frontiers | Research Topics

The role of the south atlantic on the interbasin and pole-to-pole connections

Edited by
Ronald Buss de Souza, Leticia Cotrim Da Cunha, Fabrice Hernandez
and Regina R. Rodrigues

Published in
Frontiers in Marine Science

ISSN 1664-8714
ISBN 978-2-83251-585-3
DOI 10.3389/978-2-83251-585-3

About Frontiers

Frontiers is more than just an open access publisher of scholarly articles: it is a pioneering approach to the world of academia, radically improving the way scholarly research is managed. The grand vision of Frontiers is a world where all people have an equal opportunity to seek, share and generate knowledge. Frontiers provides immediate and permanent online open access to all its publications, but this alone is not enough to realize our grand goals.

Frontiers journal series

The Frontiers journal series is a multi-tier and interdisciplinary set of open-access, online journals, promising a paradigm shift from the current review, selection and dissemination processes in academic publishing. All Frontiers journals are driven by researchers for researchers; therefore, they constitute a service to the scholarly community. At the same time, the *Frontiers journal series* operates on a revolutionary invention, the tiered publishing system, initially addressing specific communities of scholars, and gradually climbing up to broader public understanding, thus serving the interests of the lay society, too.

Dedication to quality

Each Frontiers article is a landmark of the highest quality, thanks to genuinely collaborative interactions between authors and review editors, who include some of the world's best academicians. Research must be certified by peers before entering a stream of knowledge that may eventually reach the public - and shape society; therefore, Frontiers only applies the most rigorous and unbiased reviews. Frontiers revolutionizes research publishing by freely delivering the most outstanding research, evaluated with no bias from both the academic and social point of view. By applying the most advanced information technologies, Frontiers is catapulting scholarly publishing into a new generation.

What are Frontiers Research Topics?

Frontiers Research Topics are very popular trademarks of the *Frontiers journals series*: they are collections of at least ten articles, all centered on a particular subject. With their unique mix of varied contributions from Original Research to Review Articles, Frontiers Research Topics unify the most influential researchers, the latest key findings and historical advances in a hot research area.

Find out more on how to host your own Frontiers Research Topic or contribute to one as an author by contacting the Frontiers editorial office: frontiersin.org/about/contact

The role of the south atlantic on the interbasin and pole-to-pole connections

Topic editors
Ronald Buss de Souza — National Institute of Space Research (INPE), Brazil
Leticia Cotrim Da Cunha — Rio de Janeiro State University, Brazil
Fabrice Hernandez — Institut de Recherche Pour le Développement (IRD), France
Regina R. Rodrigues — Federal University of Santa Catarina, Brazil

Citation
de Souza, R. B., Da Cunha, L. C., Hernandez, F., Rodrigues, R. R., eds. (2023). *The role of the south atlantic on the interbasin and pole-to-pole connections.* Lausanne: Frontiers Media SA. doi: 10.3389/978-2-83251-585-3

Table of contents

Frontiers in Marine Science

TYPE Editorial
PUBLISHED 23 January 2023
DOI 10.3389/fmars.2023.1137809

OPEN ACCESS

EDITED AND REVIEWED BY
Ming Li, University of Maryland, College Park, United States

*CORRESPONDENCE
Ronald Buss de Souza
ronald.buss@inpe.br

SPECIALTY SECTION
This article was submitted to Physical Oceanography, a section of the journal Frontiers in Marine Science

RECEIVED 04 January 2023
ACCEPTED 11 January 2023
PUBLISHED 23 January 2023

CITATION
Souza RB, da Cunha LC, Hernandez F and Rodrigues RR (2023) Editorial: The role of the South Atlantic on the interbasin and pole-to-pole connections.
Front. Mar. Sci. 10:1137809.
doi: 10.3389/fmars.2023.1137809

Editorial: The role of the South Atlantic on the interbasin and pole-to-pole connections

Ronald Buss Souza[1]*, Letícia Cotrim da Cunha[2,3,4], Fabrice Hernandez[5,6,7,8,9] and Regina Rodrigues Rodrigues[3,10]

[1]Divisão de Modelagem Numérica do Sistema Terrestre, Instituto Nacional de Pesquisas Espaciais (INPE), Cachoeira Paulista, Brazil, [2]Laboratório de Oceanografia Química, Faculdade de Oceanografia, Universidade do Estado do Rio de Janeiro (UERJ), Rio de Janeiro, Brazil, [3]Rede CLIMA, Instituto Nacional de Pesquisas Espaciais (INPE), São José dos Campos, Brazil, [4]Rede BrOA, Universidade Federal do Rio Grande (FURG), Rio Grande, Brazil, [5]Laboratoire d'Études en Geéophysique et Oceéanographie Spatiale (LEGOS), Université de Toulouse, Toulouse, France, [6]Centre National d'Etude Spatiale (CNES), Toulouse, France, [7]Centre National de la Recherche Scientifique (CNRS), Toulouse, France, [8]Institut de Recherche pour le Développement (IRD), Toulouse, France, [9]Université Paul Sabatier (UPS), Toulouse, France, [10]Departamento de Oceanografia, Universidade Federal de Santa Catarina (UFSC), Florianópolis, Brazil

KEYWORDS

South Atlantic Ocean, interbasin connections, pole-to-pole connections, ocean physical processes, ocean biogeochemical processes

Editorial on the Research Topic
The role of the South Atlantic on the interbasin and pole-to-pole connections

This Research Topic aimed to improve our understanding of the physical and biogeochemical processes linking the South Atlantic to other ocean basins and within the Atlantic as a whole through oceanic or atmospheric teleconnections. The South Atlantic plays an essential role in the climate of the adjacent continental areas and actively contributes to the Atlantic Meridional Overturning Circulation (AMOC), hence modulating the world's climate. The Atlantic, Pacific and Indian basins interact with each other in a two-way fashion, mainly through the tropics at the seasonal to multidecadal scales. Although not fully understood at present, the physical and biogeochemical processes involved in this interbasin interaction are essential to be addressed when we aim to increase our ability to predict the planet's weather and climate. The present volume of Frontiers in Marine Science contains ten original research articles put together by 42 different authors from 12 countries in Europe, the Americas, Asia and Africa. The articles represent state-of-the-art research aimed at understanding the variability and distributions of different properties and variables of the South Atlantic in different temporal and spatial scales. The study used *in situ* observations, satellite and modeling data and gave special attention to the characterization of the AMOC and its relations with the North Brazil Undercurrent (Liu et al., 2021), its sources and circulation pathways (Xu et al., 2022) and the feedback mechanisms between the AMOC's transport and the South Atlantic freshwater transports and content (Haines et al., 2022).

The papers by Bueno et al. (2022); Ioannou et al. (2022); Dossa et al. (2022) and Guerra et al. (2022), on the other hand, focused on the observation and characterization of ocean rings and eddies of the Atlantic Ocean, bringing relevant and new information, respectively, on the impact of these structures on the volume and heat transport within the North Brazil Current; the connectivity between eastern and western basins of the Atlantic; the role of the Atoll das Rocas and Fernando de Noronha islands favoring eddy occurrence in the South Atlantic; and the transport of mode waters from the Cape Basin towards the Southwestern Atlantic through the Agulhas Leakage. The climate variability of the eastern Tropical Atlantic was studied by Roch et al. (2021), who, using Argo floats, determined a trend of warming and freshening of the oceans' mixed layer in the study area from 2006 to 2020. Koungue et al. (2021) investigated the 2019 Benguela Niño. The authors found that this event was generated by a combination of local and remote forcing in contrast to the more frequent, classical Benguela Niño events. Risaro et al. (2022) investigated the interannual variability and trends of the sea surface temperature in the southeastern Pacific and southwestern Atlantic oceans from 1982 to 2017, pointing out that regions north (south) of 50°S presented a warming (cooling) trend of about 0.4°C (–0.3°C) per decade.

This special issue widens our knowledge of the South Atlantic variability, which still falls behind other ocean basins. The authors used all existing observing systems in the South and Tropical Atlantic Ocean: PIRATA ocean-atmosphere mooring array, Argo and other autonomous drifting ocean sensors, and satellite products reprocessed over the last four decades. They also took advantage of up-to-date ocean and atmospheric reanalyzes and dedicated numerical simulations. Even though this special issue lacked papers that directly linked the Atlantic to other ocean basins on short scales, the contribution is of paramount importance and paved the way for new research. We expect that this special issue will inspire future generations of scientists interested in studying the South Atlantic and the role of the tropical and South Atlantic on interbasin climate variability in support of the Climate and Ocean – Variability, Predictability, and Change Program (CLIVAR).

Author contributions

All authors listed have made a substantial, direct, and intellectual contribution to the work and approved it for publication.

Acknowledgments

We acknowledge all contributor authors, data providing institutions, funding agencies, the Tropical Ocean Observing System (TOOS) and the Climate and Ocean – Variability, Predictability, and Change Program (CLIVAR).

Conflict of interest

The authors declare that the research was conducted in the absence of any commercial or financial relationships that could be construed as a potential conflict of interest.

Publisher's note

frontiers in Marine Science

ORIGINAL RESEARCH
published: 20 September 2021
doi: 10.3389/fmars.2021.744833

Influence of Salinity and Temperature Gradients on the Variability of the North Brazil Undercurrent

Hao Liu[1,2,3], Zexun Wei[1,2,3]*, Ingo Richter[4], Xunwei Nie[1,2,3] and Chuanshun Li[1]

[1] First Institute of Oceanography, Ministry of Natural Resources, Qingdao, China, [2] Laboratory for Regional Oceanography and Numerical Modelling, Pilot National Laboratory for Marine Science and Technology, Qingdao, China, [3] Shandong Key Laboratory of Marine Science and Numerical Modelling, Qingdao, China, [4] Application Laboratory, Research Institute for Value-Added-Information Generation, Japan Agency for Marine-Earth Science and Technology, Yokohama, Japan

OPEN ACCESS

Edited by:
Regina R. Rodrigues,
Federal University of Santa Catarina,
Brazil

Reviewed by:
Franz Philip Tuchen,
GEOMAR Helmholtz Center for Ocean
Research Kiel, Germany
Shijian Hu,
Institute of Oceanology, Chinese
Academy of Sciences (CAS), China

***Correspondence:**
Zexun Wei
weizx@fio.org.cn

Specialty section:
This article was submitted to
Physical Oceanography,
a section of the journal
Frontiers in Marine Science

Received: 21 July 2021
Accepted: 01 September 2021
Published: 20 September 2021

Citation:
Liu H, Wei Z, Richter I, Nie X and
Li C (2021) Influence of Salinity
and Temperature Gradients on
the Variability of the North Brazil
Undercurrent.
Front. Mar. Sci. 8:744833.
doi: 10.3389/fmars.2021.744833

The North Brazil Undercurrent (NBUC) is a narrow (<1°) northward western boundary current in the tropical South Atlantic Ocean. It carries a large volume of water (>16 Sv) and plays an important role in the Atlantic Meridional Overturning Circulation and the South Atlantic Subtropical Cell. Strong salinity and temperature fronts occur over the NBUC region. The role of temperature and salinity gradients on the genesis of NBUC variability has never been explored. This study uses three high-resolution (≤0.1°) and one low-resolution (=0.25°) model outputs to explore the linear trend of NBUC transport and its variability on annual and interannual time scales. We find that the linear trend and interannual variability of the geostrophic NBUC transport show large discrepancies among the datasets. Thus, the linear trend and variability of the geostrophic NBUC are associated with model configuration. We also find that the relative contributions of salinity and temperature gradients to the geostrophic shear of the NBUC are not model dependent. Salinity-based and temperature-based geostrophic NBUC transports tend to be opposite-signed on all time scales. Despite the limited salinity and temperature profiles, the model results are consistent with the in-situ observations on the annual cycle and interannual time scales. This study shows the relationship of salinity-based and temperature-based geostrophic NBUC variations in the annual and interannual variability and trend among different models and highlights the equal important roles of temperature and salinity in driving the variability of NBUC transport.

Keywords: North Brazil Undercurrent, salinity-based geostrophic velocity, temperature-based geostrophic velocity, temporal variability, HYCOM, OFES2, GLORYS12V1

INTRODUCTION

The western tropical South Atlantic is a key conduit of the Atlantic Meridional Overturning Circulation (AMOC, Garzoli and Matano, 2011), involving a deep southward flow of cold and salty North Atlantic Deep Water (NADW) and compensating northward flows (**Figures 1A,B**) above the NADW. In the climatological mean flow fields off the eastern portion of the North Brazilian coast, the surface flow has a weak northward or even southward expression (**Figure 1B**) due to the toward shore Ekman drift (**Figure 12** from da Silveira et al., 1994). In the Southern Hemisphere, the westward zonal wind stress drives the southward coastal current, which attenuates or conceals the northward geostrophic currents (Stramma et al., 1995). Below the surface and above the NADW, the flow is northward, and the maximum velocity core is at approximately 200 m with the magnitude estimated between 0.5 m/s (da Silveira et al., 1994) and 1 m/s (Dossa et al., 2021). The subsurface current between 5 and 11°S is called the North Brazil Undercurrent (NBUC, **Figures 1A,B**). At approximately 4.8°S, the NBUC merges with the central South Equatorial Current (a surface strengthened flow, Dossa et al., 2021), forming the North Brazil Current (NBC).

The NBUC originates from the southern South Equatorial Current (sSEC; da Silveira et al., 1994; Stramma and England, 1999). It encounters the Brazilian coast at the southern sections of the 11°S zonal line, where it deflects in the south and north directions. The one deflected toward the equator (Rodrigues et al., 2007) is the NBUC. Between 11 and 4.8°S, the NBUC is generally confined between the sea surface and the upper Circumpolar Deep Water (uCDW; Reid, 1989; Larqué et al., 1997; Schott et al., 2005), the latter being defined as the temperature minimum (Larqué et al., 1997; Stramma and England, 1999; Daniel et al., 2018) at approximately 1,000–1,200 m. Estimates of the transport of the NBUC (defined as above) differ considerably across lowered acoustic Doppler current profilers (LADCPs), moorings, and other *in situ* observations, although it generally exceeds 16 Sv (Stramma et al., 1995; Schott et al., 2005; Hummels et al., 2015; Cabré et al., 2019). This is comparable to the strength of the Atlantic Meridional Overturning Circulation (AMOC, 17.2 Sv; Mccarthy et al., 2015) at 26°N. Rabe et al. (2008) has reported 36% of the Meridional Overturning Circulation variance (transport is defined as maximum integrated from the 1,200 m to surface) at 10°S is explained by NBUC. Zhang et al. (2011) reported the correlation coefficients between transport of AMOC at 40°N and NBUC is 0.8 and found that NBUC could be an index for the multi-decadal variability of AMOC. Not only the NBUC is the key component in the AMOC (Rabe et al., 2008; Zhang et al., 2011; Rühs et al., 2015), but for the subtropical cell (STC, Schott et al., 2002; Zhang et al., 2003) as well. Schott et al. (2002) have shown 13.4 ± 2.7 Sv in the NBUC region supplies the Equatorial Undercurrent. The subtropical cell (STC) transports 10 Sv of thermocline water (Zhang et al., 2003) through the interior (4 Sv) and western boundary (6 Sv). Tuchen et al. (2019) reported that there is 9.0 ± 1.1 Sv of the total STC transport in the layers below the Ekman layers and above the 26.0 kg/m^3, and 5.2 ± 0.8 Sv comes from the western boundary derived from the ship section. Thus, the total transport of the NBUC is 2–3 times larger than the STC transport within the thermocline layers of the western boundary currents. In summary, NBUC variability is vital to interpret how ocean dynamics within the South Atlantic Ocean impact global climate. Furthermore, the NBUC carries high-salinity waters ($S > 36.5$ psu, Araujo et al., 2011) in the upper 100–200 m (Liu and Qu, 2020), forming a barrier layer (Silva et al., 2009; Araujo et al., 2011), which impacts mixing processes in the vicinity. The waters carried by the NBC/NBUC are transported to the central and eastern tropical Atlantic Ocean and form a major contribution to the equatorial Atlantic cold tongue (White, 2015).

The temporal variability of the NBUC is linked to processes over a broad extent. For example, the NBUC and Brazil Current (BC, the poleward branch of the western boundary current in the South Atlantic) tend to be anti-correlated on seasonal timescales (Rodrigues et al., 2007), with the NBUC increasing when the BC decreases, and vice versa. The geostrophic component of the NBUC within the upper thermocline layers at 10°S tends to have a sign opposite to that of the South Atlantic interior transport (defined as integrated currents above 26 kg/m^3 and from 32°W to the African coast) on seasonal and interannual time scales (Tuchen et al., 2019, 2020). Furthermore, the NBUC shows anti-correlation with the North Atlantic equatorial western boundary current (defined between the sea surface and 26.8 kg/m^3 isopycnal surface from 0 to 10°N) over the seasonal cycle (Zhai et al., 2021).

Even though the NBUC transport is treated as an index for tracking AMOC variability (Rabe et al., 2008; Zhang et al., 2011), the uncertainty of its transport is still large among the model outputs. Mignac et al. (2018) compare four ocean reanalysis datasets and show that most of the inter-product difference in the maximum of the stream function or meridional heat transport at each latitude (integrated from the western to eastern coast of the South Atlantic ocean) is due to spread in the meridional velocities of the NBUC. The discrepancy was due to two reasons: lack of observations and difference in assimilation methods. As previously stated, the NBUC at the sea surface shows weak expression. Thus, the NBUC is hard to observe from the sea surface, and current reanalyses are constrained by only a few acoustic Doppler current profilers (ADCPs) or salinity and temperature profiles. The difference in data assimilation methods near the boundaries also may impact the total meridional transport. The NBUC transport might be sensitive to the treatment of observations and the parameterization of errors near the narrow band of the western boundary (Mignac et al., 2018).

The NBUC carries a variety of water masses, including subtropical underwater (STUW; Liu et al., 2021), South Atlantic Central Water (SACW), Antarctic intermediate water (AAIW), and uCDW (Schott et al., 2005; Dossa et al., 2021). These water masses are characterized by extrema in temperature and salinity distributions. The STUW is defined by a subsurface salinity maximum in the vertical directions, while the AAIW is defined by a salinity minimum in the vertical directions. The SACW is composed of subtropical mode water 18 (STMW18), which is the warmest among all types of subtropical mode waters (Souza et al., 2018; Azar et al., 2020) in the South Atlantic ocean. The uCDW is expressed as a temperature minimum in the vertical directions (Reid, 1989). Even though the STUW, AAIW, and uCDW are defined by vertical profiles, they are also marked by strong horizontal gradients in salinity and temperature (**Figures 1C–F**). Accordingly, the NBUC is collocated with strong salinity/temperature fronts. Identifying the roles of the salinity and temperature on the NBUC will be a foundation of understanding how the salinity and temperature fields are

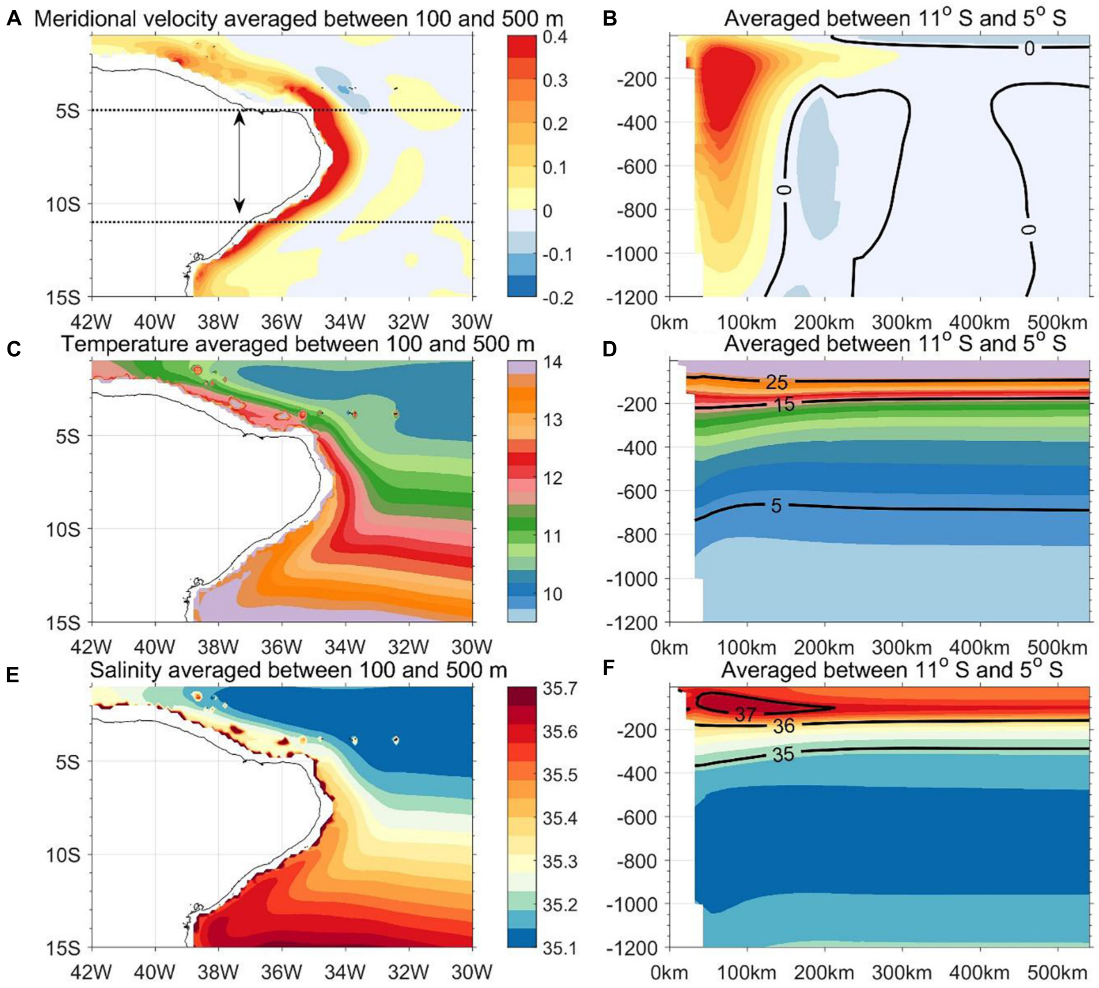

FIGURE 1 | Horizontal and vertical sections of **(A,B)** the meridional velocity, **(C,D)** conservative temperature, and **(E,F)** absolute salinity. The variables shown in the horizontal sections are averaged between 100 and 500 m by a depth-weighted method with variables on a regular 5 m intervals. The variables shown in the distance-depth sections are averaged between 11 and 5°S. The x-axis in panels **(B,D,F)** is defined as the distance from the sea surface coast. The dotted lines in panel **(A)** mark the 11 and 5°S zonal lines. The solid lines in panels **(A,C,E)** are the coastline. The solid lines in panels **(B,D,F)** are the zero velocity, isotherms from 5 to 25°C, and isohalines from 35 to 37 g/kg, respectively. The meridional velocity, temperature, and salinity are derived from the ensemble mean of three high-resolution models (including GLORYS12V1, OFES2, and HYCOM). The units for velocity are m/s, for temperature are °C, and for salinity are g/kg.

TABLE 1 | Four model outputs used in this study for identifying the variability of the North Brazil Undercurrent (NBUC).

Datasets	Data source	Underlying model	Temporal coverage and spatial resolution	References
GLORYS 12V1	Satellite sea surface temperature, sea level anomalies, T/S profiles from CORAv4.1, CERSAT sea ice concentration, initial T/S from EN4.2.0	Nucleus for European Modeling of the Ocean 3 (NEMO 3.1)	1993–2019; 1/12° (approximatively 8 km) horizontal resolution and 50 levels from 0 to 5,500 m	EU Copernicus Marine Service; Reference Number: CMEMS-GLO-PUM-001-030
OFES2	No assimilation, salinity is restored to WOA 13 version 2 with a 15-day timescale	Modular ocean model version 3 (MOM)	1958–2016; 0.1° horizontal resolution, 105 levels from the surface to 7,500 m	Sasaki et al., 2020
HYCOM 53.X	Satellite sea surface temperature, *in situ* T/S profiles, *in situ* and satellite sea surface height anomaly, satellite sea ice concentration	Data-assimilative hybrid isopycnal-sigma-pressure (generalized) coordinate ocean model	1994–2015; 0.08° horizontal resolution between 40 and 40°N, 0.04° poleward of these latitudes, 40 levels from 0 to 5,000 m	Chassignet et al., 2007
SODA 3.3.2	WOD13 and COADS2.1	MOM 5.1	1980–2017; 0.25° horizontal resolution and 50 levels from 5.03 to 5,395 m	Carton et al., 2018

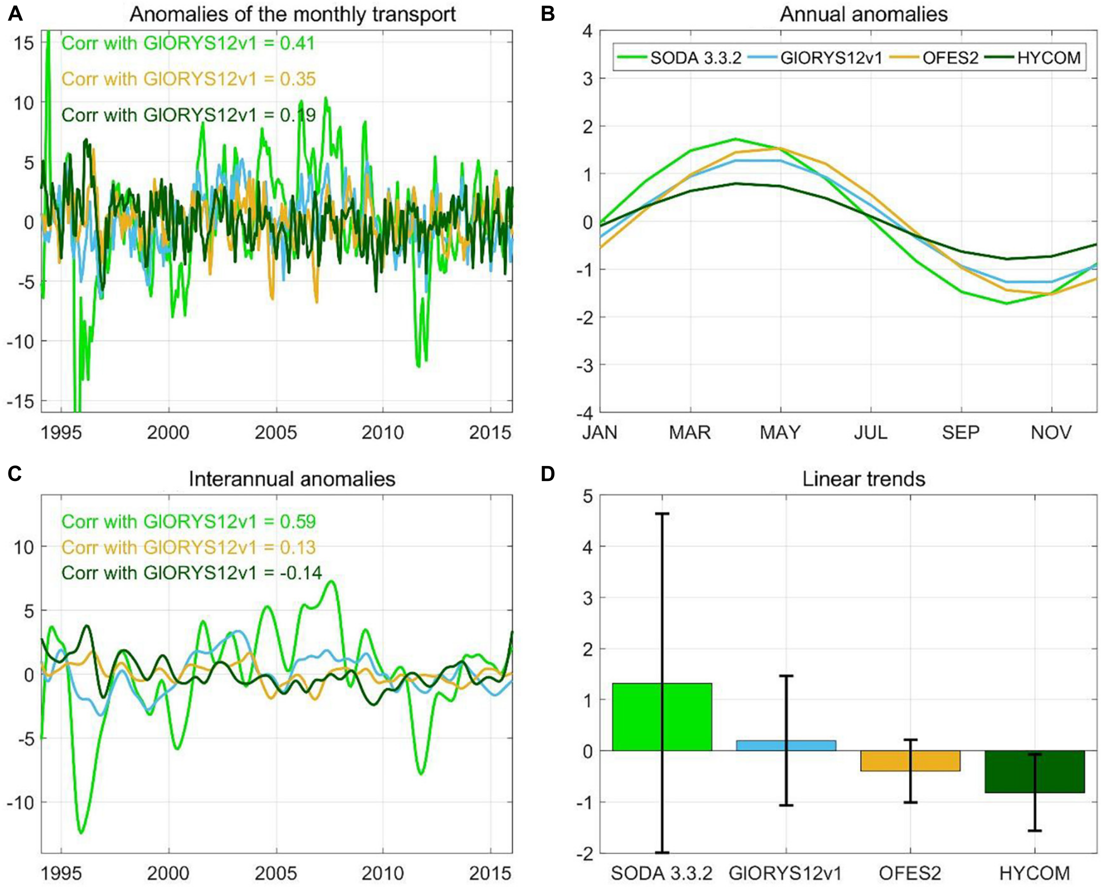

FIGURE 2 | Comparison of North Brazil Undercurrent (NBUC) geostrophic transport variability (averaged between 5 and 11°S, with 1° interval) among four products during 1994–2015. **(A)** Time series of NBUC transport anomalies, **(B)** harmonic annual cycle, **(C)** interannual NBUC transport anomalies, and **(D)** slope of linear trends. The error bars in panel **(D)** indicate the 90% confidence level of the linear trend. The correlation coefficients between monthly and interannual NBUC geostrophic transport from GLORYS12V1 and other datasets are listed in panels **(A,C)**. The units for the NBUC transport variability are Sv. The units for the slope of the linear trend are Sv/10 years.

coupled with velocities, which could assist the improvement of model simulation. The respective roles of temperature and salinity in NBUC variability have not been explored until now.

Velocity profiles over the NBUC from ADCP observations have been greatly improved our understanding of the NBUC (Hummels et al., 2015; Dossa et al., 2021). However, long-term current measurements are not available. Previous studies (e.g., Schott et al., 2005) use *in situ* hydrographic profiles as an additional data source and calculate the geostrophic components as a supplement to the analysis of the NBUC. In this study, we take a further step and decompose the density in the thermal wind equation into its temperature and salinity components. The motivation of this study is to explore the respective contributions of temperature and salinity to the NBUC transport.

We use output from three high-resolution (0.1° or higher) models and one low-resolution model (0.25°) to examine the variability of the NBUC on different time scales and its dependence on model resolution. We find that estimates vary considerably across the four models on all time scales (including the annual, interannual, and linear trends). We further decompose the geostrophic component of the NBUC into salinity and temperature contributions and found that both variables play equally important but opposite roles in the NBUC variability and that this relationship is not model-dependent. *In situ* profiles including those from Argo floats are included to confirm the model results on the annual time scale.

DATA AND METHOD

Data

Model Outputs

To identify the temporal variability in NBUC, three high-resolution models and one low-resolution model were used. There is a large amount of different model outputs available to the public. There are three criteria in choosing the products for this study. (1) The model outputs must be easy and free to access. As stated in the Data Availability section, all the four datasets used in this analysis can be freely downloaded. (2) The temporal coverage (generally longer

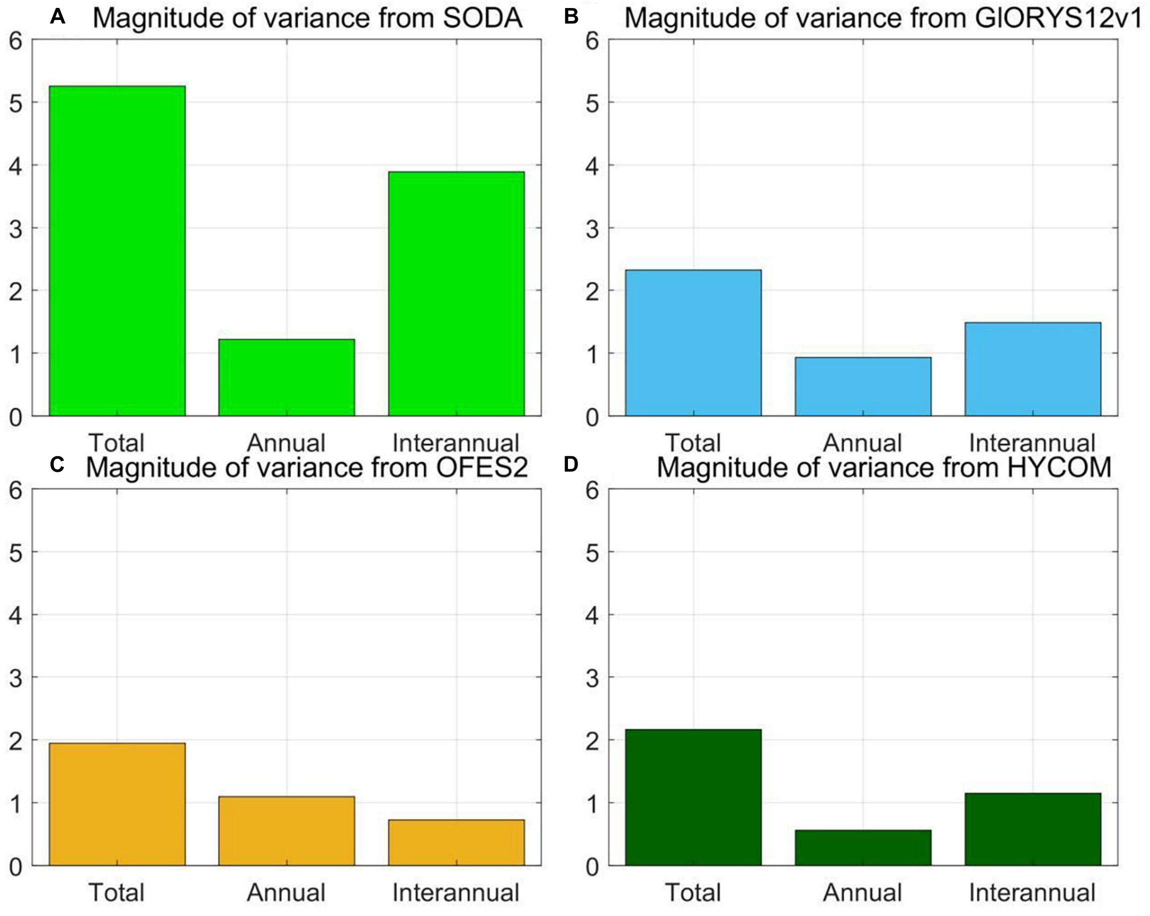

FIGURE 3 | Magnitude of the North Brazil Undercurrent (NBUC) geostrophic transport variability on the different time scales in different products: **(A)** SODA 3.3.2; **(B)** GLORYS12V1; **(C)** OFES2; and **(D)** HYCOM. The magnitude of the NBUC variability is defined as one standard deviation of each time series on different time scales, including the original (marked as total), annual, and interannual scales. The units for all the bars are Sv.

than two decades) of each model must be long enough for analysis of the interannual variations or linear trends. (3) The model must have a high horizontal resolution (at least < 0.25°), which can resolve the NBUC (width = 0.5° in the zonal direction at about 1,000 m isobar, Hummels et al., 2015) in space.

The high-resolution model-based products included the first version of the 1/12° horizontal resolution Global Ocean reanalyses and Simulation Project (GLORYS12V1, run and distributed by the EU Copernicus Marine Service), the Ocean General Circulation Model for the Earth Simulator version 2 (OFES2; Sasaki et al., 2020), and the HYbird Coordinate Ocean model (HYCOM) version 53.X (Chassignet et al., 2007). GLORYS 12V1 and HYCOM have assimilated a large number of *in situ* profiles. The relatively low-resolution reanalysis product (compared to the other three products) was Simple Ocean Data Assimilation version 3.3.2 (SODA 3.3.2, Carton et al., 2018). Details about the products are listed in **Table 1**. The HYCOM 53.X covers the period 1994–2015, which is the shortest among the four datasets. To maintain consistency in analyzing the temporal variability of the NBUC, the temporal coverage in this study is the same as that of HYCOM 53.X. All of the above products are available at a monthly resolution, which is used in this study.

In situ Profiles

In this study, we use the analyzed *in situ* hydrographic profiles from EN4.2.1 (version 4 of the Met Office Hadley Centre EN) to explore the dependence of the NBUC on temperature and salinity. EN4.2.1 provides quality-controlled data profiles. The EN4.2.1 profiles include the World Ocean Database 2013 (details are given at https://www.metoffice.gov.uk/hadobs/en4/en4-0-2-data-sources.html), Argo profiling float (Argo, 2000),[1] [2] the Global Temperature and Salinity Profile Project (Sun et al., 2010), and others. All the profiles went through strict quality-controlled analysis (Good et al., 2013) and bias correction (Gouretski and Reseghetti, 2010). In this study, only the profiles marked as "good" in the quality-controlled flags are chosen for the NBUC-related analysis.

---

[1] https://argo.ucsd.edu

[2] https://www.ocean-ops.org

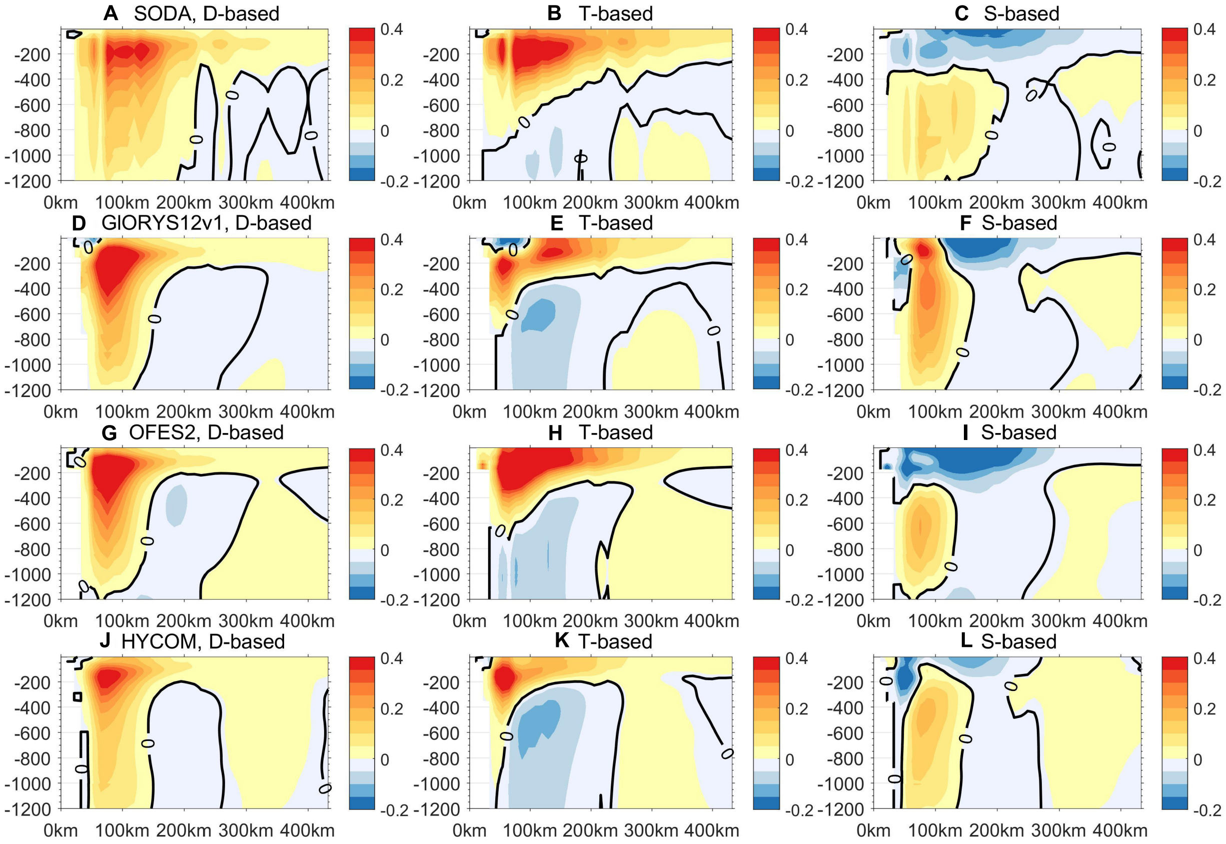

FIGURE 4 | Absolute geostrophic meridional velocities derived from density **(A,D,G,J)**, temperature **(B,E,H,K)**, and salinity **(C,F,I,L)** in SODA 3.3.2 **(A–C)**, GLORYS12V1 **(D–F)**, OFES2 **(G–I)**, and HYCOM **(J–L)**. The velocities are derived from the average between 1994 and 2015 and from 5°S to 11°S. The x-axis is defined as the distance from the sea surface coast. The black contour is zero velocity. The units are m/s.

Method

Estimation of North Brazil Undercurrent Variability

This study explores the temporal variability of the NBUC from 11 to 5°S (from the origin to transition zones; Dossa et al., 2021). NBUC transport is defined as the meridional flow from the coast to the edge of the NBUC (Zhai et al., 2021) and from the surface to 1,200 m (Hummels et al., 2015). The edge of the NBUC is defined as the location where its meridional velocity is half of the maximum meridional velocity at the same zonal lines (**Figure 2**). In the three high-resolution models, the width between the edge and the coast is generally smaller than 1°, and SODA 3.3.2 shows a slightly larger width, 1–2°. The ensemble mean of the four model outputs is smaller than 1°. A slight change in the definition of the NBUC does not impact our results (see **supplementary Figures 1, 2**). Hummels et al. (2015) defined the width of the NBUC (in their **Figure 1**) in the upper 300–400 m as 1.5° from the coast and 0.5–1° at 400–1,000 m by using alongshore velocity data from seven ship sections and moored observations. Dossa et al. (2021) did not show the width of the NBUC, but they showed that the core of the NBUC from GLORYS12V1 has shifted 15 km offshore relative to the observations from ship surveys. Nevertheless, the width of the NBUC from four model outputs in our analysis is generally consistent with the results from observations, with an acceptable difference.

The temporal variability in NBUC is divided into two components: annual (i.e., seasonal cycle) and interannual variations. The first step is to calculate the annual cycle of the NBUC based on annual harmonic least-square fitting. The annual cycle of NBUC transport is calculated as follows:

$$V(t) = V_0 + A\cos(2\pi/12 \times t + \varphi_{12}) \quad (1)$$

where V is the monthly NBUC transport, V_0 is the climatological transport, A is the amplitude, and φ_{12} is the phase. Equation (1) is applied to the time series of the NBUC transport and is subtracted from the original time series. The remaining signal $V_{residual}$ is then filtered with a 12-month low-pass Hanning filter to derive the interannual time series of the NBUC transport.

Calculation of the Geostrophic Component of the North Brazil Undercurrent

The geostrophic components of the NBUC and ADCP-measured NBUC show similar magnitudes and spatial patterns (Stramma et al., 1995; Schott et al., 2005). In this study, the absolute geostrophic currents are calculated by referencing the

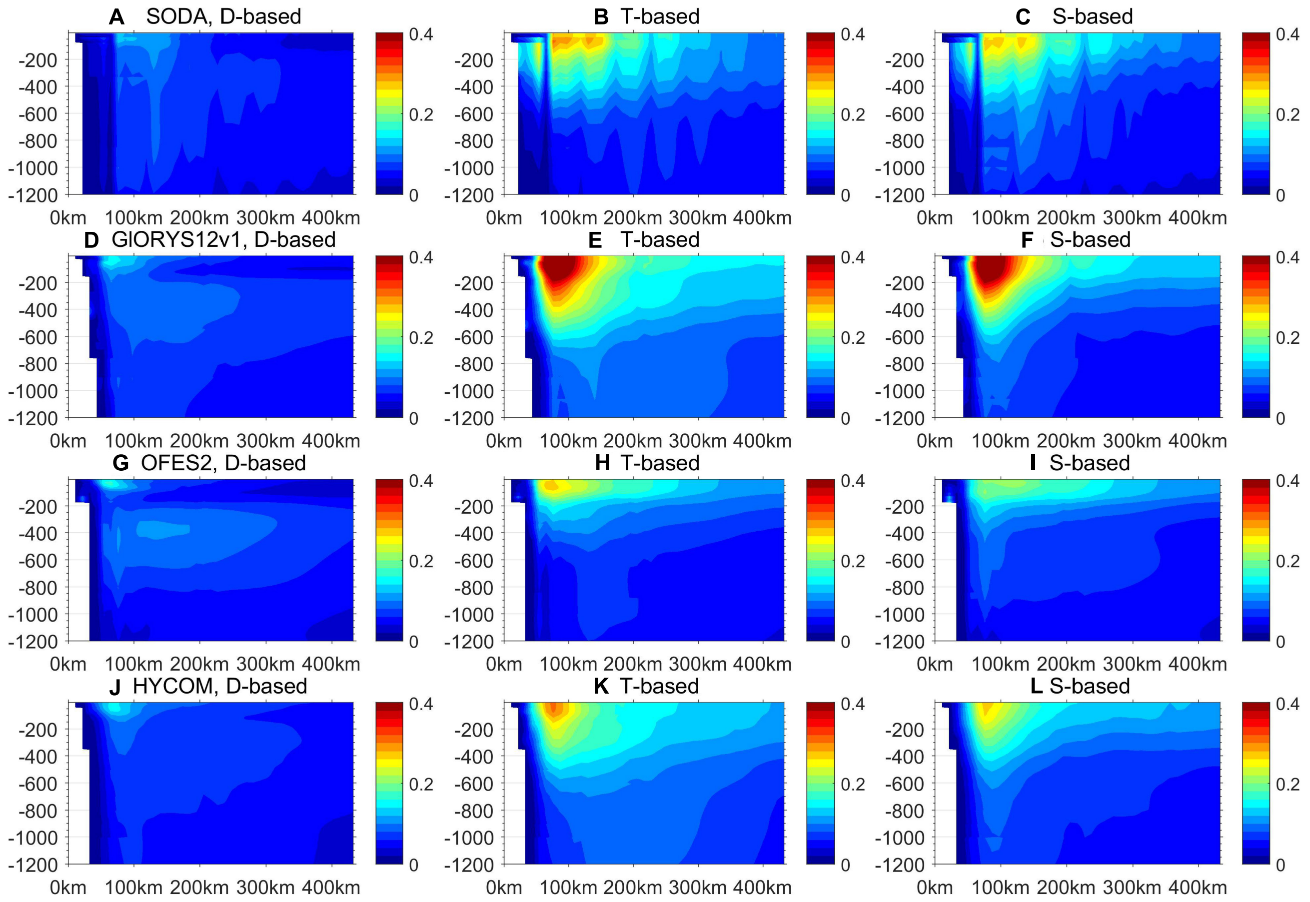

FIGURE 5 | One standard deviation of the absolute geostrophic meridional velocity derived from density **(A,D,G,J)**, temperature **(B,E,H,K)**, and salinity **(C,F,I,L)** in SODA **(A–C)**, GLORYS12V1 **(D–F)**, OFES2 **(G–I)**, and HYCOM **(J–L)**. One standard deviation of the velocities is derived from monthly values from 1994 to 2015 and averaged between 5°S and 11°S. The x-axis is defined as the distance from the sea surface coast. The units for velocity are m/s.

meridional velocity at 2,000 m from each product. We have compared the absolute geostrophic NBUC transport with that directly derived from the meridional velocity and found that the two types of transport display similar variability on all time scales (not shown). The correlation coefficients between absolute geostrophic NBUC transport and the meridional velocity are 0.75–0.95 in the four model estimates, also indicating a strong similarity between the geostrophic velocities and meridional velocities (**Supplementary Figure 3**). Thus, it also implies that the contribution of Ekman drift and ageostrophy to NBUC transport variability is small compared to the geostrophic components in the upper 1,200 m. The geostrophic velocity is calculated based on this equation :

$$\frac{\partial v}{\partial z} = -\frac{g}{\rho_0 f}\frac{\partial \rho}{\partial x} \tag{2}$$

where v is the meridional component of the geostrophic velocity; ρ is the potential density; ρ_0 is the reference density (1,027 kg/m^3); x and z are the longitude and depth, respectively; g is gravity; and f is the Coriolis parameter. In this study, the velocity derived from Eq. (2) is defined as the density-based velocity.

We express the potential density using a linearized equation of state as:

$$\rho = \rho_0[1 - \alpha(T - T_0) + \beta(S - S_0)] \tag{3}$$

where T is the conservative temperature, S is the absolute salinity, α is the thermal expansion coefficient, and β is the haline contraction coefficient. T_0 and S_0 are the constant temperature and salinity, respectively. It should be noted that T_0 and S_0 will be eliminated in the following calculation. Thus, the exact values are not our concern in this analysis. We combine Eq. (2) with Eq. (3) and write

$$\frac{\partial v_T}{\partial z} = \frac{g\alpha}{f}\frac{\partial T}{\partial x} \tag{4}$$

$$\frac{\partial v_S}{\partial z} = -\frac{g\beta}{f}\frac{\partial S}{\partial x} \tag{5}$$

where v_T is the temperature-based geostrophic velocity, and v_S is the salinity-based geostrophic velocity. Similar to Eq. (2), Eqs. (4 and 5) are integrated from 2,000 m, where the same velocity as

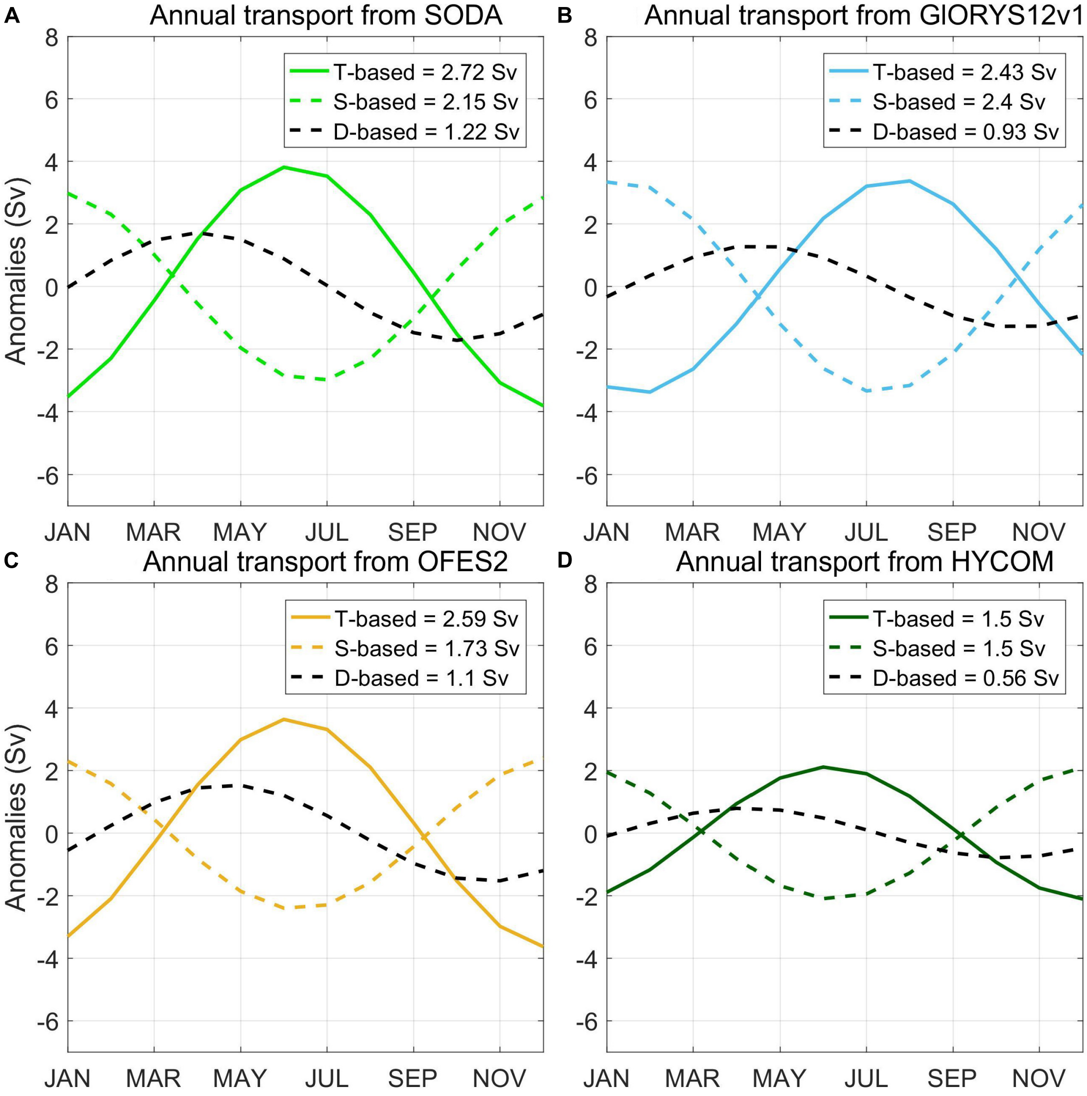

FIGURE 6 | Time series of the annual North Brazil Undercurrent (NBUC) transport anomalies in different products: **(A)** SODA 3.3.2; **(B)** GLORYS12V1; **(C)** OFES2; and **(D)** HYCOM. The colored solid lines denote the temperature-based velocity, the colored dashed lines denote the salinity-based velocity, and the black dashed lines denote the density-based velocity. One standard deviation of each type of annual variability is listed in the legend. The unit of the annual NBUC transport anomalies is Sv.

used in density-based geostrophic velocity is given, to the upper layers to calculate v_T and v_S, respectively. The density-based, temperature-based and salinity-based geostrophic velocities are referenced on the same values (velocities at 2,000 m isobar from model outputs). A change in reference would influence the magnitude of the geostrophic variability, but it will not change the relations between the three types of the geostrophic velocities. We also calculated the correlation coefficients of the absolute geostrophic velocities using 1,200 and 2,000 m as references. The correlation coefficients of NBUC transport between 1,200 and 2,000 m is 0.96, 0.79, 0.98, and 0.83 for SODA 3.3.2, GLORYS12V1, OFES2, and HYCOM, respectively. This implies that a slight change in the reference level will not impact the results in this study.

To verify the robustness of temperature and salinity decomposition, we also sum the NBUC transport derived from v_T and v_S, and compare it with the density-based geostrophic NBUC transport (**Supplementary Figure 3**). The correlation coefficients of NBUC transport between the sum and density-based geostrophic transport in SODA 3.3.2, OFES2, and HYCOM are >0.75. GLORYS12V1 has a relatively small correlation coefficient, with a magnitude of 0.45. Possible reasons could include model configurations and methods of data assimilation. Further examination is out of the scope of this study. Nevertheless, all the correlations are significant. The decomposition works at least for SODA 3.3.2, OFES2, and HYCOM. Careful attention should be taken in GLORYS12V1 when interpreting NBUC transport

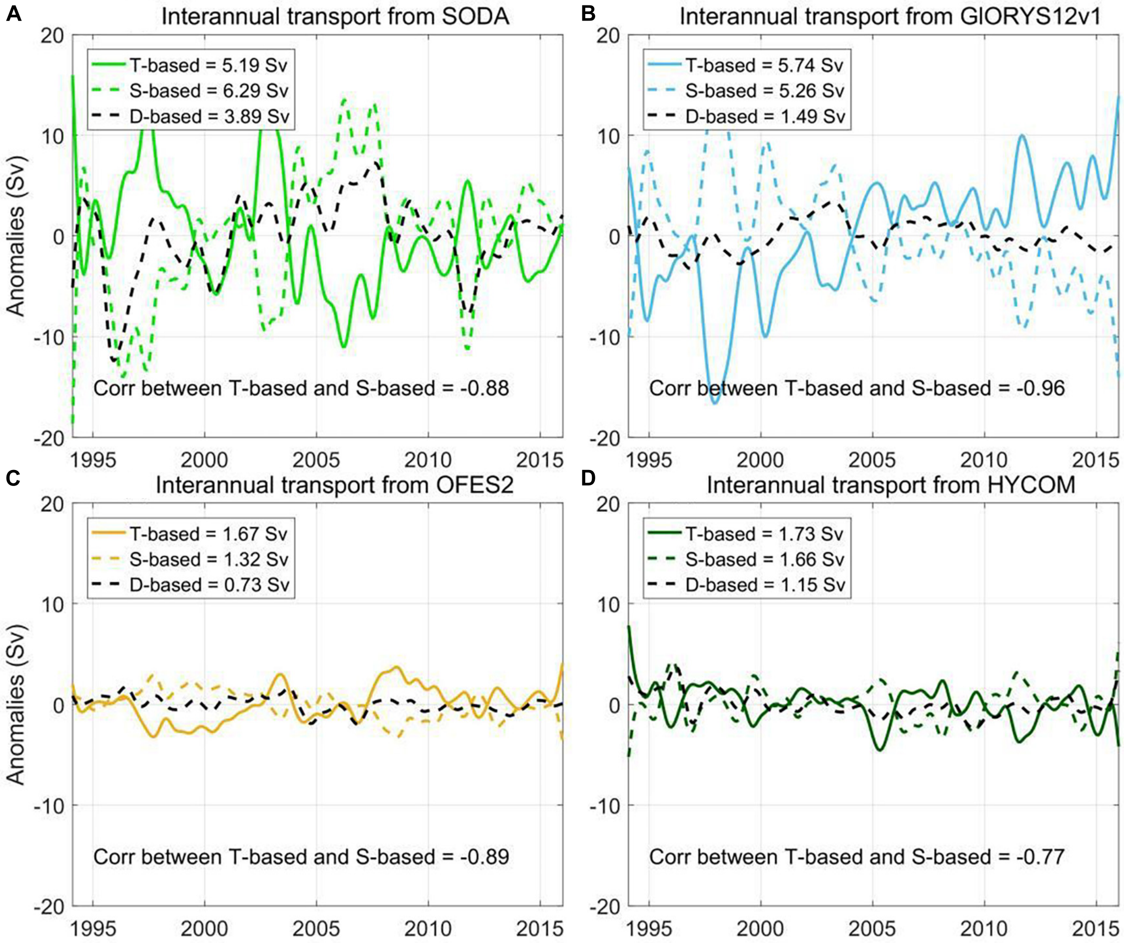

FIGURE 7 | Time series of the interannual North Brazil Undercurrent (NBUC) transport anomalies in different products: **(A)** SODA 3.3.2; **(B)** GLORYS12V1; **(C)** OFES2; and **(D)** HYCOM. The colored solid lines denote the temperature-based velocity, the colored dashed lines denote the salinity-based velocity, and the black dashed lines denote the geostrophic velocity. One standard deviation of interannual variability is listed in the legend. The correlation coefficients between the temperature-based and salinity-based NBUC time series are listed in each figure. All the correlation coefficients satisfy the 90% confidence levels (not shown). The unit of the interannual NBUC transport anomalies is Sv.

between the sum of v_T and v_S, and the density-based geostrophic velocities.

INTERCOMPARISON OF THE NORTH BRAZIL UNDERCURRENT VARIABILITY AMONG FOUR PRODUCTS

Generally, the monthly geostrophic NBUC transport varies substantially across datasets (**Figure 2A**). The correlation coefficients of monthly NBUC geostrophic transport between GLORYS12V1 and the other three datasets (**Figure 2A**) are generally small (<0.41). The correlation coefficient between GLORYS12V1 and HYCOM (a low-resolution model) is smaller than those between GLORYS12V1 and SODA 3.3.2, indicating that the resolution of the models does not play the major role in the largest difference among the inter-model comparison in this study.

However, the geostrophic NBUC transport based on different datasets agrees relatively well for the harmonic annual cycle (**Figure 2B**). The consistency between models implies that the underlying dynamics driving the annual cycle of NBUC transport are consistent among models. Transport is strongest during April-May and weakest during September-November. The results here agree with results from two surveys in spring 2015 and fall 2017, which show stronger transport during April-May 2015 than during September-October 2017 (Dossa et al., 2021). The results based on low-resolution models (Zhai et al., 2021) also show that the NBUC transport (2–10°S) reaches a maximum in May and a minimum in November-December, consistent with our results. The results from a moored array at 11°S from Schott et al. (2005) show that the minimum NBUC transport occurs in October-November, agreeing with our results. However, the maximum in NBUC transport occurs in July, which is different from other observations and our results. HYCOM shows the smallest amplitude of the annual cycle (defined as the

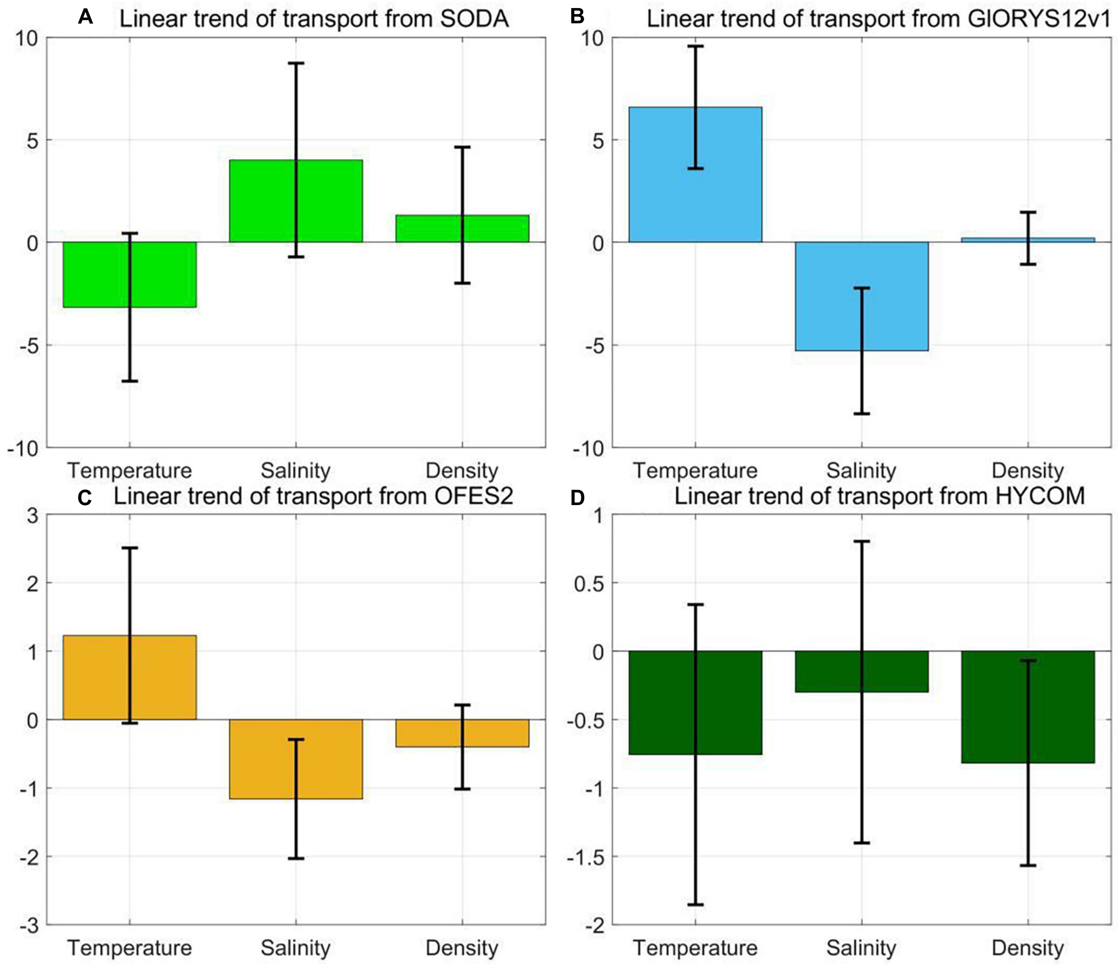

FIGURE 8 | Linear trends of NBUC transport in **(A)** SODA 3.3.2, **(B)** GLORYS 12V1, **(C)** OFES2, and **(D)** HYCOM. The error bars indicate the 90% confidence level of the linear trend. The units for the slope of the linear trend are Sv/10 years.

standard deviation) among the four datasets (**Figure 3**), with a magnitude of 0.56 Sv. SODA 3.3.2 and OFES2 show amplitudes of approximately 1.1–1.2 Sv (**Figure 3**), which are slightly smaller than the amplitudes from Schott et al. (2005), who show an annual harmonic amplitude of 1.5 Sv over 2000–2004 at 11°S. Hummels et al. (2015) find that the standard deviation of the NBUC transport obtained from a moored array between July 2013 and May 2014 is 1.8 Sv at 11°S.

On the interannual time scale (period $>$ 12 months), the NBUC transport anomalies disagree substantially between datasets (**Figure 2C**). It is, in fact, hard to find any agreement among the different products on this time scale. Even though the correlations between GLORYS12v1 and the HYCOM and OFES2 are significant at the 90% confidence level, the correlation coefficients are relatively small, with values smaller than –0.14 to 0.13. The correlation between HYCOM and GLORYS12V1 is even negative. The correlation coefficient between SODA 3.3.2 and GLORYS12V1 is 0.59, which is relatively large compared to other coefficients. The higher correlation coefficients between SODA 3.3.2 and GLORYS12V1 than the others suggest that the model's resolution is not a key component driving the difference in NBUC transport among models. However, we would like to emphasize that the low-resolution models ($>$0.5°) are incapable of resolving the NBUC width (∼0.5° at approximately 1,000 m from Hummels et al., 2015). The discrepancy between OFES2 and the other two high-resolution models (i.e., HYCOM and GLORYS12V1) could be because OFES2 is a hindcast output with no assimilation, while the other two models assimilate a large number of different types of observations (shown in **Table 1**). Large discrepancies among datasets can also be attributed to the treatment of observations and parameterization of the errors near the western boundaries (Mignac et al., 2018).

The maximum magnitude of interannual NBUC variability occurs in SODA 3.3.2, with a value of 3.89 Sv (**Figure 3**). The GLORYS12V1 and HYCOM show similar magnitudes of approximately 1.1–1.5 Sv. OFES2 has the smallest magnitude (0.72 Sv) among the four datasets. Estimates based on ship

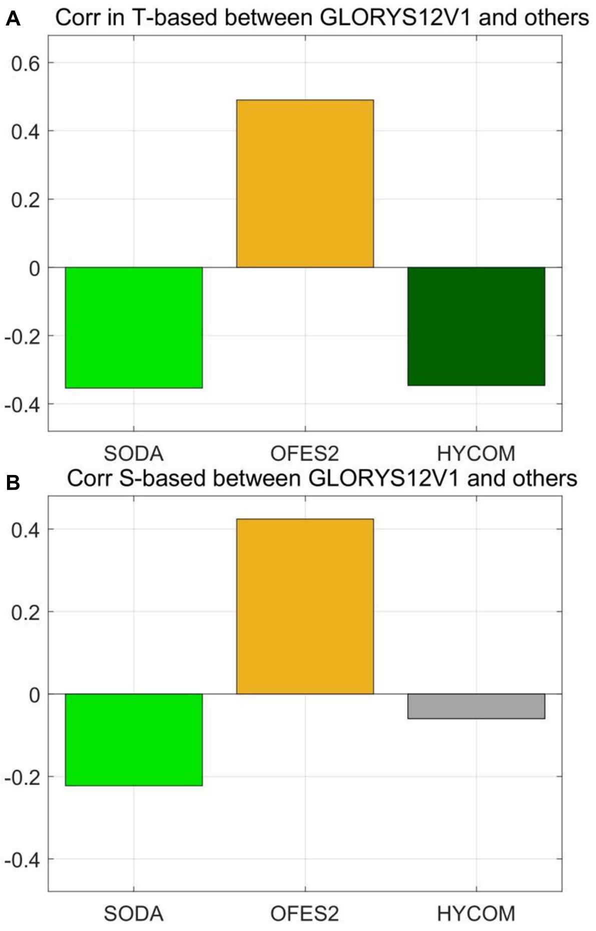

FIGURE 9 | The correlation coefficients of **(A)** temperature-based and **(B)** salinity-based NBUC transport between GLORYS12V1 and SODA 3.3.2, HYOCM and OFES2. The gray bar indicates the correlation did not pass the 90% confidence level. The NBUC transports are averaged between 5°S and 11°S.

sections (ADCP sections) and a moored array suggest an amplitude of 1.2 Sv from 2000 to 2004 (Schott et al., 2005). Thus, the results from GLORYS12V1 and HYCOM are consistent with the observations.

From 1994 to 2015, NBUC transport derived from HYCOM shows a significant negative trend, with a value of −0.8 ± 0.7 Sv per 10 years. However, the other three datasets do not show any significant trends in the annual mean NBUC transport (**Figure 2D**). Whether the NBUC has been subject to a trend over the past years is currently under debate. Hummels et al. (2015) suggested that the NBUC does not have a significant trend by using moorings, ADCP sections (2000–2004, 2013–2014), and a high-resolution ocean model (1956–2007). However, Marcello et al. (2018) found a significant positive trend (1970–2015) in NBUC using a reanalysis data. It should be noted that discrepancies between the trends of NBUC transport could result from different analysis periods. Indeed, visual inspection of Marcello et al.'s (2018) **Figure 9** does not indicate significant changes over the period 2000–2013. Thus, the two studies appear to agree on the absence of a trend for this period.

SALINITY AND TEMPERATURE CONTRIBUTIONS TO THE NORTH BRAZIL UNDERCURRENT

On the long-term average, the absolute meridional geostrophic velocity derived from the individual model estimates (**Figures 4A,D,G,J**) is consistent with the ensemble mean meridional velocity (**Figure 1**). Northward velocities with a magnitude larger than 0.4 m/s are confined west of 34°W, while weaker southward flows are found to the east of 34°W. The NBUC velocity core (maximum in NBUC velocity) is found below 100 m in all datasets. These results are consistent with previous in-situ observations, which found cores in the upper 100 to 400 m (Stramma et al., 1995; Schott et al., 2005; Dossa et al., 2021).

We use Eqs. (4 and 5) to estimate the contributions from temperature and salinity to the meridional geostrophic velocity. In the upper 1,200 m, both components are important to the density-based geostrophic velocity (**Figure 4**). The temperature-based velocity is generally dominant in the upper 400 m, while salinity-based velocity dominates below. High salinity waters formed in the subtropical gyre are being pushed to the western side (Liu and Qu, 2020), leading to saltier waters in the vicinity of the northeastern Brazilian coast and hence setting up a zonal salinity gradient. The negative zonal salinity gradient leads to a negative salinity-based velocity in the upper 400 m (Eq. 4; note that $f < 0$). At the same time, warmer waters (Stramma and England, 1999; Azar et al., 2020) are also found in the west as the SACW in the upper 400 m (this depth slightly varies between datasets), which corresponds to a positive vertical shear of the northward velocity (Eq. 3). As a result, the temperature-based velocity is opposite to the salinity-based velocity.

For the density-based meridional velocity below 400 m, the contribution of temperature-based and salinity-based velocities to the geostrophic velocity is reversed in all model outputs. The salinity-based velocity dominates the northward geostrophic velocity, and the temperature-based velocity is southward with a smaller magnitude. The zonal salinity gradient below 400 m is opposite to that in the upper layer. This is because fresh AAIW is generally transported to the Northern Hemisphere by the western boundary current (da Silveira et al., 1994; Schott et al., 2005; Fu et al., 2019). The near-coastal water at depth (AAIW located) is generally fresher than that away from the coast, leading to a negative salinity gradient and positive vertical shear.

The total variability of the meridional geostrophic velocity is calculated as one standard deviation of the monthly values from 1994 to 2015. The magnitudes in the density-based meridional geostrophic velocity variances from all model outputs are smaller than 0.2 m/s (**Figure 5**). Relatively larger variability is found between 35 and 34°W in the vicinity of

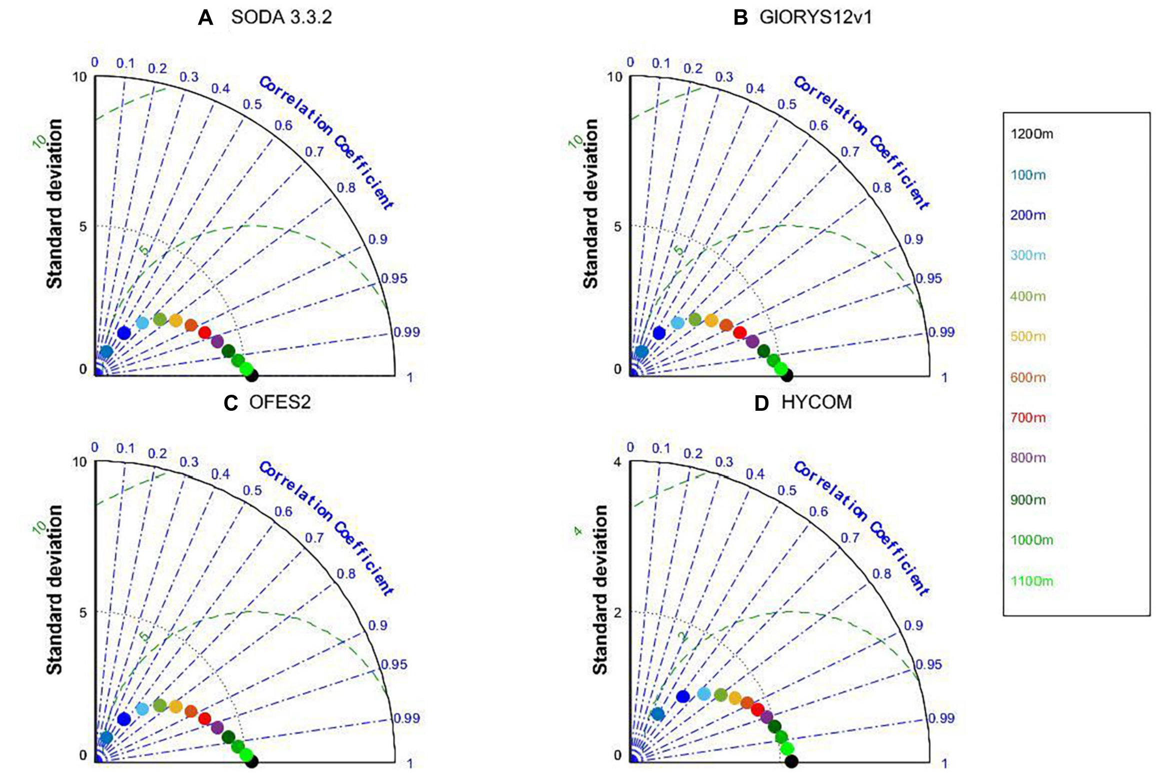

FIGURE 10 | The Taylor diagram of density-based NBUC geostrophic transport derived from **(A)** SODA 3.3.2, **(B)** GLORYS 12V1, **(C)** OFES2, and **(D)** HYCOM. Different colors show that the lower limit for the integral of the NBUC transport at certain depths (100 m is blue and 1200 m is black). The units for standard deviation for the transport is Sv.

the NBUC. The magnitude of variability of the temperature-based and salinity-based velocities shows a larger value than the density-based velocities in each model output. Furthermore, the magnitude of variability from the temperature-based and salinity-based velocities is generally larger than 0.2 m/s and shows similar spatial distributions (**Figure 5**). This suggests that the temperature and salinity contributions tend to cancel each other out.

To further explore the contribution of salinity and temperature to the variability of the meridional geostrophic velocity, temporal variability on different time scales is shown and quantified (**Figures 6–8**). On the annual time scale, the temperature-based and salinity-based velocity variances are larger than the density-based variance (**Figure 6**) in all models. Furthermore, the harmonic annual cycles of salinity-based and temperature-based velocity anomalies are 180° out of phase. From May to September, the temperature-based velocity shows positive anomalies, and the salinity-based velocity shows negative anomalies. The signs are reversed from October to the next March. The magnitude of the harmonic temperature-based variability is larger than that of salinity-based variability (or equal in results from HYCOM). The maximum/minimum density-based velocity anomalies have the same signs as the temperature-based velocity anomalies in SODA 3.3.2, OFES2, and HYCOM.

On the interannual time scale, the temperature-based and salinity-based velocity variances show a similar relationship as those on the annual time scale (**Figure 7**). The temperature-based and salinity-based velocity anomalies generally show opposite signs and the magnitude of the variances of salinity/temperature-based velocities are larger than the density-based velocity variability in all datasets. To further assess the relation between temperature-based and salinity-based velocity anomalies, correlation coefficients are calculated. The two time series show significant (over 90% confidence level) anti-correlations in all models. The largest anti-correlation coefficients occur in GLORYS12V1 (–0.96), and the smallest anti-correlation coefficients occur in HYCOM (–0.77). In SODA 3.3.2, salinity-based variability is larger than the temperature-based variability, while in the other three model estimates, temperature-based velocity variability is larger.

For the linear trend of the annual mean NBUC transport from 1994 to 2015 (**Figure 8**), the temperature-based velocity shows opposite trends to the salinity-based velocity in SODA 3.3.2, GLORYS12V1, and OFES2. The linear trend of the density-based velocity is much smaller than those of the temperature-based and salinity-based velocities. However, in HYCOM, the temperature and salinity-based velocities both show a decreasing trend (not significant), leading to a larger decreasing trend in density-based velocity.

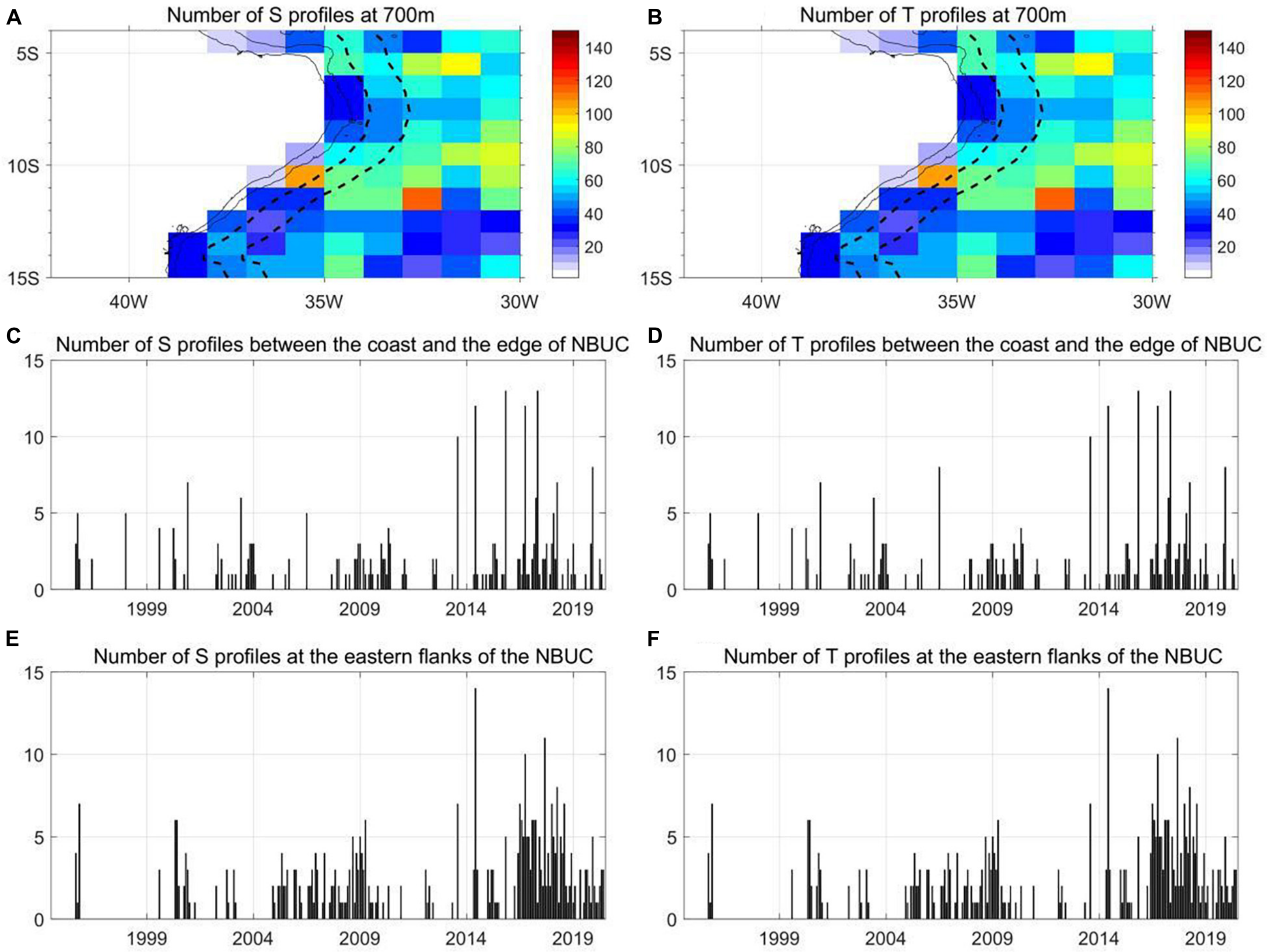

FIGURE 11 | Spatial and temporal distribution of the number of **(A,C,E)** salinity and **(B,D,F)** temperature *in situ* profiles derived from EN4. The black solid lines in panels **(A,B)** denote the coastline and 1,000 isobars under the sea surface. The black dotted lines in panels **(A,B)** denote the edge of the NBUC and the eastern section of the NBUC (which is defined as 1° eastward away from the NBUC edge). Panels **(C,D)** denote the number of *in situ* salinity/temperature profiles located between the coast and the edge of the NBUC from 11 to 5°S. Panels **(E,F)** denote the number of *in situ* salinity/temperature profiles located between the edge of the NBUC and 1° away from the edge.

In the previous section, we showed that the correlation coefficients of density-based NBUC geostrophic transport on the interannual time scales are small between models (magnitude < 0.37). **Figure 9** shows the correlation coefficients of salinity-based and temperature-based NBUC transport between GLORYS12V1 and other models. The maximum correlation of temperature-based NBUC transport occurs in GLORYS12V1 and OFES2, with a magnitude of 0.49. The maximum in correlation coefficient of salinity-based NBUC transport also occurs in GLORYS12V1 and OFES2 3.3.2, with a magnitude of 0.42. However, correlations of temperature-based or salinity-based transport between GLORYS12V1 and the other two models are negative or insignificant. If correlation is calculated between HYCOM and OFES2 or SODA 3.3.2, smaller magnitudes (−0.2 to 0.35) of correlation coefficients for both the temperature-based and salinity-based transports. The negative or small correlation coefficients in temperature-based and salinity-based transport on the interannual time scale between models indicate large differences in salinity and temperature zonal gradients, which in turn explains the large discrepancy in the NBUC geostrophic transport between products.

DISCUSSION

The Temperature and Salinity Relation in Observation

Section "Salinity and Temperature Contribution to the North Brazil Undercurrent" shows that the temperature-based and salinity-based geostrophic NBUC transport variability tends to be compensated in all models. To verify the results, we have collected profiles from EN4 datasets, and assessed the relationship between temperature and salinity within the NBUC region using *in situ* data.

The number of *in situ* observations decreases with depth. To better make use of the available hydrographic profiles, we

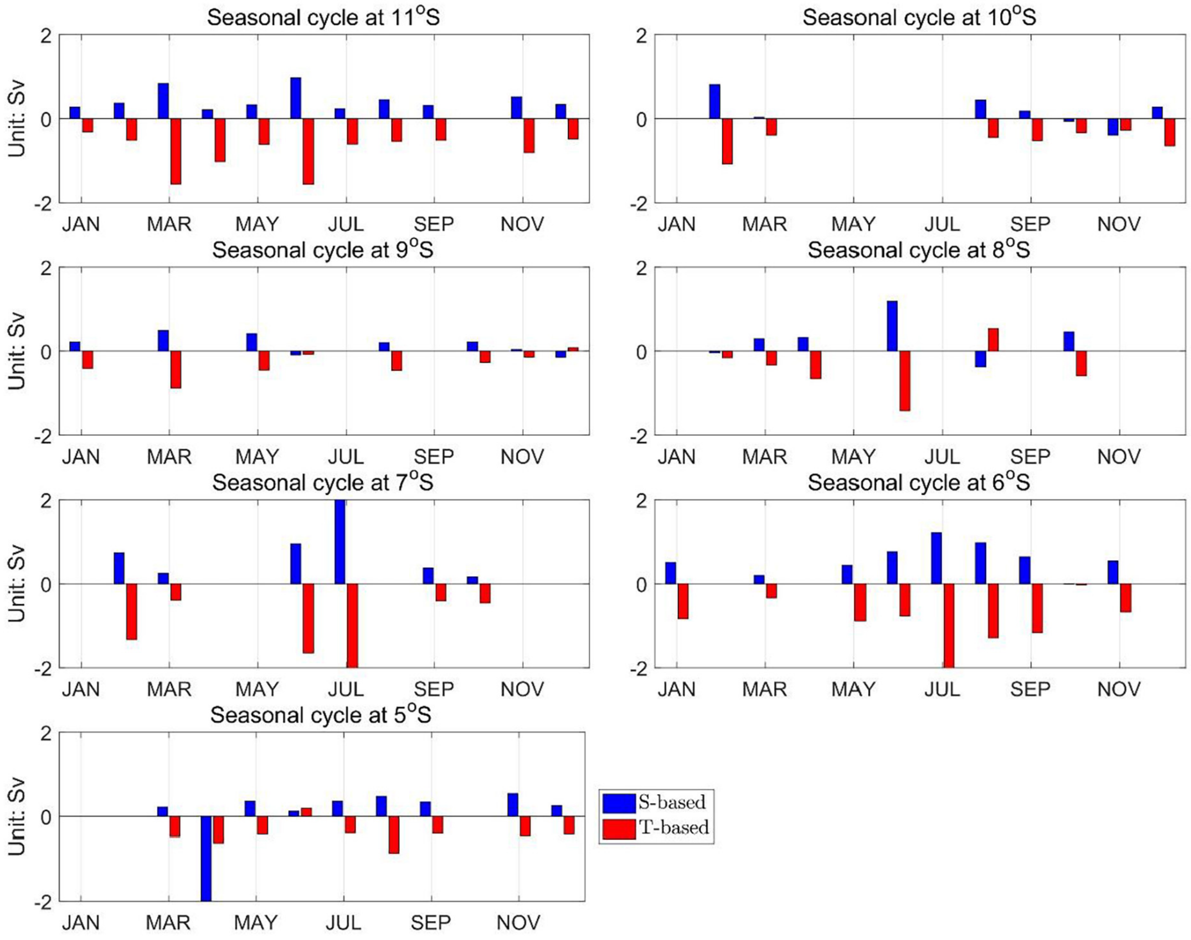

FIGURE 12 | Seasonal cycle temperature/salinity-based geostrophic transport anomalies derived from *in situ* profiles at different latitudes within the North Brazil Undercurrent (NBUC) region from 1994 to 2020. The transports are calculated from the integral of geostrophic velocity from the sea surface to 700 m. The missing data is due to lack of observations. The units for the transports are Sv.

compare the zonal density gradients averaged from the sea surface to 1,200 m with those averaged to a smaller depth. We find that the density-based geostrophic NBUC transport integrated from the surface to 700 m is not very different from that averaged from the surface to 1,200 m (**Figure 10**), with temporal correlation coefficients higher than 0.9 in all models. Thus, we selected the temperature and salinity profiles from the EN4 database that are near the NBUC and cover at least 700 m. There are only about 20–40 profiles that match our criteria between 7 and 9°S near the western boundary (**Figure 11**). At 11°S, there are 100–120 profiles in the coastal regions.

Profiles between the coast and the edge of the NBUC and those east of the NBUC are unevenly distributed. Observations mainly occur 2005–2009 and 2017–2020. At other times, observations are less frequent, which can explain why the interannual variability of the NBUC transport shows a large discrepancy between the models.

Based on *in situ* observations from EN4, we have calculated the geostrophic temperature-based and salinity-based geostrophic NBUC transport by assuming a reference level of no motion at 700 m (**Figures 12**, **13**). We emphasize that the reference level should not influence the temperature and salinity relationship because the relationship mainly depends on the zonal salinity and temperature gradients which is discussed in the following section.

From 11 to 5°S, the salinity-based and temperature-based geostrophic NBUC transport are opposite signed in most months of the annual cycle. At 11, 7, and 6°S, there is a 100% probability when the salinity-based and temperature-based geostrophic transports have opposite signs. At other latitudes, there is over 70% probability when the salinity-based and temperature-based signs are opposite. Thus, the results based on *in situ* profiles on the annual time scale are consistent with the results from models, and they show that the salinity and temperature gradients mostly compensate for each other.

From an interannual perspective, the number of temperature and salinity profiles is extremely low. For example, data cover 4 years out of 27 years (from 1994 to 2020) at 7 and 8°S. At 11°S, there are 12 years out of 27 years (from 1994 to 2020), which is the largest temporal coverage among the 5–11°S region. Thus, the

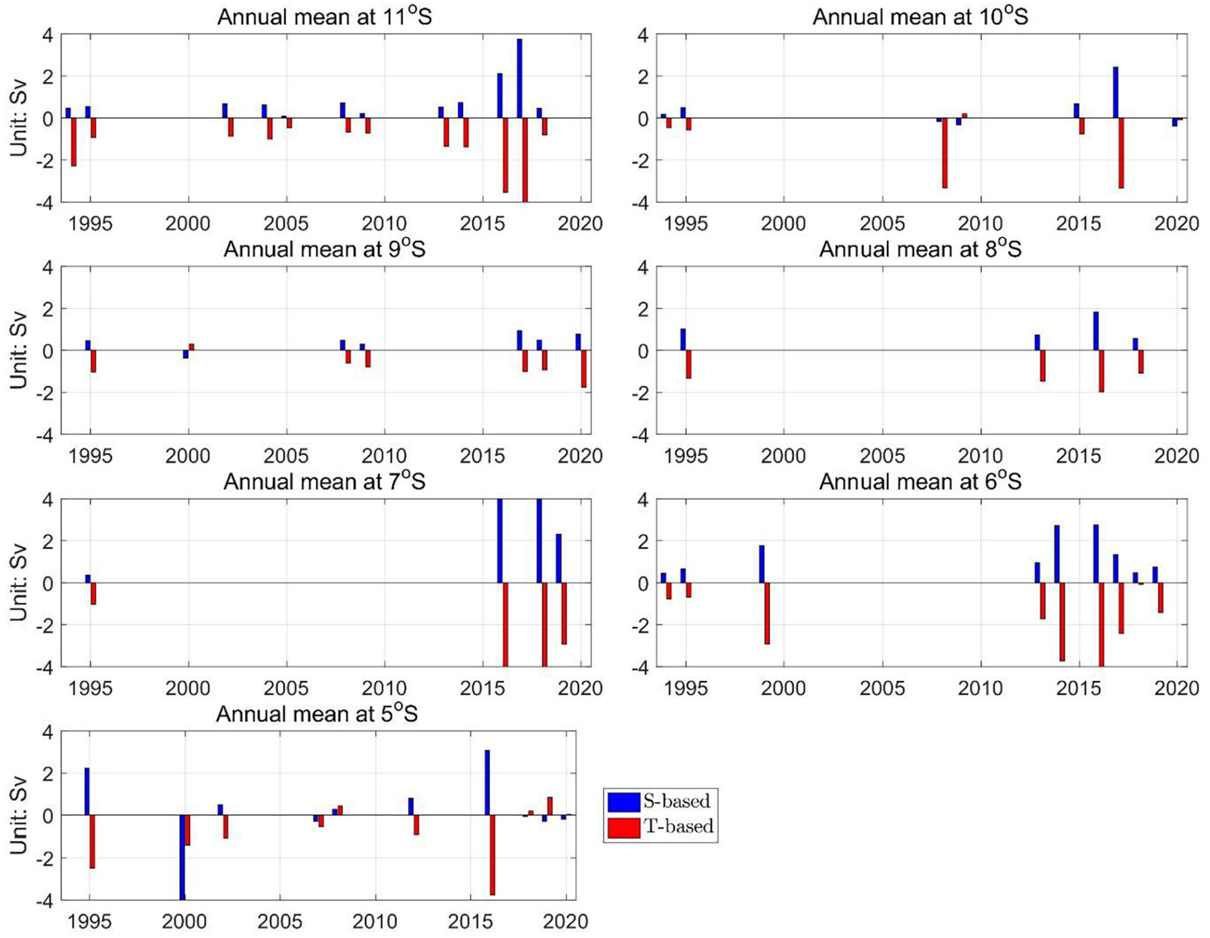

FIGURE 13 | Interannual temperature/salinity-based geostrophic transport anomalies derived from *in situ* profiles at different latitudes within the North Brazil Undercurrent (NBUC) region from 1994 to 2020. The transports are calculated from the integral of geostrophic velocity from the sea surface to 700 m. The units for the transports are Sv.

estimation of the interannual variability in geostrophic transport is likely to be biased due to the lack of data. Nevertheless, based on the available data, we find that the salinity-based and temperature-based geostrophic NBUC transport is opposite signed 90% of the time from 11 to 5°S. Thus, the compensation between salinity- and temperature-based geostrophic transport still dominates, in agreement with the model results.

Possible Cause of the Relation Between Salinity-Based and Temperature-Based Geostrophic North Brazil Undercurrent Transport

To investigate the cause of the compensation of temperature-based and salinity-based NBUC geostrophic transport, we have calculated the 0–1,200 m averaged temperature and salinity zonal gradient within the NBUC region on annual, interannual time scales, and linear trends in all models. Results show that the temperature and salinity zonal gradients also tend to be compensated on those time scales (**Supplementary Figures 4–6**), consistent with the temperature and salinity relations in geostrophic NBUC transport (**Figures 7**, **9**, 10). Saltier (warmer) waters occur near the coast in the upper 200 m than that 100–200 km away from the coast (**Figures 1D,F**). Below 200 m, fresher (cold) waters are located near the coast than those 50–100 km away from the coast. Thus, zonal salinity and temperature gradient are compensated which is probably associated with the spatial distribution of unique water masses within the NBUC. In the upper 200 m, STUW occurs below the mixed layer. Temperature and salinity within the STUW have a compensatory relationship during its equatorial transport in the North Atlantic (Qu et al., 2016). We suspect the same mechanism would also apply in the South Atlantic STUW within the NBUC. At approximately 300–500 m, the compensated temperature and salinity anomalies within the SACW (=26.3 kg/m^3) are reported to be transported from Agulhas leakage to the western South Atlantic ocean (Kolodziejczyk et al., 2014, results are based on Argo). Thus, temperature and salinity compensation are suspected to exist in those layers. The origins and causes of the compensated temperature and salinity relation (on different time scales) within the NBUC region are out of the scope of this analysis, and they should demand more thorough investigation in the future.

The Implication for Large Discrepancies in North Brazil Undercurrent Among Models and the T-S Relationship

Large discrepancies in NBUC transport among datasets are expected for low-resolution model outputs or reanalysis data but not for high-resolution model outputs. The NBUC is a narrow western boundary current. If the horizontal resolution is sparser than 0.5° (i.e., the width of the NBUC at the subsurface layers), it will generally be impossible for these models to represent the real NBUC. However, in high-resolution model outputs (resolutions $\leq$ 0.25°), the large discrepancy among datasets indicates that the mechanism driving the NBUC low-frequency variability is still unknown. We are unable to determine the real NBUC transport variability or trend, which also prevents us from identifying/exploring the role of NBUC in the AMOC. STC and AMOC have a profound impact on the Atlantic and global climate. A better understanding of the global climate demands improvement in the simulation of the NBUC. Future work is needed to investigate the causes of the discrepancy among models and the mechanism driving the NBUC variability.

In this study, we also show that the discrepancy in NBUC transport among models can be attributed to the difference in zonal temperature and salinity gradients. Furthermore, the temperature and salinity-based geostrophic transport show a compensatory relation. The results have two implications:

(1) This study shows that temperature-based geostrophic velocities deeper than 600 m isobar have an opposite sign with meridional velocity in NBUC from a climatological perspective, but in the upper 600 m, temperature-based geostrophic velocities and meridional velocity have the same sign. It could serve as the first step in understanding the role of the temperature on the NBUC, and it will be beneficial for identifying the processes associated with meridional heat fluxes across the equator.

(2) This study shows that salinity-based NBUC transport variability usually has the same order of magnitude as those from temperature-based variability (**Figures 6**, **7**). Thus, salinity observations are important for representing NBUC variability. The role of the salinity on the NBUC will be a foundation of understanding how the salinity and velocity fields are coupled, which could assist the improvement of the model simulation.

CONCLUSION

In this study, we have analyzed the trend and the variability of the NBUC transports on the annual, and interannual time scales over the 1994–2015 period. By comparing the NBUC transport from three high-resolution ($\leq$1/10°) models and one low-resolution (=0.25°) model, we find large differences in NBUC interannual variability and linear trends. Decomposing the absolute geostrophic velocity into salinity and temperature contributions, we find the following:

(1) Large differences between models occur in geostrophic NBUC transport on the interannual time scale and trend from 1994–2015.

(2) The salinity-based and temperature-based transport anomalies tend to be opposite-signed on all time scales. Thus, variability in the temperature and salinity-based geostrophic transport (and their zonal gradients) partially cancels each other out in the NBUC among model outputs.

The discrepancy in NBUC variability and trend among models in this study could be attributed to the parameterization of eddies or other variables or assimilation method (Mignac et al., 2018). The exact causes in the model discrepancy are out of the scope of this analysis. Further analysis is under way to pin out the cause of the discrepancy.

The compensated salinity/temperature-based geostrophic anomalies lead to a smaller magnitude of the density-based geostrophic transport variance. Thus, to reduce the discrepancy in NBUC transport variability among datasets, one must have reliable temperature and salinity profiles long enough for variability analysis. From 1994 to 2020, the number of *in situ* profiles in the vicinity of the NBUC region was relatively low. Thus, many questions regarding the variability of the NBUC on other time scales remain open. This demands sufficient salinity and temperature observations to derive the variability of the NBUC, which is even lacking in the Argo era (because Argo profiles near the coast are rare).

One aspect not shown in this study is the origins of the salinity and temperature compensation. Where temperature and salinity anomalies come from and how they transport will be vital in understanding the causes of NBUC variability. This study calls for a full investigation of the origins of the temperature and salinity variability.

DATA AVAILABILITY STATEMENT

GLORYS12V1 for this study can be found at the EU Copernicus Marine Service (https://resources.marine.copernicus.eu/?option=com_csw&view=details&product_id=GLOBAL_REANALYSIS_PHY_001_030). OFES2 can be found at the Japan Agency for Marine-Earth Science and Technology (https://doi.org/10.17596/0002029). HYCOM can be found at the National Ocean Partnership Program (https://www.hycom.org/data/glbv0pt08/expt-53ptx). SODA 3.3.2 can be found at the College of the Computer Mathematical and Natural Sciences, Department of Atmospheric and Oceanic Science, University of Maryland (https://www2.atmos.umd.edu/%7Eocean/index_files/soda3_readme.htm). EN4 profiles are from the Met Office Hadley Centre (https://www.metoffice.gov.uk/hadobs/en4/en4-0-2-data-sources.html). Argo profiles from EN4 were collected and made freely available by the International Argo Program and the national programs that contribute to it (https://argo.ucsd.edu, https://www.ocean-ops.org, and https://doi.org/10.17882/42182). The Argo Program is part of the Global Ocean Observing System.

AUTHOR CONTRIBUTIONS

HL and ZW conceived and led the manuscript. HL wrote the manuscript. IR, XN, and CL provided the input and/or edited the text. All authors contributed to the article and approved the submitted version.

FUNDING

This research was funded by the National Natural Science Foundation of China (42006005 and 41821004), the Postdoctoral Innovation Research Program of Shandong Province (SDSBSH202002), the Qingdao Postdoctoral Applied Research Project (QDBSH202004), and the China Ocean Mineral Resources R&D Association (DY135-S2-2).

ACKNOWLEDGMENTS

We gratefully acknowledge the efforts of all parties involved in collecting data. We thank Shan Gao from the Institute of Oceanology, Chinese Academy of Sciences for collecting the data. We also thank Ryo Furue from JAMSTEC for his valuable and instructive inputs and editing on the manuscript. We also thank Tengfei Xu from the First Institute of Oceanography for his input on the manuscript.

SUPPLEMENTARY MATERIAL

The Supplementary Material for this article can be found online at: https://www.frontiersin.org/articles/10.3389/fmars.2021.744833/full#supplementary-material

REFERENCES

Araujo, M., Limongi, C., Servain, J., Silva, M., Leite, F., Veleda, D., et al. (2011). Salinity-induced mixed and barrier layers in the Southwestern tropical Atlantic Ocean off the Northeast of Brazil. *Ocean Sci.* 7, 63–73. doi: 10.5194/os-7-63-2011

Argo (2000). *Argo Float Data and Metadata from Global Data Assembly Centre (Argo GDAC)*. SEANOE. doi: 10.17882/42182

Azar, E., Piango, A., Wallner-Kersanach, M., and Kerr, R. (2020). Source waters contribution to the tropical Atlantic central layer: new insights on the Indo-Atlantic exchanges. *Deep Sea Res. Part I Oceanogr. Res. Pap.* 168:103450. doi: 10.1016/j.dsr.2020.103450

Cabré, A., Pelegrí, J., and Vallès-Casanova, I. (2019). Subtropical-tropical transfer in the South Atlantic Ocean. *J. Geophys. Res. Oceans* 124, 4820–4837. doi: 10.1029/2019jc015160

Carton, J. A., Chepurin, G. A., and Chen, L. (2018). SODA3: a new ocean climate reanalysis. *J. Clim.* 31, 6967–6983. doi: 10.1175/JCLI-D-18-0149.1

Chassignet, E. P., Hulburt, H. E., Smedstad, O. M., Halliwell, G. R., and Hogan, P. J. (2007). The HYCOM (HYbrid Coordinate Ocean Model) data assimilative system. *J. Mar. Syst.* 65, 60–83. doi: 10.1016/j.jmarsys.2005.09.016

da Silveira, I. C., de Miranda, L. B., and Brown, W. S. (1994). On the origins of the North Brazil. *Curr. J. Geophys. Res. Oceans* 99, 22501–22512. doi: 10.1029/94JC01776

Daniel, V., Piola, A. R., Meinen, C. S., and Campos, E. J. D. (2018). Strong mixing and recirculation in the Northwestern Argentine Basin. *J. Geophys. Res. Oceans* 123, 4624–4648. doi: 10.1029/2018JC013907

Dossa, A. N., Silva, A. C., Chaigneau, A., Eldin, G., and Bertrand, A. (2021). Near-surface western boundary circulation off Northeast Brazil. *Prog. Oceanogr.* 190:102475. doi: 10.1016/j.pocean.2020.102475

Fu, Y., Wang, C., Brandt, P., and Greatbatch, R. J. (2019). Interannual variability of antarctic intermediate water in the Tropical North Atlantic. *J. Geophys. Res. Oceans* 124, 4044–4057. doi: 10.1029/2018JC014878

Garzoli, S. L., and Matano, R. (2011). The South Atlantic and the Atlantic meridional overturning circulation. *Deep Sea Res. II* 58, 1837–1847.

Good, S. A., Martin, M. J., and Rayner, N. A. (2013). EN4: quality controlled ocean temperature and salinity profiles and monthly objective analyses with uncertainty estimates. *J. Geophys. Res. Oceans* 118, 6704–6716. doi: 10.1002/2013jc009067

Gouretski, V., and Reseghetti, F. (2010). On depth and temperature biases in bathythermograph data: development of a new correction scheme based on analysis of a global ocean database. *Deep Sea Res. Part I Oceanogr. Res. Pap.* 57, 812–833. doi: 10.1016/j.dsr.2010.03.011

Hummels, R., Brandt, P., Dengler, M., Fischer, J., Araujo, M., Veleda, D., et al. (2015). Interannual to decadal changes in the western boundary circulation in the Atlantic at 11°S. *Geophys. Res. Lett.* 42, 7615–7622. doi: 10.1002/2015GL065254

Kolodziejczyk, N., Reverdin, G., Gaillard, F., and Lazar, A. (2014). Low-frequency thermohaline variability in the Subtropical South Atlantic pycnocline during 2002–2013. *Geophys. Res. Lett.* 41, 6468–6475. doi: 10.1002/2014gl061160

Larqué, L., Maamaatuaiahutapu, K., and Garçon, V. (1997). On the intermediate and deep water flows in the South Atlantic Ocean. *J. Geophys. Res. Oceans* 102, 12425–12440. doi: 10.1029/97JC00629

Liu, H., Li, S., and Wei, Z. (2021). Interannual variability in the subduction of the South Atlantic subtropical underwater. *Clim Dyn* 57, 1061–1077. doi: 10.1007/s00382-021-05758-0

Liu, H., and Qu, T. (2020). Production and fate of the South Atlantic subtropical underwater. *J. Geophys. Res. Oceans* 125:e2020JC016309. doi: 10.1029/2020JC016309

Marcello, F., Wainer, I., and Rodrigues, R. (2018). South Atlantic Subtropical gyre late 20th century changes. *J. Geophys. Res. Oceans* 123, 5194–5209. doi: 10.1029/2018JC013815

Mccarthy, G. D., Smeed, D. A., Johns, W. E., Frajka-Williams, E., Moat, B. I., Rayner, D., et al. (2015). Measuring the Atlantic meridional overturning circulation at 26°N. *Prog. Oceanogr.* 130, 91–111. doi: 10.1016/j.pocean.2014.10.006

Mignac, D., Ferreira, D., and Haines, K. (2018). South Atlantic meridional transports from NEMO-based simulations and reanalyses. *Ocean Sci.* 14, 53–68. doi: 10.5194/os-14-53-2018

Qu, T., Zhang, L., and Schneider, N. (2016). North Atlantic subtropical underwater and its year-to-year variability in annual subduction rate during the argo period. *J. Phys. Oceanogr.* 46, 1901–1916. doi: 10.1175/jpo-d-15-0246.1

Rabe, B., Schott, F. A., and Köhl, A. (2008). Mean circulation and variability of the tropical Atlantic during 1952–2001 in the GECCO assimilation fields. *J. Phys. Oceanogr.* 38, 177–192. doi: 10.1175/2007jpo3541.1

Reid, J. L. (1989). On the total geostrophic circulation of the South Atlantic Ocean: flow patterns, tracers, and transports. *Progress In Oceanography* 23, 149–244. doi: 10.1016/0079-6611(89)90001-3

Rodrigues, R. R., Rothstein, L. M., and Wimbush, M. (2007). Seasonal variability of the South Equatorial Current bifurcation in the Atlantic Ocean: a numerical study. *J. Phys. Oceanogr.* 37, 16–30. doi: 10.1175/jpo2983.1

Rühs, S., Getzlaff, K., Durgadoo, J. V., Biastoch, A., and Böning, C. W. (2015). On the suitability of North Brazil Current transport estimates for monitoring basin-scale AMOC changes. *Geophys. Res. Lett.* 42, 8072–8080. doi: 10.1002/2015GL065695

Sasaki, H., Kida, S., Furue, R., Aiki, H., and Taguchi, B. (2020). *A Global Eddying Hindcast Ocean Simulation with OFES2*. doi: 10.5194/gmd-2019-351

Schott, F. A., Brandt, P., Hamann, M., Fischer, J., and Stramma, L. (2002). On the boundary flow off Brazil at 5–10°S and its connection to the interior tropical Atlantic. *Geophys. Res. Lett.* 29:1840. doi: 10.1029/2002GL014786

Schott, F. A., Dengler, M., Zantopp, R., Stramma, L., Fischer, J., and Brandt, P. (2005). The shallow and deep western boundary circulation of the south atlantic at 5°-11°S. *J. Phys. Oceanogr.* 35, 2031–2053. doi: 10.1175/JPO2813.1

Silva, A. C., Bourles, B., and Araujo, M. (2009). Circulation of the thermocline salinity maximum waters off the Northern Brazil as inferred from in situ measurements and numerical results. *Ann. Geophys.* 27, 1861–1873. doi: 10.5194/angeo-27-1861-2009

Souza, A. D., Kerr, R., and Azevedo, J. D. (2018). On the influence of subtropical mode water on the South Atlantic Ocean. *J. Mar. Syst.* 185, 13–24. doi: 10.1016/j.jmarsys.2018.04.006

Stramma, L., and England, M. (1999). On the water masses and mean circulation of the South Atlantic Ocean. *J. Geophys. Res.* 1042, 20863–20884. doi: 10.1029/1999JC900139

Stramma, L., Fischer, J., and Reppin, J. (1995). The North Brazil Undercurrent. *Deep Sea Res. Part I Oceanogr. Res. Pap.* 42, 773–795. doi: 10.1016/0967-0637(95)00014-W

Sun, C., Thresher, A., Keeley, R., Hall, N., Hamilton, M., Chinn, P., et al. (2010). "The data management system for the global temperature and salinity profile programme," in *Proceedings of the OceanObs.09: Sustained Ocean Observations and Information for Society. Venice, Italy, 21-25 September 2009*, Vol. 2, eds J. Hall, D. E. Harrison, and D. Stammer (ESA Publication WPP-306). doi: 10.5270/OceanObs09.cwp.86

Tuchen, F. P., Lübbecke, J., Brandt, P., and Yao, F. (2020). Observed transport variability of the Atlantic Subtropical Cells and their connection to tropical sea surface temperature variability. *J. Geophys. Res. Oceans* 125:e2020JC016592. doi: 10.1029/2020JC016592

Tuchen, F. P., Lübbecke, J., Schmidtko, S., Hummels, R., and Bning, C. W. (2019). The Atlantic subtropical cells inferred from observations. *J. Geophys. Res. Oceans* 124, 7591–7605. doi: 10.1029/2019jc015396

White, R. H. (2015). Using multiple passive tracers to identify the importance of the North Brazil undercurrent for Atlantic cold tongue variability. *Q. J. R. Meteorol. Soc.* 141, 2505–2517. doi: 10.1002/qj.2536

Zhai, Y., Yang, J., and Wan, X. (2021). Cross-equatorial anti-symmetry in the seasonal transport of the Western Boundary Current in the Atlantic Ocean. *J. Geophys. Res. Oceans* 126:e2021JC017184. doi: 10.1029/2021JC017184

Zhang, D., McPhaden, M. J., and Johns, W. E. (2003). Observational evidence for flow between the subtropical and tropical Atlantic: the Atlantic subtropical cells*. *J. Phys. Oceanogr.* 33, 1783–1797.

Zhang, D., Msadek, R., Mcphaden, M. J., and Delworth, T. (2011). Multidecadal variability of the North Brazil Current and its connection to the Atlantic meridional overturning circulation. *J. Geophys. Res. Oceans* 116:C04012. doi: 10.1029/2010JC006812

Conflict of Interest: The authors declare that the research was conducted in the absence of any commercial or financial relationships that could be construed as a potential conflict of interest.

frontiers in Marine Science

ORIGINAL RESEARCH
published: 26 November 2021
doi: 10.3389/fmars.2021.748383

Southeastern Tropical Atlantic Changing From Subtropical to Tropical Conditions

Marisa Roch[1]*, *Peter Brandt*[1,2], *Sunke Schmidtko*[1], *Filomena Vaz Velho*[3] *and Marek Ostrowski*[4]

[1] GEOMAR Helmholtz Centre for Ocean Research Kiel, Kiel, Germany, [2] Faculty of Mathematics and Natural Sciences, Kiel University, Kiel, Germany, [3] Instituto Nacional de Investigação Pesqueira e Marinha, Luanda, Angola, [4] Oceanography and Climate, Institute of Marine Research, Bergen, Norway

OPEN ACCESS

Edited by:
Fabrice Hernandez,
Institut de Recherche Pour le Développement (IRD), France

Reviewed by:
Zhongxiang Zhao,
University of Washington, United States
Ru Chen,
Tianjin University, China

Correspondence:
Marisa Roch
mroch@geomar.de

Specialty section:
This article was submitted to Physical Oceanography, a section of the journal Frontiers in Marine Science

Received: *27 July 2021*
Accepted: *29 October 2021*
Published: *26 November 2021*

Citation:
Roch M, Brandt P, Schmidtko S, Vaz Velho F and Ostrowski M (2021) Southeastern Tropical Atlantic Changing From Subtropical to Tropical Conditions. Front. Mar. Sci. 8:748383. doi: 10.3389/fmars.2021.748383

A warming and freshening trend of the mixed layer in the upper southeastern tropical Atlantic Ocean (SETA) is observed by the Argo float array during the time period of 2006–2020. The associated ocean surface density reduction impacts upper-ocean stratification that intensified by more than 30% in the SETA region since 2006. The initial typical subtropical stratification with a surface salinity maximum is shifting to more tropical conditions characterized by warmer and fresher surface waters and a subsurface salinity maximum. During the same period isopycnal surfaces in the upper 200 m are shoaling continuously. Observed wind stress changes reveal that open ocean wind curl-driven upwelling increased, however, partly counteracted by reduced coastal upwelling due to weakened alongshore southerly winds. Weakening southerly winds might be a reason why tropical surface waters spread more southward reaching further into the SETA region. The mixed layer warming and freshening and associated stratification changes might impact the marine ecosystem and pelagic fisheries in the Angolan and northern Namibian upwelling region.

Keywords: southeastern tropical Atlantic Ocean, decadal variability, upper-ocean stratification increase, mixed layer warming and freshening, heave and spice anomalies, primary productivity

INTRODUCTION

The southeastern tropical Atlantic (SETA: 10–20°S, 5°W–15°E) encompasses a highly-productive ecosystem off Angola which is located just north of one of the major global coastal upwelling regions: the Benguela upwelling system (Ostrowski et al., 2009; Kopte et al., 2017). In the SETA region the thermal Angola-Benguela Front (ABF) evolves around 15–17°S where warm, tropical waters encounter cooler, subtropical waters from the Benguela upwelling system (Shannon et al., 1987; Siegfried et al., 2019). At the ABF the poleward Angola Current meets the northward Benguela Coastal Current (Siegfried et al., 2019, indicated schematically in **Figure 1a**). Siegfried et al. (2019) showed that the Angola Current is fed with tropical South Atlantic Central Water (SACW) via the eastward flowing Equatorial Undercurrent (EUC), the South Equatorial Undercurrent (SEUC) and the South Equatorial Countercurrent (SECC) (**Figure 1a**). These currents and the location of the ABF undergo large seasonal variations and hence the area influenced by the presence of tropical SACW varies as well (Rouault, 2012).

On seasonal time scales the variability of the Angola Current is affected by coastally trapped waves (CTWs) excited by remote equatorial forcing (Ostrowski et al., 2009; Bachèlery et al., 2016; Kopte et al., 2018; Tchipalanga et al., 2018). The seasonal upwelling and downwelling phases in the SETA region coincide with the corresponding four seasonal wave propagations of the CTWs. March and October are marked by downwelling and July–August and December-January by upwelling phases (Ostrowski et al., 2009). CTWs excite sea surface temperature (SST) anomalies via the thermocline feedback which can affect air-sea interactions such as heat fluxes and precipitation patterns (Shannon et al., 1986; Rouault et al., 2018).

On top of the seasonal cycle, the SST along the coast of Angola and Namibia can experience extreme warm events, the so-called Benguela Niños (Shannon et al., 1986). During these interannual warm events, the ABF is shifted anomalously poleward (Florenchie et al., 2004; Rouault et al., 2007, 2018; Lübbecke et al., 2010). Thereby, tropical SACW extends into the northern part of the Benguela upwelling region (Lübbecke et al., 2010; Siegfried et al., 2019).

Meteorologically, the SETA region is situated on the northeastern flank of the South Atlantic Subtropical High (SASH) and therefore, the wind pattern is influenced by the southeast trades (Peterson and Stramma, 1991). In the northern part of the SETA region the mainly southerly wind is considerably weak (Risien et al., 2004; Fennel et al., 2012; Lübbecke et al., 2019; Zeng et al., 2021). Besides, in austral winter when SSTs are lowest, the upwelling favorable winds are weakest and thus, the shallowing of the thermocline occurring during that part of the year is not wind-driven. Instead, enhanced biological productivity off Angola in austral winter is mainly associated with the propagation of an upwelling CTW (e.g., Ostrowski et al., 2009; Rouault, 2012; Lübbecke et al., 2019). Mixing dominantly induced by internal tides (Zeng et al., 2021) transfers the CTW upwelling signal toward the surface to further modulate near coastal SST (Imbol Koungue and Brandt, 2021) and transport nutrients upward into the euphotic zone.

In the southern part of the SETA region the wind situation differs as the southerly wind is substantially stronger. This equatorward wind weakens toward the coast and thereby produces a negative wind stress curl which leads to wind curl-driven upwelling, especially off Namibia (Fennel et al., 2012; Lübbecke et al., 2019).

Upwelling is generally considered to be the upward advection forced by Ekman dynamics (via alongshore winds and wind stress curl) and CTWs (Fennel and Lass, 2007; Fennel et al., 2012). CTWs can be generated both locally and thereby partly reducing the effect of local wind-forced upwelling (Fennel and Lass, 2007) or remotely, e.g., by equatorial forcing (Bachèlery et al., 2016). Nutrients that are important for primary productivity can be transported upward by upwelling and mixing, whereas mixing was shown to be particularly effective during upwelling CTW phases (Zeng et al., 2021).

Superimposed on the wide-spread southerly wind component in the SETA region associated with the southeast trades is the atmospheric Benguela low-level coastal jet (BLLCJ, Patricola and Chang, 2017). Low-level coastal jets are marked by strong coast-parallel equatorward winds in eastern boundary upwelling systems. Attributed to the geometry of the coastline, the BLLCJ constitutes of two local maxima in terms of frequency of occurrence around 26 and 17.5°S (Patricola and Chang, 2017; Lima et al., 2019a). The BLLCJ is formed in between the SASH and the Angolan thermal low pressure. The co-existence of these two pressure systems results in strong pressure gradient and forces the equatorward winds (Lima et al., 2019a). According to Patricola and Chang (2017), an intensification of the SASH and a shift toward the African continent strengthens the BLLCJ. The meridional wind stress component is then enhanced in the southern part, but decreasing offshore and to the north of this region.

In the high-productive SETA region both, upwelling and mixing are of great importance for small pelagic fish stocks since upward transport of nutrients directly impact primary production (Ostrowski et al., 2009; Tchipalanga et al., 2018). The extreme warm and frequently occurring Benguela Niños can have dramatic consequences for the marine ecosystem and its productivity. During a major warm event in 1995 e.g., sardinella *Sardinella aurita* and sardine *Sardinops sagax* showed a large reduction in biomass with increased mortality in Angolan waters and a southward migration to Namibian coastal waters (Gammelsrød et al., 1998). Besides, Potts et al. (2014) reported an intensified warming over the last three decades with dramatic consequences for some fish species and poleward habitat shifts. For a recent review of the impact of climate variability on the plankton, pelagic and demersal fish communities in the Benguela upwelling system the reader is referred to Jarre et al. (2015). Additionally, Jarre et al. (2015) give an outlook on possible changes of the ecosystem related to climate warming.

In general, upwelling and mixing are affected by upper-ocean stratification. Processes such as ocean ventilation and entrainment into the mixed layer depend on the density gradient at the base of the mixed layer and thus on stratification. In this study, we make use of an extensive Argo float dataset to focus on decadal variability of upper-ocean stratification. Our aim is not to investigate processes on the continental slope and shelf, as the Argo floats cannot represent the shelf region. In particular, we cannot study the effects of Benguela Niños and CTWs by using Argo data. Instead, we focus on larger scale water mass and stratification changes and discuss their possible impact on the marine ecosystem.

The common assumption based on climate projections is that global warming will result in a more stratified ocean due to enhanced warming of the ocean surface, often associated with mixed layer shoaling, reduced ventilation and weaker vertical mixing (Keeling et al., 2010; Capotondi et al., 2012; Rhein et al., 2013). Consequently, less upward nutrient supply to the euphotic zone and declining dissolved oxygen concentration are expected (Capotondi et al., 2012; Ito et al., 2019). Hence, impacts on marine ecosystems can be large. Previous work on upper-ocean stratification has mainly focused on climate models and some of these proposed feedbacks are not that straight forward as many different factors play a role. Ventilation processes for example can be further influenced by changes of the wind-driven circulation and heaving (Huang, 2015). Besides, there can be large regional

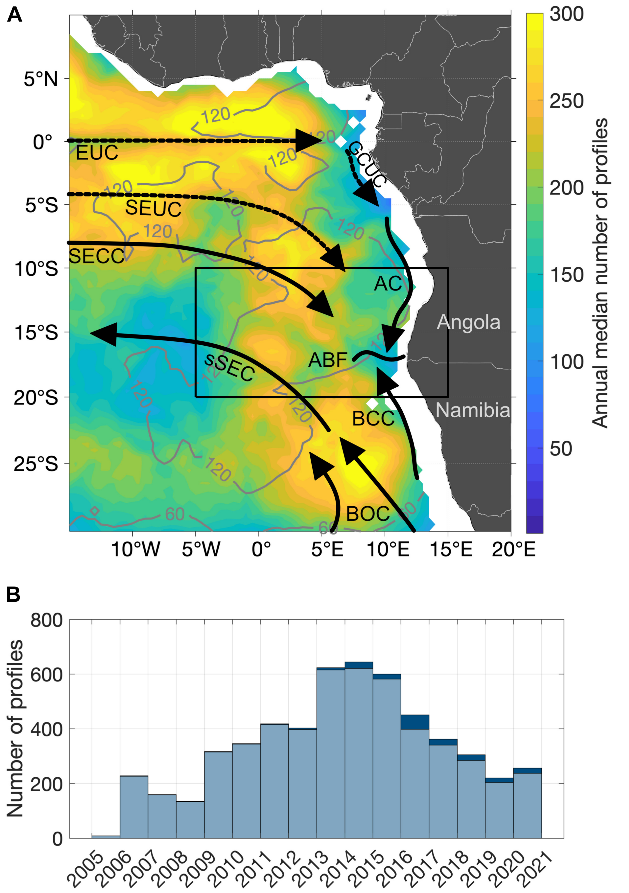

FIGURE 1 | (A) Median annual number of Argo profiles for the time period of 2006–2020. Mapping radii are ellipses with 3° in latitude and 8° in longitude at the equator changing exponentially toward circles with 6° radii in latitude and longitude at 20°S. Gray contour lines show the standard deviation of the median annual number. The black box shows the southeastern tropical Atlantic (SETA) region (10–20°S, 5°W–15°E). Additionally, currents are schematically indicated (solid arrows imply surface currents and dashed arrows thermocline currents): Equatorial Undercurrent (EUC), South Equatorial Undercurrent (SEUC), South Equatorial Countercurrent (SECC), Angola Current (AC), Benguela Coastal Current (BCC), Benguela Oceanic Current (BOC), southern branch of the South Equatorial Current (sSEC), and Gabun-Congo Undercurrent (GCUC). Besides, the location of the Angola-Benguela Front (ABF) is depicted. Shelf regions below 2,000 dbar have been blanked out. **(B)** Dark blue bars indicate the overall number of Argo profiles in the SETA region per year. Light blue bars above depict the number of Argo profiles that pass the good interquartile range filter of the vertical stratification maximum in the SETA region per year.

differences and there are observations indicating deeper mixed layers in regions with enhanced stratification (Somavilla et al., 2017; Sallée et al., 2021). This is counterintuitive and could balance the predicted reduction of vertical mixing. It reveals the general lack of understanding of how physical and biological processes are shifting due to climate warming.

Two recent studies showed increasing global stratification since the 1960s. Yamaguchi and Suga (2019) found a 40% increase of global stratification in the upper 200 m, about half of this enhancement is observed in the tropical oceans. Li et al. (2020) highlight that the global stratification in the upper 2,000 m depth is strengthening by 0.9% per decade (5.3% in total) during the period 1960–2018. Their estimate detects largest stratification increases of 5–18% in the upper 150 m.

When investigating upper-ocean stratification, it is necessary to examine mixed layer properties. Directly below the mixed layer the pycnocline/thermocline representing the vertical stratification maximum is situated. The dynamics of these two components, i.e., the mixed layer and the stratification maximum below, can be linked to each other. However, for the global ocean the evolution of water mass properties at the base of the mixed layer is much less studied than the surface warming (Clément et al., 2020).

The continuous growth of Argo observations in recent years allows us to investigate the tropical Atlantic Ocean in terms of upper-ocean stratification changes, its causes as well as its consequences for physical ocean dynamics and marine ecosystems. In this study we will focus on the SETA region as it encompasses a highly productive ecosystem and hence, investigation of upper-ocean stratification in terms of climate variability in this region is of major economic importance for the Angolan and Namibian fisheries. We aim to provide a better understanding of possible physical changes as a result of climate change and their relation to marine ecosystems.

DATA AND METHODS

Argo Observations and Stratification Estimate

The Argo project currently contains about 4,000 floats measuring hydrographic properties in the upper 2,000 m within a 10-day cycle. For this study Argo observations of the upper 200 m from 2006 to 2019 (Argo, 2019) are used. Prior 2006 the gaps in the data are too large (Roemmich et al., 2015; Desbruyères et al., 2017). Only profiles reaching at least 1000 m depth and flagged good are utilized. The tropical Atlantic from 30°N–30°S holds 121,126 profiles in the observation period. Here, we applied an interquartile range (IQR) filter, excluding data 1.5 times the IQR above/below the first/third quartile. Analyses of potential temperature, absolute salinity and potential density are performed using TEOS-10 (McDougall and Barker, 2011). Additionally, conservative temperature is estimated for the calculation of the Brunt–Väisälä frequency. Note that specifically for the analysis of the SETA region (10°S–20°S, 5°W–15°E) we extended the time series with Argo observations until November 2020, in order to overcome a gap in the data in this particular region in the mid of the year of 2019 (Argo, 2020). The SETA region constitutes 5,477 profiles from 2006 to 2020.

Argo profiles are interpolated vertically using a modified Akima piecewise cubic Hermite interpolation (makima method) as implemented in MATLAB (2019). The algorithm of Akima was first introduced by Akima (1970). Makima is a mixture of the spline and pchip interpolation methods (MathWorks Inc, 2019). Advantages are that makima respects monotonicity compared to the spline method, yet it does not cut off undulations like a pchip method. Using various vertical interpolation schemes, we found that the errors as seen in **Supplementary Figure 1B** are smallest using the makima method. Furthermore, a linear or piecewise cubic method has maxima and minima centered on measured vertical depth levels. This would lead to a bias using float data, since floats (in particular the ones that transmit the data via ARGOS, as most of them still do) have specific target depth at which they measure the oceanic properties. Thus, for the analysis of vertical maxima and minima using float data, an interpolation scheme that may have local maxima and minima between measurements is necessary and therefore, we chose the makima method. First, all profiles are interpolated on an even 0.01 kg m^{-3} density grid and second, this is followed by an interpolation on an even 1 dbar pressure grid.

The pressure interpolated profiles are used to determine the Brunt–Väisälä frequency as a measure for stratification. Argo profiles have a varying vertical resolution which impacts the estimate of the Brunt–Väisälä frequency. In order to obtain the best-possible stratification estimate with Argo measurements, we subsampled a high-resolution Conductivity-Temperature-Depth (CTD) profile from a recent cruise in the equatorial Atlantic (Meteor cruise M158, Brandt et al., 2021) onto the vertical resolution of all available Argo profiles for this study. The CTD profile was taken at 0°, 11°W in October 2019 and covers a vertical sampling rate of 1 dbar. The above explained makima interpolation method was applied to the temperature and salinity profiles subsampled according to the vertical resolution of measured Argo profiles. In a next step the Brunt–Väisälä frequency was computed on the even pressure grid. With this we derived a large amount of artificial Argo profiles which are based on the same Brunt–Väisälä frequency profile. However, they deviate from each other since they are based on different vertical resolutions. Finally, the vertical maximum in the upper 200 m of the water column was determined.

By assuming the CTD vertical stratification maximum being the "true" value, we analyzed the dependence of the vertical stratification maximum on the vertical sampling rate of the Argo profiles. The deviations are large (**Supplementary Figure 1**). However, by using the above described IQR filter and a 15-dbar window for computations, the errors were largely reduced (**Supplementary Figure 1**). This smoothing length scale was done by trial and error always in comparison to the CTD reference value. In addition, this smoothing length scale is required for the study of background stratification, ignoring other small-scale features that influence the stratification. 15-dbar seems to be the ideal range for this study as it is the balance between minimizing the noise and preserving the shape of the stratification profile (Feucher, 2016).

Mixed layer properties are determined by using the algorithm by Holte and Talley (2009). This algorithm is based on a hybrid method which combines threshold and gradient methods to specify the best mixed layer properties (Holte and Talley, 2009).

Mapping is accomplished using a least squares method which takes the uneven distribution of Argo profiles into account. Despite generally fewer profiles in the South Atlantic (**Figure 1a**), the histogram of the SETA region indicates more than 300 profiles per year from 2009 to 2018. Influence radii of the anomalies of stratification and mixed layer properties have been checked with a semivariogram analysis, in order to evaluate the spatial bias. This yielded that the spatial bias of the profiles in the SETA region is generally small. Results from 2006 to 2008 and from mid 2019 should be taken with caution due to the relatively small number of Argo profiles available (**Figure 1b**). The histogram also shows the number of profiles per year that pass the IQR filter for the vertical stratification maximum (**Figure 1b**). From those 5,477 available profiles in the SETA region 5,297 profiles pass the IQR filter.

Trends and time series of Argo observations are always computed from anomalies relative to the seasonal mean. Seasonal means are calculated on a 15-day grid resolution using overlapping 3-month means (i.e., ±45 days). In order to test statistical significance of the trends, the 95% confidence limits were determined by multiplying the t-value of the Student's t distribution for 95% significance with the standard error of the trend. In case the slopes of the upper and lower confidence limits are of the same sign, the trend is assigned to be of 95% statistical significance.

Wind Stress Data

To investigate changes of wind speed, zonal and meridional wind stress components the wind product Global Ocean Wind L4 Reprocessed Monthly Mean Observations from Copernicus Marine environment monitoring service (CMEMS) is used (Wind TAC, 2018). The measurements are based on ASCAT scatterometers on METOP-A and METOP-B satellites with the processing level L4. This product is composed of three different ASCAT products (Bentamy, 2020) spanning the global ocean with a spatial resolution of 0.25° × 0.25°. It encompasses monthly means which are estimated from at least 25 daily values at each grid point (Bentamy and Fillon, 2012). The observation period covers May 2007–December 2019. With the meridional and zonal wind stress components, the wind stress curl is computed as well. To reduce noise, the data has been transformed on a 0.5° × 0.5° horizontal grid by taking the mean of all points within ±2° in longitudinal and latitudinal direction around each grid point. The anomalies of the wind data are evaluated by subtracting the monthly means provided by CMEMS from the time series.

Heat Flux and Freshwater Products

In order to compare the results to heat and freshwater fluxes different products are used. First of all, the Objectively Analyzed air-sea fluxes (OAFlux) for the Global Oceans from Woods Hole Oceanographic Institution (WHOI) is used[1] (Yu et al., 2008). The horizontal resolution of the data is 1° × 1° in latitude and longitude and is available as a monthly mean from 1958 until present. OAFlux latent and sensible heat fluxes are computed with the COARE bulk flux algorithm and surface meteorological properties (Yu et al., 2008). For this analysis, latent heat flux, evaporation and specific humidity are used for the time period of 2006–2019.

In addition, TropFlux latent heat flux and specific humidity are compared to OAFlux data (Praveen Kumar et al., 2012).

---

[1] https://oaflux.whoi.edu/data-access/

TropFlux heat fluxes are calculated from the COARE v3 algorithm. In contrast to OAFlux, TropFlux uses ERA-I and therefore, the two datasets are to some extent not related to each other (Praveen Kumar et al., 2012). According to Praveen Kumar et al. (2012), TropFlux and OAFlux are the best-performing heat flux products. TropFlux horizontal resolution is identical to OAFlux, the monthly estimates from 2006 to 2018 are used.

Furthermore, monthly precipitation estimates from the Global Precipitation Climatology Project (GPCP) Version 2.3 are analyzed (Adler et al., 2018; Pendergrass et al., 2020). This data set has a horizontal resolution of 2.5° × 2.5° and data from 2006 to 2019 is used. GPCP combines several satellite measurements and gauge data.

Similar as for the wind data, the heat flux, evaporation and precipitation data are available as monthly estimates. Anomalies are computed by subtracting the corresponding monthly climatology. Finally, with these anomalies the linear decadal trends are computed.

Net Primary Production

Stratification changes are compared to net primary production data from the Ocean Productivity site[2] (Behrenfeld and Falkowski, 1997). The data is based on the Eppley Vertically Generalized Production Model (VGPM) which uses MODIS chlorophyll, SST data, SeaWiFs PAR and estimates of the euphotic zone depth. Net primary production is available for the period of 2002–2019 as monthly values and this study focusses on the years 2006–2019. The horizontal resolution is 1/6° in latitude and longitude but the net primary production was re-gridded on a 0.5° × 0.5° spatial grid to reduce noise.

THEORETICAL BACKGROUND

Pure Warming and Freshening Processes in Terms of Heave and Spice

To investigate possible causes for stratification changes it is important to understand that depending on the mean temperature and salinity distribution different processes can dominate. The most common cause for increasing upper-ocean stratification is surface warming, i.e., surface density reduction. Surface warming can be explored in terms of a vector summation between heave and spice (Bindoff and McDougall, 1994; Häkkinen et al., 2016). However, the sign of heave and spice depends strongly on the stability ratio in the region.

The SETA region encompasses a typical subtropical stratification, i.e., warm and saline water layered above cool and fresh water. Then a pure warming or pure freshening process (i.e., a density reduction) at a fixed depth can be interpreted by using a T-S diagram as follows: in case of a pure warming process (**Figure 2A**, orange arrow) the original thermocline (thin blue line) is shifted to a new position (thick blue line). This results into positive heaving, i.e., the original density surface is sinking downward and is replaced by a lower density on top. This heaving is then corrected by a negative spice contribution which is the temperature and salinity change on a density surface. Thus, a parcel at position 2 appears now cooler and fresher than a parcel at position 3 at the same density on the original thermocline (**Figure 2**, following Bindoff and McDougall, 1994; Häkkinen et al., 2016).

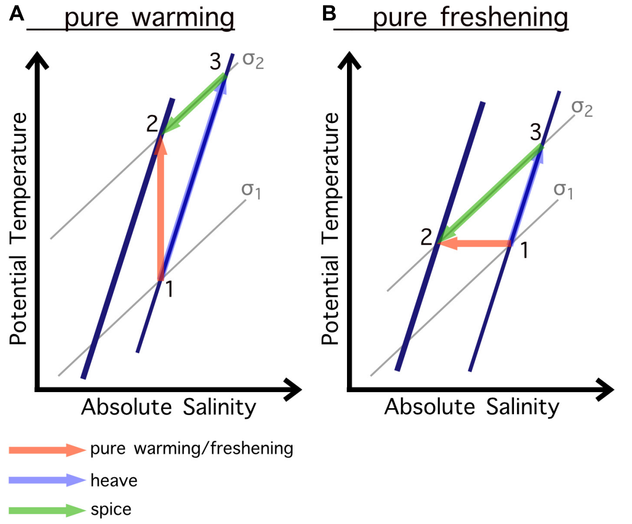

FIGURE 2 | T-S relation schematic for a pure warming process **(A)** and a pure freshening process **(B)** for a subtropical stratification (adapted from Bindoff and McDougall, 1994; Häkkinen et al., 2016). Thin blue line indicates initial thermocline, thick blue line the new thermocline. Gray lines show the potential density surfaces (σ_1 as the initial density surface and σ_2 as the density surface at the same depth after the warming/freshening process with σ_2 being smaller and thus lighter than σ_1). 1 indicates the initial starting point, 2 reveals the T-S condition at the same depth after warming/freshening. Orange arrows (1–2) denote the warming/freshening process, green arrows indicate the spice component (3–2) and blue arrows the heave component (1–3).

The same processes are active for a pure freshening (**Figure 2B**). Instead, a cooling or salinification at a fixed depth results in negative heave and positive spice, i.e., an upward displacement of the isopycnals and warm/saline conditions on the initial density surface (not shown). Note the described cases above are the simplest ones. Observed water mass changes will always be a combination of both.

Pure Heaving Process

Another process that can influence the vertical stratification is pure heaving, e.g., due to changes of wind stress curl. This mechanism is not associated with imprints in the T-S diagram (Bindoff and McDougall, 1994). If wind stress curl-driven upwelling intensifies, isopycnals will rise upward and thereby reducing the height difference between near-surface isopycnals (**Figure 3**) and correspondingly increasing the near-surface stratification or Brunt–Väisälä frequency. In case the height difference between isopycnals is increasing, the stratification decreases. Heaving can thereby alter vertical stratification and additionally may lead to shifts in the heat content (Huang, 2015).

---

[2] http://sites.science.oregonstate.edu/ocean.productivity/index.php

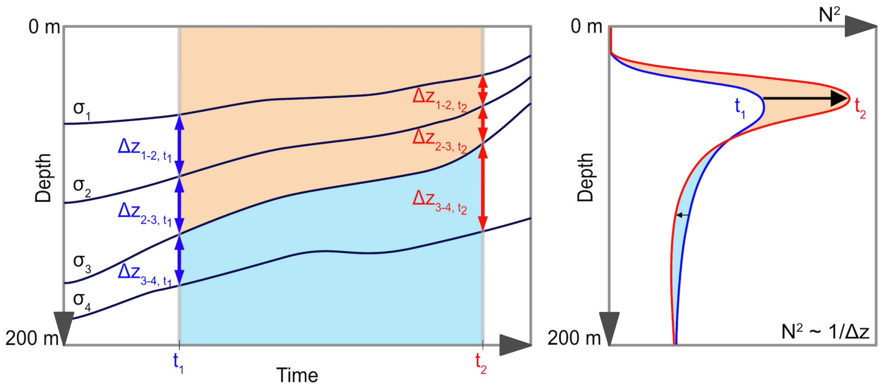

FIGURE 3 | Schematic of a pure heaving process as a result of intensified wind curl-driven upwelling. Dark blue lines indicate different isopycnals (σ_1, σ_2, σ_3, and σ_4) whose depth is changing over time. Due to the upwelling of the isopycnals, the height difference Δz between two isopycnals changes over time (compare time steps t_1 and t_2). If the Δz decreases as for the upper two pairs of isopycnals (Δz_{1-2}, Δz_{2-3}) from time step t_1 (blue double arrows) to t_2 (red double arrows), the stratification in terms of the Brunt–Väisälä frequency N^2 increases as indicated in the **right panel** by the typical stratification profile. Here the blue line of the N^2 profile corresponds to the time step t_1 as in the **left panel**. The red profile indicates the profile for t_2. In both panels the depth range where stratification increases, is shaded light orange. In contrast, if the height difference becomes larger over time as for the lower pair of isopycnals (Δz_{3-4}), stratification will be reduced. The depth range where stratification decreases is marked light blue in both panels.

RESULTS

Decadal Trends of the Tropical Atlantic

This section will deal with mean fields and decadal trend maps of vertical stratification maximum, its depth, mixed layer properties, the vertical displacement and spice of isopycnals in the tropical Atlantic. In order to receive an overview about the on-going changes and explain why we particularly focus on the SETA region (10–20°S, 5°W–15°E) for a more detailed analysis, the maps of the vertical stratification maximum and its depth are computed for the entire tropical Atlantic from 30°N to 30°S. All other maps are confined to a smaller region in the eastern tropical Atlantic ranging from 10°N–30°S, 15°W–20°E which includes the SETA region and is still large enough to explain some observed larger-scale patterns.

The vertical stratification maximum is located just below the mixed layer and is within the depth range of the thermocline. The mean of the vertical stratification maxima shows largest values within 10°N and 10°S especially close to the eastern boundary (**Figure 4A**). These areas largely coincide with areas where the mean depth of the stratification maximum is shallowest (**Figure 4B**).

The decadal trend reveals an increase of stratification in the eastern tropical North Atlantic and in most of the tropical South Atlantic away from the equatorial band with maximum increase in the region of SETA (10–20°S, 5°W–15°E) with an intensification of up to 30% (**Figure 4C**). Besides, where the stratification maximum intensifies, its depth is shoaling (**Figure 4D**). The described increase of stratification in the SETA region as well as in the northeastern tropical Atlantic (**Figure 4C**) are of 95% statistical significance.

To better characterize the above results, decadal trends of surface mixed layer characteristics have been calculated for the smaller region in the eastern tropical Atlantic (10°N–30°S, 15°W–20°E) (**Figure 5**). On average, the MLD can be found only slightly above the vertical stratification maximum. The equatorial region reveals a deepening of the mixed layer, a cooling and salinification and thus, an increase in density. Further south in the SETA region the MLT is rising, MLS is reducing and the MLD is shoaling (**Figure 5**). Indeed, at the depth of the vertical stratification maximum the patterns of temperature, salinity and density changes are similar (not shown).

In order to understand the acting processes, it is important to not only investigate changes on depth levels but also on density surfaces. Therefore, we inspect the trends of the vertical displacement (i.e., heave) and the spice of two different isopycnals (25.5 and 26.0 kg m^{-3}). These isopycnals are chosen as they are surrounding the vertical stratification maximum in the SETA region. The results of the decadal heave trend show that in most of the southeastern tropical Atlantic these two isopycnals, lying within the upper 150 m, are shoaling (**Figures 6A,B**). The strongest upwelling of the isopycnals is within 10° offshore in the SETA region whereas there is weaker upwelling along the coast (**Figures 6A,B**). Spice trends are relatively weak with a range of up to ±0.2 g kg^{-1} decade^{-1} (**Figures 6C,D**). Nevertheless, from the African coastline to 5°W–0° the spice is reducing. Westward of the Greenwich meridian the spice trend is increasing (**Figures 6C,D**).

Regional Analysis of Southeastern Tropical Atlantic Ocean Region

In this section the SETA region (10–20°S, 5°W–15°E) is investigated in more detail by analyzing its time series. SETA is the region which undergoes the largest stratification increase within the entire tropical Atlantic during the Argo period.

In fact, the 6 months running median time series of the percental change of the stratification maximum confirms the observed decadal trend in the SETA region as it continuously intensifies. From 2006 to 2016 the stratification increased by

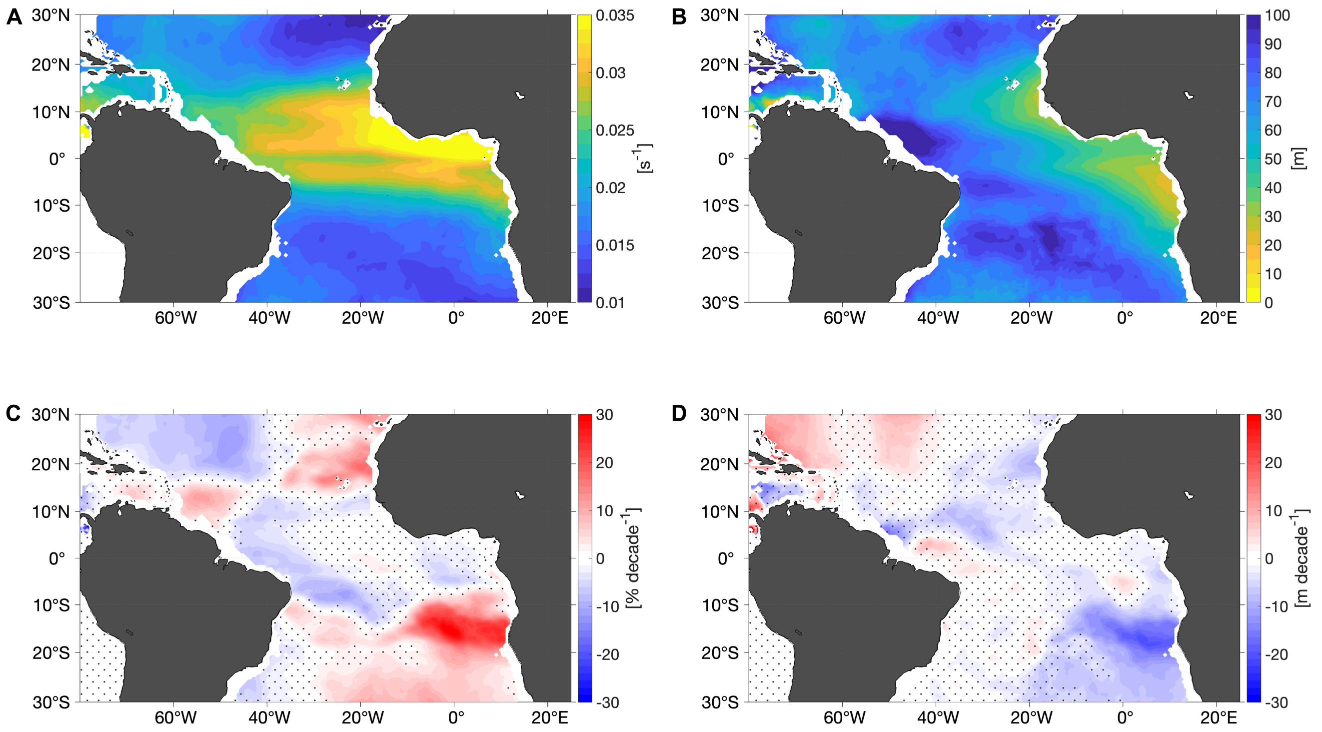

FIGURE 4 | **(A)** Mean of vertical stratification maxima inferred from Argo for the time period of 2006–2019. **(B)** Mean depth of the vertical stratification maximum from **(A)**. Panels **(C,D)** decadal trend of **(A,B)**, respectively. Trends are computed from the anomalies relative to the seasonal mean. Please note, positive trend of depth refers to a deepening. Areas where the trend is not of 95% significance are stippled. Shelf regions below 2,000 dbar are blanked out.

40% (**Figure 7A**). From 2016 until the beginning of 2020 the stratification intensified by almost another 20%. The time series of the depth anomaly onto the mean depth of the stratification maximum shows that the depth is indeed shoaling (around 50 m from 2006 to 2020, **Figure 7B**). The same accounts for the MLD which is on average 20–40 m above the depth of the vertical stratification maximum (**Figure 7B**).

The time series of MLT anomaly reveals almost 3°C temperature rise in the SETA region from 2006 to 2018 (**Figure 7C**). This temperature increase is followed by a minimum of almost -1°C in mid of 2019. At the end of 2019 and beginning of 2020 the MLT depicts a large maximum by around 3.5°C which is by far the greatest peak of the MLT timeseries. MLS is decreasing over time (more than 0.5 g kg^{-1}), however, there is a negative peak in 2008 (**Figure 7C**). Thus, as the mixed layer is becoming warmer and fresher, the density is decreasing (**Figure 7A**). The warming and freshening can be found at the depth of the vertical stratification maximum as well even though not as pronounced as in the mixed layer (not shown).

Shown as well are the time series of salinity anomalies on the isopycnals 25.5, 26.0, and 26.5 kg m^{-3} (spice anomalies). The pattern of the time series of spice changes along the 25.5 and 26.0 kg m^{-3} isopycnal surfaces is similar to that of MLS (**Figure 7D**). We observe the negative peak in 2008 and since 2011 the spice is decreasing. The spice on the 26.5 kg m^{-3} isopycnal is increasing over time indicating that at larger depths different processes are active.

In order to visualize salinity, temperature and stratification changes within the upper 200 m of the water column in the SETA region, a T-S diagram for annual averages of the Argo temperature and salinity profiles was drawn (**Figure 8**). The derived T-S diagram highlights a typical subtropical stratification with warm, saline water layered above cool, fresh water on average in the SETA region. The annual mean profiles indicate that the water column becomes more stratified during the observing period (**Figure 8**). However, this does not happen constantly on all depth levels. Largest changes are indeed found in the near-surface waters where the conditions are changing toward warmer and especially fresher characteristics. This confirms the observed mixed layer changes. Since 2009 this shift happens to be continuous and thus, the upper water column is becoming more stratified (**Figure 8**).

The T-S diagram reveals that in deeper levels the stratification is becoming slightly weaker (**Figure 8**). This is supported by mean Brunt–Väisälä frequency profiles for three time periods: 2006–2010, 2011–2015, and 2016–2020 which indicate a continuous increase of stratification in the upper 60 dbar and a decrease below 60 dbar (**Figure 9B**). In comparison to the stratification profiles, the time series of the 6 months running median pressure anomaly of the three isopycnal surfaces 25.5, 26.0, and 26.5 kg m^{-3} plus their corresponding mean pressure are shown. We can see how the isopycnals change their vertical position and how the stratification profile alters in the respective depth over the corresponding

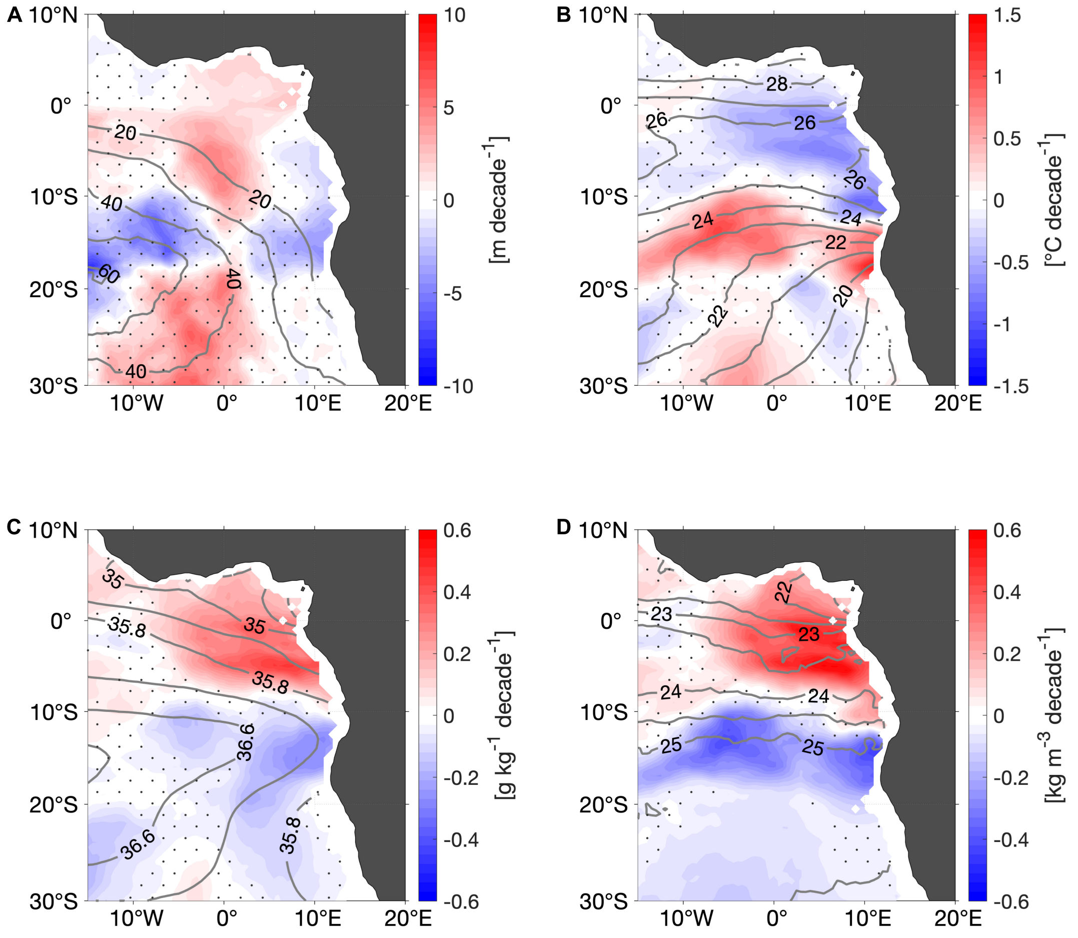

FIGURE 5 | Decadal trend of **(A)** mixed layer depth (MLD), **(B)** mixed layer temperature (MLT), **(C)** mixed layer salinity (MLS), and **(D)** mixed layer potential density anomalies from Argo for the time period of 2006–2019. Trends are computed from the anomalies relative to the seasonal mean. Mixed layer properties have been estimated with the Holte and Talley algorithm (Holte and Talley, 2009). Gray contour lines show the mean fields for the period of 2006–2019, respectively. Areas where the trend is not of 95% significance are stippled. Please note, positive trend of MLD refers to a deepening of the mixed layer. Shelf regions below 2,000 dbar are blanked out.

time period (**Figure 9A**). The time series indicate a steady upward displacement of the three isopycnals. However, the height difference between the isopycnals changes differently (**Figure 9A**). This is especially visible from the slope of the corresponding trend lines (**Figure 9A**). We find that in the depth range of the largest stratification increase, the isopycnals surfaces 25.5 and 26.0 kg m^{-3} are becoming closer to each other. Whereas below, the height difference between the 26.0 and the 26.5 kg m^{-3} enlarges. This is the same depth range where stratification weakens.

Decadal Wind Stress Changes in Southeastern Tropical Atlantic Ocean Region

In this section we contrast the prior findings of the decadal changes in the SETA region with changes of the wind stress curl, zonal and meridional wind stress components as well as wind speed. Starting with the decadal trend maps of these four variables in the eastern tropical Atlantic to achieve an overview (**Figure 10**), we discover that close to the African coast in the South Atlantic east of the mean zero-line, the wind stress curl reveals a negative trend. This implies the wind stress curl in this region is becoming more negative. West of the zero-line the wind stress curl anomaly shows a positive trend (**Figure 10A**).

The decadal trend of the wind speed anomaly shows an increase in the southern part of SETA, whereas in the northern part of SETA and around SETA the trend of wind speed is negative (**Figure 10B**). Comparing this to the zonal wind stress component, we find a negative trend in the area of intensified wind speed in SETA, i.e., intensified easterlies. The positive trend is surrounded by westerly trend. The meridional wind stress component which is on average directed northward in the SETA region depicts a negative trend in the northern part of this region, thus, indicating a weakening of southerly winds. In the southern part of SETA, the wind stress anomaly shows a slight increase of the northward component (**Figure 10D**).

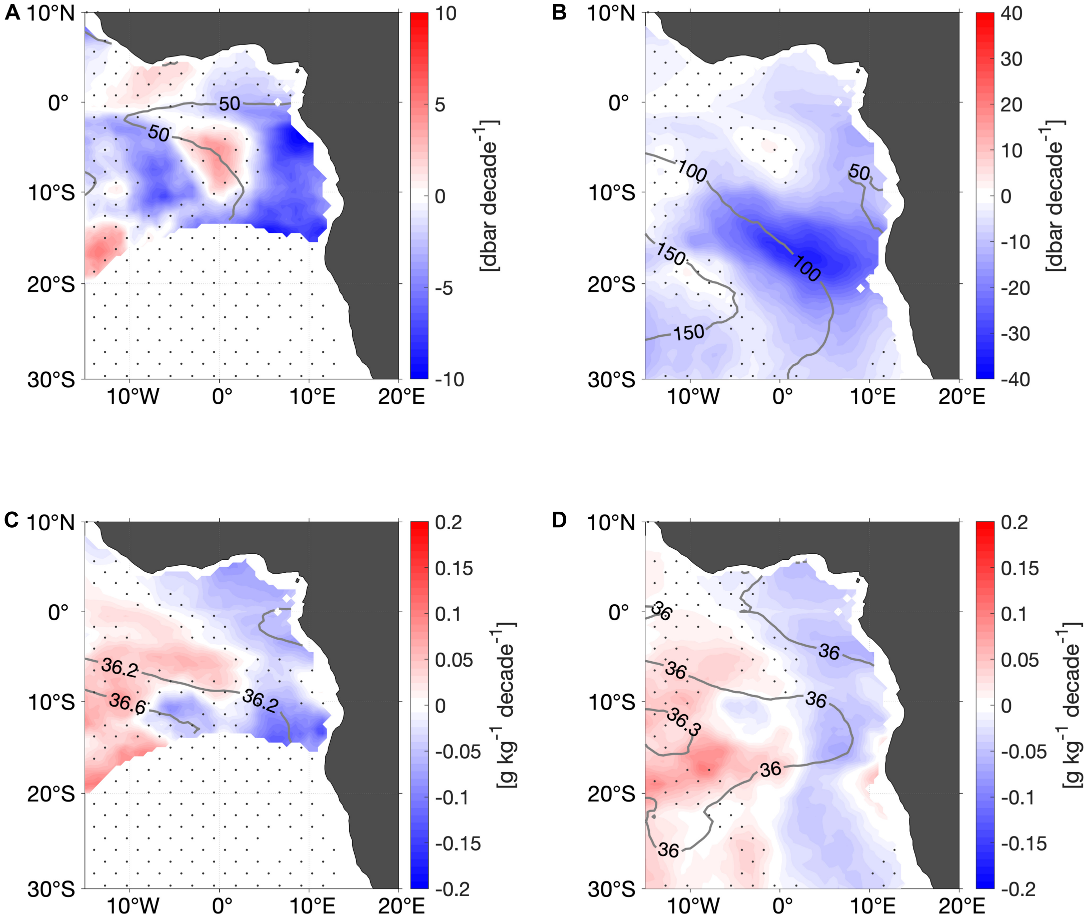

FIGURE 6 | Decadal trend of pressure of the isopycnal surfaces **(A)** 25.5 kg m^{-3} and **(B)** 26.0 kg m^{-3} and decadal trend of absolute salinity on the isopycnal surfaces **(C)** 25.5 kg m^{-3} and **(D)** 26.0 kg m^{-3} from Argo for the time period of 2006–2019. Trends are computed from the anomalies relative to the seasonal mean. Gray contour lines show the mean fields on each isopycnal surface for the time period of 2006–2019. Areas where the trend is not of 95% significance are stippled. Please note, positive trend of pressure of isopycnals surfaces refers to a deepening of the isopycnals. Shelf regions below 2,000 dbar are blanked out.

Focusing on the wind stress curl and the meridional wind stress component, the zonal sections of the 6 months running mean of the two components in the SETA region, show that indeed within 500 km of the coast the wind stress curl becomes more negative. In contrast, since 2009 meridional wind stress anomalies shift from northward to southward anomalies within about 200 km of the coast. Since 2017 again more northward anomalies are observed (**Figure 11**).

Analysis of Latent Heat Fluxes, Evaporation and Specific Humidity

In order to investigate a possible forcing of the observed mixed layer changes, in this section decadal trends of latent heat flux, precipitation, specific humidity and evaporation are evaluated for the eastern tropical Atlantic. It is important to point out that the latent heat flux and specific humidity differ substantially among the two analyzed products.

The trend of OAFlux latent heat flux shows positive values in almost the entire eastern tropical Atlantic, i.e., the oceanic latent heat loss is reduced (**Figure 12a**). Only a region around 10°S, 10°W shows an increase in oceanic latent heat loss as well as an area south of 20°S close to the Namibian coast. Accordingly, decreasing evaporation trends are observed where latent heat loss is reduced (**Figure 12c**). Contrary, oceanic latent heat loss from TropFlux shows an increase south of 5°S away from the coast. North of 5°S including the Gulf of Guinea and along the coast the latent heat loss is decreasing (**Figure 12d**).

In addition, the trend of specific humidity of OAFlux reveals increasing humidity in the equatorial region while south of that region humidity is found to be reduced. Southward from 15°S humidity increases again (**Figure 12b**). For the TropFlux product humidity increases in the Gulf of Guinea and within the coastal regions extending southward to about 10°S (**Figure 12e**). The reduction of specific humidity is spatially larger than in OAFlux and even reaches up to 25–30°S. These differences among OAFlux and TropFlux highlight the uncertainties in the heat flux trends.

Besides, GPCP precipitation trend demonstrates a decline of precipitation in the area of the equatorial region, while slightly

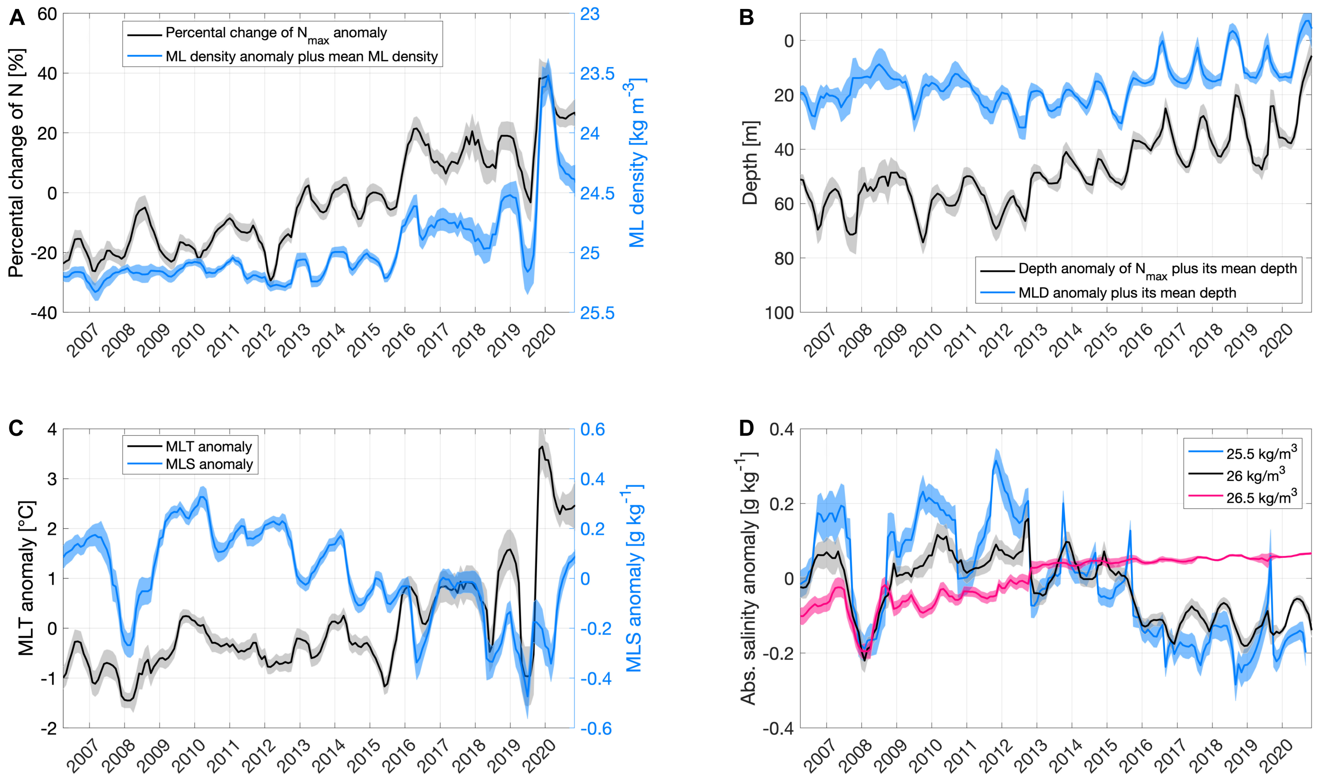

FIGURE 7 | Six months running median of **(A)** percental change of stratification anomaly of its vertical maximum N_{max} (black line, left *y*-axis) and mixed layer (ML) density anomaly plus mean ML density (blue line, right *y*-axis), **(B)** depth anomaly of the vertical stratification maximum plus its mean depth (black line, left *y*-axis) and mixed layer depth (MLD) anomaly plus mean MLD (blue line, right *y*-axis), **(C)** mixed layer temperature (MLT) anomaly (black line, left *y*-axis) and mixed layer salinity (MLS) anomaly (blue line, right *y*-axis) and **(D)** salinity anomaly on the isopycnal surfaces (i.e., spice anomaly) in SETA (10–20°S, 5°W–15°E). In **(D)** blue line denotes the 25.5 kg m^{-3} isopycnal, black line the 26.0 kg m^{-3} isopycnal and pink line the 26.5 kg m^{-3} isopycnal. All anomalies are computed relative to the seasonal mean. Shading shows the corresponding 95% confidence interval.

south of it the precipitation increases (**Figure 12f**). The Congo drainage basin reveals intensified precipitation rates.

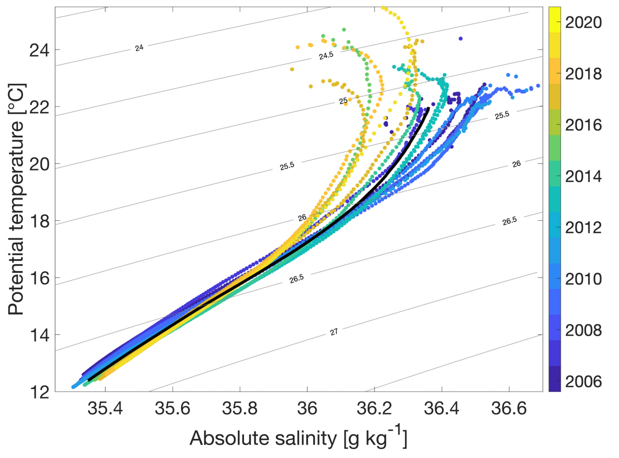

FIGURE 8 | T-S diagram of annual mean potential temperature and absolute salinity values of the upper 200 m in the SETA region (10–20°S, 5°W–15°E). Black line indicates the mean of the time period of 2006–2020.

Primary Production

The SETA upwelling system is a key region of enhanced nutrient supply to the euphotic zone that fuels local primary productivity. This section contrasts the observed signals in stratification with rates of net primary production derived from satellite observations.

The mean field of net primary production for the period of 2006–2019 shows elevated values especially within the eastern boundary regions and in the equatorial upwelling region (**Figure 13A**). The decadal trend pattern from the time series reveals that primary productivity in open ocean is increasing around 5–10% per decade almost everywhere in the eastern tropical Atlantic (**Figure 13A**). Specifically, in the SETA region primary production is intensifying as well (**Figure 13A**). North of the SETA region primary production depicts a small decreasing trend. The overall trend pattern correlates with the trend of the vertical stratification maximum except from the equatorial region, i.e., in general there is higher productivity in regions with enhanced stratification and shoaling stratification maximum (cf. **Figures 4C,D, 13A**).

Taking a closer look at the 6 months running median percental change of the net primary production in the SETA region, the time series of the median shows a maximum of above

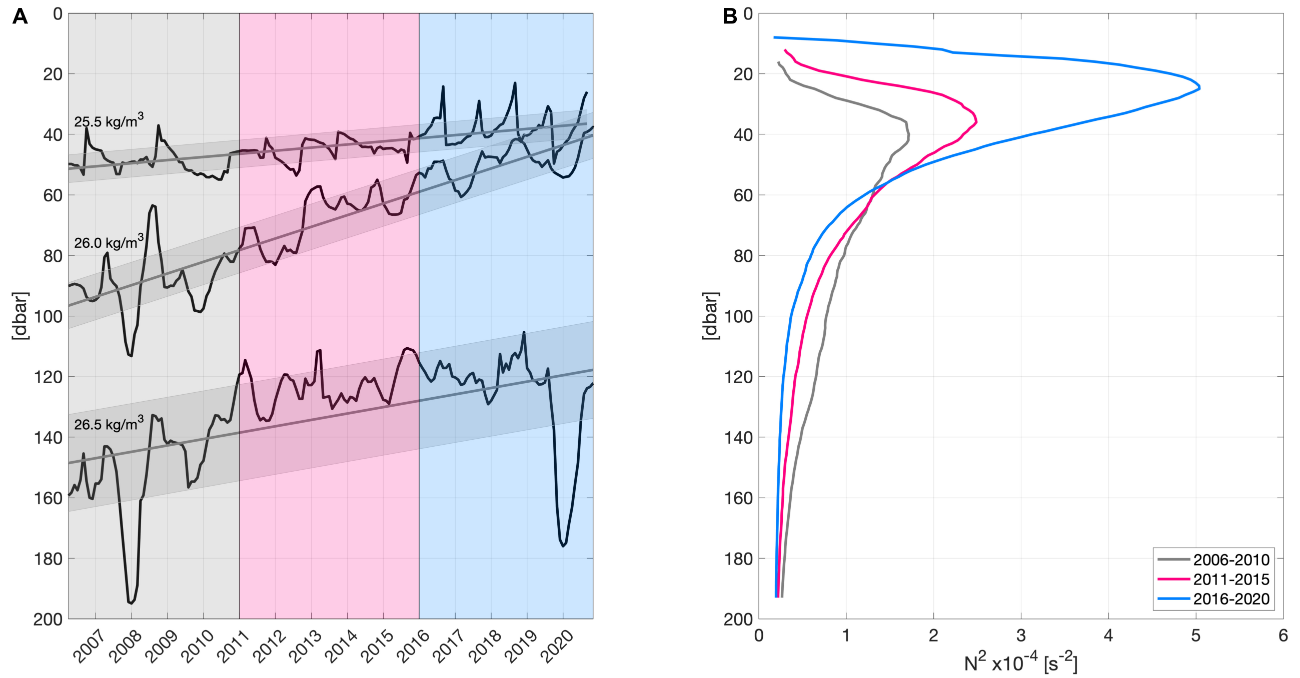

FIGURE 9 | (A) Six months running median pressure anomaly of three isopycnals (25.5, 26.0, and 26.5 kg m^{-3}) plus their corresponding mean pressure in the SETA region (10–20°S, 5°W–15°E). For each isopycnal the linear trend (gray line) and its standard error are shown (gray shading around the linear trend lines). Shaded areas indicate the time periods for the corresponding mean Brunt–Väisälä frequency profile of the upper 200 dbar in **(B)**. Gray shows the mean for the time of 2006–2010, pink denotes the mean of 2011–2015 and blue indicates the period of 2016–2020.

30% primary production in 2010 (**Figure 13B**). Except from this maximum the primary productivity seems to increase in the SETA region. For the years 2012–2019 the productivity is continuously enhancing (**Figure 13B**).

DISCUSSION

Physical Processes Leading to the Observed Stratification Changes

The findings of this study highlight locally large stratification increases within the upper 200 m in the tropical Atlantic Ocean for the Argo observation period of 2006–2019. Especially within the SETA region (10–20°S, 5°W–15°E) we observe an almost 60% intensification of the vertical stratification maximum from 2006 to 2020. This enhanced stratification is related to a warming, freshening and shoaling of the mixed layer. It represents a shift from subtropical stratification with salinity maximum water at the top toward a tropical stratification with warm and fresh surface waters (**Figure 8**). Mixed layer characteristics in the SETA region steadily change over time, i.e., changes are not confined to some single years. We observe a continuous warming of the mixed layer of 3°C during the years of 2006–2018 as well as a freshening of more than 0.5 g kg^{-1} from 2009 to 2020 (**Figure 7**). The MLT timeseries revealed a substantial temperature drop in 2019 which was followed by a warm mixed layer event at the end of the year (**Figure 7**). The negative MLT anomaly might be a result of an uneven distribution of the Argo profiles. The warm event in the beginning of 2020 can be associated to a Benguela Niño according to the classification given in Imbol Koungue et al. (2019).

Following the method of Bindoff and McDougall (1994) a pure warming or a pure freshening at a fixed depth for a typical subtropical stratification, as in the SETA region identified, should be the vector summation of negative spice and positive heave. Indeed, we observe the decline of spice on the isopycnals surrounding the vertical stratification maximum (**Figure 7D**). Yet, the isopycnals are rising (implying a negative heave, **Figure 9A**) and not deepening as anticipated for a pure warming or freshening process. Maximum upwelling of the isopycnals is observed about 10° offshore in the SETA region (**Figure 6**). Hence, another process has to be involved in the stratification increase. Wind stress curl-driven changes can lead to pure heaving (i.e., vertical adjustment of isopycnals) which is not associated with signatures in the T-S diagram (Bindoff and McDougall, 1994; Huang, 2015). In fact, we found an already negative wind stress curl becoming more negative in the SETA region, i.e., wind curl-driven upwelling is favored. As upwelling intensifies, isopycnals slope upward just as the time series show (**Figure 9A**). This suggests that the wind curl-driven upwelling is superimposed onto the pure warming and freshening processes discovered in the mixed layer and is obviously having a larger effect on the vertical displacement of the isopycnals. Besides, the heave mechanism does not contradict the stratification increase. The upper isopycnals are rising and

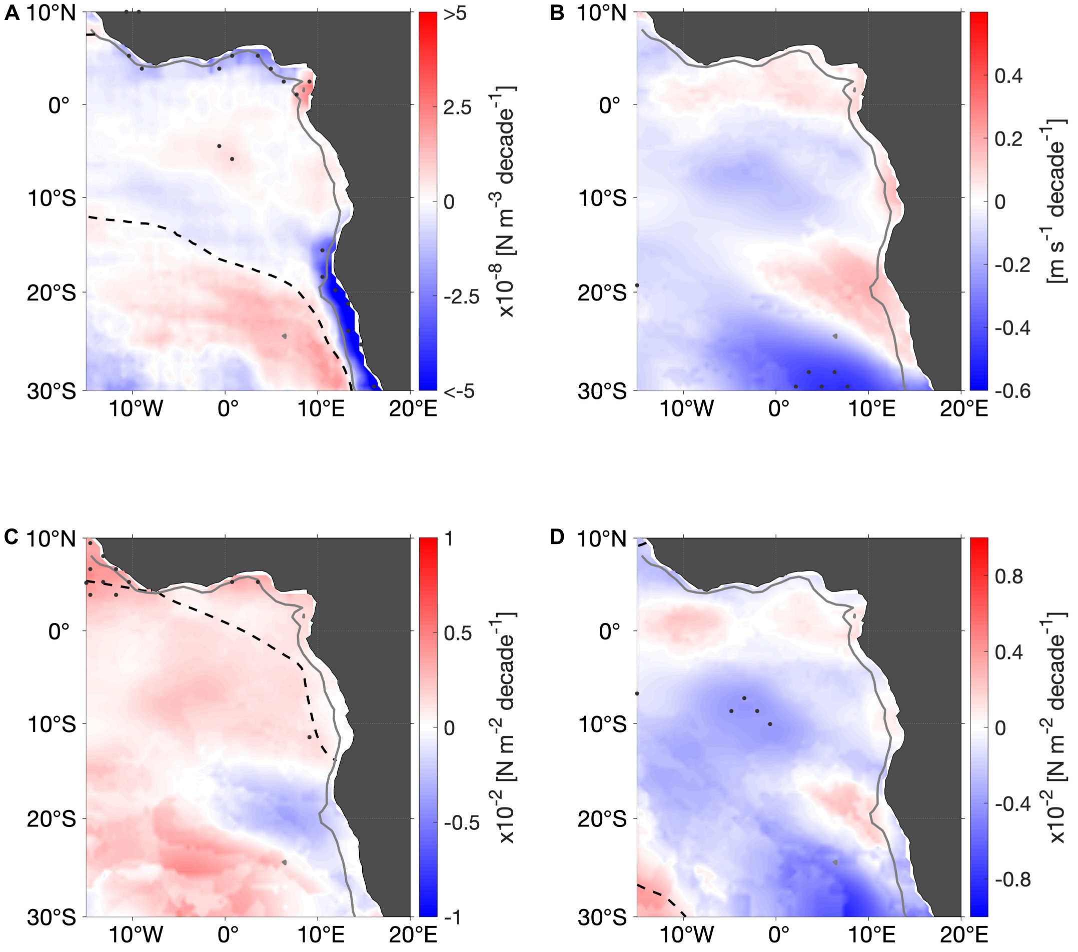

FIGURE 10 | Decadal trend of **(A)** wind stress curl, **(B)** wind speed, **(C)** zonal wind stress component, and **(D)** meridional wind stress component from monthly values from Copernicus Marine environment monitoring service (CMEMS) from ASCAT scatterometers on METOP-A and METOP-B satellites for the time period of 2007–2019. Trends are computed from the anomaly relative to the monthly mean. Black dashed lines indicate the zero-lines of the corresponding mean fields, respectively. Areas where the trend is of 95% significance are stippled. Gray line marks the 2,000 dbar isobath of the shelf regions.

thereby the distance between the 25.5 and the 26.0 kg m^{-3} is reducing and correspondingly the Brunt–Väisälä frequency is increasing (**Figure 9**). For the 26.5 kg m^{-3} isopycnal different processes seem to be involved. This deeper isopycnal is shoaling too, however, the distance between the 26.0 and the 26.5 kg m^{-3} isopycnals is becoming larger. Furthermore, the spice on the 26.5 kg m^{-3} isopycnal is slightly increasing (**Figure 7**). This indicates that stratification changes do not happen constantly at all depth levels which is confirmed by the T-S diagram with annual mean profiles of temperature and salinity (**Figure 8**) and by the mean Brunt–Väisälä frequency profiles for three different time periods (**Figure 9B**). At deeper levels (at the depth around the 26.5 kg m^{-3} isopycnal) the stratification is decreasing slightly (**Figure 9**).

Partly in contrast to the above noted findings related to the wind stress curl is that the meridional wind stress shows a shift from northward to southward anomalies within 200 km of the coast. This implies downwelling favorable conditions close to coast. However, southward wind stress anomalies could result in an increasing southward extent of near-equatorial surface waters approaching the SETA region and thereby altering the primarily subtropical stratification in the SETA region to more tropical conditions. In addition, we can compare the decadal trend pattern of wind speed and zonal wind stress, where the southern part of the SETA region reveals a slight intensification of the southeast trades. However, this area is surrounded by a westerly (positive) zonal wind stress trend, implying a weakening of the trades. Overall, it seems that the SASH is moving or extending poleward and thereby changing the prevailing winds near the African coast (**Figure 11**). Indeed, Zilli et al. (2019) found the SASH is extending further southwestward in the period of 2005–2014 compared to 1979–1991. Their results indicate that the shift produces a cyclonic anomaly of the wind over the tropical South Atlantic. Hence, this fits well to our observation of negative wind stress curl anomaly in the SETA region. Associated with the change of the SASH, the BLLCJ might have been modified, too. According to Patricola and Chang (2017), the BLLCJ shows a large intraseasonal variability linked to the SASH.

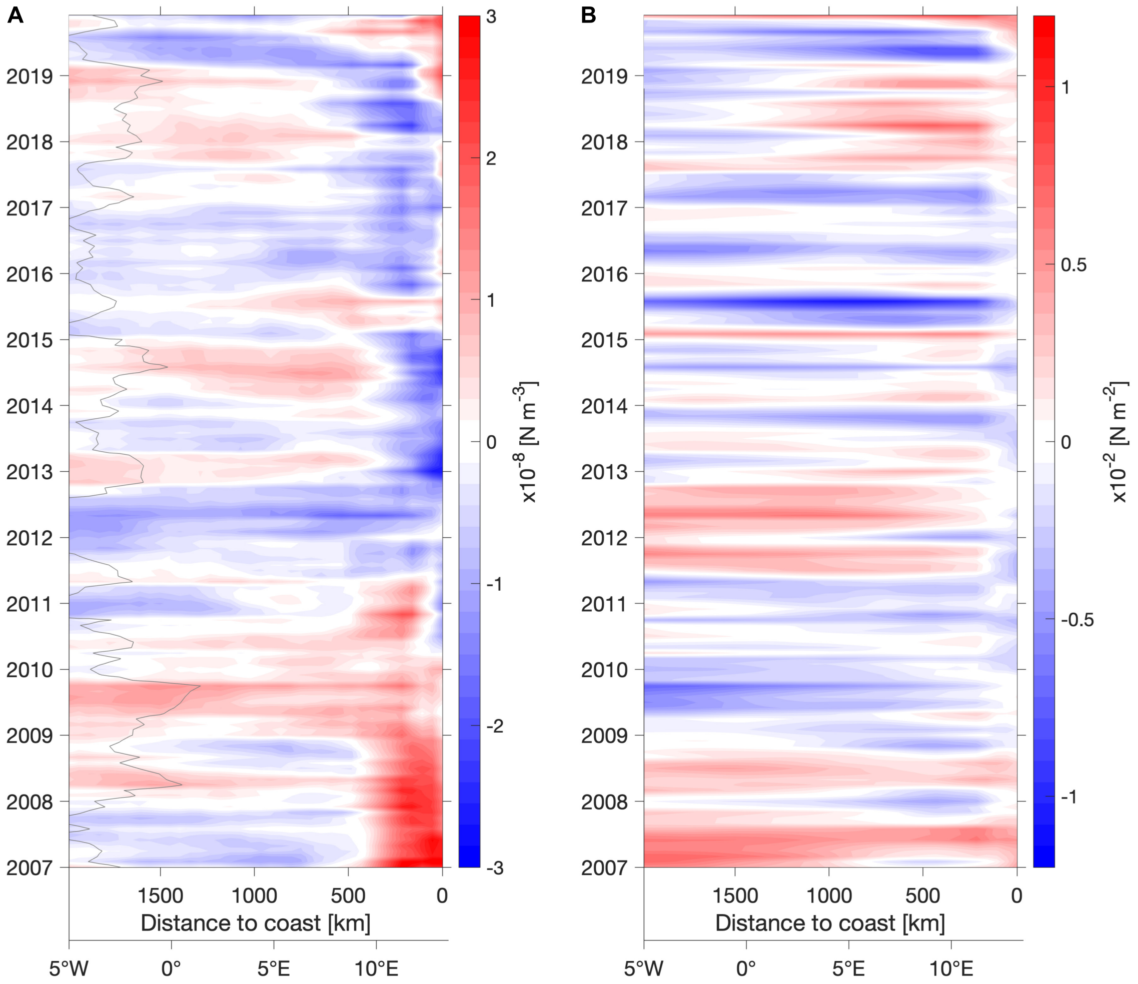

FIGURE 11 | Six months running mean of **(A)** wind stress curl anomaly and **(B)** meridional wind stress anomaly meridionally averaged in SETA (10–20°S, 5°W–15°E) as a function of distance to the coast (at about 13.5°E) and time as inferred from Copernicus Marine environment monitoring service. Anomalies are computed relative to the monthly mean of the period of 2007–2019. Gray contour line in **(A)** indicates the zero-line of the mean wind stress curl, i.e., east of this line the mean wind stress curl is negative while west of this line it is positive.

Intense jet events are found to be aligned with a strengthened SASH and increased equatorward meridional wind stress 5–10° offshore from the coast in the SETA region. Further offshore and to the north of this region, however, they found that the meridional wind stress is reduced. This pattern is similar to what our results show on decadal timescales and thus, indicates that during the observational period of our study the BLLCJ might have strengthened and led to the associated wind stress changes. In addition, future projections of Lima et al. (2019b) also show that as a result of global warming the SASH is going to intensify and therefore amplify the pressure gradient toward the Angolan low pressure. This is further associated with a poleward movement of the SASH and is assumed to cause a wind speed increase around 26°S whereas north of 17.5°S the wind speed is going to be reduced.

Nonetheless, careful attention must be taken with satellite wind products as they often do not represent coastal areas very well. The statistical significance test shows how uncertain these products are which is a problem for climatic studies. Despite this uncertainty, it is still important to point out that the isopycnals are continuously shoaling which has to be a result of intensified wind curl-driven upwelling. It indicates that the observed wind stress data has to be trustworthy to some extent.

Changes of the latent heat flux, evaporation and specific humidity strongly depend on the used product (**Figure 12**). Following the decadal trends from OAFlux, the freshening of the mixed layer could be associated with a decreased oceanic latent heat loss and thus, reduced evaporation. Conversely, latent heat flux and humidity trends from TropFlux actually indicate a decline in humidity in most of the tropical South Atlantic and increased oceanic latent heat loss. Only close to the coast and in the equatorial region the heat loss is reduced. This would rather be a sign for a salinification of the mixed layer. The large uncertainty of the heat flux products makes it difficult to interpret our findings of the mixed layer changes. Also, the test of significance mirrors the great uncertainty of these products.

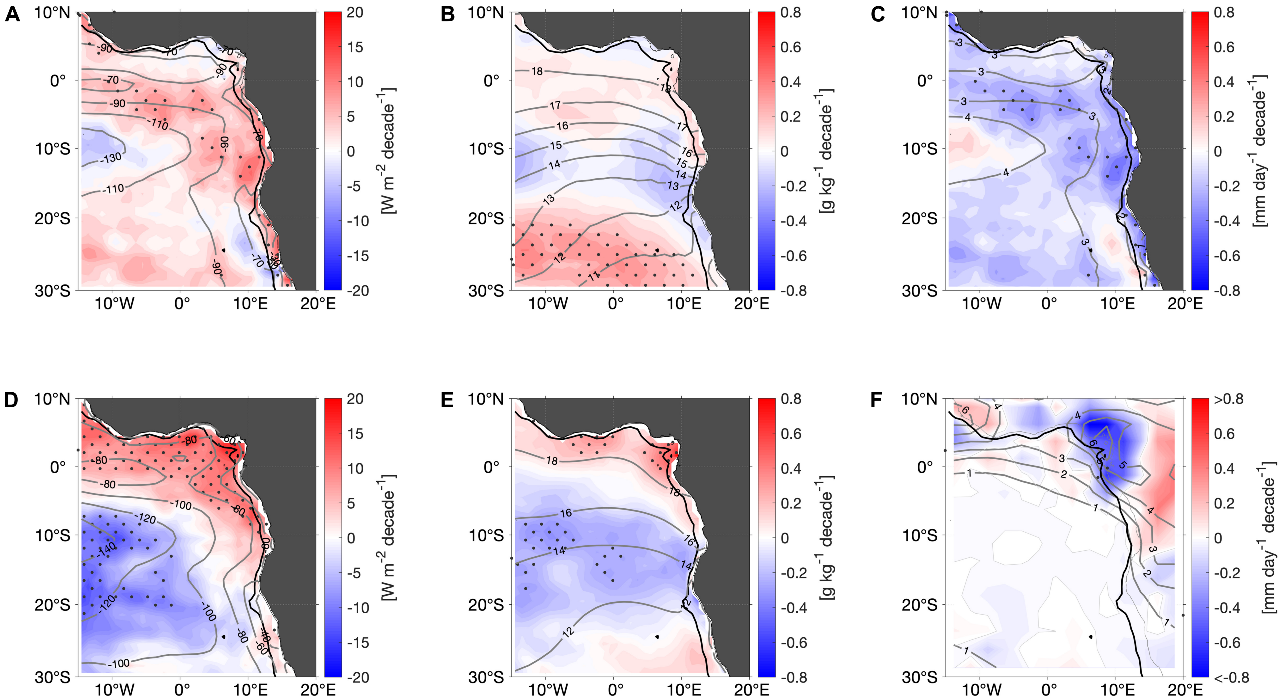

FIGURE 12 | Decadal trend of **(A)** latent heat flux anomaly, **(B)** specific humidity anomaly, and **(C)** evaporation anomaly from OAFlux data (2006–2019) and **(D)** latent heat flux anomaly and **(E)** specific humidity anomaly from TropFlux data (2006–2018) as well as **(F)** precipitation anomaly of GPCP data (2006–2019). All anomalies are computed relative to the corresponding monthly means. Note, a negative latent heat flux indicates that the ocean loses heat. Gray contour lines show the corresponding mean field. Areas where the trend is of 95% significance are stippled. Black line indicates the 2,000 dbar isobath of the shelf region.

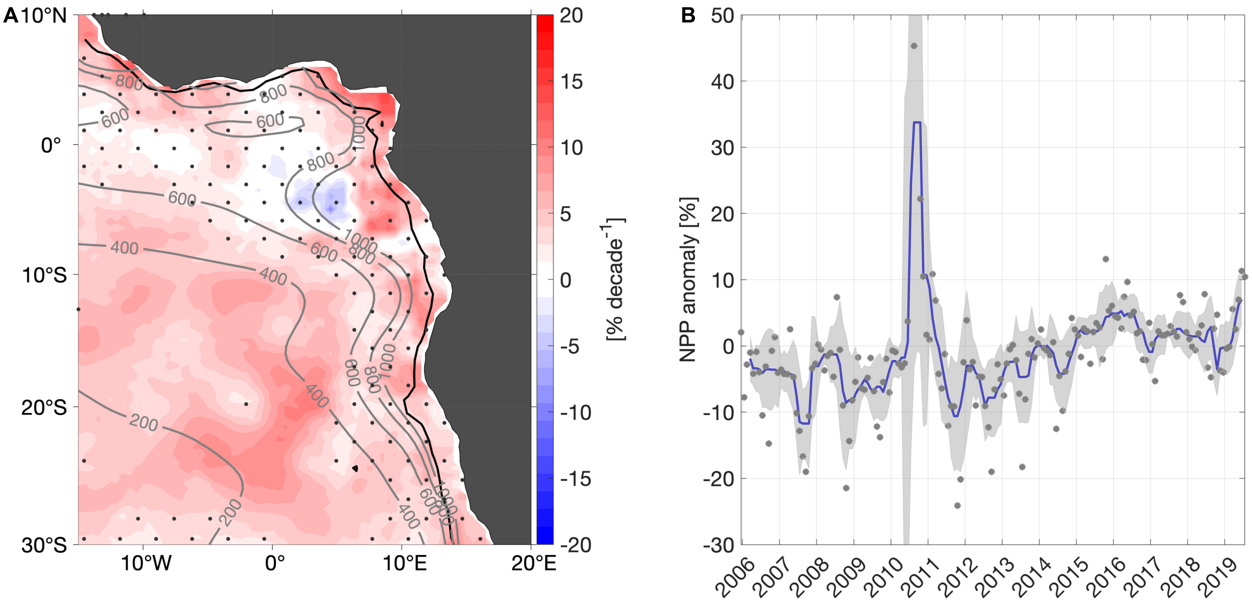

FIGURE 13 | (A) Decadal trend of net primary production (NPP) deduced from satellite observations from Ocean Productivity site for the time period of 2006–2019. The decadal trend has been evaluated from the anomalies relative to the corresponding monthly means. Areas where the trend is not of 95% significance are stippled. The gray contour lines in **(A)** show the mean NPP field. The black contour line indicates the 2,000 dbar isobath of the shelf region. **(B)** Six months running median NPP anomaly in SETA region (10–20°S, 5°W–15°E) in percent (blue line). Anomalies are computed to the monthly mean. Shading denotes the standard deviation and dots refer to the given monthly values from the product.

The GPCP precipitation data shows a rising trend in the drainage area of the Congo River. This might enhance river input and thus increase freshwater fluxes into the ocean. However, caution must be taken as precipitation data in the tropical regions is uncertain. In fact, different precipitation products show inconsistent variabilities in the tropical oceans (Sun et al., 2018 and references herein). The mean precipitation pattern is well-represented with GPCP data. Yet, there are large variations in regions with a small amount of gauge stations (Sun et al., 2018 and references herein). Besides, the significance analysis reveals barely anywhere significant trends. It is unfortunate that the meteorological data are so uncertain which makes it difficult to interpret and explain results from a climatic study like this one.

Despite the fact, that the Argo time series of the SETA region indicate mostly a steady increase or decline, we must be aware that there are uncertainties due to either an uneven distribution of the floats within the region as well as a minimum number of profiles in 2008. However, the time period of 2009–2018 shows an amount of 300 profiles and more per year allowing to achieve confident results.

As a matter of climate change, stratification is expected to increase due to the warming of ocean's surface (Capotondi et al., 2012). Yamaguchi and Suga (2019) and most recently Li et al. (2020) highlighted the continuous enhancement of the stratification in the global oceans since the 1960s with largest impacts within the upper 200 m in the tropics. Comparing their global results to our findings of the last 13 years, does not yield guarantee that the increased stratification in the SETA region is a result of the on-going global warming. Probably, the much larger trends in the SETA region compared to the global trends suggest still internal climate variability as the main reason. However, also a poleward migration of the SASH that could be forced by climate warming would contribute to enhanced warming. Thus, also the superposition of different climate-warming induced processes could result in the observed regionally enhanced trends.

Comparison of Stratification and Mixed Layer Changes to Observations of Primary Productivity

Changes in the upper-ocean stratification matter as they affect not only physical ocean dynamics such as ocean ventilation processes but also biogeochemical and ecological activities such as nutrient fluxes and fisheries. Nevertheless, the consequences of increased stratification for upwelling regions are not yet fully understood (Jarre et al., 2015). The SETA upwelling system is a key region for enhanced nutrient supply to the euphotic zone and hence, a core nutrient source for high coastal primary productivity. The nutricline is just below the mixed layer depth and within the depth range of the vertical stratification maximum in this region. The location of the nutricline was checked from individual profiles (Schlitzer, 2021). The common assumption is that increased stratification as a result of global warming will weaken mixing processes that are responsible for the upward nutrient flux to the surface waters and thereby reducing the primary production (Capotondi et al., 2012). In contradiction, our findings reveal that the net primary productivity is actually rising since 2012 in the SETA region and thereby correlating with the increase in stratification but also warming, freshening and shoaling of the mixed layer as well as the depth of the stratification maximum. In fact, this fits to enhanced observed long-term trends of chlorophyll-a data off Angola and northern Benguela recently reported by Lamont et al. (2019). Additionally, Jarre et al. (2015) discussed increased chlorophyll-a in Northern Benguela from 2006 to 2010 which was found along with a warming of the sea surface and decreased coastal upwelling. They assume that the upwelling was still in favor for primary productivity and anomalous downwelling not strong enough to suppress mixing. Actually, our findings for the SETA region indicate increased wind curl-driven upwelling associated with shoaling depths of the stratification maximum and the mixed layer. This process could instead enhance the nutrient supply into the euphotic zone and could thus explain the rising rates of primary productivity in recent years.

Furthermore, given that except from the equatorial region the trends of primary production and stratification seem to coincide, this highlights the uncertainties and lack of understanding that we are still dealing with concerning the linkage between stratification and primary production. In fact, Lozier et al. (2011) identified that there exists a direct relationship between stratification and primary productivity on seasonal time scales. Nevertheless, they concluded that on longer time scales the two variables cannot be linked so easily anymore.

Our time series shows an outstanding event in 2010 of above 30% increase of primary productivity. According to Bachèlery et al. (2016), interannual variations in biogeochemistry (such as nitrate and oxygen) off Angola, Namibia and Benguela are mainly generated by remote equatorial forcing due to CTWs. These variations of nitrate and oxygen have a large influence on the chlorophyll and primary productivity. Indeed, Bachèlery et al. (2016) state that off Angola these events are responsible for up to 30% of the mean primary productivity. Hence, such an event could have contributed to this large maximum in primary productivity in 2010. An indicator for this could be the cold event in 2010 prior to the Benguela Niño in 2011 (Imbol Koungue et al., 2019). However, this is something we cannot prove with Argo observations as they are not able to represent CTWs.

Given that the net primary productivity data is based on a satellite product, the findings should be treated with caution. Satellite products of primary production are based on empirical models as from Behrenfeld and Falkowski (1997) and are no direct measurement. These models use satellite measurements of chlorophyll and SST. Satellites only measure the surface layer (Robinson, 2010). Hence, we do not know about the primary productivity at greater depth or if there is a vertical shift of biomass. There might be a compression of the primary productivity near the surface in case of thinner mixed layers, which would be better visible in satellite data. Nevertheless, compared to situations with thicker mixed layers, this could still imply a reduction of vertically integrated primary productivity.

Possible Implications for the Pelagic Fishes

Understanding the consequences of enhanced stratification on primary productivity is key as this will have further impact on the marine food web. In fact, small pelagic fishes are sensitive to climate variability (Bakun et al., 2015; López-Parages et al., 2020; Peck et al., 2021). For instance, variations in temperature and food availability can lead to migrations of small pelagic fishes and to changes of their behavior (Brochier et al., 2018; López-Parages et al., 2020). Our observed stratification transition from subtropical to tropical conditions associated with a warmer mixed layer is likely to impact the small pelagic fishes in the SETA region. We now propose a hypothesis on the physics-to-fish relation in this region, in particular concerning the coexistence of the sardinellas *S. aurita* preferring the warm tropical waters north of the ABF and the sardines *S. sagax* favoring cooler temperatures south of the ABF (BCC, 2012). The two stocks migrate seasonally following their temperature and habitat preferences, with the SETA region being the preferred habitat for adult sardinella during austral summer (Boley and Fréon, 1980). As a result of the warming mixed layer and increasing stratification, the ABF is shifting southward. This gives the tropical sardinellas the possibility to migrate southward to stay within their best spawning and feeding environment on an all-year basis. There are indications that the tropical sardinellas of all age classes may have colonized this region during the recent decade. Indeed, Ekau et al. (2018) observed a southward shift of sardinella larvae from southern Angola to northern Namibia in the past few years. Ostrowski and Barradas (2018) reported the increasing incidence of juvenile sardinellas in trawl catches from this region during recent years. Additionally, the Benguela Current Convention (BCC, 2012) reported an increasing biomass of sardinellas off Angola and at the same time, a reduction of sardine biomass off Angola associated with a southward shift of the ABF. Sardinellas and sardines are in no feeding competition but they favor different hydrographic conditions. Besides the hydrographic parameters, there are other factors, such as the bathymetry, that impact the distribution of sardinellas and sardines which cannot be neglected.

To conclude, our results regarding the warming mixed layer and thereby stratification increase, suggest an evolution from sardine to sardinella habitat in the SETA region. Therefore, fishermen will have to adapt to new circumstances which probably will lead to economic consequences. According to Bearak and Mooney (2019), six to seven species off Angola have almost disappeared in recent years from fishermens' catches in the SETA waters, leading to substantial disturbances for the fishing industry of Southern Angola.

CONCLUSION

To summarize, this study gives an insight about recent stratification increase related to a change from subtropical toward tropical conditions in the SETA upwelling region. This is associated with mixed layer warming and freshening as well as intensified wind stress curl-driven upwelling. The impact on biological processes is still lacking of knowledge. Nevertheless, this study indicates, that the relationship between stratification and primary production is not that straight forward as previously thought. In contrast to climate projections, the satellite-derived primary production shows an increasing trend, which, however, remains to be verified by *in situ* data.

DATA AVAILABILITY STATEMENT

Publicly available datasets were analyzed in this study. This data can be found here: Argo (2019). Argo float data and metadata from Global Data Assembly Centre (Argo GDAC) – Snapshot of Argo GDAC of November 13th 2019. SEANOE. https://doi.org/10.17882/42182#68322; Argo (2020). Argo float data and metadata from Global Data Assembly Centre (Argo GDAC) – Snapshot of Argo GDAC of November 25th 2020. SEANOE. https://doi.org/10.17882/42182#78698; Brandt, Peter, Hahn, Johannes, Schmidtko, Sunke, Tuchen, Franz Philip, Kopte, Robert, Kiko, Rainer, Bourlès, Bernard, Czeschel, Rena, and Dengler, Marcus. (2021). Data and scripts used in "Atlantic Equatorial Undercurrent intensification counteracting warming induced deoxygenation" (Version 2) [Data set]. Zenodo. https://doi.org/10.5281/zenodo.4478285; Climate Data Guide: GPCP (Monthly): Global Precipitation Climatology Project. https://climatedataguide.ucar.edu/climate-data/gpcp-monthly-global-precipitation-climatology-project; Ocean Productivity Site: http://orca.science.oregonstate.edu/1080.by.2160.monthly.hdf.eppley.m.chl.m.sst.php; TropFlux – Indian National Centre for Ocean Information Services: latent heat and specific humidity: https://incois.gov.in/tropflux/tf_products.jsp; WHOI OAFlux: latent heat, evaporation and specific humidity: https://oaflux.whoi.edu/data-access/; Wind TAC (2018): WIND_GLO_PHY_CLIMATE_L4_REP_012_003 – Global Ocean Wind L4 Reprocessed Monthly Mean Observations, E.U. Copernicus Marine Service Information. Available at: https://resources.marine.copernicus.eu/?option=com_csw&view=details&product_id=WIND_GLO_PHY_CLIMATE_L4_REP_012_003.

AUTHOR CONTRIBUTIONS

MR, PB, and SS designed the study and analyzed the data. MR and SS developed the method to obtain the Brunt–Väisälä frequency by using the Argo observation array. FVV and MO provided their expertise on small pelagic fishes and their habitat. MR drafted the manuscript. All authors contributed to the writing of the manuscript.

FUNDING

This study was supported by the EU H2020 TRIATLAS project under grant agreement 817578 and by the German Federal Ministry of Education and Research as part of the BANINO project (03F0795A).

ACKNOWLEDGMENTS

We acknowledge the WHOI OAFlux project (http://oaflux.whoi.edu) funded by NOAA Climate Observations and Monitoring (COM) program for providing the global ocean heat flux and evaporation products and TropFlux data which is produced under a collaboration between Laboratoire d'Océanographie et du climat : Expérimentations et Approches Numériques (LOCEAN) from Institut Pierre Simon Laplace (IPSL, Paris, France) and National Institute of Oceanography/CSIR (NIO, Goa, India), and supported by Institut de Recherche pour le Développement (IRD, France) for the heat flux product. TropFlux relies on data provided by the ECMWF Re-Analysis interim (ERA-I) and ISCCP projects. Additionally, we acknowledge the Climate Data Guide: GPCP (Monthly): Global Precipitation Climatology Project. Achieved from https://climatedataguide.ucar.edu/climate-data/gpcp-monthly-global-precipitation-climatology-project. Furthermore, this study has been conducted using E. U. Copernicus Marine Service Information for the wind stress product.

SUPPLEMENTARY MATERIAL

The Supplementary Material for this article can be found online at: https://www.frontiersin.org/articles/10.3389/fmars.2021.748383/full#supplementary-material

REFERENCES

Adler, R. F., Sapiano, M. R., Huffman, G. J., Wang, J. J., Gu, G., Bolvin, D., et al. (2018). The global precipitation climatology project (GPCP) monthly analysis (New Version 2.3) and a review of 2017 global precipitation. *Atmosphere* 9:138. doi: 10.3390/atmos9040138

Akima, H. (1970). A new method of interpolation and smooth curve fitting based on local procedures. *J. ACM* 17, 589–602. doi: 10.1145/321607.321609

Argo (2019). *Argo Float Data and Metadata From Global Data Assembly Centre (Argo GDAC) – Snapshot of Argo GDAC of November 13st 2019*. SEANOE. doi: 10.17882/42182#68322

Argo (2020). *Argo Float Data and Metadata From Global Data Assembly Centre (Argo GDAC) – Snapshot of Argo GDAC of November 25st 2020*. SEANOE. doi: 10.17882/42182#78698

Bachèlery, M. L., Illig, S., and Dadou, I. (2016). Forcings of nutrient, oxygen, and primary production interannual variability in the southeast Atlantic Ocean. *Geophys. Res. Lett.* 43, 8617–8625. doi: 10.1002/2016gl070288

Bakun, A., Black, B. A., Bograd, S. J., Garcia-Reyes, M., Miller, A. J., Rykaczewski, R. R., et al. (2015). Anticipated effects of climate change on coastal upwelling ecosystems. *Curr. Clim. Change Rep.* 1, 85–93. doi: 10.1007/s40641-015-0008-4

BCC (2012). *Benguela Current Commission: State of Stocks Report. Report No. 2.* Available online at: http://www.benguelacc.org/index.php/en/component/docman/doc_download/120-sos-report-2012-low (accessed April 19, 2021).

Bearak, M., and Mooney, C. (2019). *2°C Beyond the Limit. A Crisis in the Water is Decimating this Once-Booming Fishing Town*. Washington Post. Available online at: https://www.washingtonpost.com/graphics/2019/world/climate-environment/angola-climate-change/ (accessed January 13, 2021).

Behrenfeld, M. J., and Falkowski, P. G. (1997). Photosynthetic rates derived from satellite-based chlorophyll concentration. *Limnol. Oceanogr.* 42, 1–20.

Bentamy, A. (2020). *Product User Manual for Wind Product - WIND_GLO_PHY_CLIMATE_L4_REP_012_003, 1*, 2 Edn. E.U. Copernicus Marine Service Information. Available online at: https://resources.marine.copernicus.eu/documents/PUM/CMEMS-WIND-PUM-012-003.pdf (accessed May 5, 2021).

Bentamy, A., and Fillon, D. C. (2012). Gridded surface wind fields from Metop/ASCAT measurements. *Int. J. Remote Sens.* 33, 1729–1754. doi: 10.1080/01431161.2011.600348

Bindoff, N. L., and McDougall, T. J. (1994). Diagnosing climate change and ocean ventilation using hydrographic data. *J. Phys. Oceanogr.* 24, 1137–1152. doi: 10.1175/1520-0485(1994)024<1137:dccaov>2.0.co;2

Boley, T., and Fréon, P. (1980). "Coastal pelagic resources," in *The Fish Resources of the Eastern Central Atlantic. Part One: The Resources of the Gulf of Guinea from Angola to Mauritania. FAO Fisheries Technical Paper No. 186.1*, eds J. P. Troadec, and S. Garcia (Rome: FAO), 13–76.

Brandt, P., Hahn, J., Schmidtko, S., Tuchen, F. P., Kopte, R., Kiko, R., et al. (2021). Atlantic Equatorial Undercurrent intensification counteracting warming induced deoxygenation. *Nat. Geosci.* 14, 278–282. doi: 10.1038/s41561-021-00716-1

Brochier, T., Auger, P. A., Pecquerie, L., Machu, E., Capet, X., Thiaw, M., et al. (2018). Complex small pelagic fish population patterns arising from individual behavioral responses to their environment. *Prog. Oceanogr.* 164, 12–27. doi: 10.1016/j.pocean.2018.03.011

Capotondi, A., Alexander, M. A., Bond, N. A., Curchitser, E. N., and Scott, J. D. (2012). Enhanced upper ocean stratification with climate change in the CMIP3 models. *J. Geophys. Res. Oceans* 117, 1–23. doi: 10.1029/2011JC007409

Clément, L., McDonagh, E. L., Marzocchi, A., and Nurser, A. J. (2020). Signature of ocean warming at the mixed layer base. *Geophys. Res. Lett.* 47, 1–10. doi: 10.1029/2019GL086269

Desbruyères, D., McDonagh, E. L., King, B. A., and Thierry, V. (2017). Global and full-depth ocean temperature trends during the early twenty-first century from Argo and repeat hydrography. *J. Clim.* 30, 1985–1997. doi: 10.1175/JCLI-D-16-0396.1

Ekau, W., Auel, H., Hagen, W., Koppelmann, R., Wasmund, N., Bohata, K., et al. (2018). Pelagic key species and mechanisms driving energy flows in the northern Benguela upwelling ecosystem and their feedback into biogeochemical cycles. *J. Mar. Syst.* 188, 49–62. doi: 10.1016/j.jmarsys.2018.03.001

Fennel, W., Junker, T., Schmidt, M., and Mohrholz, V. (2012). Response of the Benguela upwelling systems to spatial variations in the wind stress. *Cont. Shelf Res.* 45, 65–77. doi: 10.1016/j.csr.2012.06.004

Fennel, W., and Lass, H. U. (2007). On the impact of wind curls on coastal currents. *J. Mar. Syst.* 68, 128–142. doi: 10.1016/j.jmarsys.2006.11.004

Feucher, C. (2016). *Stratification Structure in Subtropical Gyres and its Decadal Variability in the North Atlantic Ocean.* Doctoral dissertation. Brest: Université de Bretagne Occidentale.

Florenchie, P., Reason, C. J. C., Lutjeharms, J. R. E., Rouault, M., Roy, C., and Masson, S. (2004). Evolution of interannual warm and cold events in the southeast Atlantic Ocean. *J. Clim.* 17, 2318–2334. doi: 10.1175/1520-0442(2004)017<2318:eoiwac>2.0.co;2

Gammelsrød, T., Bartholomae, C. H., Boyer, D. C., Filipe, V. L. L., and O'toole, M. J. (1998). Intrusion of warm surface water along the Angolan Namibian coast in February–March 1995: the 1995 Benguela Niño. *Afr. J. Mar. Sci.* 19, 41–56.

Häkkinen, S., Rhines, P. B., and Worthen, D. L. (2016). Warming of the global ocean: spatial structure and water-mass trends. *J. Clim.* 29, 4949–4963. doi: 10.1175/JCLI-D-15-0607.1

Holte, J., and Talley, L. (2009). A new algorithm for finding mixed layer depths with applications to Argo data and Subantarctic Mode Water formation. *J. Atmos. Ocean. Technol.* 26, 1920–1939. doi: 10.1175/2009JTECHO543.1

Huang, R. X. (2015). Heaving modes in the world oceans. *Clim. Dyn.* 45, 3563–3591. doi: 10.1007/s00382-015-2557-6

Imbol Koungue, R. A., and Brandt, P. (2021). Impact of intraseasonal waves on Angolan warm and cold events. *J. Geophys. Res. Oceans* 126:e2020JC017088. doi: 10.1029/2020JC017088

Imbol Koungue, R. A., Rouault, M., Illig, S., Brandt, P., and Jouanno, J. (2019). Benguela Niños and Benguela Niñas in forced ocean simulation from 1958 to 2015. *J. Geophys. Res. Oceans* 124, 5923–5951. doi: 10.1029/2019JC015013

Ito, T., Long, M. C., Deutsch, C., Minobe, S., and Sun, D. (2019). Mechanisms of low-frequency oxygen variability in the North Pacific. *Glob. Biogeochem. Cycles* 33, 110–124. doi: 10.1029/2018GB005987

Jarre, A., Hutchings, L., Kirkman, S. P., Kreiner, A., Tchipalanga, P. C. M., Kainge, P., et al. (2015). Synthesis: climate effects on biodiversity, abundance and distribution of marine organisms in the Benguela. *Fish. Oceanogr.* 24, 122–149. doi: 10.1111/fog.12086

Keeling, R. F., Körtzinger, A., and Gruber, N. (2010). Ocean deoxygenation in a warming world. *Annu. Rev. Mar. Sci.* 2, 199–229. doi: 10.1146/annurev.marine.010908.163855

Kopte, R., Brandt, P., Claus, M., Greatbatch, R. J., and Dengler, M. (2018). Role of equatorial basin-mode resonance for the seasonal variability of the Angola current at 11°S. *J. Phys. Oceanogr.* 48, 261–281. doi: 10.1175/jpo-d-17-0111.1

Kopte, R., Brandt, P., Dengler, M., Tchipalanga, P. C. M., Macuéria, M., and Ostrowski, M. (2017). The Angola current: flow and hydrographic characteristics as observed at 11°S. *J. Geophys. Res. Oceans* 122, 1177–1189. doi: 10.1002/2016jc012374

Lamont, T., Barlow, R. G., and Brewin, R. J. W. (2019). Long-term trends in phytoplankton chlorophyll a and size structure in the Benguela upwelling system. *J. Geophys. Res. Oceans* 124, 1170–1195. doi: 10.1029/2018JC014334

Li, G., Cheng, L., Zhu, J., Trenberth, K. E., Mann, M. E., and Abraham, J. P. (2020). Increasing ocean stratification over the past half-century. *Nat. Clim. Change* 10, 1116–1123. doi: 10.1038/s41558-020-00918-2

Lima, D. C., Soares, P. M., Semedo, A., Cardoso, R. M., Cabos, W., and Sein, D. V. (2019a). A climatological analysis of the Benguela coastal low-level jet. *J. Geophys. Res. Atmos.* 124, 3960–3978. doi: 10.1029/2018jd028944

Lima, D. C., Soares, P. M., Semedo, A., Cardoso, R. M., Cabos, W., and Sein, D. V. (2019b). How will a warming climate affect the Benguela coastal low-level wind jet? *J. Geophys. Res. Atmos.* 124, 5010–5028. doi: 10.1029/2018jd029574

López-Parages, J., Auger, P. A., Rodríguez-Fonseca, B., Keenlyside, N., Gaetan, C., Rubino, A., et al. (2020). El Niño as a predictor of round *Sardinella* distribution along the northwest African coast. *Prog. Oceanogr.* 186:102341. doi: 10.1016/j.pocean.2020.102341

Lozier, M. S., Dave, A. C., Palter, J. B., Gerber, L. M., and Barber, R. T. (2011). On the relationship between stratification and primary productivity in the North Atlantic. *Geophys. Res. Lett.* 38:L18609. doi: 10.1029/2011GL049414

Lübbecke, J. F., Böning, C. W., Keenlyside, N. S., and Xie, S. P. (2010). On the connection between Benguela and equatorial Atlantic Niños and the role of the South Atlantic Anticyclone. *J. Geophys. Res. Oceans* 115:C09015. doi: 10.1029/2009JC005964

Lübbecke, J. F., Brandt, P., Dengler, M., Kopte, R., Lüdke, J., Richter, I., et al. (2019). Causes and evolution of the southeastern tropical Atlantic warm event in early 2016. *Clim. Dyn.* 53, 261–274. doi: 10.1007/s00382-018-4582-8

MathWorks, Inc (2019). *Help Center: Makima*. Natick, MA. Available online at: https://de.mathworks.com/help/matlab/ref/makima.html (accessed June 25, 2021).

MATLAB (2019). *9.7.0.1190202 (R2019b)*. Natick, MA: The MathWorks Inc.

McDougall, T. J., and Barker, P. M. (2011). *Getting Started with TEOS-10 and the Gibbs Seawater (GSW) Oceanographic Toolbox, SCOR/IAPSO WG127*. 28. Available online at: www.TEOS-10.org

Ostrowski, M., and Barradas, A. (2018). *Report on the Evolution of the Angolan sardinella Stock in Relation to the Seasonal Coastally Trapped Waves Climatology and Interannual Equatorial Events 1994-2014, Extended Abstract, 2 pp., in PREFACE Deliverable D12.4, "Climate Variability and Pelagic Fish"*, 26. Available online at: https://preface.w.uib.no/files/2018/11/PREFACE-D12.4-final-20180501.pdf (accessed June 30, 2021).

Ostrowski, M., Da Silva, J. C., and Bazik-Sangolay, B. (2009). The response of sound scatterers to El Niño-and La Niña-like oceanographic regimes in the southeastern Atlantic. *ICES J. Mar. Sci.* 66, 1063–1072. doi: 10.1093/icesjms/fsp102

Patricola, C. M., and Chang, P. (2017). Structure and dynamics of the Benguela low-level coastal jet. *Clim. Dyn.* 49, 2765–2788. doi: 10.1007/s00382-016-3479-7

Peck, M. A., Alheit, J., Bertrand, A., Catalán, I. A., Garrido, S., Moyano, M., et al. (2021). Small pelagic fish in the new millennium: a bottom-up view of global research effort. *Prog. Oceanogr.* 191:102494. doi: 10.1016/j.pocean.2020.102494

Pendergrass, A., Wang, J.-J., and National Center for Atmospheric Research Staff (2020). *The Climate Data Guide: GPCP (Monthly): Global Precipitation Climatology Project*. Available online at: https://climatedataguide.ucar.edu/climate-data/gpcp-monthly-global-precipitation-climatology-project (accessed November 06, 2020).

Peterson, R. G., and Stramma, L. (1991). Upper-level circulation in the South Atlantic Ocean. *Prog. Oceanogr.* 26, 1–73. doi: 10.1016/0079-6611(91)90006-8

Potts, W. M., Henriques, R., Santos, C. V., Munnik, K., Ansorge, I., Dufois, F., et al. (2014). Ocean warming, a rapid distributional shift, and the hybridization of a coastal fish species. *Glob. Change Biol.* 20, 2765–2777. doi: 10.1111/gcb.12612

Praveen Kumar, B., Vialard, J., Lengaigne, M., Murty, V. S. N., and McPhaden, M. J. (2012). TropFlux: air-sea fluxes for the global tropical oceans—description and evaluation. *Clim. Dyn.* 38, 1521–1543. doi: 10.1007/s00382-011-1115-0

Rhein, M., Rintoul, S. R., Aoki, S., Campos, E., Chambers, D., Feely, R. A., et al. (2013). "Observations: ocean," in *Climate Change 2013: The Physical Science Basis. Contribution of Working Group I to the Fifth Assessment Report of the Intergovernmental Panel on Climate Change*, eds T. F. Stocker, D. Qin, G.-K. Plattner, M. Tignor, S. K. Allen, J. Boschung, et al. (Cambridge: Cambridge University Press).

Risien, C. M., Reason, C. J. C., Shillington, F. A., and Chelton, D. B. (2004). Variability in satellite winds over the Benguela upwelling system during 1999–2000. *J. Geophys. Res. Oceans* 109:C03010. doi: 10.1029/2003JC001880

Robinson, I. S. (2010) "Ocean biology from space," in *Discovering the Ocean from Space. Springer Praxis Books*, 1st Edn. ed. P. Blondel (Berlin: Springer), 255–267. doi: 10.1007/978-3-540-68322-3_7

Roemmich, D., Church, J., Gilson, J., Monselesan, D., Sutton, P., and Wijffels, S. (2015). Unabated planetary warming and its ocean structure since 2006. *Nat. Clim. Change* 5, 240–245. doi: 10.1038/nclimate2513

Rouault, M. (2012). Bi-annual intrusion of tropical water in the northern Benguela upwelling. *Geophys. Res. Lett.* 39:L12606. doi: 10.1029/2012GL052099

Rouault, M., Illig, S., Bartholomae, C., Reason, C. J. C., and Bentamy, A. (2007). Propagation and origin of warm anomalies in the Angola Benguela upwelling system in 2001. *J. Mar. Syst.* 68, 473–488. doi: 10.1016/j.jmarsys.2006.11.010

Rouault, M., Illig, S., Lübbecke, J., and Koungue, R. A. I. (2018). Origin, development and demise of the 2010–2011 Benguela Niño. *J. Mar. Syst.* 188, 39–48. doi: 10.1016/j.jmarsys.2017.07.007

Sallée, J.-B., Pellichero, V., Akhoudas, C., Pauthenet, E., Vignes, L., Schmidtko, S., et al. (2021). Summertime increases in upper-ocean stratification and mixed-layer depth. *Nature* 591, 592–598. doi: 10.1038/s41586-021-03303-x

Schlitzer, R. (2021). *Ocean Data View*. Available online at: odv.awi.de (acceseed September 06, 2021).

Shannon, L. V., Agenbag, J. J., and Buys, M. E. L. (1987). Large-and mesoscale features of the Angola-Benguela front. *S. Afr. J. Mar. Sci.* 5, 11–34. doi: 10.2989/025776187784522261

Shannon, L. V., Boyd, A. J., Brundrit, G. B., and Taunton-Clark, J. (1986). On the existence of an El Niño-type phenomenon in the Benguela system. *J. Mar. Res.* 44, 495–520.

Siegfried, L., Schmidt, M., Mohrholz, V., Pogrzeba, H., Nardini, P., Böttinger, M., et al. (2019). The tropical-subtropical coupling in the Southeast Atlantic from the perspective of the northern Benguela upwelling system. *PLoS One* 14:e0210083. doi: 10.1371/journal.pone.0210083

Somavilla, R., González-Pola, C., and Fernández-Diaz, J. (2017). The warmer the ocean surface, the shallower the mixed layer. how much of this is true? *J. Geophys. Res. Oceans* 122, 7698–7716. doi: 10.1002/2017JC013125

Sun, Q., Miao, C., Duan, Q., Ashouri, H., Sorooshian, S., and Hsu, K. L. (2018). A review of global precipitation data sets: data sources, estimation, and intercomparisons. *Rev. Geophys.* 56, 79–107. doi: 10.1002/2017RG000574

Tchipalanga, P., Dengler, M., Brandt, P., Kopte, R., Macuéria, M., Coelho, P., et al. (2018). Eastern boundary circulation and hydrography off Angola: building Angolan oceanographic capacities. *Bull. Am. Meteorol. Soc.* 99, 1589–1605. doi: 10.1175/bams-d-17-0197.1

Wind TAC (2018). *WIND_GLO_PHY_CLIMATE_L4_REP_012_003 - Global Ocean Wind L4 Reprocessed Monthly Mean Observations*. E.U. Copernicus Marine Service Information. Available online at:

https://resources.marine.copernicus.eu/?option=com_csw&view=details&product_id=WIND_GLO_PHY_CLIMATE_L4_REP_012_003 (accessed August 14, 2020).

Yamaguchi, R., and Suga, T. (2019). Trend and variability in global upper-ocean stratification since the 1960s. *J. Geophys. Res. Oceans* 124, 8933–8948. doi: 10.1029/2019JC015439

Yu, L., Jin, X., and Weller, R. A. (2008). *Multidecade Global Flux Datasets from the Objectively Analyzed Air-Sea Fluxes (OAFlux) Project: Latent and Sensible Heat Fluxes, Ocean Evaporation, and Related Sur- Face Meteorological Variables. OAFlux Project Technical Report. OA-2008-01*. Woods Hole, MA: Woods Hole Oceanographic Institution.

Zeng, Z., Brandt, P., Lamb, K. G., Greatbatch, R. J., Dengler, M., Claus, M., et al. (2021). Three-dimensional numerical simulations of internal tides in the Angolan upwelling region. *J. Geophys. Res. Oceans* 126:e2020JC016460. doi: 10.1029/2020JC016460

Zilli, M. T., Carvalho, L. M., and Lintner, B. R. (2019). The poleward shift of South Atlantic convergence zone in recent decades. *Clim. Dyn.* 52, 2545–2563. doi: 10.1007/s00382-018-4277-1

Conflict of Interest: The authors declare that the research was conducted in the absence of any commercial or financial relationships that could be construed as a potential conflict of interest.

frontiers
in Marine Science

ORIGINAL RESEARCH
published: 24 December 2021
doi: 10.3389/fmars.2021.800103

The 2019 Benguela Niño

Rodrigue Anicet Imbol Koungue[1]*, Peter Brandt[1,2], Joke Lübbecke[1,2], Arthur Prigent[1], Meike Sena Martins[3] and Regina R. Rodrigues[4]

[1] GEOMAR Helmholtz Centre for Ocean Research Kiel, Kiel, Germany, [2] Faculty of Mathematics and Natural Sciences, Christian-Albrechts-Universität zu Kiel, Kiel, Germany, [3] Center for Earth System Research and Sustainability, Institute of Oceanography, University of Hamburg, Hamburg, Germany, [4] Department of Oceanography, Federal University of Santa Catarina, Florianópolis, Brazil

High interannual sea surface temperature anomalies of more than 2°C were recorded along the coasts of Angola and Namibia between October 2019 and January 2020. This extreme coastal warm event that has been classified as a Benguela Niño, reached its peak amplitude in November 2019 in the Angola Benguela front region. In contrast to classical Benguela Niños, the 2019 Benguela Niño was generated by a combination of local and remote forcing. In September 2019, a local warming was triggered by positive anomalies of near coastal wind-stress curl leading to downwelling anomalies through Ekman dynamics off Southern Angola and by anomalously weak winds reducing the latent heat loss by the ocean south of 15°S. In addition, downwelling coastal trapped waves were observed along the African coast between mid-October 2019 and early January 2020. Those coastal trapped waves might have partly emanated from the equatorial Atlantic as westerly wind anomalies were observed in the central and eastern equatorial Atlantic between end of September to early December 2019. Additional forcing for the downwelling coastal trapped waves likely resulted from an observed weakening of the prevailing coastal southerly winds along the Angolan coast north of 15°S between October 2019 and mid-February 2020. During the peak of the event, latent heat flux damped the sea surface temperature anomalies mostly in the Angola Benguela front region. In the eastern equatorial Atlantic, relaxation of cross-equatorial southerly winds might have contributed to the equatorial warming in November 2019 during the peak of the 2019 Benguela Niño. Moreover, for the first time, moored velocities off Angola (11°S) revealed a coherent poleward flow in the upper 100 m in October and November 2019 suggesting a contribution of meridional heat advection to the near-surface warming during the early stages of the Benguela Niño. During the Benguela Niño, a reduction of net primary production in the Southern Angola and Angola Benguela front regions was observed.

Keywords: Benguela Niños, interannual variability, local atmospheric forcing, equatorial and coastally trapped waves, Angola Current

Edited by:
Zhiyu Liu,
Xiamen University, China

Reviewed by:
Yuanlong Li,
Institute of Oceanology, Chinese Academy of Sciences (CAS), China
Jin-Yi YU,
University of California, Irvine, United States

****Correspondence:***
Rodrigue Anicet Imbol Koungue
rodrigueanicet@gmail.com

Specialty section:
This article was submitted to Physical Oceanography, a section of the journal Frontiers in Marine Science

Received: *22 October 2021*
Accepted: *01 December 2021*
Published: *24 December 2021*

Citation:
Imbol Koungue RA, Brandt P, Lübbecke J, Prigent A, Martins MS and Rodrigues RR (2021) The 2019 Benguela Niño. Front. Mar. Sci. 8:800103. doi: 10.3389/fmars.2021.800103

INTRODUCTION

The southeastern tropical Atlantic Ocean hosts the Angola Benguela upwelling system which is one of the most productive marine ecosystems in the world (Chavez and Messié, 2009; Jarre et al., 2015) fuelled by the upwelling of nutrient-rich waters. This upwelling system is marked by the presence of a sharp meridional temperature gradient called the Angola Benguela front (ABF) located in the region between 15°S and 18°S (Mohrholz et al., 2001; Veitch et al., 2006) which separates the warm tropical waters in the north to the cold upwelled waters in the south (**Figure 1A**). The region exhibits high sea surface temperature (SST) variability at a wide range of frequencies varying from sub-monthly to decadal timescales (Bachèlery et al., 2020; Imbol Koungue and Brandt, 2021; Roch et al., 2021). The interannual timescale is marked by the occurrence of extreme warm events, the so-called Benguela Niños (Shannon et al., 1986; Florenchie et al., 2004; Rouault et al., 2007, 2018; Lübbecke et al., 2010; Bachèlery et al., 2016a, 2020; Imbol Koungue et al., 2017, 2019) and their cold counterparts, the Benguela Niñas (Florenchie et al., 2004; Koseki and Imbol Koungue, 2020). Those interannual warm and cold events usually peak in boreal spring between March and April (Rouault et al., 2007; Lübbecke et al., 2010; Imbol Koungue et al., 2019) when the SSTs are climatologically high and the intertropical convergence zone (ITCZ) reaches its southernmost position. During a Benguela Niño (Niña) event, the SSTs can be up to 3°C higher (lower) than the climatology in the Angola Benguela area (ABA, 8°E – coast; 10–20°S). Those extreme events may impact the marine ecosystem, biological productivity and fisheries in the Angola Benguela upwelling system by modulating the upward supply of nutrients (Bachèlery et al., 2016b) as they affect the upwelling intensity and upper-ocean mixing (Gammelsrød et al., 1998; Boyer et al., 2001; Blamey et al., 2015). Benguela Niños are often associated with floods in Angola and Namibia and strongly enhanced rainfall in the arid Namib desert (Rouault et al., 2003; Hansingo and Reason, 2009), whereas Benguela Niñas often lead to droughts over the Angola Benguela region (Koseki and Imbol Koungue, 2020).

Benguela Niño events are often marked by poleward intrusion of warm equatorial waters in the Angola Benguela upwelling system transported by the Angola Current (Rouault, 2012; Tchipalanga et al., 2018). Previous studies also stated that the seasonality of the Angola current is partly driven by semiannual coastal trapped waves (CTWs, Kopte et al., 2017; Tchipalanga et al., 2018). Off Angola, semiannual CTWs lead to two upwelling seasons in July–August and December–January, and two downwelling seasons in February – March and October (Ostrowski et al., 2009; Tchipalanga et al., 2018; Zeng et al., 2021).

It was recently reported that the interannual SST variability along the equatorial and in the southeastern tropical Atlantic has substantially reduced by more than 30% in May–July and March–May, respectively, in the post-2000 period compared to 1982–1999 (Prigent et al., 2020a,b; Silva et al., 2021). Those recent changes in the interannual SST variability suggest that Benguela Niños might be affected by decadal variability and/or climate warming and likely will further change in the future. This decadal modulation might also apply to the relative importance of different forcings. Previous studies have shown that Benguela Niños and Niñas can be triggered both by local and remote equatorial forcing. On the one hand, fluctuations in the local alongshore wind (Polo et al., 2008) associated with the strength and position of the South Atlantic Anticyclone (Richter et al., 2010) modulate the coastal upwelling intensity and generate positive SST anomalies in the southeastern tropical Atlantic. Moreover, Florenchie et al. (2004) suggested that local sea-air heat flux exchanges do not play a role in preconditioning the sea surface in the Angola Benguela upwelling system prior to the arrival of an event. However, the analyses of the 2016 warm event off Angola and Namibia by Lübbecke et al. (2019) revealed that the warming resulted from a combination of different local processes such as the weakening of the alongshore wind, which lead to a reduction in the latent heat loss from the ocean, as well as enhanced freshwater input through abundant precipitation and river runoffs reducing surface cooling by attenuated vertical exchange processes. Imbol Koungue et al. (2019) highlighted the influence of CTWs forced by meridional wind stress anomalies north of the Angolan region on the SST anomalies in the regions downstream. The authors found a 95% statistically significant correlation (<-0.4) at 1-month lag when the meridional wind stress anomalies north of Angola lead the SST anomalies in the Southern Angola and Angola Benguela front regions. On the other hand, Benguela Niños have been shown to be caused by remote equatorial forcing by the eastward propagation of equatorial Kelvin waves (EKWs) along the equatorial waveguide triggered by zonal wind fluctuations in the western or central equatorial Atlantic (Florenchie et al., 2003, 2004; Illig et al., 2004; Lübbecke et al., 2010; Rouault et al., 2018). Those EKWs impinging at the eastern boundary generate subsequent CTWs that propagate poleward along the Southwest African coast and impact the coastal interannual variability in the Angola Benguela upwelling system (Ostrowski et al., 2009; Rouault, 2012; Bachèlery et al., 2016a; Imbol Koungue et al., 2017; Illig et al., 2018; Illig and Bachèlery, 2019; Imbol Koungue et al., 2019; Bachèlery et al., 2020; Imbol Koungue and Brandt, 2021). A recent study by Imbol Koungue and Brandt (2021) using observations and altimetry, evidenced a thermocline feedback with the SST response lagging a thermocline displacement induced by the passage of a CTW by about 14 days. These intraseasonal CTWs are found to modulate also the intensity of the peak Benguela Niños and Niñas depending on their timing.

In the tropical Atlantic, Chenillat et al. (2021) investigated the impacts of climate modes on the interannual variability of the chlorophyll-a using satellite and reanalysis data. The authors found that during the Atlantic zonal mode (June–August), CTWs trigger by EKWs forced by zonal wind stress anomalies in the western equatorial Atlantic explain the sea surface height and chlorophyll-a variations off Southern Angola. The variability of the eastern equatorial SST in the Atlantic and Pacific Oceans has been shown to be linked to the variations of the local meridional wind at seasonal and interannual timescales (Philander and Pacanowski, 1981; Xie, 1998). Philander and Pacanowski (1981) showed that the onset of southerly winds induced low SSTs in the southeastern part of the basin as the coastal upwelling is extended to the west due to advection and Rossby wave propagations. With the onset of the southerly winds, the thermocline is anomalously deep (shallow) north (south) of the equator near 4°N (3°S). Indeed, using a forced ocean model, Philander and Pacanowski (1981) showed that the relaxation of the cross-equatorial southerly winds induced a weakening of the South Equatorial Current and Countercurrent which then resulted in a warming of the southeastern Atlantic. The same mechanism has been shown to be active in the Pacific during the growing phase

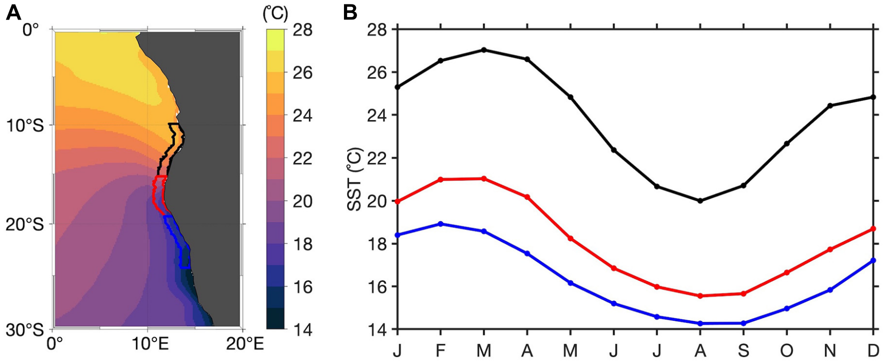

FIGURE 1 | (A) Annual climatology of SST with geographical delimitations of the coastal zones of interest overlaid: Southern Angola (10–15°S, 1°-width coastal fringe) in black, Angola Benguela front (15–19°S, 1°-width coastal fringe) in red and Northern Namibia (19–24°S, 1°-width coastal fringe) in blue. **(B)** SST climatology in the three coastal zones of interest shown in panel **(A)**. The climatology is calculated relative to the period January 1982 and April 2020.

of some El Niño events (e.g., Peng et al., 2020). A modeling study of Périgaud et al. (1997) investigated the role of meridional wind anomalies on El Niño using a coupled simulation. The authors demonstrated that during a warm (cold) event in the equatorial east Pacific, meridional wind stress anomalies drove convergent (divergent) surface currents inducing downwelling (upwelling) anomalies acting to enhance the SST and wind anomalies.

The aim of this manuscript is to describe the origin and evolution of the 2019 Benguela Niño off Angola and Namibia. This extreme warm event is atypical compared to the well-known Benguela Niño events (e.g., 1995, 2001, and 2010/2011) because of: (1) the timing of the event, and (2) the timing of the forcing mechanisms. More details are given in the section "Result." The manuscript is structured as follows: section "Data and Methods" describes the different data sets used to characterize the warming in the southeastern Atlantic as well as the methodology. Section "Results" describes the warming off Angola and Namibia and analyses the role played by the different forcing and the impact on the local net primary production. Lastly, section "Discussion and Summary" will be dedicated to the discussion of the results and the conclusion.

DATA AND METHODS

This section aims at describing the different data sets and methods used in this study.

Data

Off Angola (13°00′E; 10°50′S) at around 77 km away from the coast, a current meter mooring is measuring current velocities since July 2013 (Kopte et al., 2017; Imbol Koungue and Brandt, 2021). On the mooring cable, at 500-m depth, an upward-looking 75-kHz Long Ranger Acoustic Doppler current profiler (LR ADCP) is mounted to measure the velocity of the Angola Current up to 45 m below the sea surface with a 16-m bin size as vertical resolution. Current velocities from the moored ADCP are rotated by -34° against North to derive alongshore and cross-shore velocities (positive onshore) according to the local coastal orientation. The data are freely available at https://doi.pangaea.de/10.1594/PANGAEA.939249.

In this study, we use the gridded products of sea level anomaly (SLA) and near-surface absolute geostrophic current velocities from the delayed-time multi-mission (all satellites merged) and the near-real time that are distributed by the European Union Copernicus Marine Service Information[1] with a daily temporal resolution and available at 0.25° horizontal resolution from January 1993 to May 2020 and since April 2019, respectively. More details on the mapping algorithm procedures are provided by Pujol et al. (2016). Absolute surface geostrophic current velocities are extracted from the data point (13°07.5′E; 10°52.5′S) closest to the mooring position as in Kopte et al. (2018) and Imbol Koungue and Brandt (2021) to complement the moored velocity time series.

The daily Optimum Interpolation SST version 2 (OI-SST v2; Reynolds et al., 2007) available at 0.25° horizontal resolution from September 1981 onward is used. Data can be downloaded from the NOAA website[2]. The data is derived from daily merged *in situ* and remote sensed data.

We further use daily *in situ* temperature fields and 20°C isotherm depth from the enhanced Prediction and Research Moored Array in the Tropical Atlantic (ePIRATA, Foltz et al. (2018)[3], that are available from September 1997 to August 2020. These data are derived from buoy measurements of the PIRATA program (Servain et al., 1998; Bourlès et al., 2008; Johns et al., 2014; Bourles et al., 2019) which have successfully passed the quality control and do not need bias correction. The subsurface temperature fields are interpolated onto a uniform 5-m vertical grid. More details about the gap-filling procedures, error estimates and corrections of instrument biases can be found in Foltz et al. (2018).

The sea surface salinity (SSS) data originates from a combination of three satellite missions: Aquarius, soil moisture

---

[1] http://marine.copernicus.eu/

[2] https://www.esrl.noaa.gov/psd/data/gridded/

[3] https://www.aoml.noaa.gov/phod/epirata/

active passive (SMAP) and soil moisture and ocean salinity (SMOS). SMOS has a spatial resolution of around 0.5° and measures SSS since 2010. Aquarius satellite collected SSS measurements between 2011 and 2015 and has a coarser spatial resolution (1.35°) than SMOS. Finally, SMAP mission started in April 2015 and is running until now with a spatial resolution of around 0.36°. This initiative is part of the European space agency (ESA), which has funded the climate change initiative (CCI) SSS program (CCI+SSS). The CCI+SSS program delivers improved calibrated global SSS field data (version 3.21) which spans the period 2010 to 2020 (Boutin et al., 2021). The data set is freely available *via* https://catalogue.ceda.ac.uk/uuid/5920a2c77e3c45339477acd31ce62c3c.

Potential links to the local marine ecosystem were analyzed by presenting the anomalies of the net primary production (NPP) during the extreme warm event. Monthly means of NPP for the time period July 2002 to July 2020 are freely available online[4]. The data has a horizontal resolution of 1/6° but is interpolated on a 0.25° × 0.25° spatial grid to match with the SST anomalies. The NPP data is based on the Eppley vertically generalized production model which uses MODIS chlorophyll, SST data, SeaWiFs photosynthetically available radiation and estimates of the euphotic zone depth.

Atmospheric variables such as surface winds, air-sea heat fluxes, surface pressure, specific humidity of the air, and sea level pressure are investigated in this manuscript using the European Centre for Medium-Range Weather Forecasts (ECMWF) re-analysis 5 (ERA5; Hersbach et al., 2020). The ERA5 data is available at 0.25° horizontal resolution and the period used for the study extends from January 1982 to April 2020. Data are freely distributed *via* https://cds.climate.copernicus.eu/.

Methods

Throughout the manuscript, prior to all analyses, the linear trend estimated over the data set period (see **Figures 1–13**) has been removed and anomalies are calculated with respect to the corresponding seasonal cycle. To identify the anomalous warm or cold events along the Southwest African coast, the SST anomalies are analyzed in three 1°-width coastal fringe regions of interest (see **Figure 1A**): the Southern Angola region (in black, 10–15°S), the Angola Benguela front region (in red, 15–19°S) and the Northern Namibia region (in blue, 19–24°S). Based on these three coastal regions, the following criterion (also used in Imbol Koungue et al., 2017, 2019) is used to identify the different coastal extreme warm and cold events: an event is classified as an extreme warm or cold event when the detrended normalized SST anomalies exceed ± 1 standard deviation for at least three consecutive months and for at least two of the three coastal regions of interest.

The potential contribution to the latent heat flux from the wind speed and specific humidity difference between the sea surface and air at 10 m has been investigated. Following the bulk formula, the latent heat flux is given by:

$$Q_{lat} = \rho_a C_e l_v (q_a - q_w) U_{10} \tag{1}$$

where, Q_{lat} is the turbulent latent heat flux; ρ_a is the air density; C_e is the transfer coefficient for water vapor; l_v is the latent heat of evaporation; U_{10} is the surface wind speed at 10 m; q_w is the surface specific humidity, usually the saturated specific humidity at the temperature of the sea surface and q_a is the specific humidity of air at 10 m. The specific humidity at the sea surface has been estimated as in Imbol Nkwinkwa et al. (2019) using the formula:

$$q_w = \frac{\frac{R_{dry}}{R_{vap}} e_s(T)}{P - (1 - \frac{R_{dry}}{R_{vap}}) e_s(T)} \tag{2}$$

$$e_s(T) = a_1 exp\left[a_3\left(\frac{T - T_0}{T - a_4}\right)\right] \tag{3}$$

where, $R_{dry} = 287.0597$ J kg^{-1} K^{-1} and $R_{vap} = 461.5250$ J kg^{-1} K^{-1} are the gas constants for dry air and water vapor, respectively, P is the surface pressure (in Pa), T_0 = 273.16 K and T is the sea surface temperature (in K) from ERA5 reanalysis, $e_s(T)$ is the saturation vapor pressure (in Pa). The parameters a_1, a_3, and a_4 are set to 611.21 Pa, 17.502 and 32.19 K, respectively (Imbol Nkwinkwa et al., 2019).

RESULTS

The understanding of the SST climatology in the three coastal regions of interest (**Figure 1B**) is crucial for the interpretation of the SST anomalies. The evolution of the SST climatology is quite similar in the three coastal regions, but from the northern to the southern regions the SST climatology is shifted to lower mean SSTs. The warm season is observed in boreal spring with a maximum SST in March (February) for the Southern Angola and Angola Benguela front (Northern Namibia) regions. The cold season is observed from July to September with a minimum SST in August in the three coastal regions of interest. The normalized detrended anomalies of SST averaged over the three coastal regions are shown in **Figure 2** from January 1982 to April 2020. Based on the criterion defined in section "Methods," 14 extreme events have been identified and categorized into 6 extreme cold events, namely in 1982 (April–July), 1986–1987 (October–April), 1989–1990 (October–February), 1991-1992 (October–May), 1992 (July–September), 1996–1997 (November–June) and eight extreme warm events, namely in 1984 (February–April), 1984 (June–October), 1991 (May–July), 1995 (February–September), 1997–1998 (October–January), 2001 (March–May), 2010–2011 (December–March), and 2019 (October–January). All those extreme events have already been described in the literature (Florenchie et al., 2004; Reason et al., 2006; Rouault et al., 2007; Ostrowski et al., 2009; Rouault et al., 2009; Lübbecke et al., 2010; Rouault, 2012; Lutz et al., 2013; Imbol Koungue et al., 2017; Rouault et al., 2018; Imbol Koungue et al., 2019) except for the 2019 Benguela Niño which is the focus of this study. A complete list of manuscripts describing the previous extreme coastal events is provided in Imbol Koungue et al. (2019) in their Supplementary Table 1.

---

[4] http://sites.science.oregonstate.edu/ocean.productivity/index.php

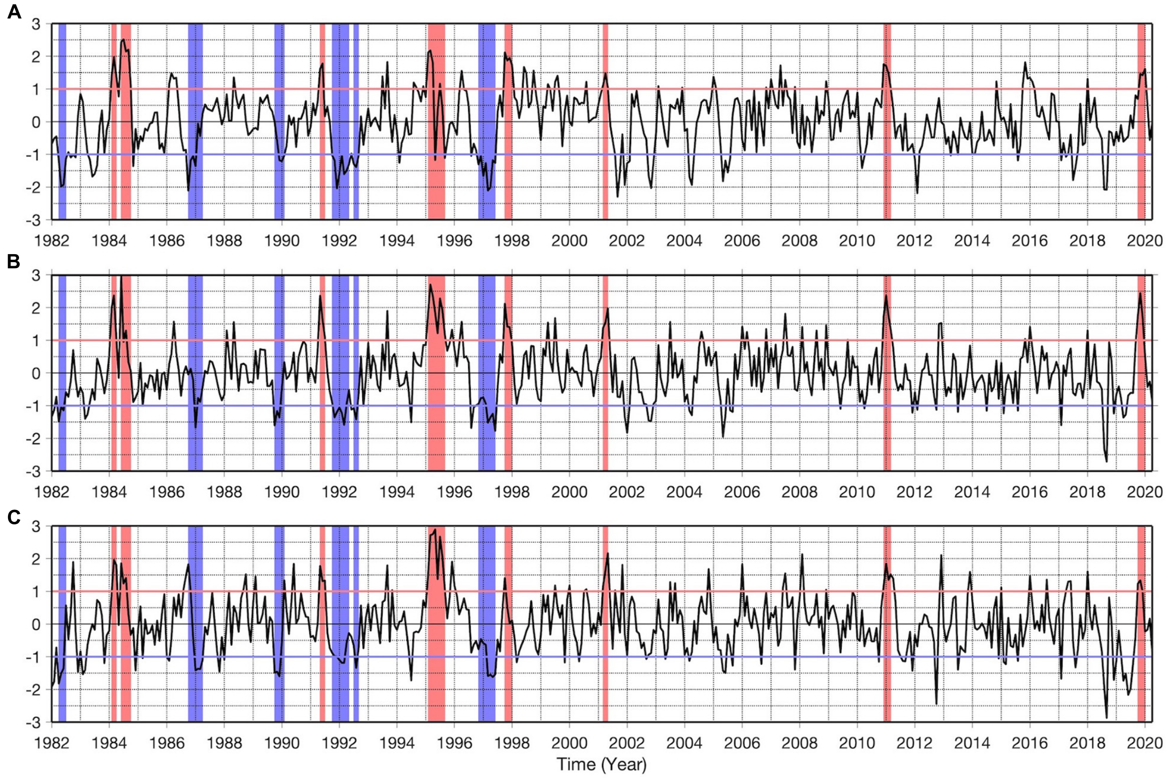

FIGURE 2 | Normalized detrended OI-SST monthly anomalies averaged in the regions of Southern Angola **(A)**, Angola Benguela front **(B)**, and Northern Namibia **(C)** between January 1982 and April 2020. The red and blue rectangles highlight Benguela Niños and Niñas, respectively. The horizontal red and blue lines indicate the ±1 standard deviation.

It is noteworthy that since 2000, there are no extreme cold events observed along the Southwest African coast, and only three extreme warm events occurring at an interval of ∼ 9 to 10 years, consistent with the results by Prigent et al. (2020b). The time series of normalized detrended anomalies of SST do portray short episodes of cold SST anomalies (for example in 2001/2002, 2005, and 2018), but they do not meet the requirements to be considered as extreme events.

Sea Surface Temperature Anomalies During 2019

This subsection aims at describing the origin and the evolution of the SST anomalies during the 2019 Benguela Niño. **Figure 3A** zooms in on the time series from **Figure 2** between January 2019 and April 2020 including the period considered to display maps of monthly SST anomalies (green rectangle). In August 2019, negative SST anomalies prevail in the southeastern tropical Atlantic with a weak warming at around 15°S (**Figure 3B**). One month later (September 2019), a warming is observed along the coast north of 20°S and extends offshore with SST anomalies greater than 1°C (**Figure 3C**), while it remains relatively cool south of 20°S along the coast. This is consistent with the time series (**Figure 3A**) which also show positive (negative) normalized detrended SST anomalies of ∼ 1 (−0.5) standard deviation in the Southern Angola and Angola Benguela front (Northern Namibia) regions. The warming persists off Southern Angola and Angola Benguela front regions, but also spreads south of 20°S in October 2019 in the Northern Namibia regions (**Figure 3D**). The peak of the 2019 Benguela Niño is observed in November 2019 (**Figure 3A**) with high SST anomalies recorded in all three coastal regions of interest but exceeding 2°C in the Angola Benguela front region (**Figure 3E**). During the peak of the event, the whole southeastern Atlantic is anomalously warm. North of 20°S, offshore maximum SST anomalies are also observed mainly in the Southern Angola region. One month after the peak of the event (December 2019), the southeastern tropical Atlantic stays warm (**Figure 3F**). The demise of the extreme warm event starts in January (February) 2020 in the Angola Benguela front and Northern Namibia (Southern Angola) regions with the appearance of cold surface waters as shown in **Figures 3G,H**. In the Southern Angola region, the SST anomalies peak in January 2020 (>2°C) with SST anomalies confined along the coast (**Figure 3G**). The area of cold SST anomalies expands northward along the southern Angola coast in March 2020 (**Figure 3I**).

Role of Local Winds and Surface Heat Fluxes

Previous studies evidenced the impact of the local wind fluctuations on the SST variability in the southeastern

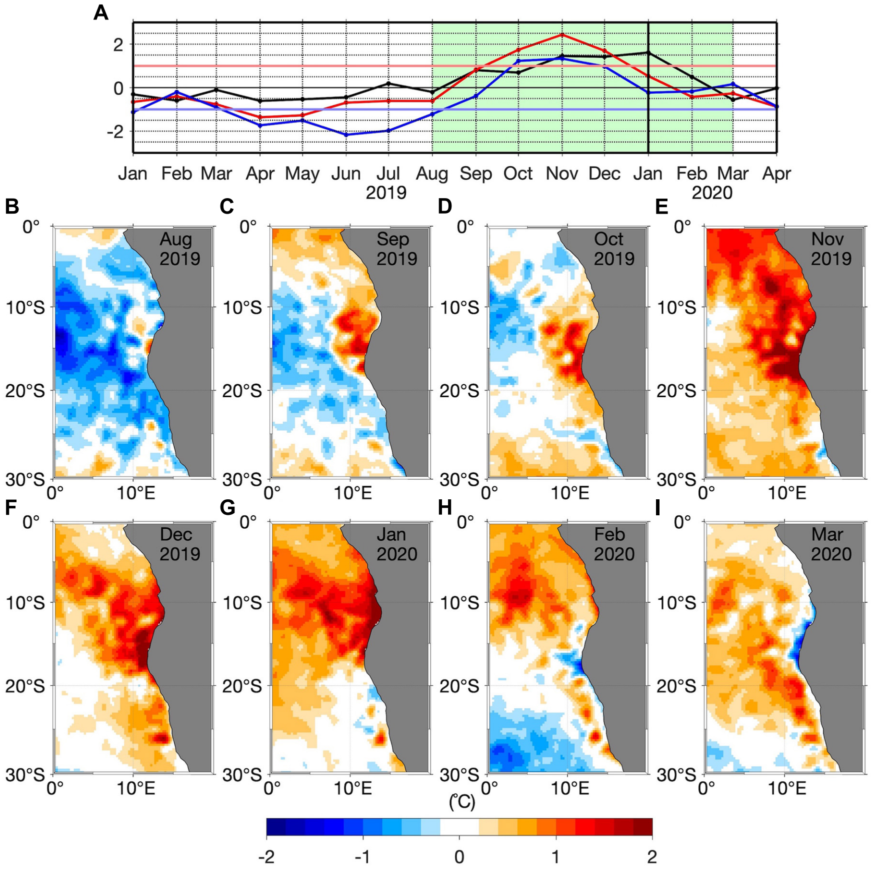

FIGURE 3 | (A) Time series of the normalized detrended OI-SST monthly anomalies from January 2019 to April 2020 shown in **Figure 2** for the regions of Southern Angola (black), Angola Benguela front (red) and Northern Namibia (blue). **(B–I)** Monthly detrended SST anomalies averaged from August 2019 to March 2020 (light green rectangle in panel **A**).

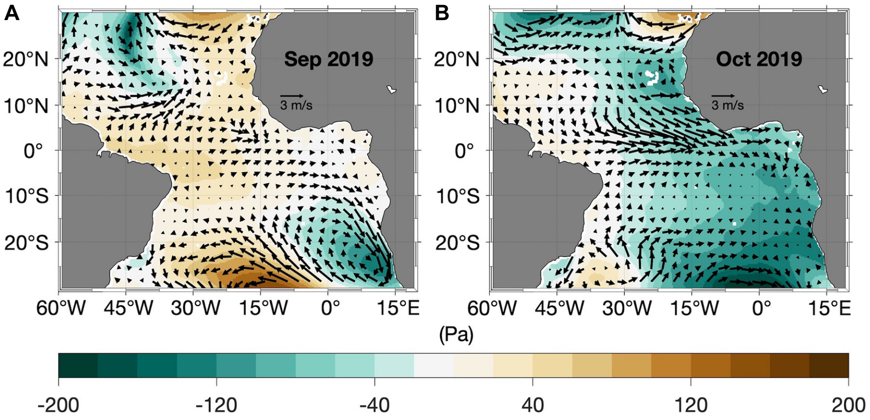

FIGURE 4 | (A,B) Detrended anomalies of ERA5 monthly sea level pressure (SLP, shading) and surface winds (arrows) from September to October 2019. The anomalies are calculated relative to the period January 1982 and April 2020.

Atlantic Ocean (Polo et al., 2008; Richter et al., 2010; Lübbecke et al., 2019). In September 2019, north-easterly wind anomalies are present south of 15°S along the West African coast, associated with a local negative SLP anomaly (**Figure 4A**). As the upwelling in northern Namibia is wind-driven (Jarre et al., 2015), the reduction of the prevailing southerly winds by the northerly wind anomalies south of 15°S is associated with reduced coastal upwelling, possibly resulting in the onset of the local warming observed in September 2019 (**Figure 3C**). In addition, the weakening of the local winds (**Supplementary Figure 1A**) is consistent with a reduction of the latent heat loss from the ocean to the atmosphere with anomalies greater than 20 W/m^2 (**Figure 5A**) even though the specific humidity difference ($q_a - q_w$, **Supplementary Figure 1D**) might also contribute. Positive anomalies of $q_a - q_w$ observed in **Supplementary Figure 1D** suggest that the air temperature at 10 m is higher than the SST. However, **Supplementary Figure 1A** reveals that the wind speed anomalies (<2 m/s) are the major contributor to the anomalous latent heat flux compared to $q_a - q_w$ which shows quite weak anomalies (<1 g/kg) south of 15°S (**Supplementary Figure 1D**). It is thus unlikely that an enhanced air temperature played an important role in the reduction of the latent heat loss from the ocean to the atmosphere during the 2019 Benguela Niño, as was observed for other warm events such as the Ningaloo Niño in the southeast Indian Ocean (Zhang et al., 2018; Guo et al., 2020). We conclude that the reduction in coastal upwelling caused by weakened local winds and the reduction of the latent heat loss from the ocean to the atmosphere resulted in the warming south of 15°S in September 2019. The onset of the warming north of 15°S will be discussed below. However, the observed offshore cold SST anomalies in September 2019 (**Figure 3C**) seems to be damped by the reduction of the latent heat loss from the ocean to atmosphere (**Figure 5A**) resulting in reduced cold SST anomalies in October 2019 (**Figure 3D**). The amplitude of the latent heat flux anomaly has considerably reduced from September to October 2019 (<15 W/m^2, **Figure 5B**), but remained positive south of 15°S. Also, a damping of the warm SST anomalies north of 25°S (**Figure 3E**) during the peak of the warm event in November 2019 is suggested by the presence of a strong latent heat loss from the ocean to the atmosphere (**Figure 5C**) along the Southwest African coast. The strong latent heat loss is explained in this case by the negative anomalies of $q_a - q_w$ (< -2 g/kg) in the Angola Benguela front region (**Supplementary Figure 1F**) as the wind speed anomalies are quite weak (**Supplementary Figure 1C**). Negative anomalies of $q_a - q_w$ highlight that in November 2019 the sea surface was warmer than the air above, due to strong sea surface temperature anomalies. Noteworthy, the similarity between the latent heat flux anomalies and the net surface heat flux anomalies, suggests the dominant role of the latent heat flux. **Figure 5D** shows that the ocean gains heat in September 2019 south of 15°S (>30 W/m^2). Positive anomalies of net surface heat flux in October 2019 (**Figure 5E**) and still reduced upwelling-favoring winds (**Figure 4B**) could have maintained the local warm SST between September–October 2019 in the Angola Benguela front region. Consistent with **Figure 5C**, in November 2019, the net surface heat flux anomaly patterns show a damping of the warm SST anomalies (**Figure 5F**) with net surface heat flux anomalies of less than -30 W m^{-2}.

Upwelling is not only driven by the alongshore wind stress but also by the wind stress curl. Anomalies of the wind stress curl are therefore shown in **Figures 6A–C** from September to November 2019. **Figure 6A** depicts a positive anomaly of the near-coastal wind stress curl in September 2019 in the Southern Angola and Angola Benguela front regions ($\sim 0.17 \times 10^{-7}$ N m^{-3} and $\sim 0.3 \times 10^{-7}$ N m^{-3}, respectively) which also extends offshore. A positive local near-coastal wind stress curl anomaly means a weakening of the mean near-coastal cyclonic wind stress curl, corresponding to weakened Ekman suction, i.e., downwelling anomalies. The reduced local upwelling, particularly off Southern Angola favors the appearance of local positive SST anomalies which could explain the warming observed in September 2019 (**Figure 3C**) in the Southern Angola region as the local wind anomalies are quite weak (**Figures 4A, 6A**). In contrast, in the Angola Benguela front region, positive SST anomalies in September 2019 are generated by a combination of positive wind stress curl anomalies and southward wind anomalies (**Figure 4A**) resulting in weakened coastal upwelling (downwelling anomalies) and a reduction of the latent heat loss from the ocean to the atmosphere (**Figure 5A**). Slight negative wind stress curl anomalies are observed south of the Southern Angola region in October 2019 (**Figure 6B**). However, in November 2019, there is an offshore extension of the positive anomaly of wind stress curl (**Figure 6C**), which might be linked to the offshore warming observed in **Figure 3E** during the peak of the event.

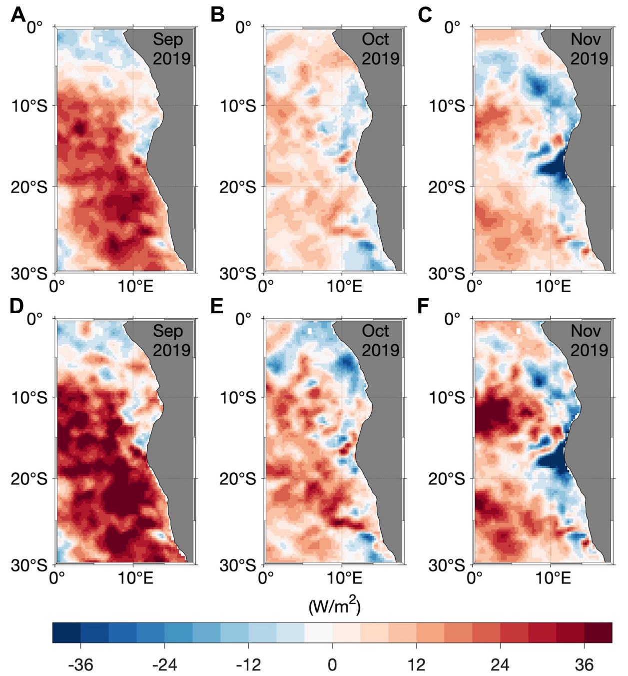

FIGURE 5 | (A–C) Monthly detrended anomalies of ERA5 surface latent heat flux (positive values mean reduced latent heat loss from the ocean to atmosphere) from September to November 2019. **(D–F)** same as **(A–C)** but for the net surface heat flux anomalies. The anomalies are calculated relative to the period January 1982 and April 2020.

Role of the Remote Forcing

Equatorial zonal wind stress fluctuations (**Figure 4B**) can excite EKWs impinging at the eastern boundary which force CTWs that propagate poleward along the West African coast and particularly in the Angola Benguela upwelling system. **Figure 7A** shows the zonal wind anomalies averaged between 40°W – 20°W and

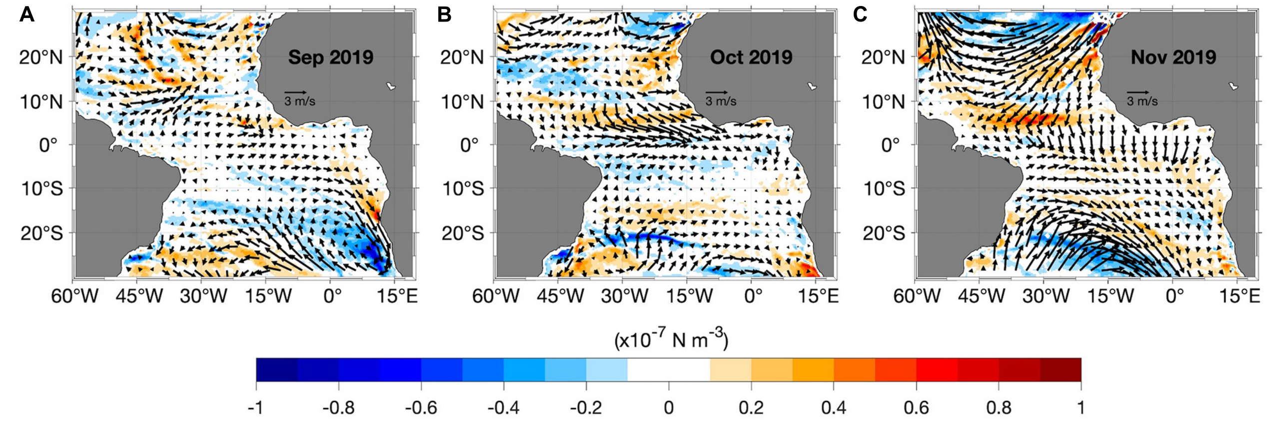

FIGURE 6 | (A–C) Monthly detrended anomalies of wind stress curl (shading) estimated from ERA5 surface winds (arrows) from September to November 2019. The anomalies are calculated relative to the period January 1982 and April 2020.

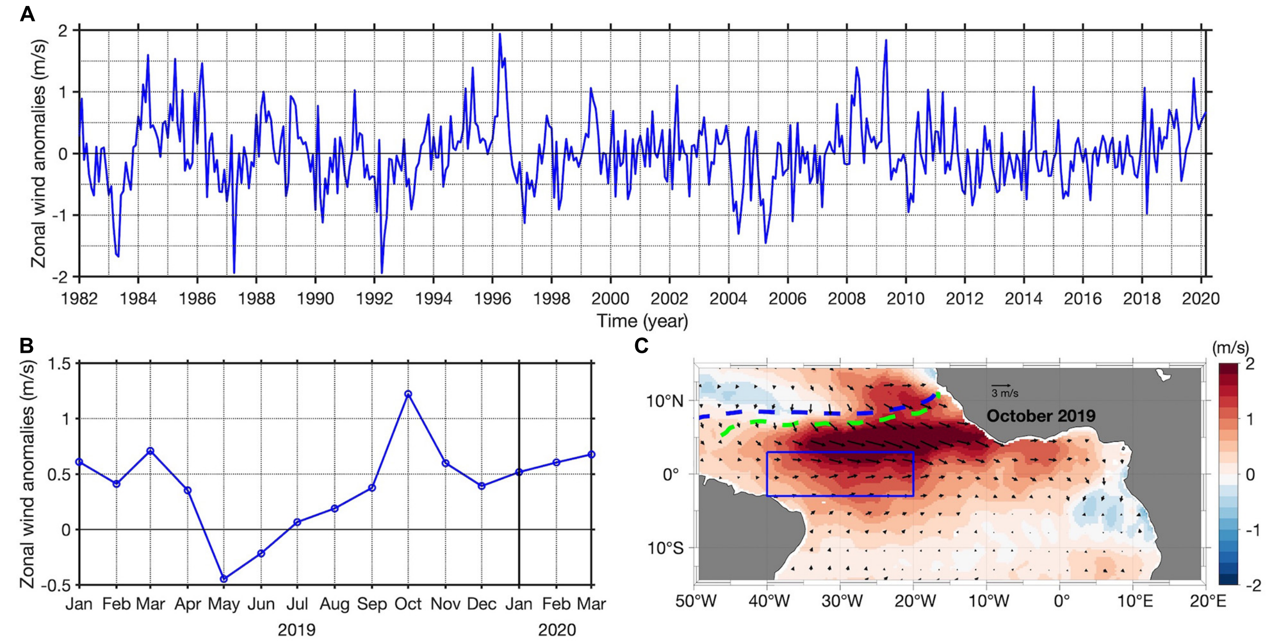

FIGURE 7 | (A) Detrended anomalies of ERA5 zonal wind averaged between 40°W and 20°W, 3°S–3°N [WAtl, blue box in panel **C**] from January 1982 to April 2020. **(B)** Zoom in 2019–2020 of the zonal wind anomalies time series in panel **A**). **(C)** Detrended anomalies of zonal wind (shading) and surface winds (arrows) in October 2019. The dashed blue line represents the climatological mean position of the Intertropical convergence zone (ITCZ) in October. The dashed green line represents the position of the ITCZ during October 2019.

3°S – 3°N (WAtl, blue box in **Figure 7C**). In the equatorial band, positive (negative) zonal wind anomalies mean weaker (stronger) easterly winds. The time series (**Figures 7A,B**) show westerly wind anomalies from January 2019 to April 2019 and again from July 2019 to March 2020 with the strongest anomaly occurring in October 2019 (>1 m/s), associated with the zonal SLP gradient observed in **Figure 4B**. A Hovmøller diagram of daily zonal wind anomalies in the equatorial Atlantic reveals that strong westerly wind anomalies (>1 m/s) prevail between the end of September and October 2019 (**Supplementary Figure 2A**). However, maximum westerly wind anomalies (>2 m/s) are located north of the equator around 2–7°N and from 35°W to 13°W (**Figure 7C**) with westerly wind anomalies still found at the equator. Climatologically, there are easterly winds in this region in October with a value of about −1 m/s (not shown). However, this area is also influenced by tropical depressions or cyclones. Particularly in October 2019, north of the equator, strong westerly wind anomalies are induced on the one hand by the zonal pressure gradient (**Figure 4B**) with positive/negative SLP anomalies to the west/east in the tropical Atlantic. On the

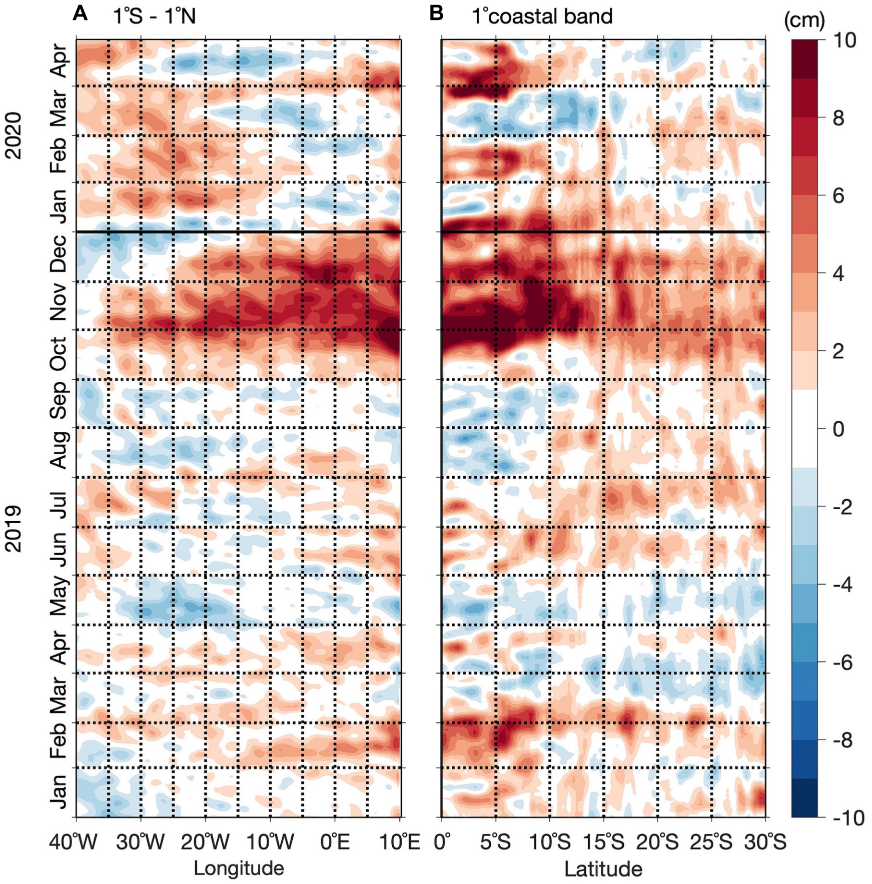

FIGURE 8 | Hovmøller diagram of detrended SLA along the equator (averaged over 1°S – 1°N) from 40°W to the African coastline in panels **(A,B)** along the Southern African coast (averaged from the coast to 1° offshore) from 0°S to 25°S from January 2019 (bottom) to April 2020 (top). The anomalies are calculated relative to the period January 1993 to April 2020.

other hand, at daily scale, there are strong cyclonic low-pressure events (not shown) that occurred in the area in the second half of October 2019 which could have contributed to maintain the westerly wind anomalies (>3.5 m/s). **Figure 7C** also shows a slight equatorward shift of the ITCZ in October 2019 (dashed green) compared to its mean October position (dashed blue line). This means that the convergence between the north-easterly and south-easterly trade winds occurred further south.

To investigate whether the wind anomalies generated EKWs, detrended sea level anomalies along the equatorial Atlantic and the West African coast are shown in **Figure 8** between January 2019 and April 2020. Altimetry data are useful to monitor the equatorial wave propagations along the equatorial and coastal waveguides. Between August and September 2019, there are no signals in SLA characterizing the propagation of downwelling EKWs (**Figure 8A**) or subsequent CTWs (**Figure 8B**). Therefore, remote equatorial forcing through ocean dynamics has not contributed to the warming along the Southwest African coast in September 2019 (**Figure 3C**). In the equatorial Atlantic, positive SLA are observed starting in October 2019 which is consistent with the dynamic height anomalies from PIRATA data (not shown). However, compared to previous Benguela Niño events such as the one in 2010/2011 (Rouault et al., 2018), the SLA signal pointing to a downwelling EKW is relative weak. Moreover, an equatorial thermocline deeper than normal (>15 m) caused by the activity of the downwelling EKW is observed between October and November 2019 (**Supplementary Figure 3**) in the monthly detrended anomalies of 20°C isotherm depth (taken as a proxy for thermocline depth) from the ePIRATA data set in the equatorial Atlantic interpolated between the PIRATA mooring locations (35°W, 23°W, 10°W, and 0°E). Detrended anomalies of subsurface temperature in the upper 200 m interpolated between the PIRATA mooring locations along the Equator are shown in **Figure 9** from August 2019 to March 2020 from the ePIRATA data. Between August and October 2019, weak positive temperature anomalies (<1.5°C) are observed in the eastern equatorial Atlantic in the upper 100 m (**Figures 9A–C**). Between 40- and 60-m depth, temperature anomalies (>2°C) are observed during the peak of the Benguela Niño in November and also in December 2019 in the eastern equatorial Atlantic (**Figures 9D,E**). The presence of strong positive temperature anomalies along the equator in November 2019 is in general agreement with the

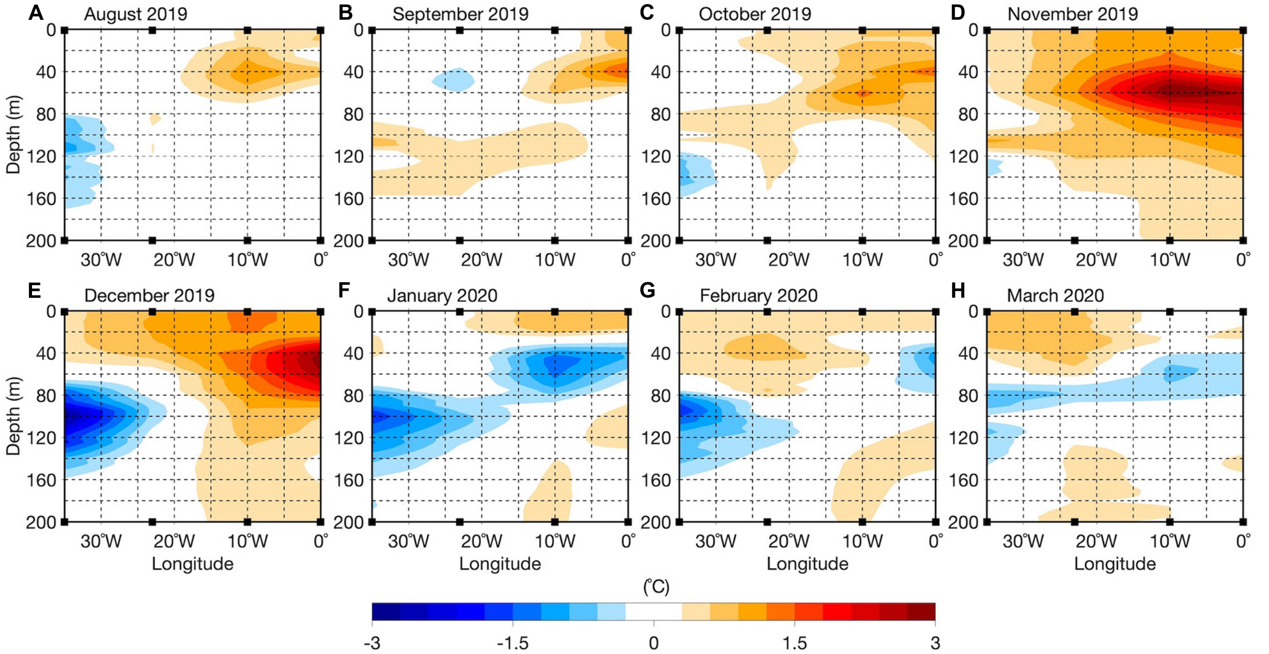

FIGURE 9 | (A–H) Detrended anomalies of temperature in the top 200 m from ePIRATA from August 2019 to March 2020 computed using interpolated temperature fields from the four equatorial moorings located at 35°W, 23°W, 10°W, and 0°E (filled black squares on the x-axes). The data are available from September 1997 to August 2020.

presence of westerly wind anomalies in October 2019 favoring the generation of a downwelling EKW (**Figure 7C**) which will deepen the equatorial thermocline (**Supplementary Figure 3**).

An additional forcing of the eastern equatorial warming in November 2019 might come from the relaxed cross-equatorial southerly winds (**Figure 10**). Indeed, the Hovmøller diagram of monthly meridional wind anomalies in the equatorial Atlantic shows prevailing reduced southerly winds (<-1 m/s) in the eastern equatorial Atlantic (0–10°E) between mid-October 2019 and mid-February 2020 (**Figure 10** and **Supplementary Figure 2B**). According to Philander and Pacanowski (1981), relaxation of cross-equatorial southerly winds causes a warming in the eastern equatorial Atlantic associated with a reduction of local upwelling. Indeed, **Figure 10** shows that during November 2019, low (high) anomalies of SLA indicative of a shallow (deep) thermocline are observed north (south) of the equator associated with reduced cross-equatorial southerly winds. Along the equator, maximum SST anomalies ($>1°C$) is observed in November 2019 with strong anomalies of SLA (>6 cm) suggesting a deepening of the thermocline as observed in **Supplementary Figure 3**. We suggest that the reduction of the cross-equatorial southerly winds might have contributed to the eastern equatorial warming in November 2019 during the peak of the 2019 Benguela Niño. In December 2019, the temperature anomaly pattern shows a sign of an anomalous relaxation of the thermocline slope in the equatorial Atlantic with a deepening in the east and a shoaling in the west (**Figure 9E**). This is consistent with **Figure 8A** which shows negative (positive) anomalies of SLA in the western (eastern) equatorial Atlantic during December 2019 and also with the observed z20 anomalies (**Supplementary Figure 3**). However, in January 2020 (**Figure 9F**), a subsurface cooling around the thermocline level is observed in the eastern equatorial Atlantic. This might be caused by the eastward propagation of an upwelling Kelvin wave induced by an upwelling Rossby wave reflecting at the western boundary which is forced by westerly wind anomalies along the equator (Nagura and McPhaden, 2010) in October 2019. This mechanism is called the delayed action oscillator (e.g., Suarez and Schopf, 1988) causing a delayed negative feedback. In addition, upwelling Rossby waves triggering upwelling Kelvin waves at the western boundary could be forced by positive anomalies of wind stress curl north of the equator west of 25°W in November 2019 (**Figure 6C**) which might have contributed to enhance the upwelling SLA signal along the equator. Weak temperature anomalies ($<0.3°C$) are observed in the near-surface in the equatorial Atlantic in February 2020 (**Figure 9G**) and are shifted westward in March 2020 ($>0.3°C$, **Figure 9H**).

Along the West African coast, downwelling poleward CTW propagations associated with SLA greater than 10 cm are observed from October 2019 to January 2020 (**Figure 8B**). These downwelling CTWs are potentially triggered by the superposition of downwelling EKWs forced by westerly wind anomalies during October 2019 (**Supplementary Figure 2A**). There might be an additional contribution from the coastal northerly wind anomalies between 5°S and 12°S (~ -2 m/s) to force downwelling CTWs in December 2019 and January 2020 (not shown). Theses CTWs trigger positive SST anomalies along the West African coast (**Figures 3D–F**). The downwelling CTW

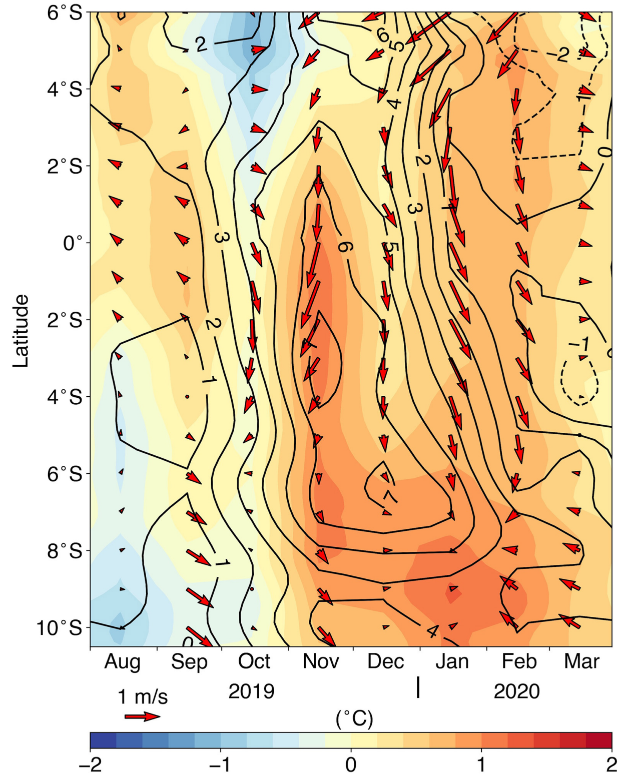

FIGURE 10 | Hovmøller diagram of detrended monthly anomalies of SST (shading), SLA (contours), and surface winds (arrows) averaged between 0°E and 10°E from August 2019 to March 2020. Anomalies are computed relative to the period January 1982 and April 2020.

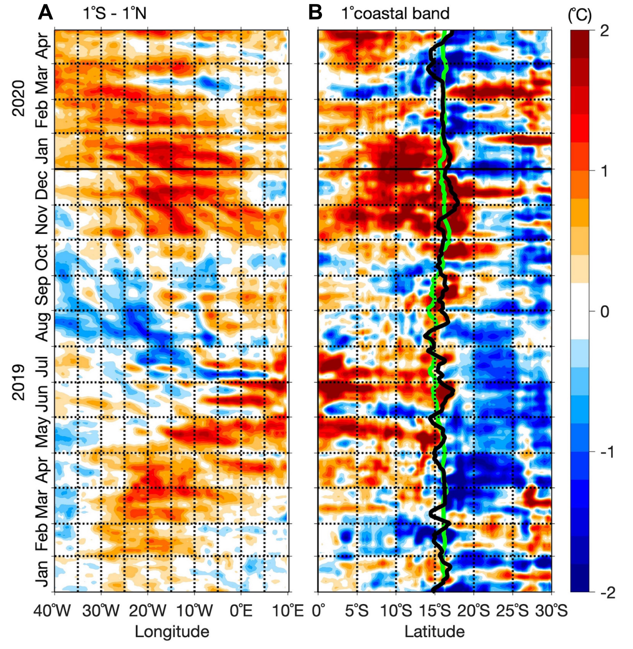

FIGURE 11 | Hovmøller diagram of detrended anomalies of daily SST along the equator (averaged over 1°S – 1°N) from 40°W to the African coastline in panel **(A)** and along the Southern African coast (averaged from the coast to 1° offshore, in panel **(B)** from 0°S to 25°S from January 2019 (bottom) to April 2020 (top). Anomalies are computed relative to the period January 1982 and April 2020. The daily mean climatology (anomalies) of the location of the maximum meridional SST gradient is represented in green (black) over **Figure 11B**. A 10-day running mean is applied to smooth the data.

propagating in January 2020 (first 10 days, **Figure 8B**) is at the origin of the peak in SST in the Southern Angola region in January (**Figure 3G**). As the signature of the CTW is weaker south of 15°S (cf. **Figure 8B**), it does not affect the regions further downstream. It is worth to mention that climatologically, this downwelling CTW propagates during the secondary, weaker upwelling season (December–January) off Angola. Similar to **Figure 8**, the detrended SST anomalies along the equator and the West African coast are presented in **Figure 11**. In agreement with the maps shown in **Figure 3**, weak positive SST anomalies (<1°C) are observed along the equator and the West African coast in September 2019 until 10°S. South of 10°S, positive SST anomalies (>1°C) are shown in the Southern Angola region (until mid-September 2019) and in the Angola Benguela front region associated with an anomalous southward position of the Angola Benguela SST front (**Figure 11B**, black line). Larger SST anomalies (>2°C) are observed south of 5°S between mid-November 2019 and January 2020. Interestingly, there might be a lag of about 14 days between the passage of the downwelling CTW at the end of October 2019 and the maximum SST anomalies (>2°C) recorded in mid-November 2019 indicative of a thermocline feedback. Relative to the climatology (**Figure 11B**, green line), a southward migration of the Angola Benguela SST front (**Figure 11B**, black line) is observed from November to December 2019 which is caused by the downwelling poleward CTW propagations during that period of the year (**Figure 8B**). The appearance of cold SST anomalies (<−1°C) south of 15°S between December 2019 and January 2020 indicates the demise of the coastal warm event. In contrast, the Southern Angola region records its largest SST anomalies (>2°C, **Figures 3G, 11B**) in January 2020 associated with a poleward downwelling CTW propagation (**Figure 8B**), before being stopped by the appearance of cold SST anomalies (<−1°C) in February 2020.

The southward shift of the ABF might be related to stronger poleward flow of warm water. The potential role of meridional advection is investigated using moored velocities off Angola (11°S) available since July 2013. **Figure 12** presents the subsurface moored alongshore velocities with the surface alongshore geostrophic current from altimetry on top. The alongshore flow off Angola is not a steady flow and is constituted of alternating periods of northward and southward velocities with maximum velocity amplitude of about 40 cm/s. In October and November 2019 (peak of the event), an enhanced vertically coherent poleward flow (<−20 cm/s in the upper 100 m) is observed off Angola. Thus, the poleward flow in the upper 100 m might have contributed to the development of the 2019 Benguela Niño through advection of warm equatorial waters downstream. Using the meridional SST gradient averaged in the ABA (8°E-14°E; 10°S-20°S) and the near-surface absolute geostrophic velocity anomaly at the mooring position (13°00′E; 10°50′S), the SST change due to the resulting anomalous meridional advection can be quantified. In October (November) 2019, the meridional SST gradient of 5.3×10^{-6} (5×10^{-6}) °C/m and the poleward near-surface velocity anomaly of 0.05 (0.08) m/s yields to an anomalous warming by poleward meridional heat advection of 0.67 (1.05) °C/month, respectively. The poleward meridional heat advection during the event was largest in October and November 2019. The averaged anomalous warming due to the meridional heat advection of 0.86°C/month overcomes the anomalous SST change between October and November 2019 that was 0.77°C/month suggesting the importance of other cooling mechanisms such as the negative feedback by the net surface heat flux discussed before (**Figure 5F**).

Link to the Net Primary Production

The Angola Benguela upwelling system which is part of the Benguela current large marine ecosystem is an area with high biological productivity (Jarre et al., 2015). Therefore, in this section, we look at the relation between the warm SST anomalies during the 2019 Benguela Niño and the local NPP. NPP values are derived using the Eppley vertically generalized production model in the southeast Atlantic Ocean. In general, the period from July to September represents the upwelling season off Angola which is typically associated with high NPP. However, note that the NPP is not necessarily only fuelled by local vertical processes (indicated here by the SST anomaly), but also by the nutrients from the Congo River discharge and the spreading of the river plume. The strongest impact of the Congo River is found between 3°S and 7°S (**Figure 13**). In August 2019, strong positive anomalies of NPP (1.5 gC m^{-2} day^{-1}, **Figure 13A**) are observed along the West African coast collocating with cold SST anomalies. In September 2019, in the Southern Angola region, the positive local near-coastal wind stress curl anomaly, i.e., downwelling anomalies (**Figure 6A**) reducing the local upwelling and favoring the local warming, are associated with local lower than normal NPP (<-1.5 gC m^{-2} day^{-1}, **Figure 13B**). Note that off Southern Angola, the NPP is climatologically high in August-September. One month later (October 2019), these negative anomalies of NPP appear slightly poleward (**Figure 13C**) compared to September 2019 and also collocate with positive SST anomalies. In November 2019 (**Figure 13D**) during the peak of the 2019 Benguela Niño, weak negative NPP anomalies (∼ -0.5 gC m^{-2} day^{-1}) are observed in the Southern Angola and Angola Benguela front regions. Note that November-December corresponds to the period of the year when the climatology of the NPP shows the lowest values off Southern Angola. Weak precipitation anomalies are recorded over the land and the ocean in November 2019 (**Supplementary Figure 4D**) south of 10°S consistent with slightly negative SSS anomalies (<-1) observed during the same period (**Supplementary Figure 5D**). **Figures 13E,F** display quite similar amplitudes of negative NPP anomalies (∼ -1 gC m^{-2} day^{-1}) in the Southern Angola and Angola Benguela front regions during December 2019 and January 2020. Likewise, north of 7°S, the distribution of the SSS anomaly in January to March 2020 looks very similar to the one of the NPP anomalies with positive NPP anomalies (**Figures 13F–H**) collocating with negative SSS anomalies (**Supplementary Figures 5F–H**). Indeed, in February to March 2020, the remarkable feature is the strong positive NPP anomalies (>2 gC m^{-2} day^{-1}) observed offshore and north of 7°S where the freshwater from Congo River (river mouth is at about 6°S) are discharged into the Atlantic Ocean. Likewise, **Supplementary Figure 4G** also shows in February 2020 strong positive precipitation anomalies (>3 mm/day) over land and in the ocean. High precipitation over land will increase the discharge of the Congo River into the Atlantic Ocean which will bring more nutrients from land into the ocean and also contribute to reduce the SSS (**Supplementary Figure 5**) with the freshwater input. However, the strength of the NPP interannual variability in the offshore area in comparison to its seasonal variability (not shown) remains unclear, especially due to the interannual variability of the Congo River discharge and its spreading which is in fact very variable. We note that the low salinity waters are not spreading southward (**Supplementary Figure 5**) and are remaining north of 12°S during the warm event.

DISCUSSION AND SUMMARY

In this manuscript, the generation, development and the demise of the 2019 Benguela Niño have been investigated using observations and the ERA5 reanalysis product in the southeastern tropical Atlantic Ocean. Compared to previous Benguela Niño events that occur during boreal spring, the 2019 Benguela Niño developed at the end of the year with SST anomalies exceeding 2°C in November 2019 in the Angola Benguela front region (**Figure 3E**). The timing is quite similar to the one of the 2010/2011 Benguela Niño described in Rouault et al. (2018) with maximum amplitude of SST anomalies (>4°C) occurring in January 2011.

The 2019 Benguela Niño was forced by the combination of local and remote forcing contrary to the canonical Benguela Niños described in the literature (e.g., Rouault et al., 2007, 2018; Richter et al., 2010; Imbol Koungue et al., 2017). On the one hand, local processes dominated in September 2019 in the Southern Angola and the Angola Benguela front regions and generated an early warming. In the Southern Angola region, the occurrence of positive near coastal wind-stress curl anomalies (**Figure 6A**) has played a predominant role in warming the region by favoring a reduction of local upwelling. Also, in the Angola Benguela front region, the downwelling anomalies in combination with the reduction of the latent heat loss from the ocean to the atmosphere (**Figure 5A**) due to weakened alongshore winds (**Figure 4A**) have generated locally positive SST anomalies. Similar local processes have been identified among the triggering mechanisms of the 2016 warm event off Angola described by Lübbecke et al. (2019). On the other hand, the westerly wind anomalies observed in the western or central equatorial Atlantic (**Figure 7C** and **Supplementary Figure 2A**) have triggered downwelling EKWs during the present extreme warm event in October 2019, but with a weak signal in SLA in contrast to classical Benguela Niños (e.g., 2001 or 2010/2011, referred to in Rouault et al., 2007, 2018). Furthermore, three downwelling CTWs with SLA of more than

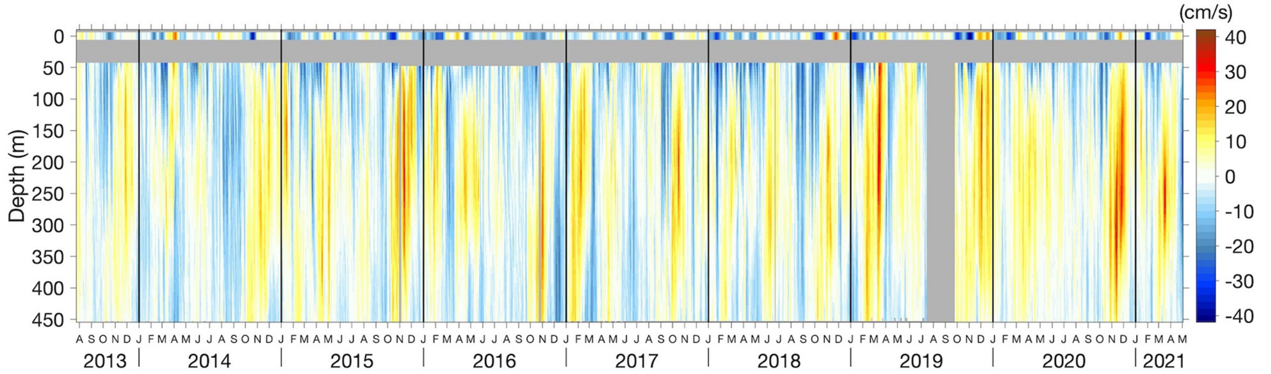

FIGURE 12 | Time series of daily alongshore velocities of surface absolute geostrophic velocities from altimetry and from moored ADCP (from 45-m depth) at 11°S.

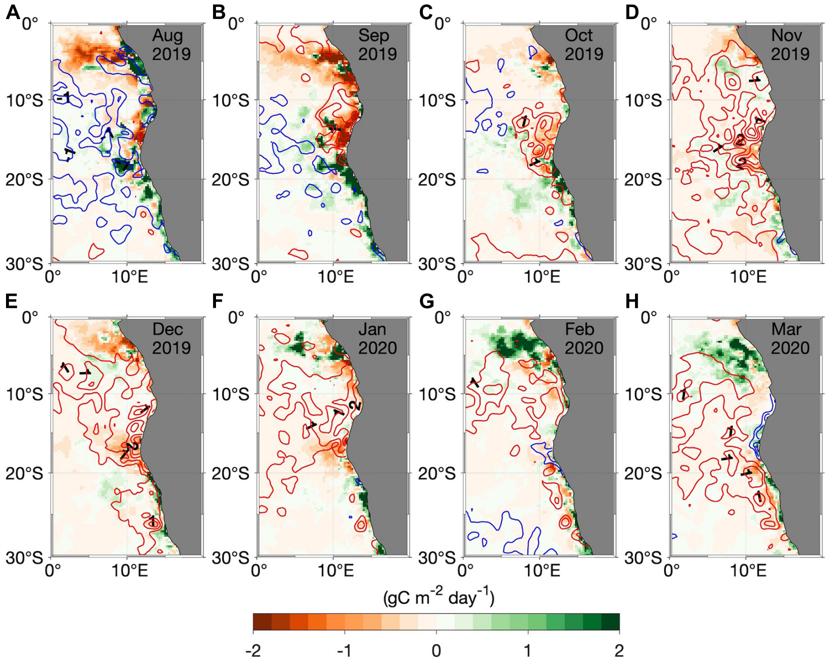

FIGURE 13 | (A–H) Monthly NPP (SST) anomalies in shading (contours) in the southeast Atlantic from August 2019 to March 2020. Blue and red contour intervals are 0.5°C and represent negative and positive SST anomalies, respectively. The anomalies are calculated relative to the period July 2002 to July 2020 for NPP and January 1982 to April 2020 for SST.

10 cm propagated along the West African coast (**Figure 8B**). They were potentially generated by the superposition of downwelling EKWs forced by westerly wind anomalies in October 2019 along the equator (**Supplementary Figure 2A**). The occurrence of these equatorial wind anomalies agrees with the results of Hu and Huang (2007) who showed from reanalysis data that locally forced warming over the Angola Benguela upwelling region is likely to generate westerly wind anomalies along the equatorial Atlantic 1 to 2 months later. This connection was also emphasized in a recent model study by Illig et al. (2020) on the timing of warm events off Angola and in the eastern equatorial Atlantic. For the 2019 extreme warm event, our results are consistent with the ones of Hu and Huang (2007) as the locally induced warming observed in September 2019 (**Figure 3C**) might have triggered westerly wind anomalies in October 2019 along the equator contributing to the generation of the Benguela Niño peaking in November 2019. This highlights that the two forcing mechanisms leading to the 2019 Benguela Niño are not independent.

In November 2019, strong positive temperature anomalies are observed along the equator (**Figure 9D**), consistent with the presence of westerly wind anomalies in October 2019 favoring the generation of a downwelling EKW (**Figure 7C**) which will anomalously deepen the equatorial thermocline (**Supplementary Figure 3**). Concomitantly, northerly wind anomalies (weakening of southerly winds) prevail east of 20°W from mid-October 2019 to mid-February 2020 (**Figure 10** and

Supplementary Figure 2B). A previous study of Philander and Pacanowski (1981) showed that in the eastern equatorial Atlantic, the weakening of the meridional wind could contribute to generate warm SST as both parameters are correlated. This highlights the importance of the meridional wind fluctuations at the eastern boundary (**Figure 10**) during the 2019 Benguela Niño.

CTWs are clearly visible with a strong signal in SLA (>10 cm, **Figure 8B**) at the end of October 2019, and about 2 weeks later strong positive SST anomalies (>2°C, **Figure 11B**) are recorded in the Angola Benguela upwelling system. This lag of $\sim$ 14 days nicely corresponds to the timescale of the thermocline feedback recently described in Imbol Koungue and Brandt (2021) at intraseasonal timescales off Southern Angola and found in the eastern equatorial Pacific (Zelle et al., 2004; Zhu et al., 2015).

Moreover, coastal northerly wind anomalies between 5°S and 12°S (~ -2 m/s) might be an additional local forcing of downwelling CTWs in December 2019 and January 2020 (not shown). This result is consistent with the one from the modeling study of Bachèlery et al. (2016a) which used a couple of sensitivity experiments to quantify the role of the local versus remote forcing in the southeastern tropical Atlantic. Their results suggested that at subseasonal timescales (<100 days), the coastal oceanic variability (currents, thermocline, and sea level) is mainly driven by local forcing.

During the peak of the event in November 2019, damping of positive SST anomalies by the latent heat flux is observed mostly in the Angola Benguela front region. Note that the latent heat flux has a major contribution in the net heat flux in the southeast Atlantic Ocean. The strong latent heat loss is mainly explained by q_w (equation 2) which is higher than q_a and meaning that the sea surface is warmer than the air above, due to strong sea surface temperature anomalies. Our findings agree with the ones of Florenchie et al. (2004) who showed using reanalysis data and model outputs, that local net heat flux act mainly through latent heat flux anomalies as a thermostat to regulate cold and warm SST. **Figure 2** shows that since 2000, there are no extreme cold events identified along the Southwest African coast, and only three extreme warm events occurring at intervals of $\sim$ 9 to 10 years. This agrees with a recent study of Prigent et al. (2020b) that showed a reduction of the interannual SST variability in the Angola Benguela region by more than 30% in the post 2000 period compared to 1982–1999. They found that the remote equatorial forcing decreased after 2000, resulting in less Benguela Niño/Niña events.

In contrast to the 2016 warm event off Angola described in Lübbecke et al. (2019), the stratification caused by freshwater inputs (precipitation and river runoffs) has not played a role during the development of the 2019 Benguela Niño. Weak salinity anomalies south of 10°S (**Supplementary Figure 5**) were recorded along the Southwest coast of Africa mainly due to the absence of precipitation. However, positive precipitation anomalies were observed north of 10°S in October 2019 (**Supplementary Figure 4C**) during the 2019 Benguela Niño whereas anomalies of latent heat flux and net heat flux show opposite sign (**Figures 5B,E**) indicating that another term in the heat budget contributes more than the latent heat flux. Indeed, **Figure 5B** shows positive anomalies of latent heat flux (less heat loss from the ocean to the atmosphere) but **Figure 5E** displays negative anomalies of net heat flux (ocean loses heat). That is related to less shortwave radiation reaching the ocean surface due to more cloud cover (not shown) and causing a cooling (**Figure 3D**). This indicates that SST anomalies in this region could also respond to cloud cover (e.g., Xie and Carton, 2004). Our result agrees with the recent results from Nnamchi et al. (2021) which showed that the precipitation which is a good proxy for the diabatic heating, leads SST variability in the equatorial Atlantic. This means that the atmosphere forces the ocean, even though the region north of 10°S is dominated by ocean dynamics.

Off Southern Angola, the occurrence of positive anomalies of near-coastal wind-stress curl (downwelling anomalies) and the weakening of alongshore winds in the Angola Benguela front region, lead to a reduction of local upwelling which agrees with reduced NPP. Note that the NPP is not necessarily only fuelled by the strength of the vertical exchange, i.e., vertical mixing and upwelling (indicated here by the SST anomaly), but also by the lateral input of nutrients with the Congo River discharge and the spreading of the river plume. Therefore, it seems not straight forward to connect the positive SST anomaly to negative NPP anomalies due to the existing strong interannual variability and also due to the influence of the Congo River. Yet, at interannual timescales, there is to our knowledge no study that established the connection between SST and NPP along the eastern boundary.

DATA AVAILABILITY STATEMENT

The original contributions presented in the study are included in the article/**Supplementary Material**, further inquiries can be directed to the corresponding author.

AUTHOR CONTRIBUTIONS

RAIK designed the study, analyzed the data, and drafted the manuscript. All authors contributed to the writing of the manuscript.

FUNDING

Financial support was provided by funding from the EU H2020 under grant agreement 817578 TRIATLAS project. This study was further supported by the German Federal Ministry of Education and Research as part of the SACUS II (03F0751A) and BANINO (03F0795A) projects and Deutsche Forschungsgemeinschaft through several research cruises with RV Maria S. Merian, RV Meteor, and RV Sonne.

ACKNOWLEDGMENTS

We would like to acknowledge the efforts made by the PIRATA project for making the mooring data freely available. We thank the captains, crews, scientists, and technicians involved in several research cruises in the tropical Atlantic who contributed to collecting data used in this study. RAIK would like to thank Arielle Stela N. Imbol Nkwinkwa for the insightful discussion and the latent heat flux analysis.

SUPPLEMENTARY MATERIAL

The Supplementary Material for this article can be found online at: https://www.frontiersin.org/articles/10.3389/fmars.2021.800103/full#supplementary-material

REFERENCES

Bachèlery, M. L., Illig, S., and Dadou, I. (2016a). Interannual variability in the South-East Atlantic Ocean, focusing on the Benguela Upwelling System: remote versus local forcing. *Geophys. Res. Lett. Oceans* 121, 284–310. doi: 10.1002/2015JC011168

Bachèlery, M.-L., Illig, S., and Dadou, I. (2016b). Forcings of nutrient, oxygen, and primary production interannual variability in the southeast Atlantic Ocean. *Geophys. Res. Lett.* 43, 8617–8625. doi: 10.1002/2016GL070288

Bachèlery, M. L., Illig, S., and Rouault, M. (2020). Interannual coastal trapped waves in the Angola-Benguela upwelling system and Benguela Niño and Niña events. *J. Mar. Syst.* 203:103262. doi: 10.1016/j.jmarsys.2019.103262

Blamey, L. K., Shannon, L. J., Bolton, J. J., Crawford, R. J. M., Dufois, F., Evers-King, H., et al. (2015). Ecosystem change in the southern Benguela and the underlying processes. *J. Mar. Syst.* 144, 9–29. doi: 10.1016/j.jmarsys.2014.11.006

Bourles, B., Araujo, M., McPhaden, M. J., Brandt, P., Foltz, G. R., Lumpkin, R., et al. (2019). PIRATA: a sustained observing system for tropical Atlantic climate research and forecasting. *Earth Space Sci.* 6, 577–616. doi: 10.1029/2018EA000428

Bourlès, B., Lumpkin, R., McPhaden, M. J., Hernandez, F., Nobre, P., Campos, E., et al. (2008). The pirata program. *Bull. Am. Meteorol. Soc.* 89, 1111–1126. doi: 10.1175/2008BAMS2462.1

Boutin, J., Vergely, J.-L., Reul, N., Catany, R., Koehler, J., Martin, A., et al. (2021). *ESA Sea Surface Salinity Climate Change Initiative (Sea_Surface_Salinity_cci): Weekly Sea Surface Salinity Product, v03.21, for 2010 to 2020. NERC EDS Centre for Environmental Data Analysis.* Available online at: https://catalogue.ceda.ac.uk/uuid/fad2e982a59d44788eda09e3c67ed7d5 (accessed October 08, 2021).

Boyer, D. C., Boyer, H. J., Fossen, I., and Kreiner, A. (2001). Changes in abundance of the northern Benguela sardine stock during the decade 1990–2000, with comments on the relative importance of fishing and the environment. *Afr. J. Mar. Sci.* 23, 67–84. doi: 10.2989/025776101784528854

Chavez, F. P., and Messié, M. (2009). A comparison of eastern boundary upwelling ecosystems. *Prog. Oceanogr.* 83, 80–96. doi: 10.1016/j.pocean.2009.07.032

Chenillat, F., Illig, S., Jouanno, J., Awo, F. M., Alory, G., and Brehmer, P. (2021). How do climate modes shape the chlorophyll-a interannual variability in the tropical Atlantic? *Geophys. Res. Lett.* 48:e2021GL093769. doi: 10.1029/2021GL093769

Florenchie, P., Lutjeharms, J. R. E., Reason, C. J. C., Masson, S., and Rouault, M. (2003). The source of Benguela Niños in the South Atlantic Ocean. *Geophys. Res. Lett.* 30:1505. doi: 10.1029/2003GL017172

Florenchie, P., Reason, C. J. C., Lutjeharms, J. R. E., Rouault, M., Roy, C., and Masson, S. (2004). Evolution of interannual warm and cold events in the southeast Atlantic Ocean. *J. Clim.* 17, 2318–2334. doi: 10.1175/1520-0442(2004)017<2318:eoiwac>2.0.co;2

Foltz, G. R., Schmid, C., and Lumpkin, R. (2018). An enhanced PIRATA data set for tropical Atlantic Ocean-atmosphere research. *J. Clim.* 31, 1499–1524. doi: 10.1175/JCLI-D-16-0816.1

Gammelsrød, T., Bartholomae, C. H., Boyer, D. C., Filipe, V. L. L., and O'Toole, M. J. (1998). Intrusion of warm surface water along the Angolan-Namibian coast in February–March 1995: the 1995 Benguela Niño. *South Afr. J. Mar. Sci.* 19, 41–56. doi: 10.2989/025776198784126719

Guo, Y., Li, Y., Wang, F., Wei, Y., and Rong, Z. (2020). Processes controlling sea surface temperature variability of Ningaloo Niño. *J. Clim.* 33, 4369–4389.

Hansingo, K., and Reason, C. J. C. (2009). Modelling the atmospheric response over southern Africa to SST forcing in the southeast tropical Atlantic and southwest subtropical Indian Oceans. *Int. J. Climatol.* 29, 1001–1012. doi: 10.1002/joc.1919

Hersbach, H., Bell, B., Berrisford, P., Hirahara, S., Horányi, A., Muñoz-Sabater, J., et al. (2020). The ERA5 global reanalysis. *Q. J. R. Meteorol. Soc.* 146, 1999–2049. doi: 10.1002/qj.3803

Hu, Z. Z., and Huang, B. (2007). Physical processes associated with the tropical Atlantic SST gradient during the anomalous evolution in the southeastern ocean. *J. Clim.* 20, 3366–3378. doi: 10.1175/JCLI4189.1

Illig, S., Bachèlery, M. L., and Lübbecke, J. F. (2020). Why do Benguela Niños lead Atlantic Niños? *J. Geophys. Res. Oceans* 125:e2019JC016003. doi: 10.1029/2019JC016003

Illig, S., and Bachèlery, M. L. (2019). Propagation of subseasonal equatorially-forced coastal trapped waves down to the Benguela upwelling system. *Sci. Rep.* 9:5306. doi: 10.1038/s41598-019-41847-1

Illig, S., Bachèlery, M. L., and Cadier, E. (2018). Subseasonal coastal-trapped wave propagations in the southeastern Pacific and Atlantic Oceans: 2. Wave characteristics and connection with the equatorial variability. *J. Geophys. Res. Oceans* 123, 3942–3961. doi: 10.1029/2017JC013540

Illig, S., Dewitte, B., Ayoub, N., Du Penhoat, Y., Reverdin, G., De Mey, P., et al. (2004). Interannual long equatorial waves in the tropical Atlantic from a high-resolution ocean general circulation model experiment in 1981–2000. *J. Geophys. Res.* 109:C02022. doi: 10.1029/2003JC001771

Imbol Koungue, R. A., and Brandt, P. (2021). Impact of intraseasonal waves on Angolan warm and cold events. *J. Geophys. Res. Oceans* 126:e2020JC017088. doi: 10.1029/2020JC017088

Imbol Koungue, R. A., Illig, S., and Rouault, M. (2017). Role of interannual Kelvin wave propagations in the equatorial Atlantic on the Angola Benguela Current system. *J. Geophys. Res. Oceans* 122, 4685–4703. doi: 10.1002/2016JC012463

Imbol Koungue, R. A., Rouault, M., Illig, S., Brandt, P., and Jouanno, J. (2019). Benguela Niños and Benguela Niñas in forced ocean simulation from 1958 to 2015. *J. Geophys. Res. Oceans* 124, 5923–5951. doi: 10.1029/2019JC015013

Imbol Nkwinkwa, N. A. S., Rouault, M., and Johannessen, J. A. (2019). Latent Heat Flux in the Agulhas Current. *Remote Sens.* 11:1576. doi: 10.3390/rs11131576

Jarre, A., Hutchings, L., Kirkman, S. P., Kreiner, A., Tchipalanga, P. C. M., Kainge, P., et al. (2015). Synthesis: climate effects on biodiver- sity, abundance and distribution of marine organisms in the Benguela. *Fish. Oceanogr.* 24, 122–149. doi: 10.1111/fog.12086

Johns, W. E., Brandt, P., Bourlès, B., Tantet, A., Papapostolou, A., and Houk, A. (2014). Zonal structure and seasonal variability of the Atlantic Equatorial Undercurrent. *Clim. Dyn.* 43, 3047–3069. doi: 10.1007/s00382-014-2136-2

Kopte, R., Brandt, P., Claus, M., Greatbatch, R. J., and Dengler, M. (2018). Role of equatorial basin-mode resonance for the seasonal variabil- ity of the Angola Current at 11°S. *J. Phys. Oceanogr.* 48, 261–281. doi: 10.1175/JPO-D-17-0111.1

Kopte, R., Brandt, P., Dengler, M., Tchipalanga, P. C. M., Macueìria, M., and Ostrowski, M. (2017). The angola current: flow and hydrograph- ic characteristics as observed at 11°S. *J. Geophys. Res. Oceans* 122, 1177–1189. doi: 10.1002/2016JC012374

Koseki, S., and Imbol Koungue, R. A. (2020). Regional atmospheric response to the Benguela Niñas. *Int. J. Climatol.* 41, E1483–E1497. doi: 10.1002/joc.6782

Lübbecke, J., Brandt, P., Dengler, M., Kopte, R., Lüdke, J., Richter, I., et al. (2019). Causes and evolution of the southeastern tropical Atlantic warm event in early 2016. *Clim. Dyn.* 53, 261–274. doi: 10.1007/s00382-018-4582-8

Lübbecke, J. F., Böning, C. W., Keenlyside, N. S., and Xie, S. P. (2010). On the connection between Benguela and equatorial Atlantic Niños and the role of the South Atlantic Anticyclone. *J. Geophys. Res.* 115:C09015. doi: 10.1029/2009JC005964

Lutz, K., Rathmann, J., and Jacobeit, J. (2013). Classification of warm and cold water events in the eastern tropical Atlantic Ocean. *Atmos. Sci. Lett.* 14, 102–106. doi: 10.1002/asl2.424

Mohrholz, V., Schmidt, M., and Lutjeharms, J. R. E. (2001). The hydrography and dynamics of the Angola–Benguela frontal zone and environment in April 1999. *South Afr. J. Sci.* 97, 199–208.

Nagura, M., and McPhaden, M. J. (2010). Wyrtki Jet dynamics: seasonal variability. *J. Geophys. Res.* 115:C07009. doi: 10.1029/2009JC005922

Nnamchi, H. C., Latif, M., Keenlyside, N. S., Kjellsson, J., and Richter, I. (2021). Diabatic heating governs the seasonality of the Atlantic Niño. *Nat. Commun.* 12:376. doi: 10.1038/s41467-020-20452-1

Ostrowski, M., da Silva, J. C., and Bazik-Sangolay, B. (2009). The response of sound scatterers to El Niño- and La Niña-like oceanographic regimes in the southeastern Atlantic. *ICES J. Mar. Sci.* 66, 1063–1072. doi: 10.1093/icesjms/fsp102

Peng, Q., Xie, S., Wang, D., Kamae, Y., Zhang, H., Hu, S., et al. (2020). Eastern Pacific Wind Effect on the Evolution of El Niño: implications for ENSO Diversity. *J. Clim.* 33, 3197–3212.

Périgaud, C., Zebiak, S. E., Mélin, F., Boulanger, J.-P., and Dewitte, B. (1997). On the role of meridional wind anomalies in a coupled model of ENSO. *J. Clim.* 10, 761–773.

Philander, S. G. H., and Pacanowski, R. C. (1981). The oceanic response to cross-equatorial winds (with application to coastal upwelling in low latitudes). *Tellus* 33, 201–210. doi: 10.3402/tellusa.v33i2.10708

Polo, I., Lazar, A., Rodriguez-Fonseca, B., and Arnault, S. (2008). Oceanic Kelvin waves and tropical Atlantic intraseasonal variability: 1. Kelvin wave characterization. *J. Geophys. Res.* 113:C07009. doi: 10.1029/2007JC004495

Prigent, A., Lübbecke, J. F., Bayr, T., Latif, M., and Wengel, C. (2020a). Weakened SST variability in the tropical Atlantic Ocean since 2000. *Clim. Dyn.* 54, 2731–2744. doi: 10.1007/s00382-020-05138-0

Prigent, A., Koungue, I. R. A., Lübbecke, J. F., Brandt, P., and Latif, M. (2020b). Origin of weakened interannual sea surface temperature variability in the southeastern tropical Atlantic Ocean. *Geophys. Res. Lett.* 47:e2020GL089348. doi: 10.1029/2020GL089348

Pujol, M.-I., FaugeÌre, Y., Taburet, G., Dupuy, S., Pelloquin, C., Ablain, M., et al. (2016). DUACS DT2014: the new multi-mission altimeter data set reprocessed over 20 years. *Ocean Sci.* 12, 1067–1090. doi: 10.5194/os-12-1067-2016

Reason, C. J. C., Florenchie, P., Rouault, M., and Veitch, J. (2006). 10 Influences of large scale climate modes and Agulhas system variability on the BCLME region. *Large Mar. Ecosyst.* 14, 223–238. doi: 10.1016/s1570-0461(06)80015-7

Reynolds, R. W., Smith, T. M., Liu, C., Chelton, D. B., Casey, K. S., and Schlax, M. G. (2007). Daily high-resolution-blended analyses for sea surface temperature. *J. Clim.* 20, 5473–5496. doi: 10.1175/2007JCLI1824.1

Richter, I., Behera, S. K., Masumoto, Y., Taguchi, B., Komori, N., and Yamagata, T. (2010). On the triggering of Benguela Niños: remote equatorial versus local influences. *Geophys. Res. Lett.* 37:L20604. doi: 10.1029/2010GL0444461

Roch, M., Brandt, P., Schmidtko, S., Vaz Velho, F., and Ostrowski, M. (2021). Southeast tropical Atlantic changing from subtropical to tropical conditions. *Front. Mar. Sci.* 8:748383. doi: 10.3389/fmars.2021.748383

Rouault, M. (2012). Bi-annual intrusion of tropical water in the northern Benguela upwelling. *Geophys. Res. Lett.* 39:L12606. doi: 10.1029/2012GL052099

Rouault, M., Florenchie, P., Fauchereau, N., and Reason, C. J. C. (2003). South East tropical Atlantic warm events and southern African rainfall *Geophys. Res. Lett.* 30:8009. doi: 10.1029/2003GL014840

Rouault, M., Illig, S., Bartholomae, C., Reason, C. J. C., and Bentamy, A. (2007). Propagation and origin of warm anomalies in the Angola Benguela upwelling system in 2001. *J. Mar. Syst.* 68, 473–488. doi: 10.1016/j.jmarsys.2006.11.010

Rouault, M., Illig, S., Lübbecke, J., and Koungue, R. A. I. (2018). Origin, development and demise of the 2010–2011 Benguela Niño. *J. Mar. Syst.* 188, 39–48. doi: 10.1016/j.jmarsys.2017.07.007

Rouault, M., Servain, J., Reason, C. J. C., BourleÌs, B., Rouault, M. J., and Fauchereau, N. (2009). Extension of PIRATA in the tropical South-East Atlantic: an initial one-year experiment. *Afr. J. Mar. Sci.* 31, 63–71. doi: 10.2989/AJMS.2009.31.1.5.776

Servain, J., Busalacchi, A. J., McPhaden, M. J., Moura, A. D., Reverdin, G., Vianna, M., et al. (1998). A pilot research moored array in the tropical Atlantic (PIRATA). *Bull. Am. Meteorol. Soc.* 79, 2019–2031.

Shannon, L. V., Boyd, A. J., Brundrit, G. B., and Taunton-Clark, J. (1986). On the existence of an El Niño-type phenomenon in the Benguela system. *J. Mar. Res.* 44, 495–520. doi: 10.1357/002224086788403105

Silva, P., Wainer, I., and Khodri, M. (2021). Changes in the equatorial mode of the Tropical Atlantic in terms of the Bjerknes Feedback Index. *Clim. Dyn.* 56, 3005–3024. doi: 10.1007/s00382-021-05627-w

Suarez, M. J., and Schopf, P. S. (1988). A delayed action oscillator for ENSO. *J. Atmos. Sci.* 45, 3283–3287.

Tchipalanga, P., Dengler, M., Brandt, P., Kopte, R., Macueìria, M., Coelho, P., et al. (2018). Eastern boundary circulation and hydrography off Angola–building Angolan oceanographic capacities. *Bull. Am. Meteorol. Soc.* 99, 1589–1605. doi: 10.1175/BAMS-D-17-0197.1

Veitch, J. A., Florenchie, P., and Shillington, F. A. (2006). Seasonal and interannual fluctuations of the Angola–Benguela Frontal Zone (ABFZ) using 4.5 km resolution satellite imagery from 1982 to 1999. *Int. J. Remote Sens.* 27, 987–998. doi: 10.1080/01431160500127914

Xie, S. (1998). Ocean–atmosphere interaction in the making of the walker circulation and equatorial cold tongue. *J. Clim.* 11, 189–201.

Xie, S.-P., and Carton, J. A. (2004). "Tropical atlantic variability: patterns, mechanisms, and impacts," in *Earth's Climate*, eds C. Wang, S. Xie, and J. Carton (Washington, DC: AGU), doi: 10.1029/147GM07

Zelle, H., Appeldoorn, G., Burgers, G., and van Oldenborgh, G. J. (2004). The relationship between sea surface temperature and thermocline depth in the eastern equatorial Pacific. *J. Phys. Oceanogr.* 34, 643–655. doi: 10.1175/2523.1

Zeng, Z., Brandt, P., Lamb, K. G., Greatbatch, R. J., Dengler, M., Claus, M., et al. (2021). Three dimensional numerical simula- tions of internal tides in the Angolan upwelling region. *J. Geophys. Res. Oceans* 126:e2020JC016460. doi: 10.1029/2020JC016460

Zhang, L., Han, W. Q., Li, Y. L., and Shinoda, T. (2018). Mechanisms for Generation and Development of the Ningaloo Nino. *J. Clim.* 31, 9239–9259. doi: 10.1175/Jcli-D-18-0175.1

Zhu, J., Kumar, A., and Huang, B. (2015). The relationship between thermocline depth and SST anomalies in the eastern equatorial Pacific: seasonality and decadal variations. *Geophys. Res. Lett.* 42, 4507–4515. doi: 10.1002/2015GL064220

Conflict of Interest: The authors declare that the research was conducted in the absence of any commercial or financial relationships that could be construed as a potential conflict of interest.

frontiers
in Marine Science

ORIGINAL RESEARCH
published: 01 March 2022
doi: 10.3389/fmars.2022.811398

Transport Structure of the South Atlantic Ocean Derived From a High-Resolution Numerical Model and Observations

Xiaobiao Xu[1]**, Eric P. Chassignet*[1]*, Shenfu Dong*[2] *and Molly O. Baringer*[2]

[1] *Center for Ocean-Atmospheric Prediction Studies (COAPS), Florida State University, Tallahassee, FL, United States,*
[2] *Atlantic Oceanographic and Meteorological Laboratory (AOML), National Oceanic and Atmospheric Administration, Miami, FL, United States*

Edited by:
Fabrice Hernandez,
Institut de Recherche Pour le Développement (IRD), France

Reviewed by:
Jian Zhao,
University of Maryland Center for Environmental Science (UMCES), United States
Antonio Fetter,
Federal University of Santa Catarina, Brazil
Louise Rousselet,
University of California, San Diego, United States

***Correspondence:**
Xiaobiao Xu
xxu3@fsu.edu

Specialty section:
This article was submitted to Physical Oceanography, a section of the journal Frontiers in Marine Science

Received: *08 November 2021*
Accepted: *28 January 2022*
Published: *01 March 2022*

Citation:
Xu X, Chassignet EP, Dong S and Baringer MO (2022) Transport Structure of the South Atlantic Ocean Derived From a High-Resolution Numerical Model and Observations. Front. Mar. Sci. 9:811398. doi: 10.3389/fmars.2022.811398

The South Atlantic Ocean plays an important role in the Atlantic meridional overturning circulation (AMOC), connecting it to the Indian and Pacific Oceans as part of the global overturning circulation system. Yet, there are still open questions regarding the relative importance of the warm water versus cold water sources in the upper limb of the AMOC and on the detailed circulation pathways of the North Atlantic Deep Water (NADW) in the lower limb. These questions are addressed using model outputs from a 60-year, eddying global ocean-sea ice simulation that are validated against observations. We find that the Pacific Antarctic Intermediate Water (AAIW) plays a role in setting the temperature and salinity properties of the water in the subtropical South Atlantic, but that the upper limb of the AMOC originates primarily from the warm Indian water through the Agulhas leakage (9.8 Sv of surface water + 3.5 of AAIW) and that only a relatively small contribution of 1.5 Sv colder, fresher AAIW originates from the Pacific Ocean. In the lower limb, the NADW flows southward as a deep western boundary current all the way to 45°S and then turns eastward to flow across the Mid-Atlantic Ridge near 42°S before leaving the Atlantic Ocean, although there is clockwise recirculation in the Brazil, Angola, and Cape Basins.

Keywords: South Atlantic, Atlantic meridional overturning circulation (AMOC), transport structure, global ocean circulation model, eddy

INTRODUCTION

In the Atlantic Ocean, warm water from the South Atlantic flows northward in approximately the upper 1000 m, loses buoyancy to the atmosphere by cooling *en route* to the northern North Atlantic, and eventually sinks and returns southward at depth as the cold North Atlantic Deep Water (NADW). The temperature difference between the upper and lower limbs of this Atlantic meridional overturning circulation (AMOC) leads to a large northward oceanic heat transport throughout the entire Atlantic basin, in contrast to the poleward (northward and southward from the equator) heat transport in the Pacific and Indian Oceans (e.g., Macdonald and Baringer, 2013). The South Atlantic Ocean, defined here as the area south of 20°S (**Figure 1**), plays an important role in that it is through this region where the upper and lower AMOC limbs are connected to the Indian and Pacific Oceans and are entangled in the global overturning circulation system (e.g., Gordon, 1986; Broeker, 1991; Schmitz, 1995, 1996; Richardson, 2008; Talley, 2013). Thus, a comprehensive knowledge of the circulation in this region is essential to our understanding of the spatial structure and temporal variability of the AMOC.

Significant observations have been made in the last 15 years or so toward quantifying and monitoring the AMOC in the South Atlantic, particularly along a latitude near 34.5°S (e.g., Baringer and Garzoli, 2007; Dong et al., 2009, 2014, 2015; Garzoli et al., 2013; Meinen et al., 2013, 2018; Goes et al., 2015). These observations, which consist of moorings, expendable Bathythermograph (XBT), and Argo float measurements, yield a time mean AMOC transport in the range of 14-20 Sv. They also showed that there is significant AMOC variability on several timescales, similar to that observed by the RAPID array at 26.5°N (e.g., Smeed et al., 2018). Beyond 34.5°S, however, the observations in the South Atlantic remain sparse and short (in time). Overall, our understanding of the spatial structure of the time mean circulation is mostly limited to the schematic of Stramma and England (1999) and even less is known about its temporal variability. Numerical studies of the AMOC have primarily dealt with the zonally integrated AMOC transport index and little on the spatial structure of the circulation; see Hirschi et al. (2020) and Roberts et al. (2020) for a recent review of AMOC representation in high-resolution ocean simulations and climate models, respectively. Furthermore, most of these numerical studies focused on the North Atlantic since it is only in the last decade or so that AMOC observations became available in the South Atlantic.

There is the long-standing debate (Gordon, 2001) regarding as to whether the upper limb of the AMOC in the South Atlantic originates from the warm, saline Indian waters through the southern rim of Africa (e.g., Gordon, 1986; Saunders and King, 1995) or from the cooler, fresher Pacific water through the Drake Passage (e.g., Rintoul, 1991; Schlitzer, 1996). Although recent studies seem to favor the warm-water route from the Indian Ocean through the Agulhas leakage (e.g., Richardson, 2007; Beal et al., 2011), the relative contributions of cold versus warm water are still uncertain (Garzoli and Matano, 2011; Bower et al., 2019). For example, Rodrigues et al. (2010) estimated a cold-water contribution of 4.7 Sv based on quasi-isobaric subsurface floats and hydrographic data. This value is close to the estimate of Rühs et al. (2019) derived from an eddy-rich model, but it is significantly higher than several other estimates of 1-2 Sv based on numerical simulations and/or reanalysis (e.g., Speich et al., 2001; Donners and Drijfhout, 2004; Friocourt et al., 2005; Rousselet et al., 2020). Furthermore, most of these estimates were computed from Lagrangian analyses and the question then arises as to how these results would compare to a volume transport structure and/or water properties estimated from a Eulerian perspective. At depth, in the lower limb of the AMOC, many of the details of the circulation are still unknown, such as the exact location/latitude where the NADW in the Deep Western Boundary Current (DWBC) turns eastward and flows across the Mid-Atlantic Ridge (MAR). In recent decades, much attention has been paid to an eastward flow of the NADW near 22°S (e.g., Speer et al., 1995; Stramma and England, 1999; Arhan et al., 2003; Hogg and Thurnherr, 2005; van Sebille et al., 2012; Garzoli et al., 2015). However, both the magnitude of this flow and the extent of the eastward penetration in the Angola Basin are still debated.

Three-dimensional circulation information beyond the existing observations is required in order to address the above questions. In this paper, these questions are addressed by performing a detailed Eulerian and Lagrangian analysis of the three-dimensional circulation of a high-resolution numerical model validated against observations. We find that the Pacific AAIW plays a role in setting the temperature and salinity properties of the water in the subtropical South Atlantic, but that the upper limb of the AMOC originates primarily from the warm Indian water through the Agulhas leakage (9.8 Sv of surface water + 3.5 Sv of AAIW) and that only a relatively small contribution of 1.5 Sv colder, fresher AAIW originates from the Pacific Ocean. In the lower limb, the NADW flows southward as a deep western boundary current all the way to 45°S and then turns eastward to flow across the Mid-Atlantic Ridge near 42°S before leaving the Atlantic Ocean, although there is clockwise recirculation in the Brazil, Angola, and Cape Basins.

The paper is structured as follows. In Section "Numerical Simulation and Validation," we first summarize the configuration and basic features of the numerical simulation. Before the model can be used to increase our understanding of the circulation on the South Atlantic, the model results must be in reasonable agreement with the existing observations. The bulk of Section "Numerical Simulation and Validation" therefore compares in detail the modeled large-scale circulation pattern and the transport structure to observations. The validated model results are then used to document the time mean circulation pattern in the South Atlantic (Section "Circulation pathways in the South Atlantic Ocean"). Summary and discussions follow in Section "Summary and Discussion".

NUMERICAL SIMULATION AND VALIDATION

The numerical results presented in this study are from a long-term global ocean-sea ice hindcast simulation performed using the Hybrid Coordinate Ocean Model (HYCOM, Bleck, 2002; Chassignet et al., 2003), coupled with the Community Ice CodE (CICE, Hunke and Lipscomb, 2008). The vertical coordinate of the HYCOM is isopycnic in the stratified open ocean and makes a dynamically smooth and time-dependent transition to terrain following in the shallow coastal regions and to fixed pressure levels in the surface mixed layer and/or unstratified seas. In doing so, the model combines the advantages of the different coordinate types in simulating coastal and open ocean circulation features simultaneously (e.g., Chassignet et al., 2006).

The simulation has a horizontal resolution of 1/12° (∼6 km in the area of interest) and a vertical resolution of 36 layers (in σ_2). It is initialized using the January temperature and salinity from an ocean climatology (Carnes, 2009), and is forced using the latest surface-atmospheric reanalysis dataset JRA55 (Tsujino et al., 2018), which has a refined grid spacing of ∼55 km and

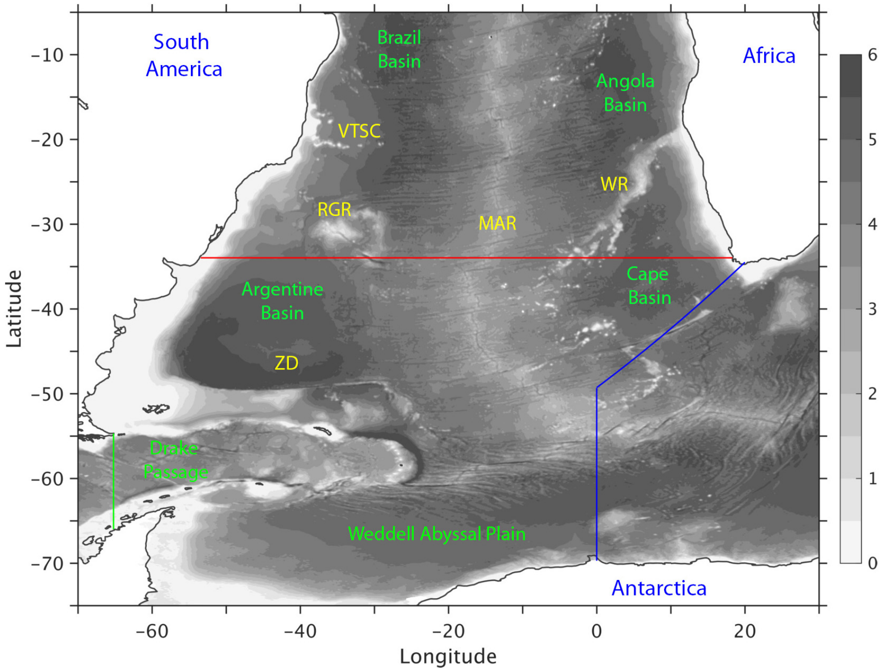

FIGURE 1 | Model bathymetry (in km) along with key topographic features in the South Atlantic Ocean: Vitoria-Trindade Seamount Chain (VTSC), Rio-Grande Rise (RGR), Mid-Atlantic Ridge (MAR), Walvis Ridge (WR), Zapiola Drift (ZD). Red, green, and blue lines denote three sections where significant observations have been obtained and the observations are used to evaluate the model results: 34°S in the South Atlantic, 65°W in Drake Passage, and the Prime Meridian-Good Hope (PM-GH) transect southwest of Africa.

temporal interval of 3 h and covers the period of 1958–2018. The surface heat flux forcing is computed using the shortwave and longwave radiations from JRA55, as well as the latent and sensible heat fluxes derived from the CORE bulk formulae of Large and Yeager (2004) and the model sea surface temperature. The surface freshwater forcing includes evaporation, precipitation, and climatological river runoffs. In addition, the model sea surface salinity is restored toward ocean climatology (Carnes, 2009) with a restoring timescale of two months, and it is constrained by an *ad hoc* assumption of zero global net flux at each time step. The wind stress is calculated from the atmospheric wind velocity and does not take into account the shear introduced by the ocean currents. The simulation starts from rest and is integrated over 1958–2018 with no data assimilation. The horizontal diffusion parameters are listed in **Supplementary Table 1**. A detailed evaluation of the modeled global ocean circulation and sea ice is provided in Chassignet et al. (2020). In this study, we focus on the South Atlantic over the last 40 years of the simulation (1979–2018), which are deemed as being representative of the time-mean circulation after spin-up.

In the remainder of this section, we first evaluate the large-scale surface circulation and then quantify the modeled transport structure at three sections in the South Atlantic: 34°S, 65°W in the Drake Passage, and a Prime Meridian-Good Hope section southwest of Africa (**Figure 1**). Significant observations have been conducted at these locations and they provide a benchmark for evaluating the realism of the modeled transports, which will be used to document the transport structure of the South Atlantic in Section "Circulation pathways in the South Atlantic Ocean."

Surface Circulation Pattern

Figure 2 compares the observed and modeled mean sea surface height (SSH), SSH variability, and eddy kinetic energy (EKE) of the surface currents in the South Atlantic. The observed mean SSH (**Figure 2A**) is from the latest mean dynamic topography climatology CNES-CLS18 (Mulet et al., 2021) while the SSH variability (**Figure 2C**) and surface EKE (**Figure 2E**) are derived from the AVISO data over 1993–2018, the same time period used for the model results. In the western side of the domain, part of the Antarctic Circumpolar Current (ACC) turns north after passing the Drake Passage and becomes the Malvinas Current (also called the Falkland Current). The latter continues to flow northward along the continental shelf of Argentina until it meets the southward flowing Brazil Current south of the Rio de la Plata estuary near 36°S. The confluence of these two western boundary currents with opposite directions and very different properties (warm salty subtropical water versus cold fresh subantarctic water) leads to numerous high-energy eddies and thus strong variability in this so-called Brazil-Malvinas confluence zone (**Figures 2C–F**). In the south between 50°W and 20°E, the ACC as a whole is mostly zonal and exhibits tighter mean SSH contours near 40°W south of the Zapiola Drift and near 10°W over the MAR. Overall, there is a good agreement between the model and the observations in the western and southern part of the domain, with the exception of a slightly lower model SSH variability

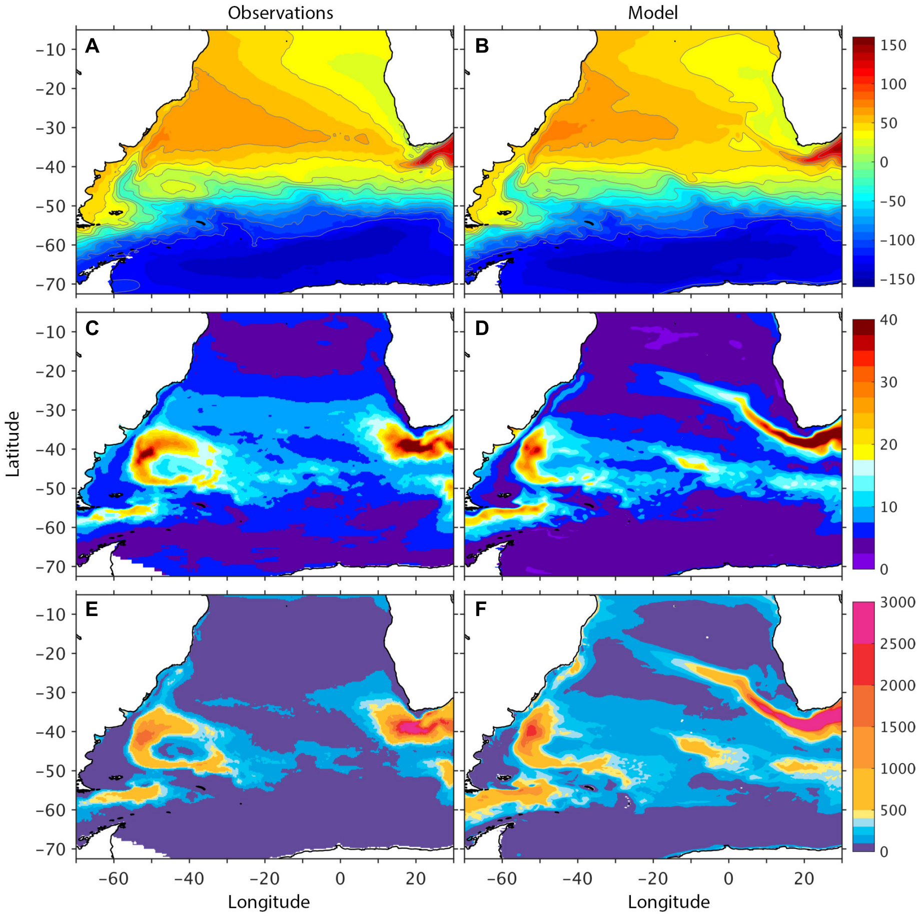

FIGURE 2 | Observed and modeled distributions of **(A,B)** time mean sea surface height (SSH, in cm), **(C,D)** SSH standard deviation (in cm), and **(E,F)** eddy kinetic energy (EKE, in $cm^2\ s^{-2}$) of the surface current in the southern Atlantic. In observation, the mean SSH is based on long-term climatology CNES-CLS18 (Mulet et al., 2021); the SSH standard deviation and EKE are based on AVISO data in 1993–2018. All model results are also in 1993–2018.

offshore in the Brazil-Malvinas confluence zone near 40°S and, likely related, a weaker signature of the Zapiola gyre in mean SSH.

West of Africa, the model results exhibit a narrow tongue of high SSH variability/EKE that extends further northwest into the South Atlantic than in observations. Plots of the SSH variability for both the model and the observations along the Prime Meridian over the observational period of 1993–2018 in **Supplexmentary Figure 1** show that the modeled Agulhas rings are stronger and cross the Prime Meridian within a smaller latitudinal range than in the observations, therefore impacting the regional circulation pattern in the eastern South Atlantic. This is a common feature for many eddying models (e.g., Maltrud and McClean, 2005; Dong et al., 2011; van Sebille et al., 2012), and there is no easy fix short of increasing the horizontal resolution to fully represent the ocean-atmospheric feedback and retain a reasonable level of surface EKE; see Chassignet et al. (2020) and discussion in the summary section.

Water Mass and Transport Across 34°S

Figures 3A–D display a vertical section of the time-mean potential temperature θ and salinity S at 34°S. The observations are based on the gridded monthly Argo profiles (2004–2014) for the upper 2000 m and the World Ocean Atlas 2013 (WOA13, Locarnini et al., 2013; Zweng et al., 2013) below 2000 m (one should note that Argo profiles are sparse in the South Atlantic and that WOA13 data are used in the upper 2000 m when Argo data are missing); the model results are 40-year means from 1979 to 2018. The water column at this latitude can be divided into four density layers of water masses characterized by their salinity (θ decreases monotonically): saline near surface water ($\sigma_2 < 35.65$ kg m^{-3}), fresh Antarctic Intermediate Water (AAIW, $35.65 < \sigma_2 < 36.58$), saline NADW ($36.58 < \sigma_2 < 37.12$), and fresh Antarctic Bottom Water (AABW, $\sigma_2 > 37.12$). There is a good agreement in the θ and S distributions, such as the warm/saline anomaly in 2000–3000 m depth range associated with the NADW in the DWBC. For a more quantitative comparison, **Figures 3E,F** display the volumetric θ-S diagram along 34°S for both observations and model results. The color shading is volume percentage of water mass calculated with a $\Delta\theta \times \Delta S$ grid resolution of 0.1°C × 0.02 psu, and the circled black/red lines are the volume weighted θ-S values calculated for each of the HYCOM density layers. The AAIW occupies ∼20%

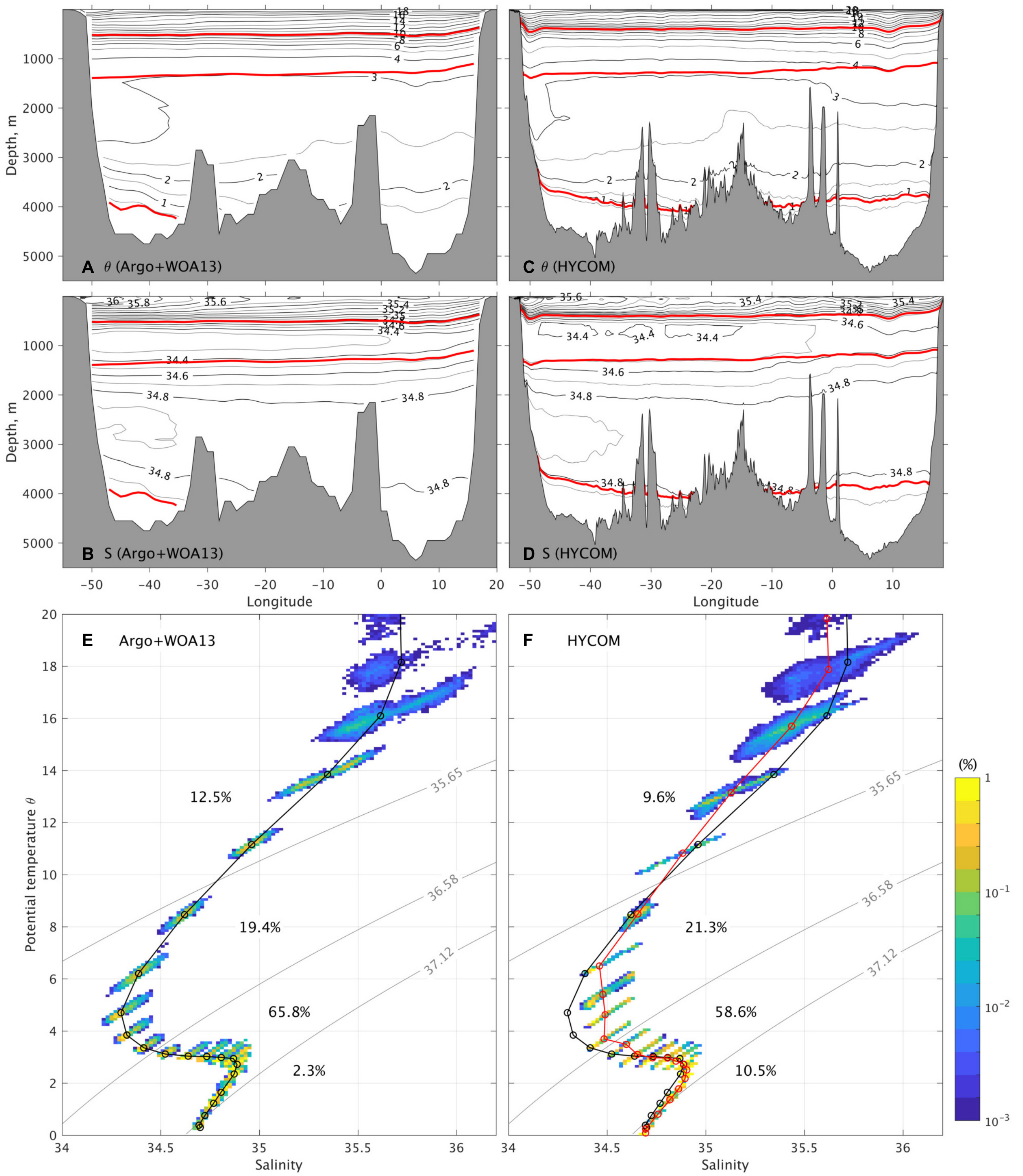

FIGURE 3 | (A–D) Potential temperature θ and salinity S distributions across 34°S. Observations are based on a combination of Argo profiles for the top 2000 m and World Ocean Atlas 2013 (WOA13) below 2000 m; model results are from the global 1/12° HYCOM simulation. Three red lines denote isopycnic surfaces (σ_2 of 35.65, 36.58, and 37.12 kg m^{-3}) that divide the water column into near surface water, Antarctic Intermediate Water (AAIW), North Atlantic Deep Water (NADW), and Antarctic Bottom Water (AABW). **(E,F)** Volumetric θ -S diagram along 34°S. Color shading shows the volume percentage for water mass with Δθ, ΔS resolution of 0.1°C, 0.02 psu (percentages for near surface water, AAIW, NADW and AABW are also listed); circled lines are volume-weighted θ -S profile in observations (black) and model results (red).

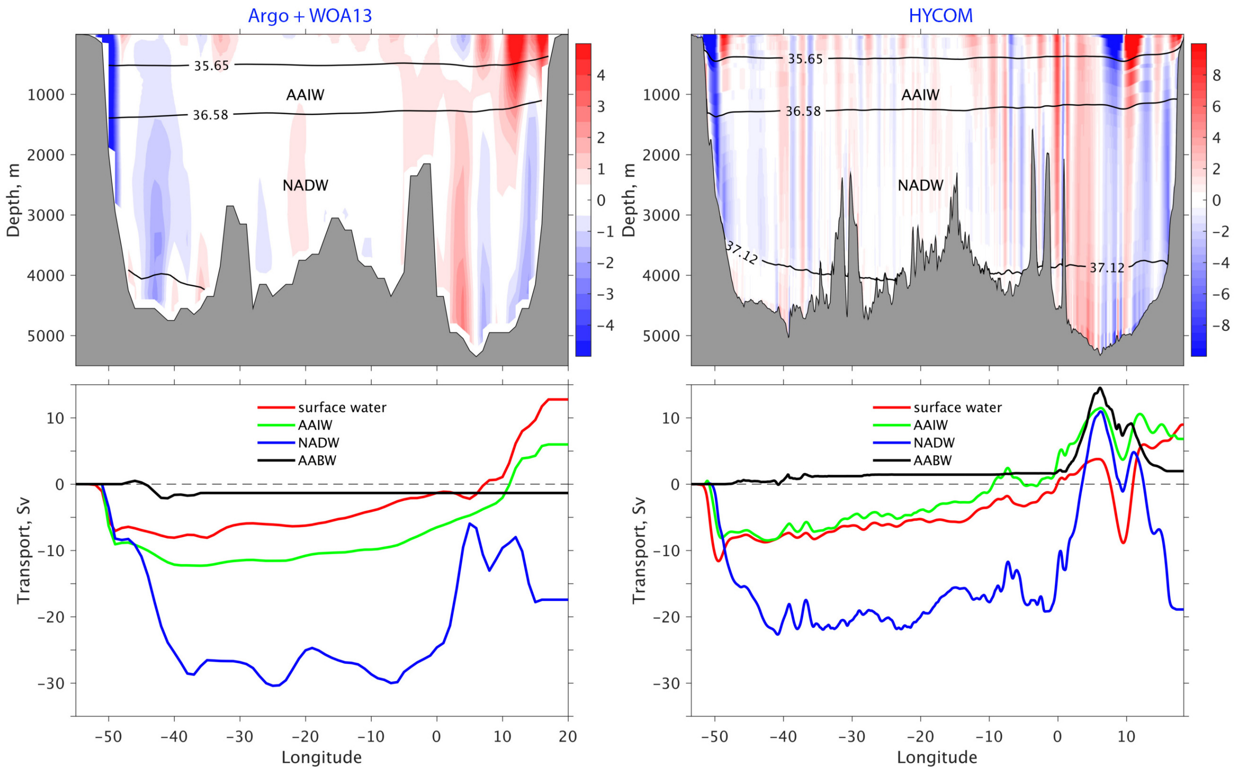

FIGURE 4 | Observed and modeled time mean meridional velocity (color shading in cm/s) across 34°S and the corresponding volume transport for the four density layers: near surface water ($\sigma_2 < 35.65$ kg m^{-3}), Antarctic Intermediate Water (AAIW, $35.65 < \sigma_2 < 36.58$), North Atlantic Deep Water (NADW, $36.58 < \sigma_2 < 37.12$), and Antarctic Bottom Water (AABW, $\sigma_2 > 37.12$). Observations are based on a combination of Argo-WOA13 profiles; model results based on the global 1/12° HYCOM simulation.

of the volume at this latitude in both the observations and model results, and this water mass as a whole is 0.35°C warmer and 0.11 psu saltier in the model than in observations (the maximum θ-S difference is ∼0.8°C and 0.18 psu for an individual density layer). Above the AAIW, the modeled near surface water is about 0.8°C warmer than observations and its salinity is very close to the observations (error on the order of 0.02 psu). Below the AAIW, the differences in θ-S properties are small (0.1°C and 0.02 psu, respectively), but the model results exhibit more AABW and less NADW than in WOA13. The latter is present in the early stage of the simulation and, to a large degree, it reflects the difference between WOA13 and the ocean climatology used for model initialization. Overall, the modeled water properties are consistent with observations – the reader is referred to Chassignet et al. (2020) for a detailed discussion of the temporal evolution of the model's temperature and salinity.

The time mean meridional velocity across 34°S and the corresponding volume transports for the four water masses defined above are shown in **Figure 4**. The observations consist of geostrophic transports derived from θ/S profiles (Argo-WOA13 data) and Ekman transports from the wind stress; see Dong et al. (2014) for details. The model results are 40-year means (1979–2018). The main circulation at this latitude consists of the South Atlantic subtropical gyre (southward Brazil Current near the western boundary and northward interior flow) and the AMOC (northward Bengula Current near the eastern boundary and southward DWBC near the western boundary). Quantitatively, the total transport of the southward western boundary current is about 42 Sv (12, 8, and 22 Sv for the surface water, AAIW, and NADW, respectively) in model, compared to 45 Sv (7, 8, and 30 Sv for the surface water, AAIW, and NADW, respectively) in observations. In the surface water and AAIW layers, the observed subtropical gyre extends from the western boundary to 0–10°E, while the northward-flowing AMOC component occupies the rest of the section to the coast of Africa. The modeled transport pattern is similar to the observations, except that the regular pathway of the Agulhas rings leads to a north/south circulation in the Cape Basin. In the NADW layer, both observations and model results show a strong southward DWBC west of 40°W and a northward return flow east of 40°W. Note that the DWBC is quite wide at this latitude and that the transport obtained by Meinen et al. (2017), 15 Sv west of 44.5°W, does not include the full DWBC (near 30 Sv in Argo-WOA13 based observations and 22 Sv in model). The return flow is mostly localized over the Walvis Ridge. In the Cape Basin, both the Argo-WOA13 based observations and the model show a recirculation of the NADW which is consistent with the results of Kersalé et al. (2019) derived from moored Current and Pressure recording Inverted Echo Sounders. This deep recirculation is likely driven by eddy activity in the upper ocean (Özgökmen and Chassignet, 1998)

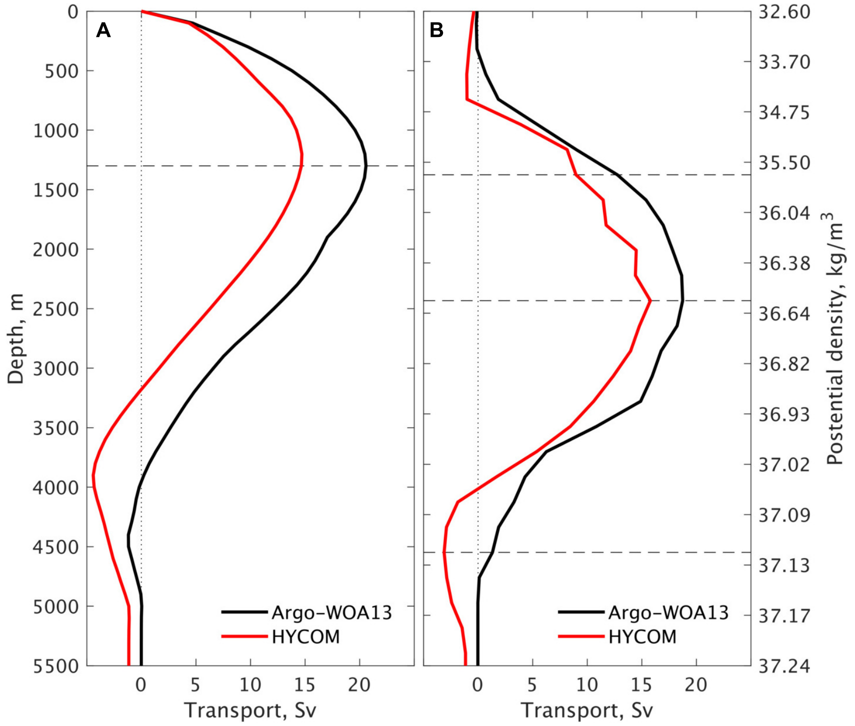

FIGURE 5 | Long-term mean meridional overturning streamfunction (in Sv) at 34°S with respect to **(A)** depth and **(B)** potential density in σ_2. Observations based on monthly mean Argo-WOA13 profiles; model results based a global 1/12° HYCOM simulation (1979–2018).

and is stronger in the model (see **Figure 4**). The pattern does not appear to be affected by the fact that the modeled Agulhas eddies follow a regular pathway. The modeled AABW transport is about 2 Sv in the western basin, much less than the 4-7 Sv estimated in observations (e.g., Hogg et al., 1982; Speer and Zenk, 1993). There is no AABW transport in the Argo-WOA13 based results.

The meridional flows across 34.5°S as shown in **Figure 4** have a significant barotropic component, and the baroclinic nature of the AMOC, i.e., northward flows in the upper limb and southward flows in the lower limb, becomes apparent only when integrated across the basin (**Figure 5**). The zonally integrated mean transport streamfunction with respect to the depth z shows a maximum overturning depth near 1300 m in both observations and model results (**Figure 5A**). The modeled mean AMOC transport is 14.7 Sv. This value agrees with the SAMOC estimate based on six years of two moored observations at the western and eastern boundaries (14.7 Sv, Meinen et al., 2018), but is significantly lower than the estimates based on nine moorings across the 34.5°S (17.3 Sv, Kersalé et al., 2020), XBT transects (18 Sv, Dong et al., 2009; Garzoli et al., 2013) and Argo-WOA13 (20 Sv, Dong et al., 2014). With respect to density (**Figure 5B**), the northward AMOC limb is above the density surface (σ_2) 36.58 kg/m^3 and the southward limb below. The modeled mean AMOC transport in density space is 15.8 Sv, compared to 18.7 Sv based on Argo-WOA13 observations. The modeled northward AMOC limb consists of 9.0 Sv warm surface water and 6.8 Sv AAIW, compared to 12.7 and 6.0 Sv, respectively, in the Argo-WOA13. This leads to a lower meridional heat transport (MHT) of 0.36 ± 0.23 PW in the model, compared to 0.68 ± 0.24 PW in the Argo-WOA13. The historical estimates of the MHT near this latitude are 0.22–0.62 PW (see Table 29.3 in Macdonald and Baringer, 2013).

At 34°S, the modeled AMOC transport variability is lower than observations on both interannual and seasonal timescales (**Figure 6**). On interannual timescale, the model AMOC transports have a standard deviation of 1.0 Sv in 2004–2014, compared to 1.9 Sv in Argo-WOA13 observations for the same period and 2.6 Sv in SAMOC results (Meinen et al., 2018) for a shorter, 6-year period (2009–2010 and 2013–2017). The time evolution of the modeled AMOC variability is similar to the Argo-WOA13 based observations in 2004–2012 but differ after 2012 (**Figure 6A**); note the Argo-WOA13 and SAMOC observations also differ in 2013–2014 when the two observations overlap. On seasonal timescale, the modeled AMOC transports have a standard deviation of 2.2 Sv, compared to 3.3 Sv in the Argo-WOA13 and 2.9 Sv in the SAMOC observations. Although the magnitude is lower, the phase of the modeled seasonal variability is consistent with the Argo-WOA13 and the SAMOC observations (**Figure 6B**).

Transport Through the Drake Passage at 65°W

The Drake Passage is an ACC chokepoint and the place where long-term sustained monitoring programs have been conducted; see Meredith et al. (2011) for a review of historical

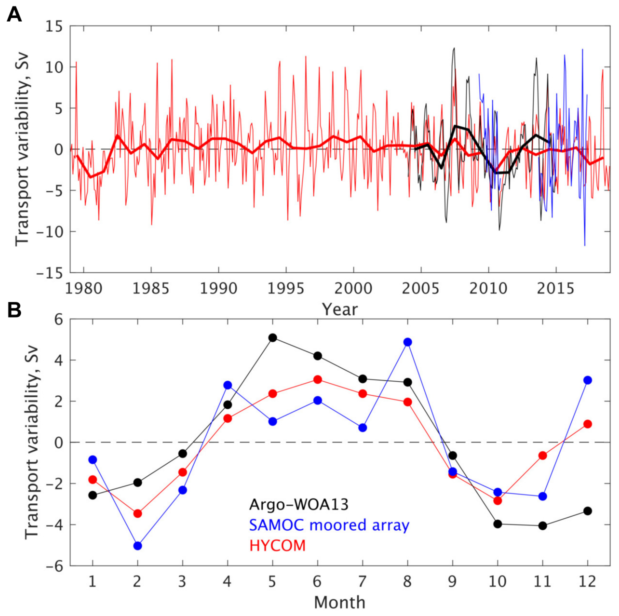

FIGURE 6 | (A) Time series of the AMOC transport variability (in Sv) at 34°S based on Argo-WOA13 (black, Dong et al., 2014), SAMOC-mooring array (blue, Meinen et al., 2018), and global HYCOM (red). The thin and thick lines represent monthly means and 12-month moving averages, respectively. **(B)** AMOC transport variability at seasonal timescale, with each dot representing the multi-year average of the monthly AMOC transport.

observations. The canonical full-depth volume transport is 133.8 ± 11.2 Sv, based on year-long current meter mooring and cruise data obtained during the International Southern Ocean Studies (ISOS, Whitworth, 1983; Whitworth and Peterson, 1985). However, based on a combination of moored current meter data from the DRAKE program (2006–2009) and satellite altimetry data (1992–2012), Koenig et al. (2014) estimated a higher full-depth transport of 141 ± 2.7 Sv. More recently, Chidichimo et al. (2014) and Donohue et al. (2016) estimated an even higher mean ACC transport of 173.3 Sv, based on the high-resolution moored bottom current and pressure measurements of the cDrake program (2007–2011).

The modeled mean ACC transport is 157.3 Sv, about the average of the estimates from DRAKE and cDrake programs. In a detailed analysis of the modeled ACC transport through the Drake passage, Xu et al. (2020) found that (a) the modeled ACC transport in the upper 1000 m of the Drake Passage is in excellent agreement with that of Firing et al. (2011) based on shipboard acoustic Doppler current profiler (SADCP) transects, and (b) the modeled exponentially decaying transport profile is consistent with the profile derived from the repeat hydrographic data from Cunningham et al. (2003) and Meredith et al. (2011). By further comparing the model results to the cDrake and DRAKE observations, Xu et al. (2020) concluded that the modeled 157.3 Sv was representative of the time-mean ACC transport through Drake Passage. The cDrake experiment overestimated the barotropic contribution in part because the array under-sampled the deep recirculation in the southern part of the Drake Passage, whereas the DRAKE experiment underestimated the transport because the surface geostrophic currents yielded a weaker near-surface transport than implied by the SADCP data.

The modeled mean zonal velocity through the Drake Passage at 65°W and the corresponding volume transports for the four density layers defined earlier (surface water, AAIW, NADW, AABW) are shown in **Figure 7A**. The ACC at this longitude exhibits four high velocity cores (indicated by arrows in **Figure 7A**), corresponding to the ACC southern boundary (SBby, south of 63°S), the southern ACC Front (SACCF, at 61–62°S), the Polar Front (PF, at 58–60°S), and the Sub-Antarctic Front (SAF, at 56–58°S). These modeled fronts are at similar locations as in Orsi et al. (1995) based on hydrographic surveys and in other studies based on SSH data (e.g., Sallée et al., 2008; Sokolov and Rintoul, 2009; Kim and Orsi, 2014).

The modeled monthly mean and 12-month moving averaged ACC transports have a standard deviation of 5.2 Sv and 2.3 Sv, respectively (panel a in **Supplementary Figure 2**). These numbers are relatively small compared to the long-term mean value of 157.3 Sv. The seasonal variability of the ACC transports is also small (with a standard deviation of 1.5 Sv) and exhibits a biannual pattern (panel b in **Supplementary Figure 2**). These results agree with the observations in Koenig et al. (2016).

Transport Across the Prime Meridian-Good Hope Transect

The wide ocean gap between Antarctica and the southern tip of Africa makes it difficult to fully measure the transport and its spatial structure. Observations have been collected mostly along the Prime Meridian (e.g., Whitworth and Nowlin, 1987; Klatt et al., 2005) from Antarctica to approximately 50°S and the Good Hope line from 0°E, 50°S to the Cape of Good Hope, South Africa (e.g., Legeais et al., 2005; Gladyshev et al., 2008; Swart et al., 2008). We refer to the combination of these two sections as the Prime Meridian-Good Hope (PM-GH) transect (**Figure 1**). The modeled net transport through PM-GH (158.5 Sv) is essentially the same as the net transport through the Drake Passage because of mass conservation, except for an additional 1.2 Sv from the Pacific-to-Atlantic Bering Strait throughflow.

The modeled circulation along the PM-GH section (**Figure 7B**) can be divided into three regimes:

i) Weddell gyre south of 55.5°S. There are two eastward and two westward jets that form the Weddell gyre. The two westward jets are found along the Antarctic Slope and the Maud Rise (MR) near 64°S, whereas the two eastward jets are found near 58–59°S and along the southern boundary (SBdy) of the ACC at 55.5°S right south of the Southwest Indian Ridge (SIR). This modeled jet pattern is consistent with the observations of Klatt et al. (2005, their Figures 4, 5). The time mean transport of the modeled Weddell gyre is 48.2 Sv, compared to 56 ± 8 Sv estimated in Klatt et al. (2005).
ii) ACC from 55.5 to 40°S. The modeled ACC exhibits high-velocity cores associated with the SACCF (52°S), PF (50.4°S

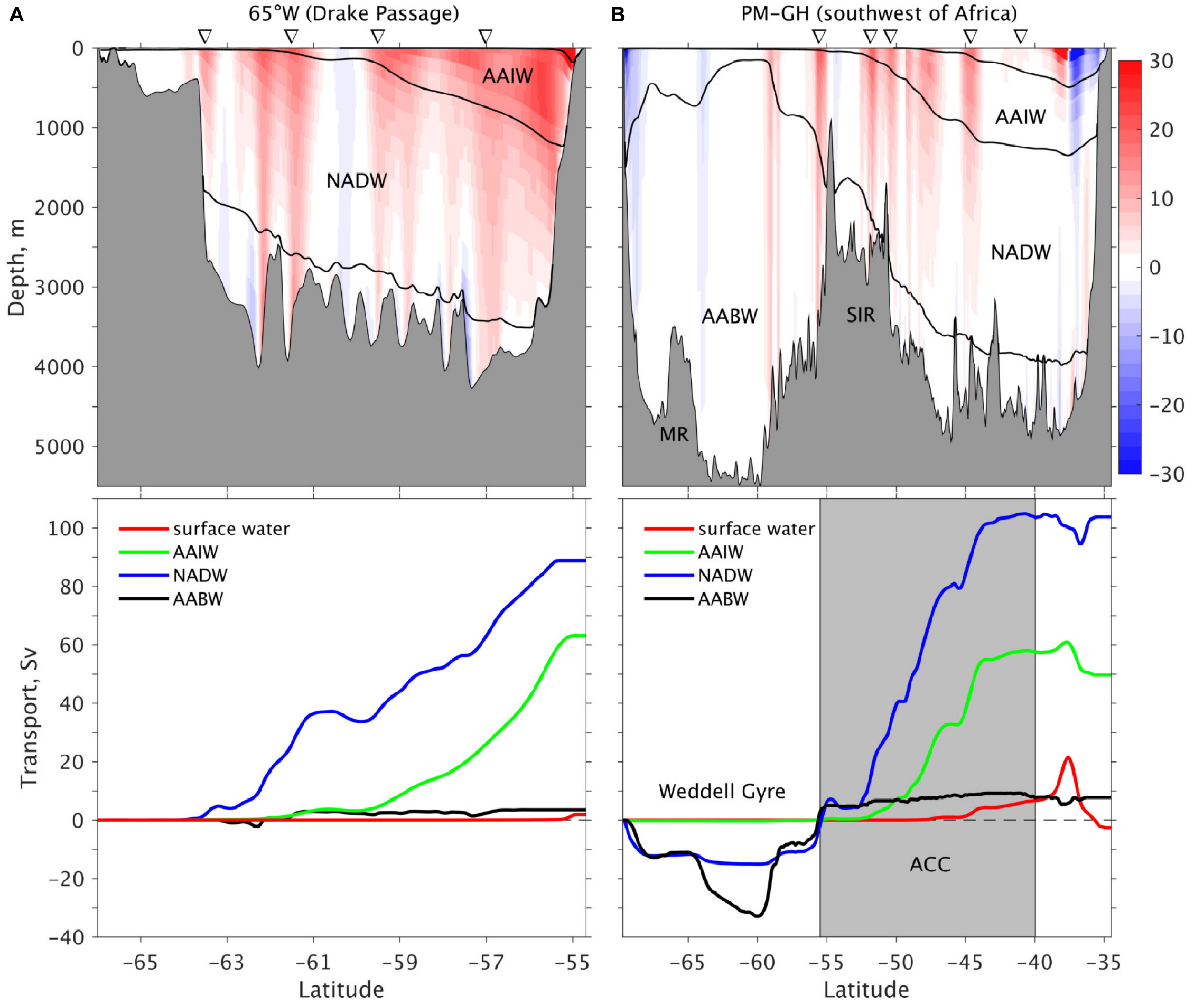

FIGURE 7 | Modeled long-term mean zonal velocity and the corresponding four-layer volume transport in four density layers across **(A)** 65°W in the Drake Passage and **(B)** the Prime Meridian-Good Hope (PM-GH) transect southwest of Africa. The triangles denote the locations of Antarctic circumpolar current (ACC) fronts, from south to north, the Southern Boundary, South ACC Front, Polar Front, Subantarctic Front, and the subtropical front in panel **(B)**. The shaded area in panel **(B)** between 40 and 55.5°S marks the ACC regime across the PM-GH transect. Transport is accumulative northward. The four layers are near surface water ($\sigma_2 < 35.65$ kg m^{-3}), Antarctic Intermediate Water (AAIW, $35.65 < \sigma_2 < 36.58$), North Atlantic Deep Water (NADW, $36.58 < \sigma_2 < 37.12$), and Antarctic Bottom Water (AABW, $\sigma_2 > 37.12$).

and 48°S), SAF (44.6°S), and the subtropical front (STF, 42°S) respectively. These front positions are close to the observations based on repeat CTD/XBT transects in this region (Swart et al., 2008, their Table 3). Note that the PF at this location is split into two fronts, with the elevated eastward velocity between 47 and 49°S corresponding to its northern expression (Gladyshev et al., 2008; Swart et al., 2008). The modeled STF is much weaker than any of the other ACC fronts as in the observations. The modeled mean ACC transport across the PM-GH transect, defined as the transport from 55.5 to 40°S including the STF as in Orsi et al. (1995), is 175 Sv, compared to 147-162 Sv estimated from CTD transects (Whitworth and Nowlin, 1987; Legeais et al., 2005; Gladyshev et al., 2008). The modeled baroclinic transport is 101.2 Sv above 2500 m, compared to 84.7–97.5 Sv derived from repeated hydrographic surveys and in combination with satellite altimetry data (Legeais et al., 2005; Swart et al., 2008).

iii) Agulhas retroflection and leakage north of 40°S. The model results show a pair of eastward and westward flows associated with the Agulhas retroflection and Agulhas Current. Slightly upstream at 28°E, the modeled full-depth Agulhas Current transport is 86.2 Sv, which is close to the observational estimate of 84 Sv in Beal et al. (2015). The "net" transports north of 40°S is 9.3 and 7.9 Sv westward for the surface water and AAIW, respectively. Thus, the Agulhas leakage in model provides slightly more transport than the 15.8 Sv in upper AMOC at 34°S.

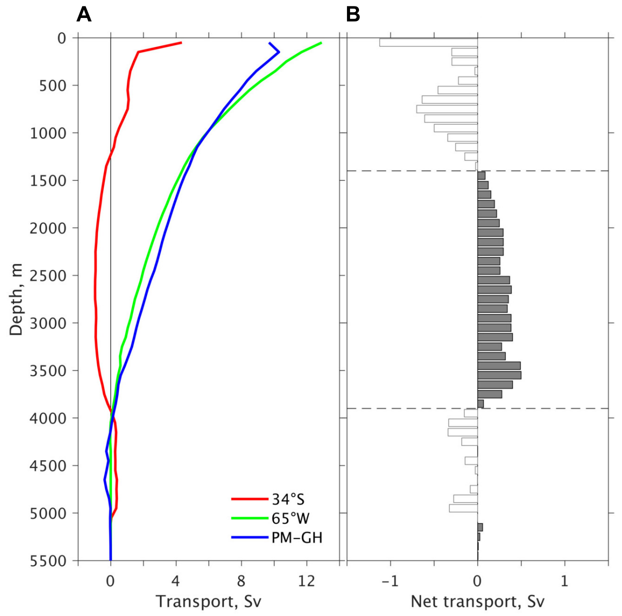

FIGURE 8 | (A) Modeled mean horizontal transports (Sv per 100 m) in the vertical across the 34°S, the 65°W, and the PM-GH transects; **(B)** The net transports into the region enclosed by the three transects, with positive (negative) values indicating net transport into (out of) the region.

The modeled transport across the full PM-GH transect decreases with depth and is eastward above 4000 m (blue line in **Figure 8A**). There is a weak westward flow below 4000 m. When compared to the vertical structure of the transport in the Drake Passage (green line in **Figure 8A**), the eastward transport through PM-GH transect is weaker in the 0–1000 m range and stronger in the 1000–4000 m range. This is due, in a large part, to the contributions to the northward-flowing upper limb and from the southward-flowing lower limb of the AMOC (red line in **Figure 8A**).

The modeled net transports into and out of the region bounded by the 34°S, Drake Passage, and PM-GH sections (see **Figure 1**) are shown in **Figure 8B**. There is a net outflow above 1400 m and below 3900 m and a net inflow between these two depths. The result implies a maximum upwelling transport of 5.6 Sv across 1400 m, consistent with the picture put forward by Schmitz (1995) and Talley (2013) that the Southern Ocean is a key upwelling region for NADW. The net transport in **Figure 8B** also implies a downward transport of 1.7 Sv across 3900 m, representing AABW formation in the model within the region bounded by the 34°S, Drake Passage, and PM-GH sections.

CIRCULATION PATHWAYS IN THE SOUTH ATLANTIC OCEAN

In the previous section, we showed that the model is able to represent the basic circulation features of the South Atlantic and the Southern Ocean, and that the modeled volume transports are consistent with observations. In this section, we use the model results to address the questions raised in the introduction on the relative importance of the warm versus cold source water in the upper limb and the detailed circulation pathways of the lower limb of the AMOC.

Upper Limb (Surface Water and Antarctic Intermediate Water)

The upper (northward) limb of the AMOC consists of two density layers: the surface water ($\sigma_2 < 35.65$) and the AAIW ($35.65 < \sigma_2 < 36.58$ kg m^{-3}). The modeled 40-year (1979–2018) mean horizontal circulation for these two layers is displayed in **Figures 9**, **10**, respectively. For the surface water (**Figure 9**), the AMOC component flows directly northwestward from the Indian Ocean via the Agulhas Leakage into the South Atlantic (red streamlines); the subtropical gyre of the South Atlantic (orange lines) flows counter-clockwise and separates the northward-flowing AMOC component and the eastward-flowing ACC. There is almost no surface water in the ACC coming from the Pacific Ocean (pink lines) and it does not contribute directly to the AMOC.

The modeled circulation pattern of the AAIW (**Figure 10**) is similar to the surface water (**Figure 9**), but it shows a meridionally more confined subtropical gyre (orange lines) and a larger contribution to the ACC from the Pacific Ocean (pink lines). There is an indication of a "supergyre" connecting the subtropical gyres of the South Atlantic and Indian Oceans, which would further prevent a direct contribution of water mass from the ACC into the upper limb of the AMOC. The patterns of modeled mean circulation in **Figures 9**, **10** are similar to the schematic of Stramma and England (1999, their Figures 3, 4), except for the recirculation in the Cape Basin which is a consequence of the unrealistic pathways of the modeled Agulhas eddies (see **Figure 2** and **Supplementary Figure 1** as well as discussion in subsection "Surface circulation pattern").

The model time-mean circulation in **Figure 10** suggests that the Pacific AAIW does not directly contribute to the upper limb of the AMOC. But this does not necessarily imply that there is no contribution by the time-varying part of the circulation, e.g., eddies and meanders. To quantify the combined contribution of the mean flow and eddies by the various water mass sources, we examine the water properties of the northward flow in the South Atlantic, by projecting the meridional transports (in Sv) on potential temperature-salinity (θ-S) plane and comparing their properties with the water masses from the Pacific and the Indian Oceans (**Figure 11**). The Pacific AAIW that flows northward across 45°S is much fresher than the Indian AAIW that flows westward across the GH section (**Figures 11A,B**). The AAIW that flows northward across 34°S and 30°S is a combination of these two sources (**Figures 11C,D**): At 34°S, 7.8 Sv of AAIW is fresher than 34.46 (Pacific) and 9.6 Sv is saltier than 34.46 (Indian). At 30°S, the Pacific contribution ($S < 34.46$) decreased to 3.6 Sv whereas the Indian contribution stayed approximately constant at 9.0 Sv. Further north at 25°S and 20°S (**Figures 11E,F**), the Pacific origin cannot be identified in the θ -S diagram, suggesting that the main contribution of the Pacific AAIW in the South Atlantic is to the subtropical gyre, not to the AMOC. However,

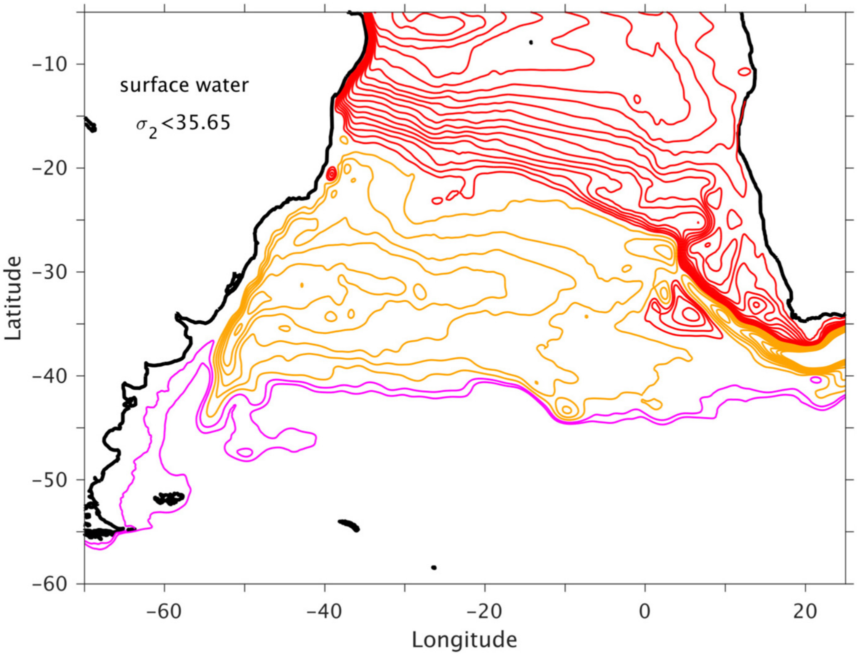

FIGURE 9 | Modeled long-term mean horizontal transport streamfunction (in Sv) for the layer of near surface water ($\sigma_2 < 35.65$ kg m^{-3}). Red and pink streamlines (increment of 1 Sv) denote AMOC contribution and ACC flow; orange streamlines (increment of 2 Sv) denote the subtropical gyre of the South Atlantic.

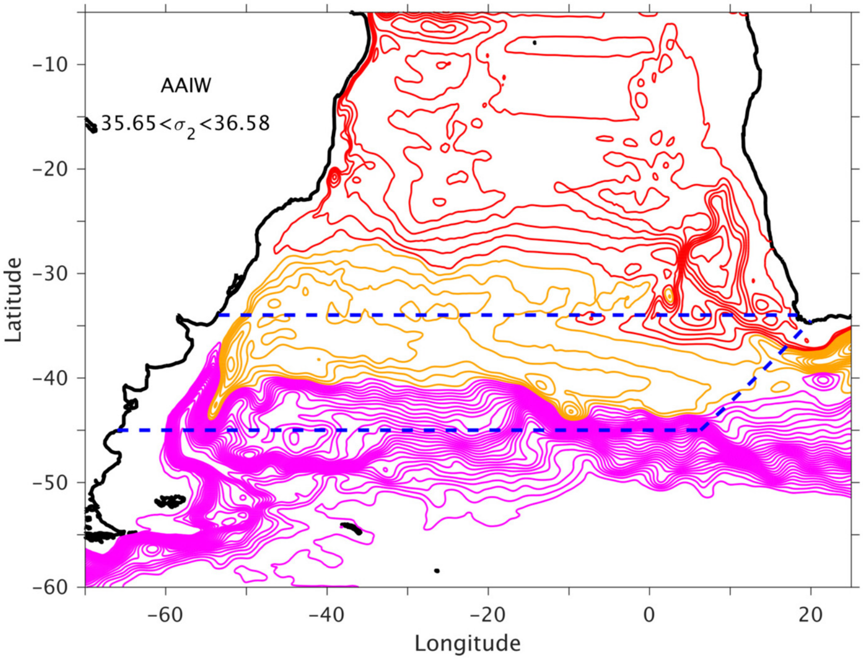

FIGURE 10 | Modeled long-term mean horizontal transport streamfunction (Sv) for the layer of AAIW ($35.65 < \sigma_2 < 36.58$ kg m^{-3}). Pink streamlines (increment of 4 Sv) is the ACC; red and orange streamlines denote AMOC contribution and the subtropical gyre of the South Atlantic (similar to **Figure 15**). The dashed blue lines denote 34°S, 45°S, and the GoodHope sections, across which the water properties of the northward and northwestward transports are examined in **Figure 14**.

the northward-flowing AAIW at 20–25°S is fresher than that at GH (the transport-weighted AAIW salinity is 34.56 at 20–25°S versus 34.60 at GH). This implies that mixing between the Indian and Pacific AAIWs takes place in the South Atlantic. In addition to this (isopycnic) mixing between the two different AAIW sources, there is also (diapycnal) mixing/water mass

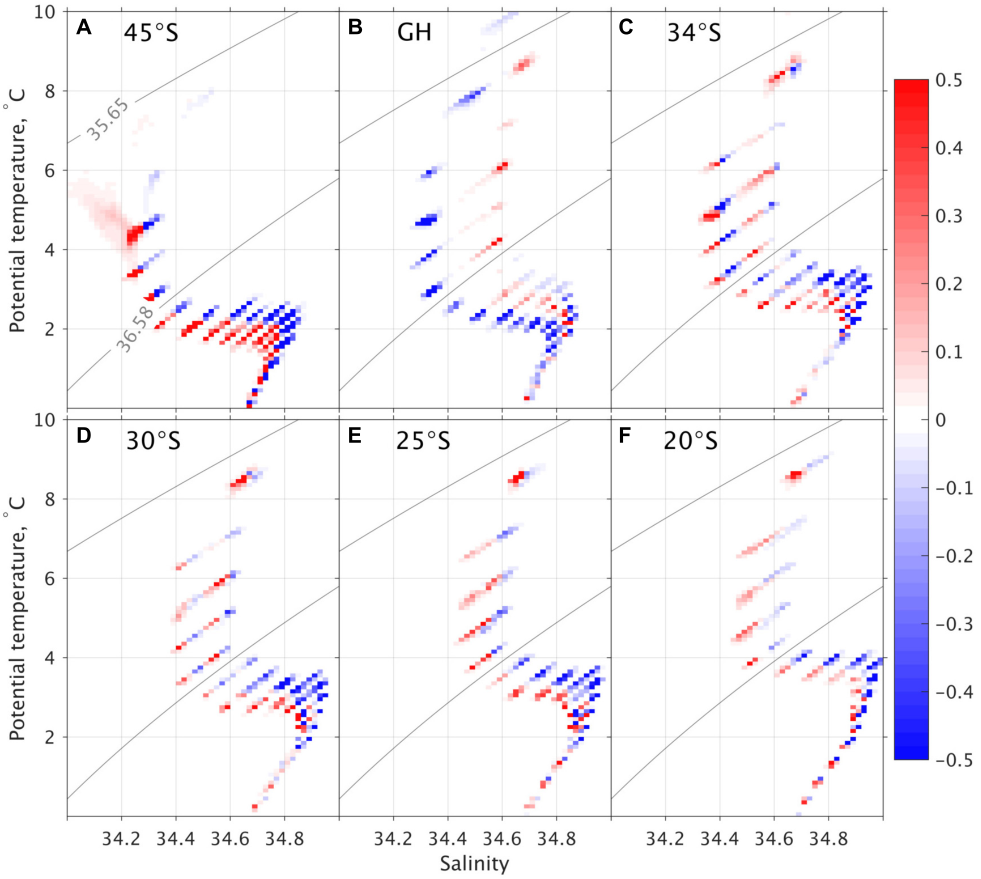

FIGURE 11 | Modeled meridional transports projected on potential temperature-salinity (θ -S) plane across 6 sections (**A–F**: 45°S, GH section, 34°S, 30°S, 25°S, and 20°S, respectively), presented in Sv over an area of (0.2°C × 0.04) in θ -S space. The red and blue colors represent north and south transports into and out of the South Atlantic. The isopycnal (σ_2) surfaces of 35.65 and 36.58 kg m^{-3} denote the upper and lower AAIW interfaces.

transformation between the AAIW and the near surface water that occurs in the South Atlantic. **Supplementary Figure 3** displays the spatial distribution of the mean AMOC transport and the AAIW and near surface water contributions. The results show that about 1.8 Sv of AAIW is transformed into near surface water between 25 and 5°S with a small decrease in overall AMOC transport of ∼1 Sv between 34 and 5°S.

To further study the contribution of Pacific versus Indian AAIW not represented in the time-mean circulation, we released numerical particles into the model AAIW density layers in the North Brazil Current (NBC) along 6°S and tracked their trajectories backward using the modeled daily velocity fields and the Lagrangian Ocean analysis toolbox OceanParcels (Delandmeter and van Sebille, 2019). At this latitude, the NBC is a boundary current that can be well-defined from coast to 33°W and the modeled NBC transport (27.7 Sv) compares well to the observed value (26.5 Sv in Schott et al., 2005). The particles were released in the northward-flowing NBC along 6°S every month in 2017–2018 and were back-tracked for 30 years. Similar to Blanke et al. (1999) and Rühs et al. (2019), the number of particles released at each grid point on the section is proportional to the model transport at that location. Each particle is tacked with a small partial volume transport (∼0.01 Sv) such that the cumulative volume transport of all the particles reflects the instantaneous total AAIW transport through the NBC each time they are released. A total of 34,016 particles were released and the majority (23,683 or ∼70%) of these particles remains in the South Atlantic, mostly north of 30°S, after 30 years of integration. Out of the 10,333 particles that "exit" the South Atlantic, 3,166 (∼30%) were found to flow through the Drake Passage box first, i.e., the cold route, and 7,167 (∼70%) through the Agulhas Leakage, i.e., the warm route. **Figures 12A,B** display the probability that one particle went through a given location in the South Atlantic from the cold and warm routes to reach the NBC at 6°S during the 30-year integration. The high probability area of cold-route particles (in **Figure 12A**) between 30 and 40°S resembles the shape of time-mean streamline of the subtropical gyre (orange contours in **Figure 10**). It indicates that, through transient eddies, particles from the ACC enter the subtropical gyre near the Malvinas confluence zone and exit the subtropical gyre into the AMOC near 30°S, 30°W. The high probability area of the warm-route particles (**Figure 12B**) follows the translation pathway of Agulhas Rings: northwestward through the Cape Basin, then zonally across the South Atlantic near 25–30°S, before

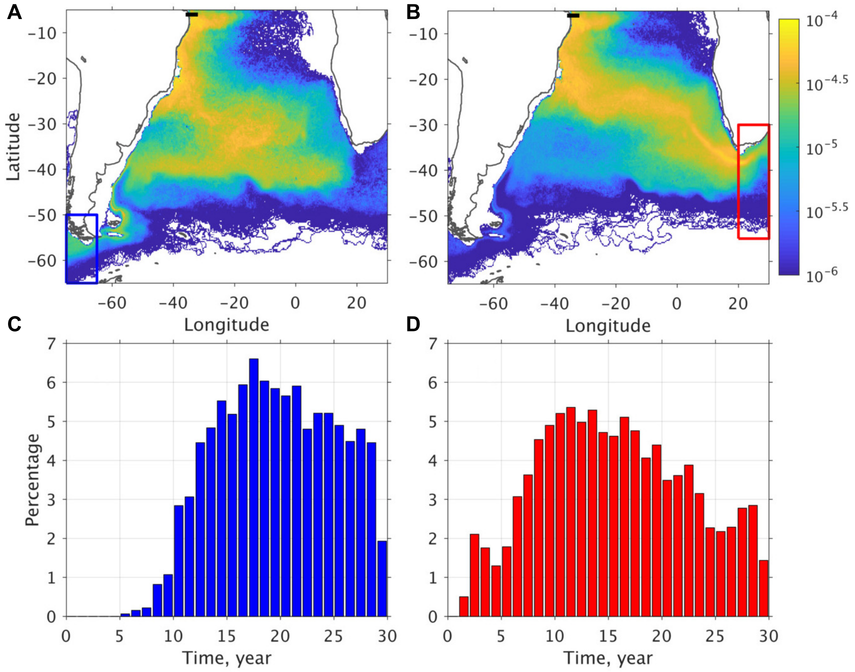

FIGURE 12 | (A,B) Probability map of the trajectory occurrence in the South Atlantic (1/4° × 1/4° grid) for the AAIW particles that were released along 6°S in the North Brazil Current (thick black line) and back-tracked for 30 year to reach **(A)** blue box in the Drake Passage (3,166 particles) and **(B)** red box in the Agulhas Leakage (7,167 particles); **(C,D)** the percentage of the particles that were back-tracked to reach **(C)** the Drake Passage and **(D)** the Agulhas Leakage as a function of time. The probabilities are computed as the number of particles landing in 1/4°x1/4° box normalized by total number of particles over time.

turning northward into the western boundary current that feeds into the NBC. This pathway is in general agreement with the time mean AAIW streamlines that contribute to the AMOC in **Figure 10** (red contours). **Figures 12C,D** displays the time scales taken by the particles from the Drake Passage and the Agulhas Leakage to reach the NBC along 6°S. The most common time for a particle to reach 6°S is about 18 and 12 years, respectively, from the Drake Passage and the Agulhas Leakage (both routes exhibit a wide range of time scales).

The volume transport carried by all the particles divided by the number of releases provides an annual mean "Lagrangian" AAIW transport for each route: 1.3 Sv for the cold route (30%) and 3.0 Sv for the warm route (70%). The sum of these two transports (4.3 Sv) is slightly lower than the "Eulerian" 5 Sv mean transport of AAIW across 6°S (**Supplementary Figure 3**). The most useful result out of the Lagrangian experiment is not the absolute transport of each route, but the ratio between the two, since many of the particles have not yet left the South Atlantic at the end of the 30-year integration and a steady state has not been reached. If one assumes that the 5.0 Sv AAIW that flows across 6°S has the warm-to-cold contribution ratio (30% to 70%) as indicated by the Lagrangian particles, then the cold and warm-route AAIW contributions are about 1.5 Sv and 3.5 Sv, respectively. Finally, only about ~2 Sv of the Drake Passage transport is in the surface water density range (**Figure 7A**), hence the surface water contribution from Drake Passage (to the AMOC) is likely negligible. Therefore, our cold-route contribution is in the order of 1.5 Sv. This is about 1/3 of the 4.7 Sv as estimated by Rühs et al. (2019) using a nested high-resolution ocean simulation. It is, however, higher than the recent estimate of 0.4 Sv by Rousselet et al. (2020) that is derived using the ECCOv4 (Estimating the Circulation and Climate of the Ocean). Note we have only considered direct contributions in this study. Some Pacific water could flow into Indian Ocean first and mix with the Indian waters before contributing to AMOC through the Agulhas Leakage (Speich et al., 2001, 2007), those would be considered as warm-route contribution.

Lower Limb (North Atlantic Deep Water)

Figure 13 shows the modeled mean circulation for the NADW layer ($36.58 < \sigma_2 < 37.12$). The modeled NADW flows southward as a DWBC along the continental slope of the Brazil and Argentine Basins, all the way to about 40°S where it encounters the northward-flowing deep Falkland Current. The NADW continues to flow southward (now offshore of the deep Falkland Current) to about 45°S where it meanders and flows eastward south of the Zapiola Drift. This modeled NADW pathway is similar to the one described in the schematic of Stramma and England (1999, their Figure 5) and is consistent with pathways derived from salinity, oxygen, and other tracers such as CFC (e.g., Koltermann et al., 2011; Garzoli et al., 2015). It is also similar to the typical NADW pathway reconstructed from Lagrangian trajectories in Rousselet et al. (2021) using reanalysis results. There is a strong counterclockwise flow around the Zapiola Drift (**Figure 13**) with a transport of approximately 25 Sv. The Zapiola anticyclone extends from surface all the way

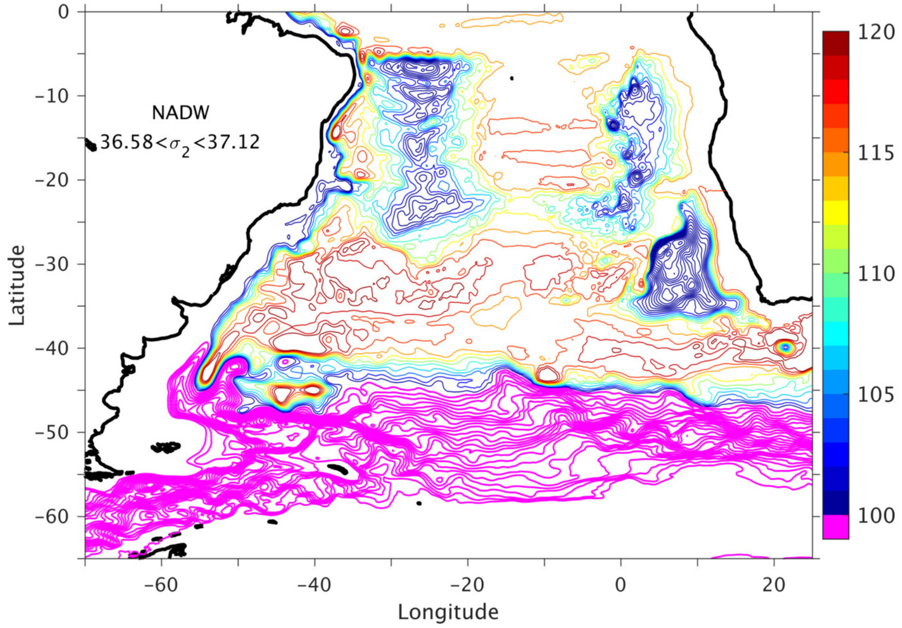

FIGURE 13 | Modeled long-term mean horizontal transport streamfunction for the layer of NADW ($36.58 < \sigma_2 < 37.12$ kg m^{-3}). Pink streamlines (4 Sv increment) indicate the eastward transport of the ACC, blue to yellow streamlines (2 Sv increment) represent the southward spreading of the NADW from north.

to the bottom, and the modeled time mean full water column transport is about 55 Sv, which is consistent with 50 Sv estimated in Saraceno et al. (2009) using the mean dynamic topography (MDT) data. The transport is highly variable, however, with a standard deviation value of 33 and 18 Sv for the monthly and annual means, respectively. Given the high variability (on intraseaonal and interannual scales), it is not surprising that significantly higher transports have been estimated, e.g., 80 Sv by Saunders and King (1995) from CTD/ADCP data and 124 Sv by Colin de Verdière and Ollitrault (2016) from Argo float data.

In addition to the DWBC, the modeled NADW layer streamfunction (**Figure 13**) suggests complex recirculation patterns in the Brazil Basin, the Angola Basin, and the Cape Basin, contrast with the smooth streamfunction pattern derived from Lagrangian studies using coarse resolution model and reanalysis (Speich et al., 2007; Rousselet et al., 2021). Hogg and Owens (1999) documented the NADW recirculation in the Brazil Basin using sub-surface float data. Their results show strong zonal flows in the interior, especially near 5–10°S and around the Vitoria-Trindade Seamount Chain near 20–25°S. These zonal flows carry NADW from the DWBC toward the interior and lead to high salinity all the way to the MAR in both the observations (WOCE lines A09 and A095) and the model (**Figure 14**). The modeled recirculation within the Cape Basin as discussed in Section "Water mass and transport across 34°S" is consistent with the observations. There is no direct observation on the Angola Basin deep circulation, but the modeled clockwise recirculation is consistent with the inverse calculation by Hogg and Thurnherr (2005) and the water property distribution.

The model exhibits a zonal flow of about 2 Sv across the MAR near 22°S (**Figures 13**, **15**), which agrees with the 2–5 Sv estimated from observations by Warren and Speer (1991), Speer et al. (1995), Hogg and Thurnherr (2005), and Garzoli et al. (2015). East of the MAR, the modeled NADW flow turns northward and circulates around the Angola Basin as in the schematic proposed by Hogg and Thurnherr (2005). Arhan et al. (2003), however, proposed a much higher transport (10.7 Sv) of NADW that flows eastward across the southern Angola Basin and southeastward into the Cape Basin. Both the observed and modeled salinity distributions at 2500 m (**Figure 14**) show that between 20 and 25°S, there is a large salinity difference between the east and west of the MAR (A15 and A14 WOCE lines, respectively). This does not support Arhan et al. (2003)'s depiction of a high-salinity NADW transport across the MAR all the way to the eastern boundary. In a numerical study performed with the JAMSTEC OFES (OGCM for the Earth Simulator) model, van Sebille et al. (2012) did find a continuous NADW flow east of the MAR, but this leads to a continuous high salinity tongue (not shown) that extends eastward across the entire Angola Basin and southeastward into the Cape Basin, a result that is not supported by the observations.

Figure 15 also shows that in NADW density range there are weak westward currents across the MAR south of 22°S which lead to a lower salinity (modeled and observed) in the west basin near 30°S (along A10) when compared to 20–25°S (A09 and A095). Overall, there is no net transport of NADW across the MAR between 20 and 40°S, thus most of the eastward NADW transport occurs near 42°S where it joins the ACC water of the same density range ($36.58 < \sigma_2 < 37.12$). The NADW/ACC streamlines turn northward when approaching the MAR and southward after crossing the MAR. This meridional shift can be explained by the conservation of potential vorticity, *f/h*, i.e., a decrease in thickness

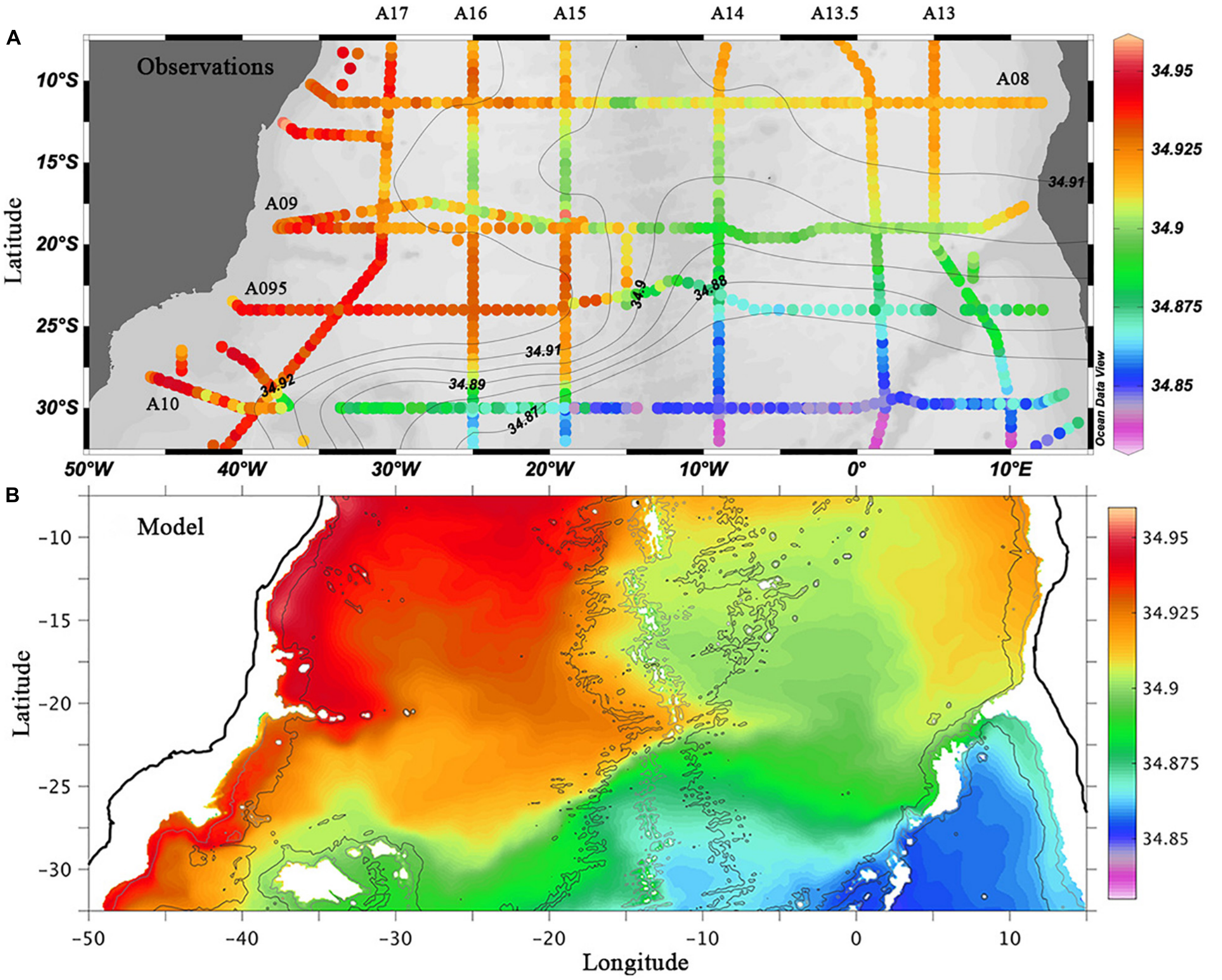

FIGURE 14 | Observed and modeled salinity distribution at 2500m in the South Atlantic. Observations are based on CTD data from GoShip program http://www.go-ship.org. Detailed vertical sections can be seen in the WOCE Atlas (Koltermann et al., 2011). The results show an eastward extension of high salinity (NADW signature) between 20 and 25°S west of the mid-Atlantic Ridge (MAR), and significantly lower salinity east of MAR.

h when approaching the MAR leads to a northward shift to reduce the planetary rotation f so that f/h is constant and vice versa. Because the MAR is slanted in a northwest-to-southeast direction in this area, the northward and southward shifts at different latitude/longitude led to a contraction of the streamlines near 10°W, which can be clearly seen in the SSH for both model and observations (**Figure 2**).

SUMMARY AND DISCUSSION

Through the South Atlantic Ocean, the AMOC is connected to the Indian/Pacific Oceans and is entangled into the global overturning circulation system. This important region is also particularly complex, featuring strong boundary currents (jets) and high eddy variability in both the western and eastern boundaries as well as in the Atlantic sector of the Southern Ocean. Observations of the full-depth circulation structure are focused on limited places, thus the three-dimensional circulation structure in the South Atlantic and the large-scale pattern of the AMOC variability are not well-determined. In this study, we used numerical results from a long-term 1/12° global simulation, along with observations, to address the questions on the mean circulation pattern that cannot be addressed using only observations. The model results are shown to represent well the transports and the vertical structure of the key circulation patterns in this region, especially, the AMOC across 34°S in the South Atlantic, the ACC at 65°W in the Drake Passage, as well as the zonal flows along the PM-GH transect in the open ocean southwest of Africa. The key results, derived from Lagrangian and Eulerian analyses, are:

1) The Pacific AAIW plays a significant role in setting the temperature and salinity properties of the water in the subtropical South Atlantic, but the upper limb of the AMOC is found to primarily originate from the

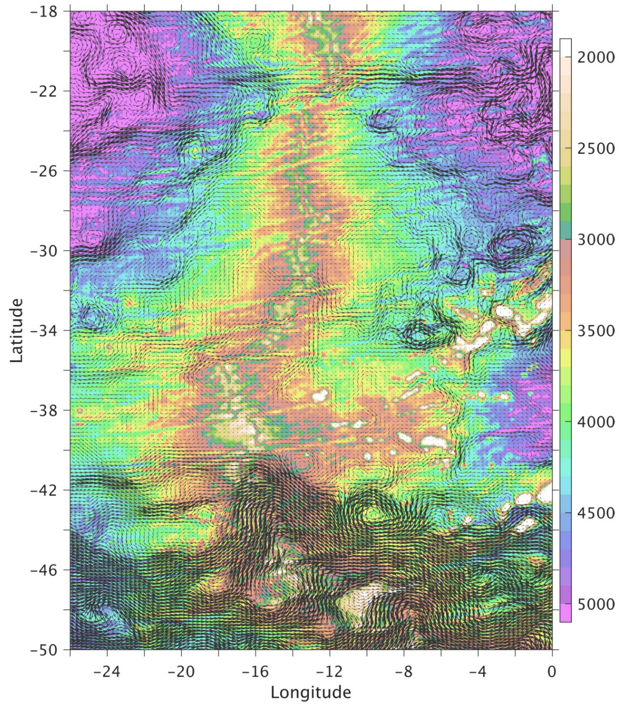

FIGURE 15 | Zoomed view of the modeled mean circulation for the density layer of NADW ($36.58 < \sigma_2 < 37.12$ kg m^{-3}) across the Mid-Atlantic Ridge in the South Atlantic Ocean.

warm Indian water through the Agulhas leakage (9.8 Sv surface water + 3.5 Sv AAIW) and only a relatively small contribution of 1.5 Sv colder, fresher AAIW originates from the Pacific Ocean through the Drake Passage.

2) In the lower limb of the AMOC, the NADW flows southward in the DWBC along the continental slope and in complex recirculation in the Brazil Basin, especially around the Vitória-Trindade Seamount Chain near 20°S. The recirculation carries the NADW and its high-salinity signature into the offshore interior. A weak zonal flow of NADW of ∼2 Sv is found to cross the MAR near 22°S. Different from the schematic of Arhan et al. (2003) based on inverse model and the previous numerical results of van Sebille et al. (2012), however, this modeled NADW does not continue to flow eastward across the Angola Basin and southeastward into the Cape Basin. Instead, it turns northward and circulates around the Angola Basin like the schematic proposed by Hogg and Thurnherr (2005). This NADW circulation pattern is consistent with the water property distribution, i.e., in both observations and model, the salinity east of MAR is significantly lower than that to the west. Virtually all of the NADW from the north flows in the DWBC all the way to 40–45°S before turning eastward to flow across the MAR near 42°S, 10°W. This crossing has a surface signature of concentrated SSH contours and is visible in satellite observations.

Although the modeled transport and vertical structure of the South Atlantic presented in this study are largely consistent with the observations, there is room for improvement. In particular, the modeled Agulhas Rings dissipate too slow and follow a regular pathway. This leads to a high EKE tongue that extends much farther to the northwest and impacts the regional circulation pattern in the eastern South Atlantic. Several remedies have been put forward to improve the realism of the circulation in the Agulhas region, namely (i) using finer horizontal resolution along with a better representation of the bathymetry features like the Agulhas Bank/Plateau as well as the continental slope and seamounts (Speich et al., 2006); (ii) using a higher order advection scheme which would lead to more irregularity in Agulhas eddy size and pathway (Backeberg et al., 2009), or (iii) including the ocean current feedback in the wind stress calculation (Renault et al., 2017; Chassignet et al., 2020). While it is indeed more physical to take into account the vertical shear between atmospheric winds and ocean currents when computing the wind stress, it does lead to an eddy damping effect that can reduce the kinetic energy by as much as 30% and a serious underestimation of EKE elsewhere in the domain (Chassignet et al., 2020). There is therefore a trade-off between a better representation of one current system (the Agulhas) and more realistic energetic and/or variability throughout the globe. A future comparison study is merited to evaluate the extent to which an improved Agulhas eddy presentation could impact the transport structure in the South Atlantic Ocean, through the interaction between the Agulhas eddies and the subtropical gyre and the exchange/mixing between warm and cold water along the eddy pathways.

DATA AVAILABILITY STATEMENT

The altimeter products used here were produced by Ssalto/Duacs and distributed by AVISO, with support from CNES (http://www.aviso.altimetry.fr/duacs); the gridded T/S fields from the Argo float measurements are available at http://www.argo.ucsd.edu; the World Ocean Atlas 2013 is available at http://www.nodc.noaa.gov/OC5/woa13; the original global model outputs are stored in the ERDC archive server and the model results presented in this study are available in HYCOM server (https://data.hycom.org/pub/xbxu/GLBb0.08/SATLx). Further inquiries can be directed to the corresponding author.

AUTHOR CONTRIBUTIONS

XX configured and performed the global simulation and analysis of the model results. EC coordinated the model configuration and analysis. SD and MB provided the observations and contributed on model-data comparison discussions. All authors participated in the interpretation of the results and in the writing of the manuscript.

FUNDING

This work was supported by the NOAA Climate Program Office MAPP Program (Award NA15OAR4310088), the NOAA Climate Variability and Predictability Program (Award GC16-210), and the Office of Naval Research (Grant N00014-19-1-2674). The numerical simulations were performed on supercomputers at the Engineer Research and Development Center (ERDC), Vicksburg, Mississippi, using computer time provided by the U.S. DoD High Performance Computing Modernization Program.

SUPPLEMENTARY MATERIAL

The Supplementary Material for this article can be found online at: https://www.frontiersin.org/articles/10.3389/fmars.2022.811398/full#supplementary-material

REFERENCES

Arhan, M., Mercier, H., and Park, Y.-H. (2003). On the deep water circulation of the eastern South Atlantic Ocean. *Deep Sea Res. Part I* 50, 889–916. doi: 10.1016/S0967-0637(03)00072-4

Backeberg, B. C., Bertino, L., and Johannessen, J. A. (2009). Evaluating two numerical advection schemes in HYCOM for eddy-resolving modelling of the Agulhas Current. *Ocean Sci.* 5, 173–190. doi: 10.5194/os-5-173-2009

Baringer, O. M., and Garzoli, S. L. (2007). Meridional heat transport determined with expendable bathythermographs. Part I: error estimates from model and hydrographic data. *Deep Sea Res. Part I* 54, 1390–1401. doi: 10.1016/j.dsr.2007.03.011

Beal, L. M., De Ruijter, W. P. M., Biastoch, A., Zahn, R., and Scor/Wcrp/Iapso Working Group 136. (2011). On the role of the Agulhas system in ocean circulation and climate. *Nature* 472, 429–436. doi: 10.1038/nature09983

Beal, L. M., Elipot, S., Houk, A., and Leber, G. M. (2015). Capturing the transport variability of a western boundary jet: results from the Agulhas Current Time-Series Experiment (ACT). *J. Phys. Oceanogr.* 45, 1302–1324.

Blanke, B., Arhan, M., Madec, G., and Roche, S. (1999). Warm water paths in the equatorial atlantic as diagnosed with a general circulation model. *J. Phys. Oceanogr.* 29, 2753–2768. doi: 10.1175/1520-0485(1999)029<2753:WWPITE>2.0.CO;2

Bleck, R. (2002). An oceanic general circulation model framed in hybrid isopycnic-Cartesian coordinates. *Ocean Model.* 37, 55–88.

Bower, A., Lozier, S., Biastoch, A., Drouin, K., Foukal, N., Furey, H., et al. (2019). Lagrangian views of the pathways of the Atlantic Meridional Overturning Circulation. *J. Geophys. Res. Oceans* 124, 5313–5335. doi: 10.1029/2019JC015014

Broeker, W. S. (1991). The great ocean conveyor. *Oceanography* 4, 79–89. doi: 10.5670/oceanog.1991.07

Carnes, M. R. (2009). *Description and Evaluation of GDEM-V3.0*. United States: Naval Research Laboratory.

Chassignet, E. P., Hurlburt, H. E., Smedstad, O. M., Halliwell, G. R., Wallcraft, A. J., Metzger, E. J., et al. (2006). Generalized vertical coordinates for eddy-resolving global and coastal ocean forecasts. *Oceanography* 19, 20–31. doi: 10.5670/oceanog.2006.95

Chassignet, E. P., Smith, L. T., Halliwell, G. R., and Bleck, R. (2003). North Atlantic simulations with the hybrid coordinate ocean model (HYCOM): impact of the vertical coordinate choice, reference pressure, and thermobaricity. *J. Phys. Oceanogr.* 33, 2504–2526.

Chassignet, E. P., Yeager, S. G., Fox-Kemper, B., Bozec, A., Castruccio, F., Danabasoglu, G., et al. (2020). Impact of horizontal resolution on global ocean-sea-ice model simulations based on the experimental protocols of the Ocean Model Intercomparison Project phase 2 (OMIP-2). *Geosci. Model Dev.* 13, 4595–4637. doi: 10.5194/gmd-2019-374-RC2

Chidichimo, M. P., Donohue, K. A., Watts, D. R., and Tracey, K. L. (2014). Baroclinic transport time series of the Antarctic Circumpolar Current measured in Drake Passage. *J. Phys. Oceanogr.* 44, 1829–1853. doi: 10.1175/JPO-D-13-071.1

Colin de Verdière, A., and Ollitrault, M. (2016). A direct determination of the World Ocean barotropic circulation. *J. Phys. Oceanogr.* 46, 255–273. doi: 10.1175/JPO-D-15-0046.1

Cunningham, S. A., Alderson, S. G., King, B. A., and Brandon, M. A. (2003). Transport and variability of the Antarctic Circumpolar Current in Drake Passage. *J. Geophys. Res. Oceans* 108:8084. doi: 10.1029/2001JC001147

Delandmeter, P., and van Sebille, E. (2019). The Parcels v2.0 Lagrangian framework: new field interpolation schemes. *Geosci. Model Dev.* 12, 3571–3584. doi: 10.5194/gmd-12-3571-2019

Dong, S., Baringer, M. O., Goni, G. J., Meinen, C. S., and Garzoli, S. L. (2014). Seasonal variations in the South Atlantic meridional overturning circulation from observations and numerical models. *Geophys. Res. Lett.* 41, 4611–4618. doi: 10.1002/2014GL060428

Dong, S., Garzoli, S., and Baringer, M. (2011). The Role of inter-ocean exchanges on decadal variations of the meridional heat transport in the South Atlantic. *J. Phys. Oceanogr.* 41, 1498–1511. doi: 10.1175/2011JPO4549.1

Dong, S., Garzoli, S., Baringer, M., Meinen, C., and Goni, G. (2009). Interannual variations in the Atlantic meridional overturning circulation and its relationship with the net northward heat transport in the South Atlantic. *Geophys. Res. Lett.* 36:L20606. doi: 10.1029/2009GL039356

Dong, S., Goni, G., and Bringas, F. (2015). Temporal variability of the South Atlantic Meridional Overturning Circulation between 20°S and 35°S. *Geophys. Res. Lett.* 42, 7655–7662. doi: 10.1002/2015GL065603

Donners, J., and Drijfhout, S. S. (2004). The Lagrangian view of South Atlantic interocean exchange in a global ocean model compared with inverse model results. *J. Phys. Oceanogr.* 34, 1019–1035.

Donohue, K. A., Tracey, K. L., Watts, D. R., Chidichimo, M. P., and Chereskin, T. K. (2016). Mean Antarctic Circumpolar Current transport measured in Drake Passage. *Geophys. Res. Lett.* 43, 11760–11767. doi: 10.1002/2016GL070319

Firing, Y. L., Chereskin, T. K., and Mazloff, M. R. (2011). Vertical structure and transport of the Antarctic Circumpolar Current in Drake Passage from direct velocity observations. *J. Geophys. Res. Oceans* 116:C08015. doi: 10.1029/2011JC006999

Friocourt, Y., Drijfhout, S., Blanke, B., and Speich, S. (2005). Water mass export from Drake Passage to the Atlantic, Indian, and Pacific Oceans: a Lagrangian model analysis. *J. Physical Oceanogr.* 35, 1206–1222. doi: 10.1175/JPO2748.1

Garzoli, S. L., Baringer, M. O., Dong, S., Perez, R. C., and Yao, Q. (2013). South Atlantic meridional fluxes. *Deep Sea Res. Part I* 71, 21–32. doi: 10.1016/j.dsr.2012.09.003

Garzoli, S. L., Dong, S., Fine, R., Meinen, C. S., Perez, R. C., Schmid, C., et al. (2015). The fate of the Deep Western Boundary Current in the South Atlantic. *Deep Sea Res. Part I* 103, 125–136. doi: 10.1016/j.dsr.2015.05.008

Garzoli, S. L., and Matano, R. (2011). The South Atlantic and the Atlantic Meridional Overturning Circulation. *Deep Sea Res. Part II* 58, 1837–1847. doi: 10.1016/j.dsr2.2010.10.063

Gladyshev, S., Arhan, M., Sokov, A., and Speich, S. (2008). A hydrographic section from South Africa to the southern limit of the Antarctic Circumpolar Current at the Greenwich meridian. *Deep Sea Res. Part I* 55, 1284–1303. doi: 10.1016/j.dsr.2008.05.009

Goes, M., Goni, G., and Dong, S. (2015). An optimal XBT-based monitoring system for the South Atlantic meridional overturning circulation at 34S. *J. Geophys. Res. Oceans* 120, 161–181. doi: 10.1002/2014JC010202

Gordon, A. L. (1986). Interocean exchange of thermocline water. *J. Geophys. Res. Oceans* 91, 5037–5046. doi: 10.1029/JC091iC04p05037

Gordon, A. L. (2001). "Interocean Exchange" in *Ocean Circulation and Climate Observing and Modelling the Global Ocean*. eds G. Siedler, J. Church, and J. Gould (London: Academic Press). 303–314. doi: 10.1016/s0074-6142(01)80125-x

Hirschi, J. J.-M., Barnier, B., Böning, C., Biastoch, A., Blaker, A. T., Coward, A., et al. (2020). The Atlantic meridional overturning circulation in high-resolution models. *J. Geophys. Res. Oceans* 125:e2019JC015522. doi: 10.1029/2019JC015522

Hogg, N. G., Biscaye, P. E., Gardner, W. D., and Schmitz, W. J. Jr. (1982). On the Transport and Modification of Antarctic Bottom Water in the Vema Channel. *J. Mar. Res.* 40, 231–263.

Hogg, N. G., and Owens, W. B. (1999). Direct measurement of the deep circulation within the Brazil Basin. *Deep Sea Res. Part II* 46, 335–353. doi: 10.1029/2004/JC002311

Hogg, N. G., and Thurnherr, A. M. (2005). A zonal pathway for NADW in the South Atlantic. *J. Oceanogr.* 61, 493–507. doi: 10.1007/s10872-005-0058-7

Hunke, E. C., and Lipscomb, W. H. (2008). *CICE: the Los Alamos Sea Ice Model Documentation and Software User's Manual, version 4.0. LA-CC-06-012.* Los Alamos: Los Alamos National Laboratory.

Kersalé, M., Meinen, C. S., Perez, R. C., Le Hénaff, M., Valla, D., Lamont, T., et al. (2020). Highly Variable Upper and Abyssal Overturning Cells in the South Atlantic. *Sci. Adv.* 6:7573. doi: 10.1126/sciadv.aba7573

Kersalé, M., Perez, R. C., Speich, S., Meinen, C. S., Lamont, T., Le Hénaff, M., et al. (2019). Shallow and Deep Eastern Boundary Currents in the South Atlantic at 34.5°S: mean structure and variability. *J. Geophys. Res. Oceans* doi: 10.1029/2018JC014554

Kim, Y. S., and Orsi, A. H. (2014). On the variability of Antarctic Circumpolar Current fronts inferred from 1992–2011 altimetry. *J. Phys. Oceanogr.* 44, 3054–3071. doi: 10.1175/JPO-D-13-0217.1

Klatt, O., Fahrbach, E., Hoppeman, M., and Rohardt, G. (2005). The transport of the Weddell Gyre across the prime meridian. *Deep Sea Res. Part II* 52, 513–528. doi: 10.1016/j.dsr2.2004.12.015

Koenig, Z., Provost, C., Ferrari, R., Sennéchael, N., and Rio, M.-H. (2014). Volume transport of the Antarctic Circumpolar Current: production and validation of a 20 year long times series obtained from in situ and satellite data. *J. Geophys. Res. Oceans* 119, 5407–5433. doi: 10.1002/2014JC009966

Koenig, Z., Provost, C., Park, Y.-H., Ferrari, R., and Sennéchael, N. (2016). Anatomy of the Antarctic Circumpolar Current volume transports through Drake Passage. *J. Geophys. Res. Oceans* 121, 2572–2595. doi: 10.1002/2015JC011436

Koltermann, K. P., Gouretski, V. V., and Jancke, K. (2011). *Hydrographic Atlas of the World Ocean Circulation Experiment (WOCE). Volume 3: atlantic Ocean.* Southampton: International WOCE Project Office.

Large, W. G., and Yeager, S. (2004). *Diurnal to Decadal Global Forcing for Ocean and Sea-ice Models: the Data Sets and Flux Climatologies.* United States: NCAR.

Legeais, J. F., Speich, S., Arhan, M., Ansorge, I. J., Fahrbach, E., Garzoli, S., et al. (2005). The baroclinic transport of the Antarctic Circumpolar Current south of Africa. *Geophys. Res. Lett.* 32:L24602. doi: 10.1029/2005GL023271

Locarnini, R. A., Mishonov, A. V., Antonov, J. I., Boyer, T. P., Garcia, H. E., Baranova, O. K., et al. (2013). *World Ocean Atlas 2013. Volume 1 Temperature.* United States: NOAA.

Macdonald, A. M., and Baringer, M. O. (2013). Ocean circulation and climate: a 21st century perspective. *Int. Geophys. Ser.* 103, 759–786. B978-0-12-391851-2.00029-5 doi: 10.1016/

Maltrud, E. M., and McClean, J. (2005). An Eddy Resolving Global 1/10° Ocean Simulation. *Ocean Model.* 8, 31–54. doi: 10.1016/j.ocemod.2003.12.001

Meinen, C. S., Garzoli, S. L., Perez, R. C., Campos, E., Piola, A. R., Chidichimo, M. P., et al. (2017). Characteristics and causes of Deep Western Boundary Current transport variability at 34.5°S during 2009–2014. *Ocean Sci.* 13, 175–194. doi: 10.5194/os-13-175-2017

Meinen, C. S., Speich, S., Perez, R. C., Dong, S., Piola, A. R., Garzoli, S. L., et al. (2013). Temporal variability of the Meridional Overturning Circulation at 34.5°S: results from two pilot boundary arrays in the South Atlantic. *J. Geophys. Res. Oceans* 118, 6461–6478. doi: 10.1002/2013JC009228

Meinen, C. S., Speich, S., Piola, A. R., Ansorge, I., Campos, E., Kersalé, M., et al. (2018). Meridional Overturning Circulation transport variability at 34.5°S during 2009–2017: baroclinic and barotropic flows and the dueling influence of the boundaries. *Geophys. Res. Lett.* 45, 4180–4188. doi: 10.1029/2018GL077408

Meredith, M. P., Woodworth, P. L., Chereskin, T. K., Marshall, D. P., Allison, L. C., Bigg, G. R., et al. (2011). Sustained monitoring of the Southern Ocean at Drake Passage: past achievements and future priorities. *Rev. Geophys.* 49:RG4005. doi: 10.1029/2010RG000348

Mulet, S., Rio, M. H., Etienne, H., Artana, C., Cancet, M., Dibarboure, G., et al. (2021). The new CNES-CLS18 Global Mean Dynamic Topography. *Ocean Sci.* 17, 789–808. doi: 10.5194/os-17-789-2021

Orsi, A. H., Whitworth, T. I. I. I., and Nowlin, W. D. Jr. (1995). On the meridional extent and fronts of the Antarctic Circumpolar Current. *Deep Sea Res. Part I* 42, 641–673. doi: 10.1038/s41467-021-24264-9

Özgökmen, T., and Chassignet, E. P. (1998). Emergence of inertial gyres in a two-layer quasi-geostrophic model. *J. Phys. Oceanogr.* 28, 461–484. doi: 10.1175/1520-0485(1998)028<0461:eoigia>2.0.co;2

Renault, L., McWilliams, J. C., and Penven, P. (2017). Modulation of the Agulhas Current retroflection and leakage by oceanic current interaction with the atmosphere in coupled simulations. *J. Phys. Oceanogr.* 47, 2077–2100. doi: 10.1175/JPOD-16-0168.1

Richardson, P. L. (2007). Agulhas leakage into the Atlantic estimated with subsurface floats and surface drifters. *Deep Sea Res. Part I* 54, 1361–1389. doi: 10.1016/j.dsr.2007.04.010

Richardson, P. L. (2008). On the history of meridional overturning circulation schematic diagrams. *Progr. Oceanogr.* 76, 466–486. doi: 10.1016/j.pocean.2008.01.005

Rintoul, S. R. (1991). South Atlantic interbasin exchange. *J. Geophys. Res. Oceans* 96, 2675–2692. doi: 10.1029/90JC02422

Roberts, M. J., Jackson, L. C., Roberts, C. D., Meccia, V., Docquier, D., Koenigk, T., et al. (2020). Sensitivity of the Atlantic meridional overturning circulation to model resolution in CMIP6 HighResMIP simulations and implications for future changes. *J. Adv. Model. Earth Syst.* 12:e2019MS002014. doi: 10.1029/2019MS002014

Rodrigues, R. R., Wimbush, M., Watts, D. R., Rothstein, L. M., and Ollitrault, M. (2010). South Atlantic mass transports obtained from subsurface float and hydrographic data. *J. Mar. Res.* 68, 819–850. doi: 10.1357/002224010796673858

Rousselet, L., Cessi, P., and Forget, G. (2020). Routes of the upper branch of the Atlantic meridional overturning circulation according to an ocean state estimate. *Geophys. Res. Lett.* 47:e2020GL089137. doi: 10.1029/2020GL089137

Rousselet, L., Cessi, P., and Forget, G. (2021). Coupling of the mid-depth and abyssal components of the global overturning circulation according to a state estimate. *Sci. Adv.* 7:eabf5478. doi: 10.1126/sciadv.abf5478

Rühs, S., Schwarzkopf, F. U., Speich, S., and Biastoch, A. (2019). Cold vs. warm water route—Sources for the upper limb of the Atlantic meridional overturning circulation revisited in a high-resolution ocean model. *Ocean Sci.* 15, 489–512. doi: 10.5194/os-15-489-2019

Sallée, J. —B., Speer, K., and Morrow, R. (2008). Response of the Antarctic Circumpolar Current to atmospheric variability. *J. Clim.* 21, 3020–30391. doi: 10.1175/2007JCLI1702.1

Saraceno, M., Provost, C., and Zajaczkovski, U. (2009). Long-term variation in the anticyclonic ocean circulation over Zapiola Rise as observed by satellite altimetry: evidence of possible collapses. *Deep Sea Res. Part I* 56, 1077–1092. doi: 10.1016/j.dsr.2009.03.005

Saunders, P. M., and King, B. A. (1995). Oceanic fluxes on the WOCE A11 section. *J. Phys. Oceanogr.* 25, 1942–1958. doi: 10.1175/1520-0485(1995)025<1942:ofotwa>2.0.co;2

Schlitzer, R. (1996). *Mass and Heat Transports in the South Atlantic Derived from Historical Hydrographie Data, in The South Atlantic.* Berlin: Springer.

Schmitz, W. J. Jr. (1995). On the interbasin-scale thermohaline circulation. *Rev. Geophys.* 33, 151–173. doi: 10.1029/95RG00879

Schmitz, W. J. Jr. (1996). *On the World Ocean Circulation: Volume I.* United States: Woods Hole Oceanographic Institution. 140.

Schott, F. A., Dengler, M., Zantopp, R., Stramma, L., Fischer, J., and Brandt, P. (2005). The shallow and deep western boundary circulation of the South Atlantic at 5–11 S. *J. Phys. Oceanogr.* 35, 2031–2053. doi: 10.1175/jpo2813.1

Smeed, D. A., Josey, S. A., Beaulieu, C., Johns, W. E., Moat, B. I., Frajka-Williams, E., et al. (2018). The North Atlantic Ocean is in a state of reduced overturning. *Geophys. Res. Lett.* 45, 1527–1533.

Sokolov, S., and Rintoul, S. R. (2009). Circumpolar structure and distribution of the Antarctic Circumpolar Current fronts: 1. Mean circumpolar paths. *J. Geophys. Res.* 114:C11018. doi: 10.1029/2008JC005108

Speer, K. G., Siedler, G., and Talley, L. (1995). The Namib Col Current. *Deep Sea Res. Part I* 42, 1933–1950.

Speer, K. G., and Zenk, W. (1993). The flow of Antarctic Bottom Water into the Brazil Basin. *J. Phys. Oceanogr.* 23, 2667–2682. doi: 10.1038/s41598-019-55226-3

Speich, S., Blanke, B., and Cai, W. (2007). Atlantic meridional overturning circulation and the Southern Hemisphere supergyre. *Geophys. Res. Lett.* 34:L23614.

Speich, S., Blanke, B., and Madec, G. (2001). Warm and cold water routes of an OGCM thermohaline conveyor belt. *Geophys. Res. Lett.* 28, 311–314.

Speich, S., Lutjeharms, J. R. E., Penven, P., and Blanke, B. (2006). Role of bathymetry in Agulhas Current configuration and behaviour. *Geophys. Res. Lett.* 33:L23611. doi: 10.1029/2006GL027157

Stramma, L., and England, M. (1999). On the water masses and mean circulation of the South Atlantic Ocean. *J. Geophys. Res.* 104, 863–883. doi: 10.1029/1999JC900139

Swart, S., Speich, S., Ansorge, I. J., Goni, G. J., Gladyshev, S., and Lutjeharms, J. R. E. (2008). Transport and variability of the Antarctic Circumpolar Current south of Africa. *J. Geophys. Res. Oceans* 113:C09014. doi: 10.1029/2007JC004223

Talley, L. D. (2013). Closure of the Global Overturning Circulation Through the Indian, Pacific, and Southern Oceans: schematics and Transports. *Oceanography* 26, 80–97. doi: 10.5670/oceanog.2013.07

Tsujino, H., Urakawa, S., Nakano, H., Small, R. J., Kim, W. M., Yeager, S. G., et al. (2018). JRA-55 based surface dataset for driving ocean-sea-ice models (JRA55-do). *Ocean Model.* 130, 79–139. doi: 10.1016/j.ocemod.2018.07.002

van Sebille, E., Johns, W. E., and Beal, L. M. (2012). Does the vorticity flux from Agulhas rings control the zonalpathway of NADW across the South Atlantic? *J. Geophys. Res. Oceans* 117:C05037. doi: 10.1029/2011JC007684

Warren, B. A., and Speer, K. G. (1991). Deep circulation in the eastern South Atlantic Ocean. *Deep Sea Res. Part I* 38, S281–S322.

Whitworth, T. III (1983). Monitoring the transport of the Antarctic Circumpolar Current at Drake Passage. *J. Phys. Oceanogr.* 13, 2045–2057.

Whitworth, T. III, and Peterson, R. G. (1985). Volume transport of the Antarctic Circumpolar Current from bottom pressure measurements. *J. Phys. Oceanogr.* 15, 810–816.

Whitworth, T., and Nowlin, W. D. (1987). Water masses and currents of the Southern Ocean at the Greenwich meridian. *J. Geophys. Res.* 92, 6462–6476. doi: 10.1029/2018JC014059

Xu, X., Chassignet, E. P., Firing, Y. L., and Donohue, K. (2020). Antarctic Circumpolar Current transport through Drake Passage: what can we learn from comparing high-resolution model results to observations? *J. Geophys. Res. Oceans* 125:e2020JC016365. doi: 10.1029/2020JC016365

Zweng, M. M., Reagan, J. R., Antonov, J. I., Locarnini, R. A., Mishonov, A. V., Boyer, T. P., et al. (2013). *Salinity. Vol. 2, World Ocean Atlas 2013*. United States: NOAA.

Conflict of Interest: The authors declare that the research was conducted in the absence of any commercial or financial relationships that could be construed as a potential conflict of interest.

frontiers in Marine Science

ORIGINAL RESEARCH
published: 04 March 2022
doi: 10.3389/fmars.2022.829144

Interannual Variability and Trends of Sea Surface Temperature Around Southern South America

Daniela B. Risaro [1,2,3]*, **María Paz Chidichimo** [1,2,4] **and Alberto R. Piola** [1,2,3,4]

[1] Departamento de Oceanografía, Servicio de Hidrografía Naval, Buenos Aires, Argentina, [2] Consejo Nacional de Investigaciones Científicas y Técnicas, Buenos Aires, Argentina, [3] Departamento de Ciencias de la Atmósfera y los Océanos, Facultad de Ciencias Exactas y Naturales, Universidad de Buenos Aires, Buenos Aires, Argentina, [4] CNRS-IRD-CONICET, UBA Instituto Franco-Argentino para el Estudio del Clima y sus Impactos (UMI 3351 IFAECI), Buenos Aires, Argentina

The interannual variability and trends of sea surface temperature (SST) around southern South America are studied from 1982 to 2017 using monthly values of the Optimally Interpolation SST version 2 gridded database. Mid-latitude (30°–50°S) regions in the eastern South Pacific and western South Atlantic present moderate to intense warming (~0.4°C decade^{-1}), while south of 50°S the region around southern South America presents moderate cooling (~ –0.3°C decade^{-1}). Two areas of statistically significant trends of SST anomalies (SSTa) with opposite sign are found on the Patagonian Shelf over the southwest South Atlantic: a warming area delimited between 42 and 45°S (Northern Patagonian Shelf; NPS), and a cooling area between 49 and 52°S (Southern Patagonian Shelf; SPS). Between 1982 and 2017 the warming rate has been 0.15 ± 0.01°C decade^{-1} representing an increase of 0.52°C at NPS, and the cooling rate has been –0.12 ± 0.01°C decade^{-1} representing a decrease of 0.42°C at SPS. On both regions, the largest trends are observed during 2008–2017 (0.35 ± 0.02°C decade^{-1} at NPS and –0.27 ± 0.03°C decade^{-1} at SPS), while the trends in 1982–2007 are non-significant, indicating the record-length SSTa trends are mostly associated with the variability observed during the past 10 years of the record. The spectra of the records present significant variance at interannual time scales, centered at about 80 months (~6 years). The observed variability of SSTa is studied in connection with atmospheric forcing (zonal and meridional wind components, wind speed, wind stress curl and surface heat fluxes). During 1982–2007, the local meridional wind explains 25–30% of the total variance at NPS and SPS on interannual time scales. During 2008–2017, the SSTa at NPS is significantly anticorrelated with the local zonal wind (r = –0.85), while at SPS it is significantly anticorrelated with the meridional wind (r = –0.61). Our results show that a substantial fraction of the interannual variability of SSTa around southern South America can be described by the first three empirical orthogonal function (EOF) modes which explain 28, 16, and 12% of the variance, respectively. The variability of the three EOF principal components time series is associated with the combined variability of El Niño–Southern Oscillation, the Interdecadal Pacific Oscillation and the Southern Annular Mode.

Keywords: sea surface temperature, Southwest South Atlantic, interannual variability, climate variability, trends, sea-air interaction, atmospheric forcing

Edited by:
Regina R. Rodrigues,
Federal University of Santa Catarina,
Brazil

Reviewed by:
Wlademir Santis,
University of São Paulo, Brazil
Paola M. Castellanos,
European University of Lisbon,
Portugal

***Correspondence:**
Daniela B. Risaro
drisaro@at.fcen.uba.ar

Specialty section:
This article was submitted to
Physical Oceanography,
a section of the journal
Frontiers in Marine Science

Received: *05 December 2021*
Accepted: *02 February 2022*
Published: *04 March 2022*

Citation:
Risaro DB, Chidichimo MP and Piola AR (2022) Interannual Variability and Trends of Sea Surface Temperature Around Southern South America. Front. Mar. Sci. 9:829144. doi: 10.3389/fmars.2022.829144

1. INTRODUCTION

The variability of Sea Surface Temperature (SST), which is highly influenced by feedbacks with the atmosphere, is a sensitive indicator of climate change. Recent observation-based estimates indicate a fast increase of global SST in the past decades as part of a long-term warming of the ocean surface since the mid-nineteenth century (Rhein et al., 2013; Abram et al., 2019). Between 1993 and 2015 global mean SST has increased at a rate of 0.016 ± 0.002°C year $^{-1}$ (Von Schuckmann et al., 2016), and this increasing rate persisted during 2016 (Von Schuckmann et al., 2018). Atmospheric CO_2 has increased substantially since the start of the Industrial Revolution generating an imbalance of energy in the Earth and therefore warming and increased absorption of CO_2 by the oceans (Ciais et al., 2014; Le Quéré et al., 2018). The majority (∼93%) of the extra thermal energy in the climate system accumulates in the ocean (Rhein et al., 2013). Consequently, the ocean heat content (OHC) has increased by 370 ± 81 ZJ since the 1960s, with contributions of 62.5% in the upper ocean (0–700 m) and 28.6% in the intermediate ocean (700–2,000 m) (Ishii et al., 2017; Cheng et al., 2020; Johnson and Lyman, 2020). Ocean warming in the past decades has led to global mean sea level rise in response to the input of freshwater by melting of glaciers and ice sheets, and to a lesser extent due to ocean thermal expansion (Church et al., 2013; Nerem et al., 2018; Oppenheimer et al., 2019). Ocean warming is considered a major driver of variability, inducing changes in circulation, mixing, oxygen content and bioavailability (Oschlies et al., 2018) which may promote the expansion of oxygen minimum zones (OMZ) and a reduction of available habitat for some species, particularly temperature and chemistry-sensitive organisms (Stramma et al., 2012; Abram et al., 2019; Bindoff et al., 2019).

Documenting fine-scale variability in temperature trends is an important step in developing and understanding the impact of climate change on marine ecosystems (Doney et al., 2012; Ramírez et al., 2017). Variations in SST can affect marine species altering their physiological functions and behavior. Shifts in the spatial ranges of their distribution are expected, such as their poleward migration (Walther et al., 2002; Parmesan and Yohe, 2003; Ling et al., 2009). Changes in species abundance and composition have also been observed, particularly in phytoplankton communities (Hays et al., 2005), which may, in turn, affect oceanic primary production and thus CO_2 sequestration (Beaugrand and Reid, 2003; Rivadeneira and Fernández, 2005). Improved knowledge on the space and time variability of SST and of its main drivers is of great climatic relevance in the current global climate change scenario.

The upper ocean temperature has been rising at global scale (Hartmann et al., 2013). However, there are significant regional variations in its pattern, characterized by warming hot spots (Hobday and Pecl, 2014) and also by regions where the ocean has been cooling (e.g., Muller-Karger et al., 2014). For example, one of the detected regional hotspots that is warming faster than the global average is the southwestern South Atlantic Ocean (SWA) (e.g., Hobday and Pecl, 2014). In contrast, since 1979 cooling trends occur in areas of the Southern Ocean associated with sea ice expansion Fan et al., 2014) that could respond to greenhouse forcing and a positive Southern Annular Mode trend (Kostov et al., 2018). Despite the significant impacts of SST variations on the marine environment, the nature of its long-term variability and trends, and the physical mechanisms that modulate those changes are still poorly understood. Though several studies addressed the impact of climate oscillations by teleconnection patterns in SST in mid and high latitudes in the North Atlantic Ocean (Lee et al., 2008; García-Serrano et al., 2017; Yang et al., 2018; Hardiman et al., 2019; Mezzina et al., 2020) very few have been carried out in the southern hemisphere (Meredith et al., 2008; Rodrigues et al., 2015; Garreaud et al., 2021). Observed changes in mid-latitude SST on timescales from months to years in the South Atlantic have been associated with remote atmospheric fluctuations in the tropical Pacific Ocean, particularly during El Niño events when the response in the extratropics may be due to the atmospheric bridge mechanism (Dong et al., 2006; Kayano and Capistrano, 2014; Rodrigues et al., 2015).

Here we focus our analyses on the productive Atlantic continental shelf off southern South America (70°–60°W, 40°–60°S), hereafter Patagonian Shelf (PS, after Piola et al., 2018). South of 40°S the climatological wind stress is relatively high, around 0.15 Pa (Palma et al., 2004), due to the strong westerly winds (Glorioso and Flather, 1995). Annual-mean climatological SST on the PS varies between 7°C south of ∼52°S and 14°C at ∼42°S with a strong seasonal cycle with ∼7°C annual amplitude (Rivas, 2010). High tidal amplitude, the inflow of low-salinity water from the Magellan Strait, and persistent westerly winds force a long-term mean northeastward circulation (Palma et al., 2004, 2008; Matano et al., 2010). Offshore from the continental shelf, the mean circulation in the SWA is characterized by the northward flowing Malvinas Current (MC) which advects nutrient-rich subantarctic waters along the upper continental slope. Near 38°S, the MC encounters the southward flowing Brazil Current (BC) characterized by warm and salty subtropical waters (e.g., Gordon and Greengrove, 1986). The region where the MC and BC encounter is referred to as Brazil-Malvinas Confluence (BMC) (see mean dynamic topography (MDT) field in **Figure 1A**).

The above-mentioned processes lead to stratification-destratification cycles, nutrients redistribution and retention zones that mediate one of the most productive marine ecosystems in the southern hemisphere (Bisbal, 1995; Falabella et al., 2009). Phytoplankton blooms occur during the spring over most of the shelf region and persist through the summer when the vertical stratification is intense, particularly near frontal regions (Acha et al., 2004; Romero et al., 2006) (**Figure 1B**). The phytoplankton productivity sustains a diverse community of species including significant fisheries and top predators that feed on and breed in its seas (e.g., Acha et al., 2004). SST variability in this region could lead to changes in the vertical stratification and therefore affect the timing and persistence of these blooms (Pecl et al., 2014; Gianelli et al., 2019).

In this study, we describe the linear trends and interannual variability of SST on the PS between 1982 and 2017, and explore the possible links with local and remote atmospheric forcing processes. We describe the observed spatial distribution

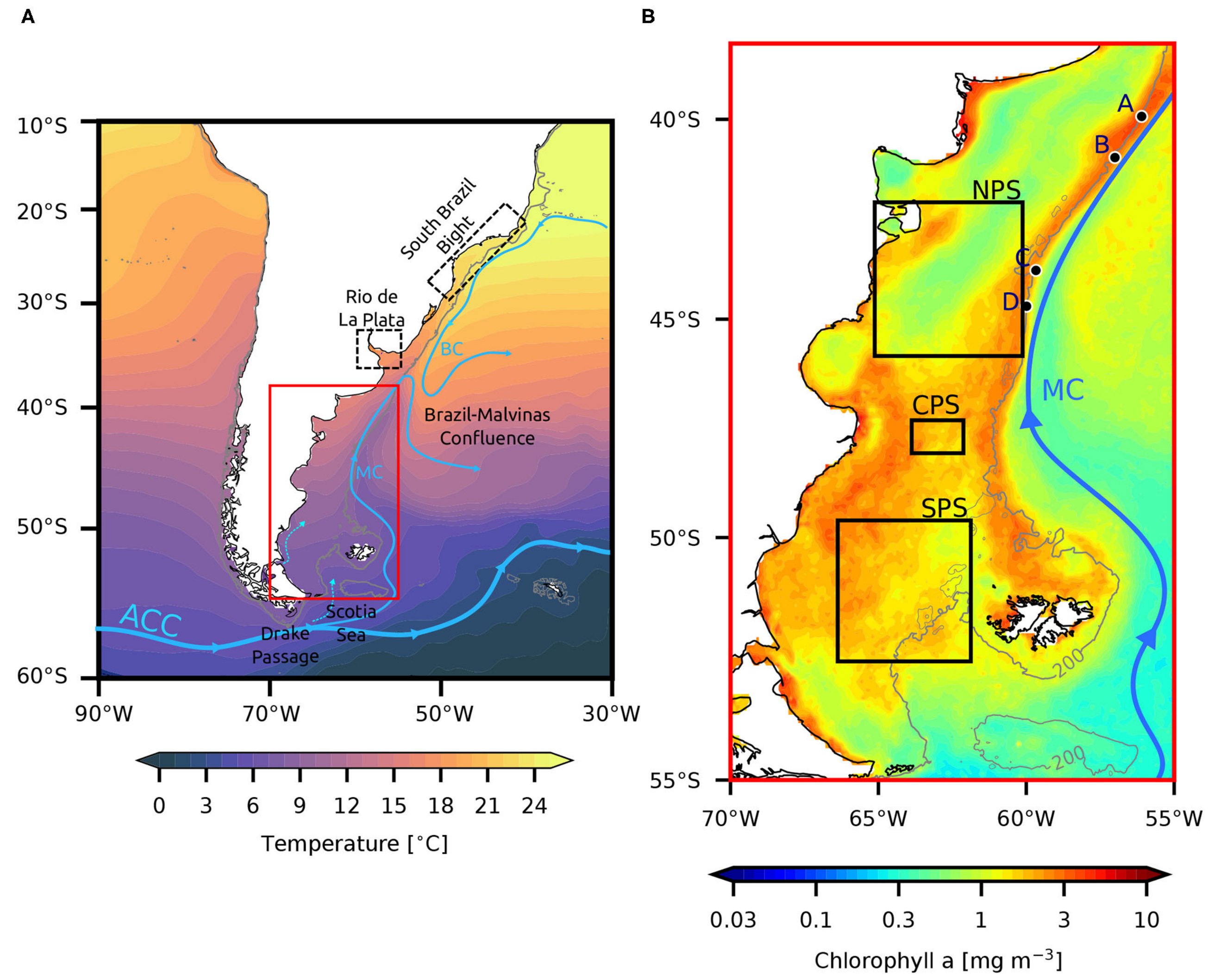

FIGURE 1 | (A) Distribution of climatological SST between 1982 and 2017 (see Section 2.1). Overlaid light blue arrows represent the schematic circulation of the Antarctic Circumpolar Current (ACC), Malvinas Current (MC) and Brazil Current (BC), based on the climatological MDT (1993–2012) from AVISO. **(B)** Climatological austral summer chlorophyll-a surface distribution (2002–2017) derived from MODIS aqua with 9 km spatial resolution. Also shown is the 200 m isobath (solid gray line, data from ETOPO1). Black dots (Sites A to D) are buoy locations of *in-situ* wind measurements (see also **Table 2**). Black rectangles indicate from North to South the main regions analyzed in this study: Northern Patagonian Shelf (NPS), Central Patagonian Shelf (CPS), and Southern Patagonian Shelf (SPS) (see Section 3.2, **Table 3**).

of long-term trends and interannual SST fluctuations focused on areas of significant warming and cooling. To understand the forcing mechanisms of the observed SST fluctuations, we analyzed the relationships between SST anomalies and local winds, air-sea heat fluxes and sea level pressure, and with teleconnection patterns associated with global ocean-atmospheric oscillations, i.e., Southern Annular Mode (SAM), El Niño Southern Oscillation (ENSO) and the Interdecadal Pacific Oscillation (IPO). This paper is organized as follows. In Section 2 we present the datasets used in this study and we describe the methodology underlying the time series analyses. The Results are presented in Section 3. Given the significant role of wind variability on SST through a variety of processes, we first analyze the performance of different wind products in the region, and then present the results and discussion of SST variability together with the local variability of local atmospheric forcing and large-scale teleconnection patterns. The discussion and final remarks are summarized in Section 4.

2. MATERIALS AND METHODS

2.1. SST

We use the Optimally Interpolation SST version 2 (OISSTv2) gridded dataset (Reynolds et al., 2007) available at http://

www.esrl.noaa.gov/psd/data/gridded from January 1982 through December 2017. This dataset has daily temporal resolution and 0.25° spatial resolution. OISSTv2 is based on measurements of the Advanced Very High-Resolution Radiometer (AVHRR) onboard NOAA polar orbiting satellites which began supplying data in late 1981. The satellite derived SST data are calibrated using *in-situ* observations. The OISSTv2 dataset improves the spatial and temporal resolution of previous versions (1° spatial resolution, weekly data) and it is chosen for this study because it employs the same type of satellites during the entire measurement period, reducing the errors associated with the use of different radiometer frequencies or orbits (i.e., microwaves, infrared or geostationary and polar orbits).

2.2. Near-Surface Atmospheric Parameters

Changes in surface wind modulate the variability of momentum and turbulent heat fluxes through the sea surface, the upper ocean circulation, and vertical stratification. Numerical studies suggest large differences in oceanic circulation patterns and volume transports on the PS when forced by different wind stress climatologies (Palma et al., 2004), underlying the sensitivity of the shelf circulation to the wind stress characteristics. It is therefore important to evaluate the relative quality of surface wind stress products. To this end we analyze *in-situ*, satellite-derived and reanalysis winds. Several studies have assessed the quality of wind reanalysis in different parts of the world ocean (Bao and Zhang, 2013; Liléo et al., 2013; Lledó et al., 2013) by comparing wind speeds with wind observations from radiosondes and tall wind towers. In the SWA, there is a single 1-month comparison between reanalysis and *in-situ* wind data (see Supplementary Material in Lago et al., 2019). For completeness, in this study we briefly evaluate the performance of reanalysis and scatterometer-derived products by comparing the surface wind with *in-situ* data using all available records in the region (see Section 2.2.3).

2.2.1. Reanalysis Products

Three widely used reanalysis products are used: The National Centers for Environmental Prediction / National Center for Atmospheric Research reanalysis (NCEPR1, Kalnay et al., 1996), the NCEP Climate Forecast System Reanalysis (CFSR, Saha et al., 2010), and the European Centre for Medium-Range Weather Forecast ERA-Interim Reanalysis (Era-Interim, Dee et al., 2011).

The selected reanalysis products cover the same period of the SST data (Section 2.1) and have different characteristics. NCEPR1 includes a full set of atmospheric variables and is available for the period 1948 to 2017. CFSR has been designed to provide the best estimate of the state of the coupled atmosphere-ocean-land surface-sea ice domains in high spatial resolution. Compared to NCEPR1, CFSR uses an improved model, finer spatial resolution, advanced assimilation schemes, and atmosphere-land-ocean-sea ice coupling. Unlike NCEPR1, because CFSR is a relatively new product, few evaluations of CFSR have been conducted so its performance is not as well-documented. ERA-Interim is produced by the European Center for Medium-Range Weather Forecasts (ECMWF). As CFSR, ERA-Interim covers the period from 1 January 1982 until August 2019.

2.2.1.1. Winds From Reanalysis

Reanalysis products of near surface (10 m) wind data are used from NCEPR1, CFSR and ERA-Interim. For NCEPR1 we select monthly wind data at 10 m, with 2.5° spatial resolution, downloaded from the NOAA/ESRL/PSD archive http://www.esrl.noaa.gov/psd/data/gridded/data.ncep.reanalysis.html. CFSR is analyzed for the period 1982–2017, and in this study, we use monthly mean wind data at 10 m, with 0.5° spatial resolution (https://rda.ucar.edu/datasets/ds093.1/). ERA-Interim is available in various spatial and temporal resolutions and in this study, we selected monthly data and a 0.25° spatial resolution (https://apps.ecmwf.int/datasets/data/interim-full-moda/levtype=sfc/).

2.2.1.2. Sea Level Pressure

We analyze monthly fields of mean sea level pressure (SLP) for the period 1982–2017 from the above-described reanalyses.

2.2.1.3. Heat Fluxes

Monthly means of daily surface heat fluxes are used for the analysis of the components of the sea-air heat flux. Net heat flux (Q_{net}) is computed as:

$$Q_{net} = SW + LW - LH - SH \tag{1}$$

where SW denotes net downward shortwave radiation flux, LW net downward longwave radiation flux, SH sensible heat flux, and LH latent heat flux. In this work, we define positive fluxes to indicate heat gained by the ocean. The time period analyzed is 1982–2017.

2.2.2. Scatterometer Winds

We use data from the Cross-Calibrated Multi-Platform gridded surface vector winds product, version 2.0 (CCMPv2, Atlas et al., 2011) in order to assess the accuracy of 10 m wind data in the SWA from different reanalyses. CCMPv2 combines radiometer wind speeds, QuikSCAT, and ASCAT scatterometer wind vectors, moored buoy wind data, and ERA-Interim model wind fields using a Variational Analysis Method (VAM) to produce 6-h maps of 0.25° gridded vector winds. The CCMPv2 dataset is available for the period 1987 to the present, and does not cover the full record of SST. The ERA-Interim reanalysis winds are used in the CCMPv2 processing as the first-guess wind field. All wind observations (satellite and buoy) and model analysis fields are referenced to a height of 10 meters. CCMPv2 winds have been processed by Remote Sensing Systems (RSS, Wentz et al., 2015) and the data are provided on the RSS website (http://www.remss.com/measurements/ccmp). The main features of wind datasets and variables considered in this work are listed in **Table 1**. The three reanalyses products are compared with CCMPv2 winds that provide an accurate depiction of the winds over the global ocean (excluding the Arctic Ocean) at high spatial and temporal resolution (0.25°, every 6 h).

2.2.3. *In-situ* Wind Measurements

The performance of wind data products from reanalyses (Section 2.2.1) and scatterometers (Section 2.2.2) is evaluated by comparing with *in-situ* data collected on moorings deployed at four locations on the PS shelf break listed in **Table 2** (Sites A to D in **Figure 1B**). Data from neither of these sites have been assimilated in any of the global data sets and thus are useful independent measurements for validating the different surface winds analyzed here. For each site, the mooring configuration consists of an oceanographic buoy holding a set of atmospheric sensors (air temperature, air pressure, humidity, and wind speed and direction). Wind speed and direction observations were collected hourly 4 m above the sea level by a JM Young 04016 Wind Monitor-JR. The intercomparison of the buoy and atmospheric reanalyses winds, as well as the scatterometer-derived wind products, is performed for the period and data points closest to the buoy's positions.

2.3. Construction of SST and Ancillary Time Series and Trends Computation

As our goal is to study regional interannual and long-term trend variability of SST fluctuations on the PS, SST monthly means are calculated at each grid point from the daily fields, as well as the record-length monthly mean climatology produced as the mean values for each month. To obtain the SST anomalies (hereafter SSTa) at each grid point we subtracted the monthly climatological annual cycle calculated for the period between 1982 and 2017 from the monthly SST record. To preserve the variability of SSTa at interannual timescales (3–7 years), we evaluated centered running mean filters by varying the windows length from 12 to 48 months. For this study we selected a 36-month window. Note that similar results are found when a longer window length is considered (not shown). We choose to be conservative and use the 36-month filter in order to lose only 18 months at the beginning and at the end of the record and yet retain most of the interannual variability.

Long-term trends of SSTa are calculated at each grid point over the domain defined by 110°-10°W and 10°-60°S by linear regression of the monthly data with regression coefficients estimated by ordinary least squares, and their significance is tested using Mann Kendall's non-parametric trend test with a 95% confidence level (Mann, 1945; Kendall, 1955; Hirsch et al., 1991; McLeod et al., 1991). The Mann Kendall trend test is a non-parametric test for randomness against the trend and has been extensively applied in meteorology and oceanography. The null hypothesis of randomness states that the data are a sample of n independent and identically distributed random variables. In this study, the number of independent variables of filtered time series was calculated following the methodology of degrees of freedom proposed by Emery and Thomson (2014). From the distribution of SSTa trends, three regions of interest are selected a posteriori on the PS because of their significance, hereafter referred to as Northern Patagonian Shelf (NPS), Central Patagonian Shelf (CPS), Southern Patagonian Shelf (SPS), which will be described in detail shortly (see **Figure 1B** and **Table 3**). The SSTa time series are spatially averaged within each region for each monthly time step resulting in three time series that represent the temporal SSTa variability at NPS, CPS, and SPS, respectively.

TABLE 1 | Wind datasets used in this work.

Wind dataset	Time frequency	Spatial resolution	Period of data (mm/yyyy)	Variables
NCEP NCAR R1	Monthly means	2.50° x 2.50°	01/1982–12/2017	u-wnd, v-wnd, wnd speed, SLP, heat fluxes
NCEP CFSR	6 h	0.50° x 0.50°	01/1982–12/2017	u-wnd, v-wnd, wnd speed, SLP, heat fluxes
ERA Interim	Monthly means	0.25° x 0.25°	01/1982–12/2017	u-wnd, v-wnd, wnd speed, SLP, heat fluxes
CCMPv2	6 h	0.25° x 0.25°	01/1982–12/2017	u-wnd, v-wnd, wnd speed

TABLE 2 | Positions, period of observation and duration of the 10 m wind records (columns 1 to 5) from meteorological buoys.

Site	Latitude (°S)	Longitude (°W)	Period of observation (dd/mm/yyyy hh:mm, UTC)	Duration (in days)	r (CCMPv2, buoy)	r (ERA-I, buoy)	r (CFSR, buoy)	r (NCEPR1, buoy)
A	39.95	56.10	21/12/2014 12:00–20/02/2015 11:00	62	0.75 (0.84)	0.74 (0.82)	0.70 (0.78)	0.71 (0.79)
B	40.98	57.00	25/09/2006 00:00–08/03/2007 23:00	165	0.71 (0.77)	0.73 (0.80)	0.70 (0.78)	0.72 (0.79)
C	43.82	59.67	15/03/2006 00:00–26/04/2006 14:00	43	0.81 (0.86)	0.81 (0.86)	0.82 (0.89)	0.72 (0.77)
C	43.82	59.67	16/10/2005 00:00–05/12/2005 11:00	51	0.74 (0.81)	0.74 (0.81)	0.71 (0.79)	0.65 (0.71)
D	44.68	59.99	16/05/2016 15:00–07/06/2016 05:00	23	0.93 (0.94)	0.90 (0.90)	0.89 (0.91)	0.74 (0.77)

*Sites (A to D) are indicated in **Figure 1B**. Correlation coefficients (r) between wind speed measured at the buoy locations and from CCMPv2, ERA-interim, CFSR and NCEPR1 are shown in columns 6, 7, 8 and 9, respectively. Correlations after removing outliers are shown in brackets. All correlation coefficients are significantly different from zero at the 95% confidence level.*

TABLE 3 | Basic statistics of Sea Surface Temperature for the regions NPS, CPS, and SPS.

Region	Latitude (°S)	Longitude (°W)	Climatological annual mean SST (°C)	Maximum climatological SST (°C)	Minimum climatological SST (°C)	Amplitude SST (°C)
NPS	42.125– 45.875	65.125– 60.125	11.5	15.6	7.9	7.7
CPS	47.375– 48.125	63.875– 62.125	9.7	13.6	6.7	6.8
SPS	49.625– 52.625	66.375– 61.875	8.0	10.5	5.8	4.7

Latitude and longitude boundaries of each region are given in columns 2–3.

To examine the relationship between local atmospheric forcing and the observed long-term trends and variability of SSTa we analyzed winds and surface heat flux anomalies. For each region, all the above-mentioned variables were monthly averaged and filtered with an 36-month running averaged identical to the SSTa (described above).

2.4. EOF Analyses

To determine the dominant spatial and temporal patterns of interannual variability of SSTa, we carried out an empirical orthogonal function (EOF) analysis (Preisendorfer and Mobley, 1988). The EOF is made over the spatial domain over the region 110°-10°W and 10°-60°S, after removing the record-length trend from the records. The temporal evolution of the spatial pattern of each EOF is described by its principal component time series (PC).

3. RESULTS

The results are presented as follows: in Section 3.1 the different wind products are evaluated against the *in-situ* observations collected with the four moored buoys (black dots in **Figure 1B**). In Section 3.2 we present the analyses of the linear trends of SSTa in the region of study. Subsequently, we analyze the possible physical drivers of observed SSTa variability at interannual time scales and the possible relationship between SSTa and the local atmospheric forcing on the PS, by evaluating the variability of surface wind, sea level pressure, and sea-air heat fluxes. Section 3.3 presents the analysis of the leading modes of SSTa variability around southern South America and their possible link with large-scale climate indices.

3.1. Performance of Wind Products

Comparisons of climatological wind stress and wind stress curl in the southeast Southeastern Pacific Ocean (SEP) and SWA estimated from NCEPR1, CFSR, Era-Interim, and CCMPv2 data during the overlapping period (1987–2017) reveal substantial differences in spatial distribution (**Figure 2**). In general, CCMPv2 wind stress curl shows more complex spatial distribution among the four products, while reanalyses display smoother patterns. This can be noted in the BMC region and around 50°S in the SWA. While the spatial patterns of ERA-Interim and CFSR agree well, there are areas where CFSR presents higher absolute values than ERA-interim. For example, the estimated wind stress curl in the Drake Passage is $-0.4\text{x}10^4$ N m^{-2} km^{-1} ERA-Interim and –0.6 x 10^4 N m^{-2} km^{-1} CFSR. Similarly, in the BMC, the wind stress curl reaches 0.5 x 10^4 N m^{-2} km^{-1} CFSR and 0.2 x 10^4 N m^{-2} km^{-1} ERA-Interim, possibly due to the higher spatial resolution of the latter. Compared with the other datasets, NCEPR1 displays a wider area of negative wind stress curl north of 36°S in the SEP. The wind stress curl is less intense in NCEPR1: in the subtropics the maximum values are $0.3\text{x}10^4$ N m^{-2} km^{-1} in NCEPR1 and larger than $0.5\text{x}10^4$ N m^{-2} km^{-1} in CCMPv2, ERA-Interim, and CFSR.

There are notable regional differences among the four wind databases analyzed here. To further investigate these differences on the PS, we compared time series of wind speed of atmospheric reanalysis (NCEPR1, CFSR and ERA-Interim) with CCMPv2 to determine which is the most suitable dataset for the region. We estimate the correlation coefficients (r) and root-mean-square error (RMSE) between wind speed for filtered and non-filtered time series at NPS, CPS, and SPS. The statistical significance of the correlation coefficients is calculated evaluating the degrees of freedom of each time series (Thomson and Emery, 2014) and are listed in **Table 4**. The highest correlation and the smallest RMSE are obtained between ERA-Interim and CCMPv2. This comparison is helpful as we wish to identify the most accurate reanalysis to analyze the atmospheric surface forcing in the study region. The correlation coefficients of the 36-month filtered wind data are higher than for non-filtered monthly records. For example, the correlation coefficients of wind speed at NPS between CCMPv2 and ERA-Interim are 0.66 and 0.86 for non-filtered and filtered data, respectively, indicating that the discrepancy between the two products increases at higher frequencies. Consistently, this is also noted in the smaller RMSE for filtered records. The correlation coefficients between ERA-Interim and CFSR (both filtered and non-filtered records) are statistically different from zero at 5% error probability. However, the highest correlations are found between CCMPv2 and ERA-Interim after 36-month low pass filtering, indicating that the latter is a suitable reanalysis to use for evaluating the atmosphere-ocean interactions on the PS. The reader is reminded that CCMPv2 uses ERA-Interim reanalysis as the first-guess wind field and therefore the data are not entirely independent from each other.

Winds in the open ocean are notoriously difficult to validate, and there are limited *in-situ* data to match the location and time of reanalyses and other wind products. Based on the above-mentioned results, in **Figure 3** we present a comparison between ERA-Interim, CCMPv2 and the longest *in-situ* wind data available in the SWA shelf break at 40.98°S, 57°W. The *in-situ* observations extend from 25 September 2006 to 8 March

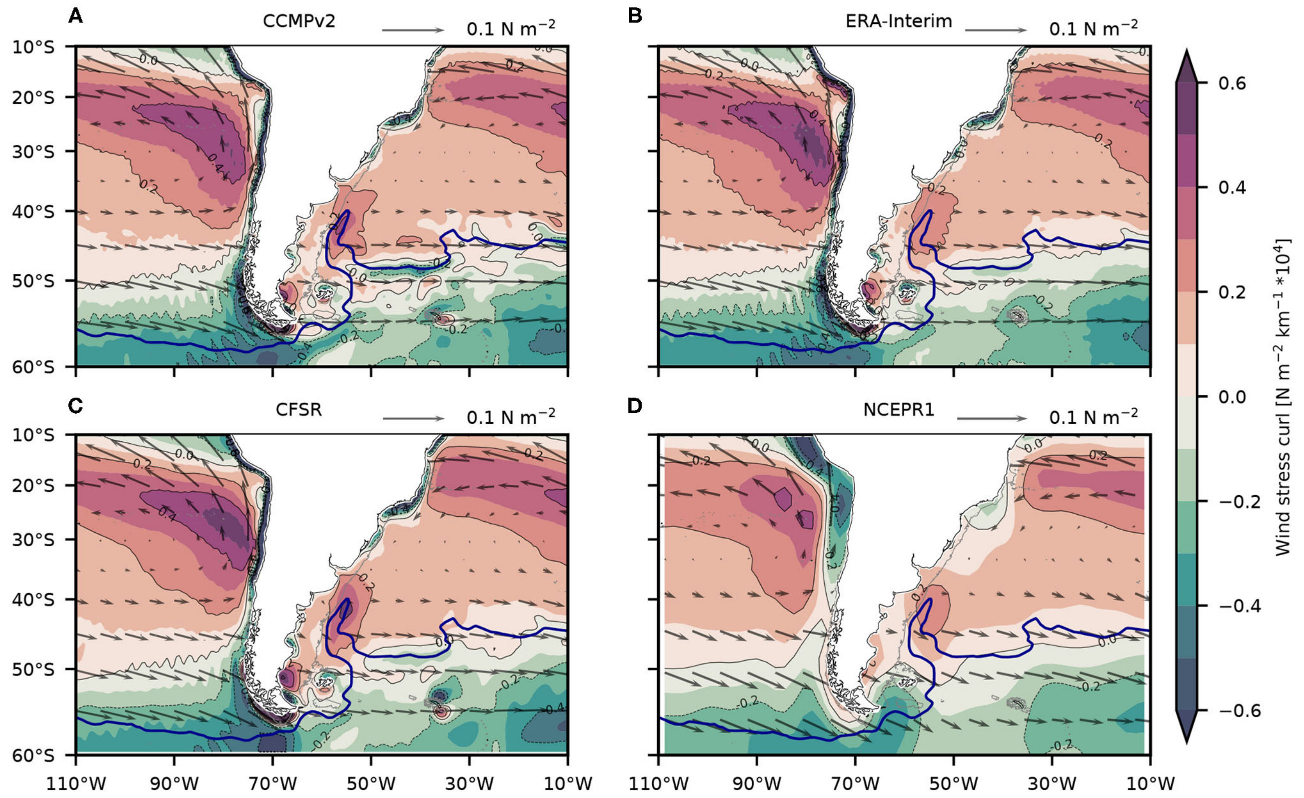

FIGURE 2 | Distribution of climatological wind stress at 10 m height (vectors) and wind stress curl (background shading) during 1988–2017 from **(A)** CCMPv2, **(B)** Era-Interim, **(C)** CFSR, and **(D)** NCEPR1. Wind data are described in Section 2.2. Positive wind stress curl indicates anticyclonic wind stress circulation and negative wind stress curl indicates cyclonic circulation. Vectors are shown every 20 gridpoints for CCMPv2 and ERA-Interim, every 10 gridpoints for CFSR and every 3 gridpoints for NCEPR1. The solid dark blue line represents the mean location of the Subantarctic Front (SAF, Kim and Orsi, 2014).

TABLE 4 | Linear correlation coefficients (r) and root-mean-square error (RMSE) of 10 m wind speed derived from CCMPv2 and from reanalysis NCEPR1, CFSR and ERA-Interim at NPS, CPS and SPS.

Region	CCMPv2 vs. NCEPR1		CCMPv2 vs. CFSR		CCMPv2 vs. ERA-Interim	
	r	RMSE (m/s)	r	RMSE (m/s)	r	RMSE (m/s)
NPS	**0.64 (0.70)**	4.57 (4.24)	**0.67 (0.77)**	4.77 (4.38)	**0.66 (0.86)**	4.22 (4.10)
CPS	**0.66 (0.81)**	4.17 (3.96)	**0.68 (0.77)**	4.33 (4.14)	**0.66 (0.90)**	3.91 (3.80)
SPS	**0.44** (0.40)	2.64 (2.16)	**0.55 (0.78)**	3.64 (3.40)	**0.61 (0.85)**	3.50 (3.34)

Correlation coefficients for 36-month running mean filtered data are shown in brackets. Correlation coefficients significantly different from zero at the 95% confidence level are indicated in bold.

2007 (Site B, **Figure 1** and **Table 2**). The hourly buoy data were sub-sampled to match the 6-h winds at 10 m (00, 06, 12, and 18 UTC) from ERA-Interim and CCMPv2. Note that wind speed is referenced at 10 m height in CCMPv2 and ERA-Interim, while buoy winds were observed at 4 m height. We adjusted the 4 m *in-situ* wind speed observations to 10 m height following Atlas et al. (2011). This adjustment leads to a 13% increase in time-mean wind speed compared to the original 4 m winds. The correlation coefficient between adjusted *in-situ* wind speed and CCMPv2 (ERA-Interim) is 0.71 (0.73). Removing outliers, defined as values above and below ± 2 standard deviations (SD), the correlation improves to ~0.80 for CCMPv2 and ERA-Interim. Correlations with and without outliers are statistically significant at 5% error probability. The linear least-square adjustment between *in-situ* and CCMPv2 data indicates that at this location the scatterometer-derived winds tend to overestimate buoy observations at wind speeds lower than 5 m s^{-1}, and underestimate it at higher wind speeds. Similar results are found for ERA-Interim reanalysis, though the transition occurs at a higher wind speed (8.5 m s^{-1}, **Figures 3C,D**). The correlation coefficients for the other deployments (Sites A, C and D, **Figure 1**) are listed in **Table 2**. The best adjustment is found at Site D, possibly because the wind speed was less variable at that site during the time of deployment. Correlation

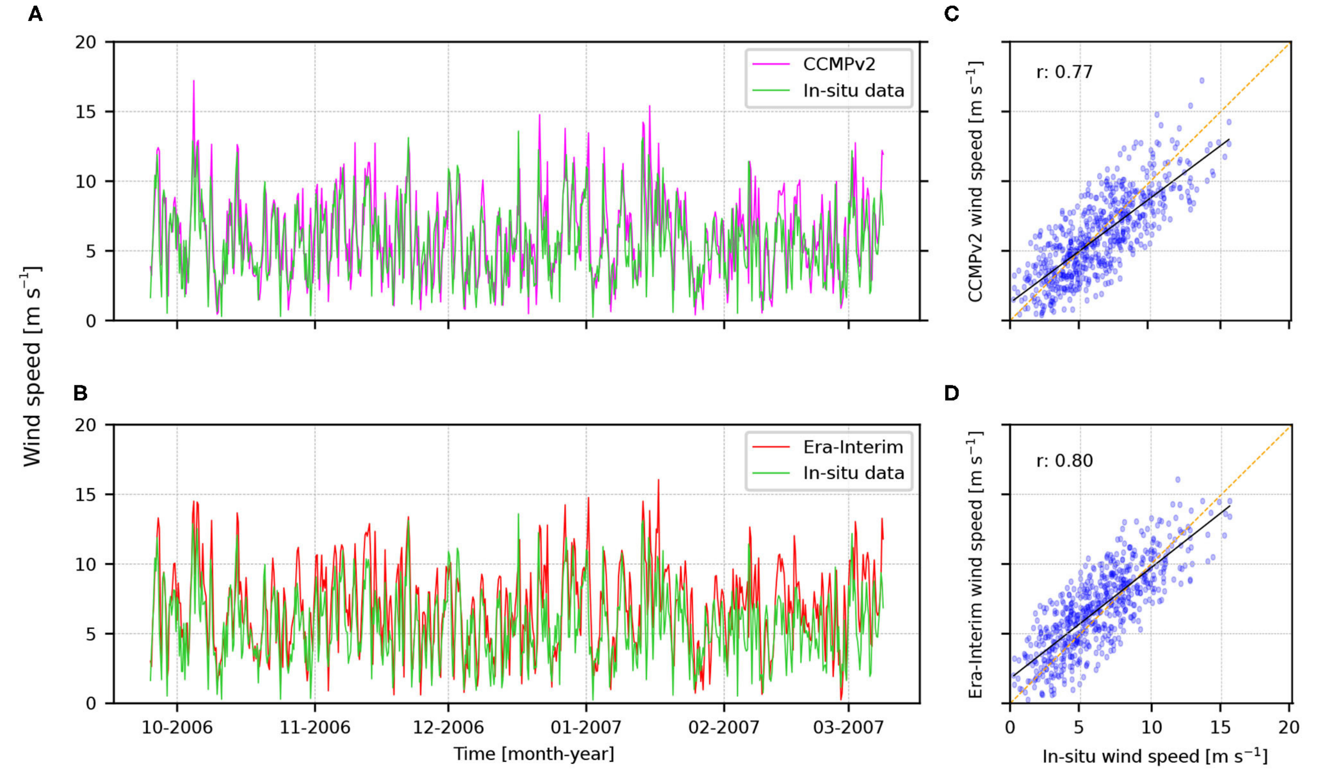

FIGURE 3 | Comparison of wind speed time series from: hourly *in-situ* data (solid green line) from an oceanographic buoy located at 40.98°S, 57°W (Site B, **Figure 1B** and **Table 2**) and **(A)** CCMPv2 (solid magenta line) and **(B)** Era-Interim (solid red line) data extracted at the nearest grid point. The wind speed data from CCMPv2 and Era-Interim used here have a 6-h temporal resolution. **(C,D)** Scatter plot between the time series shown in **(A,B)** together with the linear fit by least-squares (solid black line). r is the correlation coefficient and the line y = x is shown in orange.

coefficients between ERA-Interim/CCMPv2 and *in-situ* wind speed observations at the four locations range between 0.71 and 0.93, indicating a relatively good adjustment with ERA-Interim/CCMPv2 wind speed. Given the similar performance of both datasets and that CCMPv2 products are available only since early 1987, in the following analyses we use ERA-Interim reanalysis which also provides consistent surface heat-flux estimates and covers the same time period as the SST observations analyzed here. The same comparison was made between *in-situ* wind data and CFSR / NCEPR1 reanalysis obtaining a lower correlation compared with the correlation with ERA-Interim / CCMPv2, except for one measurement point (Site C, Period of observation 15/03/2006 00:00–26/04/2006 14:00) where the correlation coefficients with CFSR are slightly higher (**Table 2**).

3.2. Linear Trends and Temporal Variability of SSTa

3.2.1. Spatial Distribution of SSTa Linear Trends Between 1982 and 2017

The spatial distribution of record-length satellite-derived linear trends of 36-month filtered SSTa (Section 2.1) in the SEP and SWA is shown in **Figure 4** (only significant trends at the 95% confidence level are shown). The distribution of SSTa trends reflects large-scale patterns. The largest positive and negative trends are observed along the BC and the BMC (around 0.4°C decade^{-1}) and in the central Drake Passage (< -0.3°C decade^{-1}), respectively. Significant warming (positive) trends are located in mid-latitudes between 20 and 50°S. Most of these areas in the SWA are located north of the Subantarctic Front (SAF, green line in **Figure 4**, extracted from Kim and Orsi, 2014), suggesting that the majority of the warming occurs within the South Atlantic Subtropical Gyre (i.e., north of the SAF). In particular, the SWA region has been identified as a warming hotspot where SST is increasing faster compared to other regions (Hobday and Pecl, 2014; Hobday et al., 2016) and recent analyses from satellite data and models suggest that the warming is associated with a southward migration of the South Atlantic subtropical gyre and a southward penetration of the Brazil Current (e.g., Yang et al., 2020; Goyal et al., 2021). Notably, the shallow ($<$ 10 m) inner region of Rio de La Plata estuary registers the largest positive linear trend ($>$ 0.8 °C decade^{-1}). In contrast, cooling (negative) trends are found north of 25°S and south of 50°S, except for the region east of 45°W that presents moderate warming. The most intense cooling in this domain is located in the western Scotia Sea and Drake Passage (centered around 56°S–60°W). Only about 20% of the grid points in the full domain present cooling trends. Along the path of the MC, linear trends are slightly negative but mostly non-significant, except for a small region close to its northernmost extension near 39°S

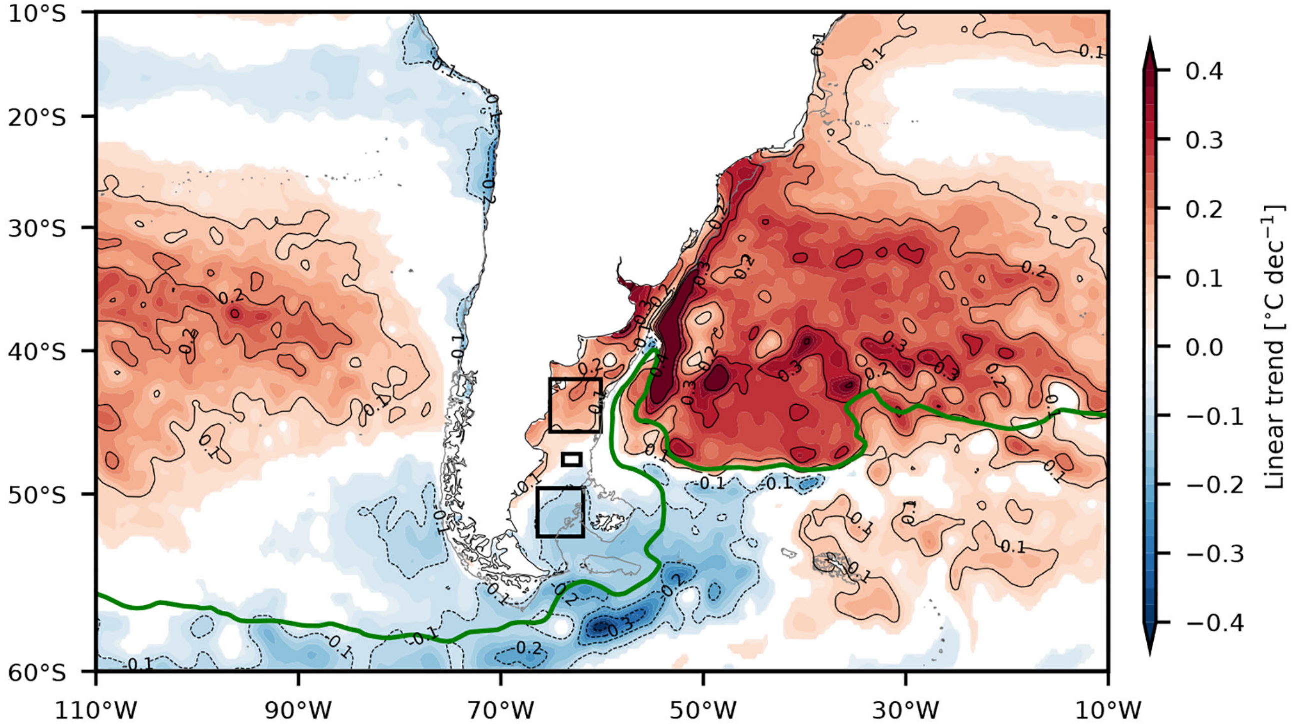

FIGURE 4 | Observational trends of filtered SST anomalies (SSTa) for the 1982–2017 period. SSTa are obtained by subtracting the climatological annual cycle calculated for the same time period from the SST record at each grid point and then smoothed by a 36-month running mean (see Section 2.1). Only regions where trends are significant at a 95% confidence level (after Mann Kendall's-test) are shaded. Black rectangles indicate the NPS, CPS, and SPS regions (identical to the boxes in **Figure 1B**). The solid dark green line represents the mean location of the Subantarctic Front (SAF, Kim and Orsi, 2014).

(< –0.2°C decade^{-1}). The large-scale meridional dipole pattern of linear trend distribution in the SWA extends over the PS, with positive trends north of 46°S, neutral trends around 48°S, and negative trends south of 49°S. Motivated by the potential impacts of SSTa variability on the productive Atlantic Patagonian Shelf, we will focus our subsequent analyses on SSTa time series constructed at the selected regions (NPS, CPS and SPS; **Figure 5**; Section 2.3). NPS and SPS are located at the positive (northern) and negative (southern) sides of the above-described dipole of meridional SSTa trends, respectively, while CPS is located in the neutral transition zone (see regions indicated in **Figure 4**), where no significant trend is observed. At NPS and SPS, the magnitude of warming and cooling trends is similar: 0.15 ± 0.01 and –0.12 ± 0.01 °C decade^{-1}, respectively. For the entire period spanning between 1982 and 2017, these linear trends represent variations of almost half a degree, with an increase of 0.52°C at NPS and a decrease of –0.42°C at SPS.

The PS presents a large amplitude seasonal cycle of SST, with mean amplitudes exceeding 5°C over most of the domain (Rivas, 1994, 2010). It is therefore relevant to determine to what extent the long-term trends are associated with specific seasons. To this end we analyzed the seasonal linear trends of SSTa (**Supplementary Figure S1**). Seasonal trends of non-filtered SSTa present warming in mid-latitudes of SEP and SWA that are larger in February and March (late austral summer) and exceed 0.3°C decade^{-1} at NPS. These positive trends remain significant but are weaker (0.2–0.3°C decade^{-1}) during April and May (austral autumn) and July and August (austral winter). The cooling signal is stronger (< –0.2°C decade^{-1}) at SPS during January and February (austral summer), indicating that summers have become colder over the period of observation analyzed here. A possible driver of the observed cooling could be enhanced vertical mixing within the upper water column. In the remaining of the year, there is no significant trend on the PS.

3.2.2. Interannual Variability of SSTa on the PS Between 1982 and 2017

The focus of this section is to study the interannual variability and the temporal evolution of SSTa linear trends in the PS. We examine the frequency distribution of the variability in the detrended time series of SSTa at NPS, CPS and SPS based on the variance preserving power spectral density of filtered and detrended time series using the Welch method (Welch, 1967; **Figure 6**). The data were divided into five 16-year segments with 75% overlap. A Hamming window was used to compute the modified periodogram of each segment. At interannual time scales, the spectra of the three records present a significant peak centered at about 80 months (~6 years) reaching maximum SSTa variance at SPS (0.032 °C^2) and minimum SSTa variance at NPS (0.02 °C^2). In both cases ~70% of the total variance is associated with the frequency band between 3 and 10 years.

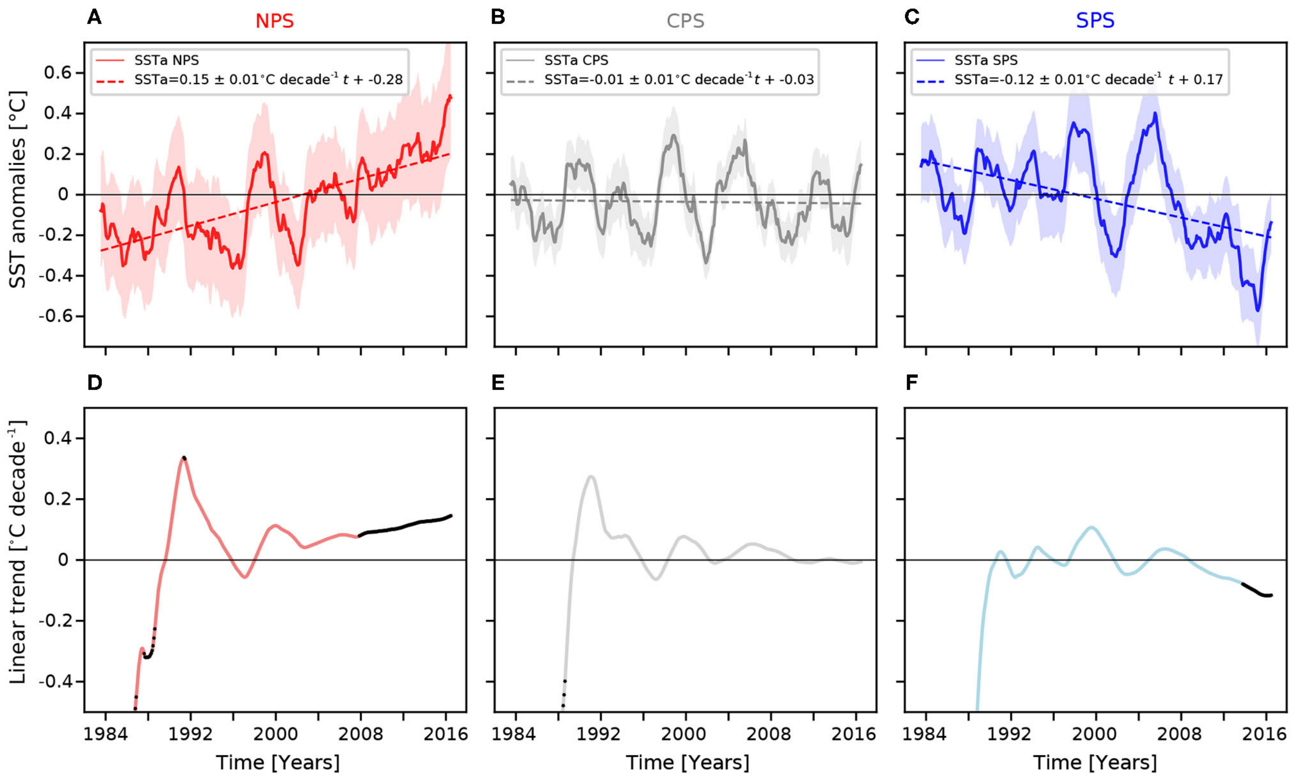

FIGURE 5 | (Top) Time series of 36-month running mean of SSTa (solid line), standard deviation (shaded) and linear trend fit (dashed line), together with their corresponding linear trends based on the SST data set described in Section 2.1 at **(A)** NPS **(B)**, CPS, and **(C)** SPS shown in **Figure 1B**. The construction of the SSTa time series for each regions is described in Section 2.3. Trends at NPS and SPS are significant at the 95% confidence level. (Bottom) Temporal evolution of linear trend slope between 1982 and 2017, at **(D)** NPS, **(E)** CPS, and **(F)** SPS. Values for the time steps when the linear trends are significant at 95% confidence level are marked in black.

Spectral variance at periods shorter than 36 months is effectively removed by the running means.

The SSTa time series at NPS and SPS present similar interannual fluctuations displaying large positive anomalies centered in 1990, late 1998, and 2005, and sharp negative anomalies in 1996 and late 2001 (**Figure 7A**). To address the similarities and differences in the temporal evolution of SSTa at NPS and SPS, we computed the time series of the correlation coefficient between both variables (**Figure 7B**). The linear correlation is positive and significant until ∼2010. After 2008 the correlation decreases and becomes progressively negative, though it does not exceed the 95% confidence level at the end of the record. Since the attribution of linear trends depends on the end-points of the time series, we define the year 2008 as a "breakpoint" and analyze the 1982–2007 and 2008–2017 periods separately instead of the entire record. Before 2008, there are no significant linear trends of SSTa at either of the three selected regions on the PS. In contrast, during 2008–2017, significant positive linear trends are observed at NPS: 0.35 ± 0.02°C decade^{-1}, at SPS –0.27 ± 0.03°C decade^{-1}, while at CPS there is no significant trend. Thus, the record-length SSTa trends observed at NPS and SPS are mostly associated with the variability observed during the last 10 years of the records.

3.2.3. Physical Drivers of Observed SSTa Trends Variability on the PS

Due to the behavior shift of the SSTa prior to and after 2008 on the PS (**Figure 7**), the spatial distribution of linear trends is analyzed over the SEP and SWA dividing the full-length record in two periods: 1982–2007 and 2008–2017. As mentioned earlier, large interannual variations of SSTa are observed on the PS (**Figure 6**). The interannual variability will be analyzed in detail in Section 4.3. To investigate the possible role of physical drivers on the observed linear SSTa trends over the SEP and SWA prior to 2007 and after 2008, we examined the relationship between the SSTa and the anomalies of the zonal and meridional wind components (u-wnda and v-wnda, respectively), wind speed (wspda), wind stress curl (curla), sea level pressure (SLPa), and net surface heat-flux (nhfa) from ERA-Interim (see Section 4.1). Subsequently, we compared SSTa with the above-mentioned atmospheric anomalies during 1982–2007, 2008–2017, and 1982–2017 (full record) at NPS, CPS, and SPS. Linear correlation coefficients between SSTa and atmospheric variables are listed in **Table 5** with significant values (95% confidence) indicated in bold. The correlation coefficients between all heat flux components (long and short-wave radiation, latent and sensible heat) and SSTa are low and non-significant

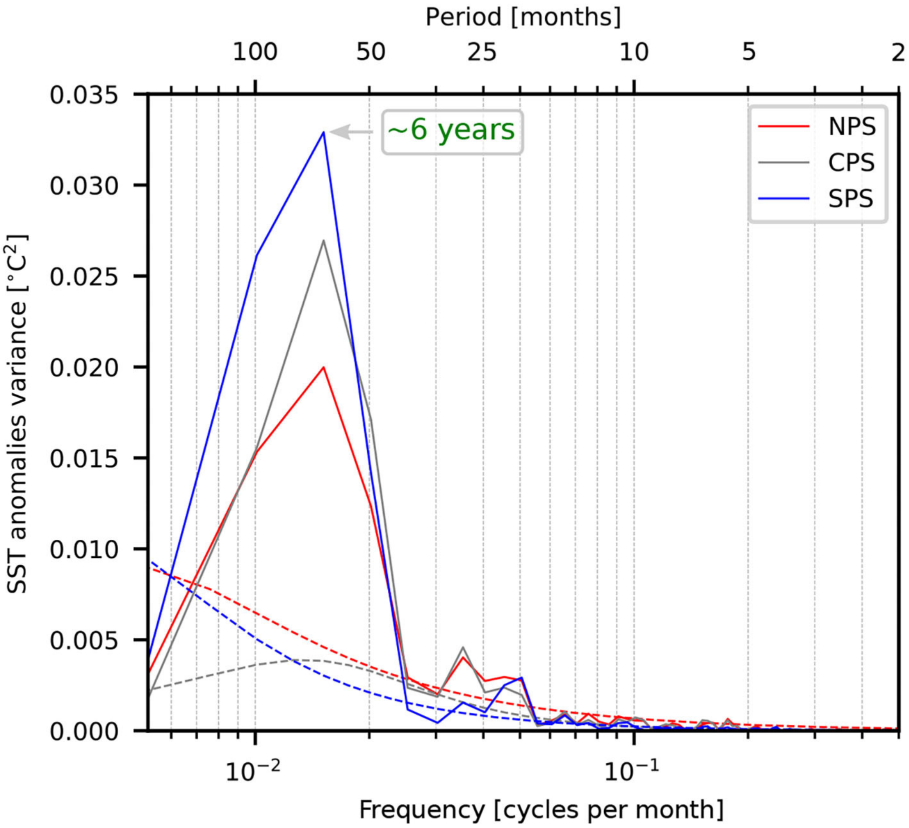

FIGURE 6 | Variance preserving Welch spectra of filtered and detrended SSTa time series (see Section 2.1) at NPS (solid red line), CPS (solid gray line) and SPS (solid blue line) shown in **Figure 1B**). Dashed lines indicate the power spectral density of red noise for each spectrum. The dashed green line indicates the period of maximum variance centered at ~6 years (see Section 3.2.2).

(not shown). Thus, only the net heat flux is presented in **Table 5**.

3.2.3.1. Linear Trends During 1982–2007

The spatial distribution of linear trends of SSTa for the period 1982-2007 exhibits moderate warming trends in the SWA (~0.2°C decade^{-1}), located over the Zapiola gyre (centered roughly at 44°S, 45°W) and south of 20°S along the main path of the BC (**Figure 8A**), while trends over the continental shelf are mostly neutral, except for the inner Río de la Plata and the South Brazil Bight. Over the SEP, significant warming greater than 0.2°C decade^{-1} is observed between 24 and 40°S and west of 90°W, which is also apparent in the SSTa trend distribution for the entire 1982–2017 period (see **Figure 4**). During 1982–2007, only weak cooling trends are observed mostly located south of 50°S.

The zonal wind component u-wnda in the SWA presents a negative trend (–0.4 m s^{-1} decade^{-1}) north of 50°S and a positive trend over a few small regions further south, with a magnitude ranging between 0.2 and 0.4 m s^{-1} decade^{-1} (**Figure 8B**). This distribution is consistent with the positive SLPa trend of around 1 hPa decade^{-1} centered near 50°S, 30°W which leads to weaker westerlies between 30 and 50°S and stronger westerlies south of 50°S (**Figure 8F**). U-wnda trends over the continental shelf are slightly positive (0.2 m s^{-1} decade^{-1}) between 40 and 50°S and negative off the Rio de la Plata. Over the SEP, positive u-wnda trends are located in mid-latitudes between 35 and 50°S, and negative north of 20°S (intensified trades) and south of 55°S (weakened westerlies). Trends in the meridional wind, v-wnda, are weak or non-significant throughout most of the domain (**Figure 8C**). Thus, the linear trend in wind speed distribution follows the spatial pattern of u-wnda trends (**Figure 8D**). Weak and mostly non-significant trends of curla are found during this period (**Figure 8E**). The distribution of nhfa trend is mostly neutral or negative over the SWA (-8 W m^{-2} decade^{-1}), particularly along the path of the BC, and over the outer continental shelf north of 50°S, where it exceeds –10 W m^{-2} decade^{-1}, and the Rio de la Plata estuary. This indicates a larger heat loss from the ocean in the southern portion of the BC and the BMC. In contrast, the estimated trend suggests a weaker heat gain in shelf break region north of 50°S (**Figure 8G**). In the SEP negative nhfa trends are observed near 10°S 100°W.

To summarize, during the 1982-2007 period the continental shelf between 35 and 55°S presents non-significant SSTa trends. The region is dominated by weak and positive u-wnda trends resulting in stronger eastward wind speed. Non-significant or very weak trends are observed in v-wnda, curla, and SLPa. There is a significant negative trend of nhfa at northern PS, on average

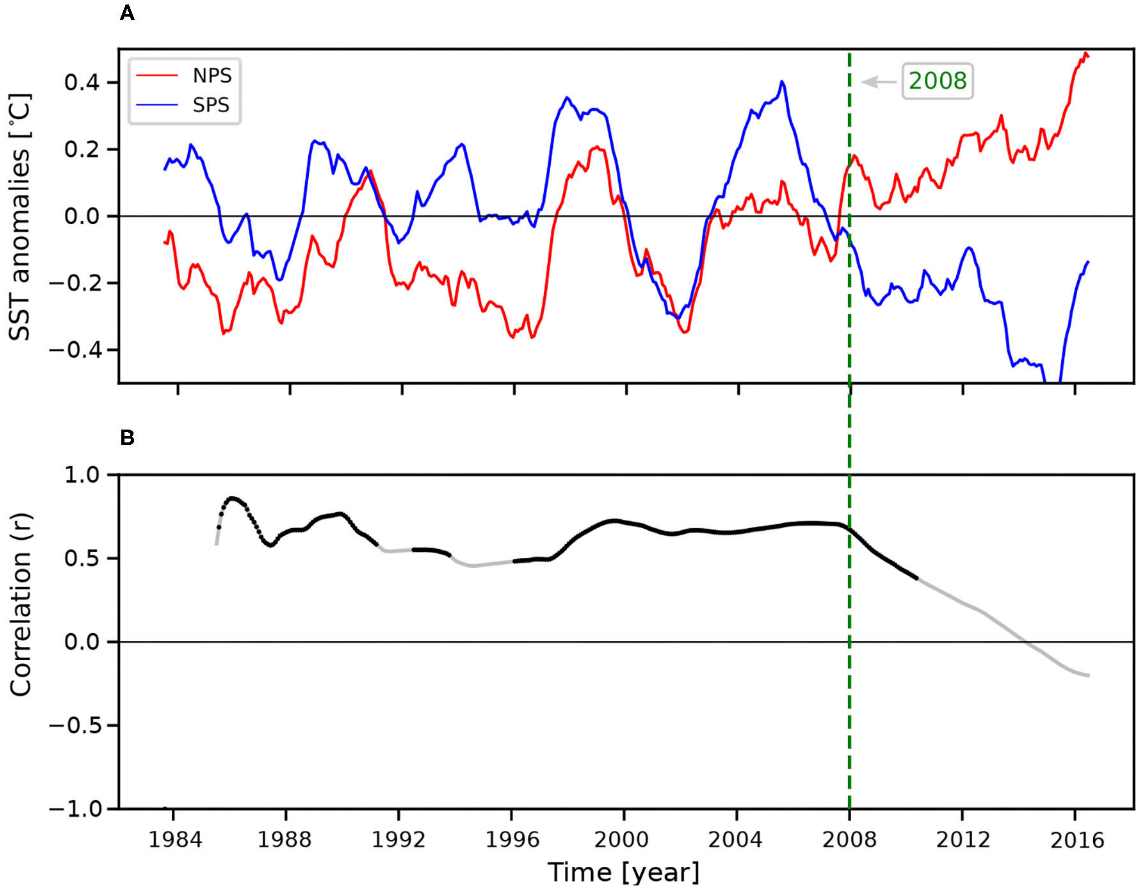

FIGURE 7 | (A) Time series of filtered SSTa at NPS (solid red line) and SPS (solid blue line). The time series are identical to those shown in **Figures 5A,C**. **(B)** Temporal evolution of the correlation coefficient (r) between SSTa at NPS and SPS. Heavy black lines indicate significant correlations at the 95% confidence level. The dashed green line indicates the “breakpoint” year centered at 2008 as identified in Section 3.2.2.

TABLE 5 | Linear correlation coefficients (r) between the time series of atmospheric forcing and SSTa at NPS, CPS, and SPS for different time periods: between 1982 and 2007, between 2008 and 2017, and for the full records between 1982 and 2017 (see Section 4.2.2).

		u-wnda	v-wnda	wspda	curla	SLPa	nhfa
NPS	1982–2007	–0.12	**–0.58**	–0.01	–0.26	0.46	–0.15
	2008–2017	**–0.85**	0.19	**–0.86**	0.62	0.67	–0.12
	1982–2017	0.16	–0.32	0.22	–0.14	0.32	–0.34
CPS	1982–2007	–0.18	**–0.50**	–0.09	0.06	0.33	–0.10
	2008–2017	–0.52	–0.03	–0.50	0.29	0.42	–0.26
	1982–2017	–0.31	–0.32	–0.26	0.14	0.38	–0.08
SPS	1982-2007	–0.15	**–0.44**	–0.14	–0.03	0.18	–0.13
	2008–2017	–0.48	**–0.61**	–0.46	0.55	–0.16	–0.20
	1982–2017	**–0.57**	–0.25	**–0.57**	0.25	0.37	–0.15

Correlation coefficients significantly different from zero at the 95% confidence level are indicated in bold.

of –8 W m^{-2} $decade^{-1}$. In conclusion, though the interannual variations remain important during this period (see Section 4.4) weak trends are observed on the PS in the wind components, wind-derived fields and the SSTa linear trend distribution.

Over the 1982–2007 period, significant negative correlations are found between SSTa and v-wnda at NPS, CPS, and SPS (*r* = –0.58, –0.50, and –0.44, respectively, **Table 5**). During this period, there is no linear trend of SSTa at the three selected regions of the PS, indicating that the observed fluctuations are, at least partially, dominated by interannual variability. The significant relationship between SSTa and v-wnda suggests that part of the SSTa variability is modulated by meridional wind variability. These fluctuations of meridional wind intensity may drive the temperature changes reported here by inducing changes in the northward advection of cold waters through the southern boundary of the continental shelf. This process will be further discussed in the next section. In contrast, there is no significant correlation between SSTa and the other variables analyzed here (**Table 5**).

3.2.3.2. Linear Trends During 2008–2017

The spatial distribution of linear trends of SSTa during 2008–2017 feature notable differences in magnitude and spatial patterns relative to the 1982–2007 period. While in 1982–2007

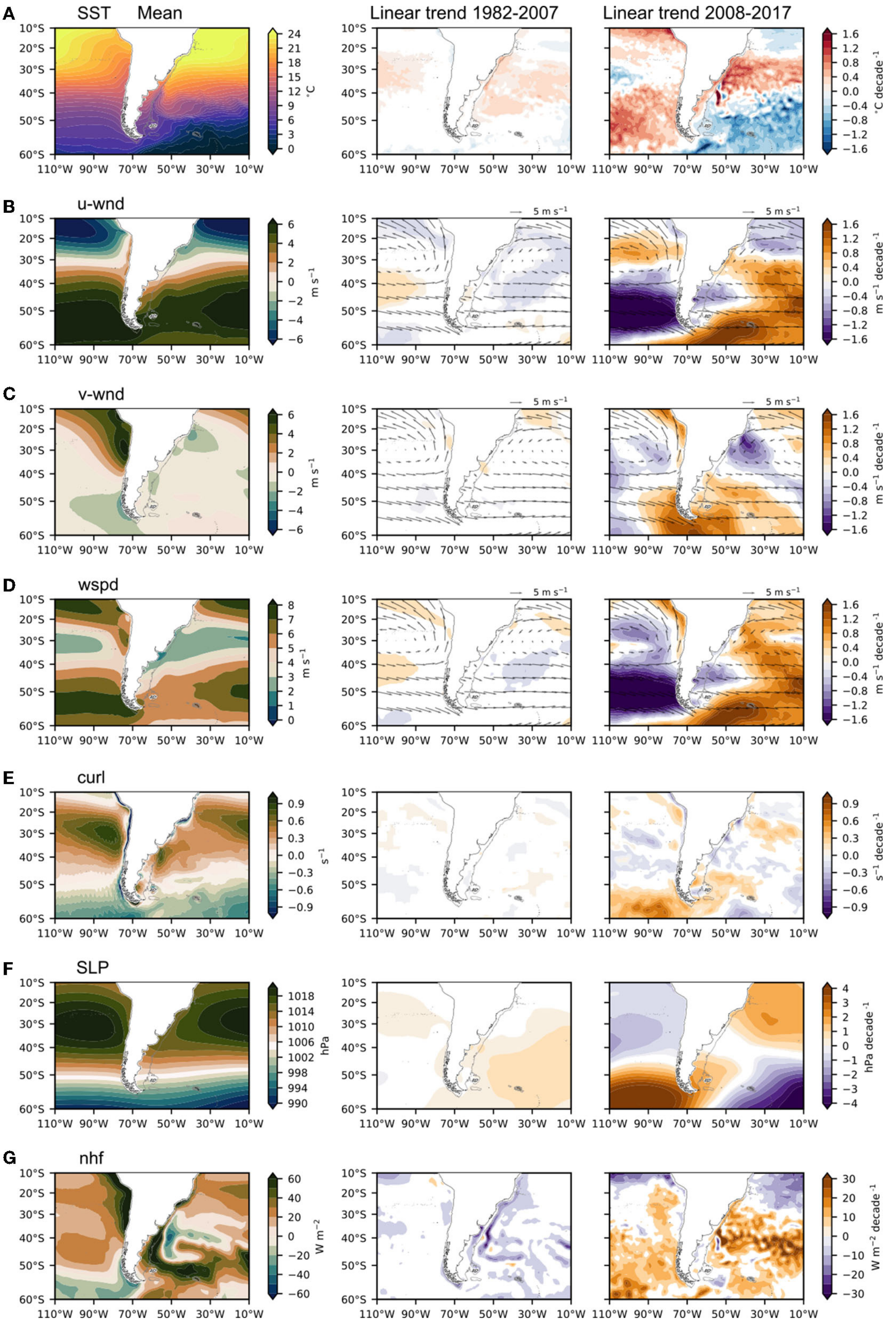

FIGURE 8 | (Left) Distribution of climatological **(A)** SST, **(B)** u-wnd, **(C)** v-wnd, **(D)** wind speed, **(E)** wind stress curl, **(F)** SLP, and **(G)** net heat flux for the 1982–2017 period. The wind speed, SLP and heat flux data are from Era-Interim (see Section 2.2). The spatial distribution of the linear trends of filtered anomalies of each variable are shown in the left panels (see Section 2.3 for methodology) calculated over 1982–2007 (center) and 2008–2017 period (right) (see details of selection of time periods in Section 3.2.2). Vectors in **(B–D)** show the distribution of climatological wind speed at 10 m height during 1982–2007 (center) and 2008–2017 (right) periods. Vectors are shown every 20 gridpoints. In every panel the 200 m isobath is also shown (solid gray line).

the SSTa trends as well as the trends of the analyzed forcing terms are null or weak (Section 4.2.3.1, center panel in **Figure 8A**), in the most recent period since 2008 the trends become stronger and significant (**Figure 8A**). Thus, this spatial pattern resembles the pattern of the full record length trends (Section 4.2.1), but the trends are now more intense. As in **Figure 4**, in the SWA significant warming trends (> 0.5°C decade^{-1}) extend over the South Atlantic subtropical gyre and the continental shelf between 25 and 40–45°S, reaching maximum values in the BMC (> 1.5°C decade^{-1}) and in the Rio de la Plata estuary (> 0.8°C decade^{-1}) (right panel in **Figure 8A**). Cooling areas in the SWA are mostly located south of 40°S in the open ocean and extend over an outer portion of the southern PS. The largest negative trends are observed in the central Drake Passage and extend eastward up to 50°W with values exceeding -1.0°C decade^{-1}. The eastern SEP presents sharp warming trends between 10–20°S and between 35–60°S, ranging from 0.2 to 1°C decade^{-1}, while in the western SEP moderate cooling extends between 30 and 35°S.

Over the SEP, positive trends of u-wnda are located in the subtropics between 15 and 35°S (i.e., weakened trades) and negative south of 35°S (i.e., weakened westerlies, **Figure 8B**). This is consistent with weakened meridional gradients of SLP suggested by the distribution of SLPa (right panel in **Figure 8F**). In the SWA south of 48°S there is a significant increase of u-wnda (reaching maximum values of about 1.2 m s^{-1} decade^{-1} in the Drake Passage, right panel in **Figure 8B**), which is consistent with the strong trends in the meridional gradient of SLPa (right panel in **Figure 8F**) at that location. The significant intensification of the westerlies could be partially responsible for the observed cooling in this region due to increased northward Ekman transport that advects cooler waters in the upper layer, and enhances the vertical mixing. In tropical latitudes in the SWA, u-wnda trends contribute to enhance easterlies north of 20°S and westerlies further south and east of 30°W by as much as 0.4 to 1 m s^{-1} decade^{-1} (right panels in **Figures 8B,D**). These changes of the lower atmospheric circulation are largely associated with the enhanced meridional SLP gradients (positive SLPa trend of ∼2.0 hPa dec-1) centered near 15°S, 25°W and negative SLPa trend further south (right panel in **Figure 8F**). On the continental shelf and adjacent deep ocean, negative u-wnda trends (–0.6 m s^{-1} decade^{-1}) are observed between 40 and 50°S and west of 45°W, which lead to weaker westerlies (right panel in **Figure 8B**). The negative trend in u-wnda leads to a similar trend in wspda (right panel in **Figure 8D**), which may contribute to the positive SSTa due to decreased wind mixing and increased vertical stratification. The distribution of v-wnda trends in the SWA basin are significant and negative between 18–40°S and 50–30°W (values of –1.4 m s^{-1} decade^{-1}) leading to increased northerly winds in this region. The trends of v-wnda are positive south of 50°S, with the highest values localized in the western Scotia Sea (1.2–1.6 m s^{-1} decade^{-1}), resulting in a meridional wind reversal (from northerly to southerly) and continuing increased southerly winds during this period. V-wnda trends are positive over most of the west coast of South America, leading to increased southerly winds north of 30°S. South of 45°S, southerly wind anomalies imply a meridional wind reversal from northerly to southerly (right panel, **Figure 8C**). V-wnda time series around southern South America indicates that during 2014 and 2015 in-phase southerly wind anomalies prevail on the Pacific and Atlantic shelves (not shown). The trend distribution of wspd-a is highly dominated by u-wnda in the entire domain (**Figure 8D**). At high latitudes, the trend of curla intensifies over the southern SEP (50°-60°S) and slightly further north over the southwestern portion of the SWA (45°-55°S) with a range of 0.4 to 1 x 10^{4} s^{-1} decade^{-1} (right panel in **Figure 8E**). Negative trends of curla are located south of 54°S and east of 50°W in the SWA (∼ −0.5 x 10^{4} s^{-1} decade^{-1}). These negative wind stress curl trends over regions of negative curl can drive stronger Ekman–induced upwelling and thereby lead to negative SSTa. At low latitudes, north of 20°S in the SEP and north of 30°S in the SWA, there is a significant negative trend of nhfa exceeding –24 W m^{-2} decade^{-1} (**Figure 8G**). In the mid to high latitudes the distribution of nhfa trends is mostly positive, with some regional maxima observed in the BMC (>30 W m^{-2} decade^{-1}) and in the central Drake Passage (∼25 W m^{-2} decade^{-1}). The localized yet intense nhfa trend dipole pattern observed over the BMC replicates the SSTa pattern, though with opposite signs (i.e., warming regions are associated with negative nhf trends and viceversa). This pattern clearly indicates that SSTa trends are not due to trends in nhfa. Since the region of warm waters north of the BMC is characterized by intense net heat loss to the atmosphere, the negative nhfa trend is consistent with a southward displacement of warm waters, and the associated positive SSTa trend along the narrow meridional strip located near 54°W between 38 and 44°S. Moreover, it suggests a strong modulation of the trends observed in the surface heat flux components by the local SSTa trends, but unraveling the dynamics of this feature is beyond the scope of this paper. Similarly, negative SSTa trends observed south of 40°S in the SWA occur with positive nhfa trends, suggesting that cooling in this region is not a direct response to sea-air heat flux trends.

The meridional dipole of SSTa trends observed on the PS during the entire record (**Figure 4**, Section 4.2.1) is similar to the one observed in 2008–2017 (right panel in **Figure 8A**), with values reaching 1°C decade^{-1} in the northern region and −0.8°C decade^{-1} in the southern region. Thus, the 2008–2017 SSTa trends shape the trends observed in the full-record, as also observed from the temporal evolution of the SSTa trends at NPS and SPS (**Figures 5**, **7**). The distribution of u-wnda displays negative trends (decreased westerlies) and the v-wnda trends (0.4–0.8 m s^{-1} decade^{-1}, right panel in **Figure 8C**) indicate southerly wind anomalies that reverse the meridional wind from northerly to southerly approximately in 2012 (not shown). These changes in surface wind imply an anticyclonic circulation anomaly which leads to the positive trend of curla observed between 40 and 51°S on the PS (right panel in **Figure 8E**). This pattern drives an anomalous convergence of surface water that could enhance the positive SSTa trend observed at NPS in 2008-2017. However, this mechanism cannot explain the negative trend of SSTa observed at SPS. At the eastern mouth of the Magellan Strait (52°S), there is a region of negative curla trend, which acts to weaken the downwelling associated with the positive record-length mean curl (left panel in **Figure 8E**). Positive SLPa trends observed on the PS south of 45°S result in strong negative trends in u-wnda north of 50°S and positive trends further south. Significant linear correlations between u-wnda (and wspda) and SSTa are found at NPS ($r = -0.85$ and -0.86, respectively). This indicates that the positive trend of SSTa observed in this region is associated with a decrease in the local zonal winds. At SPS, there is a significant correlation between SSTa and v-wnda ($r = -0.61$), indicating that the decreasing SSTa occurs partially in response to the above described reversal in meridional wind, by enhancing the northward advection of relatively cold waters. Numerical simulations suggest that the interannual variations of along-shelf transport in the southern portions of the continental shelf are moderately modulated by the meridional wind stress variability, which sets-up a cross-shelf pressure gradient through Ekman dynamics and thus geostrophically drive along-shelf transport variations (Combes and Matano, 2018; Guihou et al., 2020). Moreover, the interannual fluctuations of meridional wind are closely associated with SAM. Some small areas of significant negative nhfa trends are observed in the inner PS, while in the remaining of the PS the nhfa trends are non-significant (right panel in **Figure 8G**). At the northern PS, the negative rate of nhfa does not seem to be associated with the positive SSTa trends, indicating that heat fluxes are not responsible for the observed warming at these timescales.

During the entire period (1982–2017), significant negative correlations are found at SPS between SSTa and u-wnda ($r = -0.57$), and wspda ($r = -0.57$). These negative correlations suggest that the decreased SSTa is partially a response to enhanced vertical mixing associated with the increased u-wnda that are more intense during 2008–2017. The correlation coefficients between the SSTa and the other atmospheric variables considered (v-wnda, curla, SLPa, and nhfa) are not significant in all regions analyzed (**Table 5**).

3.3. Leading Modes of Interannual SSTa Variability

To further investigate the nature of the interannual variability which dominates the SSTa around southern South America at periods of nearly 6 years (**Figures 5**, **6**) we carry out an EOF analysis of detrended SSTa in the domain bounded by 110°-10°W, 10°-60°S. **Figure 9** depicts the leading modes of filtered SSTa during the entire record (1982–2017). Each EOF pattern is multiplied by the square root of their eigenvalues so that the amplitude of each mode is scaled in °C. The first mode (EOF1, left panel in **Figure 9A**) explains 28% of the total SSTa variance and resembles the first mode of SSTa variability documented by previous studies for different time periods (Deser et al., 2010; Messié and Chavez, 2011). This mode exhibits negative SSTa near the tropics associated with a characteristic 'horse-shoe shaped' pattern present on the tropical Pacific that usually extends along the west coast of North and South America. EOF1 presents maximum variance over the subtropics of the eastern South Pacific and over the subpolar South Atlantic east of 30°W. The second mode (EOF2, left panel in **Figure 9B**), which accounts for 16% of the total SSTa variance, displays most of the variance centered in the SWA with an out-of-phase relationship between SSTa north and south of about ∼40°S. This dipole pattern extends on the PS, though with weaker amplitudes ($< |0.1|$°C) suggesting a possible linkage between the shelf SSTa variability and a basin-scale pattern of variability. The maximum values in the southern center of action are located close to the SAF, where SSTa ranges between 0.2 and 0.3°C. EOF3 (right panel in **Figure 9C**) explains 12% of the variance with maximum positive values located close to BMC and negative values north of 20°S. Thus, the combined three leading modes explain 56% of the variance of filtered SSTa. Similar results are obtained applying running means considering shorter time windows to compute the filters: 55% of the total variance is explained by the first three modes when 24-months filter is used and the total variance explained is only slightly higher (57%) when 18-months filter is used (not shown). The variance explained by the three leading modes of non-filtered monthly SSTa decreases to 31%, suggesting that the importance of the most significant modes increases for longer time scales.

To investigate the sensitivity of the EOF to the selected spatial domain, we repeated the analysis after dividing the region into two subregions: SEP (110°-70°W, 10°-60°S) and SWA (70°-10°W, 10°-60°S) (not shown). The spatial pattern of EOF1 in SEP is nearly identical to the pattern displayed in the Pacific sector of EOF1 of the entire domain and their corresponding PC time series are almost perfectly correlated ($r = 0.97$). The spatial pattern of the Atlantic sector of EOF2 from the entire domain is similar to EOF1 of the SWA domain and the correlation between their PC time series is very high ($r = 0.99$). For the third mode, the correlation between PC3 of the entire domain and PC3 over the SWA is significant and negative ($r = -0.75$), and positive but non-significant with PC3 of SEP ($r = 0.51$). This analysis indicates that EOF1 and EOF2 of the entire domain (**Figure 9**) are associated with modes of SSTa variability centered over the SEP and SWA basins, respectively; while EOF3 combines variance from both basins. We also carried out an EOF analysis of SSTa over the continental shelf domain. The first mode, which explains 38% of the variance, resembles EOF2 of the entire domain. The second mode accounts for 16% of the total SSTa variance. This further illustrates the strong link between the western South Atlantic SST and the variability over the continental shelf at interannual time scales. In the remaining of this paper, we will only use the spatial patterns and PC time series that correspond to the full domain (right panels in **Figure 9**). The variance preserving spectra of PC1 has its most energetic fluctuations at interannual to decadal timescales (4–12 years) with a peak in spectral variance in periods of about 120 months (10 years) that accounts for ∼50% of the total variance (**Figure 9D**). The PC2 spectrum presents a similar peak, while PC3 presents spectral density accumulated in the band of 4–16 years that accounts for ∼70% of the total variance, with higher variance in comparison with PC1 and PC2. The sum of PC1 and PC2 is significantly correlated with the detrended SSTa at SPS ($r = 0.71$), accounting for 51% of the variance explained by these two principal components. The correlation with detrended SSTa at NPS is very low and non-significant ($r = 0.1$).

The observed fluctuations of SSTa on the PS are partly associated with the variability of the three previously described leading EOF modes. Thus, we will explore the relationship

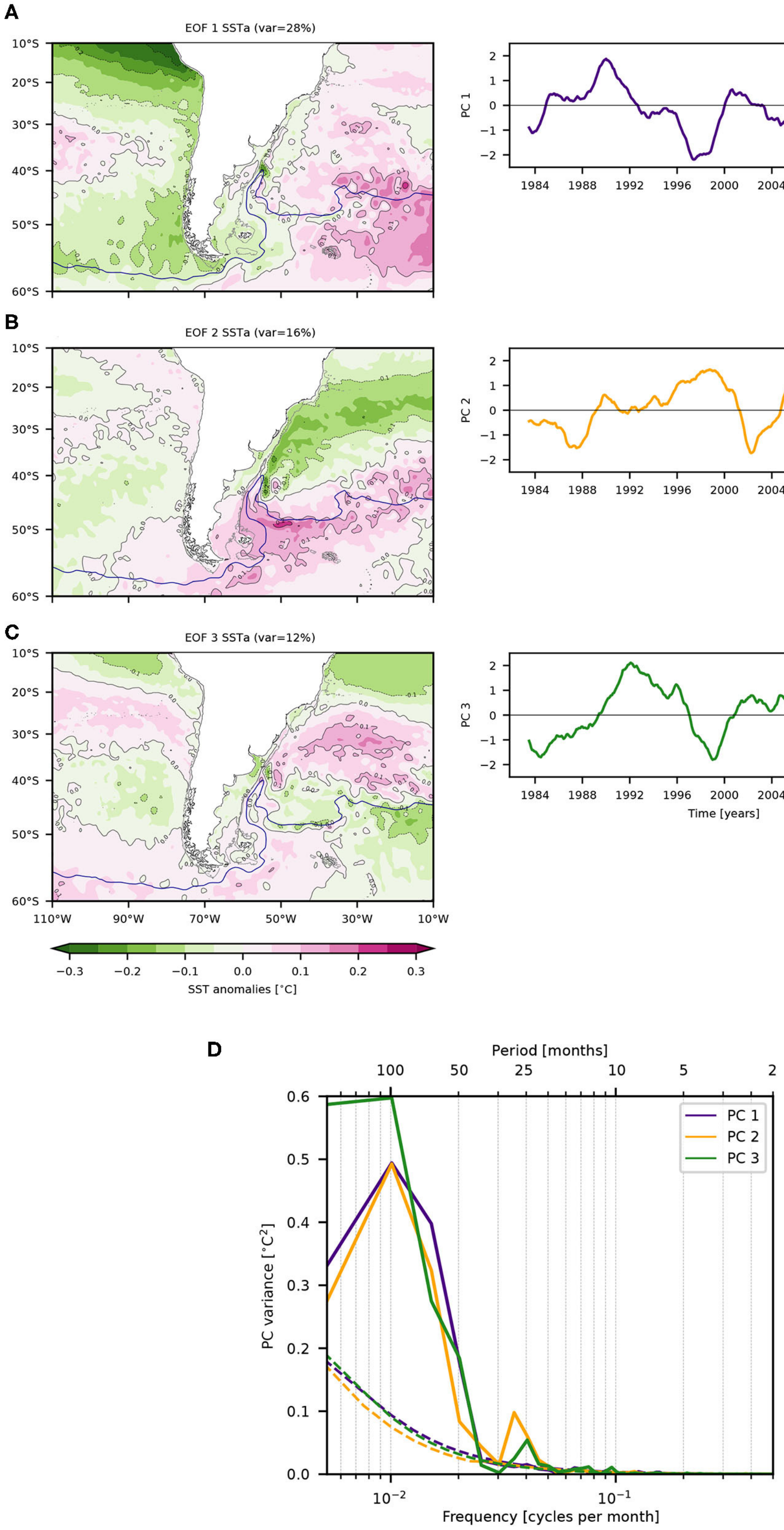

FIGURE 9 | (Left) First three **(A–C)** leading EOF of filtered and detrended SSTa estimated over the period 1982–2017 (Section 3.3) and (right) Principal Components (PC) time series of each EOF in normalized units (see Section 2.4 for methodology). The solid gray line in the EOF indicates the 200 m isobath and the solid dark blue line indicates the mean location of SAF (identical to **Figures 2**, **4**). **(D)** Variance preserving Welch spectrum of the corresponding PC time series for the three leading EOF (solid violet, orange and green lines, respectively). The power spectral density of red noise for each spectrum is indicated by the dashed lines (see Section 3.3).

between the temporal evolution of the PCs and large-scale patterns of the climate system that could drive the interannual SSTa variability by atmospheric and/or oceanic teleconnections. We focus the discussion on three main patterns of variability that are known to impact on extratropical ocean basins in the southern hemisphere on interannual to decadal timescales: Southern Annular Mode (SAM), El Niño Southern Oscillation (ENSO) and the Interdecadal Pacific Oscillation (IPO). The SAM index measures the strength of the meridional pressure gradient around Antarctica (Thompson and Wallace, 2000). The increasing trend to a positive SAM index observed during the past decades has led to the intensification and poleward shift of the westerly winds (Hall and Visbeck, 2002) affecting the local atmospheric forcing on the PS and therefore the response on the SST in that region. On the other hand, the interannual variability of tropical Pacific SST depicted by ENSO events (periods of positive ENSO 3.4 index) can trigger atmospheric Rossby waves that propagate poleward and eastward, modulating regional changes of SST in the southern SWA by local changes on zonal and meridional surface winds (Turner, 2004; Meredith et al., 2008). In addition, we include the IPO in the analysis, a broader SST pattern associated with Pacific-wide SSTs (Henley et al., 2015) on interdecadal timescales. Recent studies have shown that these decadal patterns are partially induced by tropical variability associated with ENSO events (Newman et al., 2016). Linear correlation coefficients at zero-lag between the SSTa PCs (**Figure 9**) and climate indices time series filtered with 36-month running mean are listed in **Table 6**.

Moderate but significant correlations are found between PC1 and the IPO ($r = -0.50$), and between PC2 and the IPO and ENSO 3.4 ($r = -0.42$ and -0.53, respectively). The correlations with SAM are low and non-significant for all PCs. Thus, only moderate correlations are observed between PCs and individual climate indices (**Table 6**). This suggests that the contribution of these indices to the SSTa variability on the PS is not direct. Because the interest of this work is to explain the interannual variations of SSTa on the PS through its PC, we analyzed the sum of PC1 and PC2 series (PC1+2) which explain 51% of the total variance of the SSTa at SPS and adequately represents the negative and positive SSTa periods. A multiple linear regression was performed to estimate PC1+2 values through the three climatic indices considered (SAM, ENSO 3.4, IPO). This regression significantly correlates ($r = 0.63$) with PC1+2 and explains 40% of its variance. The coefficients obtained by the multilinear regression are positive for the ENSO 3.4 and IPO indices and negative for SAM. This indicates that during positive ENSO periods, the poleward and eastward propagation of Rossby waves promotes positive values of PC1+2 and therefore positive SSTa at SPS. On the other hand, the relationship with SAM is inverse: when SAM is positive (intensified westerly winds), the northward advection of cold waters in the Ekman layer from the south to the SPS region and increased wind speeds enhance vertical mixing are promoted. In addition, as meridional wind speed variability around southern South America is negatively correlated with SAM index ($r = -0.52$) (Guihou et al., 2020), during positive SAM index periods, southerly winds can partially induce cross-shore pressure gradient and an anomalous northward geostrophic transport. These factors will likely promote negative PC1+2 anomalies and negative SSTa at SPS.

TABLE 6 | Linear correlation coefficients (r) between the PC time series of SSTa in the region spanning 110°-10°W, 60°-10°S and climate indices (ENSO 3.4, SAM, and IPO), for the period 1982–2017 (see Section 4.3).

	ENSO 3.4	SAM	IPO
PC1 SSTa	–0.38	–0.26	**–0.50**
PC2 SSTa	**–0.53**	0.26	**–0.42**
PC3 SSTa	0.40	–0.31	0.09

Correlation coefficients significantly different from zero at the 95% confidence level are indicated in bold.

This simplified multilinear regression model provides a first approach to assess the teleconnection mechanisms that are relevant for the interannual variations of SSTa on the PS. Furthermore, since the global patterns considered have a certain degree of predictability on interannual time scales (Newman, 2007), it is possible to estimate, at least, the sign of regional SSTa.

4. DISCUSSION

We analyzed linear trends and the interannual variability of SST anomaly fluctuations over the Southeastern Pacific and the Southwestern Atlantic focused on the variability over the productive Atlantic Patagonian continental shelf. The possible link between SSTa variability and local and large-scale atmospheric forcing from 1982 to 2017 was investigated using satellite and reanalysis databases. Intense positive SSTa linear trends are observed along the Brazil Current and the Brazil-Malvinas Confluence (> 0.4°C decade^{-1}), while negative trends (< -0.2°C decade^{-1}) are observed in the northernmost extension of the Malvinas Current. This meridional dipole pattern in the linear trend of SST extends over the continental shelf of the western South Atlantic, where significant positive trends north of 46°S and negative trends south of 49°S are observed. For our analysis we selected two areas of significant warming and cooling trends on the PS (NPS and SPS, respectively). We found that the observed trends in these regions represent variations of almost half a degree, with an increase of 0.52°C at NPS and a decrease of –0.42°C at SPS and that they are mostly associated with the variability observed during the past decade (2008–2017). During 2008–2017, the positive SSTa trend at NPS is strongly correlated with a decrease in the local zonal wind, i.e., to a local decline of the strength of westerly winds ($r = -0.85$). The SSTa variability at SPS is significantly correlated with the meridional wind ($r = -0.61$). This is consistent with enhanced southerly winds that reinforce northward geostrophic advection anomalies of cold waters at SPS as suggested by numerical simulations.

We find a strong interannual signal on the PS with periods centered at around 6 years. The first three leading modes of variability (EOF) in the domain bounded by 110–10°W, 10–60°S explain 28, 16, and 12% of the variance, respectively. Our analyses indicate that EOF1 and EOF2 over the above-mentioned domain represent variability associated with SSTa in the southeast Pacific and southwest Atlantic basins, respectively, while EOF3 combines variance from both basins. The sum of PC1 and PC2 (PC1+2) is significantly correlated with detrended SSTa ($r = 0.71$) and explains 51% of the variance at SPS. A multiple linear regression was performed including SAM, ENSO 3.4, IPO indices. This regression is significantly correlated ($r = 0.63$) with PC1+2 suggesting that during positive ENSO periods, the poleward propagation of atmospheric Rossby waves modulates the zonal and meridional wind variability generating anticyclonic wind anomalies (u-wnda < 0 and v-wnda > 0) that promote positive values of PC1+2 and therefore positive SSTa at SPS. In addition, the relationship with SAM is inverse: when SAM is positive (intensified westerly winds), the northward advection of cold waters to the SPS region is promoted and is further increased by intensified wind speeds that enhance vertical mixing. These two factors promote negative PC1+2 anomalies, that is negative SSTa in the SPS region. These results suggest that the SST variability observed around southern South America is partially modulated by the PDO, ENSO 3.4 and SAM, which indicate a linkage with the variability of the east-central Pacific.

To summarize, we have developed a comprehensive analysis whereby the SSTa interannual variability and trends on the SEP and SWA are forced by a combination of local and remote processes, with trends on the PS explained by local winds during the past 10 years of the records and interannual variability caused by a combination of IPO, ENSO and SAM.

DATA AVAILABILITY STATEMENT

The original contributions presented in the study are included in the article/**Supplementary Material**, further inquiries can be directed to the corresponding author.

AUTHOR CONTRIBUTIONS

DR, MPC, and AP contributed substantially to the design of this study, the analysis of the data, drafting the work, interpreting results and revising it critically. All authors have approved the final version and agreed to be accountable for all aspects of the work in ensuring that questions related to the accuracy or integrity of any part of the work are appropriately investigated and resolved.

FUNDING

This work was carried out with the aid of a grant from the Inter-American Institute for Global Change Research (IAI) CRN3070 which is supported by the U.S. National Science Foundation (grant no. GEO-1128040) and IAI grant no. SGP-HW 017.

SUPPLEMENTARY MATERIAL

The Supplementary Material for this article can be found online at: https://www.frontiersin.org/articles/10.3389/fmars.2022.829144/full#supplementary-material

REFERENCES

Abram, N., Gattuso, J.-P., Prakash, A., Cheng, L., Chidichimo, M. P., Crate, S., et al. (2019). "Framing and context of the report," in *IPCC Special Report on the Ocean and Cryosphere in a Changing Climate, Chapter 1*, 73–129. Available online at: https://www.ipcc.ch/srocc/chapter/chapter-1-framing-and-context-of-the-report/

Acha, E. M., Mianzan, H. W., Guerrero, R. A., Favero, M., and Bava, J. (2004). Marine fronts at the continental shelves of austral South America: physical and ecological processes. *J. Mar. Syst*. 44, 83–105. doi: 10.1016/j.jmarsys.2003.09.005

Atlas, R., Hoffman, R. N., Ardizzone, J., Leidner, S. M., Jusem, J. C., Smith, D. K., et al. (2011). A cross-calibrated, multiplatform ocean surface wind velocity product for meteorological and oceanographic applications. *Bull. Am. Meteorol. Soc*. 92, 157–174. doi: 10.1175/2010BAMS2946.1

Bao, X., and Zhang, F. (2013). Evaluation of NCEP-CFSR, NCEP-NCAR, ERA-Interim, and ERA-40 reanalysis datasets against independent sounding observations over the Tibetan Plateau. *J. Clim*. 26, 206–214. doi: 10.1175/JCLI-D-12-00056.1

Beaugrand, G., and Reid, P. C. (2003). Long-term changes in phytoplankton, zooplankton and salmon related to climate. *Glob. Chang Biol*. 9, 801–817. doi: 10.1046/j.1365-2486.2003.00632.x

Bindoff, N. L., Cheung, W. W., Kairo, J. G., Arístegui, J., Guinder, V. A., Hallberg, R., et al. (2019). "Changing ocean, marine ecosystems, and dependent communities," in *IPCC Special Report on the Ocean and Cryosphere in a Changing Climate, Chapter 5*, 477–587. Available online at: https://www.ipcc.ch/srocc/chapter/chapter-5/

Bisbal, G. A. (1995). The Southeast South American shelf large marine ecosystem: evolution and components. *Mar. Policy* 19, 21–38. doi: 10.1016/0308-597X(95)92570-W

Cheng, L., Abraham, J., Zhu, J., Trenberth, K. E., Fasullo, J., Boyer, T., et al. (2020). Record-setting ocean warmth continued in 2019. *Adv. Atmosphere. Sci*. 37, 137–142. doi: 10.1007/s00376-020-9283-7

Church, J. A., Clark, P. U., Cazenave, A., Gregory, J. M., Jevrejeva, S., Levermann, A., et al. (2013). *Sea level change*. Technical report, PM Cambridge University Press.

Ciais, P., Sabine, C., Bala, G., Bopp, L., Brovkin, V., Canadell, J., et al. (2014). "Carbon and other biogeochemical cycles," in *Climate change 2013: the physical science basis. Contribution of Working Group I to the Fifth Assessment Report of the Intergovernmental Panel on Climate Change, Chapter 6* (Cambridge; New York, NY: Cambridge University Press), 465–570.

Combes, V., and Matano, R. P. (2018). The Patagonian shelf circulation: drivers and variability. *Prog Oceanogr*. 167, 24–43. doi: 10.1016/j.pocean.2018.07.003

Dee, D. P., Uppala, S. M., Simmons, A., Berrisford, P., Poli, P., Kobayashi, S., et al. (2011). The ERA-Interim reanalysis: configuration and performance of the data assimilation system. *Q. J. R. Meteorol. Soc*. 137, 553–597. doi: 10.1002/qj.828

Deser, C., Alexander, M. A., Xie, S.-P., and Phillips, A. S. (2010). Sea surface temperature variability: patterns and mechanisms. *Ann. Rev. Mar. Sci*. 2, 115–143. doi: 10.1146/annurev-marine-120408-151453

Doney, S. C., Ruckelshaus, M., Emmett Duffy, J., Barry, J. P., Chan, F., English, C. A., et al. (2012). Climate change impacts on marine ecosystems. *Ann. Rev. Mar. Sci*. 4, 11–37. doi: 10.1146/annurev-marine-041911-111611

Dong, B., Sutton, R. T., and Scaife, A. A. (2006). Multidecadal modulation of El Ni no-Southern Oscillation (ENSO) variance by Atlantic Ocean sea surface temperatures. *Geophys. Res. Lett*. 33, 1–4. doi: 10.1029/2006GL025766

Falabella, V., Campagna, C., and Croxall, J. (2009). *Atlas del mar patagónico. Especies y espacios. Wildlife Conservation Society, Argentina, and BirdLife International: Buenos Aires.*). Available online at: http://www.atlas-marpatagonico.org.

Fan, T., Deser, C., and Schneider, D. P. (2014). Recent Antarctic sea ice trends in the context of Southern Ocean surface climate variations since 1950. *Geophys. Res. Lett.* 41, 2419–2426. doi: 10.1002/2014GL059239

Garcí-Serrano, J., Cassou, C., Douville, H., Giannini, A., and Doblas-Reyes, F. J. (2017). Revisiting the ENSO teleconnection to the tropical North Atlantic. *J. Clim.* 30, 6945–6957. doi: 10.1175/JCLI-D-16-0641.1

Garreaud, R. D., Clem, K., and Veloso, J. V. (2021). The South Pacific pressure trend dipole and the southern blob. *J. Clim.* 34, 7661–7676. doi: 10.1175/JCLI-D-20-0886.1

Gianelli, I., Ortega, L., Marín, Y., Piola, A. R., and Defeo, O. (2019). Evidence of ocean warming in Uruguay's fisheries landings: the mean temperature of the catch approach. *Mar. Ecol. Prog. Ser.* 625, 115–125. doi: 10.3354/meps13035

Glorioso, P. D., and Flather, R. A. (1995). A barotropic model of the currents off SE South America. *J. Geophys. Res. Oceans* 100, 13427–13440. doi: 10.1029/95JC00942

Gordon, A. L., and Greengrove, C. L. (1986). Geostrophic circulation of the Brazil-Falkland confluence. *Deep Sea Res. A Oceanogr. Res. Pap.* 33, 573–585. doi: 10.1016/0198-0149(86)90054-3

Goyal, R., England, M. H., Jucker, M., and Gupta, A. S. (2021). Response of Southern Hemisphere western boundary current regions to future zonally symmetric and asymmetric atmospheric changes. *J. Geophys. Res. Oceans* 126, e2021JC017858. doi: 10.1029/2021JC017858

Guihou, K., Piola, A. R., Palma, E. D., and Chidichimo, M. P. (2020). Dynamical connections between large marine ecosystems of austral South America based on numerical simulations. *Ocean Sci.* 16, 271–290. doi: 10.5194/os-16-271-2020

Hall, A., and Visbeck, M. (2002). Synchronous variability in the Southern Hemisphere atmosphere, sea ice, and ocean resulting from the annular mode. *J. Clim.* 15, 3043–3057. doi: 10.1175/1520-0442(2002)015andlt;3043:SVITSHandgt;2.0.CO;2

Hardiman, S., Dunstone, N., Scaife, A., Smith, D., Ineson, S., Lim, J., et al. (2019). The impact of strong El Ni no and La Ni na events on the North Atlantic. *Geophys. Res. Lett.* 46, 2874–2883. doi: 10.1029/2018GL081776

Hartmann, D. L., Tank, A. M. K., Rusticucci, M., Alexander, L. V., Brönnimann, S., Charabi, Y. A. R., et al. (2013). "Observations: atmosphere and surface," in *Climate Change 2013 the Physical Science Basis: Working Group I Contribution to the Fifth Assessment Report of the Intergovernmental Panel on Climate Change, Chapter 2* (Cambridge; New York, NY: Cambridge University Press), 159–254.

Hays, G. C., Richardson, A. J., and Robinson, C. (2005). Climate change and marine plankton. *Trends Ecol. Evolut.* 20, 337–344. doi: 10.1016/j.tree.2005.03.004

Henley, B. J., Gergis, J., Karoly, D. J., Power, S., Kennedy, J., and Folland, C. K. (2015). A tripole index for the Interdecadal Pacific oscillation. *Clim. Dyn.* 45, 3077–3090. doi: 10.1007/s00382-015-2525-1

Hirsch, R. M., Alexander, R. B., and Smith, R. A. (1991). Selection of methods for the detection and estimation of trends in water quality. *Water Resour. Res.* 27, 803–813. doi: 10.1029/91WR00259

Hobday, A. J., Alexander, L. V., Perkins, S. E., Smale, D. A., Straub, S. C., Oliver, E. C., et al. (2016). A hierarchical approach to defining marine heatwaves. *Prog. Oceanogr.* 141, 227–238. doi: 10.1016/j.pocean.2015.12.014

Hobday, A. J., and Pecl, G. T. (2014). Identification of global marine hotspots: sentinels for change and vanguards for adaptation action. *Rev. Fish. Biol. Fish.* 24, 415–425. doi: 10.1007/s11160-013-9326-6

Ishii, M., Fukuda, Y., Hirahara, S., Yasui, S., Suzuki, T., and Sato, K. (2017). Accuracy of global upper ocean heat content estimation expected from present observational data sets. *Sola* 13, 163–167. doi: 10.2151/sola.2017-030

Johnson, G. C., and Lyman, J. M. (2020). Warming trends increasingly dominate global ocean. *Nat. Clim. Chang* 10, 757–761. doi: 10.1038/s41558-020-0822-0

Kalnay, E., Kanamitsu, M., Kistler, R., Collins, W., Deaven, D., Gandin, L., et al. (1996). The NCEP/NCAR 40-year reanalysis project. *Bull. Am. Meteorol. Soc.* 77, 437–472. doi: 10.1175/1520-0477(1996)077andlt;0437:TNYRPandgt;2.0.CO;2

Kayano, M. T., and Capistrano, V. B. (2014). How the Atlantic multidecadal oscillation (AMO) modifies the ENSO influence on the South American rainfall. *Int. J. Climatol.* 34, 162–178. doi: 10.1002/joc.3674

Kendall, M. (1955). *Rank Correlation Methods. 2d Edn.* London: Charles Griffin & Co.

Kim, Y. S., and Orsi, A. H. (2014). On the variability of Antarctic circumpolar current fronts inferred from 1992-2011 altimetry. *J. Phys. Oceanogr.* 44, 3054–3071. doi: 10.1175/JPO-D-13-0217.1

Kostov, Y., Ferreira, D., Armour, K. C., and Marshall, J. (2018). Contributions of greenhouse gas forcing and the southern annular mode to historical southern ocean surface temperature trends. *Geophys. Res. Lett.* 45, 1086–1097. doi: 10.1002/2017GL074964

Lago, L., Saraceno, M., Martos, P., Guerrero, R., Piola, A., Paniagua, G., et al. (2019). On the wind contribution to the variability of ocean currents over wide continental shelves: a case study on the northern argentine continental shelf. *J. Geophys. Res. Oceans* 124, 7457–7472. doi: 10.1029/2019JC015105

Le Quéré, C., Andrew, R. M., Friedlingstein, P., Sitch, S., Hauck, J., Pongratz, J., et al. (2018). Global carbon budget 2018. *Earth Syst. Sci. Data* 10, 2141–2194. doi: 10.5194/essd-10-2141-2018

Lee, S.-K., Enfield, D. B., and Wang, C. (2008). Why do some El Ni nos have no impact on tropical North Atlantic SST? *Geophys. Res. Lett.* 35(16). doi: 10.1029/2008GL034734

Liléo, S., Berge, E., Undheim, O., Klinkert, R., and Bredesen, R. E. (2013). Long-term correction of wind measurements. State-of-the-art, guidelines and future work. *Elforsk Rep.* 13, 18. Available online at: https://energiforskmedia.blob.core.windows.net/media/19814/long-term-correction-of-wind-measurements-elforskrapport-2013-18.pdf

Ling, S., Johnson, C., Ridgway, K., Hobday, A., and Haddon, M. (2009). Climate-driven range extension of a sea urchin: inferring future trends by analysis of recent population dynamics. *Glob. Chang Biol.* 15, 719–731. doi: 10.1111/j.1365-2486.2008.01734.x

Lledó, L., Lead, T., and Dubois, J. (2013). *A study of wind speed variability using global reanalysis data. AWS* Truepower technical report, 137–142.

Mann, H. B. (1945). Nonparametric tests against trend. *Econometrica* 13, 245–259. doi: 10.2307/1907187

Matano, R., Palma, E. D., and Piola, A. R. (2010). The influence of the Brazil and malvinas currents on the southwestern atlantic shelf circulation. *Ocean Sci.* 6, 983–995. doi: 10.5194/os-6-983-2010

McLeod, A. I., Hipel, K. W., and Bodo, B. A. (1991). Trend analysis methodology for water quality time series. *Environmetrics* 2, 169–200. doi: 10.1002/env.3770020205

Meredith, M. P., Murphy, E. J., Hawker, E. J., King, J. C., and Wallace, M. I. (2008). On the interannual variability of ocean temperatures around South Georgia, Southern Ocean: Forcing by El Ni no-Southern Oscillation and the Southern Annular Mode. *Deep Sea Res. II Top. Stud. Oceanogr.* 55, 2007–2022. doi: 10.1016/j.dsr2.2008.05.020

Messié, M., and Chavez, F. (2011). Global modes of sea surface temperature variability in relation to regional climate indices. *J. Clim.* 24, 4314–4331. doi: 10.1175/2011JCLI3941.1

Mezzina, B., García-Serrano, J., Bladé, I., and Kucharski, F. (2020). Dynamics of the ENSO teleconnection and NAO variability in the north atlantic-european late winter. *J. Clim.* 33, 907–923. doi: 10.1175/JCLI-D-19-0192.1

Muller-Karger, F. E., Kavanaugh, M. T., Montes, E., Balch, W. M., Breitbart, M., Chavez, F. P., et al. (2014). A framework for a marine biodiversity observing network within changing continental shelf seascapes. *Oceanography* 27, 18–23. doi: 10.5670/oceanog.2014.56

Nerem, R. S., Beckley, B. D., Fasullo, J. T., Hamlington, B. D., Masters, D., and Mitchum, G. T. (2018). Climate-change-driven accelerated sea-level rise detected in the altimeter era. *Proc. Natl. Acad. Sci. U.S.A.* 115, 2022–2025. doi: 10.1073/pnas.1717312115

Newman, M. (2007). Interannual to Decadal predictability of tropical and North Pacific sea surface temperatures. *J. Clim.* 20, 2333–2356. doi: 10.1175/JCLI4165.1

Newman, M., Alexander, M. A., Ault, T. R., Cobb, K. M., Deser, C., Di Lorenzo, E., et al. (2016). The pacific decadal oscillation, revisited. *J. Clim.* 29, 4399–4427. doi: 10.1175/JCLI-D-15-0508.1

Oppenheimer, M., Glavovic, B., Hinkel, J., van de Wal, R., Magnan, A. K., Abd-Elgawad, A., et al. (2019). "Sea level rise and implications for low lying islands, coasts and communities," in *IPCC Special Report on the Ocean and Cryosphere in a Changing Climate, Chapter 4*. Available online at: https://www.ipcc.ch/srocc/chapter/chapter-4-sea-level-rise-and-implications-for-low-lying-islands-coasts-and-communities/

Oschlies, A., Brandt, P., Stramma, L., and Schmidtko, S. (2018). Drivers and mechanisms of ocean deoxygenation. *Nat. Geosci*. 11, 467–473. doi: 10.1038/s41561-018-0152-2

Palma, E. D., Matano, R. P., and Piola, A. R. (2008). A numerical study of the Southwestern Atlantic Shelf circulation: Stratified ocean response to local and offshore forcing. *J. Geophys. Res. Oceans* 113, C11010. doi: 10.1029/2007JC004720

Palma, E. D., Matano, R. P., Piola, A. R., and Sitz, L. E. (2004). A comparison of the circulation patterns over the Southwestern Atlantic Shelf driven by different wind stress climatologies. *Geophys. Res. Lett*. 31, 1–5. doi: 10.1029/2004GL021068

Parmesan, C., and Yohe, G. (2003). A globally coherent fingerprint of climate change impacts across natural systems. *Nature* 421, 37–42. doi: 10.1038/nature01286

Pecl, G. T., Ward, T. M., Doubleday, Z. A., Clarke, S., Day, J., Dixon, C., et al. (2014). Rapid assessment of fisheries species sensitivity to Climate Change. *Clim. Change* 127, 505–520. doi: 10.1007/s10584-014-1284-z

Piola, A. R., Palma, E. D., Bianchi, A. A., Castro, B. M., Dottori, M., Guerrero, R. A., et al. (2018). "Physical oceanography of the SW Atlantic Shelf: a review," in *Plankton Ecology of the Southwestern Atlantic* (Cham: Springer), 37–56.

Preisendorfer, R. W., and Mobley, C. D. (1988). Principal component analysis in meteorology and oceanography. *Dev. Atmosphere. Sci*. 17, 425.

Ramírez, F., Afán, I., Davis, L. S., and Chiaradia, A. (2017). Climate impacts on global hot spots of marine biodiversity. *Sci. Adv*. 3, e1601198. doi: 10.1126/sciadv.1601198

Reynolds, R. W., Smith, T. M., Liu, C., Chelton, D. B., Casey, K. S., and Schlax, M. G. (2007). Daily high-resolution-blended analyses for sea surface temperature. *J. Clim*. 20, 5473–5496. doi: 10.1175/2007JCLI1824.1

Rhein, M., Rintoul, S. R., Aoki, S., Campos, E., Chambers, D., Feely, R. A., et al. (2013). "Observations: ocean," in *Climate Change 2013: The Physical Science Basis. Contribution of Working Group I to the Fifth Assessment Report of the Intergovernmental Panel on Climate Change*, eds T. Stocker, D. P. G. -K. Qin, M. Tignor, S. Allen, J. Boschung, A. Nauels, Y. Xia, V. Bex, and P. Midgley (Cambridge: Cambridge University Press), 255–316.

Rivadeneira, M. M., and Fernández, M. (2005). Shifts in southern endpoints of distribution in rocky intertidal species along the south-eastern Pacific coast. *J. Biogeogr*. 32, 203–209. doi: 10.1111/j.1365-2699.2004.01133.x

Rivas, A. L. (1994). Spatial variation of the annual cycle of temperature in the Patagonian shelf between 40 and 50 of south latitude. *Cont. Shelf Res*. 14, 1539–1554. doi: 10.1016/0278-4343(94)90089-2

Rivas, A. L. (2010). Spatial and temporal variability of satellite-derived sea surface temperature in the southwestern Atlantic Ocean. *Cont. Shelf Res*. 30, 752–760. doi: 10.1016/j.csr.2010.01.009

Rodrigues, R. R., Campos, E. J., and Haarsma, R. (2015). The impact of ENSO on the South Atlantic subtropical dipole mode. *J. Clim*. 28, 2691–2705. doi: 10.1175/JCLI-D-14-00483.1

Romero, S. I., Piola, A. R., Charo, M., and Garcia, C. A. E. (2006). Chlorophyll-a variability off Patagonia based on SeaWiFS data. *J. Geophys. Res. Oceans* 111, 1–11. doi: 10.1029/2005JC003244

Saha, S., Moorthi, S., Pan, H.-L., Wu, X., Wang, J., Nadiga, S., et al. (2010). The NCEP climate forecast system reanalysis. *Bull. Am. Meteorol. Soc*. 91, 1015–1058. doi: 10.1175/2010BAMS3001.1

Stramma, L., Prince, E. D., Schmidtko, S., Luo, J., Hoolihan, J. P., Visbeck, M., et al. (2012). Expansion of oxygen minimum zones may reduce available habitat for tropical pelagic fishes. *Nat. Clim. Chang*. 2, 33–37. doi: 10.1038/nclimate1304

Thompson, D. W., and Wallace, J. M. (2000). Annular modes in the extratropical circulation. Part I: Month-to-month variability. *J. Clim*. 13, 1000–1016. doi: 10.1175/1520-0442(2000)013andlt;1000:AMITECandgt;2.0.CO;2

Thomson, R. E., and Emery, W. J. (2014). *Data Analysis Methods in Physical Oceanography, 3rd Edn*. Waltham, MA: Newnes.

Turner, J. (2004). The El Niño Southern Oscillation and Antarctica. *Int. J. Climatol*. 24, 1–31. doi: 10.1002/joc.965

Von Schuckmann, K., Le Traon, P.-Y., Alvarez-Fanjul, E., Axell, L., Balmaseda, M., Breivik, L.-A., et al. (2016). The copernicus marine environment monitoring service ocean state report. *J. Operat. Oceanogr*. 9(Suppl. 2):S235–S320. doi: 10.1080/1755876X.2016.1273446

Von Schuckmann, K., Le Traon, P.-Y., Smith, N., Pascual, A., Brasseur, P., Fennel, K., et al. (2018). Copernicus marine service ocean state report. *J. Operat. Oceanogr*. 11(Suppl. 1):S1–S142.

Walther, G.-R., Post, E., Convey, P., Menzel, A., Parmesan, C., Beebee, T. J., et al. (2002). Ecological responses to recent climate change. *Nature* 416, 389–395. doi: 10.1038/416389a

Welch, P. (1967). The use of fast Fourier transform for the estimation of power spectra: a method based on time averaging over short, modified periodograms. *IEEE Trans. Audio Electroacoust*. 15, 70–73. doi: 10.1109/TAU.1967.1161901

Wentz, F., Scott, J., Hoffman, R., Leidner, M., Atlas, R., and Ardizzone, J. (2015). *Remote Sensing Systems Cross-Calibrated Multi-Platform (CCMP) 6-hourly ocean vector wind analysis product on 0.25 deg grid, Version 2.0*. Santa Rosa, CA: Remote Sensing Systems.

Yang, H., Lohmann, G., Krebs-Kanzow, U., Ionita, M., Shi, X., Sidorenko, D., et al. (2020). Poleward shift of the major ocean gyres detected in a warming climate. *Geophys. Res. Lett*. 47, e2019GL085868. doi: 10.1029/2019GL085868

Yang, Y., Xie, S.-P., Wu, L., Kosaka, Y., and Li, J. (2018). ENSO forced and local variability of North Tropical Atlantic SST: model simulations and biases. *Clim. Dyn*. 51, 4511–4524. doi: 10.1007/s00382-017-3679-9

Conflict of Interest: The authors declare that the research was conducted in the absence of any commercial or financial relationships that could be construed as a potential conflict of interest.

frontiers
in Marine Science

ORIGINAL RESEARCH
published: 14 March 2022
doi: 10.3389/fmars.2022.830821

Variability and Feedbacks in the Atlantic Freshwater Budget of CMIP5 Models With Reference to Atlantic Meridional Overturning Circulation Stability

Keith Haines[1,2]*, *David Ferreira*[1] *and Davi Mignac*[1]†

[1] *Dept. of Meteorology, University of Reading, Reading, United Kingdom,* [2] *National Centre for Earth Observation (NCEO), University of Reading, Reading, United Kingdom*

Edited by:
Fabrice Hernandez,
Institut de Recherche Pour le Développement (IRD), France

Reviewed by:
Wei Cheng,
University of Washington, United States
Robert Marsh,
University of Southampton, United Kingdom
Jiang Zhu,
National Center for Atmospheric Research (UCAR), United States
Shantong Sun,
California Institute of Technology, United States

***Correspondence:**
Keith Haines
k.haines@reading.ac.uk

†Present address:
Davi Mignac,
The Met. Office,
Exeter, United Kingdom

Specialty section:
This article was submitted to Physical Oceanography, a section of the journal Frontiers in Marine Science

Received: *07 December 2021*
Accepted: *14 February 2022*
Published: *14 March 2022*

Citation:
Haines K, Ferreira D and Mignac D (2022) Variability and Feedbacks in the Atlantic Freshwater Budget of CMIP5 Models With Reference to Atlantic Meridional Overturning Circulation Stability. Front. Mar. Sci. 9:830821. doi: 10.3389/fmars.2022.830821

It has been suggested that freshwater transports by the Atlantic Meridional Overturning Circulation (AMOC) in the South Atlantic may be a useful metric for determining the stability of the AMOC because it can lead to feedbacks onto North Atlantic salinities and hence deep water formation. In this manuscript we investigate feedbacks between South Atlantic Freshwater transports, Freshwater content and AMOC transport contributions across different Atlantic latitudes, and at different timescales in centennial runs of 10 CMIP5 climate models, with both northward and southward AMOC freshwater transports in the South Atlantic. In all models, salinity variations are more important than AMOC variations in determining South Atlantic freshwater transports, especially on longer timescales >10 years. Only in the North Atlantic do AMOC variations become important in changing the meridional freshwater transports, which might then lead to feedbacks with stability implications. Closed budgets of Freshwater content show that South Atlantic transports only influence local freshwater budgets (within ∼10° latitude) and that variations in horizontal transports by the South Atlantic gyre always dominate the overturning transports in all models and timescales. These results suggest that South Atlantic freshwater transports by the AMOC is highly unlikely to be a useful metric in determining AMOC stability as meridional freshwater transports are much less meridionally coherent than the AMOC circulation itself in all 10 CMIP5 models studied.

Keywords: Atlantic freshwater, AMOC stability, CMIP5 models, southern F_{OV}, Atlantic salinity balance

INTRODUCTION

The salt-advection feedback mechanism has been suggested as a mechanism potentially leading to instability in the Atlantic Meridional Overturning Circulation (AMOC), based on ideas from box models (Stommel, 1961; Rahmstorf, 1996; De Vries and Weber, 2005). In particular, this feedback has been used to argue that the AMOCs contribution in transporting freshwater into or out of the South Atlantic basin at 34°S may be critical to AMOC stability and the existence of multiple AMOC states for a given surface freshwater forcing (i.e., bistability regime). If the AMOC exports freshwater then a weakening AMOC may lead to the whole Atlantic becoming fresher, which may then reduce deep water formation leading to further AMOC weakening, and potentially to a collapse. Recovery from such a collapsed state would require large freshwater perturbations to pull the system into a regime where a strong AMOC becomes the only possible state.

With this in mind, freshwater transport by the overturning has been assessed at the southern boundary, 34°S, in the Atlantic, leading to a focus on "$F_{ov}{}^{34S}$" as an important metric of potential instability (Drijfhout et al., 2011; Hawkins et al., 2011). The $F_{ov}{}^{34S}$ from observations is known to be slightly negative, appearing to support the possibility of AMOC instability. Many climate models have a bias in $F_{ov}{}^{34S}$, exhibiting a positive value, i.e., a freshwater transport into the Atlantic by the AMOC. It has been suggested that these models do not possess a bistable regime and are more stable to AMOC collapse than the real climate system. However, Mignac et al. (2019) argue that the observed $F_{ov}{}^{34S}$ is, most importantly, very small so that changes in the AMOC circulation have a negligible effect on freshwater transport into and out of the Atlantic basin from the south. Dijkstra (2007) did extend the freshwater feedback stability argument to emphasize freshwater convergence, thus including AMOC transports from the Arctic into the North Atlantic, but without explicitly discounting possible influence of the southern boundary transports.

Stability studies of the AMOC in climate models have usually been addressed by introducing large freshwater anomalies (Hosing experiments) into the North Atlantic (e.g., Huisman et al., 2010; Jackson, 2013; Mecking et al., 2016). Some hosing experiments in coarse ocean-only and intermediate-complexity coupled models with negative $F_{ov}{}^{34S}$, do seem to sustain a collapsed AMOC state associated with a bistable regime for longer periods, and have a slower recovery than models with positive $F_{ov}{}^{34S}$ (e.g., Rahmstorf et al., 2005). However, similar hosing experiments in more complex climate models, including eddy-permitting ocean components are less clear, revealing diverse AMOC behaviour, ranging from no evidence of an AMOC shutdown (e.g., Stouffer et al., 2006) to a situation where a collapsed AMOC was maintained for 450 years (e.g., Mecking et al., 2016). However, the sensitivity of hosing experiments to forcing timescales (Kim et al., 2021) and the strong non-linearities involved (Gent, 2018), including atmospheric feedbacks, make it difficult to study the roles of current velocity and salinity variability. Indeed, crucially, the salt-advection feedback assumes that variability in $F_{ov}{}^{34S}$ is determined by variability of the AMOC rather than variability in the salinity distribution, i.e., $dF_{ov} = \overline{\Delta S} \cdot d\psi$ (Rahmstorf, 1996). It also relies on the assumption that changes in the freshwater transport to northern water formation latitudes by other dynamics, such as the gyres or mesoscale eddies, are negligible, and these aspects cannot remain unaffected by large perturbations such as hosing.

To avoid these problems Cheng et al. (2018) instead studied the natural AMOC variability in long runs of 2 climate models and assessed the covariability between the AMOC and meridional freshwater transports throughout in the Atlantic basin. Although they found evidence for high latitude Atlantic density variability controlling AMOC strength, they found no evidence that the AMOC strength was leading to density variability through salinity transports from the South Atlantic. However, the 2 climate models used by Cheng et al. (2018), GFDL-ESM2M and CESM1, both had $F_{ov}{}^{34S} > 0$ and therefore would not have been expected to exhibit any positive feedback between the AMOC and the southern freshwater transports.

Following the work of Cheng et al. (2018), we here look at the internal variability of 10 multi-centennial CMIP5 simulations, covering both positive and negative $F_{ov}{}^{34S}$ models. We seek evidence to clarify the following points: Is the southern F_{ov} variability dominated by changes in the local circulation or in the salinities? What is the influence of southern transport by the overturning, F_{ov}, and by the gyre, F_{gyre}, in contributing to freshwater content (FWC) changes and the AMOC changes throughout the Atlantic basin? In particular, how far north can $F_{ov}{}^{34S}$ correlations be detected during internal variability?

The manuscript is organised as follows. The CMIP5 models and their main configurations are presented in Section "CMIP5 Models and Diagnostics," along with the mathematical framework used for the investigation of the salt-advection feedback mechanisms. To set the stage, Section "CMIP5 Mean Freshwater transports in South Atlantic" evaluates the mean state of the selected CMIP5 models, particularly focusing on the sensitivity of their mean F_{ov} to the vertical salinity distributions. Section "Time-Varying Freshwater Transports" evaluates the F_{ov} temporal components, by calculating the contributions of meridional velocity and salinity variations to F_{ov} anomalies on a range of timescales and across different latitudes. Freshwater budgets are calculated in Section "Atlantic Freshwater Content" to identify the main drivers of FWC changes throughout the Atlantic, from interannual to multidecadal timescales. Finally, Section "Discussion and Conclusion" discusses the findings of this work and summarises the conclusions.

CMIP5 MODELS AND DIAGNOSTICS

Models

We have selected 10 CMIP5 pre-industrial control simulations conducted by different institutions and with distinct ocean and atmospheric models (see **Table 1**). These have greenhouse gas emissions, volcanic and anthropogenic aerosols, as well as radiative forcing held constant at pre-industrial levels, therefore removing any influence of external climate forcing variations. The length of these runs ranges from 300 years in IPSL-MR to 1000 years in IPSL-LR. Further CMIP5 details can be found in Taylor et al. (2012), and individual model details can be found in the references given. Models belonging to the same institution in **Table 1** differ in the horizontal resolution employed, e.g., CMCC-CM has a much higher atmospheric resolution of 0.8° when compared to 3.7° for CMCC-CMS. All the ocean models employ z-level vertical coordinates, except for GFDL-ESM2G which has isopycnal coordinates, but its data are stored on z-levels in the CMIP5 database.

This choice of models covers a wide range of mean $F_{ov}{}^{34S}$ values, with 5 models having a negative $F_{ov}{}^{34S}$ and 5 a positive, with the $F_{ov}{}^{34S}$ range from −0.17 to +0.7 Sv, and the annual variability thereof, also shown in **Table 1**. It is notable that the

TABLE 1 | List of selected CMIP5 products with the institution that conducted the simulations, the length of each simulation, the models and their horizontal resolutions, the F_{ov} at 34°S and the AMOC strengths at 26.5°N and 34°S, ±their interannual variabilities.

Products	Institution	Years	Ocean model	Ocean resolution	Atm model	Atm resolution	$F_{ov}{}^{34S}$ (mSv)	AMOC 26.5°N 34°S (Sv)	References
*CMCC-CM	CMCC	330	NEMO	2.0° × 1.9°	ECHAM5	0.8° × 0.8°	−107 ± 37	13.9 ± 2.5 11.3 ± 1.4	Scoccimarro et al., 2011
*CMCC-CMS	CMCC	500	NEMO	2.0° × 1.9°	ECHAM5	3.7° × 3.7°	−165 ± 40	12.7 ± 2.8 11.2 ± 1.6	Scoccimarro et al., 2011
FIO-ESM	FIO	800	POP2.0	2.0° × 2.0°	CAM4	2.8° × 2.8°	−101 ± 27	15.2 ± 2.2 10.9 ± 1.5	Qiao et al., 2013
*IPSL-LR	IPSL	1000	NEMO	2.0° × 1.9°	LMDz	1.9° × 3.7°	−56 ± 31	10.3 ± 2.1 8.5 ± 1.6	Dufresne et al., 2013
*IPSL-MR	IPSL	300	NEMO	1.6° × 1.4°	LMDz	1.3° × 2.5°	−15 ± 23	12.9 ± 1.9 11.0 ± 1.7	Dufresne et al., 2013
BCC-CSM1	BCC	400	MOM4	1.0° × 1.0°	BCC-AGCM2.1	2.8° × 2.8°	145 ± 30	21.8 ± 1.8 19.5 ± 1.2	Xin et al., 2015
BNU-ESM	BNU	559	MOM4	1.0° × 1.0°	CAM4	2.8° × 2.8°	702 ± 72	25.2 ± 2.0 22.2 ± 1.6	Ji et al., 2014
CCSM4	NCAR	500	POP2.0	1.1° × 0.6°	CAM4	1.2° × 1.0°	145 ± 13	22.0 ± 1.7 14.1 ± 1.4	Danabasoglu et al., 2012
*CSIRO-Mk3	CSIRO-QCCE	500	MOM4	1.0° × 1.9°	Mk3-AGCM	1.9° × 1.9°	274 ± 48	20.3 ± 2.6 15.6 ± 1.2	Gordon et al., 2010
*GFDL-ESM2G	NOAA GFDL	500	GOLD	0.5° × 1.0°	AM2	2.0° × 2.0°	220 ± 29	21.5 ± 2.5 17.5 ± 1.6	Dunne et al., 2013

The stars before the product names indicate models for which freshwater surface fluxes are available on their ocean grids in the CMIP5 database.
CMIP5 models above and below the thick solid line have negative and positive $F_{ov}{}^{34S}$, respectively.

models with positive $F_{ov}{}^{34S}$ have slightly higher ocean resolution, although also most models with negative $F_{ov}{}^{34S}$ use a single ocean code, NEMO.

Diagnostic Framework

In order to calculate transports across each latitudinal section, following a number of earlier studies, notably Bryden and Imawaki (2001), the mean baroclinic freshwater transport is decomposed into mean vertical (overturning) and horizontal (gyre) components:

$$Fmean = F_{ov} + F_{gyre} = -\frac{1}{\hat{S}}\int_{-H}^{0} v^{*} < S > dz - \frac{1}{\hat{S}}\int_{W}^{E}\int_{-H}^{0} v'' S'' dzdx \qquad (1)$$

where H is the ocean depth, W and E correspond to the western and eastern boundaries, <.> represents the zonal mean, the double prime $''$ denotes deviations from zonal averages, $\hat{S}$ is the section averaged salinity (other reference salinity choices are possible), and v* corresponds to deviations of the zonal mean meridional velocity at each depth from its section averaged values.

F_{ov} and F_{gyre} are calculated using monthly mean model output, and the derived monthly fields are averaged over each year to produce annual-mean time series. Temporal variability in the annual-mean time series of F_{ov} is also decomposed into contributions from meridional velocity and salinity variations using the following equations:

$$F_{ov}(y) = (v.S) = (\bar{v} + v')(\bar{S} + S') = \bar{v}\bar{S} + \bar{v}S' + v'\bar{S} + v'S' \qquad (2)$$

$$\overline{F_{ov}}(y) = \bar{v}\bar{S} + \overline{v'S'} \qquad (3)$$

$$F'_{ov}(y) = F_{ov}(y) - \overline{F_{ov}}(y) = \bar{v}S' + v'\bar{S} + v'S' - \overline{v'S'} \qquad (4)$$

where y corresponds to each latitude, the overbar represents the long-term mean, the prime represents deviations from the long-term mean, and the top-to-bottom integrals of v and $-<S>/\hat{S}$ in Eq. 1 are simplified to v and S, respectively. Since the term $\overline{v'S'}$ will be shown to have negligible contribution in the analyses, the final equation can then be approximated to:

$$F'_{ov}(y) = F_{ov}(y) - \overline{F_{ov}}(y) \approx \bar{v}S' + v'\bar{S} + v'S' \qquad (5)$$

The left-hand side of Eq. 5 is the F_{ov} (y) anomaly with its long-term mean removed at each latitude. The first and second terms on the right-hand side of Eq. 5 represent, respectively, the contributions from salinity and velocity anomalies from their long-term means, whereas the last term denotes the covariations between salinity and velocity anomalies.

Fields of FWC are also obtained on a monthly basis and are then averaged over each year, according to the equation:

$$FWC = -\int_{y1}^{y2}\int_{W}^{E}\int_{-H}^{0}[S(y,x,z) - \hat{S}(y)]/\hat{S}(y)dzdxdy \qquad (6)$$

where salinity anomalies, relative to section averaged values ($\hat{S}$) at each latitude, are integrated from the bottom to the surface of the ocean and over a domain enclosed by two latitudes $y1$ and $y2$, and by the western (W) and eastern (E) boundaries.

The Atlantic freshwater budget is calculated for the 6 models which have the surface freshwater fluxes already available on their ocean grids in the CMIP5 database. These models have a star before their names in **Table 1**. Annual FWC changes are estimated as the difference between two successive Januaries, following the Deshayes et al. (2014) CMIP5 intercomparison of North Atlantic freshwater budgets. Changes in FWC can be attributed to combinations of surface fluxes, advective, and diffusive fluxes of freshwater across all lateral boundaries of the budget domain. As in Deshayes et al. (2014), a budget residual term is considered due to missing components in the CMIP5 database: (i) diffusive fluxes are not available for any models in **Table 1**; and (ii) the parameterised contributions of mesoscale processes to tracer advection, i.e., Gent-McWilliams (GM) parameterization (Gent and McWilliams, 1990), are also not available for any model. The freshwater budget equation is described as follows:

$$\Delta FWC \;=\; F^{S} + F^{N} - (E - P - R) + RES \qquad (7)$$

where ΔFWC is the temporal change, F^{N} and F^{S}, respectively, correspond to the total freshwater transports into the basin at the northern and southern boundaries, E-P-R represents the evaporation minus precipitation and runoff (each considered positive), and RES is the residual term.

To evaluate the main drivers of FWC changes between any two latitudes in the Atlantic the covariance of each budget term with FWC changes is normalised by the variance of FWC changes, and will satisfy the following equation:

$$\frac{\mathrm{cov}(\mathrm{F_{ov}}^{\mathrm{S}},\,\mathrm{FWC})}{\sigma^{2}(FWC)} + \frac{\mathrm{cov}(\mathrm{F_{gyre}}^{\mathrm{S}},\,\mathrm{FWC})}{\sigma^{2}(FWC)} + \frac{\mathrm{cov}(\mathrm{F_{ov}}^{\mathrm{N}},\,\mathrm{FWC})}{\sigma^{2}(FWC)} + \frac{\mathrm{cov}(\mathrm{F_{gyre}}^{\mathrm{N}},\,\mathrm{FWC})}{\sigma^{2}(FWC)} + \frac{\mathrm{cov}(\mathrm{E-P-R},\,\mathrm{FWC})}{\sigma^{2}(FWC)} + \frac{\mathrm{cov}(RES,\,\mathrm{FWC})}{\sigma^{2}(FWC)} = \frac{\mathrm{cov}\,(\mathrm{FWC},\ \mathrm{FWC})}{\sigma^{2}(FWC)} \;=\; 1 \qquad (8)$$

It is worth noting that all the analyses are performed on the original model grid and the time-series have their linear trends removed.

CMIP5 MEAN FRESHWATER TRANSPORTS IN THE SOUTH ATLANTIC

Figures 1A,B show the zonal and run averaged salinity between 34°S and 20°S, as a function of depth, for the two CMIP5 groups based on $F_{ov}{}^{34S}$ sign. The observed zonal and time averaged salinity from EN4.2.1 is also shown on both plots. Models with positive $F_{ov}{}^{34S}$ (**Figure 1A**) are much fresher than the observations through the top 500 m and have a mainly salty bias below 1200 m, with quite a large spread of values. The zonal mean AMOC flow reverses around 1200 m so this vertical salinity distribution explains the northward freshwater transport of the AMOC in these models. In contrast the models with negative $F_{ov}{}^{34S}$ (**Figure 1B**) match observed salinities much better in the top 500 m: they have a small 0.4 psu salty bias between 500 and 1200 m but otherwise fit the observations well below 1200 m with only a small spread. For convenience we follow Mignac et al. (2019) and define ΔS_{1200m} as the zonal mean difference between salinities averaged in the top 1200 m and averaged below 1200 m.

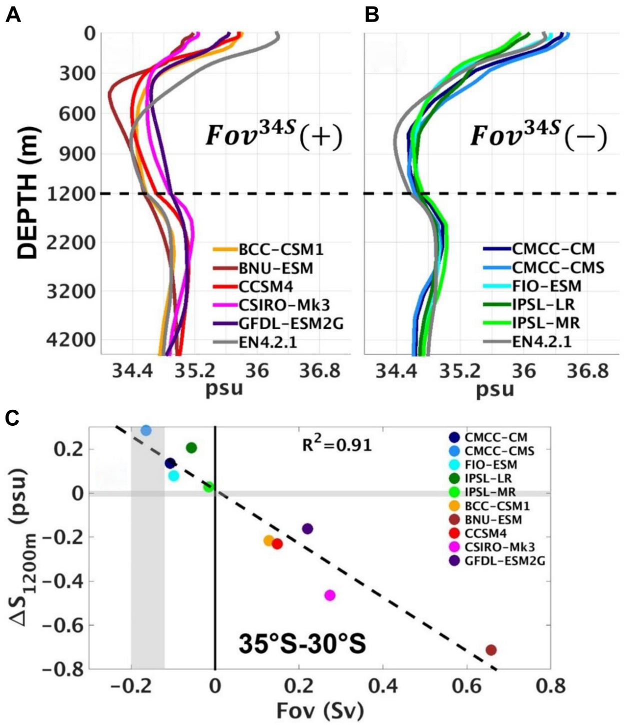

FIGURE 1 | The zonally averaged salinity profiles between 34°S and 20°S for the 10 chosen CMIP5 models, divided into groups with **(A)** positive and **(B)** negative $F_{ov}{}^{34S}$. The EN4.2.1 observations are also shown for comparison. Note the stretched vertical axis in **(A,B)** between 0 and 1200 m, compared to 1200 and 4500 m. **(C)** Scatter plot of mean ΔS_{1200m} and F_{ov} between 35°S and 30°S for the 10 chosen CMIP5 models. The vertical grey shading represents F_{ov} observational range in the southern Atlantic from Garzoli et al. (2013), whereas the horizontal grey shading corresponds to the small annual range of EN4.2.1 $\Delta S_{1200m} \sim 0.02$ psu.

The positive and negative S biases within different depth ranges may be associated with salinity discrepancies in the formation regions of water masses (Sallée et al., 2013; Zhu et al., 2018). For example, all models with positive $F_{ov}{}^{34S}$ have their salinity minimum between 300 and 600 m indicating a shallow AAIW layer, with a strong fresh bias at these levels which also extends right up to the surface. This shallow AAIW minimum, with too fresh waters reaching the surface, along with too salty waters below 1200 m. produces the positive $F_{ov}{}^{34S}$ bias. The models with negative $F_{ov}{}^{34S}$ better reproduce the AAIW minimum position, and although the AAIW does not extend deeply enough the transports between 500 and 1200 m are weak enough not to cause large $F_{ov}{}^{34S}$ bias.

Figure 1C shows the very tight relationship between ΔS_{1200m} and $F_{ov}{}^{35-30S}$, with a linear regression coefficient of 0.91 amongst all these models. This is consistent with the key role of salinity differences in controlling F_{ov}, as also noted by Mignac et al. (2019) when comparing ocean reanalysis datasets (ORA) and free running models (FRM). This also explains the large sensitivity of $F_{ov}{}^{34S}$ when salinity bias corrections are applied in the CMIP5 models (Mecking et al., 2017).

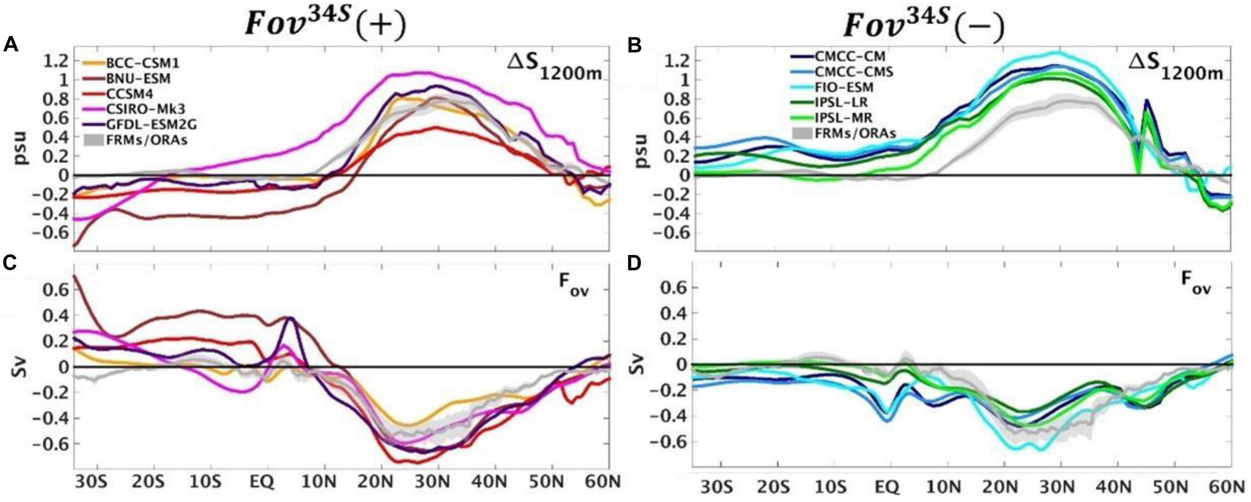

FIGURE 2 | The mean **(A,B)** ΔS_{1200m} (psu), and **(C,D)** F_{ov} (Sv), divided into two CMIP5 groups of positive (left) and negative (right) $F_{ov}{}^{34S}$, respectively.

The influence of ΔS_{1200m} over F_{ov} extends throughout the Atlantic basin. **Figure 2** shows ΔS_{1200m} and F_{ov}, as a function of latitude throughout the Atlantic basin. The positive $F_{ov}{}^{34S}$ models (**Figure 2**, left), show that the greater spread in ΔS_{1200m}, and $F_{ov}{}^{34S}$ seen in **Figure 1A** relative to **Figure 1B**, extends throughout the Atlantic basin. Although ΔS_{1200m} controls the $F_{ov}{}^{34S}$ strength, **Table 1** shows that the models with positive $F_{ov}{}^{34S}$ also have larger AMOC strengths than models with negative $F_{ov}{}^{34S}$. Mecking et al. (2017) also noticed the inter-model correlation of 0.73 between the AMOC strength at 26.5°N and $F_{ov}{}^{34S}$ and proposed an indirect connection whereby CMIP5 models with stronger AMOCs lead to warmer SSTs and more evaporation in the North Atlantic, making the north saltier and denser and hence able to maintain the strong AMOC. For consistency the extra evaporation in the North Atlantic then requires freshwater import by the AMOC into the southern Atlantic, a positive $F_{ov}{}^{34S}$, and transport up into the northern basin. Conversely, models with weak AMOCs would have less evaporation in the North Atlantic and require less import of freshwater through the southern Atlantic. We will look for any evidence of these connections in the following section.

TIME-VARYING FRESHWATER TRANSPORTS

In this section we look at the correlated variability in the AMOC and the freshwater transports in the different models. Despite the large AMOC strength differences between the two groups of CMIP5 models in **Table 1**, the interannual AMOC variability at 34°S and 26°N is insensitive to $F_{ov}{}^{34S}$, with very small linear regression coefficients of 0.05 and 0.09, respectively (**Figure 3**). Although interannual Ekman transports are included in AMOC variability, stability differences between models could still lead to larger AMOC variability for the more unstable models, however, there is no indication of a relationship to the mean $F_{ov}{}^{34S}$.

An implicit assumption of the salt-advection feedback is that temporal F_{ov} variability is primarily determined by the meridional velocity variability rather than by the salinity variability throughout the Atlantic (Rahmstorf, 1996). In **Figure 4** (left), the decadal F_{ov}^{34S} timeseries variability is decomposed into contributions from salinity and velocity variations, together with the contributions due to their covariability (see Eq. 5). Regardless of $F_{ov}{}^{34S}$ sign, 7 out of 10 CMIP5 models in **Table 1** have F_{ov}^{34S} variability more correlated (R^2 on plots) with local salinity variations than with local

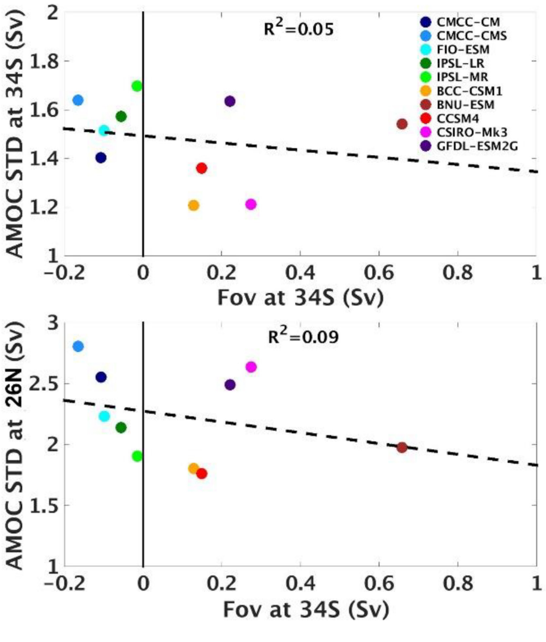

FIGURE 3 | Scatter plot of interannual AMOC variability (Sv) at 34°S **(top)** and at 26°N **(bottom)** against F_{ov} (Sv) at 34°S for the 10 CMIP5 models.

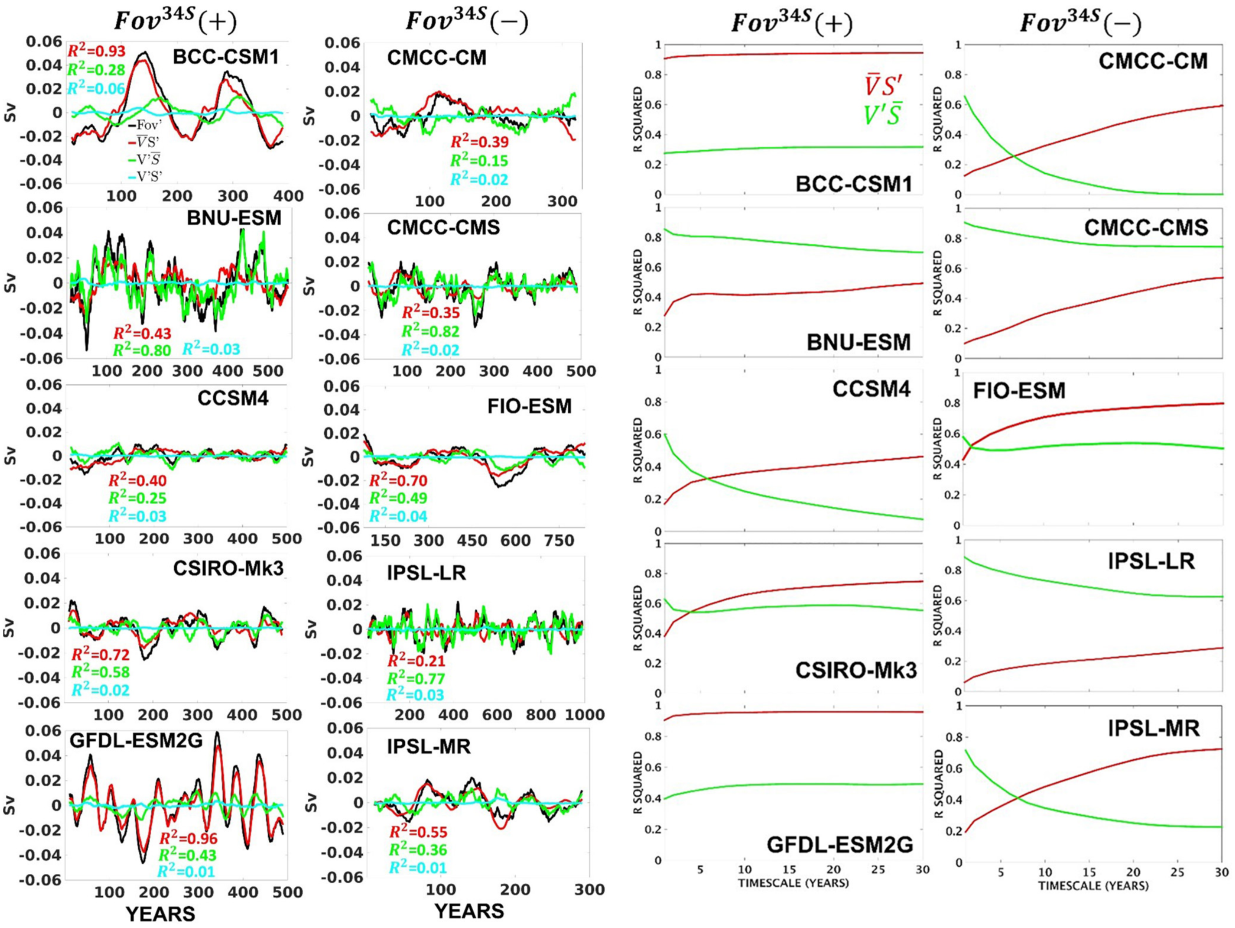

FIGURE 4 | (Left): Eleven-point running averages of the annual-mean time series of F_{ov}' (black lines; Sv), with contributions from salinity (red line) and velocity (green line) variability, as well as from their covariability (cyan line) for the region between 34°S and 20°S. The R^2 values between F_{ov}' and its components are indicated by the respective colours. Note the different time intervals for each CMIP5 model. **(Right)**: R^2 of F_{ov} anomalies with contributions from salinity (red) and velocity (green) anomalies, as a function of timescale, for the region 34°S to 20°S. The CMIP5 models with positive and negative ${F_{ov}}^{34S}$ are displayed on the left and right panels, respectively, in both sections.

circulation changes. For example, in BCC-CSM1 and GFDL-ESM2G, $\bar{v}\ S'$ has 0.93 and 0.96 correlation with southern F_{ov} variability, much larger than the 0.28 and 0.43 correlations with $v'\ \bar{S}$, respectively. Although the relative contributions of meridional velocity anomalies are slightly larger in CSIRO-Mk3, CCSM4, CMCC-CM, FIO-ESM, and IPSL-MR, these models still show a dominance of $\bar{v}\ S'$ over $v'\ \bar{S}$ on decadal timescales.

In **Figure 4** (right), the R^2 coefficients of F_{ov}' with $\bar{v}\ S'$ and $v'\ \bar{S}$ are shown as a function of timescale. Many CMIP5 models show a rapid increase (decrease) of $\bar{v}\ S'$ ($v'\ \bar{S}$) contributions with increasing timescale. In most models S' becomes larger than $v'\ \bar{S}$ contributions on timescales greater than approximately 5 years. In models, such as BCC-CSM1 and GFDL-ESM2G, the ${F_{ov}}^{34S}$ variability is driven almost entirely by salinity variations, with $\bar{v}\ S'$ dominating on all timescales. In all models and timescales, it is variability of salinity in the top 1200 m that leads to F_{ov}' variability, rather than salinity variability below (not shown).

The F_{ov} variability timeseries and its components between 26°N and 40°N are shown in **Figure 5** [Left]. In contrast to the South Atlantic, the north shows clear dominance of the meridional velocity variations in determining F_{ov} variability, with contributions of salinity anomalies $\bar{v}\ S'$, for all the 10 CMIP5 models remaining small, or very small and comparable to $v'S'$. This is consistent with Cheng et al. (2018), who showed that the decadal F_{ov} variability in the two CMIP5 models they studied was dominated by salinity variations, except in the subtropical North Atlantic (i.e., 20N–40N). The change in R^2 coefficient with timescale, for the north Atlantic is shown in **Figure 5** [Right], demonstrating the dominance of $v'\ \bar{S}$, i.e., the local circulation changes, in controlling F_{ov} variability on all timescales.

ATLANTIC FRESHWATER CONTENT

In this section we look at the impact of ${F_{ov}}^{34S}$ transport contributions to the freshwater budget integrated throughout the Atlantic basin, and any influence on the meridional FWC gradient variations that might feedback onto the AMOC. To

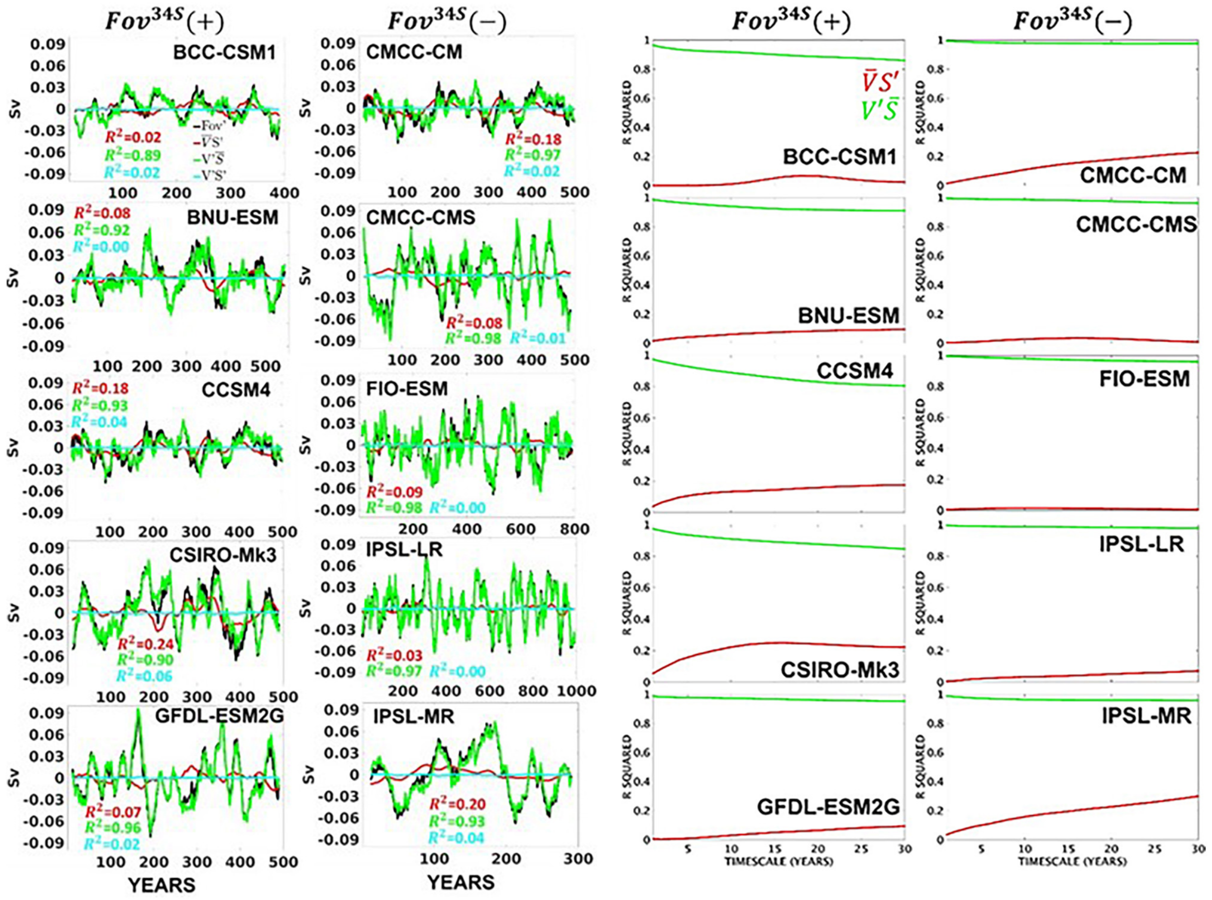

FIGURE 5 | (Left): As in **Figure 4** but for F_{ov}' averaged between 26°N and 40°N. The column headings are only used to classify the models into the two groups.

investigate this we follow the freshwater budget approach developed previously by Deshayes et al. (2014) for the North Atlantic subpolar gyre. **Table 2** shows the freshwater budget components between 34°S and 40°N, along with their variability on decadal timescales. This was only done for the 6 models denoted with * in **Table 1**, which provide the surface freshwater fluxes on their ocean grids. Note that the transports do not include lateral diffusion terms (Redi, 1982) or the effects of Gent and McWilliams (1990) parameterizations. Even so the budget residuals and their variability remain small, showing that the causes of freshwater changes can be well attributed in all of these models.

To first order, the budgets show that the net evaporation over 34°S–40°N is balanced by a convergence of the FWT transports by resolved advection in all models. The residual term, accounting for parameterised eddy fluxes or the way the salinity reference, $\hat{S}$, is defined, only amounts to 5–15% of the E-P-R, while FWC change terms are negligible on these timescales. The models with positive ${F_{ov}}^{34S}$ and stronger AMOCs (**Table 1**), such as CSIRO-Mk3 and GFDL-ESM2G, also have larger mean total freshwater transports at 34°S, and larger E-P-R compared to most of the models with negative ${F_{ov}}^{34S}$. This supports Mecking et al. (2017) suggestion that models with stronger AMOCs lead to more evaporation in the North Atlantic, along with more freshwater import in the south.

Decadal variability of the freshwater convergence, however, is dominated by northern boundary transports in almost all models, and it can also be seen from the amplitude of their

TABLE 2 | Decadal freshwater budget components (mSv) and their decadal standard deviations between 34°S and 40°N.

Model	FWT 34°S (mSv)	FWT 40°N (mSv)	FWT conv. (mSv)	E-P-R (mSv)	FWC changes (mSv)	Residual (mSv)
CMCC-CM	263 ± 19	442 ± 38	705 ± 43	817 ± 39	−5 ± 39	107 ± 8
CMCC-CMS	194 ± 29	477 ± 32	671 ± 39	760 ± 44	−1 ± 35	88 ± 9
IPSL-LR	273 ± 22	489 ± 39	762 ± 44	853 ± 28	0 ± 38	91 ± 11
IPSL-MR	361 ± 23	519 ± 30	880 ± 32	996 ± 40	−3 ± 31	113 ± 6
CSIRO-Mk3	480 ± 19	441 ± 38	921 ± 45	1012 ± 29	−9 ± 41	82 ± 8
GFDL-ESM2G	373 ± 32	518 ± 47	891 ± 58	957 ± 40	0 ± 52	64 ± 13

The second and third columns represent the total freshwater transport at 34°S and 40°N, respectively, whereas the fourth column corresponds to the freshwater transport convergence into this region. CMIP5 models above and below the thick solid line have negative and positive ${F_{ov}}^{34S}$*, respectively. The transport signs are positive when the flux is into the budget domain.*

decadal variability in relation to the total variability, that the southern and northern freshwater transport variations appear to be uncorrelated. There is no indication that freshwater anomalies crossing the southern boundary are connected to transports into the high latitude North Atlantic where they would be needed to affect the AMOC.

Figure 6 evaluates these FWC budget components between 34°S and 40°N on a range of timescales using the normalised covariance of each budget term with the FWC changes (Eq. 8). The total freshwater transports are also decomposed into F_{ov} and F_{gyre} for a more detailed investigation of the budget contributions. The most important driver of 34°S–40°N FWC changes varies between E-P-R and the northern F_{ov}, depending on the model and timescale. There is generally a larger contribution of the advective fluxes, particularly the northern F_{ov}, with increasing timescale. In CMCC-CM, CMCC-CMS and IPSL-MR, the contribution of the southern F_{gyre} also increases with timescale, becoming the largest advective flux on multidecadal timescales.

The ${F_{ov}}^{34S}$ explains less than 12% to FWC budget in all models, regardless of timescale, and it provides the smallest contribution to the freshwater budget variations, apart from the residual term. This strongly suggests that any influence it might have on variability in North Atlantic water formation would be very minimal. In contrast to the northern boundary transports, the southern F_{gyre} is always equal to, or more important than, ${F_{ov}}^{34S}$ in **Figure 6**, reinforcing the key role played by the southern F_{gyre} in contributing to South Atlantic freshwater budgets (e.g.,

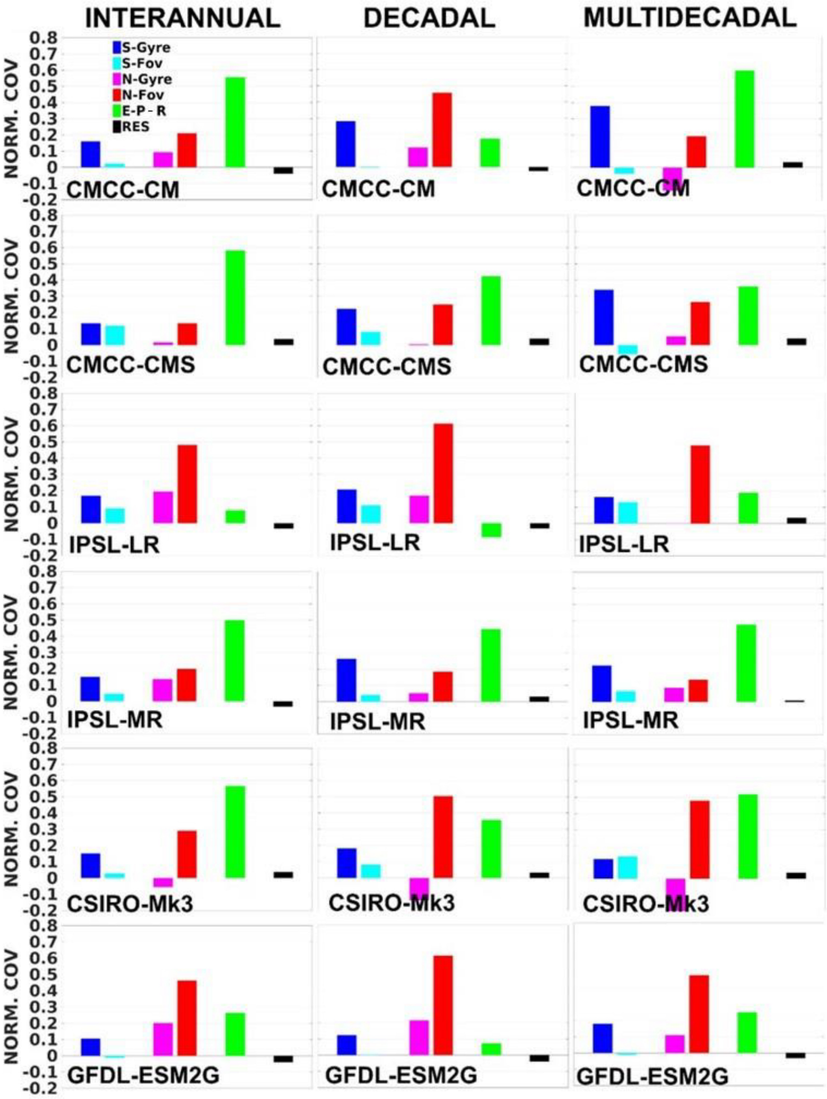

FIGURE 6 | The covariance of each budget term with FWC changes normalised by the variance of FWC changes (Eq. 8, considering the region between 34°S and 40°N). The sum of all normalised covariances, including from the residual term, equals 1. The normalised covariances are evaluated on interannual, decadal, and multidecadal timescales. The prefixes "S-" and "N-" denote southern and northern transports, respectively.

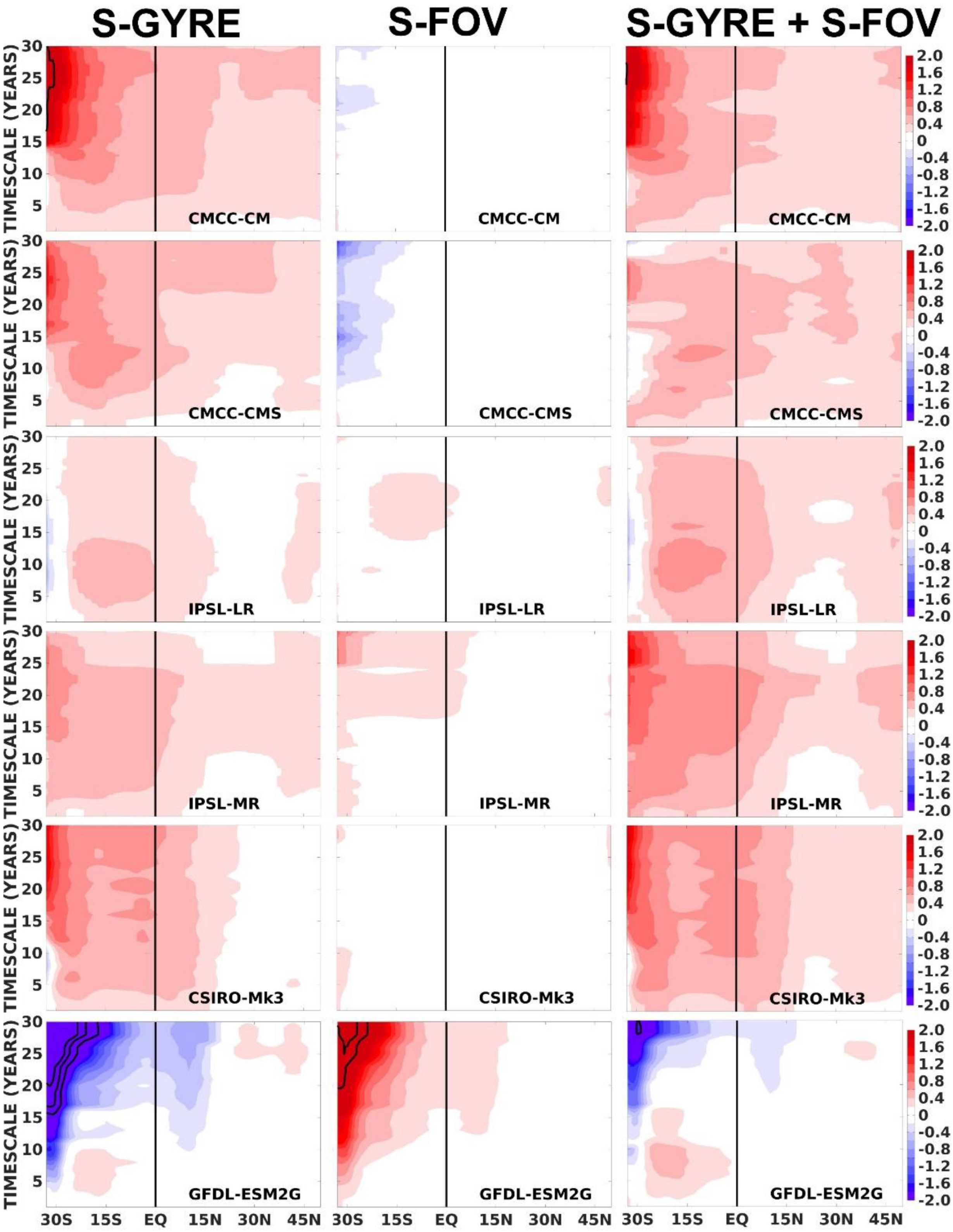

FIGURE 7 | Normalised covariances of the southern F_{gyre}, F_{ov}, and total transports with FWC changes, as in Eq. 8, considering a fixed southern boundary at 34°S and a moving northern boundary from 33°S to 50°N. The spatially varying normalised covariances are evaluated from interannual to multidecadal timescales. The black contours correspond to either negative or positive normalised covariance values of >3.

De Vries and Weber, 2005; Sijp, 2012; Ferreira et al., 2018). At higher resolutions additional FWC variability may come from Agulhas leakage (Biastoch et al., 2008).

In **Figure 7** we can see how far into the Atlantic basin the 34°S freshwater transports F_{ov} and F_{gyre} can influence the FWC on different timescales, using the normalised covariances of each budget term in Eq. 8, where the latitude determines the northern boundary of the FWC budgets down to 34°S. The contribution of $F_{ov}{}^{34S}$ in driving FWC changes decreases rapidly as the region considered extends northward. Its contribution is always restricted to south of the equator, and is systematically smaller than $F_{gyre}{}^{34S}$ in all models. In contrast, the influence

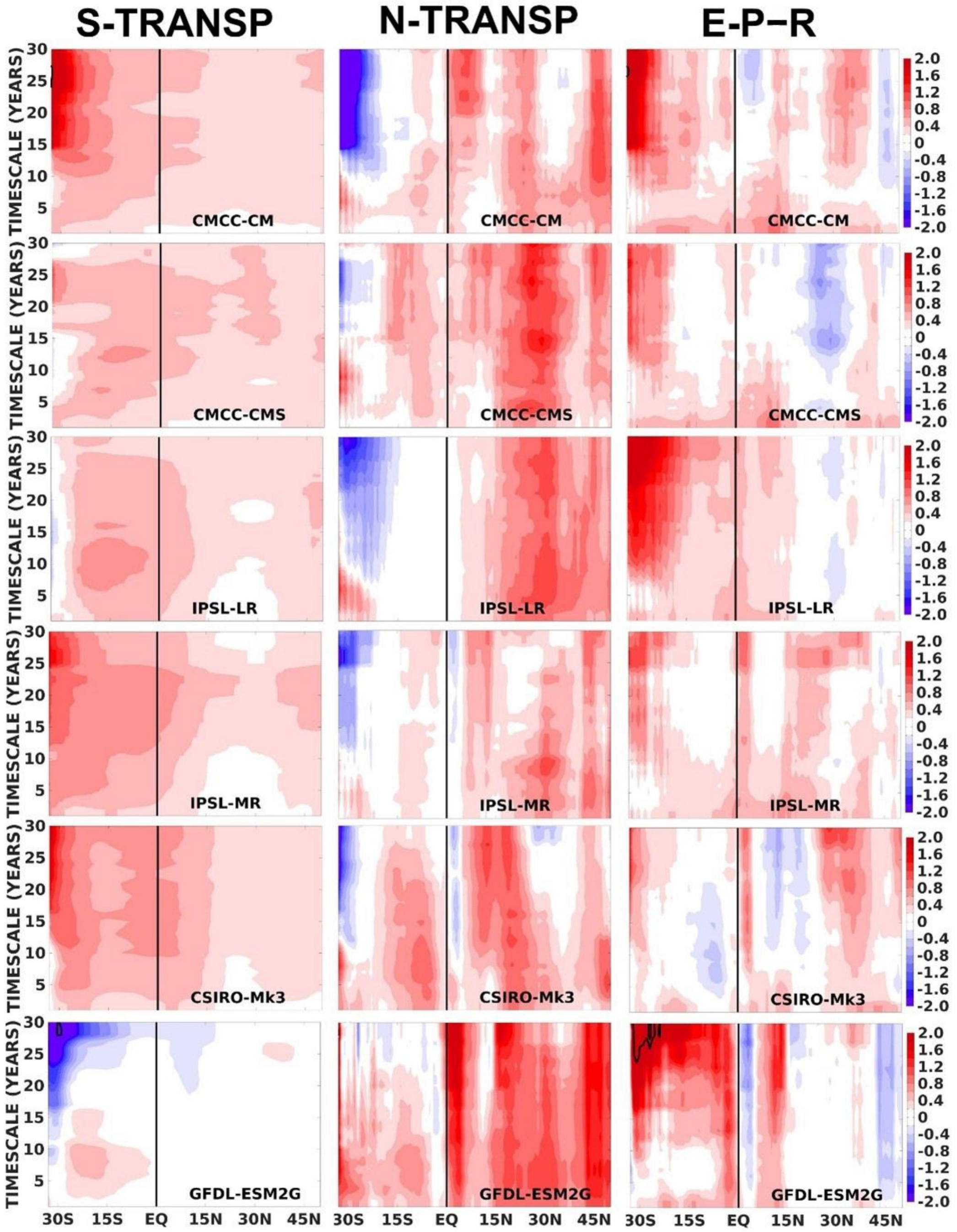

FIGURE 8 | Normalised covariances of the total southern transports, total northern transports and E-P-R with FWC changes as in Eq. 8, considering a fixed southern boundary at 34°S and a moving northern boundary from 33°S to 50°N. The spatially varying normalised covariances are evaluated from interannual to multidecadal timescales. The black contours correspond to either negative or positive normalised co-variance values >3.

of $F_{gyre}{}^{34S}$ extends across the equator in CMCC-CM, CMCC-CMS and IPSL-MR, particularly on longer timescales. In fact, the budget contributions from the total transports at 34°S are always dominated by F_{gyre} rather than F_{ov}, even for GFDL-ESM2G, which shows a strong compensation of the contributions from $F_{gyre}{}^{34S}$ and $F_{ov}{}^{34S}$ through the southern Atlantic. $F_{gyre}{}^{34S}$ usually drives FWC changes (i.e., positive covariances) in all models, except for GFDL-ESM2G where $F_{gyre}{}^{34S}$ acts to dampen FWC changes (i.e., negative covariances). When the domain is limited to the southern hemisphere, F_{ov} coming from the north show negative covariances with FWC, i.e., tending to dampen variability in FWC content south of ∼15°S (**Supplementary Figure A**).

Figure 8 shows the total advective fluxes at both the southern and northern boundaries, along with E-P-R. The latitude defines the moving northern boundary representing the budget terms for the region down to 34°S. The budget residuals are not shown since they always represent <20% of the total FWC changes for all regions and timescales. E-P-R is a strong driver of FWC change (positive covariances) especially in the southern hemisphere where it is often larger than the total (overturning + gyre) transports across 34°S. Transports across the northern boundary are usually dampening the FWC variability in the southern hemisphere, especially south of 15°S. When the domain of the budget extends well into the northern hemisphere, the role of surface fluxes reverses and weakens. The dominant driver of FWC changes becomes the transport across the northern boundary, which is dominated by F_{ov} (not shown), and the surface fluxes are then usually acting to dampen these northern transport driven FWC changes. The southern boundary transports have very weak impact on FWC changes once the budget box extends across the Equator.

Although there are common patterns in the budgets, such as the clear dominance of $F_{gyre}{}^{34S}$ over $F_{ov}{}^{34S}$ in contributing to FWC changes in the South Atlantic, it is evident that the budgets do greatly vary among these CMIP5 models. Considering only the budget domain between 34°S and 40°N (**Figure 6**), some models have E-P-R as the main driver of FWC changes, whereas other models have the advective fluxes, particularly the northern F_{ov}, as the main driver. The models also show very different dominant timescales contributing to FWC variations. In the southern hemisphere, the main outlier is GFDL-ESM2G which has the role of the northern and southern boundaries reversed compared to the other models (**Figure 8**). However, for larger budget boxes (extending across the equator), the GFDL model shows similar behaviour to other models. Similar CMIP5 variations were also found by Deshayes et al. (2014) in the North Atlantic subpolar freshwater budgets, where the roles of surface fluxes and advection in governing FWC changes were also seen to be model-dependent.

DISCUSSION AND CONCLUSION

The salt-advection feedback is characterised by a feedback loop between the AMOC, the meridional advection of salt, and the meridional density gradient, which was proposed to be triggered by changes in the southern Atlantic. This basin-scale feedback has its origin in simple box models. Here, we have evaluated the internal variability in 10 pre-industrial CMIP5 simulations (**Table 1**) in an attempt to detect signatures of the salt-advection feedback mechanisms on different timescales.

From these 10 centennial-timescale simulations, two groups of five models are defined, with opposite signs of mean $F_{ov}{}^{34S}$. Supporting previous results of Jackson (2013) and Mecking et al. (2017), the $F_{ov}{}^{34S}$ sign depends on the CMIP5 salinity biases and how they project onto the upper and lower AMOC branches (i.e., ΔS_{1200m}) at 34°S (although these same biases are consistent in all models throughout the South Atlantic). Models with positive $F_{ov}{}^{34S}$ have a very shallow AAIW layer, showing too fresh waters near the surface and too saline waters at depth in the South Atlantic (i.e., $\Delta S_{1200m} < 0$). Conversely, models with negative $F_{ov}{}^{34S}$ are closer to observations but still tend to show the opposite bias structure, being too saline mainly in the lower thermocline, 500–1200 m, and too fresh at deeper levels (i.e., $\Delta S_{1200m} > 0$). In addition to the sign of F_{ov}, ΔS_{1200m} also controls its magnitude, explaining 90% of the inter-model spread in $F_{ov}{}^{34S}$. This reinforces the findings of Mignac et al. (2019) that F_{ov} strength is primarily determined by the salinity contrasts between the upper and lower branches of the AMOC, rather than by the AMOC strength itself, throughout the South Atlantic.

The dominance of the salinity in determining the southern F_{ov} also extends to the time variability, particularly on 5-year and longer timescales. For instance, in 7 out of 10 CMIP5 models, decadal F_{ov} anomalies between 34°S and 20°S are determined by local salinity variations, rather than local circulation changes. In the northern subtropics (i.e., 26°N–40°N), however, it is the meridional velocity which clearly dominates F_{ov} variability in all models and on all timescales. This evidence, built upon the variability of multiple climate models, is then not consistent with the box-model assumption that southern F_{ov} fluctuations are primarily dominated by circulation rather than salinity changes, at least on 5-year and longer timescales.

The AMOC salt-advection feedback also relies on F_{ov} being able to alter the N-S FWC differences on some timescale, which can then drive AMOC changes (Rahmstorf, 1996). However, FWC variability, and therefore meridional N-S FWC differences, are always dominated by FWC changes in the northern hemisphere rather than in the southern ocean in all CMIP5 models. This is shown by the role of the North Atlantic in governing the long-term variability of the north-south density gradients (Danabasoglu, 2008; de Boer et al., 2010; Cheng et al., 2018). This therefore implies that $F_{ov}{}^{34S}$ would have to influence the FWC well into the northern hemisphere before AMOC feedbacks could occur.

We then show that the FWC budget in 6 of the models can be closed within ∼10%, neglecting GM advection and lateral diffusion terms which are not available, and that the $F_{ov}{}^{34S}$ contribution to driving FWC changes on all timescales is restricted to the South Atlantic, and even then is always smaller than the influence of $F_{gyre}{}^{34S}$. We also find that the surface fluxes, E-P-R, drive as much variability in the South Atlantic FWC as the total 34°S transports, with freshwater transports from the north tending to oppose FWC changes on longer timescales.

As the domain gets larger to include both the South and North Atlantic, the F_{ov} in the northern hemisphere, along with E-P-R, become the most important contributors to FWC change, although $F_{gyre}{}^{34S}$ may also contribute weakly on 30-year timescales in some models. These general conclusion about the budgets must be seen in the context of large differences across CMIP5 models. As in Deshayes et al. (2014), the roles of surface fluxes and advection in governing basin-wide FWC changes vary greatly depending on the specific CMIP5 model.

All the evidence gathered here from the internal variability of 10 centennial-scale simulations seems to refute any role for the South Atlantic in salt-advection feedbacks effects on AMOC strength. This is the case for all CMIP5 models in **Table 1**, regardless of their mean F_{ov}^{34S} sign, and it strongly suggests that F_{ov}^{34S} is not a useful metric for assessing AMOC stability. Additional targeted numerical experiments, where the system is forced to change more systematically than the natural variability studied in these control runs, may shed more light on other feedbacks and mechanisms controlling the AMOC behaviour.

DATA AVAILABILITY STATEMENT

The CMIP5 data used for this study are all freely available from global repositories, and were originally downloaded from PCMDI (https://pcmdi.llnl.gov/mips/cmip5/).

AUTHOR CONTRIBUTIONS

All technical work and production of figures were performed by DM as part of his Ph.D. thesis. The first draft of this work appears in Mignac (2020). The rewriting of the work into a manuscript was performed by KH and DF. All authors contributed to the article and approved the submitted version.

FUNDING

DM like to acknowledge the financial support of the CAPES Foundation, Brazil (proc. BEX 1386/15—8) in supporting these studies. Supervisors KH and DM also acknowledge the support of NCEO strategic grant in developing this work.

ACKNOWLEDGMENTS

This work was performed as part of the Ph.D. research of DM.

SUPPLEMENTARY MATERIAL

The Supplementary Material for this article can be found online at: https://www.frontiersin.org/articles/10.3389/fmars.2022.830821/full#supplementary-material

REFERENCES

Biastoch, A., Böning, C., and Lutjeharms, J. (2008). Agulhas leakage dynamics affects decadal variability in Atlantic overturning circulation. *Nature* 456, 489–492. doi: 10.1038/nature07426

Bryden, H. L., and Imawaki, S. (2001). "Ocean heat transport," in *Ocean Circulation and Climate*, eds G. Siedler, J. Church, and J. Gould (London: Academic Press), 455–474.

Cheng, W., Weijer, W., Kim, W. M., Danabasoglu, G., Yeager, S. G., Gent, P. R., et al. (2018). Can the salt-advection feedback be detected in internal variability of the atlantic meridional overturning circulation? *J. Clim.* 31, 6649–6667. doi: 10.1175/JCLI-D-17-0825.1

Danabasoglu, G. (2008). On multidecadal variability of the Atlantic meridional overturning circulation in the community climate system model version 3. *J. Clim.* 21:55245544. doi: 10.1175/2008JCLI2019.1

Danabasoglu, G. S. C. B., Briegleb, B. P., Jayne, S. R., Jochum, M., Large, W. G., Peacock, S., et al. (2012). The CCSM4 ocean component. *J. Clim.* 25, 1361–1389. doi: 10.1175/jcli-d-11-00091.1

de Boer, A. M., Gnanadesikan, A., Edwards, N. R., and Watson, A. J. (2010). Meridional density gradients do not control the Atlantic overturning circulation. *J. Phys. Oceanogr.* 40, 368–380.

De Vries, P., and Weber, S. L. (2005). The Atlantic freshwater budget as a diagnostic for the existence of a stable shut down of the meridional overturning circulation. *Geophys. Res. Lett.* 32:1450. doi: 10.1029/2004GL021450

Deshayes, J., Curry, R., and Msadek, R. (2014). CMIP5 model intercomparison of freshwater budget and circulation in the North Atlantic. *J. Clim.* 27, 3298–3317.

Dijkstra, H. A. (2007). Characterization of the multiple equilibria regime in a global ocean model. *Tellus Dyn. Meteorol. Oceanogr.* 59, 695–705. doi: 10.1111/j.1600-0870.2007.00267.x

Drijfhout, S. S., Weber, S. L., and van der Swaluw, E. (2011). The stability of the MOC as diagnosed from model projections for pre-industrial, present and future climates. *Clim. Dyn.* 37, 1575–1586. doi: 10.1007/s00382-010-0930-z

Dufresne, J.-L., Foujols, M. A., Denvil, S., Caubel, A., Marti, O., Aumont, O., et al. (2013). Climate change projections using the IPSL-CM5 earth system model: from CMIP3 to CMIP5. *Clim. Dyn.* 40, 2123–2165.

Dunne, J., John, J., Shevliakova, E., Ronald, S., Krasting, J., Malyshev, S., et al. (2013). GFDL's ESM2 global coupled climate–carbon earth system models. part II: carbon system formulation and baseline simulation characteristics. *J. Clim.* 26, 2247–2267. doi: 10.1175/JCLI-D-12-00150.1

Ferreira, D., Cessi, P., Coxall, H. K., de Boer, A., Dijkstra, H. A., Drijfhout, S. S., et al. (2018). Atlantic-pacific asymmetry in deep water formation. *Ann. Rev. Earth Plan. Sci.* 46, 327–352.

Garzoli, S. L., Baringer, M. O., Dong, S., Perez, R., and Yao, Q. (2013). South atlantic meridional fluxes. *Deep Sea Res. Part I* 71, 21–32. doi: 10.1038/nature05222

Gent, P. R. (2018). A commentary on the Atlantic meridional overturning circulation stability in climate models. *Ocean Mod.* 122, 57–66. doi: 10.1016/j.ocemod.2017.12.006

Gent, P. R., and McWilliams, J. C. (1990). Isopycnal mixing in ocean circulation models. *J. Phys. Oceanogr.* 20, 150–155. doi: 10.1175/1520-0485(1990)020<0150:imiocm>2.0.co;2

Gordon, H., O'Farrell, S., Collier, M., Dix, M., Rotstayn, L., Kowalczyk, E., et al. (2010). *The CSIRO Mk3.5 Climate Model, CAWCR Technical Report No. 021*. Available online at: www.cawcr.gov.au/technical-reports/CTR_021.pdf (accessed March 15, 2019).

Hawkins, E., Smith, R. S., Allison, L. C., Gregory, J. M., Woolings, T. J., Pohlmann, H., et al. (2011). Bistability of the Atlantic overturning circulation in a global climate model and links to ocean freshwater transport. *Geophys. Res. Lett.* 38:208. doi: 10.1029/2011GL047208

Huisman, S. E., den Toom, M., Dijkstra, H. A., and Drijfhout, S. S. (2010). An indicator of the multiple equilibria regime of the Atlantic meridional overturning circulation. *J. Phys. Oceanogr.* 40, 551–567. doi: 10.1175/2009JPO4215.1

Jackson, L. C. (2013). Shutdown and recovery of the AMOC in a coupled global climate model: the role of the advective feedback. *Geophys. Res. Lett.* 40, 1182–1188.

Ji, D., Wang, L., Feng, J., Wu, Q., Cheng, H., Zhang, Q., et al. (2014). Description and basic evaluation of beijing normal university earth system model (BNU-ESM) version 1. *Geosci. Model Dev.* 7, 2039–2064.

Kim, H.-J., An, S.-I., Kim, S.-K., and Park, J.-H. (2021). Feedback processes modulating the sensitivity of atlantic thermohaline circulation to freshwater forcing timescales. *J. Clim.* 34, 5081–5092. doi: 10.1175/JCLI-D-20-0897.1

Mecking, J. V., Drijfhout, S. S., Jackson, L. C., and Andrews, M. B. (2017). The effect of model bias on Atlantic freshwater transport and implications for AMOC bi-stability. *Tellus* 69, 1–14. doi: 10.1175/jcli-d-20-0614.1

Mecking, J. V., Drijfhout, S. S., Jackson, L. C., and Graham, T. (2016). Stable AMOC off state in an eddy-permitting coupled climate model. *Clim. Dyn.* 47, 2455–2470.

Mignac, D., Ferreira, D., and Haines, K. (2019). Decoupled freshwater transport and meridional overturning in the south Atlantic. *GRL* 46, 2178–2186.

Mignac, D. (2020). *Atlantic Transports From Free Model Runs, Reanalyses and Coupled Simulations, Ph. D, Thesis*. University of Reading.

Qiao, F., Song, Z., Bao, Y., Song, Y., Shu, Q., Huang, C., et al. (2013). Development and evaluation of an earth system model with surface gravity waves. *J. Geophys. Res. Oceans* 118, 4514–4524. doi: 10.1002/jgrc.20327

Rahmstorf, S. (1996). On the freshwater forcing and transport of the Atlantic thermohaline circulation. *Clim. Dyn.* 12, 799–811.

Rahmstorf, S., Crucifix, M., Ganopolski, A., Goosse, H., Kamenkovich, I., Knutti, R., et al. (2005). Thermohaline circulation hysteresis: a model intercomparison. *Geophys. Res. Lett.* 35:L23605.

Redi, M. H. (1982). Oceanic isopycnal mixing by coordinate rotation. *J. Phys. Oceanogr.* 12, 1154–1158.

Sallée, J. B., Shuckburgh, E., Bruneau, N., Meijers, A., Wang, Z., and Bracegirdle, T. (2013). Assessment of southern ocean water mass circulation in CMIP5 models: historical bias and forcing response. *J. Geophys. Res.* 118, 1830–1844.

Scoccimarro, E., Gualdi, S., Bellucci, A., Sanna, A., Fogli, P. G., Manzini, E., et al. (2011). Effects of tropical cyclones on ocean heat transport in a high-resolution coupled general circulation model. *J. Clim.* 24, 4368–4384.

Sijp, W. P. (2012). Characterising meridional overturning bistability using a minimal set of state variables. *Clim. Dyn.* 39, 2127–2142. doi: 10.1007/s00382-011-1249-0

Stommel, H. M. (1961). Thermohaline convection with two stable regimes of flow. *Tellus* 13, 224–230.

Stouffer, R. J., Yin, J., Gregory, J., Dixon, K., Spelman, M., Hurlin, W., et al. (2006). Investigating the causes of the response of the thermohaline circulation to past and future climate changes. *J. Clim.* 19, 1365–1387. doi: 10.1175/JCLI3689.1

Taylor, K. E., Stouffer, R. J., and Meehl, G. A. (2012). An overview of CMIP5 and the experiment design. *BAMS* 485–498.

Xin, X.-G., Tong-Wen, W., and Jie, Z. (2015). Introduction of CMIP5 experiments carried out with the climate system models of beijing climate center. *Adv. Clim. Change Res.* 4, 41–49.

Yin, J., and Stouffer, R. J. (2007). Comparison of the stability of the Atlantic thermohaline circulation in two coupled atmosphere-ocean general circulation models. *J. Clim.* 20, 4293–4315.

Zhu, C., Liu, Z., and Gu, S. (2018). Model bias for South Atlantic Antarctic intermediate water in CMIP5. *Clim. Dyn.* 50, 3613–3624.

Conflict of Interest: The authors declare that the research was conducted in the absence of any commercial or financial relationships that could be construed as a potential conflict of interest.

frontiers | Frontiers in Marine Science

ORIGINAL RESEARCH
published: 14 June 2022
doi: 10.3389/fmars.2022.835260

Characterizing Mesoscale Eddies of Eastern Upwelling Origins in the Atlantic Ocean and Their Role in Offshore Transport

Artemis Ioannou, Sabrina Speich and Remi Laxenaire*

Laboratoire de Météorologie Dynamique LMD-IPSL, Ecole Normale Supérieure, Paris, France

Motivated by the recurrent formation of eddies in the eastern upwelling areas, we examine cross-basin connectivity that is promoted by coherent, long-lived and long-propagating mesoscale eddies in the Atlantic Ocean. By applying the TOEddies detection and tracking algorithm to daily satellite observations (AVISO/DUACS) of Absolute Dynamic Topography (ADT), we characterize mesoscale eddy activity and variability in the North and South Atlantic. This method provides a robust eddy-network reconstruction, enabling the tracking of eddies formed in the Atlantic eastern upwelling systems together with any merging and splitting events they undergo during their lifetime as long as they remain detectable in the altimetry field. We show that during the years of observations, mesoscale eddies are long-lived coherent structures that can ensure oceanic connectivity between the eastern and the western boundaries, as a result of complex inter-eddy interactions. Moreover, alignment of South Atlantic eddies of eastern boundary origins with available Argo floats achieves a mean cross-basin connectivity signal from both anticyclonic and cyc5lonic eddies which is particularly evident at depth, along thermocline isopycnal layers of γ^n = 26 - 27 kg m^{-3}. We explore two individual cyclonic eddy trajectories from *in-situ* measurements gathered by different Argo profiling floats trapped inside the eddy cores. Our results support the hypothesis that mesoscale eddies sustain and transport water masses while subducting during their westward propagation.

Keywords: mesoscale eddies, eastern boundary upwelling systems, oceanic connectivity, cross-basin exchanges, subduction, Agulhas Cyclones

OPEN ACCESS

Edited by:
Regina R. Rodrigues,
Federal University of Santa Catarina,
Brazil

Reviewed by:
Yuntao Wang,
Ministry of Natural Resources, China
Iury T. Simoes-Sousa,
University of Massachusetts
Dartmouth, United States

****Correspondence:***
Artemis Ioannou
innartemis@gmail.com

Specialty section:
This article was submitted to
Physical Oceanography,
a section of the journal
Frontiers in Marine Science

Received: *14 December 2021*
Accepted: *16 May 2022*
Published: *14 June 2022*

Citation:
Ioannou A, Speich S and Laxenaire R
(2022) Characterizing Mesoscale
Eddies of Eastern Upwelling Origins
in the Atlantic Ocean and Their
Role in Offshore Transport.
Front. Mar. Sci. 9:835260.
doi: 10.3389/fmars.2022.835260

1 INTRODUCTION

Eastern boundary upwelling systems (EBUS) are dynamically complex circulation systems characterized by enhanced mesoscale activity (Correa-Ramirez et al., 2007; McGillicuddy et al., 2007; Stramma et al., 2013; Amos et al., 2019). In the Atlantic Ocean, the Canary Current upwelling system (CCUS) and the Benguela Current upwelling system (BCUS) are among the major EBUS of the world ocean. These areas support highly productive marine ecosystems and sustain significant fisheries (Hutchings et al., 2009; Harvey et al., 2020). Their particular dynamics, influenced by the combined effect of strong Ekman transport of surface waters and upwelled waters along the coast, give rise to various flow instabilities including the formation of mesoscale eddies (Chaigneau et al., 2009; Chelton et al., 2011; Pegliasco et al., 2015).

Eddies in the CCUS and BCUS are *a priori* expected to be generated by instabilities of the upwelling current fronts (Marchesiello et al., 2003; Marchesiello and Estrade, 2007; Moscoso et al., 2021). Wang et al. (2015, 2021) showed a strong correlation between frontal activity (estimated from Sea Surface Temperature fields) and the variability of alongshore winds. Nevertheless, both upwelling systems have their own specificities and it is difficult to separate the physical mechanisms that are involved in eddy generation. As far as CCUS is concerned, the presence of islands near its upwelling shelf (Canary Islands in the north and Cape Verde in the south) contributes to eddy generation through island-induced mechanisms (Sangrà et al., 2005; Caldeira et al., 2014; Stegner, 2014; Ioannou et al., 2020a; Ioannou et al., 2020b) while downstream of the Gran Canaria, the shedding of both cyclonic and anticyclonic eddies is observed (Arístegui et al., 1994; Arístegui et al., 1997; Basterretxea et al., 2002; Barton et al., 2004; Arístegui and Montero, 2005; Sangrà et al., 2005; Sangrà et al., 2007). On the other hand, high eddy occurrences are found near the African coast (Schütte et al., 2016a) where various instabilities and coastal processes are involved in eddy generation (Dilmahamod et al., 2021). Continuous interactions between island-induced eddies and eddies or filaments from the upwelling have also been reported to entrain nutrient-rich waters further offshore (Arístegui et al., 1994; Arístegui et al., 1997; Basterretxea et al., 2002; Arístegui and Montero, 2005; Sangrà et al., 2005; Sangrà et al., 2007). On the basis of 14 years of satellite observations (1992-2006), Sangrà et al. (2009) have furthermore noted the westward propagation of long-lived eddies from the upwelling. Distinct eddy corridors along which organic matter could be exported into the oligotrophic subtropical gyre in the North Atlantic were documented.

Meanwhile, in the South Atlantic, the BCUS upwelling regime, especially its southern part, is intrinsically bounded to the Agulhas Leakage (Doglioli et al., 2007; Blanke et al., 2009; Veitch and Penven, 2017) that together with the regional circulation, also shapes particularly energetic and dynamically complex local dynamics. The intrusion of warm salty Indian water *via* the spawning of Agulhas Rings from the Agulhas Current retroflection (Arhan et al., 1999; Matano and Beier, 2003; Giulivi and Gordon, 2006; Guerra et al., 2018; Laxenaire et al., 2018; Laxenaire et al., 2019; Laxenaire et al., 2020), along with the BCUS dynamics as well as the complex bathymetry in the Cape Basin (Matano and Beier, 2003), causes strong interactions between cyclonic and anticyclonic eddies (Boebel et al., 2003; Richardson and Garzoli, 2003; Giulivi and Gordon, 2006; Souza et al., 2011). Numerous eddies with high cyclonic versus anticyclonic ratios are observed, (3:2 in favor of cyclones (Boebel et al., 2003)), while various exchanges and water-mass modification processes take place (Rusciano et al., 2012). Indeed, satellite imagery has revealed the strong influence of the Agulhas Rings in the Cape Basin that may also entrain and export cold upwelling waters along their pathway beyond the upwelling shelf (Duncombe Rae et al., 1992). Yet there are only a few studies (Giulivi and Gordon, 2006; Arhan et al., 2011; Souza et al., 2011) that emphasize on the role of cyclonic eddies from the upwelling and their dynamical characteristics. During a recent hydrographic transect along 34.5°S, an Agulhas cyclone originated from an instability along the Benguela upwelling system has been observed near the Southern Africa shelf (Manta et al., 2021). Vessel Mounted Acoustic Doppler Profiler (VM-ADCP) measurements revealed intense velocities for the cyclone that reached 80 cm/s at 100 dbar. Strong temperature anomalies extended between 100 - 700 dbar.

Generally however until now, with the sole exception of the multi-year observations reported in Sangrà et al. (2009), the characterization of eddies with upwelled origins has been surveyed only occasionally and open questions are still raised on how far such eddies may travel in the Atlantic Ocean. Unlike waves, coherent eddies, characterized by rotational speeds greater than their translating motion (Flierl, 1981; Chelton et al., 2011; Polito and Sato, 2015), can trap water masses in their cores for long periods and remain physically isolated from outside perturbations while propagating. Sparse yet significant observations made *via* Argo floats that stayed trapped inside eddies for significant time periods (Ioannou et al., 2017; Guerra et al., 2018; Laxenaire et al., 2018; Laxenaire et al., 2019; Nencioli et al., 2018) confirm the existence of such long-lived and long-propagating eddies.

Combined hydrographic observations in the CCUS (Basterretxea et al., 2002; Brandt et al., 2015; Schütte et al., 2016a; Schütte et al., 2016b; Karstensen et al., 2017) have pointed out that upwelled eddies may substantially contribute to the global offshore transport of properties. Given that eddies inhibit lateral exchanges with the outside environment, they may be responsible for the gradual development of anoxic environments within their cores (Brandt et al., 2015; Schütte et al., 2016b; Karstensen et al., 2017). Eddy-resolving numerical models (Gruber et al., 2011; Nagai et al., 2015) have shown that such eddies can act as the main exporters of nutrients and biological components out of coastal areas. Subduction of upwelling filaments is also suggested as a possible mechanism contributing to the offshore transport of upwelled waters affecting biological productivity by moving phytoplankton and nutrients in or out the euphotic zone. In other upwelling systems, their contribution to the offshore transport of nutrient- and carbon-rich coastal waters has also been highlighted (Amos et al., 2019). In the global ocean, increased chlorophyll concentrations have been continuously reported within eddies (McGillicuddy et al., 2007; Lehahn et al., 2011; Villar et al., 2015; Dufois et al., 2016; Cornec et al., 2021a; Cornec et al., 2021b). Mesoscale eddies may thus significantly alter the distribution of properties along their propagation. Further characterization and quantification of eddies shed from upwelling areas is therefore crucial in order to deepen our understanding of cross-shore export of properties, the dynamical processes shaping local marine ecosystems and marine connectivity.

Satellite altimetry remains a powerful tool for characterizing the ocean mesoscale. Despite its various limitations and uncertainty (Amores et al., 2018; Laxenaire et al., 2018; Stegner et al., 2021), the development of automatic eddy detection algorithms has made the characterization of eddies from satellite altimetry an easier task, allowing them to be quantified and their temporal variability followed over long time periods. Automatic detection and tracking algorithms can thus identify eddies *via* their imprints on sea surface height, locate their centers and quantify their main horizontal dynamical parameters such as size, intensity, surface geostrophic velocity, drifting speed, etc. Recent techniques (Li et al., 2014; Le Vu et al., 2018; Laxenaire et al., 2018; Cui et al., 2019) now also provide methods to identify merging and splitting events. In this study, we use the TOEddies Global Atlas to detect and follow eddies in the Atlantic Ocean, building on the approach taken by Laxenaire et al. (2018) to investigate the Agulhas Rings in particular. The TOEddies Atlas not only provides information on eddy dynamical characteristics together with their merging and splitting events, but also reconstructs a complex eddy network, linking eddy trajectories associated with the merging with other eddies or the splitting into two or more eddies. TOEddies is among the few algorithms that has been qualified against an independent dataset, with eddies derived from surface drifter trajectories and dubbed as "loopers" (Lumpkin, 2016). Moreover, in recent years TOEddies has successfully aided the positioning and tracking of eddies in near-real time during several oceanographic cruises (Manta et al., 2021; Stevens et al., 2021). The TOEddies Atlas furthermore incorporates available colocalized vertical information from Argo floats with its eddy detection (Laxenaire et al., 2018; Laxenaire et al., 2020). This combination of satellite altimetry with autonomous measurements has been proven especially useful for analyzing the vertical properties of eddies (Chaigneau et al., 2011; Pegliasco et al., 2015; de Marez et al., 2019; Laxenaire et al., 2019; Laxenaire et al., 2020)

Indeed, vertical information on eddies offers to shed valuable light on their structure and behavior. For example, Pegliasco et al. (2015), through comparisons of the surface and subsurface characteristics of long-lived eddies originating from four of the major EBUS in the global ocean, found a high percentage of anticyclonic and cyclonic eddies to be subsurface-intensified. Surface-intensified eddies that experience summer restratification can potentially separate from the surface, becoming subsurface-intensified eddies and retaining a homogeneous water layer in their core. Such "mode-water"eddies, as they are called in the scientific literature, have been surveyed in the Canary upwelling system (Schütte et al., 2016a; Schütte et al., 2016b; Karstensen et al., 2017; Dilmahamod et al., 2021) and in the Cape Basin (Laxenaire et al., 2019; Laxenaire et al., 2020). Karstensen et al. (2017) surveyed an anticyclonic mode water eddy reporting low oxygen in its eddy core that originated from the Mauritanian upwelling region. Barceló-Llull et al. (2017) also discussed a subtropical intrathermocline four-months-old anticyclonic eddy in the Canary eddy corridor in 2014. In the south Atlantic, Laxenaire et al. (2019, 2020) found that Agulhas Rings subside gradually in deeper ocean layers, transforming in subsurface-intensified eddies along their westward propagation. This transition is associated with an important decrease in their surface imprint on altimetry maps and other properties such as sea surface temperature and salinity. Even if the surface signal of such eddies attenuate over time, the reconstructed eddy vertical structure shows no significant changes. The intense heat loss that these eddies experience at the Agulhas Current retroflection and during their displacement in the southern Cape Basin area can lead to significant cooling and increased density of the rings' upper 400-600 m layers (Arhan et al., 2011). As a result, a subsidence transition from surface to subsurface eddies occurs while drifting westward and encountering the warmer South Atlantic subtropical gyre waters (Laxenaire et al., 2019; Laxenaire et al., 2020). This transition to subsurface introduces a new challenge when identifying mesoscale eddies from satellite observations as the altimetric signal can capture as well as surface-intensified eddies and subsurface-intensified ones (Assassi et al., 2016; Dilmahamod et al., 2018; Laxenaire et al., 2020). Also, when the eddy signal disappears from altimetry maps, this is very likely not due to the eddy's dissipation but to its increased penetration at depth.

In this paper, we examine the contribution of mesoscale eddies with origins in the EBUS to the offshore export, transport and distribution of properties in the Atlantic Ocean. Our approach consists in characterizing the horizontal and vertical extent of mesoscale eddies with a combination of satellite altimetry and Argo floats measurements using the TOEddies Atlas (Laxenaire et al., 2018; Laxenaire et al., 2020). We focus on the two major eastern boundary upwelling systems of the Atlantic Ocean, namely the Benguela Current upwelling system (BCUS) and the Canary Current upwelling system (CCUS), that are characterized by enhanced mesoscale activity. We thus explore the oceanic connectivity that is potentially promoted by coherent, long-lived and long-propagating mesoscale eddies across basins.

The paper is organized as follows: in section 2 we describe the various datasets that we used, with an overview of the TOEddies Dynamical Atlas and the available Argo float measurements. Section 3, presents the dynamical characteristics of eddies in the Atlantic Ocean and in the upwelling systems considered in this study. We then discuss the mean horizontal and vertical structure of oceanic connectivity that is achieved by mesoscale eddies of eastern upwelling origins. We also present two cyclonic eddies that were sampled by a high number of vertical profiles over a one-year period along their dynamical evolution in the South Atlantic. Finally our results are summarized in section 4.

2 DATA AND METHODS

2.1 TOEddies Global Dataset and Argo Profiles Co-Location

To characterize mesoscale eddies, we used the TOEddies Global Atlas dataset (Laxenaire et al., 2018) that provides daily eddy detection and tracking from satellite observations of Sea Surface Height (SSH), over a 24-year period from 1993 to 2018. The TOEddies Global Atlas is applied on fields of Absolute Dynamic Topography (ADT) that are projected on a $\frac{1}{4}°$ ($dX\simeq 25\ km$) all-sat-merged dataset and distributed by AVISO/DUACS.

Firstly, eddies are identified by TOEddies as points of extreme ADT. ADT fields are chosen over Sea Level Anomaly (SLA) fields even though the latter have been widely used (Chelton et al., 2011; Cui et al., 2019; Tian et al., 2019), since SLA fields represent a deviation of SSH from a temporal SSH mean and potentially lead to misinterpretations of the eddy signals (Pegliasco et al., 2020). Next, closed contours of SSH that exceed an eddy amplitude threshold, delimit the eddy outer boundary. Once the eddy outer boundary is identified, the SSH contour of maximum azimuthal speed V_{max} is also detected. The latter delimits the eddy dynamical core that physically remains uninterrupted by lateral exchanges with the environment. The outer $\langle R_{out} \rangle$ and characteristic radius $\langle R_{max} \rangle$ of an eddy can be then estimated. The mean radii will correspond to the same area as that of a circular disc would have when enclosed by the characteristic and the outer contour respectively. In this study, we mainly use R_{max} and V_{max} to quantify the eddy size and the intensity respectively.

To follow eddies over time, TOEddies requires eddy areas to overlap between successive time steps. This overlapping criterion is additionally combined with a cost-function that takes into account dynamical characteristics such as the eddy size, intensity and distance (Laxenaire et al., 2018; Le Vu et al., 2018) in order to reconstruct the eddy trajectories when eddies split or merge. This technique allows the identification of unique segments of eddies rather than eddy occurrences. Eddies that interact with each other, either by a merging or a splitting event, are assigned orders of interactions and can be tracked in the AVISO time-series. In this way, the TOEddies algorithm reconstructs a complex eddy network and enables the tracking of eddies of specific origins (Laxenaire et al., 2018). The accurate detection of merging and splitting events is necessary as successive eddy-eddy interactions can alter the main eddy pathways and impact the reconstruction of eddy trajectories (Du et al., 2014; Li et al., 2014; Le Vu et al., 2018; Cui et al., 2019).

Moreover, TOEddies combines its derived daily eddy detection with vertical information on temperature and salinity from autonomous Argo floats measurements over the period 2000-2017. For this study, we restricted our analysis to the Atlantic Ocean (80°W-30°E and 60°S-60°N) and around ~ 25% of the total colocalisation dataset corresponding to 276,259 individual Argo profiles of temperature and salinity collected by 3,024 different floats. The spatial distribution of available profiles in the North and South Atlantic is shown in **Figure S1**. For each profile, temperature and salinity were converted to potential temperature and absolute salinity using TEOS-10 (McDougall and Barker, 2011). Potential density σ_θ and neutral density γ^n profiles were also estimated. To reconstruct the hydrography of the "no-eddy" environment around a given position and a given date, Argo profiles were separated in two groups: those detected inside mesoscale eddies by TOEddies, or outside of them (outside the last eddy contour). The latter were considered to sample the environment and are used to construct climatological profiles of T, S and σ in the given area. Thus, the "no-eddy" climatology consists of all profiles located outside of eddies at a radial distance ≤1° around the selected position and during a ±30 day period from the given date (regardless of the year) over the 17 years.

We further limited our selection of Argo floats that were located inside eddies from the different eddy network reconstructions that are considered in this study (see subsection 3.3). To analyze mean vertical properties of the eddy networks, we grouped profiles in 1° × 1° bins. For each bin and at each depth level, we computed the mean characteristics of temperature and salinity as well as their corresponding anomalies with respect to the climatology. Mean properties were also analyzed at different sigma levels by interpolating all properties to constant density layer intervals ($\Delta\sigma_\theta = 0.01$ kg m^{-3}).

2.2 Sea Surface Temperature and Atmospheric Data

We used the ERA-Interim data-set to compute the seasonal and interannual variations of wind forcing and sea surface temperature for the upwelling areas. This reanalysis provided the atmospheric fields at $\frac{1}{4}°$ spatial resolution and temporal resolution of 1 h. Sea surface wind components at 10 m and sea surface temperature were obtained from the ERA-Interim synoptic fields from 1993 to 2018 (Hersbach et al., 2018). Wind stress components and the wind stress curl were calculated with the standard bulk formula $[\underline{\tau} = \rho_{air} C_D V_{wind} \underline{V_{wind}} (Nm^{-2})] =$ with ρ_{air} = 1.25 kg m^{-3} and a constant C_d coefficient (C_d = 1.6 10^{-3}). We considered four different upwelling subsystems, separating the CCUS and BCUS into two sub-systems in the North (nCCUS and nBCUS) and the South (sCCUS and sBCUS) as discussed further in section 3.2 (**Figure 6**). We built the monthly mean estimates of wind forcing and sea surface temperature for the different subsystems and compared their temporal variability.

3 CHARACTERIZATION OF MESOSCALE EDDIES IN THE ATLANTIC OCEAN

3.1 Mesoscale Activity in the Atlantic Ocean

The TOEddies dynamical dataset detects and tracks more than 14,169,103 eddies (with lifetimes of at least 7 days) and 408,202 eddy trajectories in the Atlantic Ocean.

To characterize mesoscale eddy activity, we present in **Figure 1**, separately for cyclones and anticyclones, histograms of eddy lifetimes, characteristic radii and velocities. Histograms of eddy dynamical characteristics are shown separately for the North and South Atlantic. In these diagrams we have filtered out mesoscale eddies with radius smaller than ≤ 18 km, in order to avoid small-scale features that are not accurately captured by altimetry. We find an almost equal percentage of cyclonic and anticyclonic eddies with lifetimes exceeding 16 weeks even if cyclones are slightly higher in number than anticyclones (cyclonic eddies represent 51.7% of the total for the North and 53.1% for the South Atlantic). Around 57% of the tracked eddies were detected in the North Atlantic. In total, eddies with lifetimes less than 4 and 16 weeks respectively represent almost 75% and 95% percentile of the eddy lifetime distribution as provided by satellite altimetry maps (**Figures S2, S9**) On average, we detected cyclonic eddies with lifetimes more than 16 weeks to have slight smaller radii (by 3%) than anticyclones in both hemispheres, while their characteristic velocities exceeded that of the anticyclones, mostly in the North Atlantic, by 14%.

Figure 2 shows trajectories of mesoscale eddies in the Atlantic ocean as tracked by TOEddies. Eastward versus westward trajectories were identified by estimating their net displacement between their first and last position. Eastward propagating eddies with lifetimes ≥16 weeks accounted for only 17.5% of the total trajectories and they corresponded mainly to eddies tracked in the Antarctic Circumpolar Current (ACC) and in the subpolar North Atlantic (north of 40°N) (**Figure 1**). In line with previous studies (Chelton et al., 2011), the majority of long-lived eddies in the North and South Atlantic were found to propagate westward influenced by the β-effect (**Figure 2** shows westward eddies with lifetimes ≥52 weeks). The total number of westward-propagating eddies in the North Atlantic was higher than the ones of the South Atlantic (representing 59% of the total westward trajectories).

Eddy trajectories were also sorted on the basis of their estimated lifetimes in **Figure 3**. The ratio of cyclone versus anticyclone lifetimes was similar only for eddies with lifetimes of less than 52 weeks (**Figure 1** and **Figures S2B, C**). In agreement with previous findings (Chelton et al., 2011; Tian et al., 2019), eddies with longer lifetimes (≥52 weeks, approximately 1.5 years) were mostly anticyclonic (**Figures S2**). In the South Atlantic, around 60% of eddy trajectories were indeed anticyclonic, while in the North Atlantic the percentage of eddies of both polarities remained close (51% anticyclonic over 49% cyclonic). Nevertheless, the TOEddies algorithm detected a higher number of long-lived cyclones originating in the upwelling systems of both hemispheres.

Figure 4 compares the cumulative number of Atlantic mesoscale eddy first (A, B) and last detections (C, D) as well as eddy-eddy interactions (merging and splitting events) (E, F) computed on a 1° × 1° gridded map as detected daily during the study period (1993 - 2018). In order to account for all possible eddy-eddy interactions, we counted centroids of eddies that were tracked for at least 4 weeks. Hot spots of eddy activity were characterized by high density of eddy generations exceeding $N > 30$ eddies per degree square. We found a higher rate of eddy generation near the eastern boundary of the ocean basin and, in particular, within the major eastern upwelling boundary systems (Canary in the North and Benguela in the South Atlantic) as well as within the western boundary currents (Brazil Current in the South Atlantic and the Gulf Stream in the North Atlantic).

Several areas where eddies were frequently generated were also areas where eddies disappeared from altimetry maps. Nevertheless, the difference on average between generation and termination points (not shown here) consists mostly of areas favorable for the generation of eddies. We noted that high spatial distribution of merging and splitting events also occurred in similar places, a fact that emphasizes the importance of accounting for eddy-eddy interactions to provide a complete dynamical description of the evolution of detected eddies. Merging and splitting events in the North Atlantic involved 53% of cyclonic eddies while in the South Atlantic a similar percentage of 54% was associated with interactions between anticyclonic eddies.

Areas of strong mesoscale activity are usually identified by estimating their eddy kinetic energy (EKE). Similarly to Chelton et al. (2011), we computed the total kinetic energy (KE) from the geostrophic velocity fields as derived from the daily ADT maps, namely by subtracting the temporal mean of the velocity geostrophic components over the study period

$$KE = \frac{1}{N}\sum_{i=1}^{N}(u(x,y,t) - \bar{u}(x,y))^2 + (v(x,y,t) - \bar{v}(x,y))^2 \qquad (1)$$

where $\bar{u} = \frac{1}{N}\sum_{i=1}^{N}u(x,y,t)$ and $\bar{v} = \frac{1}{N}\sum_{i=1}^{N}v(x,y,t)$. Based on TOEddies daily eddy detection, we were further able to distinguish the percentage of EKE attributed only to anticyclonic and cyclonic eddies respectively, and thus recover areas of eddy kinetic energy associated only with mesoscale eddy activity. This is achieved with a delta function $\delta(x, y, t)$ set to zero when the KE lay outside the last eddy contour and 1 when inside

$$EKE = \frac{1}{N}\sum_{i=1}^{N}((u(x,y,t) - \bar{u}(x,y))^2 + (v(x,y,t) - \bar{v}(x,y))^2)\delta(x,y,t) \qquad (2)$$

We plotted in **Figure 5**, the ratio of eddy kinetic energy versus total kinetic energy separately for cyclonic and anticyclonic eddies. The eastern upwelling areas are among the most energetic areas in the Atlantic Ocean. In the CCUS upwelling areas, the signatures of both cyclonic and anticyclonic eddies contribute to this eddy kinetic energy. In the BCUS, strong KE signal are mostly associated with cyclonic eddies near the upwelling areas, while the intense Agulhas eddy contribution to KE is visible in the right panel of **Figure 5**.

3.2 Dynamical Characteristics of EBUS Trajectories

The mean statistical properties of all the eddies detected by TOEddies in the Atlantic Ocean show that the EBUS represent areas of increased eddy density due to frequent eddy generations, interactions as well as high EKE. In particular, several long-lived and long-propagating eddies were found to originate from the EBUS.

To investigate the eddies' role in greater detail, we firstly defined eddies originating from the upwelling systems as those

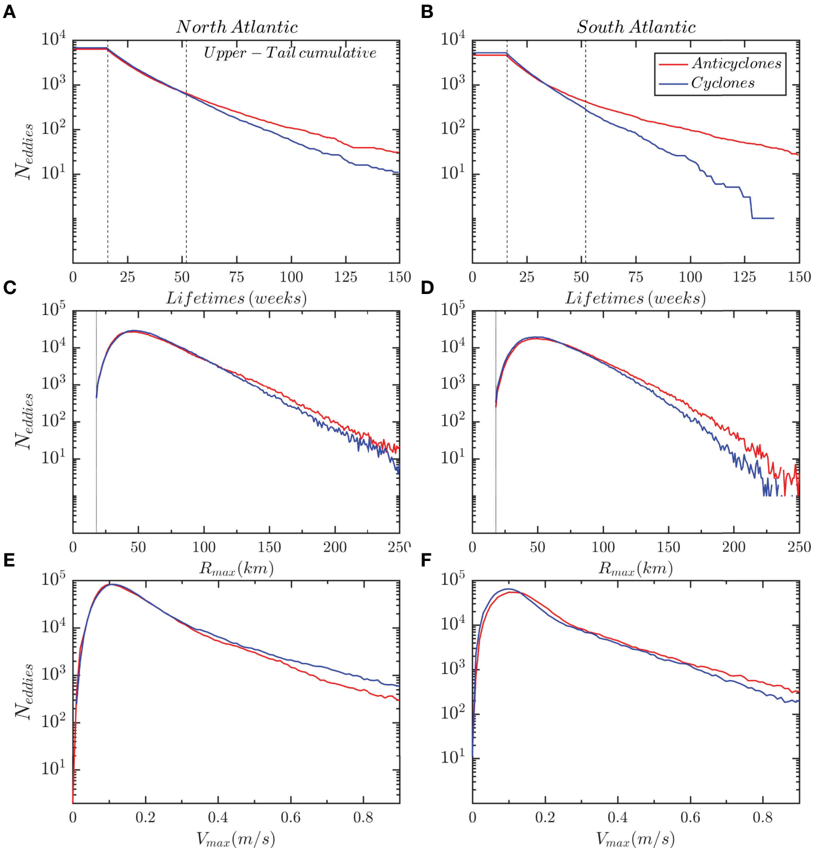

FIGURE 1 | Upper-tail cumulative histograms of eddy lifetimes (weeks) **(A, B)** and histograms of eddy characteristic radius R_{max} (km) **(C, D)** and velocity V_{max} (m/s) **(E, F)** of anticyclonic (red colors) and cyclonic eddies (blue colors) for the North (left panels) and South (right panels) Atlantic Ocean during the 1993-2018 period. We consider only mesoscale eddies having lifetimes ≥ 16 weeks and characteristic radii larger than R_{max} ≥ 18 km as indicated by the dashed lines in panels **A–D** respectively.

initially detected within the BCUS and CCUS regions before propagating into the Atlantic Ocean. To represent the upwelling fronts and broadly capture eddies generated from shelf's instabilities, we chose the 4,000 m isobath. In accordance with previous studies (Cury and Shannon, 2004; Desbiolles et al., 2014; Ndoye et al., 2014), we additionally divided the BCUS upwelling system into two subsystems: the north and south upwelling cells (nBCUS and sBCUS) at approximately 26.5°S near Lüderitz. This south and north division has been reported to be distinct in terms of climatological wind conditions and regional frontal dynamics (Wang et al., 2015; Wang et al., 2021) but also in terms of biological clustering (Blamey et al., 2015; Kirkman et al., 2016). A similar north and south division was made for the CCUS at around 20°N near Cape Blanc (nCCUS and sCCUS) (Barton et al., 1998; Benazzouz et al., 2014; Pelegrí and Benazzouz, 2015). The different upwelling subregions are indicated in **Figure 6** in different colors (blue for the north and green for the south).

In **Figures 6A, B** and **E, F** we display the eddy trajectories originating from the different subsystems that could be tracked from satellite altimetry maps for more than 16 weeks during the 1993-2018 period. Taking all eddy trajectories into account, both cyclonic and anticyclonic eddies were found to populate the upwelling subregions. In total numbers, TOEddies tracked more eddies originating from the CCUS subsystems than from the BCUS while the highest number of individual eddy trajectories was found for the nCCUS. The number of tracked cyclones was consistently higher than that of the anticyclones with the nCCUS being the only subsystem to be populated by an equal mixture of eddy types (50% cyclones/49% anticyclones). The asymmetry between cyclonic and anticyclonic eddies was the strongest for the sBCUS where 83% of the eddies are cyclonic. Slightly lower percentage (67%) was found for the sCCUS, while cyclonic eddies originating from the nBCUS were almost double the number of the anticyclonic ones. These findings are in line with previous observations (Boebel et al., 2003).

Moreover, eddy generation can vary considerably from year to year (**Figures 6C, G**). On average, in the sCCUS, the rate of cyclonic eddy generation was close to 8 ± 1.8 eddies per year (lifetimes ≥ 16 weeks in **Figure S4**). Stronger interannual variations with an average rate of 7.7 ± 2.6 cyclones/year were found for the sBCUS. In the nBCUS, this rate was estimated close to 5.3 ± 1.7 cyclones/year. Anticyclonic and cyclonic generation in the nCCUS yielded similar rates, close to 8 ± 2

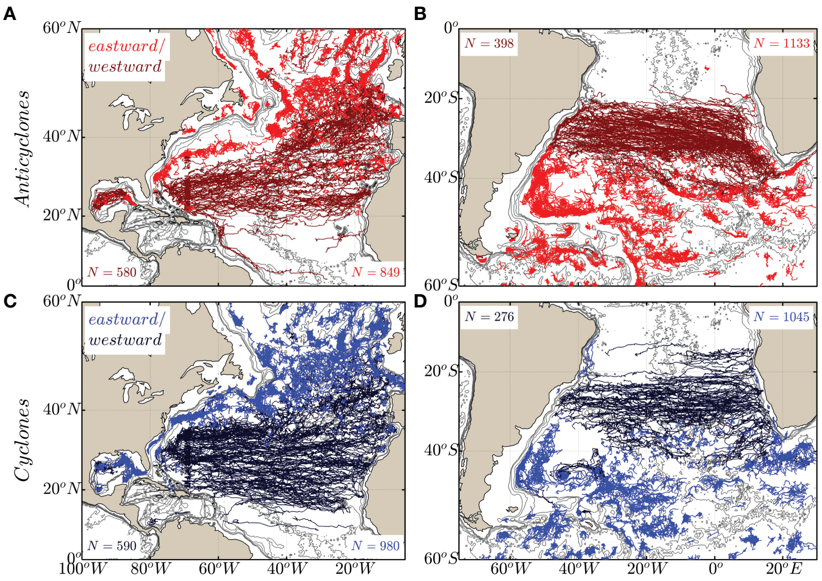

FIGURE 2 | Trajectories of eastward (lighter colors) versus westward (darker colors) propagating eddies with lifetimes longer than ≥16 weeks and ≥52 weeks respectively. Anticyclonic **(A, B)** and cyclonic **(C, D)** are indicated by blue and red, as detected *via* the TOEddies algorithm over a 24-year period (1993-2018). Bathymetry shallower than 4,000 m is indicated by gray lines.

eddies/year. Conversely, anticyclonic generation rates were consistently lower in the other systems: below 4.2 ± 1.8/year for the sCCUS, 2.8 ± 1.2/year for the nBCUS and 1.9 ± 1/year for the sBCUS.

During specific years, eddies originating from the Atlantic EBUS were tracked for longer periods of time while propagating westward. After generation, cyclones from the sCCUS and nCCUS mainly translated westward and north-westward, while anticyclones followed very different trajectories and tended to propagate south-westward. Meanwhile, cyclones generated in the nBCUS and sBCUS mainly translated westward and south-westward, towards the southern branch of the South Equatorial

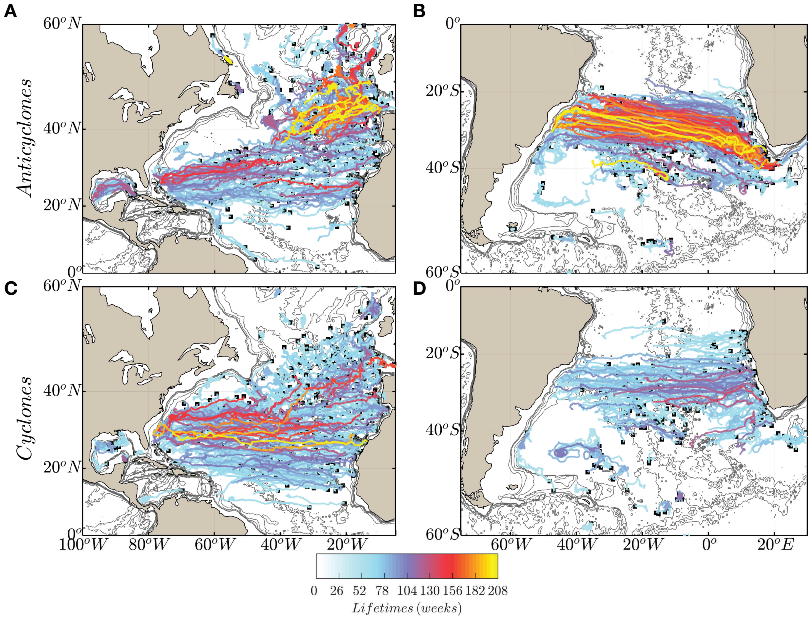

FIGURE 3 | Trajectories of anticyclonic **(A, B)** and cyclonic **(C, D)** eddies as detected *via* the TOEddies algorithm over a 24-year period (1993-2018) having a lifetime longer than ≥ 52 weeks. Each trajectory is colored on the basis of their estimated lifetimes (weeks). Bathymetry shallower than 4,000 m is indicated by gray lines.

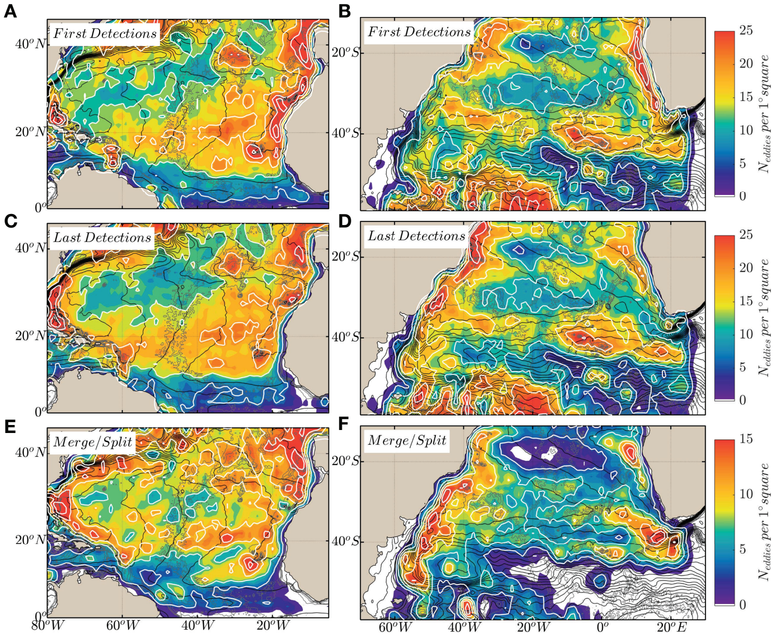

FIGURE 4 | Frequency maps of first (panel **A**, **B**), last (panel **C**, **D**) detection points and merging and splitting points (panel **E**, **F**) of mesoscale eddies with lifetimes longer than ≥ 4 weeks as detected in the South and North Atlantic from the TOEddies global Atlas over a 24-year period (1993-2018) gridded over 1° × 1° bins (smoothed using a 1° × 1° window). The mean dynamic topography (MDT in cm) is shown by black contours and bathymetry shallower than 4,000 m depth by gray lines.

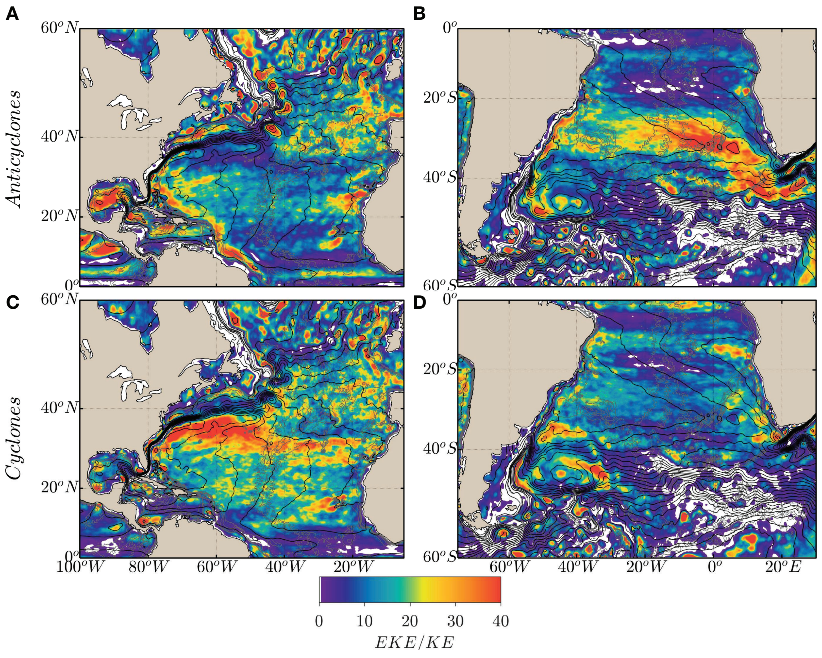

FIGURE 5 | Ratio of the contribution of mesoscale eddy kinetic energy (EKE) to the total kinetic energy (KE) in the North (left panels) and South Atlantic (right panels), respectively for anticyclonic **(A, B)** and cyclonic **(C, D)** eddies gridded over 1° × 1° bins. The mean dynamic topography (MDT in cm) is shown by black contours and bathymetry shallower than 4,000 m depth by gray lines.

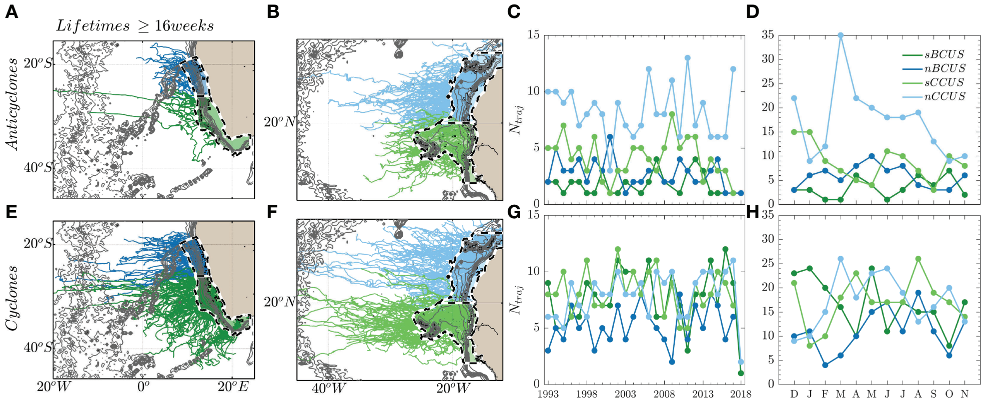

FIGURE 6 | Eddy trajectories originating from the four upwelling subsystems: nBCUS and sBCUS **(A, E)** and sCCUS and nCCUS **(B, F)** as obtained from TOEddies Global Atlas with lifetimes more than ≥ 16 weeks. The mean annual and monthly number of eddies are indicated in panels **C**, **G** and **D**, **H** respectively for anticyclonic and cyclonic trajectories. The north and south upwelling regions of the BCUS and CCUS are indicated by the blue and green patch areas respectively.

Current (Majumder et al., 2019; Luko et al., 2021). Thus, equatorward/poleward deflections for anticyclones/cyclones respectively were also confirmed here in agreement with previous findings (Morrow, 2004; Chaigneau et al., 2009; Chelton et al., 2011; Schütte et al., 2016a). Among these long-lived mesoscale eddies, several stood out with lifetimes exceeding 2 years and propagation distances exceeding 2,000 km (**Figure S5**).

If we assume that eddy generation in the BCUS and CCUS is mainly driven by instabilities of the upwelling thermal front, we can then expect their formation to be associated with the upwelling seasonal variations. We therefore explored the seasonal variations of different indices for the four Atlantic EBUS subsystems examined in the present study (see **Supplementary Material Figures S6, S7**). The mean monthly variations of all upwelling indicators showed the nCCUS and nBCUS upwelling subregions to exhibit a permanent upwelling regime while the sCCUS and sBCUS subregions undewent a marked upwelling seasonal cycle (Benazzouz et al., 2014; Pelegrí and Benazzouz, 2015; Brandt et al., 2015).

Even if mesoscale eddies are expected to form more frequently when the upwelling seasonal variations are the strongest, we found that eddy generation does not exhibit marked seasonal variations (**Figure 6**). Moreover, when a seasonal cycle is detectable in the eddy generation, it does not always coincide with an intenser upwelling seasonal phase (**Figure S6**). For instance, in the nCCUS, cyclonic and anticyclonic eddy generation peaks in March just after the maximum SSTa (Sea Surface Temperature anomaly) that peaks during winter (November/December). Similarly, in the sCCUS cyclonic eddy generation peaks in August, a period of weak upwelling intensity. On the other hand, in the sBCUS, cyclonic eddy generation peaks in May, at the end of the most intense upwelling season, when the SSTa is at its minimum (**Figure S6D**). In the nBCUS, increased cyclonic eddy generation is observed from February till May (peak in May for AEs), a fact that could be associated with the minimum SSTa during May. Nevertheless, the maximum number of CEs is observed during August, which is out of phase with any upwelling index considered (SSTa or WSCa,- (**Figures S6D, E**). Even though we have found no direct correlation, we suspect that eddy generation in the upwelling regions is controlled by nonlinear processes involved. For instance, Marchesiello et al. (2003) have shown mesoscale eddy variability in the California current system to be linked with alongshore current instabilities. Marchesiello and Estrade (2007) have further demonstrated that stratification and topography alone can substantially affect the available potential energy initially provided by regional wind forcing. This suggests that more thorough investigations are necessary to understand the connections between regional forcing and eddy generation.

In **Figure 7**, we compare the mean horizontal characteristics of the eddies from the four upwelling subsystems. Histograms of eddy characteristic radii and velocities were plotted separately for cyclonic and anticyclonic eddies. Eddy lifetimes longer than 16 weeks were considered. In the nBCUS and nCCUS, the characteristic radii of cyclonic eddies were estimated at $\langle R_{max} \rangle = 67.1 \pm 23$ km and $\langle R_{max} \rangle = 59.4 \pm 21$ km, 13% and 5% larger than the equivalent average radius of the anticyclones. We found similar sizes (66.3 ± 23 km) for sCCUS cyclones and anticyclones. Cyclones originating from the sBCUS had a mean size of $\langle R_{max} \rangle = 63.4 \pm 22$ km. These were the most intense eddies among the four upwelling systems with mean characteristic velocities reaching almost $\langle V_{max} \rangle = 30 \pm 19$ cm/s, which was twice those of the sCCUS cyclonic eddies (14 ± 7 cm/s), nCCUS (14 ± 15 cm/s) and nBCUS (12 ± 6 cm/s). We noted that the mean horizontal characteristics of eddies from the upwellings were associated with large standard deviations indicating that eddy sizes and intensities could vary substantially among the years of observations.

To investigate the mean vertical structure of eddies from each subsystem, we further investigated certain long-lived trajectories of **Figure 6**, limiting ourselves only to those that were additionally

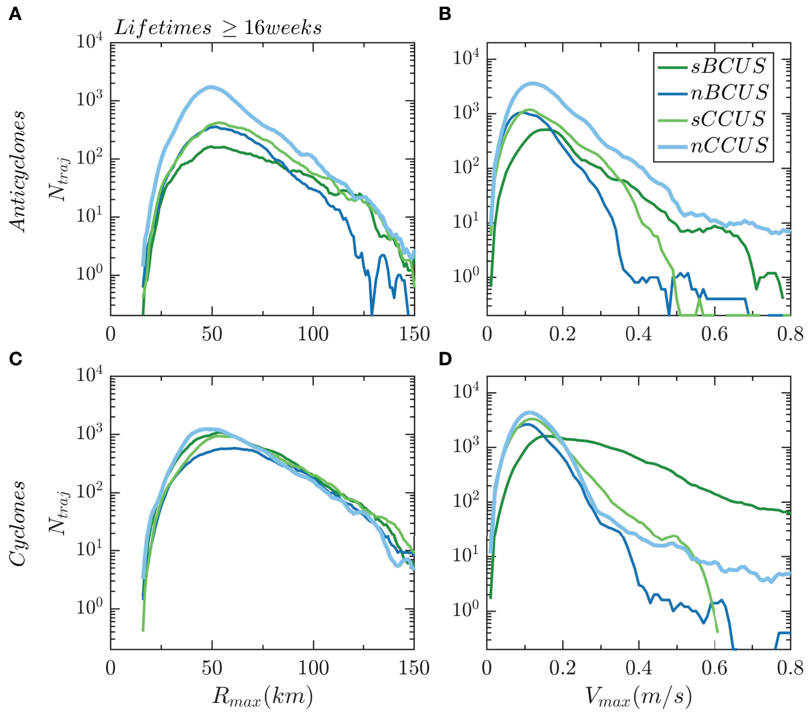

FIGURE 7 | Histograms of eddy characteristic radii R_{max} (km) and velocities V_{max} (m/s) for anticyclonic **(A, B)** and cyclonic **(C, D)** trajectories originating from the different upwelling subsystems considered in this study (lifetimes ≥ 16 weeks).

sampled by at least 1 Argo float at a radial distance smaller than or equal to the eddy characteristic radius ($d_{argo} \leq R_{max}$). **Figure 8** shows the mean vertical structure of temperature and density anomalies of AEs and CEs from each upwelling subsystem. On average, the CEs presented larger anomalies than the AEs. Moreover, BCUS cyclones seemed to contain waters from the environment colder by -1.76°C in the sBCUS and by -1.22°C in the sBCUS in comparison with cyclones from the CCUS whose anomalies remained below 1°C (-0.46°C and -0.7°C in the sCCUS and nCCUS). On average, CCUS eddies displayed shallower vertical extents, occupying mostly shallower and less dense layers (γ^n = 25.2 - 27.1 kg m^{-3}) in comparison with eddies from the BCUS that extended further deeper at higher density intervals (γ^n = 26.5 - 27.14 kg m^{-3}). CEs in the sCCUS were characterized by the shallower vertical extent (γ^n = 25.96 kg m^{-3} ~ 70 m depth) in comparison with CEs from the sBCUS whose maximum anomaly in temperature centered at γ^n = 27.07 kg m^{-3} and at almost 430 m depth. It should be pointed out that all above properties were derived from Argo floats that sampled eddies of the upwelling subregions at different radial distances, while always remaining inside the eddy dynamical core. This selection was made in order to retain a relatively large number of Argo floats for each subregion ($N_{Argo} \geq 20$), in our calculation of the estimated mean EBUS vertical properties. Nevertheless, when taking into account floats located at distances close to the eddy center ($d_{argo} \leq 0.5\ R_{max}$), we found that the mean eddy hydrological anomalies intensified by at least 30% (even growing to 60% for the sBCUS and sCCUS subregions). Accordingly, we suggest that the distance from the eddy center should be taken into further consideration when investigating its impact on nutrient or chlorophyll distribution (Wang et al., 2018).

3.3 Mean Upwelled Eddy Connectivity Signal

The main exporters of nutrient-rich waters from the CCUS and BCUS seem to be mostly associated with cyclonic features. Apart being areas of frequent eddy generation these EBUS are also associated with large eddy-eddy interactions that lead to numerous eddy splitting and merging events (**Figure 4**). Such events alter the main eddy pathways and are supposedly linked with significant transfers of waters. It is hence essential to identify merging and splitting events of both eddy types in order to understand the evolution of eddies.

Following Laxenaire et al. (2018), we reconstructed an eddy network comprising all trajectories related with various filiations to eddies of upwelled origins. By assigning the order of eddy-eddy interactions, the resulting eddy trajectories network assembles all eddies connected *via* merging or splitting and traces them from the upwelling areas further offshore in the Atlantic. **Figure 9** shows the eddy-network reconstruction for the two key areas the BCUS and the CCUS upwelling systems. Trajectories indicated in black are the reference trajectories that originated from the shelf and are assigned an order zero. The order number increases in relation to the number of interactions that are needed to trace back or forward to a reference trajectory.

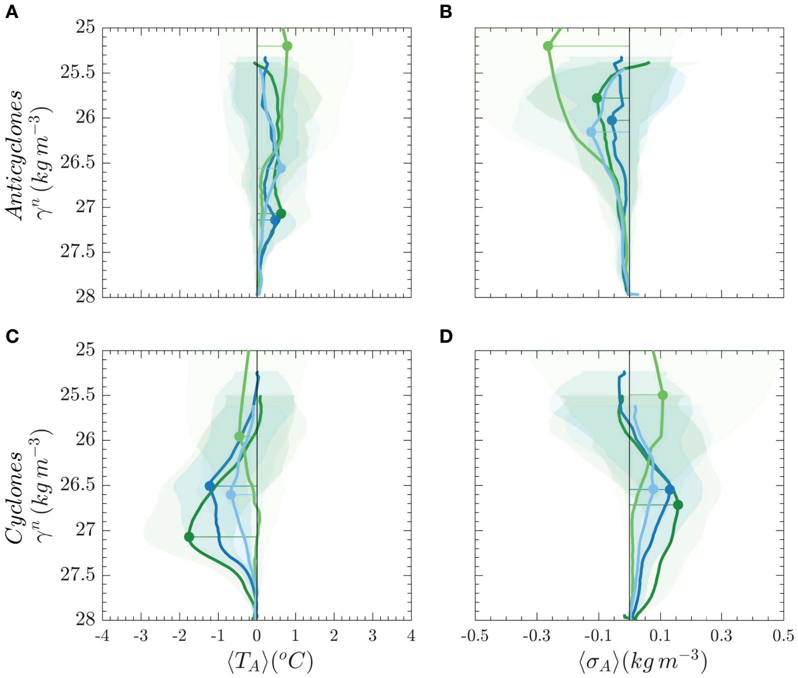

FIGURE 8 | Mean temperature $\langle T_A \rangle$ (°C) and density $\langle \sigma_A \rangle$ (kg m^{-3}) anomalies as derived from Argo profiles tracked inside anticyclonic **(A, B)** and cyclonic trajectories **(C, D)** with lifetimes more than ≥ 16 weeks originating from the different upwelling subsystems considered in this study. Only Argo profiles located at a radial distance of less than R_{max} from the estimated eddy center were kept ($d_{argo} \leq R_{max}$).

In total, the BCUS and the CCUS eddy networks were composed of 11,764 and 12,969 eddy trajectories respectively (with lifetimes larger than 4 weeks). Overall, eddies from upwelling networks account for only 10% of the total number of trajectories tracked in the Atlantic by the TOEddies algorithm. However, if we only consider long-lived eddies from these networks (with lifetimes greater than 52 weeks), this percentage increases to 61%. Mesoscale eddies of order zero (originating from the upwelling areas) were mostly cyclonic, accounting for 75% of the order-zero eddy trajectories for the BCUS and 57% for the CCUS (lifetimes ≥ 16 weeks). Nevertheless, anticyclonic eddies were also involved in the advection of properties when higher orders of interactions are considered. Indeed, the role of anticyclonic eddies on the advection and entrainment of upwelled waters when situated near upwelling coastal areas has been previously highlighted for both the CCUS and the BCUS (Duncombe Rae et al., 1992; Arístegui et al., 1997). When merging and splitting events are taken into account, both eddy types ensured connections between the eastern and western boundaries contributing to a mean connectivity signal (**Figure 9**).

The EBUS eddy-network reconstruction shows that long-lived and long-propagating eddies, along with their frequent interactions, may potentially transport waters from the upwelling regions further offshore and in some cases even reach the western Atlantic boundaries (Guerra et al., 2018; Nencioli et al., 2018; Laxenaire et al., 2018; Laxenaire et al., 2019) In order to investigate whether these connections concern only upper-ocean dynamics, we selected all Argo floats co-localised with the TOEddies Atlas that were identified inside the BCUS and CCUS network trajectories (**Figure 9**). Together, BCUS and CCUS eddy networks were sampled by 28,554 Argo profiles in various positions inside eddies. Around 21% of the total EBUS network trajectories were sampled by at least 1 Argo float. Out of these, 64% sampled anticyclones and 36% cyclones.

In order to estimate the mean connectivity signal represented by these mesoscale eddies in comparison with the adjacent environment, in **Figure 10** we plotted mean anomalies of potential temperature estimated from the CCUS and BCUS eddy networks in the upper ($\langle \gamma^n \rangle$ = 25 - 26 kg m^{-3}) and thermocline ($\langle \gamma^n \rangle$ = 26 - 27 kg m^{-3}) isopycnal layers. Anomalies were computed by subtracting the non-eddy climatology in each isopycnal surface. Positive and negative temperature anomalies corresponded to anticyclonic and cyclonic eddies respectively. These properties concerned only Argo floats trapped inside eddy trajectories with origins from the eastern upwelling system (we limited the estimate to up to order 5 trajectories in **Figure 9**). The subsurface extent of eddy properties was visible well below the surface, reaching intermediate depths.

On average, for the CCUS network, anticyclones were associated with mean temperature/salinity anomalies of about 0.45 ± 0.91°C/0.02 ± 0.14 g/kg in the upper layers and 0.26 ± 0.47°C/0.04 ± 0.09 g/kg for denser layers. For the BCUS, these mean temperature/salinity anomalies were stronger for both, the upper layers (0.93 ± 1.29°C/0.1 ± 0.18 g/kg) and for denser layers

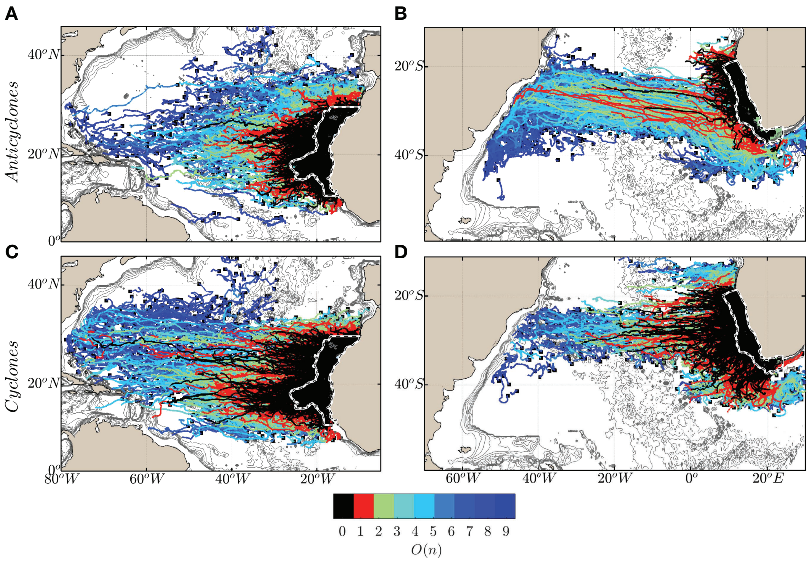

FIGURE 9 | Eddy network of anticyclonic **(A, B)** and cyclonic **(C, D)** trajectories from the CCUS (left panels) and the BCUS (right panels). Each eddy trajectory is colored according to their assigned order. Bathymetry shallower than 4,000 m is indicated by gray lines.

(0.95 ± 0.94°C/0.12 ± 0.12 g/kg). For CCUS cyclonic eddies, the mean temperature/salinity anomalies were estimated at -0.4 ± 1°C/-0.004 ± 0.12 g/kg for the upper layers and slightly weaker at greater depth (-0.39 ± 0.6°C/-0.04 ± 0.1 g/kg). Finally, BCUS anomalies for cyclones were found to be even positive in the upper isopycnal layers 0.08 ± 1°C/-0.04 ± 0.15 g/kg but reached -0.67± 0.9°C/-0.08 ± 0.11 g/kg for deeper layers.

The mean properties from the eddy networks demonstrated an additional contribution and spreading of heat and salt by mesoscale eddies in comparison with the environment. The comparison between upper and deeper isopycnal layer anomalies indicated that cross-basin connectivity achieved by mesoscale eddies not only concerns the upper layers but seems to extend down to the main thermocline. For BCUS cyclones the maximum of intense anomalies was found to be even stronger in the denser layers here considered ($\langle \gamma^n \rangle = 26 - 27$ kg m^{-3}) than in the upper layers.

3.4 Individual Eddy Trajectories

In the previous section, by combining available hydrographic properties from Argo floats with the eddy trajectory networks built for the CCUS and BCUS, we estimated the mean temperature and salinity anomalies within isopycnal layers related to mesoscale eddies of EBUS origins in the Atlantic. These mean anomalies of properties associated with eddies are not restricted in the surface layers but can extend through the thermocline. In order to further evaluate vertical eddy properties and how they evolve over time we searched for individual eddy trajectories that were sufficiently sampled by Argo floats among the years of observations.

From the total eddy trajectories networks, we therefore selected specific examples of cyclonic and anticyclonic trajectories that were sampled by more than 30 Argos floats over periods of more than one year, allowing us to gather information on their internal structure along their en-route propagation. Among these, we firstly identified several Agulhas Rings that were previously described in Laxenaire et al. (2019, 2020) and for this reason, omit their discussion in this paper. We further isolated two specific cases of cyclonic eddies in the years 2012 and 2015 that were sampled by a total of 41 and 44 Argo profiles, the dynamical evolution of which we will describe in the following section. To our knowledge, these are among the few occurrences of Argo floats remaining trapped inside coherent cyclones for significant long time periods, providing us with information on their vertical structure and evolution.

3.4.1 BCUS Cyclones: Eddy Signature on Subduction

Figure 11 A shows the trajectories of two cyclonic eddies, C0 and C1, one originating from the nBCUS and one from the sBCUS and sampled by more than 30 profiles (magenta points) during their lifespans. These two cyclones were formed in late fall, in March 2012 (C1) and April 2015 (C0) respectively. They moved mainly west-southwestward and were tracked for more than 1 year with TOEddies. The movies of the two cyclones' dynamical evolution (see Supporting Information) show their daily tracking by TOEddies in the sea surface height fields along with their sampling rate from the Argo floats.

Several snapshots along the temporal evolution of the surface signature of these eddies are presented in **Figure 12**. Cyclone C0 was initially detected on 5 January 2015 in the nBCUS upwelling frontal zone and was tracked with TOEddies till 1 April 2016, for almost 65 weeks (approximately 1.5 years). The eddy drifted westward covering a distance of 1,793 km, while an Argo float (WMO 1901310) sampled C0 at various radial distances from the eddy center providing in total 44 T/S profiles. According to the

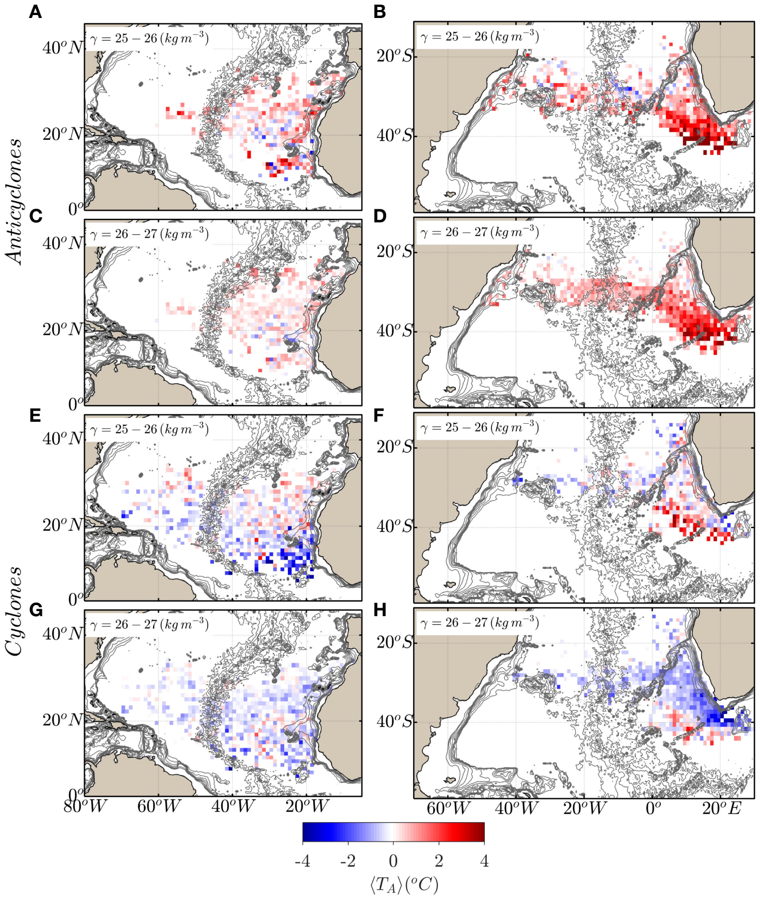

FIGURE 10 | Mean temperature anomalies $\langle T_A \rangle$ (°C) at upper ($\gamma = 25$ - 26 kg m^{-3}) **(A, B, E, F)** and deeper ($\gamma = 26$ - 27 kg m^{-3}) **(C, D, G, H)** isopycnal layers as measured by Argo floats trapped inside anticyclones and cyclones from the CCUS (left panels) and the BCUS (right panels) eddy trajectory networks. Bathymetry shallower than 4,000 m is indicated by gray lines.

TOEddies network reconstruction, this cyclone merged on 25 Feb 2015 with a short-lived cyclone (less than one month old) initially detected on 18 January 2015 (**Figure 12A**). It also seems that this eddy detached from the nBCUS slightly south of C0 (11.39°E, 26.55°S), and was sampled by the same Argo float that later remained trapped in C0 for almost 8 months. During eddy generation, while eddy scales and the distance from the shore remain relatively small, we cannot guarantee that satellite altimetry resolution is sufficiently accurate to resolve such rapid interactions between eddies. Nevertheless, this detachment was identified as a merging event by TOEddies. The Argo T/S profiles before and after the merging event showed that the eddy water masses were not significantly impacted. During the months that followed, the eddy propagated westward reaching and crossing the Walvis Ridge during the austral winter (June, July, August) of 2015 (**Figures 12C, D**).

Meanwhile, cyclone C1 was initially detected in sBCUS on 27 February 2012, north-west of Cape Town. This cyclone was tracked with TOEddies for almost 71 weeks (16 months). From March 2012 several different Argo floats sampled the eddy until 12 July 2013 when the eddy was last detected, providing 41 vertical profiles. From August 2012, the cyclone drifted westward while starting to interact with and propagate along an Agulhas Ring that was in the vicinity (**Figures 12G–H**). Such cyclone-anticyclone interactions in the Cape Basin have been previously documented from observations (Boebel et al., 2003; Souza et al., 2011) and numerical simulations (Doglioli et al., 2007).

Figures 11B, C depict the daily evolution of the geostrophic dynamical characteristics of the radii and azimuthal velocities of the two eddies under investigation. The time series for C1 and C0 show distinct dynamical periods for the eddies. During generation, when the eddies were moving away from the continental slope, variations in their velocity and radius were observed. After generation both cyclones increased in radius and velocity. The latter thus reached a maximum of 40 cm/s and 60 cm/s for cyclones C0 and C1 respectively, 6 months after generation (**Figure 11C**). It is worth noting that the maximum eddy intensities are at least twice as high as than the mean CE intensities shown in Section 3.2. Indeed, for C0, during the austral summer, the eddy diameter remained constant whereas the eddy tangential speed increased when the eddy crossed the Walvis Ridge. During that period, its translation speed was

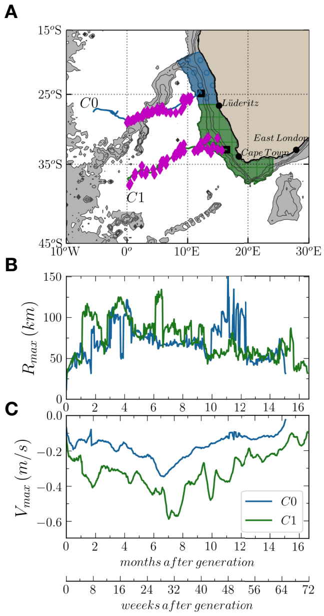

FIGURE 11 | Trajectories of long-lived cyclones C0 and C1 originating from the sBCUS (green patch) and nBCUS (blue patch) as detected from the TOEddies database for the years 2012 and 2015 respectively are shown in **A**. Bathymetry shallower than 4,000 m is indicated by gray shading. The temporal evolution of dynamical characteristics of characteristic radius R_{max} (km) and velocity V_{max} (m/s) is shown in **B**, **C**.

relatively weak (~ 7 km/day), and its shape remained almost circular with ellipticity below $\epsilon = 0.3$. A decay in the eddy velocity was then observed.

In order to investigate the evolution of the vertical structure of the eddies core, we selected only Argo profiles that were located at a radial distance of ≤ 55 km from their estimated centers (**Figures 13A, B**). This corresponds to a mean ratio between the Argo radial distance and the eddy characteristic radius of about 50% (maximum ratio of about 74%). The temporal evolution of the temperature and density anomalies in the cores of the two cyclones is shown in **Figures 13C, D** along with the estimation of their mixed layer depth (MLD). The latter was determined by computing the depth at which the Brunt–Väisälä frequency squared ($N^2 = -\frac{g}{f}\frac{\partial \rho}{\partial z}$) was found to be at its minimum. We then estimated the density anomaly induced by the eddies on the basis of the climatological eddy background containing a no-eddy signature (**Figures 13E, F**). To quantify the vertical extent of the eddy we computed the depth of the maximal density anomaly.

According to **Figure 13** during the first 3 months of the formation of C0, the density anomaly of the eddy seemed weak in comparison with the surrounding environment. This makes sense when considering that the eddy had not yet detached from the shelf and the upwelling tongue: during this period the eddy was mainly trapped in the upwelled waters that were not significantly different from the adjacent environment. Once the eddy started to propagate westward, we then detected a temperature and salinity anomaly located

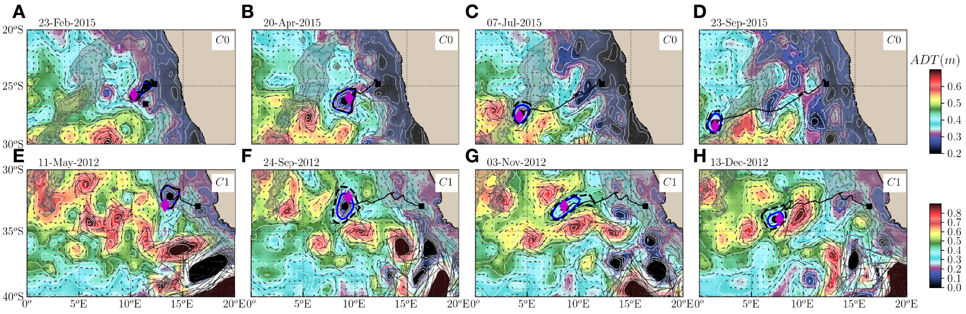

FIGURE 12 | Snapshots along the temporal evolution of cyclones C0 **(A–D)** and C1 **(E–H)**. The background colors correspond to the ADT while the gray arrows correspond to surface geostrophic velocities. The characteristic and outer contours detected by TOEddies are shown by the solid blue and dashed black lines. The Argo floats trapped in the eddies are shown by magenta diamonds points. Bathymetry shallower than 4,000 m is indicated by gray shading.

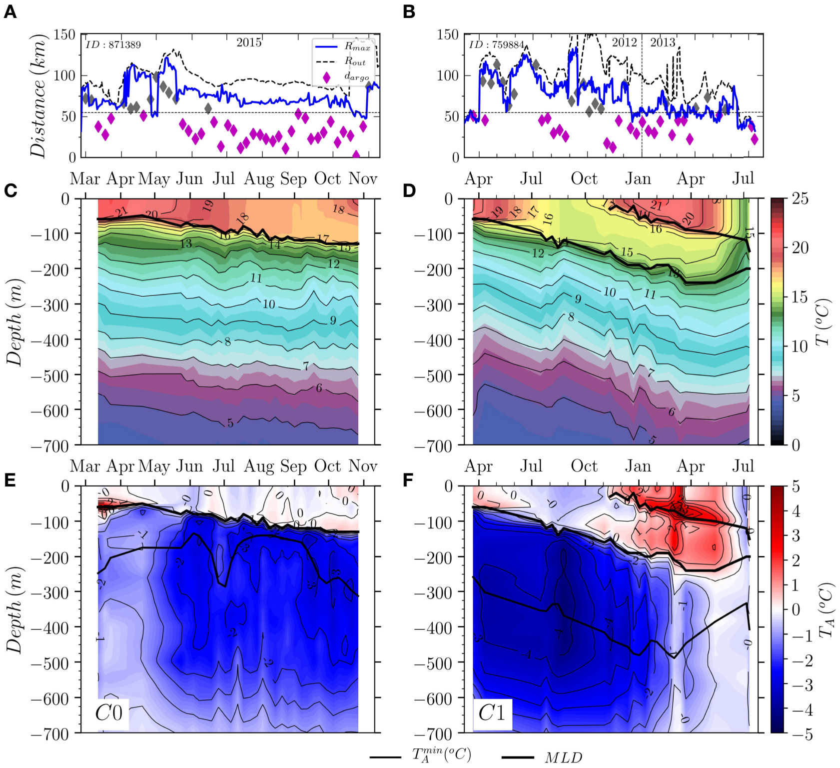

FIGURE 13 | The temporal evolution of eddy characteristic R_{max} (km) and outermost radius R_{out} (km) is shown in panels **(A, B)**, with the blue and black dashed lines indicating cyclones C0 and C1 respectively. The magenta diamond points illustrate the position of the Argo profiles as a function of their distance from the eddy center. Vertical profiles of temperature T (°C)as obtained from the Argo floats trapped in the eddy are shown in panels **(C, D)**. The vertical temperature T_A (°C) anomalies are shown in panels **(E, F)** relative to the TOEddies climatology.

at between -200 and -700 m depth, which was -2.8°C/-0.3 g/kg colder and fresher than the environment. The density anomaly of C0 was confined to between -100 and -700 m depth with a maximal density anomaly of σ_A = 0.34 kg m^{-3} that was located at -190 m in May 2015. Two months later, the maximal density anomaly seemed to deepen further, reaching Z_{max} = -210 m on 30 July 2015. In September 2015, the maximal density anomaly reached a depth of Z_{max} = -240 m while remaining relatively strong σ_A = 0.37 kg m^{-3} (with -3.4°C/-0.37 g/kg temperature and salinity anomalies). Unfortunately, no other Argo float was detected inside the eddy after November 2015 despite TOEddies managing to track it until 1 April 2016 (5.5°W, 27.54°S).

As for C1, one month after its formation (on 22 March 2012), the eddy density anomaly was σ_A = 0.52 kg m^{-3} at -80 m. Five months later, the maximal σ_A remained the same in intensity while deepening, reaching a depth of Z_{max} = -180 m on 25 August 2012, with corresponding temperature and salinity anomalies of -4.4°C/-0.47 g/kg. In November 2012, the maximal density anomaly deepened further reaching Z_{max} = -250 m probably as a result of air-sea interactions that cooled and mixed the eddy upper layers, deepening its MLD. Indeed, during that period the eddy's upper layers seemed to be connected to the surface. From November till at least March 2013 (austral summer), in the upper eddy structure, a seasonal thermocline appeared, whereas the eddy core seemed to penetrate further in depth while gradually separating from the ocean surface. Afterwards, the eddy propagated south-westward (0.57°E, 37.9°S) until 12 July 2013 when it was last detected.

The vertical sampling of the two BCUS cyclones, C0 and C1, shows that these eddies accounted for density anomalies of σ_A = 0.5 kg m^{-3} and temperature anomalies of 4.4°C in the Cape Basin. Both cyclonic eddies showed a progressive deepening of their vertical structure and a clear separation from the ocean surface, suggesting that they subsided and became subsurface-intensified eddies as they left the upwelling area and penetrated the Cape Basin. This transition was accompanied by a gradual decay of both eddy surface intensities whereas subsurface anomalies remained relatively unchanged.

Such behavior has been already observed and described for anticyclonic eddies, in particular for Agulhas Rings and for CCUS specific anticyclones (Schütte et al., 2016a; Karstensen et al., 2017; Barceló-Llull et al., 2017; Guerra et al., 2018; Laxenaire et al., 2019; Laxenaire et al., 2020). (Laxenaire et al., 2019; Laxenaire et al., 2020) showed that the majority of Agulhas Rings become subsurface-intensified eddies along their route. However, the results we discuss in the present study, represent the first evidence of such behavior for cyclonic eddies in the South Atlantic.

4 SUMMARY AND CONCLUSION

Motivated by the fact that EBUS are areas of high productivity as well as of frequent eddy generation, we examined cross-basin oceanic connectivity that is promoted by coherent, long-lived and long-propagating mesoscale eddies with eastern upwelling origins in the Atlantic Ocean. We characterized the dynamical properties of mesoscale eddies over a 24-year period (1993 to 2018) throughout the Atlantic with the TOEddies Dynamical Dataset that uses daily satellite observations of ADT.

Among all the mesoscale eddies detected in the Atlantic Ocean with the TOEddies dataset, a small fraction of them will be long-lived (10% with lifetimes more than 52 weeks). In agreement with previous studies (Chaigneau et al., 2009; Chelton et al., 2011), we found that long-lived eddies propagate mainly westward and are predominantly anticyclonic. However, at least 60% of these long-lived westward eddies were found to either originate or interact with eddies from eastern boundary upwelling systems. We have then specifically qualified from the whole Atlantic TOEddies dataset the eddies spawn from the four upwelling subsystems (north and south CCUS and BCUS), analyzing their seasonal and interannual variabilities. By using co-localized Argo float profiles, also provided by the TOEddies Atlantic Atlas, we characterized their mean vertical structures, retaining only the Argo profiles sampling the eddies' dynamical cores.

To estimate the contribution of eddies on oceanic connectivity, we reconstructed the eddy-trajectory network linking eddies of upwelled origins to all nearby eddies connected to them *via* merging/and splitting events. The mean eddy connectivity signal was then derived on the basis of a synthesis of the CCUS and BCUS eddy networks with 17 years of *in-situ* observations from Argo floats. A comparison between eddies from the four upwelling subsystems showed that a higher number of eddy trajectories is associated with cyclonic than anticyclonic eddies. The only exception to this observation is the nCCUS subsystem characterized by an equal proportion of eddies of each polarity. In total numbers, more eddies were detected to originate from the CCUS than the BCUS. On the other hand, our study suggests that the sBCUS is mainly characterized by cyclonic eddies (83%), the mean tangential velocity of which is about double the intensity of cyclones from the other subsystems. Our comparisons with mean upwelling indicators as derived from ERA5 datasets showed that seasonal variations in eddy formation do not always coincide with the mean upwelling climatology. Further investigation of possible connections between specific eddy formations and the processes responsible for their variability is therefore required (Marchesiello et al., 2003; Marchesiello and Estrade, 2007; Moscoso et al., 2021).

We retracted the Canary eddy corridor, first introduced in Sangrà et al. (2009), for the CCUS, while also tracking long-lived eddies that propagated even farther than 35°W. Similar eddy westward pathways were found for the BCUS. Poleward/equatorward deflections for cyclonic/anticyclonic eddies were also confirmed in our study. Nevertheless, cyclones originating from the sCCUS and nBCUS were found to propagate mostly westward, also joining the southern branch of the South Equatorial Current (Majumder et al., 2019; Luko et al., 2021). Several of the upwelled-origin eddies that we investigated, contributed to a mean oceanic connectivity across basins, for example when they managed to reach the western boundary current systems. Eddy mean lifetimes may exceed 1 year and propagation distances of 2,000 km. Moreover, we noted that these eddies were not isolated but often merged and splitted with other structures. We expect that during such events, the resulting eddies will remain stable and retain some fraction of the initial trapped waters. Besides, coherent eddies may interact and exchange properties *via* their mutual deformation (Dritschel, 1995; Yasuda, 1995; Yasuda and Flierl, 1995; Carton, 2001; Flament et al., 2001; Brandt and Nomura, 2010; Carton et al., 2015). When taking into account eddy-eddy interactions, both cyclonic and anticyclonic eddies are important in transporting water properties across-basins. The mean thermohaline structure as derived from the combination of eddy trajectories with available Argo float measurements displays a mean connectivity signal between eastern and western boundaries that does not only concern surface layers but may extend deeper. On average the vertical extent of eddies from the CCUS was found to be shallower (maximum temperature anomalies ranging between 50 - 190 m, γ^n = 25.2 - 27.1 kg m^{-3}) than that of eddies from the BCUS which occupyied deeper and denser layers (150 - 530 m, γ^n = 26.5 - 27.14 kg m^{-3}). Mean anomalies associated with BCUS cyclonic eddies were found to be even stronger along the lower thermocline isopycnal layers (γ^n = 26.5 - 27 kg m^{-3}).

Finally, we focused on two specific years in which two cyclonic eddies originating from the nBCUS and sBCUS were formed. During these years, Argo profilers were trapped for several months in their cores, allowing us to compare the temporal evolution of their hydrological properties. The two cyclonic eddies that were sampled by Argo floats along their en-route propagation provided additional observational evidence of the transport of properties by coherent eddies. The temporal evolution of their anomalies revealed a progressive deepening of the eddy core into deeper thermocline layers while being advected further west, suggesting a subduction and a transformation of these eddies from surface-intensified to subsurface-intensified structures. Cyclone C0 originating from the nBCUS crossed the Walvis Ridge and left the Cape Basin, contrary to previous findings (Matano and Beier, 2003). Moreover, the multi-month vertical sampling of this eddy by Argo floats showed that the eddy's core remained unchanged while crossing the Walvis Ridge. While the subduction process has previously been evidenced for Agulhas Rings (Laxenaire et al., 2019; Laxenaire et al., 2020), to our knowledge, this study represents the first description of subduction for cyclonic eddies. Indeed, subsurface eddies have already been surveyed in similar EBUS areas, for example in the CCUS (Schütte et al., 2016a,b; Karstensen et al., 2017; Dilmahamod et al., 2021).

We note that our study provides information for only a small fraction of eddies whose signature is detectable from altimetry maps. With the current satellite and *in-situ* observations and the TOEddies algorithm, we can only observe part of all mesoscale eddy processes that occur in the ocean, and even these provide only partial glimpses of these events. We hope that with the upcoming altimetry SWOT mission together with dedicated field experiments, it will be possible to gain new insight. The SWOT wide-swath altimetric signal is expected to capture, with higher accuracy, ocean-surface topography globally but also near the BCUS area. Nevertheless, our results already suggest that the Atlantic eastern boundary upwelling systems are important sources of long-lived eddies that may efficiently export heat, salt and other water properties further offshore from the coastal upwelling areas. As documented in this study for two cyclonic eddies spawn from the BCUS, or Agulhas Rings (Laxenaire et al., 2019, Laxenaire et al., 2020) or anticyclones in the CCUS (Schütte et al., 2016a, b; Karstensen et al., 2017; Dilmahamod et al., 2021), many eddies subduct into the subsurface while drifting westward. We therefore suggest that most of the eddies that disappear from altimetry maps do not immediately dissipate but continue to drift into the open ocean, masked by upper-ocean layer stratification. Their potential impact on thermocline ventilation and coastal ecosystems should be addressed in future studies. Indeed, these eddies trap and advect water properties as well as plankton and fish larvae from the nutrient-rich upwelling shelfs. Their ability to connect distant environments should thus be investigated further.

DATA AVAILABILITY STATEMENT

The data used for this paper are available at the following repository and can be accessed through the following link (10.5281/zenodo.6443096). The gridded satellite altimetry data we used in this work were produced by SSALTO/DUACS and distributed by the Copernicus Marine Environment Monitoring Service (https://marine.copernicus.eu/). The Argo data were collected and made freely available by the International Argo Program and the national programs that contribute to it (https://coriolis.eu.org).

AUTHOR CONTRIBUTIONS

AI and SS designed the study and contributed to the writing. AI performed the data analysis while RL provided TOEddies dataset and automatic eddy detection for the study area. All authors contributed to the article and approved the submitted version.

FUNDING

This paper was supported by the TRIATLAS project, which has received funding from the European Union's Horizon 2020 research and innovation programme under grant agreement No 817578.

ACKNOWLEDGMENTS

We would like to gratefully acknowledge and thank the two reviewers for their comments that helped us improve the manuscript and Johannes Karstensen from the GEOMAR Helmholtz Centre for Ocean Research in Kiel for his helpful suggestions and bibliographic input. This work was supported by the European Union's Horizon 2020 research and innovation program under grant agreements no. 817578 (TRIATLAS), the TOEddies and BIOSWOT CApeCauldron CNES-TOSCA and the ENS Chaire Chanel research grants. We also acknowledge the mesoscale calculation server CICLAD (http://ciclad-web.ipsl.jussieu.fr) dedicated to Institut Pierre Simon Laplace modeling effort for technical and computational support.

SUPPLEMENTARY MATERIAL

The Supplementary Material for this article can be found online at: https://www.frontiersin.org/articles/10.3389/fmars.2022.835260/full#supplementary-material

REFERENCES

Amores, A., Jordà, G., Arsouze, T., and Le Sommer, J. (2018). Up to What Extent Can We Characterize Ocean Eddies Using Present-Day Gridded Altimetric Products? *J. Geophys. Res.: Oceans* 123, 7220–7236. doi: 10.1029/2018JC014140

Amos, C. M., Castelao, R. M., and Medeiros, P. M. (2019). Offshore Transport of Particulate Organic Carbon in the California Current System by Mesoscale Eddies. *Nat. Commun.* 10, 1–21. doi: 10.1038/s41467-019-12783-5

Arhan, M., Mercier, H., and Lutjeharms, J. R. E. (1999). The Disparate Evolution of Three Agulhas Rings in the South Atlantic Ocean. *J. Geophys. Res.: Oceans* 104, 20987–21005. doi: 10.1029/1998JC900047

Arhan, M., Speich, S., Messager, C., Dencausse, G., Fine, R., and Boye, M. (2011). Anticyclonic and Cyclonic Eddies of Subtropical Origin in the Subantarctic Zone South of Africa. *J. Geophys. Res.: Oceans* 116, 1–22. doi: 10.1029/2011JC007140

Arístegui, J., and Montero, M. F. (2005). Temporal and Spatial Changes in Plankton Respiration and Biomass in the Canary Islands Region: The Effect of Mesoscale Variability. *J. Mar. Syst.* 54, 65–82. doi: 10.1016/j.jmarsys.2004.07.004

Arístegui, J., Sangrá, P., Hernández-León, S., Cantón, M., Hernández-Guerra, A., and Kerling, J. (1994). Island-Induced Eddies Canary Islands. *Deep-Sea Res.* 41, 1509–1525. doi: 10.1016/0967-0637(94)90058-2

Arístegui, J., Tett, P., Hernández-Guerra, A., Basterretxea, G., Montero, M., Wild, K., et al. (1997). The Influence of Island-Generated Eddies on Chlorophyll Distribution: A Study of Mesoscale Variation Around Gran Canaria. *Deep-Sea Res. I* 44, 71–96. doi: 10.1016/s0967-0637(96)00093-3

Assassi, C., Morel, Y., Vandermeirsch, F., Chaigneau, A., Pegliasco, C., and Morrow, R. (2016). An Index to Distinguish Surface- and Subsurface-Intensified Vortices From Surface Observations. *J. Phys. Oceanography* 46, 2529–2552. doi: 10.1175/JPO-D-15-0122.1

Barceló-Llull, B., Sangrà, P., Pallàs-Sanz, E., Barton, E. D., Estrada-Allis, S. N., Martínez-Marrero, A., et al. (2017). Anatomy of a Subtropical Intrathermocline Eddy. *Deep Sea Res. Part I: Oceanogr. Res. Papers* 124, 126–139. doi: 10.1016/j.dsr.2017.03.012

Barton, E., Arístegui, J., Tett, P., Cantón, M., García-Braun, J., Hernández-León, S., et al. (1998). The Transition Zone of the Canary Current Upwelling Region. *Prog. Oceanography* 41, 455–504. doi: 10.1016/S0079-6611(98)00023-8

Barton, E. D., Arístegui, J., Tett, P., and Pérez, E. N. (2004). Variability in the Canary Islands Area of Filament-Eddy Exchanges. *Prog. Oceanography* 62, 71–94. doi: 10.1016/j.pocean.2004.07.003

Basterretxea, G., Barton, E., Tett, P., Sangrá, P., Navarro-Perez, E., and Arístegui, J. (2002). Eddy and Deep Chlorophyl Maximum Response to Wind-Shear in the Lee of Gran Canaria. *Deep-Sea Res. I* 49, 1087–1101. doi: 10.1016/S0967-0637(02)00009-2

Benazzouz, A., Mordane, S., Orbi, A., Chagdali, M., Hilmi, K., Atillah, A., et al. (2014). An Improved Coastal Upwelling Index From Sea Surface Temperature Using Satellite-Based Approach – The Case of the Canary Current Upwelling System. *Cont. Shelf Res.* 81, 38–54. doi: 10.1016/j.csr.2014.03.012

Blamey, L. K., Shannon, L. ., Bolton, J. J., Crawford, R. J., Dufois, F., Evers-King, H., et al. (2015). Ecosystem Change in the Southern Benguela and the Underlying Processes. *J. Mar. Syst.* 144, 9–29. doi: 10.1016/j.jmarsys.2014.11.006

Blanke, B., Penven, P., Roy, C., Chang, N., and Kokoszka, F. (2009). Ocean Variability Over the Agulhas Bank and its Dynamical Connection With the Southern Benguela Upwelling System. *J. Geophys. Res.* 114, 1–15. doi: 10.1029/2009JC005358

Boebel, O., Lutjeharms, J., Schmid, C., Zenk, W., Rossby, T., and Barron, C. (2003). The Cape Cauldron: A Regime of Turbulent Inter-Ocean Exchange. Deep Sea Research Part II: Topical Studies in Oceanography. *Earth System Science Data* 50, 57–86. doi: 10.1016/s0967-0645(02)00379-x

Brandt, P., Bange, H. W, Banyte, D., Dengler, M., Didwischus, S.-H., and Fischer, T. (2015). On the Role of Circulation and Mixing in the Ventilation of Oxygen Minimum Zones With a Focus on the Eastern Tropical North Atlantic. *Biogeosciences* 12, 489–512. doi: 10.5194/bg-12-489-2015

Brandt, L. K., and Nomura, K. K. (2010). Characterization of the Interactions of Two Unequal Co-Rotating Vortices. *J. Fluid Mech.* 646, 233–253. doi: 10.1017/s0022112009992849

Caldeira, R. M. A., Stegner, A., Couvelard, X., Araújo, I. B., Testor, P., and Lorenzo, A. (2014). Evolution of an Oceanic Anticyclone in the Lee of Madeira Island: *In Situ* and Remote Sensing Survey. *J. Geophys. Res.: Oceans* 119, 1195–1216. doi: 10.13140/2.1.4081.7926

Carton, X. (2001). Hydrodynamical Modeling Of Oceanic Vortices. *Surveys Geophys.* 22, 179–263. doi: 10.1023/a:1013779219578

Carton, X., Ciani, D., Verron, J., Reinaud, J., and Sokolovskiy, M. (2015). Vortex Merger in Surface Quasi-Geostrophy. *Geophys. Astrophys. Fluid Dynamics* 110, 1–22. doi: 10.1080/03091929.2015.1120865

Chaigneau, A., Eldin, G., and Dewitte, B. (2009). Eddy Activity in the Four Major Upwelling Systems From Satellite Altimetr–2007). *Prog. Oceanography* 83, 117–123. doi: 10.1016/j.pocean.2009.07.012

Chaigneau, A., Le Texier, M., Eldin, G., Grados, C., and Pizarro, O. (2011). Vertical Structure of Mesoscale Eddies in the Eastern South Pacific Ocean: A Composite Analysis From Altimetry and Argo Profiling Floats. *J. Geophys. Res.: Oceans* 116, 1–16. doi: 10.1029/2011JC007134

Chelton, D. B, Schlax, M. G., and Samelson, R. M. (2011). Global Observations of Nonlinear Mesoscale Eddies. *Prog. Oceanography* 91, 167–216. doi: 10.1016/j.pocean.2011.01.002

Cornec, M., Claustre, H., Mignot, A., Guidi, L., Lacour, L., Poteau, A., et al. (2021a). Deep Chlorophyll Maxima in the Global Ocean: Occurrences, Drivers and Characteristics. *Global Biogeochem. Cycles* 35, e2020GB006759. doi: 10.1029/2020gb006759

Cornec, M., Laxenaire, R., Speich, S., and Claustre, H. (2021b). Impact of Mesoscale Eddies on Deep Chlorophyll Maxima. *Geophys. Res. Lett.* 48, e2021GL093470. doi: 10.1029/2021gl093470

Correa-Ramirez, M. A., Hormazábal, S., and Yuras, G. (2007). Mesoscale Eddies and High Chlorophyll Concentrations Off Central Chile (29°–39°s). *Geophys. Res. Lett.* 34, 1–5. doi: 10.1029/2007GL029541

Cui, W., Wang, W., Zhang, J., and Yang, J. (2019). Multicore Structures and the Splitting and Merging of Eddies in Global Oceans From Satellite Altimeter Data. *Ocean Sci.* 15, 413–430. doi: 10.5194/os-15-413-2019

Cury, P., and Shannon, L. (2004). Regime Shifts in Upwelling Ecosystems: Observed Changes and Possible Mechanisms in the Northern and Southern Benguela. *Prog. Oceanography* 60, 223–243. doi: 10.1016/j.pocean.2004.02.007

de Marez, C., L'Hégaret, P., Morvan, M., and Carton, X. (2019). On the 3D Structure of Eddies in the Arabian Sea. *Deep Sea Res. Part I: Oceanogr. Res. Papers* 150, 103057. doi: 10.1016/j.dsr.2019.06.003

Desbiolles, F., Blanke, B., Bentamy, A., and Grima, N. (2014). Origin of Fine-Scale Wind Stress Curl Structures in the Benguela and Canary Upwelling Systems. *J. Geophys. Res.: Oceans* 119, 7931–7948. doi: 10.1002/2014JC010015

Dilmahamod, A. F., Aguiar-González, B., Penven, P., Reason, C. J. C., Ruijter, W. P. M. D., Malan, N., et al. (2018). SIDDIES Corridor: A Major East-West Pathway of Long-Lived Surface and Subsurface Eddies Crossing the Subtropical South Indian Ocean. *J. Geophys. Res.: Oceans* 123, 5406–5425. doi: 10.1029/2018jc013828

Dilmahamod, A. F, Karstensen, J., Dietze, H., Löptien, U., and Fennel, K. (2021). Generation Mechanisms of Mesoscale Eddies in the Mauritanian Upwelling Region. *J. Phys. Oceanography* 52(1), 161–182. doi: 10.1175/jpo-d-21-0092.1

Doglioli, A., Blanke, B., Speich, S., and Lapeyre, G. (2007). Tracking Coherent Structures in a Regional Ocean Model With Wavelet Analysis: Application to Cape Basin Eddies. *J. Geophys. Res.* 112, 1–12. doi: 10.1029/2006jc003952

Dritschel, D. G. (1995). A General Theory for Two-Dimensional Vortex Interactions. *J. Fluid Mech.* 293, 269–303. doi: 10.1017/s0022112095001716

Dufois, F., Hardman-Mountford, N. J, Greenwood, J., Richardson, A. J, Feng, M., and Matear, R. J. (2016). Anticyclonic Eddies are More Productive Than Cyclonic Eddies in Subtropical Gyres Because of Winter Mixing. *Sci. Adv.* 2, e1600282. doi: 10.1126/sciadv.1600282

Duncombe Rae, C., Shillington, F., Agenbag, J., Taunton-Clark, J., and Gründlingh, M. (1992). An Agulhas Ring in the South Atlantic Ocean and its Interaction With the Benguela Upwelling Frontal System. Deep Sea Research Part A. *Oceanogr. Res. Papers* 39, 2009–2027. doi: 10.1016/0198-0149(92)90011-H

Du, Y., Yi, J., Wu, D., He, Z., Wang, D., and Fuyuan, L. (2014). Mesoscale Oceanic Eddies in the South China Sea From 1992 to 2012: Evolution Processes and Statistical Analysis. *Acta Oceanol. Sin.* 33, 36–47. doi: 10.1007/s13131-014-0530-6

Flament, P., Lumpkin, R., Tournadre, J., and Armi, L. (2001). Vortex Pairing in an Unstable Anticyclonic Shear Flow: Discrete Subharmonics of One Pendulum Day. *J. Fluid Mech.* 440, 401–409. doi: 10.1017/s0022112001004955

Flierl, G. R. (1981). Particle Motions in Large-Amplitude Wave Fields. *Geophys. Astrophys. Fluid Dynamics* 18, 39–74. doi: 10.1080/03091928108208773

Giulivi, C. F, and Gordon, A. L. (2006). Isopycnal Displacements Within the Cape Basin Thermocline as Revealed by the Hydrographic Data Archive. *Deep Sea Res. Part I: Oceanogr. Res. Papers* 53, 1285–1300. doi: 10.1016/j.dsr.2006.05.011

Gruber, N., Lachkar, Z., Frenzel, H., Marchesiello, P., Münnich, M., McWilliams, J. C., et al. (2011). Eddy-Induced Reduction of Biological Production in Eastern Boundary Upwelling Systems. *Nat. Geosci.* 4, 787–792. doi: 10.1038/ngeo1273

Guerra, L. A. A., Paiva, A. M, and Chassignet, E. P. (2018). On the Translation of Agulhas Rings to the Western South Atlantic Ocean. *Deep Sea Res. Part I: Oceanogr. Res. Papers* 139, 104–113. doi: 10.1016/j.dsr.2018.08.005

Harvey, C. J., Fisher, J. L., Samhouri, J. F., Williams, G. D., Francis, T. B, Jacobson, K. C., et al. (2020). The Importance of Long-Term Ecological Time Series for Integrated Ecosystem Assessment and Ecosystem-Based Management. *Prog. Oceanography* 188, 102418. doi: 10.1016/j.pocean.2020.102418

Hersbach, H., Bell, B., Berrisford, P., Biavati, G., Horányi, A., Muñoz Sabater, J., et al. (2018). *ERA5 Hourly Data on Single Levels From 1979 to Present*. Copernicus Climate Change Service (C3S) Climate Data Store (CDS). doi: 10.24381/cds.adbb2d47

Hutchings, L., van der Lingen, C., Shannon, L., Crawford, R., Verheye, H., Bartholomae, C., et al. (2009). The Benguela Current: An Ecosystem of Four Components. *Prog. Oceanography* 83, 15–32. doi: 10.1016/j.pocean.2009.07.046

Ioannou, A., Stegner, A., Dubos, T., Le Vu, B., and Speich, S. (2020a). Generation and Intensification of Mesoscale Anticyclones by Orographic Wind Jets: The Case of Ierapetra Eddies Forced by the Etesians. *J. Geophys. Res.: Oceans* 125, e2019JC015810. doi: 10.1029/2019jc015810

Ioannou, A., Stegner, A., Dumas, F., and Vu, B. L. (2020b). Three-Dimensional Evolution of Mesoscale Anticyclones in the Lee of Crete. *Front. Mar. Sci.* 7. doi: 10.3389/fmars.2020.609156

Ioannou, A., Stegner, A., Le Vu, B., Taupier-Letage, I., and Speich, S. (2017). Dynamical Evolution of Intense Ierapetra Eddies on a 22 Year Long Period. *J. Geophys. Res.: Oceans* 122, 9276–9298. doi: 10.1002/2017jc013158

Karstensen, J., Schütte, F., Pietri, A., Krahmann, G., Fiedler, B., Grundle, D., et al. (2017). Upwelling and Isolation in Oxygen-Depleted Anticyclonic Modewater Eddies and Implications for Nitrate Cycling. *Biogeosciences* 14, 2167–2181. doi: 10.5194/bg-14-2167-2017

Kirkman, S., Blamey, L., Lamont, T., Field, J., Bianchi, G., Huggett, J., et al. (2016). Spatial Characterisation of the Benguela Ecosystem for Ecosystem-Based Management. *Afr. J. Mar. Sci.* 38, 7–22. doi: 10.2989/1814232X.2015.1125390

Laxenaire, R., Speich, S., Blanke, B., Chaigneau, A., Pegliasco, C., and Stegner, A. (2018). Anticyclonic Eddies Connecting the Western Boundaries of Indian and Atlantic Oceans. *J. Geophys. Res.: Oceans* 123, 7651–7677. doi: 10.1029/2018JC014270

Laxenaire, R., Speich, S., and Stegner, A. (2019). Evolution of the Thermohaline Structure of One Agulhas Ring Reconstructed From Satellite Altimetry and Argo Floats. *J. Geophys. Res.* 124, 8969–9003. doi: 10.1029/2018jc014426

Laxenaire, R., Speich, S., and Stegner, A. (2020). Agulhas Ring Heat Content and Transport in the South Atlantic Estimated by Combining Satellite Altimetry and Argo Profiling Floats Data. *J. Geophys. Res.: Oceans* 125, e2019JC015511. doi: 10.1029/2019jc015511

Lehahn, Y., d'Ovidio, F., Lévy, M., Amitai, Y., and Heifetz, E. (2011). Long Range Transport of a Quasi Isolated Chlorophyll Patch by an Agulhas Ring. *Geophys. Res. Lett.* 38, 1–6. doi: 10.1029/2011GL048588

Le Vu, B., Stegner, A., and Arsouze, T. (2018). Angular Momentum Eddy Detection and Tracking Algorithm (AMEDA) and Its Application to Coastal Eddy Formation. *J. Atmos. Oceanic Technol.* 35, 739–762. doi: 10.1175/jtech-d-17-0010.1

Li, Q.-Y., Sun, L., Liu, S.-S., Xian, T., and Yan, Y.-F. (2014). A New Mononuclear Eddy Identification Method With Simple Splitting Strategies. *Remote Sens. Lett.* 5, 65–72. doi: 10.1080/2150704X.2013.872814

Luko, C. D., Silveira, I. C. A., Simoes-Sousa, I. T., Araujo, J. M., and Tandon, A. (2021). Revisiting the Atlantic South Equatorial Current. *J. Geophys. Res.: Oceans* 126, e2021JC017387. doi: 10.1029/2021jc017387

Lumpkin, R. (2016). Global Characteristics of Coherent Vortices From Surface Drifter Trajectories. *J. Geophys. Res.: Oceans* 121, 1306–1321. doi: 10.1002/2015jc011435

Majumder, S., Goes, M., Polito, P. S, Lumpkin, R., Schmid, C., and Lopez, H. (2019). Propagating Modes of Variability and Their Impact on the Western Boundary Current in the South Atlantic. *J. Geophys. Res.: Oceans* 124, 3168–3185. doi: 10.1029/2018jc014812

Manta, G., Speich, S., Karstensen, J., Hummels, R., Kersalé, M., Laxenaire, R., et al. (2021). The South Atlantic Meridional Overturning Circulation and Mesoscale Eddies in the First GO-SHIP Section at 34.5°S. *J. Geophys. Res.: Oceans* 126, e2020JC016962. doi: 10.1029/2020JC016962

Marchesiello, P., and Estrade, P. (2007). Eddy Activity and Mixing in Upwelling Systems: A Comparative Study of Northwest Africa and California Regions. *Int. J. Earth Sci.* 98, 299–308. doi: 10.1007/s00531-007-0235-6

Marchesiello, P., McWilliams, J. C, and Shchepetkin, A. (2003). Equilibrium Structure and Dynamics of the California Current System. *J. Phys. Oceanography* 33, 753–783. doi: 10.1175/1520-0485(2003)33<753:esadot>2.0.co;2

Matano, R., and Beier, E. (2003). A Kinematic Analysis of the Indian/Atlantic Interocean Exchange. *Deep Sea Res. Part II: Topical Stud. Oceanography* 50, 229–249. doi: 10.1016/s0967-0645(02)00395-8

McDougall, T. J, and Barker, P. M. (2011). *Getting Started With TEOS-10 and the Gibbs Seawater (GSW) Oceanographic Toolbox*. Intergovernmental Oceanographic Commission IOC of Unesco

McGillicuddy, D. J., Anderson, L. A, Bates, N. R, Bibby, T., Buesseler, K. O, Carlson, C. A., et al. (2007). Eddy/Wind Interactions Stimulate Extraordinary Mid-Ocean Plankton Blooms. *Science* 316, 1021–1026. doi: 10.1126/science.1136256

Morrow, R. (2004). Divergent Pathways of Cyclonic and Anti-Cyclonic Ocean Eddies. *Geophys. Res. Lett.* 31, 1–5. doi: 10.1029/2004gl020974

Moscoso, J. E, Stewart, A. L, Bianchi, D., and McWilliams, J. C. (2021). The Meridionally Averaged Model of Eastern Boundary Upwelling Systems (Mamebusv1.0). *Geosci. Model. Dev.* 14, 763–794. doi: 10.5194/gmd-14-763-2021

Nagai, T., Gruber, N., Frenzel, H., Lachkar, Z., McWilliams, J. C, and Plattner, G.-K. (2015). Dominant Role of Eddies and Filaments in the Offshore Transport of Carbon and Nutrients in the California Current Systems. *J. Geophys. Res.: Oceans* 120, 5318–5341. doi: 10.1002/2015JC010889

Ndoye, S., Capet, X., Estrade, P., Sow, B., Dagorne, D., Lazar, A., et al. (2014). SST Patterns and Dynamics of the Southern Senegal-Gambia Upwelling Center. *J. Geophys. Res.: Oceans* 119, 8315–8335. doi: 10.1002/2014jc010242

Nencioli, F., Olmo, G. D, and Quartly, G. D. (2018). Agulhas Ring Transport Efficiency From Combined Satellite Altimetry and Argo Profiles. *J. Geophys. Res.: Oceans* 123, 5874–5888. doi: 10.1029/2018jc013909

Pegliasco, C., Chaigneau, A., and Morrow, R. (2015). Main Eddy Vertical Structures Observed in the Four Major Eastern Boundary Upwelling Systems. *J. Geophys. Res: Oceans* 120, 6008–6033. doi: 10.1002/2015JC010950

Pegliasco, C., Chaigneau, A., Morrow, R., and Dumas, F. (2020). Detection and Tracking of Mesoscale Eddies in the Mediterranean Sea: A Comparison Between the Sea Level Anomaly and the Absolute Dynamic Topography Fields. *Adv. Space Res* 68(2), 401–419. doi: 10.1016/j.asr.2020.03.039

Pelegrí, J. L, and Benazzouz, A. (2015). Coastal Upwelling Off North-West Africa. *Oceanogr. Biol. Features Canary Curr. Large Mar. Ecosyst.* 115, 93–103.

Polito, P. S, and Sato, O. T. (2015). Do Eddies Ride on Rossby Waves? *J. Geophys. Res.: Oceans* 120, 5417–5435. doi: 10.1002/2015jc010737

Richardson, P., and Garzoli, S. (2003). Characteristics of Intermediate Water Flow in the Benguela Current as Measured With RAFOS Floats. *Deep-Sea Res. II* 50, 87–118. doi: 10.1016/S0967-0645(02)00380-6

Rusciano, E., Speich, S., and Ollitrault, M. (2012). Interocean Exchanges and the Spreading of Antarctic Intermediate Water South of Africa. *J. Geophys. Res.: Oceans* 117, 1–21. doi: 10.1029/2012JC008266

Sangrà, P., Auladell, M., Marrero-Díaz, A., Pelegrí, J., Fraile-Nuez, E., Rodríguez-Santana, A., et al. (2007). On the Nature of Oceanic Eddies Shed by the Island of Gran Canaria. *Deep-Sea Res. I* 54, 687–709. doi: 10.1016/j.dsr.2007.02.004

Sangrà, P., Pascual, A., Rodríguez-Santana, Á., Machín, F., Mason, E., McWilliams, J. C., et al. (2009). The Canary Eddy Corridor: A Major Pathway for Long-Lived Eddies in the Subtropical North Atlantic. *Deep Sea Res. Part I: Oceanogr. Res. Papers* 56, 2100–2114. doi: 10.1016/j.dsr.2009.08.008

Sangrà, P., Pelegrí, J. L, Hernández-Guerra, A., Arregui, I., Martín, J. M, Marrero-Díaz, A., et al. (2005). Life History of an Anticyclonic Eddy. *J. Geophys. Res.* 110, 1–19. doi: 10.1029/2004JC002526

Schütte, F., Brandt, P., and Karstensen, J. (2016a). Occurrence and Characteristics of Mesoscale Eddies in the Tropical Northeastern Atlantic Ocean. *Ocean Sci.* 12, 663–685. doi: 10.5194/os-12-663-2016

Schütte, F., Karstensen, J., Krahmann, G., Hauss, H., Fiedler, B., Brandt, P., et al. (2016b). Characterization of 'Dead-Zone' Eddies in the Eastern Tropical North Atlantic. *Biogeosciences* 13, 5865–5881. doi: 10.5194/bg-13-5865-2016

Souza, J. M. A., de Boyer Montégut, C., and Traon, P.-Y. L. (2011). Comparison Between Three Implementations of Automatic Identification Algorithms for the Quantification and Characterization of Mesoscale Eddies in the South Atlantic Ocean. *Ocean Sci.* 7, 317–334. doi: 10.5194/os-7-317-2011

Stegner, A. (2014). Oceanic Island Wake Flows in the Laboratory, in Modeling Atmospheric and Oceanic Flows: Insights From Laboratory Experiments and Numerical Simulations. *Remote Sens. Lett.*, 265–276. doi: 10.13140/2.1.4081.7926

Stegner, A., Vu, B. L, Dumas, F., Ghannami, M. A, Nicolle, A., Durand, C., et al. (2021). Cyclone-Anticyclone Asymmetry of Eddy Detection Ongridded Altimetry Product in the Mediterranean Sea. *J. Geophys. Res.: Oceans* 126, e2021JC017475. doi: 10.1029/2021JC017475

Stevens, B., Bony, S., Farrell, D., Ament, F., Blyth, A., Fairall, C., et al. (2021). EUREC4A. Earth System Science Data 13, 4067–4119. doi: 10.5194/essd-13-4067-2021

Stramma, L., Bange, H. W, Czeschel, R., Lorenzo, A., and Frank, M. (2013). On the Role of Mesoscale Eddies for the Biological Productivity and Biogeochemistry in the Eastern Tropical Pacific Ocean Off Peru. *Biogeosciences* 10, 7293–7306. doi: 10.5194/bg-10-7293-2013

Tian, F., Wu, D., Yuan, L., and Chen, G. (2019). Impacts of the Efficiencies of Identification and Tracking Algorithms on the Statistical Properties of Global Mesoscale Eddies Using Merged Altimeter Data. *Int. J. Remote Sens.* 41, 2835–2860. doi: 10.1080/01431161.2019.1694724

Veitch, J. A., and Penven, P. (2017). The Role of the Agulhas in the Benguela Current System: A Numerical Modeling Approach. *J. Geophys. Res.: Oceans* 122, 3375–3393. doi: 10.1002/2016JC012247

Villar, E., Farrant, G. K, Follows, M., Garczarek, L., Speich, S., Audic, S., et al. (2015). Ocean Plankton. Environmental Characteristics of Agulhas Rings Affect Interocean Plankton Transport. *Science* 348, 1261447–1261447. doi: 10.1126/science.1261447

Wang, Y., Castelao, R. M, and Yuan, Y. (2015). Seasonal Variability of Alongshore Winds and Sea Surface Temperature Fronts in Eastern Boundary Current Systems. *J. Geophys. Res.: Oceans* 120, 2385–2400. doi: 10.1002/2014jc010379

Wang, Y., Liu, J., Liu, H., Lin, P., Yuan, Y., and Chai, F. (2021). Seasonal and Interannual Variability in the Sea Surface Temperature Front in the Eastern Pacific Ocean. *J. Geophys. Res.: Oceans* 126, e2020JC016356. doi: 10.1029/2020jc016356

Wang, Y., Zhang, H.-R., Chai, F., and Yuan, Y. (2018). Impact of Mesoscale Eddies on Chlorophyll Variability Off the Coast of Chile. *PLoS One* 13, e0203598. doi: 10.1371/journal.pone.0203598

Yasuda, I. (1995). Geostrophic Vortex Merger and Streamer Development in the Ocean With Special Reference to the Merger of Kuroshio Warm Core Rings. *J. Phys. Oceanogr.* 25, 979. doi: 10.1175/1520-0485(1995)025<0979:gvmasd>2.0.co;2

Yasuda, I., and Flierl, G. R. (1995). Two-Dimensional Asymmetric Vortex Merger: Contour Dynamics Experiment. *J. Oceanography* 51, 145–170. doi: 10.1007/BF02236522

Conflict of Interest: The authors declare that the research was conducted in the absence of any commercial or financial relationships that could be construed as a potential conflict of interest.

frontiers | Frontiers in Marine Science

ORIGINAL RESEARCH
published: 11 July 2022
doi: 10.3389/fmars.2022.831098

Volume and Heat Transports by North Brazil Current Rings

Luana F. Bueno[1]*, *Vladimir S. Costa*[1,2], *Guilherme N. Mill*[1,3] and *Afonso M. Paiva*[1]

[1] Ocean Engineering Program – COPPE, Universidade Federal do Rio de Janeiro, Rio de Janeiro, Brazil, [2] Ocean Predictions and Applications Division, Centro Euro-Mediterraneo sui Cambiamenti Climatici, Lecce, Italy, [3] Department of Oceanography, Universidade Federal do Espírito Santo, Vitória, Brazil

A methodology that combines a 24-year long (January 1993 to December 2016) global dataset of eddy trajectories, derived from altimetry, with vertical temperature and salinity profiles from the EN4.2.0 database, derived from XBTs/MBTs, CTDs and Argo floats, was used to reconstruct the mean vertical structure of North Brazil Current (NBC) rings, and to calculate some of their properties. The number of NBC rings formed each year varied from 2 to 8, with an annual-mean formation of 5.3 ± 1.5. During the analyzed period, 112 rings were sampled at least once, at various distances from the center of the rings, leading to a total of 1323 (604) temperature (salinity) profiles available to compute the mean NBC ring, depicting a large, surface intensified, and relatively shallow ring, with intense temperature and salinity anomalies. The meridional volume transport was estimated in 1.3 Sv (1Sv = 10^6 m^3s^{-1}) per ring, leading to an annualized transport of ~7 ± 2 Sv. The amount of South Atlantic Water (SAW) within the mean ring was estimated in ~40 to 60% of the ring volume. According to these estimates, NBC rings may be responsible in different years for approximately 20 to 80% of the northward volume transport associated with the upper limb of the Atlantic Meridional Overturning Circulation (AMOC), and approximately 15 to 55% of the meridional heat transport in the tropical Atlantic.

Keywords: inter-hemispheric exchange, AMOC, South Atlantic Water transport, NBC ring variability, NBC mean ring

Edited by:
Ronald Buss de Souza,
National Institute of Space Research (INPE), Brazil

Reviewed by:
Rafael Cervantes,
Instituto Politécnico Nacional (IPN), Mexico
Mark Jury,
University of Puerto Rico at Mayagüez, Puerto Rico

Correspondence:
Luana F. Bueno
luferraz06@hotmail.com

Specialty section:
This article was submitted to Physical Oceanography, a section of the journal Frontiers in Marine Science

Received: *08 December 2021*
Accepted: *25 May 2022*
Published: *11 July 2022*

Citation:
Bueno LF, Costa VS, Mill GN and Paiva AM (2022) Volume and Heat Transports by North Brazil Current Rings. Front. Mar. Sci. 9:831098. doi: 10.3389/fmars.2022.831098

1 INTRODUCTION

The North Brazil Current (NBC) is an intense western boundary current which crosses the equator and retroflects around 6° to 8°N, feeding the North Equatorial Counter Current - NECC (Schott et al., 1998). Throughout the year, the NBC retroflection sheds isolated warm-core rings that can reach more than 450 km in overall diameter (Johns et al., 1990; Richardson et al., 1994; Fratantoni et al., 1995; Johns et al., 2003). These large features propagate northwestward along the South American coast (Ffield, 2005) and represent a major contribution to the transport of South Atlantic water that crosses the equator into the North Atlantic Subtropical Gyre (Jonhs et al., 1990; Didden & Schott, 1993; Richardson et al., 1994). Such upper-ocean transport is required, as part of the Atlantic Meridional Overturning Circulation (AMOC), in order to compensate for the southward export of North Atlantic Deep Water (NADW) in the deep ocean. The remainder of the AMOC upper-ocean flow in this region is transported by shallow coastal currents along the South American shelf

(Halliwell et al., 2003) and by Ekman transport in the ocean interior (Candela et al., 1992). The NBC rings may also present a significant contribution to the total meridional heat transport at low latitudes (Garzoli et al., 2003).

After being shed at the retroflection the NBC rings translate for three to four months until they reach the Lesser Antilles, experiencing significant depth variations of the water column (from approximately 500 to 4000m, in particular at their southwestern border) along their trajectories. Interaction with the complex bottom topography may have an impact on the rings' pathway, and in some cases on their shape, dynamics, and vertical structure (Fratantoni et al., 1995; Fratantoni and Glickson, 2002). Different vertical structures may also reflect different conditions at the retroflection, leading to shallow surface-intensified rings, deep-reaching surface-intensified rings, and subsurface intensified rings (Wilson et al., 2002). Surface intensified rings are associated with positive sea level anomaly (SLA), which can be tracked with satellite altimetry data, while subsurface intensified rings have little or no surface signal (Johns et al., 2003).

Estimates on the number of NBC rings formed per year vary from 2 to 9 in the literature, since they were first identified by Johns et al. (1990) using color scanner imagery, as more data from *in situ* and satellite observations have become available. Didden and Schott (1993) were able to track 5 rings, from their formation at the retroflection until 60°W, in approximately two and a half years of Geosat sea level anomaly (SLA) data. Shortly after, Richardson et al. (1994) followed 6 different rings along their trajectory, from 1989 to 1992, using surface and subsurface drifters. Goni and Johns (2001) provided the first satellite-based census of NBC rings, based on Topex/Poseidon data from 1992 to 1998, and found 2 to 7 rings forming each year. From a total of 34 rings identified during the 6-year long period of available observations, 24 originated at the retroflection and 10 possibly so, resulting in an average of 4 to almost 6 NBC rings per year. Latter, Goni and Johns (2003) updated these estimates with a longer (10 years) period of altimetry data, finding 3 to 7 rings formed at different years. Their average of 5-6 rings per year is close to the 6 NBC rings identified each year from September 1997 to September 2000 by Fratantoni and Glickson (2002), using ocean color data. Johns et al. (2003) raised these estimates to 8-9 NBC rings per year, based on 20 months of direct measurements taken on cruise surveys and moored current meters. Sharma et al., 2009 using drifting buoys, ADCP and satellite data identified during 8 years the formation of 5 to 8 rings over the period of 1 year. More recently, long period studies such as Jochumsen et al. 2010, which used 15 years of modeling data, estimated an averaged shedding of 6.8 rings per year. Mélice and Arnault (2017) provided an updated census based on almost 23 years of altimeter data and found from 2 to 7 NBC rings formed at different years, with an average of 5 rings per year. Recently, Aroucha et al. (2020) applied an eddy detection algorithm based on dynamical and geometrical constraints in the NBC region for 24 years of altimetry data found an averaged shedding rate of 5 rings per year.

Estimates on the volume transport per ring have been more consistent throughout the literature, and most authors agree with the average value of roughly 1Sv first proposed by Johns et al. (1990). If one considers the large range of values reported for the number of rings formed each year, such estimates lead to annualized transports as low as 2Sv or as high as 9Sv. These figures correspond to 15% up to 70% of the canonical 13Sv required to close the AMOC transport at low latitudes (Schmitz Jr. and McCartney, 1993). More recent estimates performed by Johns et al. (2003), based on *in situ* observations of a large number of NBC rings, indicate a transport of 1.1Sv per ring, corresponding solely to that portion of water with origin in the South Atlantic ocean.

The contribution of NBC rings to the meridional heat transport has been estimated considering their volume transport, and the difference between the temperature within the ring and that of the deep portions of the AMOC. Fratantoni et al. (1995) evaluated 5 rings sampled during one year by a fixed mooring line, finding a total transport of 0.18PW, with an average of 0.036PW per ring. Garzoli et al. (2003) computed the volume transport for 11 NBC rings sampled for 18 months and assumed a fixed temperature difference of 15°C, finding a mean annualized transport of 0.54PW, with an averaged 0.07PW per ring. These two estimates place the contribution of NBC rings to the meridional heat transport at low latitudes (~1PW, according to Ganachaud and Wunsch, 2000) as something between 20% and 50% of the total transport.

The large variation on the estimates provided by previous studies leads to uncertainties regarding the real contribution of NBC rings to the total meridional volume and heat transports of the AMOC. In order to improve on these estimates, the present study makes use of two extensive and continuous series of surface and subsurface data. Ring shedding and translation are identified from the 24-year long Mesoscale Eddy Trajectory Atlas – META product (Schlax and Chelton, 2016) derived from satellite altimetry data. Historical temperature and salinity profiles compiled by the Met Office Hadley Center (EN4.2.0) are used to analyze the vertical structure of the rings. By combining both products, the vertical structure of the mean NBC ring is reconstructed, its heat and salt anomalies are evaluated, and the associated annual volume and heat transports are estimated.

This paper is organized as follows. The automatic eddy detection global dataset and the historical compilation of vertical temperature and salinity profiles are described in section 2, together with the methodology used to reconstruct the mean NBC ring. In section 3, results are presented detailing the NBC ring formation during the 24 years of analysis, the vertical structure of the mean NBC ring, and the annualized volume, and heat transports. Two individual rings that were intensely sampled, one by Eulerian methods (hydrographical profiles) and one by Lagrangian methods (ARGO floats) are also analyzed, and their structure is compared to that of the mean ring. A general discussion on the contribution of the NBC rings to the total volume and heat transports of the AMOC, and the main conclusions are then presented in section 4.

2 DATASETS AND METHODS

2.1 The Data

META2.0 DT is an altimetry-based global dataset of eddy trajectories and properties, from January 1993 to December 2016, distributed by Archiving Validation and Interpretation of Satellite Data in Oceanography (AVISO – https://www.aviso.altimetry.fr/en/data/products/). The methodology of Schlax and Chelton (2016), which is a modified version of Chelton et al. (2011), employs an automatic detection and tracking algorithm applied to daily high-pass filtered grid fields of Sea Level Anomaly (SLA), which contains only mesoscale variability. Anticyclonic (cyclonic) eddies are identified and tracked as coherent structures surrounding local SLA maximum (minimum) values. On each local maximum or minimum, the algorithm searches the points around it to extend the area detected as an eddy, following some rules, such as: the tested area must be equal or smaller in amplitude than the area already defined; the distance between the two remotest points must be less than 700km for latitudes lower than +/-25° of latitude; the maximum area must not exceed 2000 pixels; and no-holes are not allowed on the edges and within the interior of the area. If the tested area is not already included in the detection region of another eddy, an eddy is considered as detected. Any further detection on this area is stopped. Only eddy trajectories longer than (or equal to) 4 weeks are retained. For each eddy detected, the following properties are defined: (i) amplitude, which is the difference between the maximum (minimum) sea surface high (SSH) value and the averaged SSH over the edge pixels that define the outer perimeter of the eddy; (ii) radius of maximum velocity; and (iii) rotational velocity, which is the average of geostrophic speed over the radius of maximum velocity. This same methodology has been successful applied by other authors, such as Arur et al. (2014) in their study of eddies in the Indian Ocean, Jufaili and Piontkovski (2020) for eddies in the western Arabian Sea, and Brokaw et al. (2020) for eddies generated by the Loop Current in the eastern Gulf of Mexico. A newer version of mesoscale eddy trajectory atlas product META3.1 DT was made available recently and uses a different algorithm based on py-eddy-tracker to detect eddies. According to Pegliasco et al. (2022) the major differences between both dataset comes from the detection algorithm and the newest version contains smaller eddies and shorter trajectories, aspects that are not mandatory for the objective of this study, since small eddies of shorter lifetime are poorly sampled.

The temperature (T) and salinity (S) profiles from the EN4.2.0 dataset (https://www.metoffice.gov.uk/hadobs/en4/), used to compute the mean vertical structure of the NBC rings, combine data from WOD09 (World Ocean Database), GTSPP (Global Temperature and Salinity Profile Program), and Argo Global Data Assembly Centers (GDACs), and is available from 1900 to the present. This data has undergone quality control, as described by Good et al. (2013). However, bad data were still identified between 1993 and 2016 in our study area, and based on Pegliasco et al. (2015) a more restrictive criterion has been applied in which the depth difference between two consecutive data does not exceed the following threshold: 25 m for the 0–150 m layer, 50 m for the 150–300 m layer, 75 m for the 300–500 m layer and 100 m below 500 m depth. Only profiles that extend beyond 500m, and with data within three standard deviations from the local average were retained.

2.2 Identification and Tracking of the NBC Rings

The NBC rings were identified as those anticyclonic eddies in the META product that originated between 3°N and 10°N, and 44°W and 55°W (**Figure 1**). The ring formation area was defined considering: (a) the mean position of the NBC retroflection, between latitudes 6°N and 8°N, and longitudes 49°W and 50°W (Didden and Schott, 1993; Richardson et al., 1994); (b) its reported seasonal variability, oscillating between 45°W and 55°W (Flagg et al., 1986; Schott et al., 1998; Garzoli et al., 2004; Goes et al., 2005); and (c) previous identification in the literature of NBC rings up to 10°N (Richardson et al., 1994; Goni and Johns, 2001;

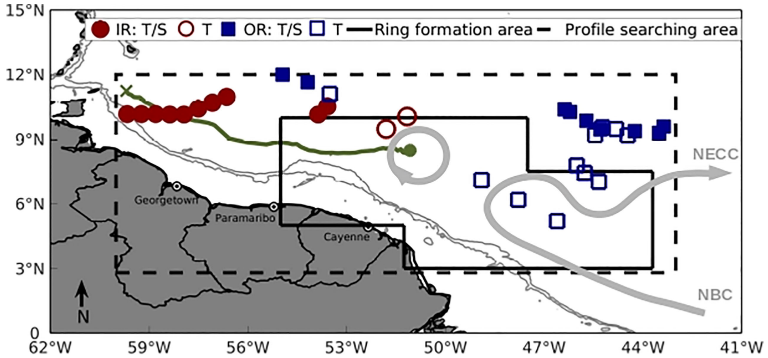

FIGURE 1 | Searching area (dashed lines) for T and S profiles and for ring trajectories originated at the NBC retroflection (ring formation area, defined by solid lines). See text for details. The green line indicates the trajectory of one NBC ring, originated near 51°W and 8°N, illustrating the selection of T and S profiles as IR (circles) or OR (squares). Filled markers indicate that T and S profiles were available (from CTD casts or ARGO floats), while empty markers indicate that only T profiles were available (from MBTs or XBTs). The ring, the NBC and NECC are illustrated schematically by the thick gray lines, for reference. The thin gray lines are the 200 and 1000 m isobaths.

Fratantoni and Glickson, 2002; Garzoli et al., 2003). Rings originating from other regions that crossed the ring formation area were not classified as NBC rings and were disregarded in the following analysis, which take into account only the anticyclonic rings that had their first and unique appearance within the established area. NBC rings were then followed along their northwestward trajectories until reaching 12°N or 60°W. These end-limits were imposed in order to eliminate from the analysis the rings after they interact with the bathymetric obstacles established by the Lesser Antilles Arc System, which significantly deform their shape, and possibly their vertical structure.

2.3 Reconstructing the Mean Ring

After identification and tracking, META and EN4.2.0 datasets were combined by selecting and classifying, within the study area, those T and S profiles that were taken either inside or outside a ring. Inside ring profiles were used to reconstruct the mean vertical structure of the NBC ring. The mean ring volume transport and its T and S anomalies compared to the outside environment (evaluated from the outside ring profiles) were then calculated. Considering the total number of rings formed each year (as provided by META) it was then possible to estimate the total contribution of NBC rings to the meridional volume and heat transports.

The area inside a NBC ring was assumed as that within 2R from the ring center, in which R is the radius of maximum speed provided by the META product. Once defined the limits of the ring influence, the T and S profiles were classified into two categories depending on their distances from the center of the ring, considering all profiles within the searching area (dashed rectangle in **Figure 1**) and the ring location for a given date during its trajectory. The profiles captured by the rings, or those located within a maximum distance of 2R from the center, were classified as Inside-Ring (IR) profiles. IR profiles were used to reconstruct the mean NBC ring. The profiles located at distances larger than 2.5R from the center, and limited by the searching area were classified as Outside-Ring (OR) profiles. OR profiles were used to estimate the mean state of the area of occurrence of NBC rings, and to evaluate the rings T and S anomalies. Profiles located between 2R and 2.5R were not considered in the analysis, to avoid uncertainties regarding the real extent of the influence of each ring.

This methodology is illustrated in **Figure 1** for one single NBC ring, the trajectory of which is shown as the green line originating near 51°W and 8°N. From a total of 32 profiles that were taken from the time this ring was first identified within the ring formation area (solid lines in the figure) until it left the searching area (dashed lines), 10 T/S profiles and 2 T-only profiles (filled and empty circles, respectively) where located within 2R from the center of the ring and were classified as IR, while 9 T/S profiles and 10 T-only profiles (filled and empty squares, respectively) where beyond 2.5R and were classified as OR. Care was taken in order not to duplicate OR profiles when two or more rings were observed simultaneously within the searching area. This was possible since each profile in the EN4.2.0 dataset has a unique code, allowing for duplicated profiles to be excluded at the end of the profile selection. From the total number of profiles originally identified within the searching area in the EN4.2.0 dataset, 70% of the T profiles (or 5772) and 60% of the S profiles (or 2746) remained after the quality control procedure. A total of 1323 T and 604 S profiles were classified as IR, and 4449 T and 2142 S profiles as OR (**Table 1** and **Figure 2**). Circa 50% of the temperature data were profiled by XBTs/MBTs, which explains why the number of T profiles is larger than the number of S profiles (originated from CTD casts and ARGO floats). The OR ARGO and XBT profiles are homogeneously distributed within the profile searching area, while IR profiles are concentrated along the path of the NBC rings, as expected (see **Figure 2**). The OR CTD casts are somewhat more concentrated at the NBC retroflection region, with only four sections (64 T and 65 S profiles) sampling NBC rings. More than half of OR and IR and ARGO and CTD profiles reach 2000m depth, while XBTs are somewhat well distributed among 1000, 12000 and 2000m. Considering all the NBC rings identified and followed along their trajectories, about 88% were sampled by T and/or S profiles at least once.

In order to obtain the three-dimensional structure of the mean NBC ring, the T and S IR profiles were interpolated following Yang et al. (2013). First, the location of all profiles was transformed into a normalized ring-coordinate space (**Figure 3**), according to:

$$D_{MR} = \frac{D_R}{R_R} R_{MR} \tag{1}$$

in which D_{MR} is the profile equivalent distance from the ring center for the reconstructed mean ring, D_R is the instantaneous distance from each profile to the observed ring center (considering the geographical locations given by EN4.2.0 and META datasets), R_R is the instantaneous radius of maximum speed for each ring, taken from META at the same time as the profile observations, and R_{MR} is the average radius for all rings (also from META). Assuming circular rings (as implicit in Eq. 1) may not be perfectly true (see, for instance, Fratantoni and Glickson, 2002), in particular in latter stages of their life cycle in which interaction with topography may have deformed somewhat their shape. It is, however, a limitation of the META dataset in which the ring radius is taken as that of a circle which better represents, on an average sense, the region of maximum swirl velocities.

The resulting distribution of T and S profiles is relatively uniform over the composite ring area (**Figure 3B**), providing adequate data for deriving the mean NBC ring structure. Less data is observed at the southwest quadrant, possibly reflecting the

TABLE 1 | Number of temperature and salinity profiles from the EN4.2.0 dataset remaining after quality control.

	Inside Ring (IR) profiles		Outside Ring (OR) profiles	
Equipment	Temperature	Salinity	Temperature	Salinity
XBT/MBT	687	-	2100	-
Argo Floats	572	539	2144	1938
CTD	64	65	205	204

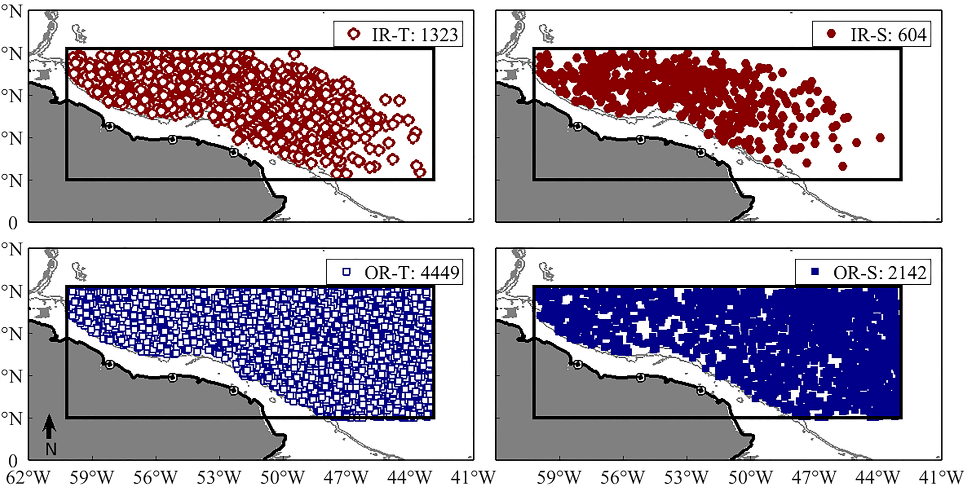

FIGURE 2 | Spatial distribution of the Inside Ring (IR) profiles (upper panels) and Outside Ring (OR) profiles (lower panels) within the searching area from 1993 to 2016, from the EN4.2.0 dataset. Empty markers (left panels) indicate T profiles, while filled markers (right panels) indicate S profiles. The rectangle defined by solid lines delineates the searching area (see text and **Figure 1** for details). The gray lines are the 200 and 1000 m isobaths.

interaction of the rings with topography along the continental margin. The longitudinal distributions of T and S profiles (**Figure 3C**), however, show that more than half (about 77% for T and 71% for S profiles) are distributed eastward of 54°W, indicating that most profiles sampled newly formed rings, which have been little influenced or modified by the interaction with topography. The mean NBC ring T and S cross-sections were calculated assuming symmetry in all directions, projecting all profiles into one side of the ring's radial axis, and mirroring them to the opposite side. This approach is also not perfectly true, but ensures more confidence in the analysis, and leads to a more robust estimate of the mean ring.

Following Souza et al. (2011), a 7th degree Lagrange polynomial was used to fit the T and S data at each depth. This polynomial captures the approximate Gaussian shape of the anomaly distribution corresponding to anticyclonic rings. Both normalization and fitting are essential to obtain the vertical structure of the mean ring. The corresponding NBC mean ring T and S anomaly sections were then calculated, by removing the mean state of the searching area calculated with all the OR

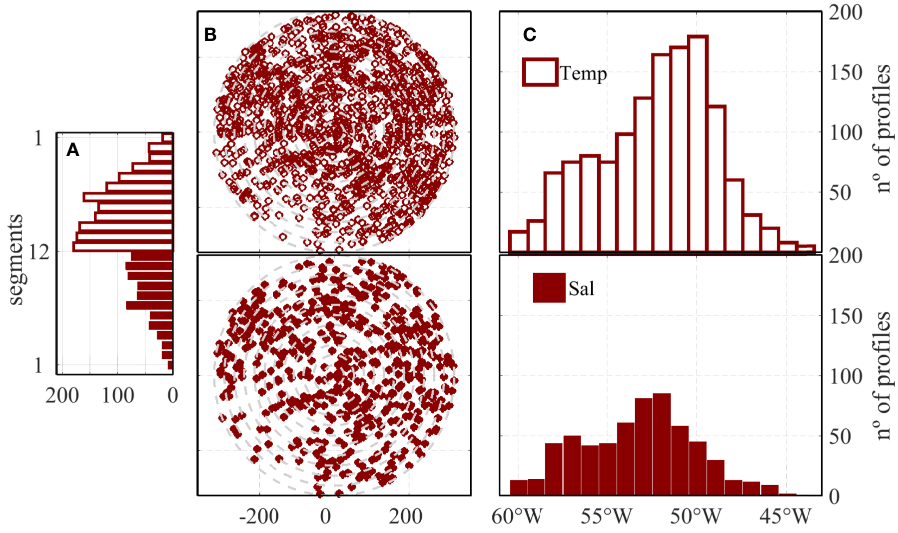

FIGURE 3 | Distribution of the selected IR profiles: **(A)** number of T (upper) and S (lower) profiles in 12 equally spaced intervals along the radius of the mean ring, after normalization according to equation 1; **(B)** spatial distribution of all selected T (upper) and S (lower) profiles, after normalization; and **(C)** number of T (upper) and S (lower) profiles for different longitudinal bands.

profiles. A similar procedure (see details in *Analysis Along Isopycnals*) was then carried out along isopycnals (instead of depth levels) taking into consideration only IR profiles for which T/S pairs were available (so that density could be calculated for each profile). This approach was applied to allow for an estimation of the percentage contribution of South Atlantic waters to the total transport of the mean ring.

3 RESULTS

3.1 Ring Census

A total of 128 NBC rings were identified in the META dataset, originating at the NBC retroflection between January 1993 and December 2016, leading to a mean formation of 5.3 ± 1.5 rings per year. Significant inter-annual variability was observed during these 24 years, with minimum formation of 2 (in 2006 and 2009) and maximum formation of 8 (in 1999) rings per year (**Figure 4A**). Apart from 2006 and 2009, at least four rings were formed each year for the entire period, while 7 or more rings were formed only in 7 different years. Maximum ring formation can be distinctly observed in the boreal summer, with 35 rings (27% of the total) formed in June or July, but large values also occur in the Winter and early Spring months (**Figure 4B**). The lowest formation occurs both in May and from September to November, with no more than 7 rings formed in each month for the entire period of observations. While a semiannual cycle is apparent, with maximum formation both in summer and winter, and minimum in spring and autumn, no clear seasonal cycle could be established for the NBC ring formation based on the META dataset, in accordance with previous studies (Fratantoni et al., 1995; Pauluhn and Chao, 1999; Goni and Johns, 2001; Fratantoni and Glickson, 2002; Goni and Johns, 2003; Johns et al., 2003).

After formation, most rings follow a relatively well-defined path towards the Caribbean (**Figure 5**). In their journey along the South American continental margin, the NBC rings travel on average 840 ± 320 km, with a lifetime of 80 ± 50 days. The large standard deviations reflect the fact that the SSH signal is lost for several rings before reaching the Lesser Antilles. It is not clear, however, if that indicates the demise of such rings or just that the signal has fallen below a detection threshold. About half of the total (68 rings) reach the Antilles, with 2 rings passing through the Caribbean.

Table 2 presents the mean properties of the 128 NBC rings, taken from the META dataset, which are within the range of previously estimated values, such as Johns et al., 1990; Didden and Schott, 1993; Richardson et al., 1994; Fratantoni et al., 1995; Pauluhn and Chao, 1999; Goni and Johns, 2001; Fratantoni and Glickson, 2002; Wilson et al., 2002; Garzoli et al., 2003; Goni and Johns, 2003; Johns et al., 2003 (**Table 3**). Also shown in **Table 2** are the same properties computed only for those 112 rings that were sampled at least once by T and/or S profiles, and that were used to reconstruct the mean NBC ring. Most significant differences are observed for the ring radius (138 ± 43 km for the former, and 160 ± 41 km for the latter), albeit not beyond the reach of the standard deviations, pointing to the fact that the present estimate of the rings mean vertical structure may favor somewhat larger rings. It is interesting to note that the ratio between the azimuthal velocity and the translation speed is larger than one for the mean ring (and also for most individual rings considering their standard deviation), indicating that NBC rings

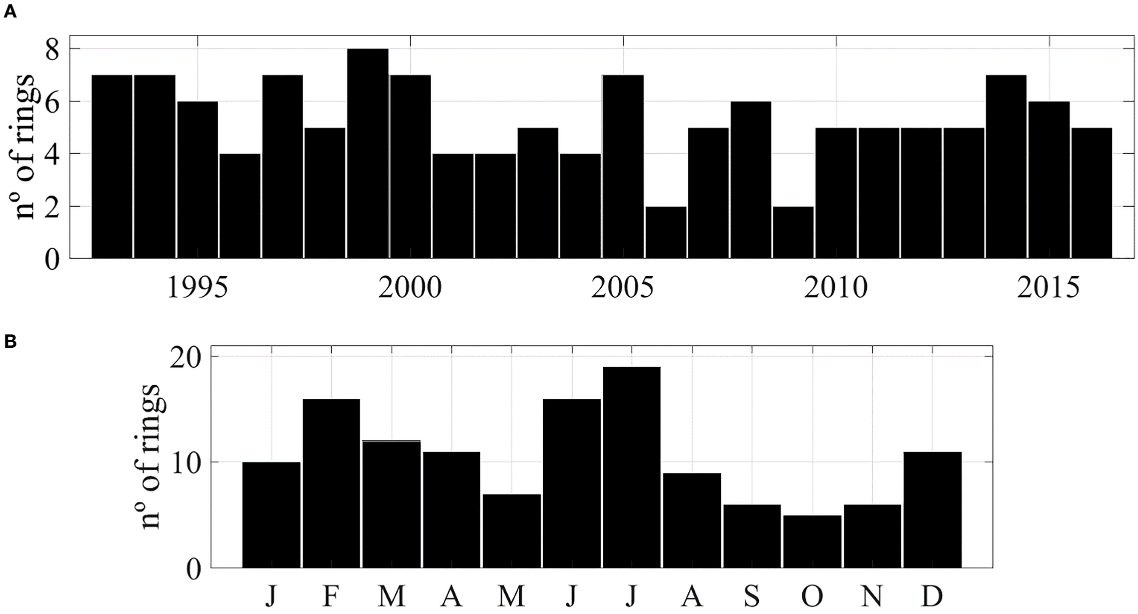

FIGURE 4 | Total number of NBC rings identified in the META dataset: **(A)** for each year, from 1993 to 2016; and **(B)** for each month, for the entire 24-year period. The annual and monthly values were calculated based on the date when each ring was identified for the first time within the ring formation area.

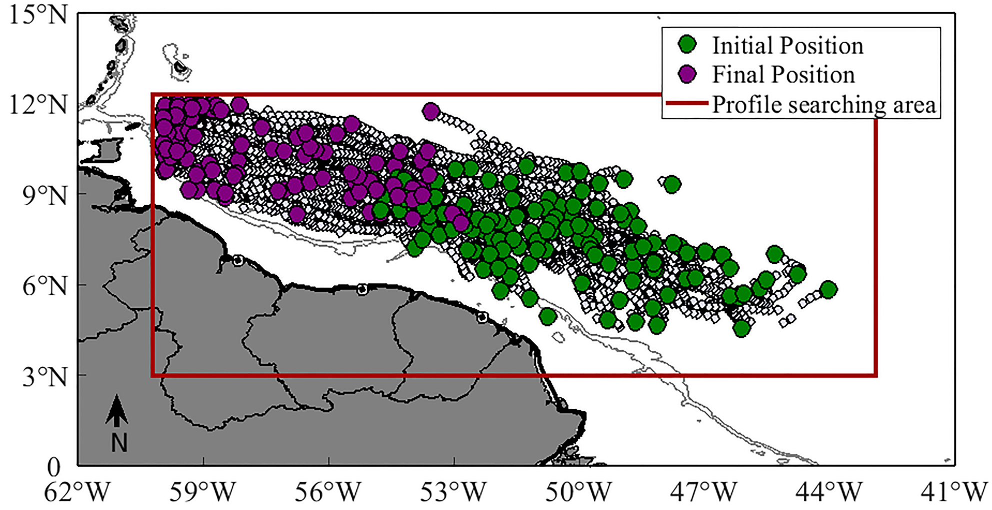

FIGURE 5 | The trajectory of the 128 NBC rings identified in the META dataset (white dots), between 1993 and 2016. Green dots indicate their initial position, and purple dots their final position within the searching area (defined by the red retangle). The gray lines are the 200 and 1000 m isobaths.

TABLE 2 | Mean NBC ring properties derived from the META dataset: radius of maximum surface geostrophic velocities (km), amplitude (10^{-2}m), maximum surface velocity and translation speed (ms^{-1}), estimated for all 128 rings identified in the META dataset, and for the 112 rings that were sampled at least once by T and/or S profiles.

Number ofRings	Radius(km)	Amplitude (10^{-2} m)	Maximum surface velocity (ms^{-1})	Translation speed (ms^{-1})
128	138 ± 43	9 ± 5	0.40 ± 0.01	0.16 ± 0.08
112	160 ± 41	10 ± 4	0.45 ± 0.12	0.16 ± 0.07

TABLE 3 | NBC ring properties from previous observational studies.

References	Number of analyzed rings	Radius of max. velocity (km)	Amplitude (10^{-2} m)	Maximum surface velocity (ms^{-1})	Translation speed (ms^{-1})
Johns et al. (1990)	7	200	–	–	0.11 – 0.17
Didden and Schott (1993)	2	130	10-14	0.4	0.15
Richardson et al. (1994)	7	125	–	0.8	0.09 – 0.14
Fratantoni et al. (1995)	5	112 ± 30	–	0.42 ± 0.15	–
Goni and Johns (2001)	8	100 ± 17	8	–	0.14
Fratantoni and Glickson (2002)	5	100-150	–	–	0.15
Johns et al. (2003)	16	85-160	15-25	1.0	–
Garzoli et al. (2003)	11	195	–	–	0.14
Goni and Johns (2003)	52	100 ± 27	–	–	0.09 - 0.3
Fratantoni and Richardson (2006)	10	125 ± 25	–	0.75 ± 0.15	0.17 ± 0.02*
Sharma et al. (2009)	44	50-250	–	0.7 – 2.0	0.17
Aroucha et al. (2020)	121	138 ± 23.6	9.4 ± 4	0.27 ± 0.08	–

**Evaluated for 6 rings.*

are fairly non-linear and trap water in their interior (Chelton et al., 2011).

3.2 The Mean NBC Ring

3.2.1 Analysis Along Constant Levels

The mean NBC ring, computed for constant levels with the IR profiles according to the methodology presented in section 2, is better visualized as vertical sections of T and S anomalies with respect to the mean OR profile (**Figures 6A, B**). These sections depict a moderately shallow ring, with positive anomalies penetrating down to approximately 500m. Geostrophic velocities referred to 500db (**Figure 6C**) also depict a shallow, surface intensified mean NBC ring. Swirl velocities above 0.1 m/s are observed in the upper 150 to 200 m, while the maximum geostrophic velocity reaches 0.36 m/s, at a distance of ~160km from the center of the mean ring. The 500m depth level

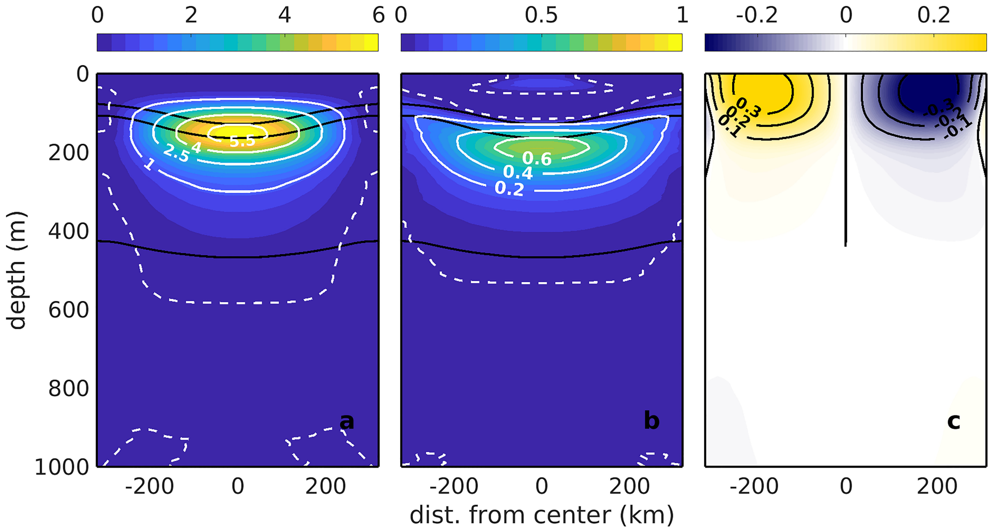

FIGURE 6 | Vertical sections across the mean NBC ring. In **(A, B)** the T and S anomalies, respectively, calculated by subtracting the T and S of all IR profiles from the mean T and S of all OR profiles. The white dashed lines represent the zero anomaly isolines, and the black lines are (from top to bottom) the 24.5, 25.5 and 27.1 kgm^{-3} isopycnals. In **(C)** the anticyclonic geostrophic velocities (in ms^{-1}) of the mean NBC ring, referred to 500db and computed for the Coriolis parameter corresponding to a mean latitude of 8.7°N.

corresponds to the approximate depth of the 27.1 kgm^{-3} isopycnal within the mean ring (also shown in **Figure 6**), which marks the transition between Antarctic Intermediate Waters - AAIW and South Atlantic Central Waters – SACW in the tropics (Stramma and England, 1999). This correspondence indicates that the mean ring transports primarily thermocline waters, or more specifically surface tropical and subsurface central water masses.

The anticyclonic mean ring is, as expected, warmer and saltier than the environment (**Figures 6A, B**). Maximum T and S anomalies at the ring core reach 5.9°C at ~150m depth, and 0.7 at 180m depth, respectively. On the one hand, these are intense anomalies, when contrasted to those reported for anticyclonic mean rings in different regions of the world, and computed with similar methodology, as for example T (S) anomalies of ~2.0°C (0.1) for the Kuroshio region (Yang et al., 2013); ~2°C (0.2 - 0.3) for the southeastern Indian ocean (Yang et al., 2015); ~0.5 to 1.0°C (0.1) for eastern boundary current regions (Pegliasco et al., 2015); and ~2.5°C for Agulhas rings (Souza et al., 2011). On the other hand, the mean NBC ring T and S anomalies compare well with those computed with *in situ* data for three individual NBC rings by Fratantoni and Glickson (2002), which varied from approximately 3 to 6°C, and 0.5 to 1.0, respectively, in the depth range from 100 to 200m. Also in agreement with observations, the surface signature of the NBC mean ring is significantly reduced within the shallow surface mixed layer, due to intense mixing associated with heat and mass exchanges with the atmosphere.

Calculating the outside ring average T and S profiles is an important step to compute the mean NBC ring anomalies. In order to evaluate these profiles estimated based on the OR data from EN4.2.0, the T and S anomalies were compared to those calculated with respect to the WOA13 climatology (World Ocean Atlas 2013, available at www.nodc.noaa.gov/OC5/woa13/). This comparison is illustrated in **Figure 7**, which shows the total T and S anomalies obtained by subtracting the mean IR profile from both the mean OR profile and the WOA13 mean profile for the searching area (defined in **Figure 1**). T and S maximum anomalies (~1.7°C at ~160m, and ~0.3 at ~170m, respectively) are lower than those presented in **Figure 6** as expected, since these estimates take into account the total mean profile for the entire ring, but are very similar for both the EN4.2.0 and the WOA13 cases. Within the mean ring core, S anomalies show no significant difference, while T anomalies computed with respect to the OR profiles are somewhat warmer (by ~0.3°C) than those computed with the WOA13 climatology. This possibly reflects the fact that the climatological profile was computed with all information within the searching area, without distinguishing the inside and outside ring data. Larger differences are observed near the surface, associated with the large T and S spatial variability in the tropical region.

The mean NBC ring was assumed to have a Gaussian shape and to carry the volume of a cylinder, $V = \pi R^2 h$, where R is the radius of maximum velocity and h is the vertical extension. Thus, the volume of the mean NBC ring was estimated in $4 \times 10^{13} m^3$, based on a radius of the maximum velocity of 160km and a vertical extension of 500m, leading to an annualized volume transport of ~1.3Sv per ring by dividing its volume by the number of seconds in one year (following Johns et al., 1990 and Didden and Schott, 1993; Fratantoni and Glickson, 2002; Johns et al., 2003). This value is on the same order, but somewhat larger than the canonical 1Sv, generally assumed in the literature since Johns et al. (1990), but is within the range of previous estimates for individual rings, based on satellite or *in situ* data (see, for instance, Didden and

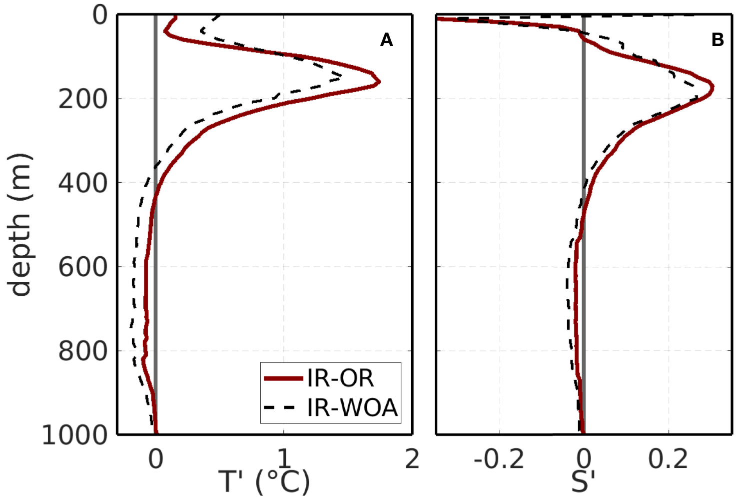

FIGURE 7 | Total mean T **(A)** and S **(B)** NBC ring anomalies with respect to the OR mean profile from EN4.2.0 (solid red line) and to the WOA13 climatology (dashed black lines).

Schott, 1993; Johns et al., 2003). The contribution of the mean NBC ring to the heat transport in the tropics can be estimated using $\rho V c_p \Delta T$, in which ρ is a reference density, V is volume transport, c_p is the specific heat and ΔT is the difference between the mean temperature of the ring and that of a reference level, divided by the number of seconds in one year. A similar computation can be done for the freshwater transport, estimated as $\rho V(1-\Delta S/1000)$, in which ΔS is the difference between the mean salinity of the ring and that at the same reference level. Using the composite structures of T and S, the average temperature of the mean ring was estimated at 16°C and the average salinity was 35.5. Assuming that the water carried by the NBC rings is compensated by the opposite flow of NADW (Garzoli et al., 2003), with mean T~3°C (Broecker, 1991) and mean S~34.9 (Reid and Lynn, 1971), the heat and freshwater transports of the mean NBC ring were estimated in 0.07PW and $0.45\text{x}10^6 \text{kgs}^{-1}$. On the one hand, such an estimate for the heat transport of the mean NBC ring is higher than the averaged transport per ring of 0.036PW, which can be inferred from the results presented by Fratantoni et al. (1995) for five individual rings sampled from 1987 to 1988, of variable size and temperature (which varied from 0.010 ± 0.008 to 0.066 ± 0.019 PW). On the other hand, it is numerically the same average transport computed by Garzoli et al. (2003), from the analysis of eleven individual rings (ranging from 0.06 to 0.10PW) sampled from 1998 to 2000.

3.2.2 Analysis Along Isopycnals

In order to estimate the contribution of waters originating in the South Atlantic to the total volume transport of the mean ring, the previous analysis was also conducted along constant potential densities. In this case, however, only profiles containing both T and S values were considered, corresponding to 1653 OR profiles, 463 profiles within 2R, and 95 profiles within 1R from the ring center. The ratio of South Atlantic Waters - SAW within the mean ring was computed following Johns et al. (2003), considering the salinity values (S) of the mean ring relative to the expected salinity for South (S_S) and North (S_N) Atlantic waters, at each density, given by:

$$SAW = \frac{(S_N - S)}{(S_N - S_S)} \tag{2}$$

In equation 2, S_S and S_N are evaluated as the average of the 10% minimum and maximum salinity values, respectively, for all the available profiles within the study area. As in Johns et al. (2003), such estimates do not differ much from climatological values for S_S, and are slightly saltier for S_N. The curves for S, S_S and S_N are shown in the S-σ_θ diagram in **Figure 8A**.

The mean NBC ring is fresher (negative anomalies, for S-S_N) then North Atlantic waters in density space, from the surface to the lower limits of SACW (σ_θ ~ 27.1kgm^{-3}), indicating northward transport of waters with a distinct South Atlantic signature (e.g., Emery and Dewar, 1982). This picture is in contrast with the positive anomalies computed in depth levels (see **Figure 7**) due to the heaving effect of isopycnals, characteristic of anticyclonic eddies. Maximum anomalies (absolute values of ~0.55) are observed for densities around 25 to 26 kgm^{-3} (**Figure 8B**), corresponding to thermocline levels located roughly from 150 to 200m deep, decreasing towards lower (upper) and higher (deeper) densities (levels). Negative anomalies (absolute values of ~0.02) are also observed within the AAIW domain (σ_θ ~ 27.25kgm^{-3}), decreasing to zero for densities within the North Atlantic Deep Water – NADW. Anomalies computed with all profiles within 2R from the ring center are somewhat lower, but close to those computed only with profiles within 1R from the ring center.

The percentage of SAW in the water column (derived from eq. 2) is shown in density space in **Figure 9**, from the surface down to intermediate levels. Percentages vary from 40 to 60% for the entire

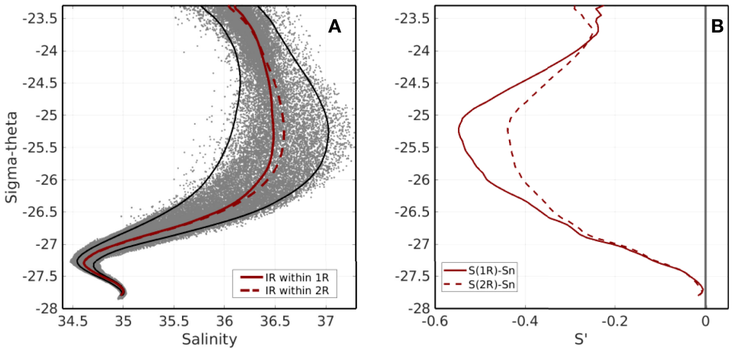

FIGURE 8 | **(A)** S-σ_θ diagram for all IR + OR profiles within the searching area (gray dots), from the subset containing observations with both T and S values. The black lines are the S_S (left) and S_N (right) curves, respectively. The red lines are the average salinity (S) for the mean ring, computed with all IR profiles located within 1R (solid) and 2R (dashed) from the ring center. One standard deviation (not shown) is about 0.5 for σ_θ = 25.5 kgm^{-3}, decreasing for lower and higher densities. **(B)** Salinity anomaly, in density space, of the mean ring with respect to the expected salinity of North Atlantic waters (S_N), for the IR profiles located within 1R (solid) and 2R (dashed) from the ring center.

density range (average of ~50%) with two local maxima at upper SACW or thermocline levels (σ_θ ~ 24 to 25 kgm^{-3}) and at lower SACW and AAIW levels (σ_θ ~ 27.0 to 27.25 kgm^{-3}). Percentages are somewhat lower (average of ~45%) when the anomalies are computed for a mean profile considering the IR profiles within 2R of the ring center, as expected. Considering, as before, a mean ring with geometrical volume of 4x10^{13}m^3, computed for a radius of 160 km (corresponding to the maximum geostrophic velocities) and total depth of 500m, and integrating the SAW ratio from the surface to σ_θ = 27.1 kgm^{-3}, the annualized transport by the mean NBC rings is reduced by approximately 50%, from 1.3Sv to 0.66Sv. This new estimate would represent, in fact, the annualized transport of SAW by the mean NBC ring (see *Discussion and Conclusions* for a discussion on these estimates). Johns et al. (2003) suggest that the anomalies and percentages calculated for σ_θ below 24.5 kgm^{-3} are not reliable, since there is no clear definition of the water mass sources near the surface, and assume a constant percentage value from this isopycnal to the surface. This approach is sensible, but does not change the previous calculations by more than 3%.

3.3 Sampling Two Individual NBC Rings

Two NBC rings, among the 128 identified in this study (or 112 with T and/or S profiles), were more intensely sampled during their lifetime, allowing for a detailed view of their vertical structure. One ring (hereafter ring A) was sampled by a CTD section midway between the retroflection and the Antilles, providing a synoptic view across the center of the

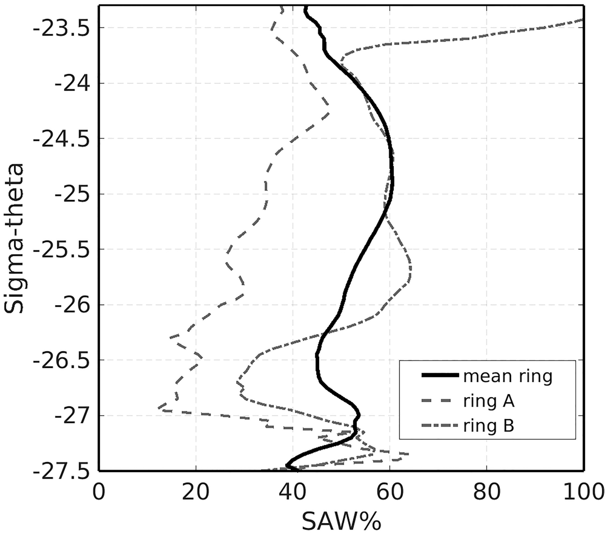

FIGURE 9 | Percentage of South Atlantic Water (SAW) estimated according to Eq. 2 for the mean NBC ring (solid line), ring A (dashed line) and for ring B (dotted-dashed line), considering only profiles located within 1R from the ring center.

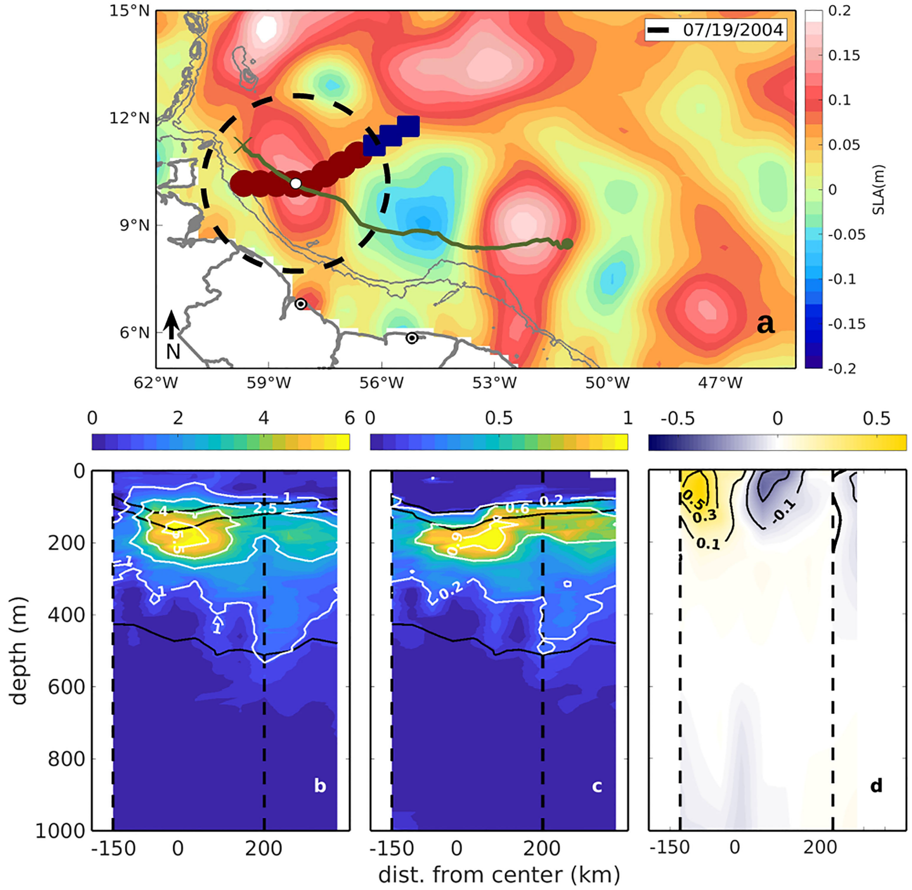

FIGURE 10 | Ring A seen as a positive sea level anomaly near 59°W in **(A)**. The green line is the ring trajectory from the META dataset; the dashed circle corresponds to twice the ring radius (2R), and the brown and blue markers are the positions of the IR and OR profiles, respectively. The T and S anomalies with respect to the ring exterior (the OR profiles) are presented in panels **(B, C)** together with the 24.5, 25.5 and 27.1 kgm^{-3} isopycnals (black lines, from top to bottom); and the geostrophic velocities referred to 550db in panel **(D)**. The vertical dashed lines indicate the limits for the IR profiles. No smoothing was applied to the CTD data.

ring (**Figure 10**). A second ring (hereafter ring B), was sampled by an ARGO float during 64 days, for circa 800 km, providing a Lagrangian view for a significant part of its lifetime (**Figure 11**). Sections of T and S anomalies, with respect to the OR profiles, and geostrophic velocities (for ring A) were built, and the percentages of SAW transported by each ring were calculated, helping to evaluate how representative the mean NBC ring is.

Ring A was first observed in the META dataset on May 30th, 2004, near 8.5°N and 51°W, traveling for approximately two months before its signal was lost near 10°N and 60°W. The CTD section sampled the ring around July 19th, leading to 8 IR profiles and 3 OR profiles, spaced on average by 53 km (**Figure 10A**). The samples were taken down to 2600 m, with the closest profile located approximately 8km from the ring center. The mean radius of Ring A (~134 km) was below average considering the 112 rings sampled by T and S profiles, and average sized considering the 128 tracked in the altimeter data (see **Table 2**). Maximum T anomalies reached ~5.5°C, centered around 150 to 200m depth, similar to the mean ring (compare **Figures 6A**, **10B**). Maximum S anomalies reached ~0.9, about 30% larger than the mean ring, also centered around 150 to 200 m depth (same depth of the maximum T anomaly, unlike the mean ring which presented a somewhat deeper S anomaly core). Both T and S anomaly fields suggest an approximately symmetric ring, somewhat deeper at the offshore side. Geostrophic velocities indicate a surface intensified ring, with significant velocities above 0.1 m/s concentrated in the upper 200m. The inshore side of the ring is more intense than its offshore side, with northwestward (southwestward) velocities reaching 0.5 m/s (0.3 m/s), possibly reflecting the interaction with the continental margin, which tends to squeeze the inshore side of the ring. The velocity structure of Ring A is similar to those of the surface intensified rings classified by Fratantoni et al. (1995) and Wilson et al. (2002) based on *in situ* data.

The volume of the ring A was estimated in 3.1x10^{13}m^3 based on its radius of maximum velocity of 134km and a vertical extension of 550m, leading to an annualized volume transport of 0.98Sv, about 75% of the volume transport of the mean ring. The

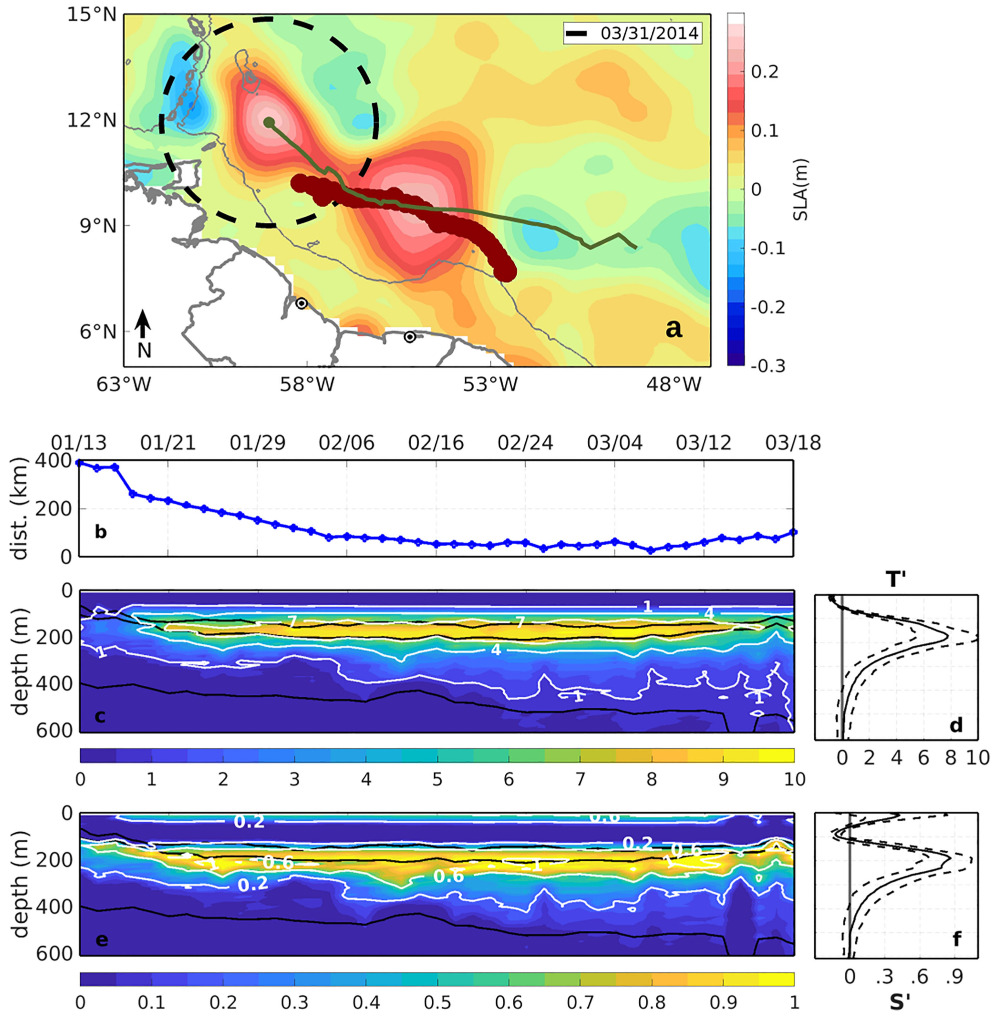

FIGURE 11 | Ring B seen as a positive sea level anomaly at the end of its recorded trajectory in the META dataset in **(A)**. The green line is the ring trajectory, the dashed circle corresponds to twice the ring radius (2R), and the brown markers are the locations of the IR profiles from ARGO. The distances from the ring center to the ARGO profiles is shown in panel **(B)**. The T and S anomalies with respect to the ring exterior (OR profiles) are presented in panels **(C, E)** together with the 24.5, 25.5 and 27.1 kgm^{-3} isopycnals (black lines, from top to bottom); and their time average (plus and minus one standard deviation) in panels **(D, F)**. No smoothing was applied to the ARGO data.

percentage of SAW transported by ring A (considering profiles located within 1R from the ring center) is shown in **Figure 9**. The maximum percentage (~43%) occurs at shallower levels than the mean ring, decreasing to less than 20% in the lower thermocline. The average percentage of ~30%, computed within the depth range of ring A, is significantly lower than that of the mean ring, leading to an annualized transport of SAW of ~0.3Sv. It is unclear from the data if these differences reflect different conditions during the ring formation or, otherwise, result from the erosion of the SAW composition due to mixing. It is noteworthy that ring A was sampled near the end of its life cycle, suggesting that the latter may be true. Using the composite structures of T and S, its average temperature was 15.5°C and average salinity 35.5, leading to a heat transport of 0.05PW and freshwater transport of 0.4x10^{6}kgs^{-1}. These figures are about 30% and 20% lower than the corresponding ones for the mean ring, and are associated primarily with the smaller radius, and therefore smaller volume of Ring A.

Ring B was first identified in the altimeter dataset on January 8th, 2014, near 8°N and 49°W, and traveled for three months until it crossed the 12°N threshold and left the searching area near 60°W (**Figure 11A**). The ARGO float was captured by the ring just after its separation from the retroflection. The float traveled within the ring for 64 days, and over 800km, maintaining an average distance of ~60km from the rings center for at least 30 days. The mean ring radius of 157km was close to the average size for the 112 rings sampled by T and/or S profiles (see **Table 2**). The average T anomaly at the ring core is ~7.5°C (larger than the T anomaly of the mean ring) with maximum observed anomalies reaching 10°C (**Figures 11C, E**).

The average S anomaly at the ring core is ~0.7 (similar to the S anomaly of the mean ring) with maximum observed anomalies reaching 0.9 (**Figures 11D, F**). The S anomaly core is located around the depth of 200m, somewhat deeper than the T anomaly core, similar to the mean ring.

The volume of ring B was estimated at $3.8\text{x}10^{13}\text{m}^3$, based on its radius of maximum velocity of 157km and vertical extension of 500m, leading to an annualized volume transport of 1.2Sv, close to the volume transport of the mean ring. The percentage of SAW transported by ring B (considering profiles located within 1R from the ring center) is shown in **Figure 9**. The maximum percentage (~62%) is somewhat larger and occurs at lower levels and higher densities (σ_θ ~ 25.7kgm^{-3}) when compared to the mean ring. The percentage of SAW is lower than that of the mean ring for higher densities, and similar to that of the mean ring for lower densities (until σ_θ ~23.8kgm^{-3}). Near the surface, for $\sigma_\theta < 23.8\text{kgm}^{-3}$, anomalies with respect to S_N increase significantly, with the percentage of SAW reaching 100% at the surface. Following Johns et al. (2003), as discussed above, these near surface anomalies are disregarded and an average of 54% is estimated within the depth range of ring B, similar to the mean ring, leading to an annualized transport of ~0.66Sv of SAW. The heat transport of Ring B is 0.07PW, similar to the mean NBC ring, and its fresh water transport $0.26\text{x}10^6\text{kgs}^{-1}$ (about 42% lower).

Rings A and B are surface intensified rings, with anomalous T and S vertical structures similar to that of the mean ring, both in terms of vertical extension and core location. Ring A, however, is significantly saltier and has a somewhat deeper T core, while Ring B presents both saltier and warmer cores. The relatively oversampling of these two rings may raise some concerns that the estimation of the mean ring might be somewhat biased towards these two well sampled events. In order to address this issue, the mean ring was recomputed, eliminating all the IR profiles that sampled rings A and B. The resulting mean NBC ring is virtually indistinguishable from the previous estimate shown in **Figure 6**, giving confidence in the representativeness of the mean NBC ring.

4 DISCUSSION AND CONCLUSIONS

The vertical structure of the mean NBC ring was reconstructed from a combined analysis of two global datasets, spanning 24 years (1993 to 2016) of freely distributed altimetry products and hydrographic data. The mean NBC ring depicts a large, moderately intense and relatively shallow feature, with radius of ~160km, surface velocities reaching $\sim 0.36\text{ms}^{-1}$, and significant temperature and salt anomalies present in the upper 500m of the water column. Maximum T and S anomalies (5.9°C and 0.7, respectively) are found at subsurface levels, near 150 to 200m deep. A mean NBC ring formation of 5.3 ± 1.5 rings per year was estimated from the altimetry data. This value agrees with previous estimates based on satellite data, but is derived from a much longer dataset comprising 24 years of altimetry data, as opposed to the 6 and 10 years analyzed by Goni and Johns (2001 and 2003, respectively). More recent studies (Mélice and Arnault, 2017, and Aroucha et al., 2020), also based on longer time series of satellite data, find average formation rates similar to that of the present study.

A high variability in the number of NBC rings formed each year was found in the present study, with a minimum of 2 and a maximum of 8 rings. This is an interesting and important aspect, which should be taken with care since it will lead to a large inter-annual variability in the contribution of NBC rings to volume and heat transport in the tropics. Such a variability was also found by previous authors, such as the early studies of (Goni and Johns 2001; 2003) who found from 2 to 7 rings per year, and in more recent estimates based on longer time series of data, such as Mélice and Arnault (2017), who found 2 to 7 rings per year, and Aroucha et al. (2020), who found 3 to 8 NBC rings per year.

No clear correlation could be established between the annual formation of NBC rings and the Northern Tropical Atlantic Index, as previously speculated by Goni and Johns (2003). Very weak correlation was also found when comparing the number of NBC rings shed per year and the maximum SSH anomaly identified with the Oceanic Niño Index (ONI), similar to what was obtained by Aroucha et al. (2020). These authors actually attempted to correlate several Atlantic climate indexes with NBC parameter anomalies, but could not find significant correlations. Their higher value was only 0.34, obtained for SSH anomalies and the Atlantic Multidecadal Oscillation - AMO (a value of 0.26 was found in the present study in this case). Other studies (e.g., Fonseca et al., 2004; Hormann et al., 2012) have associated the ring formation with the position of the retroflection, the northward displacement of the NECC, and the wind stress curl over the tropical Atlantic. Sharma et al. (2009), on the other hand, indicated that ITCZ migration and forcing by trade winds are not the main factors influencing the shed of NBC rings during the year. To further investigate the causes of the observed inter-annual variability is beyond the scope of the present study, in which such variability is relevant insofar as it affects the estimates of NBC volume and heat transport.

An annualized transport of ~1.3Sv was computed for the mean NBC ring in the present study. Combined with the mean formation of 5.3 ± 1.5 rings per year, the total contribution of NBC rings to the meridional volume transport reaches approximately 7 ± 2Sv. Considering the canonical 13Sv of newly formed North Atlantic Deep Water that flows southward in the deep ocean (Schmitz Jr. and McCartney, 1993), these estimates amount to rough estimates of 40 to 70%, with an average of circa 50% of the upper ocean transport required to close the Atlantic Meridional Overturning Cell (AMOC) at low latitudes. The heat transport by the mean NBC ring was estimated at 0.07PW. Compared to a total heat transport of 1PW, according to Ganachaud and Wunsch (2000), and taking into consideration the average number of rings formed per year, the NBC rings may account for approximately 25 to 50% of the meridional heat transport in the tropical Atlantic, highlighting their important role for the earth's climate. This estimate is consistent and reinforces those made by Fratantoni et al. (1995) and Garzoli et al. (2003), who placed the contribution of NBC rings to the meridional heat transport at low latitudes as something between 20% and 50% of the total transport.

These estimates, despite being derived from a large amount of altimetry and hydrographic data, should be evaluated with care. A major issue is to determine how much of the total volume transports actually correspond to waters with South Atlantic origin. This aspect will be tackled in the following discussion, but first some uncertainties in calculating the mean ring volume, from which the annualized transport is derived, must be taken into consideration. The mean NBC ring volume was estimated at $4x10^{13}m^3$ for a radius of maximum geostrophic velocities of ~160km and maximum penetration depth of 500m. A first, and possibly minor issue, is the estimated penetration depth of the mean ring. As long as the *in situ* data, sampling 112 different rings, may be considered as representative of a large variety of rings with different vertical penetration, which has been observed to occur in the observations of individual rings (e.g, Johns et al., 2003) this should not be a major concern. The 500m seems to be a robust value, determined both from the average depth of zero T and S anomalies, and from the depth of the σ_θ = 27.1kgm^{-3} isopycnal (the limit between SACW and AAIW, as discussed below), but a reasonable uncertainty of ~50m for this estimated penetration depth should lead per se to a 10% variation in the volume transport of the mean ring.

A second issue is related to the radius of maximum geostrophic velocity. The value of 160km was calculated from the individual observations of the 112 rings for which T and/or S profiles were available. This favors somewhat larger rings, when compared to the average radius of 138km calculated from the individual observations of the 128 rings detected by altimetry. The question of why there is less hydrographic information for smaller rings (despite ring A discussed in Section 3.3) is beyond the scope of the present investigation. But if one assumes that the average anomalies computed for the mean NBC ring could be extended to all the rings presented in the altimetry dataset, different values of volume and transport could be estimated. Such a transport, for a radius of 138km, would drop to 0.95Sv (closer to previous estimates reported in the literature) and the total contribution of NBC rings to the AMOC would vary accordingly. A related issue is that the average radius in the altimetry data set seems to decrease from east to west, suggesting that larger rings are more representative of their conditions at the formation region, and shorter rings reflect a general decay during their lifetime. It is unclear whether these two factors compensate each other or not.

With these assumptions regarding the ring volume taken into account, there remains the issue that the value of 1.3Sv for the annualized transport by the mean ring is somewhat larger than the canonical 1Sv, generally assumed in the literature since Johns et al. (1990). This agreement in the literature between different estimates of the volume transport per ring, however, is possibly somewhat fortuitous since they have been made based on several simplified, and sometimes contradictory assumptions. Johns et al. (1990), for instance, obtained a transport of 0.8Sv computing the volume of a cylinder with a diameter of 400km, corresponding to the outer edge under the rings influence (based on the available satellite images) and 200m height, or the thickness of the upper-layer South Atlantic water. Didden and Schott (1993) considered the same diameter, but estimated the volume for a scale height of 350m, or the average depth of the 10°C isotherm in the equatorial region, obtaining a volume transport of ~1.4Sv (closer to the present estimate). Shortly after, Richardson et al. (1994) observed that the signature of the NBC rings in the subsurface drifters reached more than 900m in the water column and that the diameter of the rings was reduced by ~50% at these depths. Their estimated 0.9Sv of volume transport was only possible because they assumed a lower surface diameter of 250km, much lower than the two previous estimates, corresponding to the radial distance of maximum swirl velocity. Fratantoni and Glickson (2002) tracked 12 rings using SeaWiFS chlorophyll-*a* signature and assumed their shape as elliptical cylinders, with an average major (minor) axis of 304 (213) km, and vertical height of 600m based on the oxygen signature from three sampled rings, obtaining a volume transport of 1.0 ± 0.4Sv. The large range of values obtained for individual rings by these authors, from 0.55Sv and 1.73Sv, points also to a large variability around these estimated values of transport per ring.

In order to compute the amount of SAW transported by the mean NBC ring, anomalous salinity in density space within the ring could not be computed with respect to the average salinity of the OR profiles, as done for the analysis at constant depth levels. Such anomalies, otherwise, were evaluated with respect to "endpoint" salinities (S_N), or the average of the highest 10% salinities for each density in the S-σ_θ diagram. This points to the fact that significant percentages of SAW are present outside NBC rings in the tropical western Atlantic, and SAW is also sampled by the OR profiles. This is observed to occur at all density levels from intermediate to subsurface and surface waters, and is illustrated in **Figure 12** for σ_θ = 25.5 kgm^{-3}. Higher percentages, above 40%, are observed in the eastern domain, within the region of the NBC retroflection, and along the general trajectory of NBC rings in the western domain. Westward from 55°W, lower percentages are observed both to the south and to the north of the average ring trajectory, indicating transport by the NBC rings. High percentages of SAW for OR profiles in the eastern domain may indicate both transport by the NBC and NECC, and mixing within the retroflection. Otherwise, high percentages for OR profiles and low percentages for IR profiles in the western domain possibly indicates mixing of SAW transported by NBC rings with the surrounding waters. The general pattern seen in **Figure 12** is similar for all density levels within the range of SACW, and to some extent in the upper part (lower densities) of AAIW. At intermediate levels in the eastern domain, however, a larger meridional variability is observed and values above 40% are rare north of 9°N.

Computing the percentage of SAW transported by the NBC rings, and by the mean ring, is relatively easy when the averages are done in density space (see Eq. 2), but actually depends on some different and possibly controversial approaches.

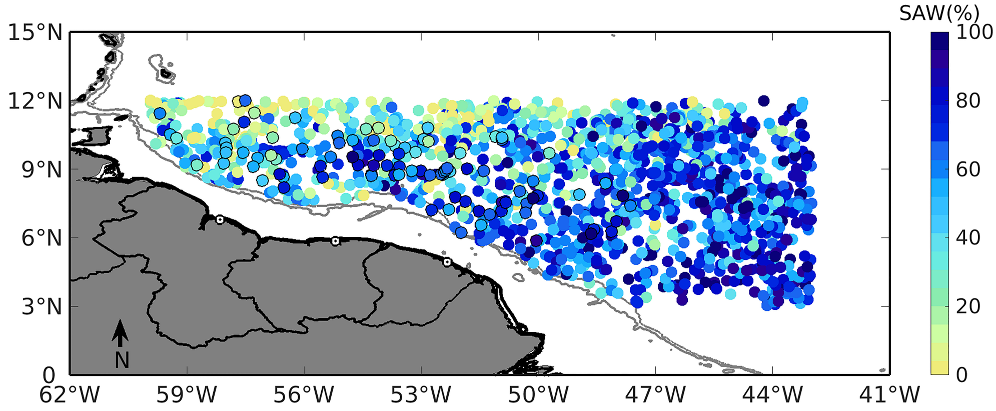

FIGURE 12 | Percentage of SAW for the σ_θ = 25.5 kgm^{-3} density level, for all IR and OR profiles containing T/S pairs, within the sampling region. Each dot is one individual profile, and dots with highlighted perimeter represent the IR profiles.

Considering the salinity anomalies for density surfaces below σ_θ = 27.1kgm^{-3} leads to, on average, approximately 50% of SAW (circa 0.66Sv) being transported by the mean ring. This should reduce the contribution of NBC rings to the AMOC to about 20 to 35%, but should not influence their contribution to the meridional heat transport. Such an estimate was done considering salinity anomalies and ring volumes calculated for profiles located within 1R from the ring center. Johns et al. (2003), however, suggests that such a calculation (for individual rings, in their case) should be performed not within 1R (R being the radius of maximum geostrophic velocities) but within the ring outer edge. This is defined in their work as the radial distance in which the swirl velocity drops below ~15cms^{-1}, and is justified by the authors with respect to Flierl (1981) ideas on the water trapping within rings, and penetration depths in which the swirl velocity drops below 10cms^{-1}, a rather arbitrary value. Such approach is sensible and, applied to the mean ring would lead to radial distances close to 2R in the present case, although it is arguable whether it makes sense considering average instead of instantaneous velocities. Taking all profiles within 2R, and penetration depth of 200m (see **Figure 6** for the average depth in which the velocities of the mean ring are ~10cms^{-1}), the SAW transport by the mean NBC ring is raised by approximately 40%, from 0.66 to 0.92Sv. This estimate is close to the average SAW transport of 1.1Sv, and within the range from 0.2 to 2.3Sv in individual rings, estimated by Johns et al. (2003).

The estimates of SAW by Johns et al. (2003) also include a portion of intermediate waters. These are not considered in the present study, since waters with densities above σ_θ = 27.1kgm^{-3} are located below the penetration depth of the mean NBC ring. It is certain that some intermediate waters are carried by NBC rings, since observations have shown that some individual rings reach depth levels below 1000m, with densities in the range of AAIW. What percentage of AAIW is transported by NBC rings, or otherwise by the mean flow, can not be asserted in the present study. At the same time, subsurface intensified rings, with little or no surface SSH signal, also considered by Johns et al. (2003), are probably absent, or under-sampled (since some degree of coupling may exist between surface and subsurface rings) in the present analysis. Fratantoni and Richardson (2006) verified that more intense surface-intensified rings which translate relatively quickly are able to overtake smaller and slower subsurface rings. At the same time, the lowest observed value of SSH anomaly by the tracking method was 1.0 cm, similar to the minimum values observed by Aroucha et al. (2020), who used a hybrid algorithm of eddy detection based on geostrophic velocity at 50m. Of the total of 128 rings identified in the entire period of analysis, 7 of them were first identified with the minimum SSH anomaly value of 1cm and that might indicate the META dataset is able to identify rings with small surface signals, such as the subsurface ones. Whether the mean NBC ring, and the associated meridional transports are representative of the full set of NBC rings or only of those shallow and surface-intensified is still to be determined. Numerical studies, such as that performed by Garrafo et al. (2003), in which surface and subsurface intensified rings are generated, may help to shed some light as to the degree of coupling between such rings, and whether subsurface rings may be detected but their surface signal.

The present study, despite the limitations inherent to the data, is an attempt to improve on the estimates of volume and heat transport by NBC rings, proposing an assemblage of a large amount of data, from different but complementary observational approaches. The geometric volume, associated heat transport, and percentage of SAW within the mean NBC ring appear to be robust estimates. To infer the annualized meridional volume transport by the rings and the percentage contribution by SAW, however, depends on several assumptions on the limits for integrating the ring anomalies, and the uncertainties may be higher. This limitation is not restricted to the present study. Taking also into account the large variability on the number of rings formed at individual years, from a minimum of 2 to a maximum of 8 rings, the total contribution of NBC rings to the upper limb of the AMOC may be considered to vary within a large range, from ~20 to 80% in different years.

DATA AVAILABILITY STATEMENT

Publicly available datasets were analyzed in this study. This data can be found here: The META dataset is made available at https://www.aviso.altimetry.fr/en/data/products/, and The EN4.2.0 dataset is made available at https://www.metoffice.gov.uk/hadobs/en4/.

AUTHOR CONTRIBUTIONS

LB developed this work during a master program under the supervision of AP, VC, and GM. All authors contributed to the writing of the manuscript. All authors contributed to the article and approved the submitted version.

FUNDING

The first author was funded with a fellowship by the Brazilian National Council for Scientific and Technological Development (CNPq).

ACKNOWLEDGMENTS

The authors would like to thank the SSALTO/DUACS team for running and distributing the "Mesoscale Eddy Trajectory Atlas" product, which was developed and validated in collaboration with D.Chelton and M. Schlax at Oregon State University. The EN4.2.0 dataset is made freely available by the Met Office Hadley Centre observations datasets, who join all types of ocean profiling instruments that provide temperature and (if available) salinity information.

REFERENCES

Aroucha, L. C., Veleda, D., Lopes, F. S., Tyaquiçã, P., Lefèvre, N., and Araujo, M. (2020). Intra- and Inter-Annual Variability of North Brazil Current Rings Using Angular Momentum Eddy Detection and Tracking Algorithm: Observations From 1993 to 2016. *J. Geophys. Res.: Ocean.* 125, e2019JC015921. doi: 10.1029/2019JC015921

Arur, A., Krishnan, P., George, G., Goutham Bharathi, M. P., Kaliyamoorthy, M., Hareef Baba Shaeb, K., et al. (2014). The Influence of Mesoscale Eddies on a Commercial Fishery in the Coastal Waters of the Andaman and Nicobar Islands, India. *Int. J. Remote Sens.* 35 (17), 6418–6443. doi: 10.1080/01431161.2014.958246

Broecker, W. S. (1991). The Great Ocean Conveyor. *Oceanography* 4 (2), 79–89. doi: 10.5670/oceanog.1991.07

Brokaw, R. J., Subrahmanyam, B., Trott, C. B., and Chaigneau, A. (2020). Eddy Surface Characteristics and Vertical Structure in the Gulf of Mexico From Satellite Observations and Model Simulations. *J. Geophys. Res.: Ocean.* 125 (2), e2019JC015538. doi: 10.1029/2019JC015538

Candela, J., Beardsley, R. C., and Limeburner, R. (1992). Separation of Tidal and Subtidal Currents in Ship-Mounted Acoustic Doppler Current Profiler Observations. *J. Geophys. Res.* 97, 769–788. doi: 10.1029/91JC02569

Chelton, D. B., Schlax, M. G., and Samelson, R. M. (2011). Global Observations of Nonlinear Mesoscale Eddies. *Prog. Oceanogr.* 91 (2), 167–216. doi: 10.1016/j.pocean.2011.01.002

Didden, N., and Schott, F. (1993). Eddies in the North Brazil Current retroflection region observed by Geosat altimetry. *J. Geophys. Res.: Ocean.* 98 (C11), 20121–20131. doi: 10.1029/93JC01184

Emery, W. J., and Dewar, J. S. (1982). Mean Temperature-Salinity, Salinity-Depth and Temperature-Depth Curves for the North Atlantic and the North Pacific. *Prog. Oceanogr.* 11 (3), 219–305. doi: 10.1016/0079-6611(82)90015-5

Ffield, A. (2005). North Brazil Current Rings Viewed by TRMM Microwave Imager SST and the Influence of the Amazon Plume. *Deep-Sea. Res. Part I.: Oceanogr. Res. Pap.* 52 (1), 137–160. doi: 10.1016/j.dsr.2004.05.013

Flagg, C. N., Gordon, R. L., and McDowell, S. (1986). Hydrographic and Current Observations on the Continental Slope and Shelf of the Western Equatorial Atlantic. *J. Phys. Oceanogr.* 16 (8), 1412–1429. doi: 10.1175/1520-0485(1986)016<1412:HACOOT>2.0.CO;2

Flierl, G. R. (1981). Particle Motions in Large-Amplitude Wave Fields. *Geophys. Astrophys. Flui. Dyn.* 18 (1-2), 39–74. doi: 10.1080/03091928108208773

Fonseca, C. A., Goni, G. J., Johns, W. E., and Campos, J. D. (2004). Investigation of the North Brazil Current Retroflection and North Equatorial Countercurrent Variability. *Geophys. Res. Lett.* 31, L21304. doi: 10.1029/2004GL020054

Fratantoni, D. M., and Glickson, D. A. (2002). North Brazil Current Ring Generation and Evolution Observed With SeaWiFS. *J. Phys. Oceanogr.* 32 (3), 1058–1074. doi: 10.1175/1520-0485(2002)032<1058:NBCRGA>2.0.CO;2

Fratantoni, D. M., Johns, W. E., and Townsend, T. L. (1995). Rings of the North Brazil Current: Their Structure and Behavior Inferred From Observations and a Numerical Simulation. *J. Geophys. Res.: Ocean.* 100 (C6), 10633–10654. doi: 10.1029/95JC00925

Fratantoni, D. M., and Richardson, P. L. (2006). The Evolution and Demise of North Brazil Current Rings. *J. Phys. Oceanogr.* 36 (7), 1241–1264. doi: 10.1175/JPO2907.1

Ganachaud, A., and Wunsch, C. (2000). Improved Estimates of Global Ocean Circulation, Heat Transport and Mixing From Hydrographic Data. *Nature* 408 (6811), 453–457. doi: 10.1038/35044048

Garraffo, Z. D., Johns, W. E., Chassignet, E. P., and Goni, G. J.. (2003). "North Brazil Current rings and transport of southern waters in a high resolution numerical simulation of the North Atlantic," In: *Elsevier Oceanography Series* Eds. G. J. Goni and P. Malanotte-Rizzoli (Amsterdam: Elsevier). vol. 68, 375–409.

Garzoli, S. L., Ffield, A., Johns, W. E., and Yao, Q. (2004). North Brazil Current Retroflection and Transports. *J. Geophys. Res.: Ocean.* 109 (C1), 1–14. doi: 10.1029/2003JC001775

Garzoli, S. L., Ffield, A., and Yao, Q. (2003). "North Brazil Current Rings and the Variability in the Latitude of Retroflection," in *Elsevier Oceanography Series* 68. Elsevier Science), 357–373. doi: 10.1016/S0422-9894(03)80154-X

Goes, M., Molinari, R., da Silveira, I., and Wainer, I. (2005). Retroflections of the North Brazil Current During February 2002. *Deep-Sea. Res. Part I.: Oceanogr. Res. Pap.* 52 (4), 647–667. doi: 10.1016/j.dsr.2004.10.010

Goni, G. J., and Johns, W. E. (2001). A Census of North Brazil Current Rings Observed From TOPEX/POSEIDON Altimetry: 1992–1998. *Geophys. Res. Lett.* 28 (1), 1–4. doi: 10.1029/2000GL011717

Goni, G. J., and Johns, W. E. (2003). "Synoptic Study of Warm Rings in the North Brazil Current Retroflection Region Using Satellite Altimetry," in *Elsevier Oceanography Series*, Vol. 68. (Elsevier Science), 335–356. doi: 10.1016/S0422-9894(03)80153-8

Good, S. A., Martin, M. J., and Rayner, N. A. (2013). EN4: Quality Controlled Ocean Temperature and Salinity Profiles and Monthly Objective Analyses With Uncertainty Estimates. *J. Geophys. Res.: Ocean.* 118 (12), 6704–6716. doi: 10.1002/2013JC009067

Halliwell, G. R.Jr., Weisberg, R. H., and Mayer, D. A. (2003). "A Synthetic Float Analysis of Upper-Limb Meridional Overturning Circulation Interior Ocean Pathways in the Tropical/Subtropical Atlantic," in *Interhemispheric Water Exchange in the Atlantic Ocean*, vol. Vol. 68 . Eds. G. J. Goni and P. Malanotte-Rizzoli (Elsevier Science).

Hormann, V., Lumpkin, R., and Foltz, G. R. (2012). Interannual North Equatorial Countercurrent Variability and its Relation to Tropical Atlantic Climate Modes. *J. Geophys. Res.* 117, C04035. doi: 10.1029/2011JC007697

Jochumsen, K., Rhein, M., Hüttl-Kabus, S., and Böning, C. W.. (2010). “On the Propagation and Decay of North Brazil Current Rings. *J. Geophys. Res.: Oceans* 115, C10004. doi: 10.1029/2009JC006042

Johns, W. E., Lee, T. N., Schott, F. A., Zantopp, R. J., and Evans, R. H. (1990). The North Brazil Current Retroflection: Seasonal Structure and Eddy Variability. *J. Geophys. Res.: Ocean.* 95 (C12), 22103–22120. doi: 10.1029/JC095iC12p22103

Johns, W. E., Zantopp, R. J., and Goni, G. J. (2003). “Cross-Gyre Transport by North Brazil Current Rings,” in *Elsevier Oceanography Series*, (Elsevier Oceanography: Elsevier Science) 68, 411–441. doi: 10.1016/S0422-9894(03)80156-3

Jufaili, S. M. A., and Piontkovski, S. A. (2020). Seasonal and Interannual Variations of Sardine Catches Along the Omani Coast. *Int. J. Ocean. Oceanogr.* 14 (1), 77–99. doi: 10.37622/IJOO/14.1.2020.77-99

Mélice, J. L., and Arnault, S. (2017). Investigation of the Intra-Annual Variability of the North Equatorial Countercurrent/North Brazil Current Eddies and of the Instability Waves of the North Tropical Atlantic Ocean Using Satellite Altimetry and Empirical Mode Decomposition. *J. Atmosph. Ocean. Technol.* 34 (10), 2295–2310. doi: 10.1175/JTECH-D-17-0032.1

Pauluhn, A., and Chao, Y. (1999). Tracking Eddies in the Subtropical North-Western Atlantic Ocean. *Phys. Chem. Earth. Part A.: Solid. Earth Geodes.* 24 (4), 415–421. doi: 10.1016/S1464-1895(99)00052-6

Pegliasco, C., Chaigneau, A., and Morrow, R. (2015). Main Eddy Vertical Structures Observed in the Four Major Eastern Boundary Upwelling Systems. *J. Geophys. Res.: Ocean.* 120 (9), 6008–6033. doi: 10.1002/2015JC010950

Pegliasco, C., Delepoulle, A., Mason, E., Morrow, R., Faugère, Y., and Dibarboure, G. (2022). META3.1exp: A New Global Mesoscale Eddy Trajectory Atlas Derived From Altimetry. *Earth Syst. Sci. Data* 14, 1087–1107. doi: 10.5194/essd-14-1087-2022

Reid, J. L., and Lynn, R. J. (1971). “On the Influence of the Norwegian-Greenland and Weddell Seas Upon the Bottom Waters of the Indian and Pacific Oceans,” in *Deep-Sea Research and Oceanographic Abstracts Oceans*, Vol. 18. (Elsevier), 1063–1088. doi: 10.1016/0011-7471(71)90094-5

Richardson, P. L., Hufford, G. E., Limeburner, R., and Brown, W. S. (1994). North Brazil Current Retroflection Eddies. *J. Geophys. Res.: Ocean.* 99 (C3), 5081–5093. doi: 10.1029/93JC03486

Schlax, M. G., and Chelton, D. B. (2016). “The “Growing Method” of Eddy Identification and Tracking in Two and Three Dimensions,” in *College of Earth, Ocean and Atmospheric Sciences*, vol. 8. (Corvallis, Oregon: Oregon State University).

Schmitz, W. J.Jr., and McCartney, M. S. (1993). On the North Atlantic Circulation. *Rev. Geophys.* 31 (1), 29–49. doi: 10.1029/92RG02583

Schott, F. A., Fischer, J., and Stramma, L. (1998). Transports and Pathways of the Upper-Layer Circulation in the Western Tropical Atlantic. *J. Phys. Oceanogr.* 28 (10), 1904–1928. doi: 10.1175/1520-0485(1998)028<1904:TAPOTU>2.0.CO;2

Sharma, N., Anderson, S. P., Brickley, P., Nobre, C., and Cadwallader, M. L. (2009). “Quantifying the Seasonal and Inter-Annual Variability of the Formation and Migration Pattern of North Brazil Current Rings. *Oceans*, 1–7. doi: 10.23919/OCEANS.2009.5422142

Souza, J. M. A. C., de Boyer Montégut, C., Cabanes, C., and Klein, P. (2011). Estimation of the Agulhas Ring Impacts on Meridional Heat Fluxes and Transport Using ARGO Floats and Satellite Data. *Geophys. Res. Lett.* 38 (21), 1–5. doi: 10.1029/2011GL049359

Stramma, L., and England, M. (1999). On the Water Masses and Mean Circulation of the South Atlantic Ocean. *J. Geophys. Res.* 104 (C9), 20863–20883. doi: 10.1029/1999JC900139

Wilson, W. D., Johns, W. E., and Garzoli, S. L. (2002). Velocity Structure of North Brazil Current Rings. *Geophys. Res. Lett.* 29 (8), 114–111. doi: 10.1029/2001GL013869

Yang, G., Wang, F., Li, Y., and Lin, P. (2013). Mesoscale Eddies in the Northwestern Subtropical Pacific Ocean: Statistical Characteristics and Three-Dimensional Structures. *J. Geophys. Res.: Ocean.* 118 (4), 1906–1925. doi: 10.1002/jgrc.20164

Yang, G., Yu, W., Yuan, Y., Zhao, X., Wang, F., Chen, G., et al. (2015). Characteristics, Vertical Structures, and Heat/Salt Transports of Mesoscale Eddies in the Southeastern Tropical Indian Ocean. *J. Geophys. Res.: Ocean.* 120 (10), 6733–6750. doi: 10.1002/2015JC011130

Conflict of Interest: Author VC, despite being currently employed by Fugro GeoConsulting, was an exclusive part of the university's research group at the time of the development of this research.

The remaining authors declare that the research was conducted in the absence of any commercial or financial relationships that could be construed as a potential conflict of interest.

frontiers | Frontiers in Marine Science

TYPE Original Research
PUBLISHED 01 November 2022
DOI 10.3389/fmars.2022.886617

OPEN ACCESS

EDITED BY
Zhiyu Liu,
Xiamen University, China

REVIEWED BY
Shijian Hu,
Institute of Oceanology, Chinese Academy of Sciences (CAS), China
Xiaolin Bai,
Xiamen University, China

*CORRESPONDENCE
Alina N. Dossa
nath2dossa@gmail.com

SPECIALTY SECTION
This article was submitted to Physical Oceanography, a section of the journal Frontiers in Marine Science

RECEIVED 28 February 2022
ACCEPTED 30 September 2022
PUBLISHED 01 November 2022

CITATION
Dossa AN, da Silva AC, Hernandez F, Aguedjou HMA, Chaigneau A, Araujo M and Bertrand A (2022) Mesoscale eddies in the southwestern tropical Atlantic.
Front. Mar. Sci. 9:886617.
doi: 10.3389/fmars.2022.886617

Mesoscale eddies in the southwestern tropical Atlantic

Alina N. Dossa[1,2]*, Alex Costa da Silva[1], Fabrice Hernandez[1,3], Habib M. A. Aguedjou[2,3], Alexis Chaigneau[2,3], Moacyr Araujo[1,4] and Arnaud Bertrand[1,5,6]

[1]Laboratório de Oceanografia Física Estuarina e Costeira, Deptoartamento de Oceanografia, UFPE, Recife, PE, Brazil, [2]International Chair in Mathematical Physics and Applications (ICMPA), Université d'Abomey-Calavi, Cotonou, Benin, [3]Laboratoire d'Études en Géophysique et Océanographie Spatiale (LEGOS), Université de Toulouse, CNES/CNRS/IRD/UPS, Toulouse, France, [4]Brazilian Research Network on Global Climate Change – Rede CLIMA, São José dos Campos, Brazil, [5]MARBEC, Univ Montpellier, CNRS, Ifremer, IRD, Sète, France, [6]Universidade Federal Rural de Pernambuco (UFRPE), Recife, Brazil

The southwestern tropical Atlantic is a region of complex ocean dynamic where originates the strong western boundary current system composed of North Brazil current and North Brazil undercurrent. The region includes a variety of features including the Atoll das Rocas (AR) and Fernando de Noronha (FN) ridge that may favour mesoscale eddy dynamics. However, origin, occurrence and characteristics of mesoscale eddies were still not described in the region. Using satellite altimetry data from 1993 to 2018 off Northeast Brazil (37-25°W; 13-1°S), we reconstruct eddy trajectories and analyse the main eddy surface characteristics (e.g., size, amplitude, polarity) and their spatiotemporal variations. The study reveals two distinct dynamic regions before quantifying mesoscale eddies characteristics. Approximately 2000 mesoscale eddies crossed the region during the study period, among which 76% were generated inside the region, with amplitudes and radii ranging between 1 and 2 cm and 25 and 205 km, respectively. Eddies are preferentially formed between August and September and propagate westward. In the region around the FN Archipelago (36-26°W; 6-1°S), the formation of cyclonic eddies is likely favoured by barotropic instabilities of surface currents and the wind stress curl. On the other hand, in the south of the region (36-26°W; 12-8°S), eddies formation is likely associated with the barotropic instabilities, wind stress curl and the meandering of surface currents. Based on vertical temperature and salinity profiles from Argo floats' data, we determined that in average, the core of cyclonic eddies is centred at ~ 130 m (140 m) in the northern (southern) region while the core of anticyclonic eddies is centred at ~90 m (125 m) in the northern (southern) region. Moreover, mesoscale eddies formed in the tropical Atlantic do not connect the eastern tropical Atlantic and northeast Brazil.

KEYWORDS

mesoscale eddies, eddy characteristics, southwestern tropical Atlantic, wind stress curl, barotropic instability

Introduction

Mesoscale eddies, which are a common feature of the World Ocean, are one of the main contributors to oceanic variability. During their formation, they can trap local water inside their core and transport its properties over long distances toward remote regions (see for instance Chelton et al. (2011) or Laxenaire et al. (2018), for very long-lived eddies). Therefore, they can significantly contribute to the transport and redistribution of heat, salt, nutrients and other biogeochemical properties (Wunsch, 1999; Chelton et al., 2011; Gaube et al., 2014; Dufois et al., 2016; Gaube et al., 2019). Moreover, on their pathway, they can influence ocean-atmosphere exchanges by affecting heat-fluxes at the air-sea interface, winds, cloud cover and precipitations (e.g., Frenger et al., 2013; Villas Bôas et al., 2015). They can also affect temperature, salinity and velocity fields from the sea surface to ~1000 m depth (Kang and Curchitser, 2015; Pegliasco et al., 2015; Keppler et al., 2018; Aguedjou et al., 2021).

In the south tropical Atlantic Ocean (STAO), mesoscale eddies are frequently formed in the Benguela eastern boundary upwelling system (EBUS) (10-30°S; 0-30°E) (e.g., Chaigneau et al., 2009; Chelton et al., 2011; Pegliasco et al., 2015) and the region of the Brazil current (RBC) (10-20°S) (e.g., Campos, 2006; Soutelino et al., 2011; Arruda et al., 2013; Soutelino et al., 2013; Aguedjou et al., 2019). In the Benguela EBUS, mesoscale eddies are mostly generated from baroclinic/barotropic instabilities, topographic features, strong wind shear, and large-scale currents interaction with the shelf (e.g., Djakouré et al., 2014) (Djakouré et al., 2014) while in the RBC, mesoscale eddies generation are mainly due to the Brazil Current (BC) meandering along the shelf break, topographic and baroclinicity effect (e.g., Schmid et al., 1995; Campos, 2006).

From a biogeochemical point of view, mesoscale eddies contribute to the horizontal and vertical transport of mineral and organic matter in the ocean (e.g., Mahadevan, 2014). In general, surface intensified cyclonic eddies (CE) are associated with a pycnocline rise and hence nutrient vertical transport into the euphotic layer, while surface intensified anticyclonic eddies (AE) are associated with a pycnocline deepening and hence nutrient deficiency in the euphotic layer. Nevertheless, for subsurface eddies, the opposite can be observed. The northeastern Brazil (NEB) is an oligotrophic region due to the presence of a permanent thermocline preventing nutrient-rich subsurface waters from being advected to the surface (e.g., Assunção et al., 2020). This region is characterized by various water masses advected in the region by large-scale currents. The relatively warm (T> 25°C) tropical water is observed above ~100 m depth. At ~ 80-150 m depth, lays the subtropical underwater (SUW). Below the SUW down to ~500 m depth is encountered the South Atlantic central water, characterized by large temperature (T~10-23°C) and salinity (>35) ranges. Then, below lays the Antarctic Intermediate Water, characterized by low salinity. During their propagation, mesoscale eddies can contribute to the transport and mixing of these water masses, connecting the open ocean and regional seas (Huang et al., 2021) or the eastern boundary and the western boundary of Atlantic Ocean (Laxenaire et al., 2018). Nevertheless, a probable connection between the NEB and the eastern tropical Atlantic remains unexplored.

The western part of the STAO, the region enclosing the concave coastline between Maceio and Natal (Northeast Brazil, 10-3°S; 37-30°W), constitutes the pathway of two major western boundary currents, the North Brazil undercurrent (NBUC) and the North Brazil current (NBC) (Figure 1A). It is also a region of complex bathymetry, with the presence of Islands (Fernando de Noronha and Atoll das Rocas) and seamounts (along the Fernando de Noronha ridge) acting as obstacles for large-scale circulation (Silva et al., 2021). In the near-shore region, the main northward undercurrent, the NBUC, shifts from northeastward to northwestward at about 7.5°S as the coast orientation change (Dossa et al., 2021). Moreover, the central branch of the south equatorial current (cSEC), which flows westward across the tropical Atlantic, coalesces with the NBUC at about 4 - 5°S, to form the NBC (e.g., Schott et al., 1995; Schott et al., 1998; Dossa et al., 2021).

In the western STAO, very few studies emphasized the mesoscale activity. Using a series of XBT data Bruce (1984), observed mesoscale eddy occurrence off North Brazilian coast. These eddies mostly occur in boreal summer and fall between 3°-10°N and can extend up to 300 – 400 m depth vertically. In the Northeast region, Silveira et al. (1994) was the first to observe a clockwise recirculation of the cSEC at the surface, when it approaches the northeast Brazil coast at ~33°W. However, the authors suggested that it might be occasional and seasonal. Then, based on numerical simulations, Silva et al. (2009) pointed out the high surface mesoscale activity along the cSEC patches close to the northeast Brazil region. More recently, mesoscale activity was studied in the region based on altimetry data at specific periods (Dossa et al., 2021; Silva et al., 2021). However, to the best of our knowledge, no study provided a general vision of the characteristics of mesoscale activity and its seasonal variation in northeast Brazil (NEB). Here, we took advantage of 26 years of altimetry data to determine the origin, occurrence and characteristics of mesoscale eddies within the NEB. We depicted the presence of two regions with different characteristics. The region of the Fernando de Noronha ridge was characterized by the dominance of cyclonic eddies while in the region where the sSEC bifurcates both cyclonic and anticyclonic eddies occurred comparably. Moreover, we reveal that there is no any connection between the eastern tropical Atlantic and the NEB.

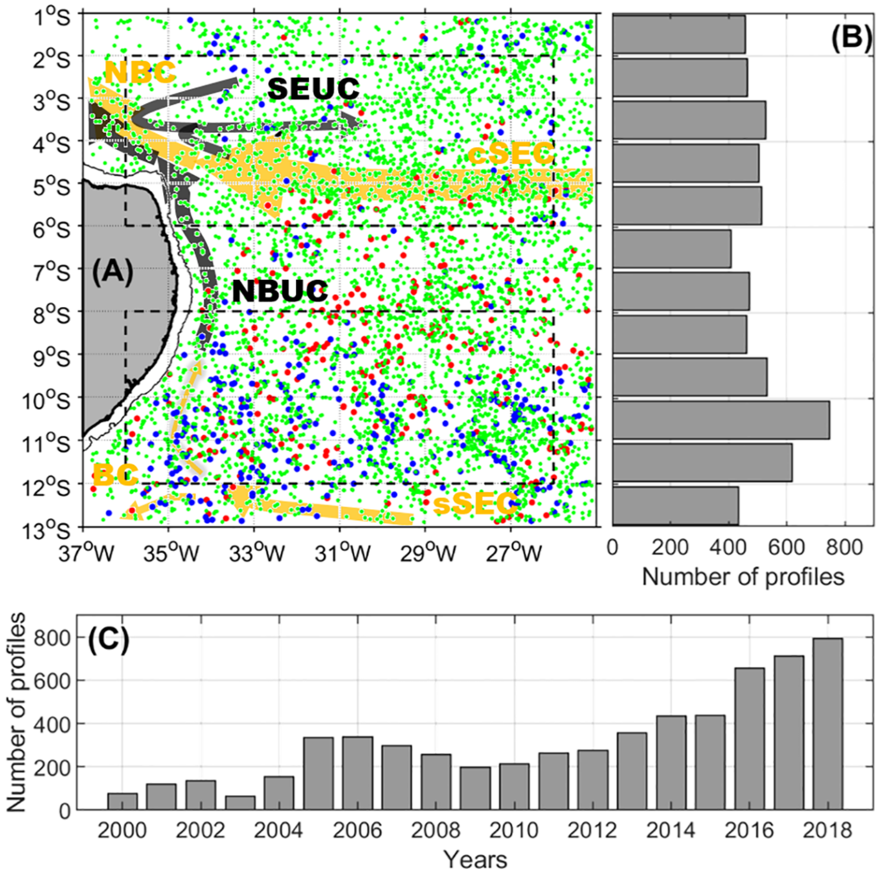

FIGURE 1
Spatio-temporal distribution of the 6134 Argo valid profiles used in this study. **(A)** Position of Argo profiles and schematic representation of mean currents off northeast Brazil. Blue (red) dots indicates Argo profiles inside CE (AE). Green dots indicate Argo profile outside eddies (AE & CE). Solid orange (black, respectively) lines indicate surface (subsurface) currents. sSEC, southern branch of South Equatorial Current; cSEC, central branch of South Equatorial Current; BC, Brazil Current; NBC, North Brazil Current; NBUC, North Brazil Undercurrent; SEUC, South Equatorial Undercurrent. **(B)** Meridional variation of the number of valid Argo profiles in one-degree latitudinal bands. **(C)** Yearly variation (2000-2018) of the number of valid Argo profiles.

Data and methods

Altimetry data and eddy tracking

To investigate mesoscale activity off northeast Brazil, we used altimetry observations including absolute dynamic topography (ADT) and derived surface geostrophic velocities data available from January 1993 to December 2018. These data were produced by Ssalto/DUACS multi-mission products with support from CNES (http://www.AVISO.altimetry.fr/duacs/). Multi-mission products refer to the combination of all satellites data available at one time: Jason-3, Sentinel-3A, HY-2A, Saral/AltiKa, Cryosat-2, Jason-2, Jason-1, T/P, ENVISAT, GFO, and ERS1/2. This dataset is mapped daily onto a 0.25° × 0.25° latitude/longitude grid (Ablain et al., 2015; Dupuy et al., 2016) and distributed by the Copernicus Marine Environment Monitoring Service (CMEMS: http://marine.copernicus.eu).

Mesoscale eddy identification is based on ADT daily maps, using the eddy detection algorithm from Chaigneau et al. (2008; Chaigneau et al., 2009). This algorithm finds the possible eddy centres corresponding to local extrema of ADT (maxima for AE, minima for CE), and defines the outermost closed contour around these extrema as eddy edges. Most previous studies on mesoscale eddies, have based eddy detection on sea level anomaly (SLA) fields because of inaccuracies in the geoid definition. However, recent improvements in estimation of the Mean Dynamic Topography, depending on the geoid (Rio et al., 2011; 2014) allowed to provide more accurate ADT fields. Thus, following Laxenaire et al. (2018) and Aguedjou et al. (2021), and the recommendations of Pegliasco et al. (2021), mesoscale eddies were detected on ADT fields instead of SLA. Eddy trajectories were then reconstructed using the tracking method developed by Pegliasco et al. (2015).

For each detected eddy, several properties were computed. The eddy amplitude corresponds to the absolute value of the difference between the ADT at the eddy centre and at the eddy edge. In our study, only eddies with amplitudes higher than 1 cm were retained. The eddy radius corresponds to the equivalent radius of a disk having the same area than the eddy. Only eddies with radii larger than 25 km were retained. The eddy kinetic energy (EKE) was computed as the average EKE inside the eddy, based on the geostrophic velocity components. Eddies with lifetime higher than 14 days were retained in the present study.

Relative vorticity (ζ) of large-scale currents is determined from the zonal (U) and meridional (V) geostrophic velocity components as:

$$\zeta = \frac{\partial V}{\partial x} - \frac{\partial U}{\partial y} \tag{1}$$

Barotropic instability, associated with the change of sign of the gradient of absolute vorticity (C), could drive eddy generation (Johns et al., 1990; Aguedjou et al., 2019). Indeed, it occurs in the region with weak value of C. As in Aguedjou et al. (2019), we computed the gradient of absolute vorticity as:

$$C = \vec{\nabla}\ (f + \zeta)\,.\,\vec{n} \tag{2}$$

where $\vec{n} = \frac{\overrightarrow{\nabla(\psi)}}{(\| \overrightarrow{\nabla(\psi)} \|)}$ is the unit vector perpendicular to geostrophic streamlines, $\psi = -\frac{g}{f} ADT$ is the stream function, f is the Coriolis parameter, g the gravitational acceleration.

To investigate eddy occurrence off Northeast Brazil (NEB) (37°-25°W;13°-1°S), we first build maps of spatial distribution of the number of detected eddies, eddy polarity, eddy properties (radius, amplitude), EKE, as well eddy speed of propagation and eddy life time. Eddy mean properties are accessed after gridding the region onto on 1° × 1° cells. The mean eddy properties correspond to the mean of all eddy-like features with lifetime > 14 days that occur in each cell. The analysis was performed over the study period (January 1993 - December 2018). Eddy number maps were built by considering the number of eddies with lifetime > 14 days within each cell. These maps show individual observations of eddies. For instance, if an eddy is stationary within a cell for 4 days, it will count as four observations within that cell. The eddy polarity is the probability for an eddy to be a cyclone (polarity < 0) or an anticyclone (polarity >0) and is defined as follow (Chaigneau et al., 2009):

$$P = \frac{N_{AE} - N_{CE}}{N_{AE} + N_{CE}} \tag{3}$$

where N_{AE} is the number of AE while N_{CE} correspond to the number of CE.

Mean EKE maps correspond to the average mean EKE of eddy detected in each cell over the period of study.

Mean propagation maps of eddy were also built by considering the mean propagation speed of eddies with lifetime > 14 days within each cell. The eddy speed within each grid cell corresponds to the mean propagation speed of all eddy detected in each grid cell. Note that the eddy speed is the speed of a detected eddy from its location at time t to its next location at time $t+1$.

Argo dataset and classification of Argo profiles

To investigate the vertical structure of mesoscale eddies in the NEB region; we used the available Conductivity Temperature Depth (CTD) profiles acquired from autonomous floats of the Argo international program. These temperature and salinity vertical profiles are available at https://www.coriolis.eu.org/Observing-the-Ocean/ARGO. Vertical profiles from the Argo program in the Tropical Atlantic are available after 2000 (e.g., Aguedjou et al., 2021), reason why we limit our analysis to 2000-2018.

The mean thermohaline structure was first investigated by estimating the mixed layer depth (MLD), the isothermal layer depth (ILD) and the upper and lower limits of isothermal, halocline and pycnocline layers. The MLD was estimated using the criterion recently applied in the region (e.g., Araujo et al., 2011; Assunção et al., 2020). The MLD corresponds to the depth where the density is equal to the density at the reference depth (10 m), plus an increment corresponding to temperature change of 0.5 °C. The ILD was estimated using the same temperature criterion, assuming that it correspond to the depth where the temperature was 0.5°C below the temperature at the reference depth. The upper limit of the thermocline and the halocline/pycnocline corresponds to ILD and MLD respectively while the lower limit of both corresponds to the depth where the buoyancy frequency (N^2) ≥ 10^{-4} (Assunção et al., 2020).

Then, a composite analysis of the eddy vertical structures were performed following Aguedjou et al. (2021). First, we retained only vertical profiles with at least 30 data between 15 m and 950 m depth, and with no significant vertical gap between each data (see Aguedjou et al. (2021) for more details). In the study region, 6134 profiles were retained (Figure 1). Second, these profiles were classified into three categories, whether they surfaced inside AE, CE or outside eddies. In average, between 400 and 500 profiles are available in each band of one degree of latitude (Figure 1B), and a maximum of 730 profiles were acquired between 11°S and 12°S (Figure 1B). The temporal distribution shows that the number of profiles was less than 200 between 2000 and 2004 (Figure 1C). The number of profile decreased from 334 in 2005 to 198 in 2005, from where it linearly increased to 800 in 2018.

Wind data

Wind data were used to investigate the contribution of wind stress and wind stress curl in the formation of mesoscale eddies in the study region. The wind dataset used in the present study is the quality-assured monthly update of the ECMWF Reanalysis v5 (ERA5) available from 1979 to 2019 on the grid 0.25° x 0.25°. The dataset includes zonal and meridional wind component estimated at 10 m above sea level. The data is produced by Copernicus Climate Change Service (C3S) and is available at https://www.ecmwf.int/en/forecasts/datasets/reanalysis-datasets/era5. We used zonal and meridional component of the wind to estimate the wind stress and the wind stress curl within the northeast Brazil. The wind stress and its curl were estimated based on Gill and Adrian (1982) and considering a non-linear drag coefficient from Large and Pond (1981) modified for low wind speed (Trenberth et al., 1990).

Surface current data

To provide a more comprehensive picture of upper layer's dynamic, we used the near-surface velocities climatological data derived from Global Drifter Program (GDP). Velocities are obtained from satellite-tracked drifting buoys drogued at 15 m depth. The climatology was built from dataset spanning from 1979 to 2015. The data were low-pass filtered to remove high-frequency currents and oscillations associated with local inertial periods. The data is monthly available on the grid 0.25° x 0.25°. This climatology is an update version of the older version described in Laurindo et al. (2017) (https://www.aoml.noaa.gov/phod/gdp/mean_velocity.php).

Results

Eddy density and mean properties off northeast Brazil

In the NEB, about 1500 eddies with radius larger than 25 km, amplitude larger than 1 cm and lifespan longer than 14 days were identified including 40% (60%) of AE (CE). The spatial distribution of mean annual number (1993 - 2018) of detected eddies (Figure 2A) revealed that eddies are much more numerous south of 8°S where up to 50 eddies per square degree per year were identified than north of 6°S (≤11 eddies per square degree). Considering this main feature, we defined two regions, the northern region A (36-26°W; 6°S-2°S) and the southern region B (36°-26°W; 8°-12°S).

In region A, CE eddies were strongly dominant (85% CE and 15% AE) with a mean polarity that can reach -1 in some cells (Figure 2B). In region B, the proportion of AE and CE was alike (58% CE and 42% AE) with the polarity that can locally reach 1 or -1.

Eddy amplitude ranged between 1 and 2 cm with no clear spatial pattern (Figure 3A). Eddy radii ranged between 25 and 205 km with radii decreasing from North (> 110 km) to South (Figure 3B) in agreement with the decrease of the Rossby radius of deformation. EKE was much stronger in the equatorial region, North of 5°S, where it reached 210 cm^2 s^{-2} than in region B where it was < 70 cm^2 s^{-2} (Figure 3C). The mean meridional variation of eddy characteristics shown that eddies formed north of 3°S have higher mean characteristics (Figure 3D).

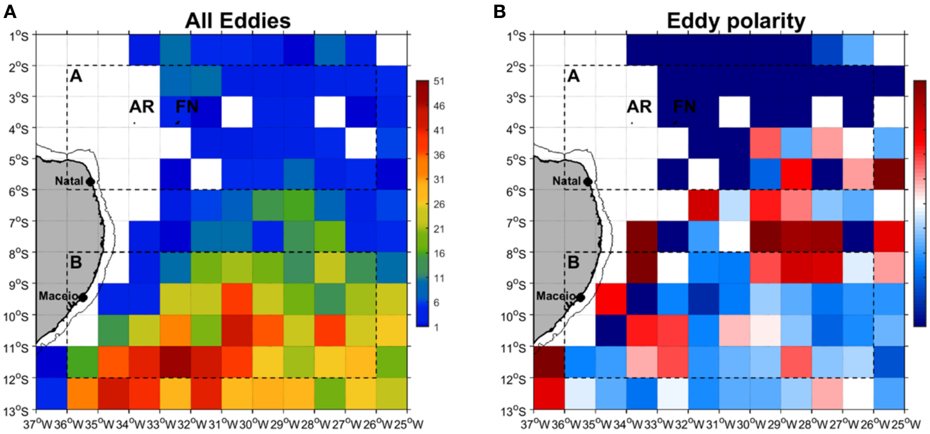

FIGURE 2
Spatial distribution of mean annual number of detected eddies per degree square over 1993-2018 period: **(A)** all eddies, **(B)** eddy polarity. The dashed rectangles delimit the northern (region A) and southern (region B) part of the NEB. The northern region A includes the Atoll das Rocas (AR) and Fernando de Noronha (FN) archipelago. The black solid line indicates the bathymetric contour at 70 m.

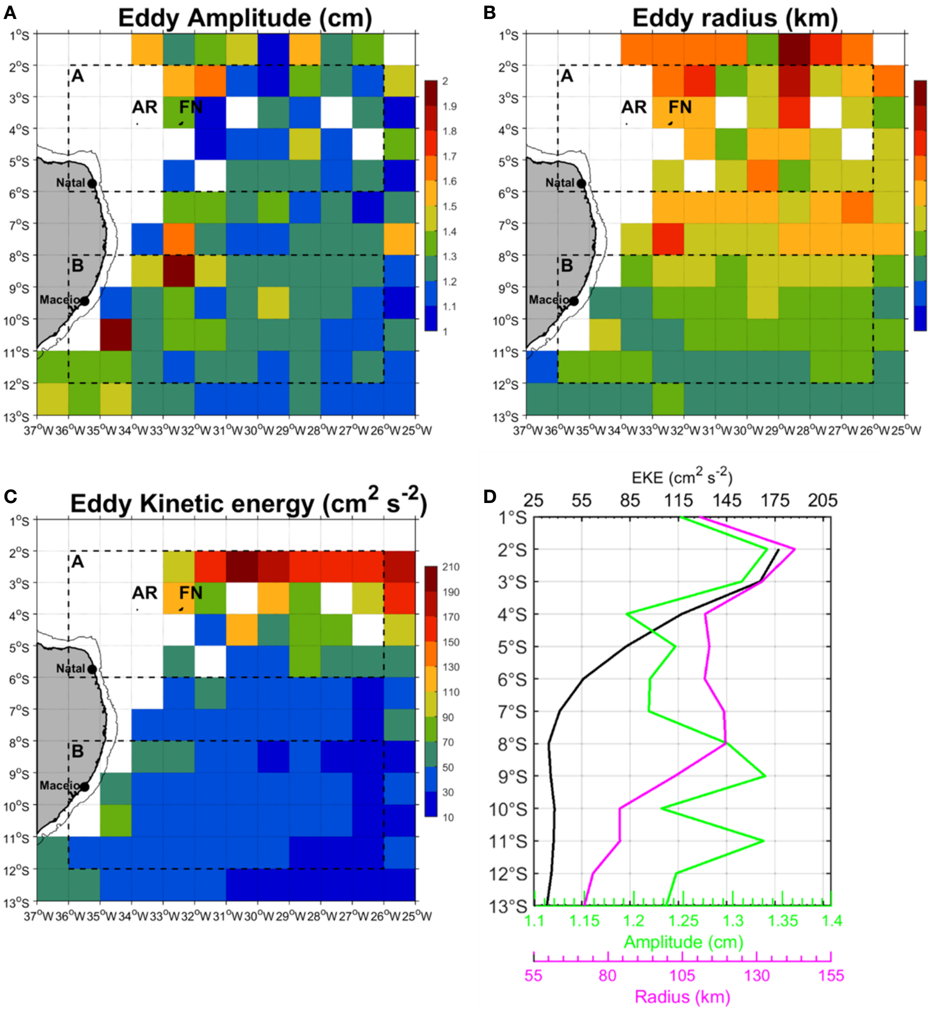

FIGURE 3
Spatial distribution of mean eddy characteristics per degree square over 1993 -2018 period: **(A)** eddy amplitude (cm), **(B)** eddy radius (km), **(C)** eddy kinetic energy (cm^2 s^{-2}) and **(D)** mean meridional variation of eddy characteristics.

Eddy genesis and propagation off northeast of Brazil

We detected and analysed 1950 eddy trajectories crossing the NEB (60% of CE and 40% of AE). About 25% of these eddies were formed outside the NEB mainly to the east from where they propagated westward into the study region, due to the beta effect (Figure 4). In region A, very few eddy trajectories were detected and they were mostly CE (85%). No AE propagated along the Fernando de Noronha Ridge. In contrast, most of eddy trajectories were concentrated in region B. In the near-coastal zone of region B, from the shelf-break to about 30 km offshore, only AE trajectories were observed.

Over the NEB region, eddies mostly propagate westward (Figure 5A). They were faster (> 10 cm s^{-1}) and less persistent (< 30 days) in region A than region B (< 10 cm s^{-1}; > 30 days). Eddies formed near the shelf-break west of 33°W had relatively low velocities and short lifetimes likely due to the interaction with the coast. Eddies within NEB lasted more when they have weak speed of propagation (Figure 5B).

Eddy properties within the NEB and regions A and B are summarized in Table 1. On average, 1950 eddies trajectories crossed the NEB between 1993 and 2018. They are subdivided into 775 AE and 1173 CE. Among, these eddies, 1470 (583 AE, 887 CE) were generated within the NEB. The average amplitude of both type of eddies are alike (~ 1.3 cm). However, CE exhibited greater average EKE (51 cm s^{-2}) than AE (35 cm s^{-2}). In region A, only 175 eddy trajectories (41 AE, 134 CE) passed within the region over the period of study while only 94 eddies were formed in the region over the same period. Both types of eddy formed in region A have alike

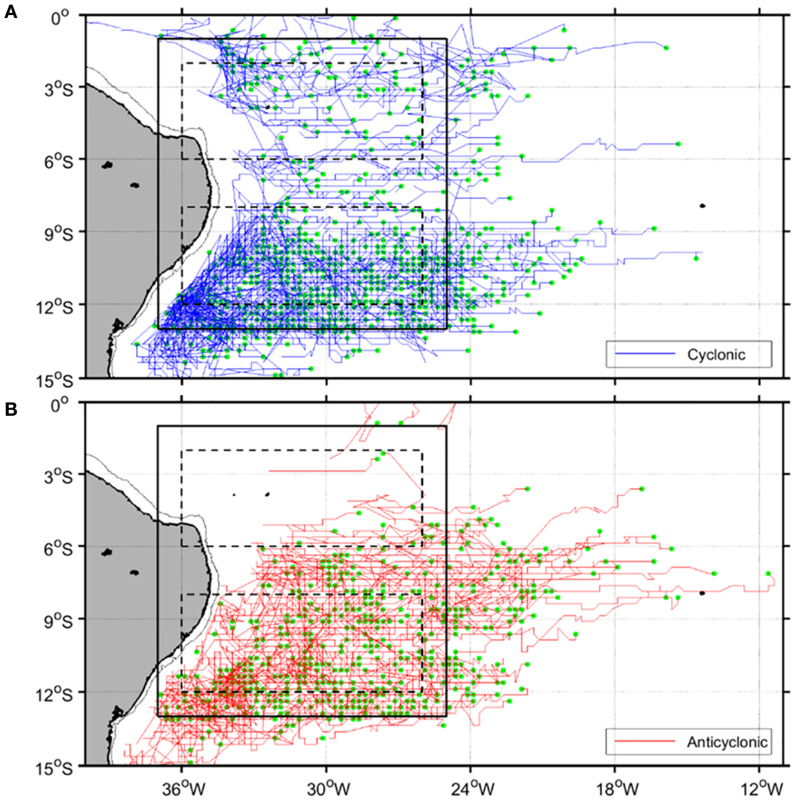

FIGURE 4
Trajectories of **(A)** cyclonic and **(B)** anticyclonic eddies which crossed the Northeast Brazil (NEB) region between January 1993 and December 2018. Green dots indicate the positions where these eddies were first identified. Black boxes indicate the NEB region while dashed boxes show regions **(A, B)** as in Figure 3.

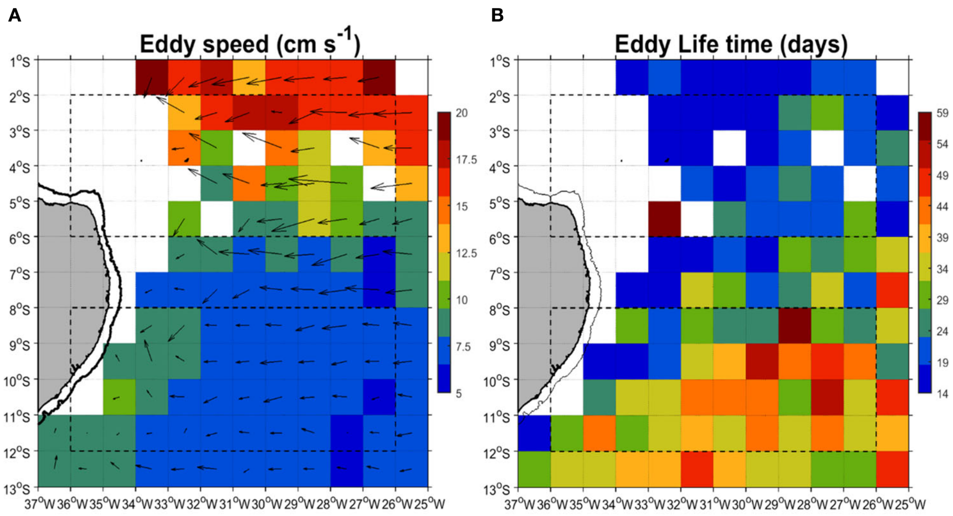

FIGURE 5
Spatial distribution per degree square over 1993-2018 period of **(A)** mean eddy propagation speed (colors) and direction (arrows) and **(B)** mean eddy life time off northeast Brazil.

TABLE 1 Mean properties and characteristics of AE and CE within NEB and northern part of NEB (A) and southern part of NEB (B).

Mean (STD)

	NEB		A		B	
	AE	CE	AE	CE	AE	CE
Number of trajectories crossing	775	1173	41	134	448	666
Number of eddies generated within	583	887	14	80	326	442
Amplitude (cm)	1.2 (0.3)	1.3 (0.3)	1.2 (0.2)	1.3 (0.3)	1.2 (0.3)	1.3 (0.5)
Radius (km)	94.7 (23.8)	90.3 (26.2)	121.5 (18.1)	130.0 (46.3)	91.4 (29.1)	86.2 (29.0)
EKE (cm^2 s^{-2})	35.0 (14.0)	51.0 (32.0)	79.0 (4.1)	132.0 (32.1)	32.0 (12.0)	38.0 (21.0)
Speed (cm s^{-1})	7.4 (1.6)	8.6 (3.2)	11.0 (2.3)	14.3 (3.4)	7.2 (1.3)	7.7 (1.8)
Lifetime (days)	32(24)	35 (26)	21 (5)	21 (8)	33 (22)	41 (29)

Standard deviation values (STD) are indicated in brackets.

average amplitudes. However, CE have greater average radius, EKE, speed than AE. On other side, 1114 eddy trajectories crossed the region B including 448 AE and 666 CE. Among these eddies, 768 (326 AE, 442 CE) were formed within the region before propagating out of the region or decaying within it. Both type of eddies have alike amplitude (1.2 ± 0.3 cm for AE; 1.3 ± 0.5 for CE). Average radius for AE was greater (91.4 ± 29 km). However, CE exhibited greatest lifetime (41 ± 29 days).

Eddy seasonal variability and mechanisms behind its formation off northeast Brazil

In the NEB region, CE dominated over AE throughout the year except in June when the proportion of both types were alike (Figure 6) This seasonal variation is similar with the observation of Bruce, 1984 in the northern latitude (3- 10°N). However, the seasonal variation was alike for both types of eddies with a maximum in August-September and minimum in February-March (but a local minimum in June for CE).

We further estimated the seasonal variation of the number of AE and CE as well as the wind stress curl and wind stress magnitude by region. In region A, CE dominated AE from April to November with a peak in October while between December and March the proportion of both eddies was alike (Figure 7A). The seasonal variation of CE in this region seems related to the seasonal variation of wind stress curl (Figure 7A). The wind stress curl was negative throughout the year within region A. Between June and October; it shows similar variations as the number of CE, increasing from -1.6×10^{-8} N m^{-3} in June to 0.8×10^{-8} in October. On other side, the magnitude of the wind stress exhibited a clear seasonal cycle (Figure 7C) within region A from less than 0.03 N m^{-2} in March-April to 0.06 N m^{-2} in August-September.

In region B, less seasonal variation was observed for the number of both eddy types (Figure 7B). However, AE and CE were respectively minimum in April and June and maximum in August and October. The wind stress curl within the region showed a clear seasonal variation. Two distinct periods of variability were observed: a negative wind stress curl between January and August and a positive wind stress curl between

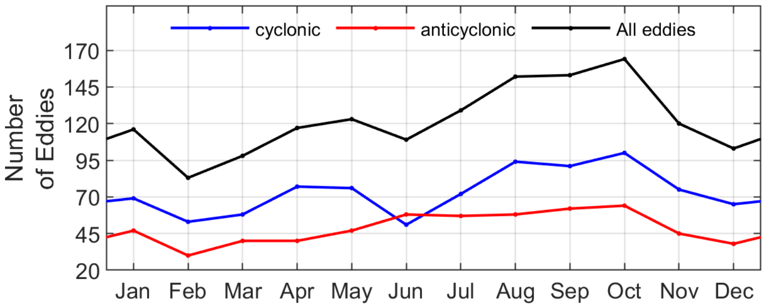

FIGURE 6
Seasonal cycle of the number of eddies generated off Northeast Brazil.

September and December. The maximum wind stress curl (0.7×10^{-8} N m^{-3}) occurred in November while the minimum wind stress curl (- 1.7×10^{-8} N m^{-3}) occurred in July. On other side, wind stress magnitude depicted a clear seasonal variation (Figure 7C), increasing from ~0.035 N m^{-2} in March to ~0.06 N m^{-2} in July. In both regions, the wind stress curl and the wind stress seem to contribute to the generation of eddies. However, other mechanisms could induce eddy formation in the region.

Indeed, several other mechanisms such as the topographic effect, barotropic and baroclinic instabilities are susceptible to promote the formation of eddies in the world ocean. According to the Rayleigh (1880) criterion extended to nonparallel steady currents and applied in the geostrophic context, barotropic instabilities increase in regions where the gradient of the absolute vorticity (C) of large-scale currents almost vanished. This criterion was recently applied in the region of the NECC retroflection in the tropical Atlantic (Aguedjou et al., 2019) where more than 55% of eddies are formed in areas of weak vorticity gradient. In the same way, we first estimated the seasonal cycle (1993 – 2018 monthly mean maps) of the gradient of absolute vorticity gradient superimposed with the formation position of each eddy detected in regions A and B (Figure 8). In a second step, we assessed the variation of the number of eddies formed in each region as a function of the absolute vorticity gradient (Figure 9).

The NEB region was dominated by large positive vorticity values throughout the year. Nevertheless, negative gradient values can be observed in some areas (Figure 8). In region A, the distribution did not show a well pronounced seasonal cycle. The region was dominated by positive gradients. However, intense positive values can be observed in some areas. For example, at the northern limit of the region along 2°S, at ~30-25°W, a positive intensification of gradient was observed from January to August, but disappeared in September-October before reappearing in November. At the western limit of the region (36-35°W) at ~ 4 - 3°S, a negative intensification superimposed by a positive intensification was observed all year long. Still, in some places, we can observe some strong positive values of vorticity gradient.

During the first trimester (January-March), very few eddies were formed in the area. Among these, we observed just two CE in January that were formed in areas of gradient close to zero. Between April and October, most of eddies (AE, CE) were formed in low gradient areas.

In the southern part of NEB, in region B, the spatial distribution of the gradient of absolute vorticity showed a strong seasonal cycle. Between April and August, the region was dominated with negative gradient of absolute vorticity, which was much extended during June – July. Between September and March, when the gradient within the region was dominantly positive, very few eddies were generated in the area of weak gradient. Therefore, a better estimation of number of eddies generated within region of weak gradient is necessary. For this purpose, we provided the mean number of eddies generated within regions A and B in function of gradient of vorticity at position of each detected eddy (Figure 9).

In region A, 34% of CE were formed within areas where the gradient of absolute vorticity (C) was close to zero (± 0.1×10^{-10} m^{-1} s^{-1}) (Figure 9A) while only one AE was formed in regions of

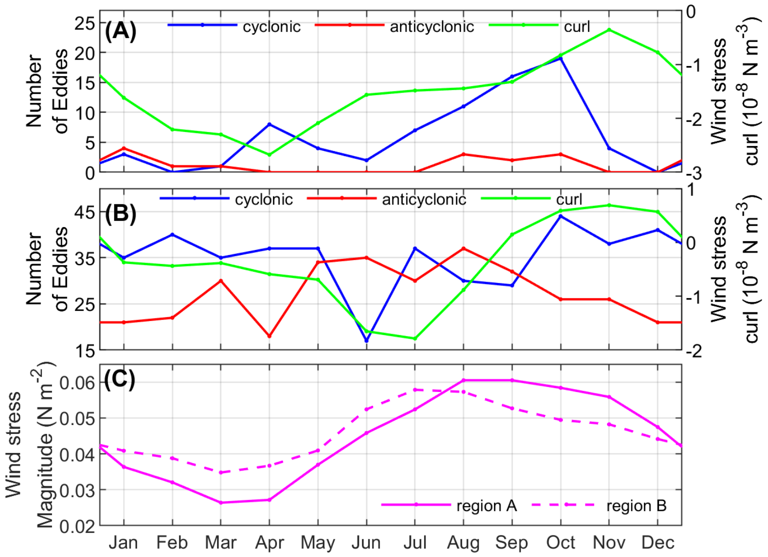

FIGURE 7

Seasonal cycle of **(A)** number of AE and CE (red and blue lines respectively) and wind stress curl (green line) within northern part of NEB (region A), **(B)** number of AE and CE (red and blue lines respectively) and wind stress curl (green line) within southern part of NEB (region B), and **(C)** wind stress magnitude in regions A (magenta solid line) and B (dashed magenta line).

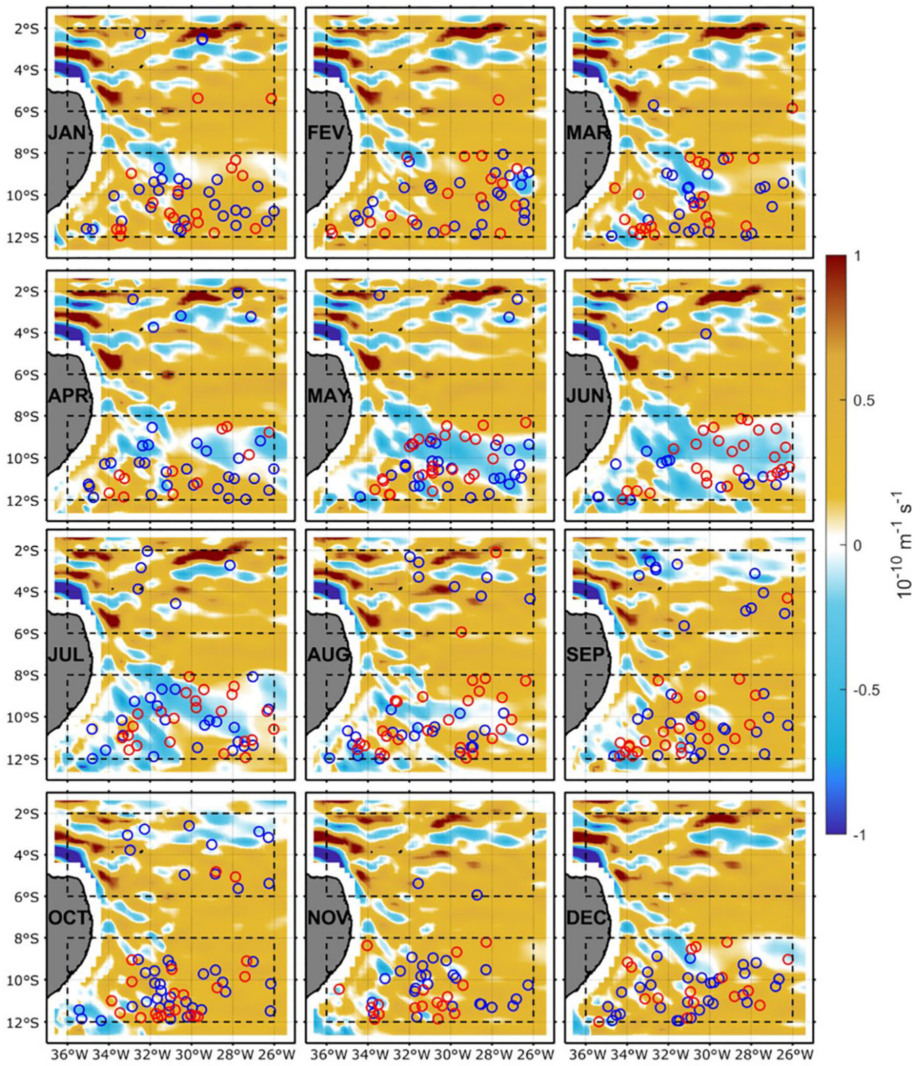

FIGURE 8
1993 – 2018 monthly mean maps of gradient of absolute vorticity of large-scale currents (color shading) superimposed with eddy location of long-lived eddies generated off northeast Brazil between 1993 and 2018 (blue and red circles for cyclonic and anticyclonic eddies respectively).

weak C. Therefore, others mechanisms may be involved into the formation of both types of eddies within this region. In the southern part of NEB, in region B, most eddies were generated within areas of weak gradient of vorticity (Figure 9B). Among CE formed in the region, ~57% were formed in region of weak C (± 0.1×10^{-10} m^{-1} s^{-1}) against 54% for AE. Hence, barotropic instabilities mostly control eddy formation in region B. Due to the complex dynamics of the region, the horizontal shear of the surface currents could also contribute to the formation of eddies off NEB.

Surface current analysis from near-surface drifter data provides information on upper layer dynamics. It revealed a dominant zonal current north of 5°S (Figure 10). Along the coast, current velocities exhibited a seasonal variability. They intensified progressively from January to July with the occurrence of strong values in May-June when the speed can reach 1 m s^{-1} north of 5°S and 0.8 m s^{-1} south of 8°S. These velocities along the coast weakened from July to December.

In region A, the circulation was mainly westward (characteristic of the cSEC) at the beginning of the year (January-February-March). In April, the current velocities strengthened (>0.8 m s^{-1}). During this month, a cyclonic recirculation around 2°S between 26°-30°W was noted at the northern limit of the region, and remained permanent until May, when it gradually disappeared. From May onward, the circulation slightly changed of direction and progressively shifted to the southwest around 3°S, East of 28°W. This orientation became noticeable in most of the region until

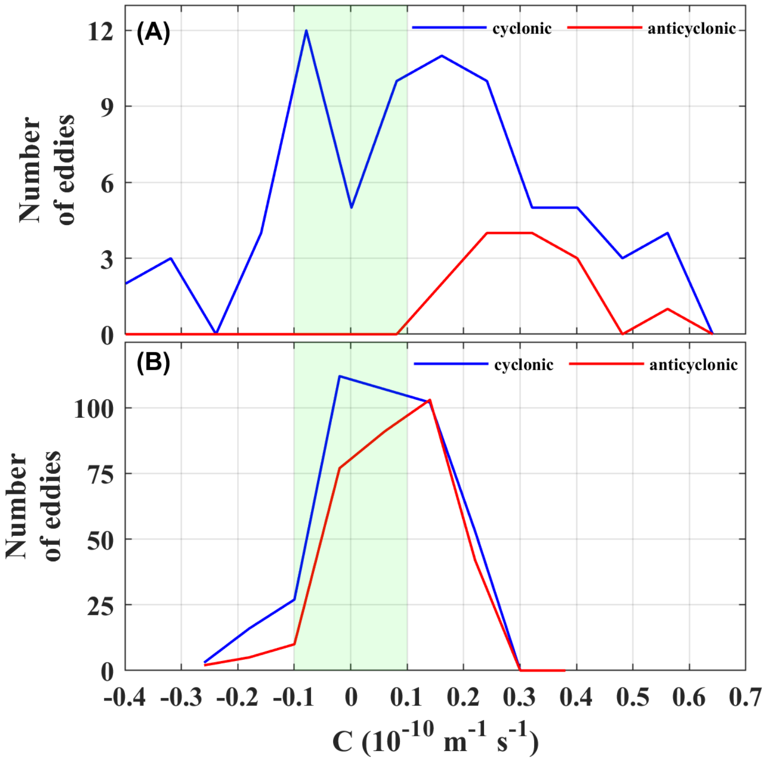

FIGURE 9
Distribution of the number of detected cyclonic and anticyclonic eddies as function of the gradient of large-scale absolute vorticity C at eddy generation sites for all eddies generated between 1993 and 2018 within: **(A)** northern part of NEB (region A) and **(B)** southern part of NEB (region B). Green vertical in **(A, B)** indicate interval values C within $\pm$ 0.1×10^{-10} m^{-1} s^{-1}.

August. However, from this month, the strength of the current weakened in the region and became westward until the end of the year.

On the other hand, the current velocities in region B were weaker than those in region A throughout the year. Moreover, the circulation was not as organized as in region A. Early in the year, cyclonic structures were observed around 28°W between 10°-8°S. In addition, around 10°S to about 34°W, there was a retroflection of a zonal flow from the east, remarkable from February. During the retroflection, the zonal flow split in two, one was directed to the north and the other to the south. This southward flow recirculates further south and enter into the northward coastal flow. In April, we noticed that the retroflection occurred a little further north around 8°S, while the recirculation of the southward flow occurred around 10°S. This retroflection remains permanent around 8°S throughout the year. On the other hand, the cyclonic recirculation of the southward flow occurred progressively further south. In July-August, it was quite remarkable around 12°S to ~36°S. Between September and December, it occurs much more to the south. In addition, east of the region at 10°-8°S; 30-28°W, a meander of the surface current was present between August and September.

Eddies connecting eastern and western tropical Atlantic

To investigate possible connection between the northeast Brazil and the eastern tropical Atlantic we used the trajectories crossing three key distinctive regions along the western tropical Atlantic (Figure 11). Few eddy trajectories formed in the tropical Atlantic (40° S- 40°N; 60° W- 30°E) crossed the Amazon River plume (AMZ) (Figure 11A). Most trajectories observed in the region were originated within the region. Very few AE trajectories originated from the eastern Atlantic crossed the AMZ while no CE trajectories originated from the eastern coast crossed it (Figure 11A). South of the AMZ, off the NEB, most trajectories were originated within the region. No eddy trajectories (AE, CE) originated from the eastern tropical Atlantic were observed. The region thus does not have any connection with the eastern tropical Atlantic through mesoscale eddies. Finally, a clear connection between the southeastern Atlantic and the southwestern tropical was revealed (Figure 11C), in agreement with Laxenaire et al. (2018). The connection was mostly made through AE, with up to 8 trajectories originating from the southeastern tropical Atlantic

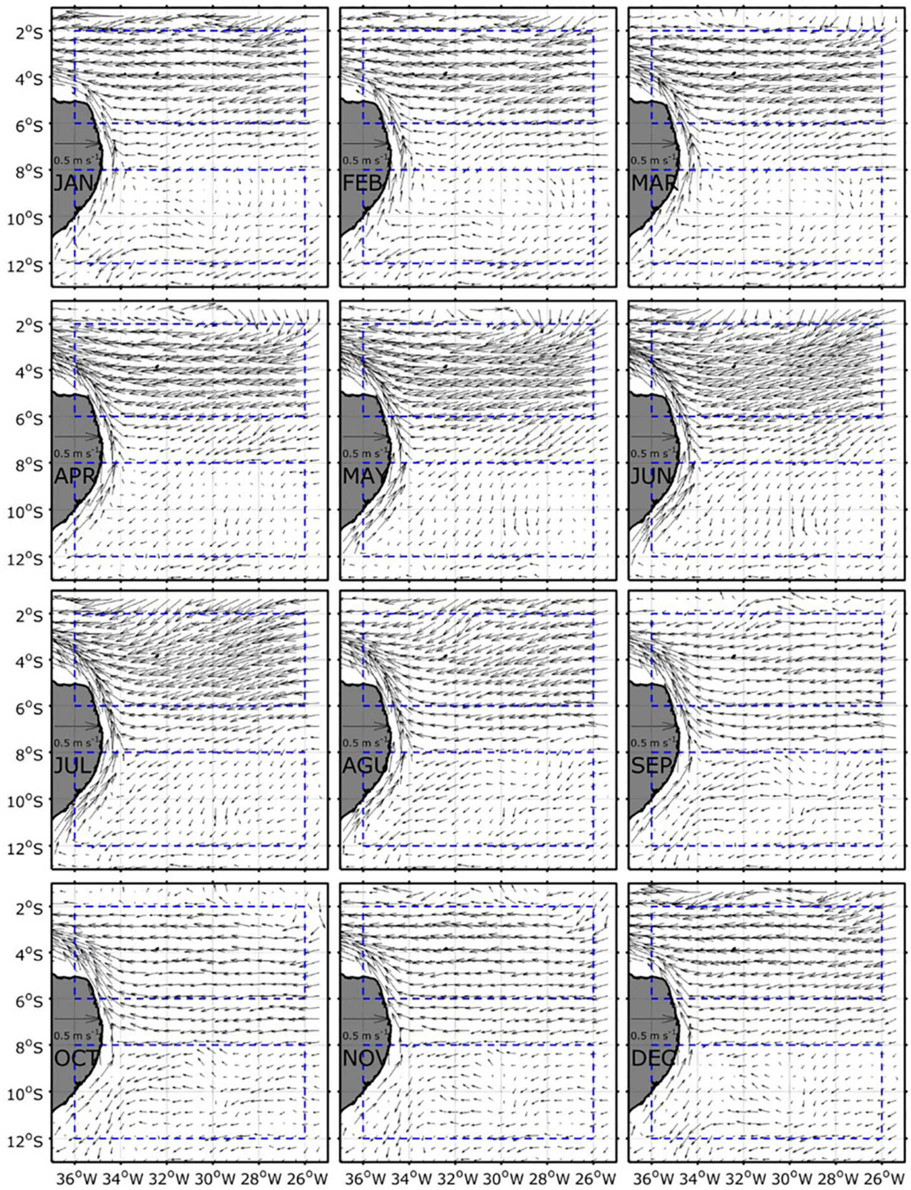

FIGURE 10
Mean monthly (1979 - 2015) map of surface currents from drifter off NEB.

(east of 7°E). On other side, only one CE originated from the southeastern Tropical Atlantic crossed the basin.

Eddy vertical extent

In order to study eddy vertical extent in the NEB, we first provide the mean temperature, salinity and density profiles from Argo floats in regions A and B (Figure 12). In region A, The MLD and the ILD were respectively 51 m and 56 m. The temperature profile was characterized by relatively weak stratification above 200 m with thermocline extending from 56 to 146 m depth while halocline and pycnocline extending between 51 and 146 m depth (Figure 12A). In region B, the MLD and the ILD were 55 m and 63 m, respectively (Figure 12B). The mean temperature, salinity and density profiles exhibited low stratification, characterized by thermocline extending from 63 m to 185 m depth. The halocline/pycnocline ranged at 55 – 185 m depth.

In region A and B, vertical profiles of the mean temperature, salinity and density anomalies were largest within eddies than outside eddies (Figure 13). In region A, the largest mean

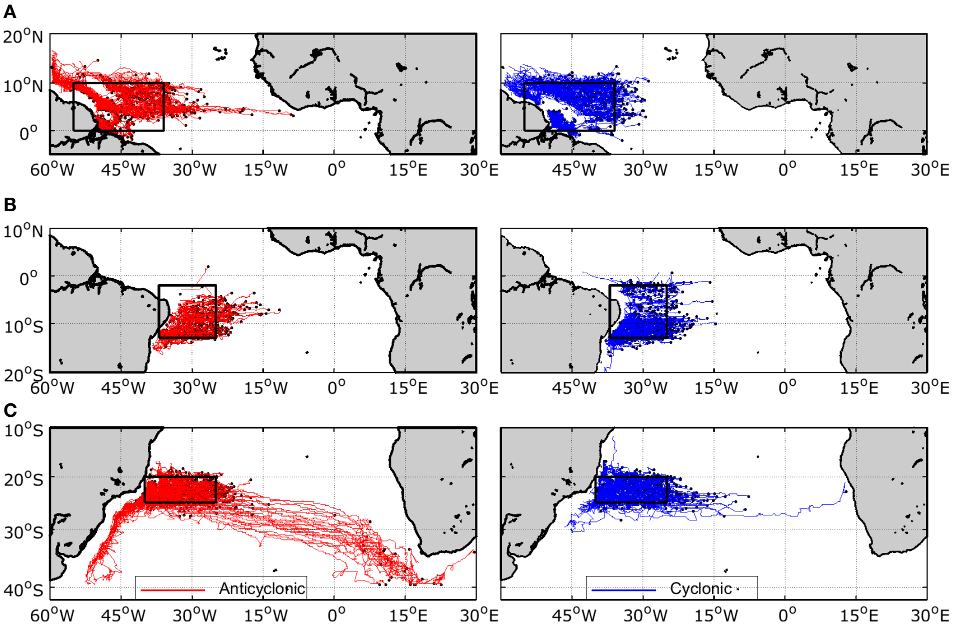

FIGURE 11
Mesoscale eddy trajectories detected in the tropical Atlantic crossing the: **(A)** Amazon river plume region (55°– 36°W; 0° – 10°N), **(B)** northeast Brazil region (37° – 25°W; 13° - 2°S) and **(C)** southwestern tropical Atlantic (40° – 25°W; 25° - 20°S). Red (blue) lines indicate AE (CE) trajectories. Black dots indicate eddy generation position.

temperature anomalies (> 0.2°C) in AE were located at ~ 60 – 180 m depth, with a maximum anomaly of 1.4°C at 105 m depth (Figure 13A). The corresponding salinity anomalies were weaker in AE (< 0.1). Salinity anomalies inside AE were negative above 85 m depth. Below this depth, at ~ 85 – 220 m, the anomalies were positive, with largest values (> 0.01) observed between 90 m and 190 m depth. The maximum anomaly (0.09) was reached at ~135 m depth. Below 220 m depth, the anomaly changed sign and became slightly negative. Inside CE, temperature anomalies were mostly positive (Figure 13A) and largest temperature anomalies (< -0.1°C) were observed between ~ 40 and 230 m depth, with an extremum (-1.25°C) at 90 m depth. The corresponding salinity anomalies were positive above 65 m depth, but the highest anomalies in absolute value located practically at the same depth. The extremum in salinity anomaly was reached at 115 m depth. Profile of mean density anomalies were mostly consistent with the temperature anomaly profiles (except in the upper surface layer), demonstrating that in region A, the density distribution is mostly driven by temperature changes. As expected outside eddies, the mean temperature, salinity, and density anomalies were almost null.

In region B, above 200 m depth, the mean temperature, salinity, and density anomalies within (outside) both types of eddy were weaker (higher) than in region A. Inside AE of region B, the highest temperature anomalies (> 0.2°C) were located at ~60- 230 m depth, with an extremum (0.5°C) at 155 m depth. The corresponding salinity anomalies were negative above 105 m. Below this depth, these anomalies become positive along with the depth until ~800 m depth where they almost vanished. The largest positive anomalies (0.01) ranged at ~100 – 270 m depth, with an extremum (0.09) at 150 m depth. In the CE of the region, the highest temperature anomalies in absolute value (> 0.2 °C) were observed at ~ 60 – 230 m depth with an extremum (-0.6) at 140 m. Salinity anomalies were also positive in the near-surface layer (above 90 m) and below 890 m depth (Figure 13B) and were maximum (> 0.01) at ~110 – 270 m depth. On other side, the profile of mean density anomalies was similar with the profile of mean temperature anomalies (Figures 13A, C), demonstrating that change in temperature also controlled most of the density distribution in region B. Mean sea water properties and associated anomalies at depth where the density is maximum are summarized in Table 2.

The definition of the lower limit of the eddy extent in the water column is a challenging task. In the present study, we based our definition on the isotherm and isohaline threshold. Following Sandalyuk and Belonenko (2021), we defined the lower limit of eddy extent as the depth where both temperature and salinity anomalies within eddies correspond to about 10% of the maximum anomalies. Using this criterion, we observed that in region A, AE (CE) lower limit is located at ~ 180 m (250 m) while in region B, AE (CE) extended up to ~ 250 m (270 m).

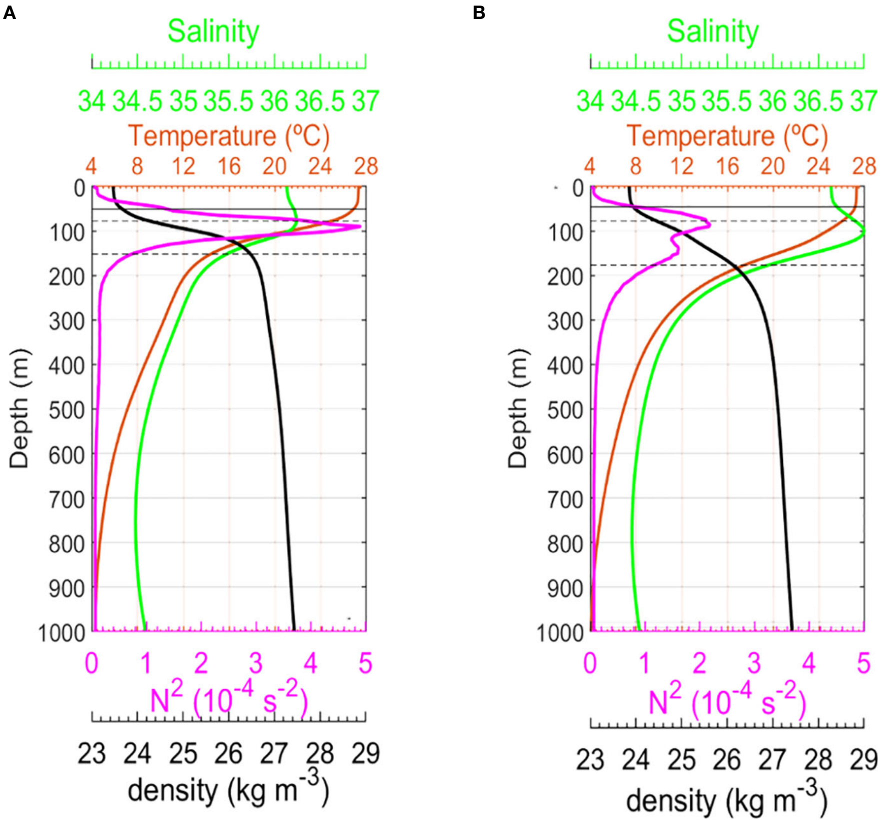

FIGURE 12
Mean Temperature, salinity, density, and squared buoyancy frequency (N^2) inside eddies in the regions **(A, B)** Solid horizontal line indicates the base of the mixed layer depth while the dashed horizontals lines indicate the upper and lower thermocline depth. The lower thermocline depth also corresponds to the pycnocline depth.

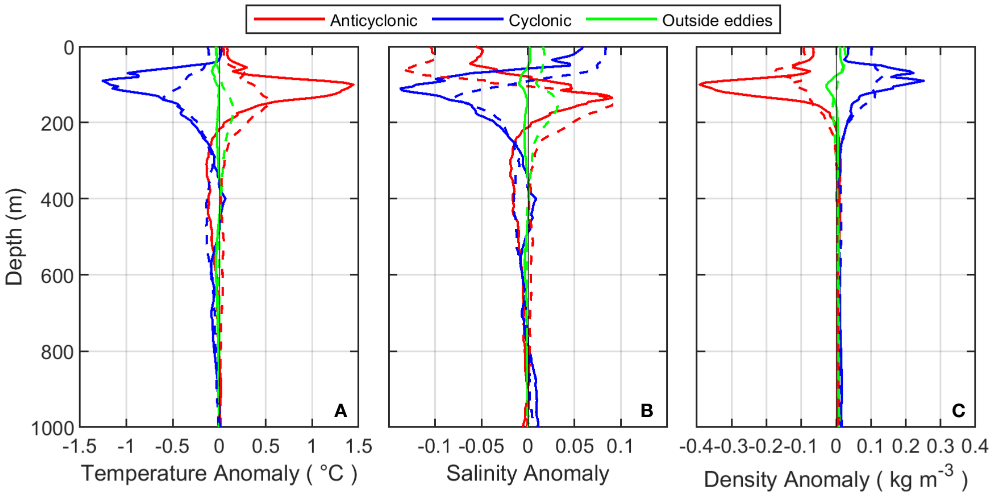

FIGURE 13
Mean vertical profiles of **(A)** temperature anomaly, **(B)** salinity anomaly, and **(C)** density anomaly in regions A and **(B)** Solid lines (dashed lines) correspond to the mean profiles obtained in region A **(B)** for the composite CE (blue lines), AE (red lines) and outside eddies (green lines).

Discussion and conclusion

Based on altimetry data and Argo data, this study characterized the mesoscale eddies and the possible mechanisms involved in their generation off Northeast Brazil. Gradients of absolute vorticity from AVISO geostrophic velocity fields allowed us to observe the contribution of barotropic instabilities in the eddy generation within the region of interest. Then, wind data from ERA5 and surface velocities data from near-surface drifters enabled us to emphasize the contribution of wind stress curl and dynamics of surface currents, respectively. In addition, an important finding is that mesoscale eddies do no directly connect the eastern tropical Atlantic to the NEB region.

Automatic eddy detection and tracking algorithms applied to daily ADT maps from January 1993 to December 2018 allowed us to reveal 1950 eddies trajectories crossing the NEB. Among these eddies, 1470 eddies (40% AE and 60% CE) were formed within the region of interest. There was no clear geophysical preference for both types of eddy in NEB as observed in the Global ocean (Chelton et al., 2011) and specifically in the tropical Atlantic (Aguedjou et al., 2019).

Our results reveal that in the northern part (region A), eddies are rather rare. They tend to have a large radius, a large EKE, low amplitudes and do not live too long. This is due to the baroclinic Rossby radius deformation (e.g., Chaigneau et al., 2009). CE dominate region A. Although barotropic instabilities can contribute to the formation of the CE in the region, negative wind stress curl associated with an increase intensity of wind stress seems to also favour their formation (Figures 7A, C, 8, 9) in accordance with Rodrigues et al. (2007) for the region.

More eddies were formed in the south (region B) than in the northern part of the NEB indicating that different physical processes control the eddy dynamics in each region. Indeed, in region A lies the Fernando de Noronha ridge, which encompasses seamounts, the Fernando de Noronha archipelago and Atoll das Rocas (Figure 2). It is also a region where the intense surface current NBC is formed when the cSEC crossing the region enters the western boundary system (e.g., Dossa et al., 2021). Most of eddies observed in this region were formed in the eastern part of the FN archipelago from where the cSEC flows (Figure 4A). West of AR, few eddy trajectories were observed, but none of them was formed in this region. This is not consistent with the theory indicating that the disruption of the current flow by the islands can induce the generation of eddies in the wake of the obstacle (e.g., Arístegui et al., 1997). This inconsistency may be because the altimeter resolution near the equator is too large and did not allow to capture eddies with lower amplitude. This suggests the need of Surface water and ocean Topography (SWOT) to access fine mesoscale geostrophic currents in near equatorial region, to better capture eddies in the region. Moreover, Silva et al. (2021) showed that the presence of the FN Archipelago induces strong disturbances of the cSEC with a splitting of its core upstream of the archipelago. They also highlighted the effect of the topography around islands on the intensity and direction of the currents, which can favour eddy generation at the wake of the FN archipelago. At the western extremity of region A, where one would expect eddy formation due to the interaction of the cSEC with the western boundary system, no eddies were observed because, eddies in this region have small life and propagate very fast.

More eddies (AE, CE) were observed in region B (Table 1). Several processes are likely to promote their formation. First, it is

TABLE 2 Depths of mixed layer, isothermal layer, lower thermocline limit, maximum temperature anomaly and maximum salinity anomaly inside eddies in region A and B.

	Region A		Region B	
	CE	AE	CE	AE
MLD (m)	49		55	
ILD (m)	54		63	
LTD (m)	146		185	
Depth of maximum Temperature anomaly (m)	90 (40 – 230)	135 (60 – 180)	140 (60 -230)	155 (60 - 230)
Depth of maximum Salinity anomaly (m)	115 (40 - 230)	90 (40 - 230)	130 (110 -270)	150 (100 - 270)
Depth of maximum density anomaly (m)	90 (45 – 185)	95 (75 - 140)	75 (50 - 175)	70 (30 - 160)
Temperature (°C)	22.08 (3.32)	23.32 (2.63)	26.07 (0.60)	26.52 (0.63)
Salinity	36.15 (0.25)	36.27 (0.23)	36.95 (0.12)	36.77 (0.22)
Density (kg m^{-3})	25.02 (0.74)	24.78 (0.57)	24.50 (0.22)	24.20 (0.30)
Temperature anomaly (°C)	-1.2 (2.8)	1.3 (1.6)	-0.3 (0.7)	0.3 (0.6)
Salinity anomaly	-0.009 (0.061)	0.03 (0.18)	0.04 (0.15)	-0.12 (0.21)
Density anomaly (kg m^{-3})	0.2 (0.2)	- 0.4 (0.3)	0.1 (0.3)	- 0.2 (0.3)

MLD, ILD and LTD values correspond to the mean values inside both type of eddy (AE & CE); Mean seawater properties (temperature, salinity and density) and their anomalies observed in eddies cores at the depth where density anomalies are maximum. Depths values in brackets indicate the approximative depth range of large temperature, salinity, and density anomalies while anomalies values in brackets indicate standard deviation.

a region where lies the Pernambuco Plateau at ~8°S (Silva et al., 2022). The interaction of the large-scale currents with this plateau could generate eddies (e.g., Herbette et al., 2003). Dossa et al. (2021) showed that the northward meridional flow originating from the south of the region is slightly shifted eastward until ~7.5°S (northern extremity of the region) where it changes direction to the west as the coast orientation changes. This suggests that the formation of about five AE eddies observed in region B over the continental slope (Figure 4A) may be favoured by the interaction of near-coastal circulation with the topography.

Second, region B constitutes part of the sSEC retroflection zone (10°-14°S, Rodrigues et al., 2007) where the NBUC (BC) is formed and flows northward (southward). The latitude of the retroflection is subjected to south-north migration due to the change in wind stress curl (wind stress curl < 0 or > 0) near the coast (Rodrigues et al., 2007) which is favourable for the generation of eddies. Similarly, we observed that the negative wind stress curl between January and September observed within region B is correlated with the seasonal cycle of the number of CE (Figure 7B). Therefore, the negative wind stress curl likely contributes to the generation of CE formed in region B.

Third, barotropic instabilities also contribute to the formation of both types of eddies in region B. Almost 57% (54%) of the CEs (AEs) formed in this region, are generated in regions where the gradient of absolute vorticity is close to 0, justifying the strong contribution of barotropic instabilities associated with horizontal shear of surface currents in the region (Figure 10).

In both regions (A, B) of the NEB, the formation of both types of eddies seems to be driven not only by the mechanisms highlighted here (barotropic instabilities, wind stress curl, topographic effect), but other mechanisms such as baroclinic instabilities (e.g., von Schuckmann et al., 2008) could be involved in the eddy generation within NEB. The formation of eddies downstream of the islands and the topographic effect need to be investigated through a high-resolution numerical model to better understand their role in the formation of eddies.

Through eddy tracking algorithm in the tropical Atlantic, we did not observe any eddy connecting the eastern tropical Atlantic and the Northeast Brazil (Figure 11A). However, some mesoscale eddies originating from western Africa (southeastern boundary) can eventually propagate until the Amazon River plume (southwestern tropical Atlantic) (Figures 11B, C). The latter connection was also observed by Laxenaire et al. (2018). These authors have reported that anticyclonic eddies can travel from the Indian Ocean from where they carry salty and warm water to the southeastern Atlantic.

The composite analysis of Argo profile revealed that the occurrence of mesoscale eddies have an influence on thermohaline structure off northeast Brazil. In the northern region, CE tend to stretch the thermocline and the halocline vertically of 45 m in depth (Figures 12A, 13A, B and Table 2). AE only stretch the halocline and moved the thermocline 6 m in depth with a vertical extent of ~30 m (Figures 12A, 13A, B and Table 2). In the southern region, both type of eddy (AE & CE) have similar influence on the thermocline and the halocline. They tend to stretch to thermocline 45 m in depth and move the halocline 55 m in depth with an extent of ~50 m (Figures 12B, 13A, B and Table 2). Eddies plays same role on the thermohaline structure in the southern region, because, they have almost the same vertical extent (Table 2).

Data availability statement

All the data used in this study are publicly available. The altimetry datasets can be obtained from the Copernicus Marine Environment Monitoring service (CMEMS: http://marine.copernicus.eu). The sea surface velocities current from DRIFTER are available at https://www.aoml.noaa.gov/phod/gdp/mean_velocity.php. The wind datasets are publicly available at https://www.ecmwf.int/en/forecasts/datasets/reanalysis-datasets/era5. Argo profiles are available at https://www.coriolis.eu.org/Observing-the-Ocean/ARGO.

Author contributions

AND, AS and AB conceptualized the work. AND, HA and AC worked in data processing. AND provided the original draft. All authors contributed to the article and approved the submitted version.

Funding

This work was supported by the CAPES/PRINT (n° 88887.470036/2019-00) through a PhD internship scholarship grant for AND. This work was a contribution to the LMI TAPIOCA, the SMAC project (CAPES/COFECUB no. 88881.142689/2017–01), the PADDLE project (funding by the European Union's Horizon 2020 Research and Innovation Programme—Grant Agreement 73427) and EU H2020 TRIATLAS project under Grant Agreement 817578.

Acknowledgments

This work was supported by the CAPES/PRINT (n° 88887.470036/2019-00) through a PhD internship scholarship grant for A.N.D. This work was supported by the CAPES (Coordenação de Aperfeiçoamento de Pessoal de Nível Superior) through a PhD scholarship grant for A.N.D. MA thanks the Brazilian Research Network on Global Climate Change—Rede CLIMA (FINEP-CNPq 437167/2016-0) and the Brazilian National Institute of Science and Technology for Tropical Marine Environments—INCT AmbTropic (CNPq/ FAPESB 565054/2010-4 and 8936/2011) for their support. This work is a contribution to the In- ternational Joint Laboratory TAPIOCA (www.tapioca.ird.fr), to the SMAC project (CAPES/COFECUB n° 88881.142689/2017–01), the PADDLE project (funding by the European Union's Horizon 2020 research and innovation programme - grant agreement No. 73427), and to the TRIATLAS project, which has also received funding from the European Union's Horizon 2020 research and innovation program under grant agreement No 817578.

Conflict of interest

The authors declare that the research was conducted in the absence of any commercial or financial relationships that could be construed as a potential conflict of interest

Publisher's note

References

Ablain, M., Cazenave, A., Larnicol, G., Balmaseda, M., Cipollini, P., Faugère, Y., et al. (2015). Improved sea level record over the satellite altimetry era, (1993-2010) from the climate change initiative project. *Ocean Sci.* 11, 67–82. doi: 10.5194/os-11-67-2015

Aguedjou, H. M. A., Chaigneau, A., Dadou, I., Morel, Y., Pegliasco, C., Da-Allada, C. Y., et al. (2021). What can we learn from observed temperature and salinity isopycnal anomalies at eddy generation sites? application in the tropical Atlantic ocean. *J. Geophys. Res. Ocean* 126, 1–27. doi: 10.1029/2021JC017630

Aguedjou, H. M. A., Dadou, I., Chaigneau, A., Morel, Y., and Alory, G. (2019). Eddies in the tropical Atlantic ocean and their seasonal variability. *Geophys. Res. Lett.* 156–164. doi: 10.1029/2019GL083925

Araujo, M., Limongi, C., Servain, J., Silva, M., Leite, F. S., Veleda, D., et al. (2011). Salinity-induced mixed and barrier layers in the southwestern tropical Atlantic ocean off the northeast of Brazil 63–73. doi: 10.5194/os-7-63-2011

Arístegui, J., Tett, P., Hernández-Guerra, A., Basterretxea, G., Montero, M. F., Wild, K., et al. (1997). The influence of island-generated eddies on chlorophyll distribution: A study of mesoscale variation around gran canaria. *Deep Res. Part I Oceanogr. Res. Pap.* 44, 71–96. doi: 10.1016/S0967-0637(96)00093-3

Arruda, W. Z., Campos, E. J. D., Zharkov, V., Soutelino, R. G., and da Silveira, I. C. A. (2013). Events of equatorward translation of the vitoria eddy. *Cont. Shelf Res.* 70, 61–73. doi: 10.1016/j.csr.2013.05.004

Assunção, R. V., Silva, A. C., Roy, A., Bourlès, B., Silva, C. H. S., Ternon, J. F., et al. (2020). 3D characterisation of the thermohaline structure in the southwestern tropical Atlantic derived from functional data analysis of *in situ* profiles. *Prog. Oceanogr.* 187, 102399. doi: 10.1016/j.pocean.2020.102399

Bruce, J. G. (1984). Comparison of eddies off the north Brazilian and Somali coasts. *J. Phys. Oceanogr.* 14 (4), 825–832. doi: 10.1175/1520-0485(1984)014<0825:COEOTN>2.0.CO;2

Campos, E. J. D. (2006). Equatorward translation of the vitoria eddy in a numerical simulation. *Geophys. Res. Lett.* 33, 1–5. doi: 10.1029/2006GL026997

Chaigneau, A., Eldin, G., and Dewitte, B. (2009). Eddy activity in the four major upwelling systems from satellite altimetry, (1992-2007). *Prog. Oceanogr.* 83, 117–123. doi: 10.1016/j.pocean.2009.07.012

Chaigneau, A., Gizolme, A., and Grados, C. (2008). Mesoscale eddies off Peru in altimeter records: Identification algorithms and eddy spatio-temporal patterns. *Prog. Oceanogr.* 79, 106–119. doi: 10.1016/j.pocean.2008.10.013

Chelton, D. B., Schlax, M. G., and Samelson, R. M. (2011). Global observations of nonlinear mesoscale eddies. *Prog. Oceanogr.* 91, 167–216. doi: 10.1016/j.pocean.2011.01.002

Djakouré, S., Penven, P., Bourlès, B., Veitch, J., and Koné, V. (2014). Coastally trapped eddies in the north of the gulf of Guinea. *J. Geophys. Res. Ocean* 119, 6805–6819. doi: 10.1002/2014JC010243

Dossa, A. N., Silva, A. C., Chaigneau, A., Eldin, G., Araujo, M., and Bertrand, A. (2021). Near-surface western boundary circulation off northeast Brazil. *Prog. Oceanogr.* 190, 102475. doi: 10.1016/j.pocean.2020.102475

Dufois, F., Hardman-Mountford, N. J., Greenwood, J., Richardson, A. J., Feng, M., and Matear, R. J. (2016). Anticyclonic eddies are more productive than cyclonic eddies in subtropical gyres because of winter mixing. *Sci. Adv.* 2, 1–7. doi: 10.1126/sciadv.1600282

Dupuy, S., Pujol, M.-I., Picot, N., Ablain, M., Faugère, Y., Taburet, G., et al. (2016). DUACS DT2014: the new multi-mission altimeter data set reprocessed over 20 years. *Ocean Sci.* 12, 1067–1090. doi: 10.5194/os-12-1067-2016

Frenger, I., Gruber, N., Knutti, R., and Münnich, M. (2013). Imprint of southern ocean eddies on winds, clouds and rainfall. *Nat. Geosci.* 6, 608–612. doi: 10.1038/ngeo1863

Gaube, P., McGillicuddy, D. J., Chelton, D. B., Behrenfeld, M. J., and Strutton, P. G. (2014). Regional variations in the influence of mesoscale eddies on near-surface chlorophyll. *J. Geophys. Res. Ocean* 119, 8195–8220. doi: 10.1002/2014JC010111

Gaube, P., McGillicuddy, J.D., and Moulin, A. J. (2019). Mesoscale eddies modulate mixed layer depth globally. *Geophys. Res. Lett.* 46, 1505–1512. doi: 10.1029/2018GL080006

Gill, A. E., and Adrian, E. (1982). *Atmosphere-ocean dynamics (Vol. 30)* (Academic press).

Herbette, S., Morel, Y., and Arhan, M. (2003). Erosion of a surface vortex by a seamount. *J. Phys. Oceanogr.* 33, 1664–1679. doi: 10.1175/2382.1

Huang, M., Liang, X., Zhu, Y., Liu, Y., and Weisberg, R. H. (2021). Eddies connect the tropical Atlantic ocean and the gulf of Mexico. *Geophys. Res. Lett.* 48, 1–10. doi: 10.1029/2020GL091277

Johns, W. E., Lee, T. N., Schott, F. A., Zantopp, R. J., and Evans, R. H. (1990). The north Brazil current retroflection: Seasonal structure and eddy variability. *J. Geophys. Res.* 95, 22103. doi: 10.1029/jc095ic12p22103

Kang, D., and Curchitser, E. N. (2015). Energetics of eddy-mean flow interactions in the gulf stream region. *J. Phys. Oceanogr.* 45, 1103–1120. doi: 10.1175/JPO-D-14-0200.1

Keppler, L., Cravatte, S., Chaigneau, A., Pegliasco, C., Gourdeau, L., and Singh, A. (2018). Observed characteristics and vertical structure of mesoscale eddies in the southwest tropical pacific. *J. Geophys. Res. Ocean* 123, 2731–2756. doi: 10.1002/2017JC013712

Large, W. G., and Pond, S. (1981). Open ocean momentum flux measurements in moderate to strong winds. *J. Phys. Oceanogr.* 11 (3), 324–336. doi: 10.1175/1520-0485(1981)011<0324:OOMFMI>2.0.CO;2

Laurindo, L. C., Mariano, A. J., and Lumpkin, R. (2017). An improved near-surface velocity climatology for the global ocean from drifter observations. *Deep Res. Part I Oceanogr. Res. Pap.* 124, 73–92. doi: 10.1016/j.dsr.2017.04.009

Laxenaire, R., Speich, S., Blanke, B., Chaigneau, A., Pegliasco, C., and Stegner, A. (2018). Anticyclonic eddies connecting the Western boundaries of Indian and Atlantic oceans. *J. Geophys. Res. Ocean* 123, 7651–7677. doi: 10.1029/2018JC014270

Mahadevan, A. (2014). Eddy effects on biogeochemistry. *Nature* 506, 168–169. doi: 10.1038/nature13048

Pegliasco, C., Chaigneau, A., and Morrow, R. (2015). Main eddy vertical structures observed in the four major Eastern boundary upwelling systems. *J. Geophys. Res. Ocean* 120, 6008–6033. doi: 10.1002/2015JC010950

Pegliasco, C., Chaigneau, A., Morrow, R., and Dumas, F. (2021). Detection and tracking of mesoscale eddies in the Mediterranean Sea: A comparison between the Sea level anomaly and the absolute dynamic topography fields. *Adv. Sp. Res.* 68, 401–419. doi: 10.1016/j.asr.2020.03.039

Rayleigh, L. (1880). On the stability, or instability, of certain fluid motions. *Proc. London Math. Soc* 9, 57–70.

Rio, M. H., Guinehut, S., and Larnicol, G. (2011). New CNES-CLS09 global mean dynamic topography computed from the combination of GRACE data, altimetry, and *in situ* measurements. *J. Geophys. Res. Ocean* 116, 1–25. doi: 10.1029/2010JC006505

Rio, M. H., Mulet, S., and Picot, N. (2014). Beyond GOCE for the ocean circulation estimate: Synergetic use of altimetry, gravimetry, and *in situ* data provides new insight into geostrophic and ekman currents. *Geophys. Res. Lett.* 41, 8918–8925. doi: 10.1002/2014GL061773

Rodrigues, R. R., Rothstein, L. M., and Wimbush, M. (2007). Seasonal variability of the south equatorial current bifurcation in the Atlantic ocean: A numerical study. *J. Phys. Oceanogr.* 37, 16–30. doi: 10.1175/JPO2983.1

Sandalyuk, N. V., and Belonenko, T. V. (2021). Three-dimensional structure of the mesoscale eddies in\vspace {.3pc} the agulhas current region from hydrological and altimetry data. *Russ. J. Earth Sci.* 21, 1–19. doi: 10.2205/2021es000764

Schmid, C., Schafer, H., Podesta, G., and Zenk, W. (1995). The vitoria eddy and its relation to the Brazil current. *J. Phys. Oceanogr.* 25, 2532–2546. doi: 10.1175/1520-0485(1995)025<2532:tveair>2.0.co;2

Schott, F. A., Fischer, J., and Stramma, L. (1998). Transports and pathways of the upper-layer circulation in the Western tropical Atlantic. *J. Phys. Oceanogr.* 28, 1904–1928. doi: 10.1175/1520-0485(1998)028<1904:TAPOTU>2.0.CO;2

Schott, F. A., Stramma, L., and Fischer, J. (1995). The warm water inflow into the western tropical Atlantic boundary regime, spring 1994. *J. Geophys. Res.* 100, 24745. doi: 10.1029/95JC02803

Silva, M., Araujo, M., Servain, J., Penven, P., and Lentini, C. A. D. (2009). High-resolution regional ocean dynamics simulation in the southwestern tropical Atlantic. *Ocean Model.* 30, 256–269. doi: 10.1016/j.ocemod.2009.07.002

Silva, A., Chaigneau, A., Dossa, A. N., and Eldin, G. (2021). Surface circulation and vertical structure of upper ocean variability around Fernando de noronha archipelago and rocas atoll during spring 2015 and fall 2017. doi: 10.3389/fmars.2021.598101

Silva, M. V. B., Ferreira, B., Maida, M., Queiroz, S., Silva, M., Varona, H. L., et al. (2022). Flow-topography interactions in the western tropical Atlantic boundary off northeast Brazil. *J. Mar. Syst.* 227, 103690. doi: 10.1016/j.jmarsys.2021.103690

Silveira, I. C. A., de Miranda, L. B., and Brown, W. S. (1994). On the origins of the north Brazil current. *J. Geophys. Res.* 99, 22501. doi: 10.1029/94JC01776

Soutelino, R. G., Da Silveira, I. C. A., Gangopadhyay, A., and Miranda, J. A. (2011). Is the Brazil current eddy-dominated to the north of 20°S? *Geophys. Res. Lett.* 38, 1–5. doi: 10.1029/2010GL046276

Soutelino, R. G., Gangopadhyay, A., and da Silveira, I. C. A. (2013). The roles of vertical shear and topography on the eddy formation near the site of origin of the Brazil current. *Cont. Shelf Res.* 70, 46–60. doi: 10.1016/j.csr.2013.10.001

Trenberth, K. E., Large, W. G., and Olson, J. G. (1990). The mean annual cycle in global ocean wind stress. *J. Phys. Oceanogr.* 20, 1742–1760. doi: 10.1175/1520-0485(1990)020<1742:tmacig>2.0.co;2

Villas Bôas, A. B., Sato, O. T., Chaigneau, A., and Castelão, G. P. (2015). The signature of mesoscale eddies on the air-sea turbulent heat fluxes in the south Atlantic ocean. *Geophys. Res. Lett.* 42, 1856–1862. doi: 10.1002/2015GL063105

von Schuckmann, K., Brandt, P., and Eden, C. (2008). Generation of tropical instability waves in the Atlantic Ocean. *J. Geophys. Res.* 113, C08034. doi: 10.1029/2007JC004712

Wunsch, C. (1999). Where do ocean eddy heat fluxes matter? *J. Geophys. Res. Ocean* 104, 13235–13249. doi: 10.1029/1999jc900062

frontiers | Frontiers in Marine Science

TYPE Original Research
PUBLISHED 24 November 2022
DOI 10.3389/fmars.2022.958733

OPEN ACCESS

EDITED BY
Ronald Buss de Souza,
National Institute of Space Research (INPE), Brazil

REVIEWED BY
Erik Van Sebille,
Utrecht University, Netherlands
Rémi Laxenaire,
Florida State University, United States

*CORRESPONDENCE
Luiz Alexandre A. Guerra
laguerra@petrobras.com.br

SPECIALTY SECTION
This article was submitted to Physical Oceanography, a section of the journal Frontiers in Marine Science

RECEIVED 31 May 2022
ACCEPTED 31 October 2022
PUBLISHED 24 November 2022

CITATION
Guerra LAA, Mill GN and Paiva AM (2022) Observing the spread of Agulhas Leakage into the Western South Atlantic by tracking mode waters within ocean rings. *Front. Mar. Sci.* 9:958733. doi: 10.3389/fmars.2022.958733

Observing the spread of Agulhas Leakage into the Western South Atlantic by tracking mode waters within ocean rings

Luiz Alexandre A. Guerra[1,2]*, Guilherme N. Mill[2,3] and Afonso M. Paiva[2]

[1]PETROBRAS/CENPES, Cidade Universitária, Rio de Janeiro, Brazil, [2]Programa de Engenharia Oceânica – PEnO/COPPE, Universidade Federal do Rio de Janeiro (UFRJ), Centro de Tecnologia, Cidade Universitária, Rio de Janeiro, Brazil, [3]Centre of Excellence, Vale S.A. - Vitória, Espírito Santo, Brazil

The Agulhas rings transport warm and salty waters that feed the surface limb of the Atlantic Meridional Overturning Circulation. Some studies have focused on the conveying capacity of ocean eddies, and recently, the role of the Agulhas rings in advecting water masses and organisms has been explored. Here we show evidence that the Agulhas rings are responsible for the advection of mode waters from the Cape Basin to the western side of the Atlantic. We analyzed more than 3,200 temperature profiles and 2,400 salinity profiles from historical databases collocated with 52 long-lived Agulhas rings tracked from 1993 through 2016. An automated algorithm was used to identify thermostads in the profiles acquired within the rings. The data revealed mode water layers trapped inside 88% of the rings. The joint distribution of temperature and salinity indicated two types of mode waters in the range 16.2 ± 0.6°C, 35.6 ± 0.1 (Type I) and 12.9 ± 0.7°C, 35.2 ± 0.1 (Type II). The majority (67%) of the rings carrying mode waters had both types detected inside. Moreover, considering only those rings sampled west of the Mid-Atlantic Ridge, we found that 45% of them advected mode waters to the western basin. Therefore, our results demonstrate that, despite the long journey, interaction with the bottom topography and other vortices, ocean-atmosphere exchanges, and decay, the Agulhas rings are responsible for spreading mode waters initially available at the Cape Basin throughout the South Atlantic, contributing to a positive anomaly in temperature and salinity along the eddy corridor joining the Cape Basin to the Brazil Basin.

KEYWORDS

South Atlantic, mode water, Agulhas rings, Agulhas Leakage, AMOC, thermocline ventilation, Argo, XBT

1 Introduction

The Agulhas Leakage refers to the transferring of warm and salty Indian Ocean waters into the Atlantic, whose main component is the spawning of anticyclonic rings from the retroflection of the Agulhas Current that takes place south of Africa (de Ruijter and Boudra, 1985; Gordon, 1985; Gordon, 1986; Lutjeharms and Gordon, 1987; Lutjeharms and van Ballegooyen, 1988; Lutjeharms, 1996; de Ruijter et al., 1999; Richardson, 2007).

Several studies have explored the role of the Great Agulhas System on the Earth's climate. The retroflection works like a gateway to the warm return flow of the Atlantic Meridional Overturning Circulation (AMOC) (de Ruijter et al., 1999; Beal et al., 2011). So as the retroflection behavior depends on its position, determined by the wind field, the leakage variability has been known to range from interannual to decadal periods (Witter and Gordon, 1999; Biastoch et al., 2009; van Sebille et al., 2009; Backeberg et al., 2012). As an example, Rouault et al. (2009) point out that since the 1980s, a temperature increase in the Agulhas system has been observed due to the wind's intensification with maximum southward displacement. The increased leakage has implications for stabilizing the AMOC, which may counterpoint a trend toward weakening the thermohaline circulation in a scenario of glaciers melting in Greenland (Weijer et al., 2002; Beal et al., 2011).

Fossil records from the Cape Basin indicate that the exchanges between the Indian and Atlantic oceans have been highly variable, alternating water cooling during glacial periods and warming in interglacial intervals in the last 450,000 years (Rau et al., 2002). Some studies have suggested that the onset of an increased Agulhas Leakage is crucial in glacial terminations resulting in a resumption of the AMOC (Peeters et al., 2004). However, there was doubt due to a lack of evidence of leakage spread reaching the West and eventual deep-water convection in the North Atlantic. Recently, Ballalai et al. (2019) put forward the results of a comparative analysis of a new fossil record from the Brazilian coast and another from the Cape Basin, which suggest a common mechanism responsible for increasing the salinity on both sides of the Atlantic. The authors proposed that the observed salinity anomaly responded to an increased Agulhas Leakage through Agulhas rings' progression connecting both sides of the Atlantic. The arrival of Agulhas rings to the western border, once hypothesized (Gordon and Haxby, 1990; Byrne et al., 1995; Nof, 1999; Azevedo et al., 2012), was recently confirmed with *in situ* evidence by Guerra et al. (2018). Subsequently, Laxenaire et al. (2018) conducted research on the role of Agulhas rings connecting the western boundaries of the Indian and Atlantic Oceans, using a new technique for eddy tracking that keeps records of merging and split-off events.

Vortices are well known for their capacity for transporting heat, mass, and other scalars trapped in the inner core, isolated from the external world (Danabasoglu et al., 1994; Volkov et al., 2008; Dong et al., 2014; Jayne and Marotzke, 2002; Souza et al., 2011; Zhang et al., 2014; Wang et al., 2015). Even though Agulhas rings experience an exponential decay, with a reduction of ~80% in amplitude within a year after shedding (Byrne et al., 1995; Schouten et al., 2000; van Sebille et al., 2010; Guerra et al., 2018), many studies have identified mode waters inside rings in the Cape Basin and beyond the Walvis Ridge at the Mid-Atlantic (McCartney and Woodgate-Jones, 1991; Olson et al., 1992; Toole and Warren, 1993; McDonagh et al., 2005; Guerra, 2011). New estimates of the transport of Agulhas rings heat content showed that most heat anomalies are associated with the mode water layers advected westward during the rings translation along the South Atlantic (Laxenaire et al., 2020).

Mode waters (MWs) are vertical homogeneous layers of the thermocline waters formed by subduction from the mixed layer during wintertime conditions (Hanawa and Talley, 2001). Different types of MW have been identified and described in the literature in the South Atlantic. The South Atlantic Central Water comprises three MWs with distinct ranges of properties (Provost et al., 1999; Sato and Polito, 2014). Each MW was observed in different regions of the subtropical gyre: the western side of the gyre near the Brazil Current recirculation, the southern edge of the gyre in the central and eastern South Atlantic, and on the east side of the basin, including the Cape Basin region (Sato and Polito, 2014; Bernardo and Sato, 2020).While it is generally agreed that there are three varieties of subtropical MW (STMW) in the South Atlantic, there is less consensus over whether or not they are influenced by remote central waters or locally formed. De Souza et al. (2018) revisited data from WOCE cruises and Argo floats and found an important contribution of the Subtropical Indian MW (SIMW) in the thermocline waters of the South Atlantic. Surprisingly, the presence of the SIMW increased westward, and the authors suggested that this tendency was related to the advection of Indian MW trapped inside Agulhas rings as they traveled westward. Using numerical modeling, Capuano et al. (2018) demonstrated the role of turbulence and instabilities in the Cape Basin on the transformation of water masses from the Indian Ocean and subduction of MW inside Agulhas rings. Using a new algorithm to detect MW in Argo profiles, including outcropping MW, Chen et al. (2022) suggested a new interpretation of the origin and formation of the MWs found in the upper thermocline of the South Atlantic Ocean. Their results led to a redefinition of the three types of South Atlantic STMW, where the origins of both the lightest and the densest varieties were found mainly inside the southeastern Cape Basin, related to the Agulhas Leakage, while Sato and Polito (2014) argued that two varieties are related to the Brazil-Malvinas Confluence.

These previous studies (op. cit.) mainly focused on detecting STMW along the South Atlantic using Argo profiles without giving a detailed comparative analysis of the thermocline waters inside and outside Agulhas rings. Therefore, this paper analyzes twenty-three years (1993-2016) of *in situ* measurements collocated with Agulhas rings to clarify their role in Agulhas Leakage spreading. Temperature and salinity profiles from free-drifting Argo floats provided a view of the time evolution of the ring's cores, while data from multiple cruises crossing rings provided a synoptic view of their vertical structure in several opportunities. The use of water masses to track the Agulhas Leakage may be complex because of the similarity between thermocline waters from the South Indian and South Atlantic (Gordon and Haxby, 1990; van Aken et al., 2003). Nevertheless, mode waters, which present a unique vertical homogeneity and whose formation occurs at specific spots under certain well-known winter conditions, can work as tracers (McCartney, 1982). We sought profiles with a low vertical temperature gradient using an automated algorithm, looking for MW signals. Our results showed that 45% of the Agulhas rings sampled at the western basin carried at least one type of MW initially available at the Cape Basin.

The paper is organized as follows. Section 2 presents the data sets, a description of the automated collocation method between the rings' trajectories and hydrographic profiles, the detection of MW, and the two-layer model with reduced gravity to estimate ring properties. In Section 3, we summarize the results of the MW classification, show their advection throughout the South Atlantic, and explore in detail three particular cases of super-sampled Agulhas rings. These rings, named Ana, Eliza, and Jeannette, spent two consecutive winters in the Cape Basin but in different years. They were sampled in Lagrangian and Eulerian forms, inside and outside the basin, showing the presence of MW. A discussion about the formation of MW, rings decay and conveyor capacity, and their possible sinking at the western basin is presented in Section 4. Finally, Section 5 is dedicated to the concluding remarks.

2 Methods

2.1 Rings detection and tracking

The method used in this study to detect and track eddies on altimetric maps consists of an automated hybrid algorithm that combines closed contours of sea surface height and the Okubo-Weiss parameter. The eddy's radius is calculated by fitting a circle of area equivalent to that defined by the maximum radial velocity around the eddy, regardless of whether it is circular or not. A thorough description of the entire method is available in Halo et al. (2014) and Guerra et al. (2018).

The daily maps of sea level anomaly are from the multi-satellite global DUACS DT2014, delayed time, provided on a regular Cartesian grid of 1/4° × 1/4° (Le Traon et al., 1998; Ducet et al., 2000; Le Traon et al., 2003). A detailed description of the altimetry dataset can be found in Pujol et al. (2016).

The eddy tracking data used here, the same as in Guerra et al. (2018), spans January 1993 to May 2016. Among the whole set of anticyclones and cyclones detected in the South Atlantic, the original dataset also includes 74 Agulhas rings with life spans longer than one year. In the present study, we focused on those 56 rings that crossed the Mid-Atlantic Ridge, reaching the western South Atlantic Basin (Figure 1A). A discussion about the skills of the method to detect and track Agulhas rings, including a comparison with the Chelton atlas, is presented in Guerra et al. (2018).

2.2 Temperature and salinity profiles

We sought profiles coincident in time with eddies. All profiles occurring within an area defined by twice the respective eddy radius were selected. Nevertheless, as mentioned, the eddy radius is an approximation, and it is not rare that the actual eddy does not fit a circular form. Thus, the chosen search radius aims to increase the chance of capturing coincident profiles close to the eddy edge (see Supplementary Figure 1).

We used the vertical profiles from the EN4.2.1 dataset (Good et al., 2013). The EN4.2.1 dataset includes eXpendable BathyThermograph (XBT) and Conductivity-Temperature-Depth (CTD) profiles from different cruises and programs (e.g., data from the XBT transects AX18 and AX97, provided by the NOAA/AOML High-Density Transects Program, and Argo profiles as well). Temperature and salinity profiles passed through an automatic analysis based on a quality control manual (U.S. Integrated Ocean Observing System, 2020).

2.3 Detecting mode waters

Temperature and salinity profiles were interpolated to a regular vertical interval of 5 meters using a piecewise cubic Hermite interpolating polynomial (Fritsch and Carlson, 1980). A difference criterion was applied to determine the mixed layer depth, defined as the depth where the temperature deviates by 0.5°C from the sea surface temperature (Foltz et al., 2003). Between the mixed layer depth and the 1,000 m depth, an automated algorithm identified layers defined by a threshold of vertical temperature gradient of 0.01°C/m ($d\theta/dz<0.01$°C/m) (Provost et al., 1999; Sato and Polito, 2014). Only thermostads with temperatures in the range 18.0°C > t > 10.5°C, with a minimum thickness of 50 meters, and entirely inserted in the referred depth interval were considered. Afterward, each profile was visually inspected to guarantee that the thermostads were detected appropriately inside a ring (e.g., Supplementary Figure 1).

2.4 Rings properties

We used a two-layer model with reduced gravity to study the structure and dynamics of the Agulhas rings following

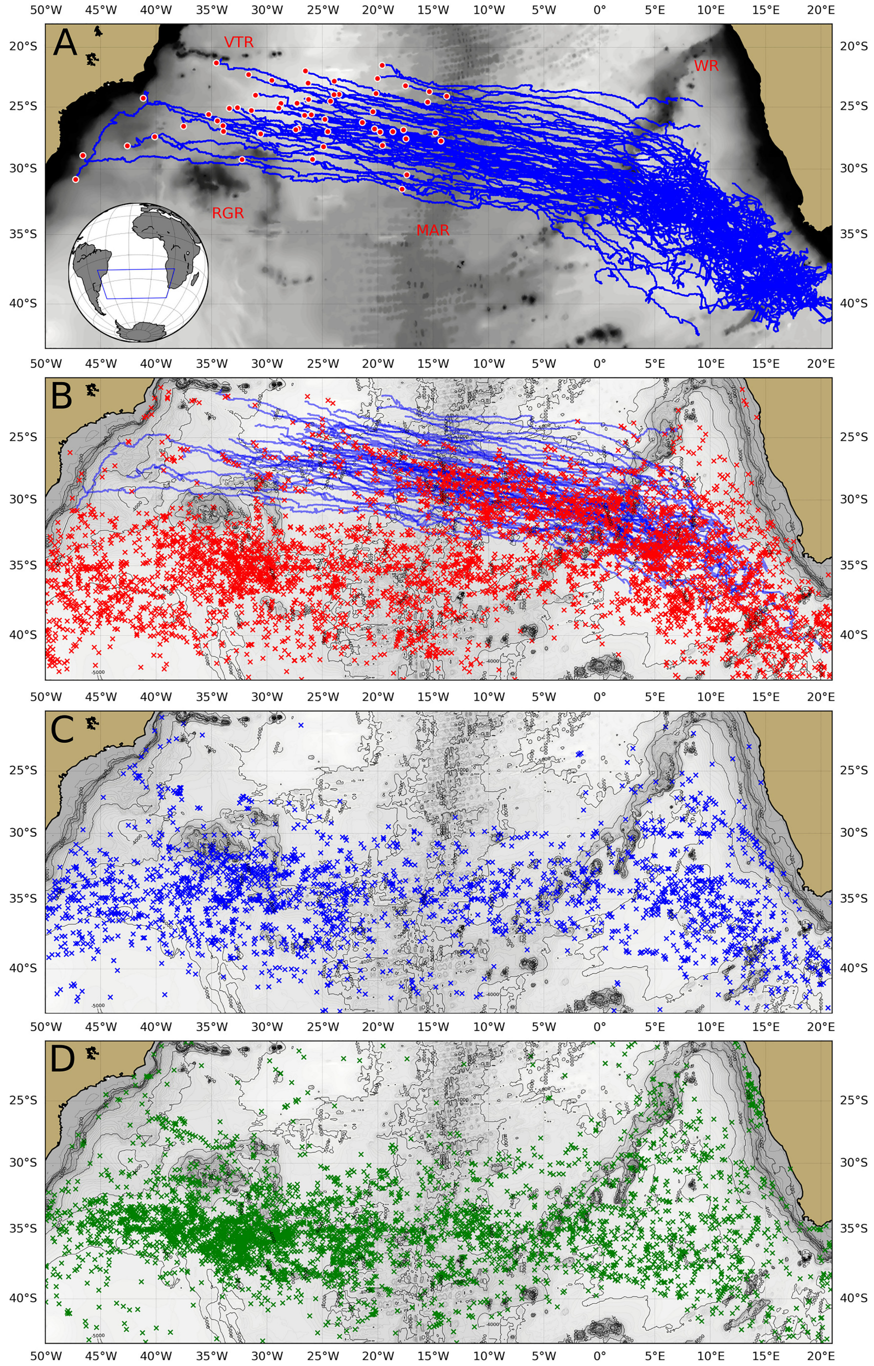

FIGURE 1
(A) Tracks of 56 long-lived Agulhas rings (blue lines) between 1993 and 2016 identified using an automatic algorithm. The set includes only the rings that reached the western basin. The acronyms WR, MAR, VTR, and RGR refer to Walvis Ridge, Mid-Atlantic Ridge, Vitória-Trindade Ridge, and Rio Grande Rise, respectively. The red circles mark the final tracking position of each ring. The bottom topography is shown in the background in gray. **(B)** Map with the paths of the Agulhas rings (blue lines) and the sites of detection of thermostads coincident with anticyclones (red x). **(C)** Map with the sites of detection of thermostads coincident with cyclones (blue x). **(D)** Map with the sites of detection of thermostads in profiles outside eddies (green x).

Olson et al. (1985). In this model, a cylindrical coordinate system has its origin at the ring's center, and the interface between the two layers with different densities ($\rho_1<\rho_2$) is approximately defined by an isotherm representing the main thermocline. Considering the high correlation between the sea surface height and the 10°C isotherm depth at the Agulhas Retroflection vicinities and along the rings' corridor, this isotherm was used as a proxy for the thermocline (Olson and Evans, 1986; Garzoli et al., 1997).

The assessment of the volume and energy of the rings in the upper layer was performed using formulations derived from the model as follows:

$$Vol = \int_A (h_1 - h_\infty) dA \tag{1}$$

$$APE = \frac{\rho_1 g'}{2} \int_A (h_1 - h_\infty)^2 dA \tag{2}$$

$$KE = \frac{\rho_1}{2} \int_A (h_1 v^2) dA \tag{3}$$

where h_1 is the depth of the thermocline within the ring, h_∞ is the depth of the undisturbed thermocline in the far-field, A is the surface area of the ring, g' is the reduced gravity, and v is the azimuthal velocity. Considering that the rings are frequently associated with other vortices that disturb the mass field in the actual ocean, we used the 10°C isotherm climatological mean depth from the World Ocean Atlas 2018 (WOA18) (Garcia et al., 2019). The azimuthal velocity (v) was calculated as the maximum of the average geostrophic speeds around the closed contours of sea surface height inside the ring, according to Chelton et al. (2011).

The reduced gravity that measures the restoring force and depends on local stratification was calculated according to:

$$g'(x,y) = \frac{\rho_2(x,y) - \rho_1(x,y)}{\rho_2(x,y)} g \tag{4}$$

where g=9.8 m/s^2 is the gravitational acceleration, ρ_1 and ρ_2 are the mean potential density of the upper and lower layers calculated using temperature and salinity from the WOA18. The density integration in the lower layer was limited to 1,500 m depth or the ocean bottom when in shallow waters.

The instantaneous upper layer thickness in the center of the eddy was computed from the satellite sea level anomaly and the known mean thermocline depth and reduced gravity, using the following equation (Goni et al., 1996):

$$h_1(x,y,t) = \overline{h_1}(x,y) + \frac{g}{g'(x,y)}[\eta'(x,y,t) - \overline{B'}(x,y)] \tag{5}$$

where $\overline{h_1}$ is the mean upper layer thickness, equivalent to the thermocline depth at the far-field, η' is the amplitude of the ring, that is the difference between the sea surface height in the center and at the border of the ring (Chelton et al., 2011), obtained from the altimetry, and B' is the barotropic contribution to the sea surface level anomaly, where $\overline{B'} = 0$, since $|B'| \ll |\eta'|$.

Additionally, we calculated the upper layer thickness fitting a Gaussian function to the depth of the thermocline obtained at different distances from the ring center by temperature profiles, following Olson et al. (1985) and Goni et al. (1997):

$$h_1(r) = h_0 e^{-r^2/(2L^2)} + h_\infty \tag{6}$$

where r is the radial distance measured from the center of the ring, assuming it is radially symmetrical, h_0 is the maximum depth of the thermocline measured from h_∞ at the ring's center, and L is the ring radius. This method was used in two cases where at least five temperature profiles were synoptically available.

3 Results

We started exploring the occurrence of thermostads in the South Atlantic between the latitudes 20°S and 43°S from January 1993 through May 2016. The analysis included 99,167 profiles, of whom 10.4% (10,281) displayed thermostads. We found that 49.6% (49,186) of the profiles were collected within eddies, considering a search distance of twice the length of the radius centered on each eddy. When using a search distance of one eddy radius, we obtained percentages similar to Sato & Polito (2014), despite analyzing a more extended period and a dataset with three times the number of profiles. Most thermostad detections were inside vortices (62.8% of detections, or 6.5% of the profiles), with the number of occurrences in anticyclones being twice as many as in cyclones (see Supplementary Table 1).

Figure 1B shows the occurrence of thermostads within anticyclones (4,385). They extend along the parallel 35°S with concentrations west of 20°W and in the Cape Basin, east of 0°W. This pattern is roughly repeated for the thermostads within cyclones (Figure 1C) and thermostads outside eddies (Figure 1D). However, a distinctive characteristic is their spread along the eddy corridor depicted by the paths of long-lived Agulhas rings (Figure 1B). In contrast, regarding the thermostads in cyclones and thermostads outside eddies, there is a clear space along the corridor (Figures 1C, D). In the Cape Basin, there is a predominance of thermostads within anticyclones. While west of 20°W, thermostads outside vortices are more frequent.

The general picture emerging from this analysis is that the occurrence of thermostads inside anticyclones along the eddy corridor crossing the South Atlantic seems to be related to the translations of long-lived Agulhas rings. We will analyze this matter in detail below.

Our principal analysis focused on the 56 long-lived Agulhas rings tracked from the origin at the Cape Basin until the Brazil Basin between 1993-2016 (Figure 1A). The general characteristics of this subset of Agulhas rings are very similar to those presented by Guerra et al. (2018) for the original set of long-lived rings. The average lifetime of the 56 rings is 1,041 ± 213 days, and the average travel distance is 6,268 ± 1,286 km (mean ± standard deviation), including parent rings in case of merging and split-off events in the Cape Basin.

The interior of the Cape Basin is a well-known spot of turbulent mixing and stirring, where the anticyclonic Agulhas rings interact with topography, other anticyclones, and cyclones, resulting in dissipation, intensification, splitting, and merging events (see Boebel et al., 2003; Dencausse et al., 2010). Consequently, several short trajectories are crowded in the Cape Basin until the ring shows up as an isolated eddy ready to cross the Walvis Ridge (Figure 1A). The rings leave the Cape Basin after overcoming the Walvis Ridge (WR) and continue in a west-northwest course to eventually cross the Mid-Atlantic Ridge (MAR), in the case of long-lived ones. They reach the western basin in a latitudinal band, limited North by the Vitória-Trindade Ridge (VTR) and South by the Rio Grande Rise (RGR).

The number of identified coincident profiles with the Agulhas rings sums to 3,217 temperature profiles and 2,476 salinity profiles, produced by 741 XBT, 70 CTD, and 2,406 Argo profilers. The quality control rejected 141 temperature profiles and 282 salinity profiles. There is a corresponding temperature profile for every approved salinity profile in the qualified set. Figure 2, top panel, shows the number of coincident temperature profiles along the path of the 56 sampled Agulhas rings. The data reveal that roughly 75% of the coincident profiles occurred east of the Mid-Atlantic Ridge, while the other 25% sampled 38 rings in the western.

Aiming to find signs of MW within the Agulhas rings, the set of coincident profiles was examined by an automated algorithm for thermostads searching, followed by a visual inspection. The search returned a total of 912 thermostads. Figure 2, left panel, illustrates a MW detection, presenting a temperature profile acquired within an Agulhas ring, in which we observe two thermostads: 16.5°C between 125-215 m, and 12.5°C between 385-505 m. As shown in the figure, when the vertical temperature gradient threshold is crossed, the limits of the layers are determined.

We examined the relationship between thermostads detection and profile distance from the ring center. Despite being detected throughout the entire range, from the center of the ring to twice the radius, it is noticeable that thermostads

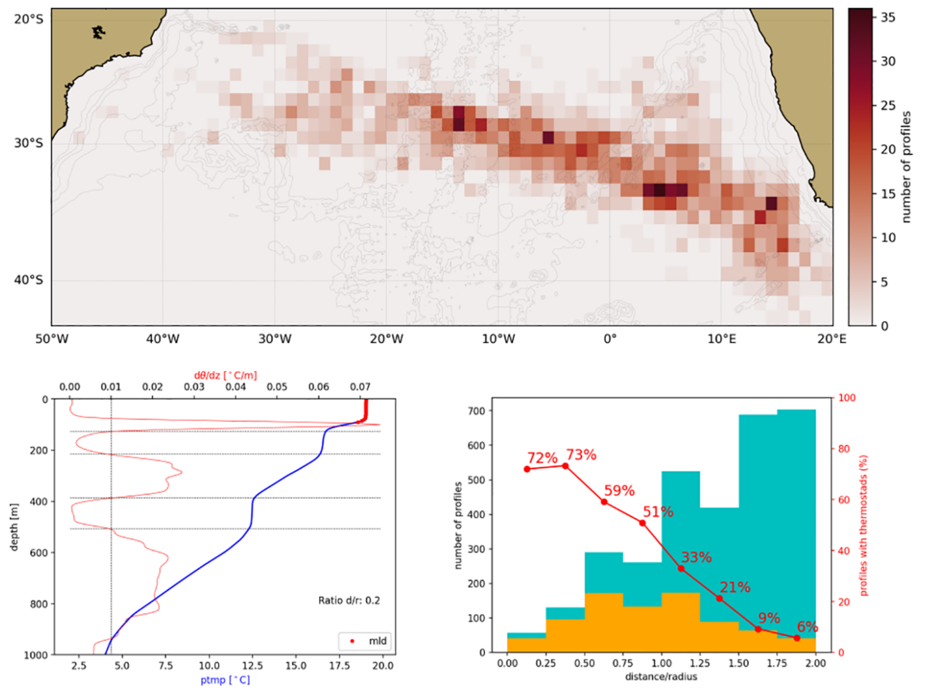

FIGURE 2
Temperature profiles inside Agulhas rings along the South Atlantic between 1993 and 2016. Top) Distribution of coincident temperature profiles and Agulhas rings, totaling 3,076 profiles, in a 1° x 1° resolution grid. The bottom topography is shown in the background in faded gray lines. Left) Temperature profile acquired within an Agulhas ring on the geographic coordinates 27.92°S of latitude and longitude 20.22°W, on 27-Jul-2006, close to the ring center (ratio distance/radius = 0.2). The red line indicates the vertical temperature gradient, and the red dots mark the mixed layer. The vertical dashed line marks the threshold for the vertical temperature gradient at 0.01°C/m. Right) The number of profiles acquired within Agulhas rings versus the ratio between the distance from the ring center and ring radius. Cyan: all the profiles; Orange: profiles with mode water signal. Red line: the percentage of profiles with detected thermostad in each class interval of distance.

detection is relatively more frequent at a distance within a half-ring radius, where 73% of the profiles showed thermostads. As the distance from the center increases, the lesser the chances to detect them, as indicated by the decreasing percentage of profiles with MW towards the ring's periphery (Figure 2, right panel).

Figure 3 shows a graphic summary of the classification of the Agulhas rings according to sampling and geographical distribution of MWs. Only 52 of the 56 long-lived Agulhas rings were sampled during the journey. We found the occurrence of thermostads in 46 rings, but only 38 of them were sampled in the western basin. Of those, 45% (17) had MW detected west of the Mid-Atlantic Ridge. On the other hand, 12 rings had MW detected during the life span but were not sampled on the western basin. Thus, for this specific subset, it is not possible to affirm that they were able to transport MW to the western basin. Half of the 34 rings sampled on the western side, with previous records of MW, did not show any signal west of the Mid-Atlantic Ridge. Thus, these figures should be considered with some caution due to the nature of the sampling. Besides, the mentioned 17 rings with no detected thermostads west of the Mid-Atlantic Ridge had four rings sampled a maximum of five times and whose profiles were undertaken at distances greater than one ring radius, which implies a lower probability of MW detection.

The temperature and salinity of the isopycnal layers showed bimodal distributions (Figure 4, top and right panels). A hypothesis test, applied separately for temperature and salinity, confirmed the difference between the two modes, with a p=0.0001. Then, we used the k-means method (Lloyd, 1982) to distinguish the two populations and determine their statistics, considering the pairs of temperature-salinity. The analysis evidenced two clusters of MW, which we named Type I (16.2 ± 0.6°C, 35.6 ± 0.1) and Type II (12.9 ± 0.7°C, 35.2 ± 0.1). The Type I MW is centered near the 26.2 isopycnal, and it is lighter than the Type II (centroid close to the 26.6 isopycnal). Figure 4, central panel, presents the clusters' centroids (white circles) and the temperature-salinity pairs (triangles) corresponding to the pycnostads.

The Type I MW was present in 45 rings, while Type II was in 32 rings. A total of 31 rings showed more than one variety of MW at least once during the lifetime. Only one ring studied in this work showed the isolated occurrence of Type II without the presence of Type I. When evaluating this single case, which is a ring sliced in a meridional section at position 27°S/9°W, we found remnants of a layer with the characteristics of Type I MW but already quite eroded.

Examining profiles with simultaneous occurrence of Type I and Type II MW in the environment outside eddies, we found 11 cases: five in the Cape Basin, three east of MAR, and three west of MAR. This subset represents 0.003% of the total number of profiles with detected thermostads outside eddies (3,820).

The spread of each type of MW trapped inside the rings is shown in Figure 5. Both types of MW were detected inside Agulhas rings from the southeastern region of the Cape Basin until the western basin at 34°W. They spread along the eddy corridor crossing the South Atlantic. Type I was more frequent than Type II, in general, as shown in the map and TS diagram (Figure 4), but the second was also detected at the westernmost recorded position. Type I was relatively more frequent westward from meridian 10°E.

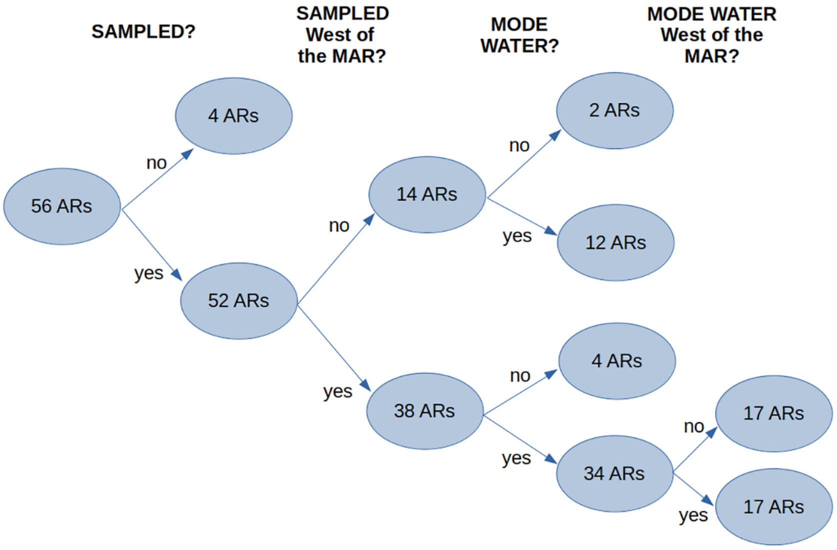

FIGURE 3
The Agulhas rings (ARs) classification according to sampling and presence of mode waters passed through a dichotomous tree. The 13°W meridian was used as a watershed for the South Atlantic, representing the Mid-Atlantic Ridge (MAR).

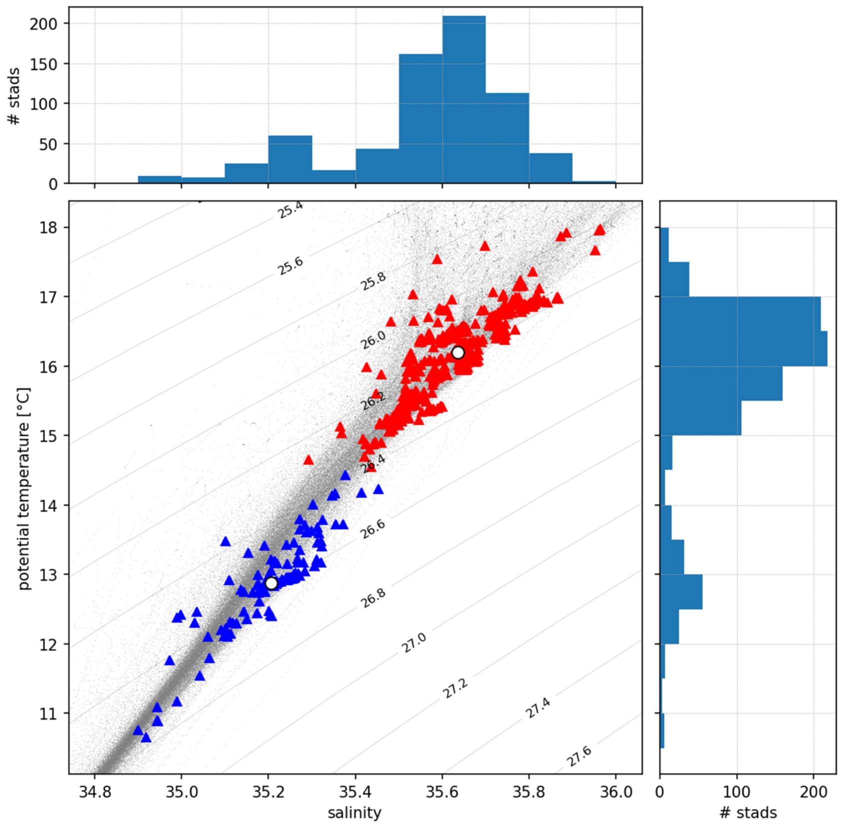

FIGURE 4
Temperature-salinity diagram including all qualified profiles acquired inside the rings (gray dots), and histograms of mean salinity (top) and mean temperature (right) of the pycnostads identified. The triangles show the t-s pairs of the pycnostads, and the white circles show the centroids of each mode water cluster (Type I in red and Type II in blue). The centroids have the following characteristics: Type I (16.2 ± 0.6°C, 35.6 ± 0.1 psu, 26.2 ± 0.1 σ_θ) and Type II (12.9 ± 0.7°C, 35.2 ± 0.1 psu, 26.6 ± 0.1 σ_θ).

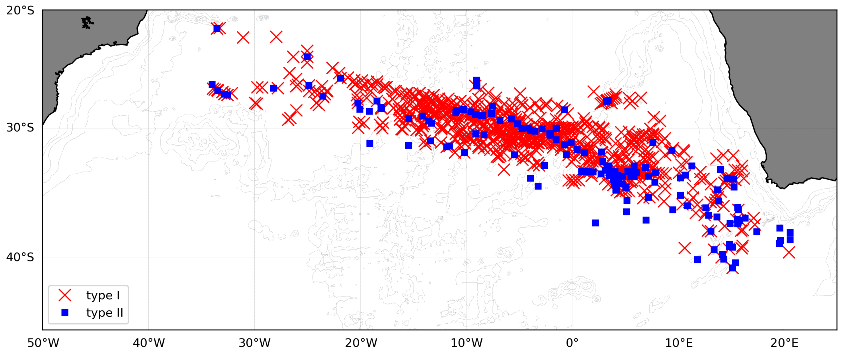

FIGURE 5
Map of occurrence of mode waters in Agulhas rings. Both mode water varieties were detected from the Cape Basin until the western basin. The bottom topography is shown in the background in faded gray lines.

We assumed the meridian 13°W as the watershed of the eastern and western basins, representing the Mid-Atlantic Ridge, to compare the characteristics of mode waters Type I and Type II on both sides of the South Atlantic Ocean. The total number of detections in the east is four times larger than in the west. Comparing the MW layers on both sides of the Atlantic, the maximum thicknesses for Type I and Type II are more prominent on the eastern, but there is no significant difference in the mean for the two types (295 m for both; see Supplementary Table 2). However, there is a significant increase in the depth of the core of Type I in the west. While on the eastern side, the average vertical distance between the two cores within the rings is 259 m, this space shrinks to 230 m on the opposite side. Ultimately, the temperature and salinity show no variation from the eastern to the western side, evidence that the water masses in the core of the rings may be preserved for time scales of years.

3.1 Particular cases: Three supersampled Agulhas rings

After a general description of the MW properties and spreading throughout the South Atlantic inside Agulhas rings, we will focus on three supersampled rings, whose MW characteristics and evolution were captured both in Lagrangian and in Eulerian sampling.

3.1.1 Ring Ana

The first ring, referred to as Ring Ana, was first detected at 38.26°S/17.10°E on 15-Aug-2004 and tracked until north of the Rio Grande Rise at 33°W, on 09-May-2007, in the western basin. Around longitude 7°W, the Argo float number WMO (World Meteorological Organization) 1900487 was captured by the ring and carried for more than 2,000 kilometers, performing 36 profilings inside the ring for 350 days (from 09-Nov-2005 to 25-Oct-2006). The trajectory of the advected Argo exhibits seven anticyclonic loops (Figure 6 - yellow triangles) between the eastern and the western side of the Mid-Atlantic Ridge. Two other Argo floats also profiled the ring, but for shorter times: WMO 1900525 (24-Oct-2005 to 21-Feb-2006) and WMO 1900285 (12-Mar-2006 to 31-May-2006).

The time evolution of the temperature and salinity vertical profiles made with the Argo 1900487 data showed two regions of the water column with low potential vorticity, with potential temperatures ranging between 16-17°C and 12-13°C, and their respective halostads of 35.6-35.7 and 35.1-35.2, between depths of 70-280 m and 400-550 m (Figure 7). They were classified as Type I and Type II MW, respectively, and they are present in this record only during the period the profiler was trapped inside the ring, as shown in Figure 7. The associated pycnostads for Type I and II were 1,026.1-1,026.2 kg/m^3 and 1,026.6-1,026.7 kg/m^3, respectively. The vertical dashed lines mark the period the Argo 1900487 was trapped (ratio distance/radius< 2). Before and after this period, it is possible to observe the surrounding stratification outside the ring, showing no thermostads or halostads in the same range of the properties of the two types of MW.

While Type I is noticed in the ring throughout the entire sampling duration, Type II is more evident during three periods only (February-March 2006, June-August 2006, and September 2006), when the profiling occurred closer to the ring's center (d/r<1) (Figure 7, top panel). The thickness oscillation of the pycnostads suggests a lenticular shape of the MW layers, thicker as much closer to the ring's center and thinner in its peripheral region. The profiler was entrapped during the austral spring and stayed sampling inside the ring until the following spring. The two other mentioned profilers (WMO 1900285 and WMO 1900525) confirm the temperature and salinity values (vertical profiles not shown) of the two MW at the same depth ranges. Despite the winter's surface cooling, the recapture of the 16-17°C layer did not occur, evidencing the role of the ring in transporting MW away from the formation zone. The Argo data provide clear evidence that a well-defined front

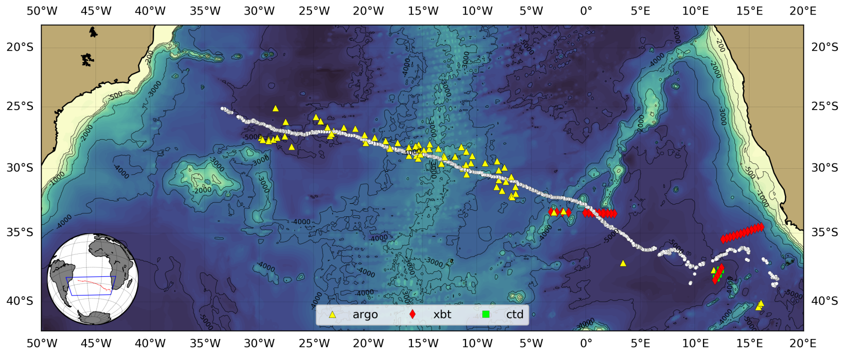

FIGURE 6
The path of the Ring Ana between 15-Aug-2004 and 09-May-2007 (white dots) and the locations of Argo (yellow), XBT (red diamonds), and CTD (green squares) profiles within the ring radius. The bottom topography is shown in the background.

at the ring's edge retains the MW in its interior core as the Argo profiles acquired outside the ring exhibit no signal of them. These Lagrangian observations provided by the Argo profilers unequivocally evidenced that MW can be preserved within the Agulhas rings for long distances.

Just before Ring Ana leaves the Cape Basin (near the Greenwich meridian), it was sampled by XBT probes from an AX18 cruise on 25-26-May-2005 (Figure 8, left panel). Even though the Type I MW was present trapped inside the ring five months later (Figure 7), the temperature profiles in May show alternatively a presence of a well-developed 12°C thermostad (classified as Type II) with 300 m thickness and a surface signal of the 17°C (Figure 8, right panel) associated with the local mixed layer. These results suggest that the formation of the Type I MW may occur even on the verge of the ring leaving Cape Basin and translating to the ocean interior. Unfortunately, the analyzed data could not capture the subduction of Type I, and it is hypothesized that the MW formation had occurred in the interval between the sampling events.

3.1.2 Ring Eliza

The second ring, referred to as Ring Eliza, results from a split-off occurring approximately on position 38°S/16°E from a ring shed from the retroflection on 01-Aug-2007, just one month before the split-off. It was tracked for 1,007 days from the shedding until its demise in the western basin near 29°W on 04-May-2010 (Figure 9).

Along its path, the ring was sampled on different occasions but remarkably at longitudes 8°W, 16°W, and 24°W, by three consecutive AX18 cruises in February and July 2009 and January 2010, respectively, when it was sliced. During the cruises, XBT probes were deployed every 50 km, reaching a depth of 850 m. The temperature sections illustrate the vertical structure of the ring in distinct moments of its evolution (Figure 10). On all three occasions, the data showed a large volume of Type I MW (16.4°C) inside the ring, with a thickness of approximately 200 m, evidencing the lenticular structure of the imprisoned water.

The first section was sampled in February 2009 before the ring crossed the Mid-Atlantic Ridge, while the second, in July 2009, was just after. We could find no signs of any possible influence of the ridge on the ring's structure after its passage. In January 2010, the section sliced the ring closer to the center. On that occasion, the thermocline depth inside the Ring Eliza, represented by the 10°C isotherm, was 150 m below its undisturbed depth outside the ring. The thickness of the lenticular-shaped MW was approximately 250 m near the center of the ring. Like what was observed on Ring Ana, the surrounding waters outside Ring Eliza showed no thermostads in the same depth range.

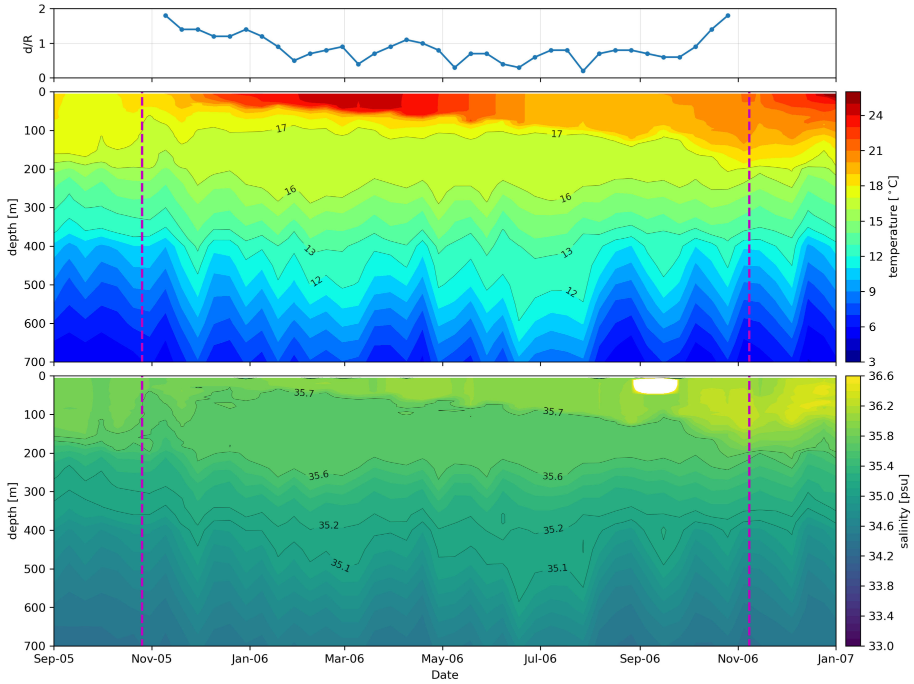

FIGURE 7
Temperature and salinity sections from Argo 1900487. Vertical dashed lines delimit the time the Argo remained inside the ring (from 09-Nov-2005 to 25-Oct-2006). It is possible to see two thick thermostads (16-17°C and 12-13°C) and halostads (35.6-35.7 and 35.1-35.2), classified as Type I and Type II. Top panel: the ratio between profile distance from the ring center and ring radius.

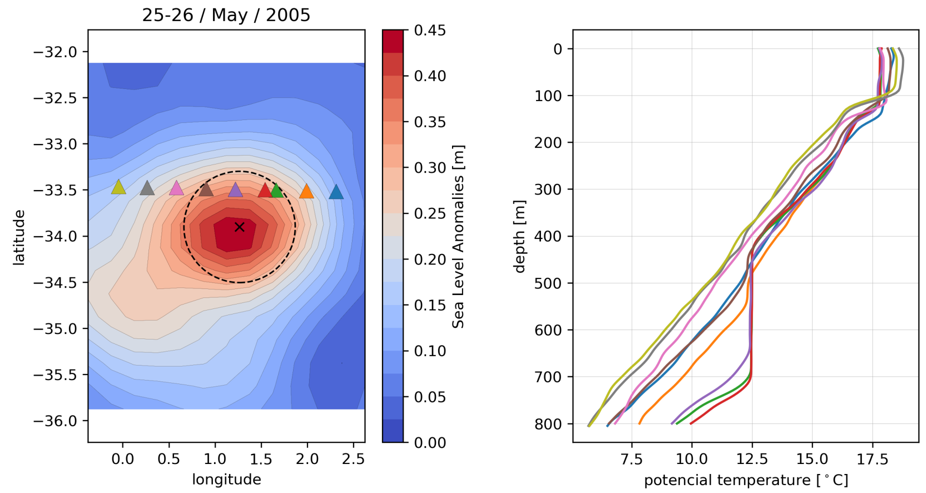

FIGURE 8
Left panel: Altimetry map showing the Ring Ana just before leaving Cape Basin and XBT launches in a section crossing it towards the west. The dashed circle marks the radius of the ring, estimated at 67 km. Right panel: Temperature profiles from the XBT section. The profile colors identify the deployments.

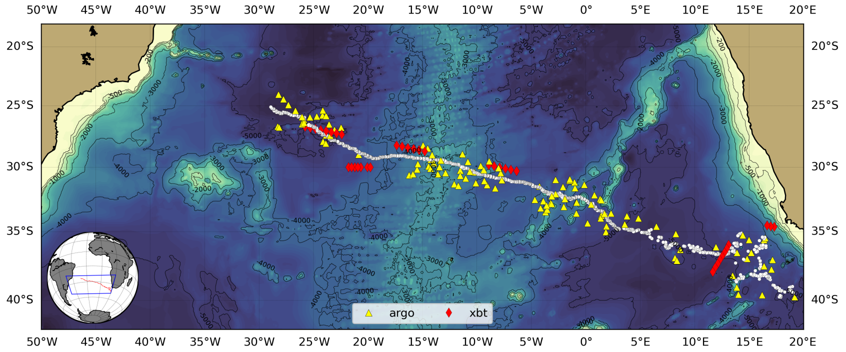

FIGURE 9
The path of the Ring Eliza between 01-Aug-2007 and 04-May-2010 (white dots) and the locations of Argo (yellow) and XBT (red diamonds) profiles within the ring radius. The bottom topography is shown in the background.

Between 25°W and 29°W, Ring Eliza was sampled 13 times by three Argo floats until its demise (Figure 9). Four profiles confirmed the presence of a 115 m thickness pycnostad with a temperature of 16.4°C and a salinity of 35.7. The surface signal of the ring was faint past 29°W, and the tracking algorithm could not continuously follow its trajectory except for short periods. Instead, a positive sea level anomaly was going west at the same speed as the ring but not as a coherent eddy. We decided to follow it visually and search for profiles nearby. We could find eleven profiles produced by four Argo floats (Figure 11, left panel). Despite the altimetric signature of the ring as a coherent feature weakening since 29°W, which could indicate the dismantling of the ring, the Argo profiles showed the persistence of the previously detected thermostad with temperature centered at 16.4°C (Figure 11, right panel) and salinity of 35.7 (not shown) until reaching the meridian 38°W, approaching the continental slope region dominated by the southward flow of the Brazil Current.

3.1.3 Ring Jeannette

The track of the ring referred to as Ring Jeannette begins on 28-Jan-2012 at 39°S/17°E and finishes on 27-Dec-2015 at 21°S/35°W, at the southern flank of the Vitória-Trindade Ridge, Brazilian coast (Figure 12).

Ring Jeannette is one of those thirty-ones observed rings that carried both types of mode water. Two XBT sections crossed the

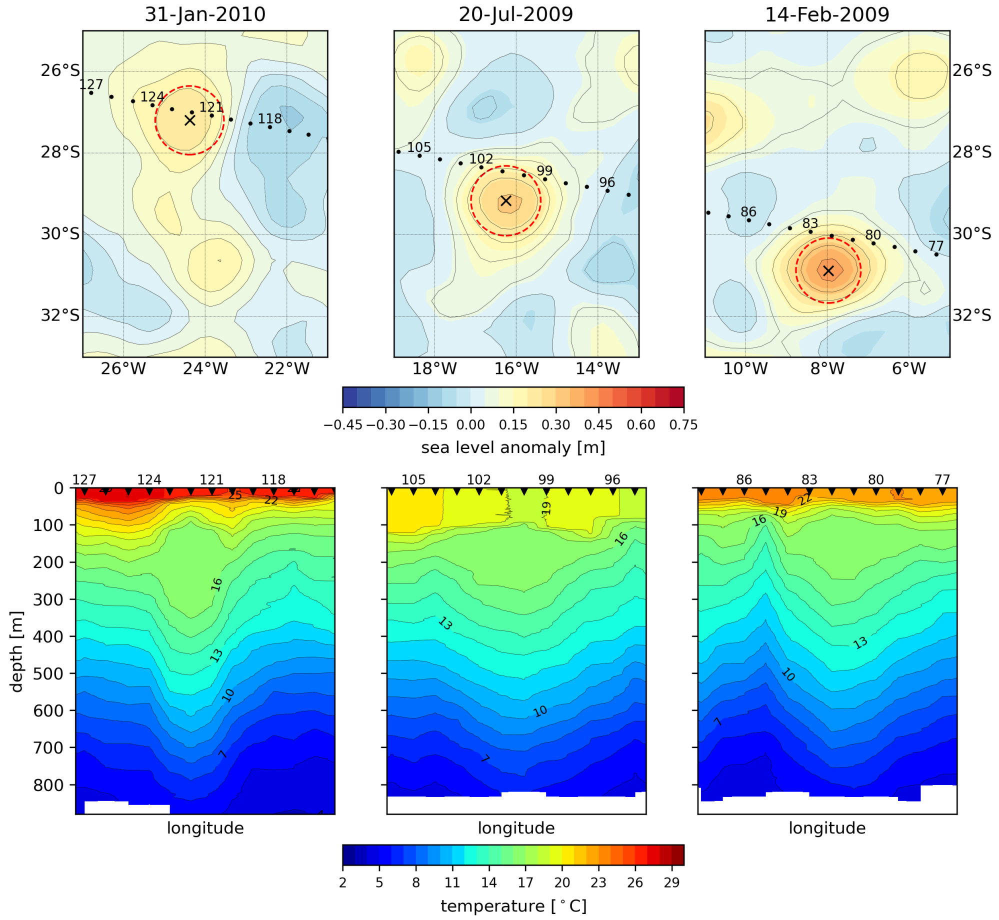

FIGURE 10
Three temperature sections were sampled across the Ring Eliza in successive AX18 cruises in February 2009, July 2009, and January 2019. The top panels show altimetric maps of the ring with numbered deployment stations. The red circle delimits the area defined by one ring radius (93 km, 95 km, and 88 km, from older to younger). The bottom panels show the three temperature sections.

ring, the first in the Cape Basin and the other next to the Brazilian coast just before its demise. The temperature sections clearly show the two thermostads on both occasions (Figure 13). The temperature shift in the thermostads is more pronounced in the shallow one. While its mean temperature was 15.6°C in the Cape Basin, and two and half years after, close to the Brazilian coast, it was 16.3°C, the deep thermostad conserved 13.8°C on both sides of the Atlantic. However, examining the Argo profiles between the two XBT sections, we observed that the shifting occurred possibly at the passage through the Walvis Ridge. Previous studies reported the role of the Walvis Ridge on the transformation of Agulhas rings due to volume exchanges with the environment (Richardson, 2007; Nencioli et al., 2018). Furthermore, the thicknesses of the thermostads are roughly two times larger in the Cape Basin. The vertical extension was shrunk with the aging of the ring, as previously observed in Agulhas rings by other studies (Guerra et al., 2018; Nencioli et al., 2018), evidencing its erosion.

The ring that propagated along the track shown in Figure 12, and that we named Ring Jeannette, was also studied by Nencioli et al. (2018). However, the authors followed it in two steps. They reported a spawning of a ring, called B12, from the merging of two Agulhas rings at the Mid-Atlantic Ridge. The seminal rings were formed in the Cape Basin and translated to the west in parallel tracks until the encounter. They called the north track AN1 and the south AS2. The entire track of our Ring Jeannette comprises Nencioli's south track AS2 and B12. A possible interpretation for this distinction is that our tracking algorithm, in the case of merging, continues the track of the nearest eddy from the previous time step (for details, see Guerra et al., 2018).

We examined the profiles coincident with the north track (AN1), including an XBT section crossing the ring, and observed only the shallow thermostad (Type I). Nevertheless, the analysis of the southern track (AS2), coincident with our track, revealed the presence of both Type I and Type II MW. Our findings are consistent with Nencioli's results showing the southern track

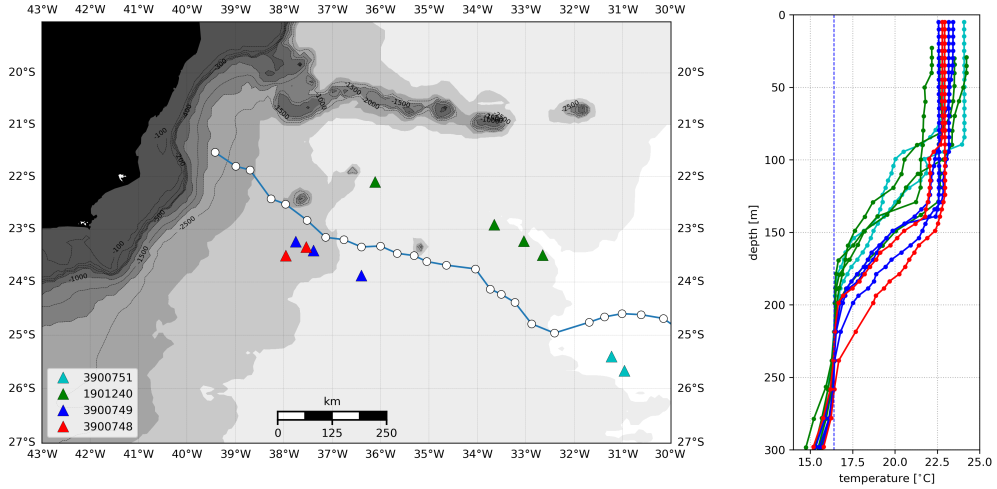

FIGURE 11
Trajectory of the sea level anomaly related to the Ring Eliza between 30°W and the Brazilian coast at 39°W (18-May-2010 through 02-Nov-2010). Left: Triangles mark the positions of the Argo floats that sampled the Type I mode water within a radius of 150 km from the center of the feature. The bottom topography is shown in the background in gray. Right: Temperature profiles measured by the Argo floats. The vertical dashed blue line marks the thermostad temperature at 16.4°C.

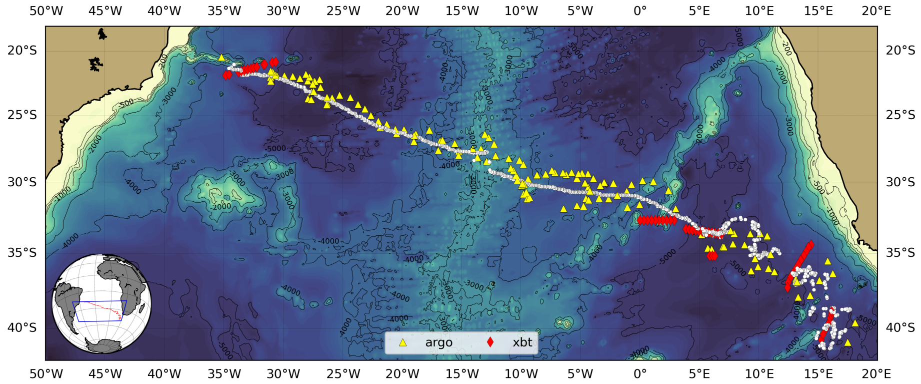

FIGURE 12
The path of the Ring Jeannette between 28-Jan-2012 and 27-Dec-2015. Besides the Argo profiles distributed along its route through the Atlantic, two XBT sections crossed the ring, one in the Cape Basin and the other next to the Brazilian coast. The bottom topography is shown in the background.

(AS2) as the main contributor to the B12. An interesting side finding was that after a merging event, it is possible to identify water masses from the core of the seminal vortices in the newborn vortical feature.

4 Discussion

The Cape Basin receives warm subtropical waters from the Agulhas Retroflection and intense subpolar winds (Gordon, 1985; Gordon et al., 1987). The air-sea fluxes in the region exceed any other in the Southern Hemisphere (Bunker, 1988; Walker & Mey, 1988). Under these conditions, MWs are produced with potential temperatures of 17.4-17.8°C, and those most weathered with temperatures of ~16.5°C, predominantly found around Agulhas Retroflection but also trapped in Agulhas rings, as discussed in the literature (e.g., Olson et al., 1992). The occurrence of deep 17°C mixed layers in the late winter in the Cape Basin is confirmed by several Argo and XBT profiles analyzed in this study (see Figure 8 and

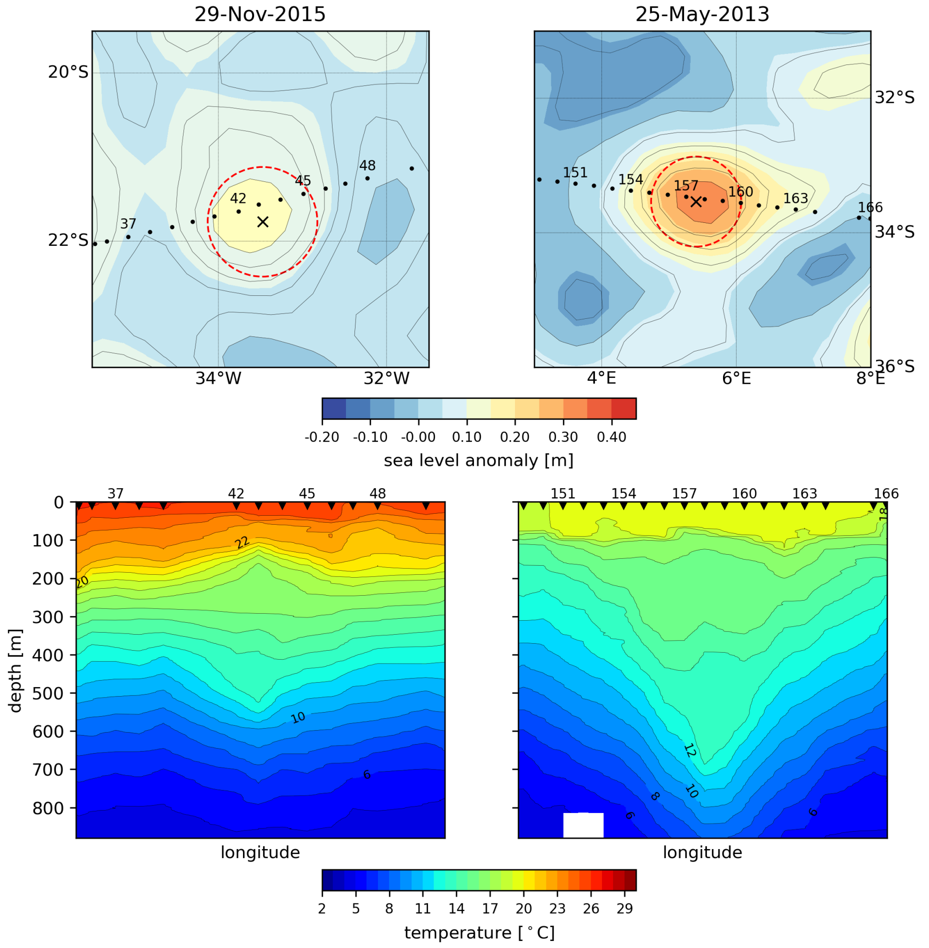

FIGURE 13
Temperature sections were sampled across the Ring Jeannette in the Cape Basin (right) and next to the Brazilian coast (left) in May 2013 and November 2015. The top panels show altimetric maps with numbered XBT deployments. The red circle delimits the area defined by one ring radius (72 km in Nov/2015 and 74 km in May/2013). The bottom panels show the temperature sections.

Supplementary Figures 2, 3). Figure 14 shows the WOA18 sea surface temperature for September, at the end of the austral winter, in the Southeastern Atlantic Ocean. In the Cape Basin, the average surface temperature is lower than 17°C, while temperatures are higher in the adjacent Angola Basin and Agulhas Retroflection region. The analysis of the trajectories of the three supersampled rings (Ana, Eliza, and Jeannette) reveals that while in the Cape Basin, they experienced two consecutive winters in the region of occurrence of temperatures associated with the Type I MW. The stars in the figure show the positions of the rings in September. The general picture emerging from the analysis is that the Type I MW is formed in the Cape Basin, a region with the necessary conditions to produce it, rather than a modified SIMW. This finding is congruent with the works of Capuano et al. (2018) and Laxenaire et al. (2019), who claimed that the 16-17°C STMW found within Agulhas rings is, in fact, the Agulhas Ring Mode Water (ARMW).

The Type II MW, characterized by a deeper 12°C thermostad, was also observed inside Agulhas rings, as shown in detail for rings Ana and Jeannette. Some papers have documented such occurrences and earlier attempts to identify their origin (McCartney, 1977; McCartney & Woodgate-Jones, 1991). Previous research has supported the hypothesis that the 12°C thermostad would be a variety of South Indian Ocean Subantarctic Mode Water (SAMW) (McDonagh and Heywood, 1999). Other authors have argued that it results from entraining cold low-salinity Subantarctic Surface Water injected from south to north in the retroflection region as a wedge during the ring-spawning process (Gordon et al., 1987; Lutjeharms and van Ballegooyen, 1988). The high levels of oxygen of this alleged local variety of SAMW provide convincing evidence in favor of a possible origin directly from wintered surface waters from the south of the Subtropical Front, close to the Retroflection, instead of being derived from the Indian Ocean *via* leakage (Gordon et al.,

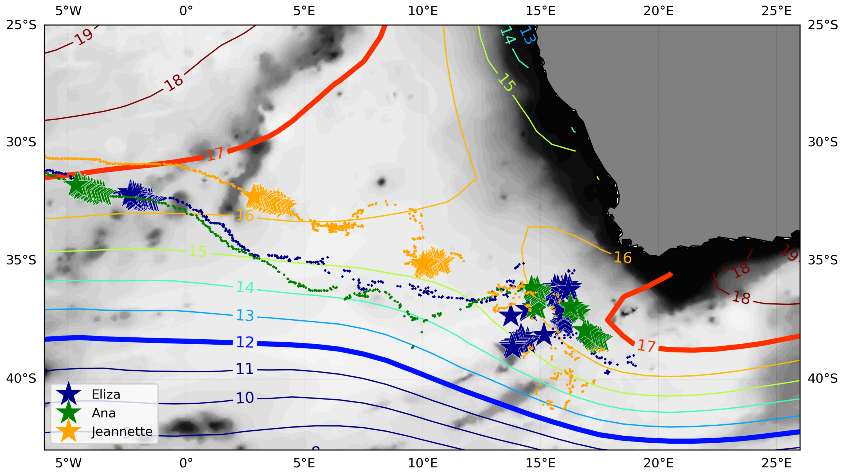

FIGURE 14
Mean sea surface temperature, in degrees Celsius, for the Cape Basin in September (WOA18). The trajectories of the three supersampled rings are plotted over the map. The stars mark the positions of the rings in September, the end of the austral winter. The bottom topography is shown in the background in gray.

1987; Arhan et al., 1999; Schmid et al., 2003). Gladyshev et al. (2008), after a detailed analysis of transect data from South Africa until the southern limit of the Antarctic Circumpolar Current, crossing three Agulhas rings, showed that both ways are possible.

More recently, Chen et al. (2022) proposed a redefinition of the three STMWs discussed by Sato and Polito (2014). They reasoned that only one variety originates from the Brazil Current recirculation, whereas the other two develops into the Cape Basin under the influence of the Agulhas leakage. Our Type I MW relates to the most saline variety (SASTMW2), and the Type II MW to the densest variety (SASTMW3). Corroborating the conclusions of McDonagh and Heywood (1999); Chen et al. (2022) demonstrated that, contrary to the findings of Smythe-Wright et al. (1996), a ring in the southeast Atlantic carrying MW with a potential temperature of 13°C and salinity of 35.2 psu originated at the Agulhas Retroflection and not at the Brazil-Malvinas Confluence as initially supposed, corroborating the conclusions of McDonagh and Heywood (1999). Whether the 12-13°C thermostad, by origin, is subantarctic or subtropical, from a remote site in the South Indian Ocean, or locally formed, remains controversial and deserves more research.

Each Agulhas ring is unique, having its characteristics related to its formation, depending on the staying period in the Cape Basin, the intensity of air-sea fluxes, and interactions with other eddies (e.g., Arhan et al., 1999). Several studies reported the occurrence of rings with or without thermostads (van Ballegooyen et al., 1994; McDonagh et al., 1999; Arhan et al., 1999; Garzoli et al., 1999). As shown in Figure 14, the three rings (Ana, Eliza, and Jeannette) had similar trajectories, approached the climatological position of the surface 12°C isotherm, and remained at least two winters east of the Walvis Ridge, but in different years. Unlike rings Ana and Jeannette, the Ring Eliza did not show the Type II MW in any vertical profile, inside or outside the Cape Basin. This result might indicate that this MW was not available during the ring formation. Thirteen other rings analyzed in the present study also contained the Type I MW exclusively.

Conversely, our data show that 31 distinct rings presented Type I and Type II MW during their life span, detected simultaneously or not. That was the most frequently observed situation (67% of the 46 rings with detected thermostads). The causes for some rings having only the Type I MW and others doing both types are still unclear. It is noteworthy that only one ring showed the isolated occurrence of Type II without the presence of Type I.

From the beginning of systematic satellite altimetry with the Geosat until nowadays' multi-satellite altimetry, some decay curves for Agulhas rings have been proposed, all showing the exponential decline of amplitude along the trajectory (Gordon & Haxby, 1990; Byrne et al., 1995; Schouten et al., 2000; Guerra et al., 2018). The decay curves suggest that most rings disintegrate and diffuse their content within the subtropical gyre. Byrne et al. (1995) argued that mode water volume decays with distance from the formation zone at the same rate as the ring's sea surface height. However, rings' structure and hydrography variations while they cross the South Atlantic Ocean are barely known. Our results demonstrate that Agulhas rings can advect mode waters for long distances throughout the South Atlantic Ocean, reaching distances superior to 4,000 km until the western basin. This reinforces the idea that Agulhas rings are essential to the ventilation of the South Atlantic thermocline with relatively warm and saline waters, not restricted to the eastern sector of the subtropical gyre. Regarding the decay rate of the mode water content, the sampling provided by Argo profilers is insufficient to solve this puzzle. Hypothetically, a time series of the thermocline depth at the ring's center would be necessary to illustrate the erosion of its core. Although Ring Ana has been continuously sampled for more than one year by Argo profilers, it is impossible to confirm the hypothesis since it occurred at different positions relative to the ring's center and sparsely in time. Oscillations of the thermostads thicknesses associated with profile distance to the ring center (Figure 7) suggest a lenticular shape of the isopycnal layers, but nothing to state about volume.

In the case of Ring Eliza, a serendipitous coincidence of three sequential cruises and the ring trajectory within one year produced slices that reveal its internal structure while crossing the subtropical gyre. Ring Jeannette was also surveyed on two cruises lagged by two and a half years, being the first just before the ring leaves the Cape Basin and the last next to the Vitória-Trindade Ridge. Table 1 presents the volume and energetics of the rings Eliza and Jeannette and the parameters used in the reduced gravity model, calculated as described in Section 2.4.

The amplitude and radius of the rings were determined from the altimetry. The mean upper layer thickness, $\overline{h_1}$, was obtained from WOA18 climatology. The instantaneous upper layer thickness, h_1, was calculated using altimetry and verified with the *in situ* data. The radial distribution of profiles along the rings' sections made a Gaussian curve fitting possible to determine the thermocline depth within the rings, even if the section had not crossed its center. The root mean squared error (rmse) expresses the difference between the thermocline depth measured by each profile and the value from the Gaussian fitting (i.e., how well the curve fits the data). The derived Volume, APE and KE, were computed from the h_1 estimated by the two methods. Using *in situ* data, we could then examine the time evolution of the ring's characteristics (Volume, APE, and KE) and assess the uncertainties of estimates based exclusively on altimetry data.

Olson et al. (1985) remind us that a simple diagnosis of eddy evolution could be made by assessing its volume. The decay curves are generally time functions of eddies' amplitude obtained from satellite altimetry. The high correlation between the sea surface height and thermocline depth turns possible to assess the eddies' volume. However, the analysis of the rings Eliza and Jeannette using synoptic *in situ* measurements revealed significant differences from satellite estimates (see Table 1). The volume calculated using temperature profiles for Ring Eliza was 6%, 40%, and 86% larger than the satellite estimates. The same was observed for Ring Jeannette with 107% and 210%. The difference is because the observed thermocline within the rings is deeper than the estimated with the altimetry.

Regarding the APE, the difference between the values calculated from the altimetry for both rings and the mean values presented by Guerra et al. (2018) for the Agulhas rings along the Atlantic is not significant. Nevertheless, the APE values calculated with *in situ* data show a significant increase since the difference between the thermocline depth within the ring and its undisturbed mean is squared. On the other hand, the KE values present an average increase of just 17%.

The numbers indicate that the usual estimates based on satellite altimetry could be overrated regarding the decay rate. The volume of Ring Eliza estimated with altimetric data reduced by 44% between February 2009 and January 2010, while the calculated with *in situ* data decreased by 2%. The analysis of Ring Jeannette displayed a distinct scenario where the variation of satellite estimates and *in situ* data converge. Between May 2013 and November 2015, its altimetric volume reduced by 78% and 67% for the in situ. At least for Ring Eliza, there was a negligible mass loss in the studied interval, despite the decay indicated by the altimetry. The results provide preliminary evidence that the rings' decay rate based on satellite altimetry might not be an accurate measure to evaluate their life span and, ultimately, their impact on circulation.

A remarkable fact about the Ring Eliza is its sinking and consequent loss of coherence on the surface. As Laxenaire et al. (2019) observed, a reduction in the eddy surface intensity may not necessarily be associated with its dissipation but with its subsidence. Future studies will have to investigate further why some rings do not fit the model estimate.

In addition, the thermostads within anticyclones west of 20°W and north of 30°S might be related to Agulhas rings even if

TABLE 1 Parameters used in the two-layer model with reduced gravity. The values of $\overline{h_1}$ were obtained from the WOA18 climatology, while η' and L came from the altimetric map. The depth h_1 at the center of the ring, Volume, Available Potential Energy, and Kinetic Energy were calculated from the model and from the *in situ* data for rings Eliza and Jeannette.

Ring	Date	η' (m)	$\overline{h_1}$ (m)	L (km)	h_1(m)			Vol (10^{12}m^3)		APE (10^{15}J)		KE (10^{15}J)	
					model	in situ	rmse	model	in situ	model	in situ	model	in situ
Eliza	Feb/09	0.21	485	88	647	658	13	7.9	8.4	4.3	4.9	3.2	3.6
Eliza	Jul/09	0.14	500	95	600	641	23	5.7	8.0	1.9	3.8	1.7	2.0
Eliza	Jan/10	0.12	510	93	590	660	23	4.4	8.2	1.3	4.4	2.5	2.8
Jeannette	May/13	0.16	480	74	610	750	34	4.5	9.3	1.9	8.4	1.6	1.8
Jeannette	Nov/15	0.05	485	72	515	590	12	1.0	3.1	0.1	1.0	0.3	0.4

apparently without connection with the trajectories depicted in Figure 1B (blue lines). We tracked the Agulhas rings that left the Cape Basin without considering splitting or merging during their journey. Nevertheless, Laxenaire et al. (2018) developed an interesting concept of a network of Agulhas rings that included the seminal rings (122 trajectories) and their descendants resulting from splitting and merging, linking impressive 730,481 eddies into 6,363 segments over 24 years of satellite altimetry. Therefore, it is probable that those anticyclones were Agulhas rings' descendants not followed by our algorithm or Agulhas rings that had lost the surface signal but followed existing in the subsurface, just like the super-sampled Ring Eliza.

5 Conclusions

This work analyzed temperature and salinity profiles collocated with 52 long-lived Agulhas rings between 1993 and 2016. We found that 88% (46/52) of the rings carried mode waters. Our results demonstrate that the Agulhas rings can advect mode waters for long distances through the South Atlantic Ocean, crossing the MAR and reaching the western basin, where 45% (17/38) of the rings sampled still carried significant amounts of mode waters. Most long-lived Agulhas rings disappear on the altimetric maps when they reach 30-40°W, where they may dissipate or coalesce with other vortices. Nevertheless, we present new *in situ* evidence that rings may lose surface signature and continue moving westward below the surface, marked by the low potential vorticity of the mode water core and possibly interacting with the Brazil Current system.

Two types of mode waters were determined in the range 16.2 ± 0.6°C, 35.6 ± 0.1 (Type I) and 12.9 ± 0.7°C, 35.2 ± 0.1 (Type II). Their spread along the eddy corridor crossing the South Atlantic defines a positive anomaly in temperature and salinity, supporting the concept that the Agulhas rings have an essential role in the ventilation of the South Atlantic thermocline not restricted to the eastern sector of the subtropical gyre. The necessary conditions to form the Type I MW can be found in the Cape Basin. Field data show a ring with a well-developed Type II thermostad and an outcropped Type I. Both mode waters were present inside that ring five months later and continued being sampled for one year while crossing the Atlantic.

The occurrence of rings with both Types I and II MW was most frequent (67%). The analysis of three rings with similar trajectories in the Cape Basin, where they remained for two winters but in different years, revealed that only one of them did not show the Type II MW. It has been hypothesized that different processes may influence the formation and the properties variability of MW inside Agulhas rings. Indeed, a common argument is that the intense air-sea fluxes and turbulent mixing play an essential role in setting the water properties inside the rings translating along the Cape Basin. The absence of the Type II MW in the ring could be caused by its scarcity during the ring formation. However, our results do not permit a conclusion about the factors that induced the MW properties or the simultaneous occurrence of different MWs.

Synoptic *in situ* data revealed issues regarding the volume and decay assessments of Agulhas rings using satellite altimetry. Two rings were examined, and volumes were either 86% or 210% larger than satellite estimates. We also found that the decay rate based on satellite altimetry was, for one ring, twenty times larger than the calculated from *in situ* measurements, while the rates for the other ring did not differ significantly. A possible interpretation of this finding is that in some cases, for reasons not yet apprehended, the decay of Agulhas rings can be significantly less than that of the usual estimates based on satellite data, which might be related to subsidence and not necessarily to dissipation. Consequently, previous studies may have underestimated the life span and volume transported by the rings.

Data availability statement

Publicly available datasets were analyzed in this study. This data can be found here: https://www.metoffice.gov.uk/hadobs/en4/ https://www.aviso.altimetry.fr/en/data/products/sea-surface-height-products/global.html https://www.ncei.noaa.gov/data/oceans/woa/WOA18/DATA/ https://www.researchgate.net/publication/360932544_Agulhas_rings_tracks https://www.researchgate.net/publication/363762371_eddies_aviso_19930101_20160505_20170607_msla_tracking.

Author contributions

LG led the conceptualization, writing, analyses, preparation of figures, and manuscript editing. GM contributed with the mode water detection method, analyses, writing, and AP discussed concepts and revised the manuscript. All authors contributed to the article and approved the submitted version.

Funding

This work was supported by Petróleo Brasileiro S.A. (PETROBRAS) and the Brazilian Oil Regulatory Agency (ANP) within the project EV-00405 - "Ocean Forecast System", part of the Oceanographic Modeling and Observation Network (REMO).

Acknowledgments

The SSALTO/DUACS altimeter products were produced and distributed by the Copernicus Marine and Environment Monitoring Service (CMEMS) (http://www.marine.copernicus.

eu). The Argo data were collected and made freely available by the international Argo Program and the national programs that contribute to it (http://www.argo.ucsd.edu; http://argo.jcommps.org). The Argo Program is part of the Global Ocean Observing System (https://doi.org/10.17882/42182). The XBT data are made freely available on the Atlantic Oceanographic and Meteorological Laboratory and are funded by the NOAA Office of Climate Observations.

Conflict of interest

Author GNM is currently employed by Vale S.A.

The authors declare that the research was conducted in the absence of any commercial or financial relationships that could be construed as a potential conflict of interest.

Publisher's note

Supplementary material

The Supplementary Material for this article can be found online at: https://www.frontiersin.org/articles/10.3389/fmars.2022.958733/full#supplementary-material

References

Arhan, M., Mercier, H., and Lutjeharms, J. R. E. (1999). The disparate evolution of three Agulhas rings in the South Atlantic Ocean. *J. Geophys. Res.* 104, 20987–21005. doi: 10.1029/1998jc900047

Azevedo, J. L. L., Nof, D., and Mata, M. M. (2012). Eddy-train encounters with a continental boundary: A South Atlantic case study. *J. Phys. Oceanography* 42 (9), 1548–1565. doi: 10.1175/JPO-D-11-027.1

Backeberg, B. C., Penven, P., and Rouault, M. (2012). Impact of intensified Indian Ocean winds on mesoscale variability in the Agulhas system. *Nat. Climate Change* 2 (8), 608–612. doi: 10.1038/nclimate1587

Ballalai, J. M., Santos, T. P., Lessa, D. O., Venancio, I. M., Chiessi, C. M., Johnstone, H. J. H., et al. (2019). Tracking spread of the Agulhas leakage into the western South Atlantic and its northward transmission during the last interglacial. *Paleoceanography and Paleoclimatology* 34, 1744–1760. doi: 10.1029/2019PA003653

Beal, L. M., De Ruijter, W. P., Biastoch, A., and Zahn, R. (2011). On the role of the Agulhas system in ocean circulation and climate. *Nature* 472 (7344), 429–436. doi: 10.1038/nature09983

Bernardo, P. S., and Sato, O. T. (2020). Volumetric characterization of the South Atlantic subtropical mode water types. *Geophysical Res. Lett.* 47, e2019GL086653. doi: 10.1029/2019GL086653

Biastoch, A., Böning, C. W., Schwarzkopf, F. U., and Lutjeharms, J. R. E. (2009). Increase in Agulhas leakage due to poleward shift of southern hemisphere westerlies. *Nature* 462 (7272), 495–498. doi: 10.1038/nature08519

Boebel, O., Lutjeharms, J., Schmid, C., Zenk, W., Rossby, T., and Barron, C. (2003). The Cape Cauldron: A regime of turbulent inter-ocean exchange. *Deep-Sea Res. Part II: Topical Stud. Oceanography* 50 (1), 57–86. doi: 10.1016/S0967-0645(02)00379-X

Bunker, A. F. (1988). Surface energy fluxes of the South Atlantic Ocean. *Mon. Weather Rev.* 116, 809–823. doi: 10.1175/1520-0493(1988)116<0809:SEFOTS>2.0.CO;2

Byrne, D. A., Gordon, A. L., and Haxby, W. F. (1995). Agulhas eddies: A synoptic view using geosat ERM data. *J. Phys. Oceanogr.* 25, 902–917. doi: 10.1175/1520-0485(1995)025<0902:AEASVU>2.0.CO;2

Capuano, T. A., Speich, S., Carton, X., and Blanke, B. (2018). Mesoscale and submesoscale processes in the southeast Atlantic and their impact on the regional thermohaline structure. *J. Geophysical Research: Oceans* 123, 1937–1961. doi: 10.1002/2017JC013396

Chelton, D. B., Schlax, M. G., and Roger, M. (2011). Global observations of nonlinear mesoscale eddies. *Prog. Oceanography* 91.2, 167–216. doi: 10.1016/j.pocean.2011.01.002

Chen, Y., Speich, S., and Laxenaire, R. (2022). Formation and transport of the South Atlantic subtropical mode water in eddy-permitting observations. *J. Geophysical Research: Oceans* 127, e2021JC017767. doi: 10.1029/2021JC017767

Danabasoglu, G., McWilliams, J. C., and Gent, P. R. (1994). The role of mesoscale tracer transports in the global ocean circulation. *Science* 264 (5162), 1123–1126. doi: 10.1126/science.264.5162.1123

Dencausse, G., Arhan, M., and Speich, S. (2010). Routes of Agulhas rings in the southeastern Cape Basin. *Deep-Sea Res. Part I: Oceanographic Res. Papers* 57 (11), 1406–1421. doi: 10.1016/j.dsr.2010.07.008

de Ruijter, W. D., Biastoch, A., Drijfhout, S. S., Lutjeharms, J. R. E., Matano, R. P., Pichevin, T., et al. (1999). Indian-Atlantic Interocean exchange: Dynamics, estimation and impact. *J. Geophysical Research: Oceans* 104 (C9), 20885–20910. doi: 10.1029/1998JC900099

de Ruijter, W. P., and Boudra, D. B. (1985). The wind-driven circulation in the South Atlantic-Indian Ocean–i. Numerical experiments in a one-layer model. *Deep Sea Research Part A. Oceanographic Res. Papers* 32 (5), 557–574. doi: 10.1016/0198-0149(85)90044-5

de Souza, A. G. Q., Kerr, R., and de Azevedo, J. L. L. (2018). On the influence of subtropical mode water on the South Atlantic Ocean. *J. Mar. Syst.* 185, 13–24. doi: 10.1016/j.jmarsys.2018.04.006

Dong, C., McWilliams, J. C., Liu, Y., and Chen, D. (2014). Global heat and salt transports by eddy movement. *Nat. Commun.* 5, 1–6. doi: 10.1038/ncomms4294

Ducet, N., Le Traon, P. Y., and Reverdin, G. (2000). Global high-resolution mapping of ocean circulation from TOPEX/Poseidon and ERS-1 and -2. *J. Geophys Res.* 105, 419–477. doi: 10.1029/2000JC900063

Foltz, G. R., Grodsky, S. A., Carton, J. A., and McPhaden, M. J. (2003). Seasonal mixed layer heat budget of the tropical Atlantic Ocean. *J. Geophysical Research: Oceans* 108 (C5), 1–13. doi: 10.1029/2002JC001584

Fritsch, F. N., and Carlson, R. E. (1980). Monotone piecewise cubic interpolation. *SIAM J. Numerical Anal.* 17 (2), 238–246. doi: 10.1137/0717021

Garcia, H. E., Boyer, T. P., Baranova, O. K., Locarnini, R. A., Mishonov, A. V., Grodsky, A., et al. (2019). *World ocean atlas 2018: Product documentation*. Ed. A. Mishonov (Silver Spring, MD)

Garzoli, S. L., Goñi, G. J., Mariano, A. J., and Olson, D. B. (1997). Monitoring the upper southeastern Atlantic transports using altimeter data. *J. Mar. Res.* 55, 453–481. doi: 10.1357/0022240973224355

Garzoli, S. L., Richardson, P. L., Duncombe Rae, C. M., Fratantoni, D. M., Goñi, G. J., and Roubicek, A. J. (1999). Three Agulhas rings observed during the Benguela Current experiment. *J. Geophys. Res.* 104, 20971–20986. doi: 10.1029/1999JC900060

Gladyshev, S., Arhan, M., Sokov, A., and Speich, S. (2008). A hydrographic section from South Africa to the southern limit of the Antarctic Circumpolar Current at the Greenwich meridian. *Deep Sea Res. Part I: Oceanographic Res. Papers* 55 (10), 1284–1303. doi: 10.1016/j.dsr.2008.05.009

Goni, G. J., Garzoli, S. L., Roubicek, A. J., Olson, D. B., and Brown, O. B. (1997). Agulhas ring dynamics from TOPEX/POSEIDON satellite altimeter data. *J. Mar. Res.* 55, 861–883. doi: 10.1357/0022240973224175

Goni, G., Kamholz, S., Garzoli, S., and Olson, D. (1996). Dynamics of the Brazil-Malvinas Confluence based on inverted echo sounders and altimetry. *J. Geophysical Research: Oceans* 101 (C7), 16273–16289. doi: 10.1029/96JC01146

Good, S. A., Martin, M. J., and Rayner, N. A. (2013). EN4: quality controlled ocean temperature and salinity profiles and monthly objective analyses with uncertainty estimates. *J. Geophysical Research: Oceans* 118, 6704–6716. doi: 10.1002/2013JC009067

Gordon, A. L. (1985). Indian-Atlantic Transfer of thermocline water at the Agulhas Retroflection. *Science* 227, 1030–1033. doi: 10.1126/science.227.4690.1030

Gordon, A. L. (1986). Interocean exchange of thermocline water. *J. Geophys. Res.* 91, 5037–5046. doi: 10.1029/JC091iC04p05037

Gordon, A. L., and Haxby, W. F. (1990). Agulhas eddies invade the South Atlantic: Evidence from Geosat altimeter and shipboard survey. *Journal of Geophysical Research* 95, 3117–3125. doi: 10.1029/JC095iC03p03117

Gordon, A. L., Lutjeharms, J. R. E., and Gründlingh, M. L. (1987). Stratification and circulation at the Agulhas Retroflection. *Deep Sea Research Part A* 34, 565–599. doi: 10.1016/0198-0149(87)90006-9

Guerra, L. A. A. (2011). Vórtices das Agulhas colidem com a Corrente do Brasil? (Doctoral dissertation, Universidade Federal do Rio de Janeiro). ("Do Agulhas rings collide with the Brazil Current?" in Portuguese).

Guerra, L. A. A., Paiva, A. M., and Chassignet, E. P. (2018). On the translation of Agulhas Rings to the western South Atlantic Ocean. *Deep Sea Res. Part Oceanogr. Res. Pap.* 139, 104–113. doi: 10.1016/j.dsr.2018.08.005

Halo, I., Backeberg, B., Penven, P., Ansorge, I., Reason, C., and Ullgren, J. E. (2014). Eddy properties in the Mozambique Channel: A comparison between observations and two numerical ocean circulation models. *Deep Sea Res. Part II Top. Stud. Oceanogr.* 100, 38–53. doi: 10.1016/j.dsr2.2013.10.015

Hanawa, K., and Talley, L. D. (2001). Mode waters. *In Int. Geophysics (Vol. 77* pp, 373–386). doi: 10.1016/S0074-6142(01)80129-7

Jayne, S. R., and Marotzke, J. (2002). The oceanic eddy heat transport. *J. Phys. Oceanography* 32 (12), 3328–3345. doi: 10.1175/1520-0485(2002)032<3328:TOEHT>2.0.CO;2

Laxenaire, R., Speich, S., and Alexandre, S. (2019). *Evolution of the thermohaline structure of one Agulhas Ring reconstructed from satellite altimetry and Argo floats. J. Geophys. Res:: Oceans*, 124. doi: 10.1029/2019JC015210

Laxenaire, R., Speich, S., Blanke, B., Chaigneau, A., Pegliasco, C., and Stegner, A. (2018). Anticyclonic eddies connecting the western boundaries of Indian and Atlantic oceans. *J. Geophys. Res:: Oceans* 123, 7651–7677. doi: 10.1029/2018JC014270

Laxenaire, R., Speich, S., and Stegner, A. (2020). Agulhas ring heat content and transport in the South Atlantic estimated by combining satellite altimetry and Argo profiling floats data. *J. Geophys. Res:: Oceans* 125, e2019JC015511. doi: 10.1029/2019JC015511

Le Traon, P. Y., Faugère, Y., Hernandez, F., Dorandeu, J., Mertz, F., Ablain, M., et al. (2003). Can we merge GEOSAT follow-on with TOPEX/Poseidon and ERS-2 for an improved description of the ocean circulation? *J. Atmospheric Ocean. Technol.* 20, 889–895. doi: 10.1175/1520-0426(2003)020<0889:CWMGFW>2.0.CO;2

Le Traon, P. Y., Nadal, F., and Ducet, N. (1998). An improved mapping method of multisatellite altimeter data. *J. Atmospheric Ocean. Technol.* 15, 522–534. doi: 10.1175/1520-0426(1998)015<0522:AIMMOM>2.0.CO;2

Lloyd, S. (1982). Least squares quantization in pcm. *IEEE Trans. Inf. Theory* 28 (2), 129–137. doi: 10.1109/TIT.1982.1056489

Lutjeharms, J. R.E. (1996). "The exchange of water between the South Indian and the South Atlantic," in *The south Atlantic: Present and past circulation*. Eds. G. Wefer, W. H. Berger, G. Siedler and D. J. Webb (Berlin, Heidelberg: Springer), 125–162. doi: 10.1007/978-3-642-80353-6

Lutjeharms, J. R. E., and Gordon, A. L. (1987). Shedding of an Agulhas Ring observed at sea. *Nature* 325 (6100), 138–140. doi: 10.1038/325138a0

Lutjeharms, J. R. E., and Van Ballegooyen, R. C. (1988). The retroflection of the Agulhas Current. *J. Phys. Oceanography* 18 (11), 1570–1583. doi: 10.1175/1520-0485(1988)018<1570:TROTAC>2.0.CO;2

McCartney, M. S. (1977). "Subantarctic mode water," in *A voyage of discovery: George deacon 70th anniversary*. Ed. M. V. Angel (Oxford: Supplement to Deep-Sea Research, Pergamon Press), 103–119.

McCartney, M. S. (1982). The subtropical recirculation of mode waters. *J. Mar. Res.* 40 (Suppl.), 427–464.

McCartney, M. S., and Woodgate-Jones, M. E. (1991). A deep-reaching anticyclonic eddy in the subtropical gyre of the eastern South Atlantic. *Deep Sea Res. Part A. Oceanographic Res. Papers* 38, 1. doi: 10.1016/S0198-0149(12)80019-7

McDonagh, E. L., Bryden, H. L., King, B. A., Sanders, R. J., Cunningham, S. A., and Marsh, R. (2005). Decadal changes in the South Indian Ocean thermocline. *J. Clim.* 18, 1575–1590. doi: 10.1175/JCLI3350.1

McDonagh, E. L., and Heywood, K. J. (1999). The origin of an anomalous ring in the southeast Atlantic. *Journal of Physical Oceanography* 29 (8), 2050–2064. doi: 10.1175/1520-0485(1999)029<2050:TOOAAR>2.0.CO;2

McDonagh, E. L., Heywood, K. J., and Meredith, M. P. (1999). On the structure, paths, and fluxes associated with Agulhas Rings. *J. Geophysical Research: Oceans* 104 (C9), 21007–21020. doi: 10.1029/1998JC900131

Nencioli, F., Dall'Olmo, G., and Quartly, G. D. (2018). Agulhas ring transport efficiency from combined satellite altimetry and argo profiles. *J. Geophysical Research: Oceans* 123, 5874–5888. doi: 10.1029/2018JC013909

Nof, D. (1999). Strange encounters of eddies with walls. *J. Mar. Res.* 57 (5), 739–761. doi: 10.1357/002224099321560555

Olson, D., and Evans, R. (1986). Rings of the Agulhas Current. *Deep Sea Res.* 33, 27–42. doi: 10.1016/0198-0149(86)90106-8

Olson, D. B., Fine, R. A., and Gordon, A. L. (1992). Convective modifications of water masses in the Agulhas. *Deep Sea Res.* 39, S163—–S181. doi: 10.1016/s0198-0149(11)80010-5

Olson, D. B., Schmitt, R. W., Kennelly, M., and Joyce, T. M. (1985). A two-layer diagnostic model of the long-term physical evolution of warm-core ring 82B. *J. Geophys. Res.* 90, 8813. doi: 10.1029/JC090iC05p08813

Peeters, F. J. C., Acheson, R., Brummer, G. J. A., De Ruijter, W. P. M., Schneider, R. R., Ganssen, G. M., et al. (20047000). Vigorous exchange between the Indian and Atlantic oceans at the end of the past five glacial periods. *Nature* 430, 661–665. doi: 10.1038/nature02785

Provost, C., Escoffier, C., Maamaatuaiahutapu, K., Kartavtseff, A., and Garçon, V. (1999). Subtropical mode waters in the South Atlantic Ocean. *J. Geophysical Research: Oceans* 104 (C9), 21033–21049. doi: 10.1029/1999JC900049

Pujol, M.-I., Faugère, Y., Taburet, G., Dupuy, S., Pelloquin, C., Ablain, M., et al. (2016). DUACS DT2014: The new multi-mission altimeter data set reprocessed over 20 years. *Ocean Sci.* 12, 1067–1090. doi: 10.5194/os-12-1067-2016

Rau, A. J., Rogers, J., Lutjeharms, J. R. E., Giraudeau, J., Lee-Thorp, J. A., Chen, M. T., et al. (2002). A 450-kyr record of hydrological conditions on the western Agulhas Bank slope, south of Africa. *Mar. Geology* 180 (1–4), 183–201. doi: 10.1016/S0025-3227(01)00213-4

Richardson, P. L. (2007). Agulhas leakage into the Atlantic estimated with subsurface floats and surface drifters. *Deep Sea Res. Part I: Oceanographic Res. Papers* 54 (8), 1361–1389. doi: 10.1016/j.dsr.2007.04.010

Rouault, M., Penven, P., and Pohl, B. (2009). Warming in the Agulhas Current system since the 1980's. *Geophysical Res. Lett.* 36 (12), 1–5. doi: 10.1029/2009GL037987

Sato, O. T., and Polito, P. S. (2014). Observation of South Atlantic subtropical mode waters with argo profiling float data. *J. Geophys. Res.* 118, 2860–2881. doi: 10.1002/2013JC009438

Schmid, C., Boebel, O., Zenk, W., Lutjeharms, J. R. E., Garzoli, S. L., Richardson, P. L., et al. (2003). Early evolution of an Agulhas Ring. *Deep-Sea Res. Part II* 50, 141–166. doi: 10.1016/S0967-0645(02)00382-X

Schouten, M. W., de Ruijter, W. P. M., van Leewen, P. J. V., and Lutjeharms, J. R. E. (2000). Translation, decay and splitting of Agulhas Rings in the southeastern Atlantic ocean. *J. Geophys. Res.* 105, 21913–21925. doi: 10.1029/1999JC000046

Smythe-Wright, D., Gordon, A. L., Chapman, P., and Jones, M. S. (1996). CFC-113 shows Brazil eddy crossing the South Atlantic to the Agulhas Retroflection region. *J. Geophysical Research: Oceans* 101 (C1), 885–895. doi: 10.1029/95JC02751

Souza, J. M. A. C., De Boyer Montégut, C., Cabanes, C., and Klein, P. (2011). Estimation of the Agulhas ring impacts on meridional heat fluxes and transport using ARGO floats and satellite data. *Geophysical Res. Lett.* 38 (21), 1–5. doi: 10.1029/2011GL049359

Toole, J. M., and Warren, B. A. (1993). A hydrographic section across the subtropical South Indian Ocean. *Deep Sea Res. Part I: Oceanographic Res. Papers* 40, 1973–2019. doi: 10.1016/0967-0637(93)90042-2

U.S. Integrated Ocean Observing System (2020). "Manual for real-time quality control of in-situ temperature and salinity data version 2.1," in *A guide to quality control and quality assurance of in-situ temperature and salinity observations* (MD, U.S: Silver Spring), 50pp. Department of Commerce, National Oceanic and Atmospheric Administration, National Ocean Service, Integrated Ocean Observing System. doi: 10.25923/x02m-m555

van Aken, H. M., Van Veldhoven, A. K., Veth, C., De Ruijter, W. P. M., Van Leeuwen, P. J., Drijfhout, S. S., et al. (2003). Observations of a young Agulhas Ring, Astrid, during MARE in march 2000. *Deep-Sea Res. Part II: Topical Stud. Oceanography* 50 (1), 167–195. doi: 10.1016/S0967-0645(02)00383-1

van Ballegooyen, R. C., Gründlingh, M. L., and Lutjeharms, J. R. E. (1994). Eddy fluxes of heat and salt from the southwest Indian Ocean into the southeast Atlantic Ocean: A case study. *J. Geophys. Res.* 99, 14053. doi: 10.1029/94JC00383

van Sebille, E., Barron, C. N., Biastoch, A., Van Leeuwen, P. J., Vossepoel, F. C., and De Ruijter, W. P. M. (2009). Relating Agulhas leakage to the Agulhas

Current retroflection location. *Ocean Sci.* 5 (4), 511–521. doi: 10.5194/os-5-511-2009

van Sebille, E., Van Leeuwen, P. J., Biastoch, A., and De Ruijter, W. P. M. (2010). On the fast decay of Agulhas rings. *J. Geophysical Research: Oceans* 115 (3), 1–15. doi: 10.1029/2009JC005585

Volkov, D. L., Lee, T., and Fu, L. L. (2008). Eddy-induced meridional heat transport in the ocean. *Geophysical Res. Lett.* 35 (20), 1–5. doi: 10.1029/2008GL035490

Walker, N. D., and Mey, R. D. (1988). Ocean/atmosphere heat fluxes within the Agulhas Retroflection region. *J. Geophysical Research: Oceans* 93, 15473–15483. doi: 10.1029/JC093iC12p15473

Wang, Y., Olascoaga, M. J., and Beron-Vera, F. J. (2015). Coherent water transport across the South Atlantic. *Geophysical Res. Lett.* 42 (10), 4072–4079. doi: 10.1002/2015GL064089

Weijer, W., De Ruijter, W. P. M., Sterl, A., and Drijfhout, S. S. (2002). Response of the Atlantic overturning circulation to South Atlantic sources of buoyancy. *Global Planetary Change* 34 (3–4), 293–311. doi: 10.1016/S0921-8181(02)00121-2

Witter, D. L., and Gordon, A. L. (1999). Interannual variability of South Atlantic circulation from 4 years of TOPEX/POSEIDON satellite altimeter observations. *J. Geophysical Research: Oceans* 104 (C9), 20927–20948. doi: 10.1029/1999JC900023

Zhang, Z., Wang, W., and Qiu, B. (20146194). Oceanic mass transport by mesoscale eddies. *Science* 345, 322–324. doi: 10.1126/science.1252418

Frontiers in
Marine Science

Explores ocean-based solutions for emerging global challenges

The third most-cited marine and freshwater biology journal, advancing our understanding of marine systems and addressing global challenges including overfishing, pollution, and climate change.

Discover the latest Research Topics

See more →

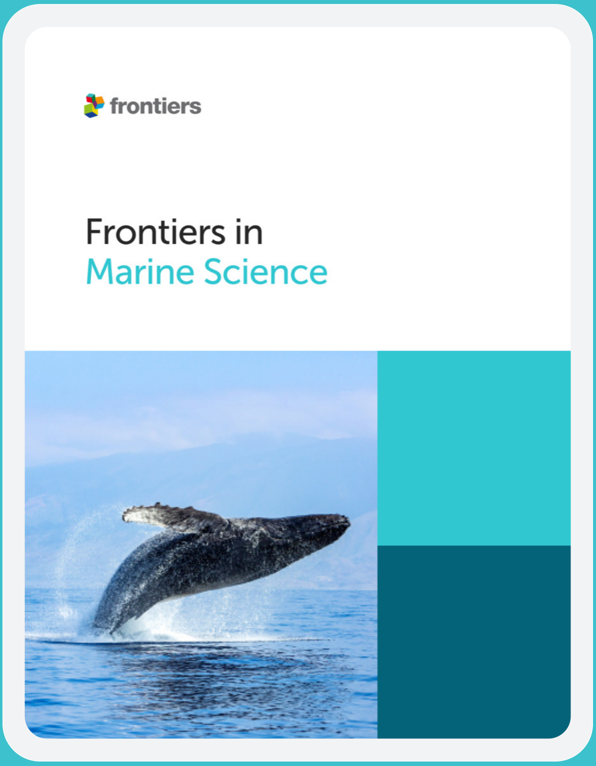
frontiers

Frontiers in
Marine Science

Frontiers

Avenue du Tribunal-Fédéral 34
1005 Lausanne, Switzerland
frontiersin.org

Contact us

+41 (0)21 510 17 00
frontiersin.org/about/contact